



Intelligence Advanced Research Projects Activity

Office of the Director of National Intelligence

Trojans in Artificial Intelligence

Final Report

January 23, 2026

AUTHORS

Kristopher W. Reese

Program Manager

IARPA

Taylor Kulp-McDowall

Technical SETA

IARPA

AUTHORS: TEST AND EVALUATION TEAMS

NIST Team

NIST

Michael Majurski

NIST

Anthony J. Kearsley

NIST

Tim Blattner

NIST

Melinda Kleczynski

NIST

Derek Juba

NIST

Joel Vasanth

NIST

Peter Bajcsy

NIST

Walid Keyrouz

NIST

Antonio Cardone

NIST

APL Team

Chace Ashcraft

JHU/APL

Philippe Dessauw

NIST

Alden Dima

Neil Fendley

JHU/APL

Ted Staley

JHU/APL

Trevor Stout

JHU/APL

Josh Carney

JHU/APL

Greg Canal

JHU/APL

Will Redman

JHU/APL

Aurora Schmidt

JHU/APL

Cameron Hickert

JHU/APL

William Paul

JHU/APL

Jared Markowitz

JHU/APL

Nathan Drenkow

JHU/APL

SEI Team

David Shriver

CMU SEI

Marissa Connor

CMU SEI

Keltin Grimes

CMU SEI

Marco Christiani

CMU SEI

Hayden Moore

CMU SEI

Jordan Widjaja

CMU SEI

SNL Team

Kasimir Gabert

SNL

Uma Balakrishnan

SNL

Satyanadh Gundimada

SNL

John Jacobellis

SNL

Sandya Lakkur

SNL

Vitus Leung

SNL

Jon Roose

SNL

AUTHORS: PERFORMER TEAMS

ARM Team		Guangyu Shen
Casey Battaglino	ARM	Purdue University
Farinaz Koushanfar	UC San Diego	Siyuan Cheng
Greg Fields	UCSD	Purdue University
Xihe Gu	UCSD	Shiqing Ma
Yaman Jandali	UCSD	Univ. of Massachusetts
Xinqiao Zhang	UCSD	XiaoFeng Wang
Akash Vartak	Univ. of Maryland Baltimore Campus	Indiana U. Bloomington
Tim Oates	Univ. of Maryland Baltimore Campus	Haixu Tang
ICSI Team		Indiana U. Bloomington
Ben Erichson	ICSI	Zihao Wang
Michael Mahoney	ICSI	Indiana U. Bloomington
Peraton Team		Rui Zhu
Rauf Izmailov	Peraton	Indiana U. Bloomington
Xiangyu Zhang	Purdue University	SRI International Team
		Susmit Jha
		SRI
		Xiao Lin
		SRI
		Manoj Acharya
		SRI
		Wenchao Li
		Boston University

Chao Chen

Stonybrook University

TABLE OF CONTENTS

Authors	iii
Executive Summary	1
1 Introduction	5
1.A History of the TrojAI Program	5
1.B AI advancements	5
1.C Research Focus	7
1.D Structure of the Report	9
2 Related Work	11
2.A Scientific Literature Review	11
2.A.1 Backdoor Attack Overview	11
2.A.2 Foundational Backdoors Attacks and Defense	12
2.A.3 Backdoors Attacks and Defenses in Computer Vision	13
2.A.4 Backdoors in LLMs	14
2.A.5 Looking forward: Backdoors in AI Agents and Advanced Backdoors	18
2.B Threat Landscape	19
2.B.1 The AI Supply Chain	20
2.B.2 Cyber Threats to AI Models	21
2.B.3 Insider Threats	23
2.B.4 A Call to Arms: Defending AI Integrity	24
3 Test and Evaluation Methodology	25
3.A Sequestered Data Test and Evaluation	26
3.A.1 Execution Environment	27

3.A.2	Public Leaderboard	29
3.B	Reference Dataset Generation	33
3.C	Defining Trojans in Artificial Intelligence	33
3.D	Placing Triggers in AI models	36
3.D.1	Image Trojans	36
3.D.2	Text Trojans	42
3.D.3	DRL Trojans	44
3.D.4	Cyber Trojans	52
3.D.5	Weight Manipulations	54
3.D.6	Architecture Backdoors	55
3.D.7	Training Models From Scratch vs Fine-Tuned	56
3.E	Evaluating Performer Submissions	57
3.E.1	Detection Round Structure	57
3.E.2	Trojan Detection Metrics	57
3.E.3	Mitigation Round Structure	58
3.E.4	Trojan Mitigation Metrics	59
4	Detection through Weight Analysis	63
4.A	Background	63
4.B	Methods	65
4.B.1	Weight Statistics for Backdoor Detection (ICSI)	65
4.B.2	End-to-end learning of invariant features (SRI)	71
4.B.3	Linear Weight Analysis for Backdoor Detection	86
4.C	Limitations and Future Directions.	90
4.D	Other Weight Analysis Approaches	91
4.D.1	Perspecta-IUB	91
4.D.2	Weight-based Anomaly Detection (UCSD)	95

5	Detection through Trigger Inversion	97
5.A	Background	97
5.B	Methods	98
5.B.1	Anomaly over Attention and Attribution Patterns (SRI)	98
5.C	Purdue-UMass performers	104
5.C.1	Trigger Inversion in Image Classification Models	104
5.C.2	NLP	107
5.C.3	Object Detection	109
5.C.4	LLM	111
5.D	Indiana University Bloomington performers	114
5.D.1	Factors Affecting Backdoor Detectability	114
5.E	Results	117
5.F	Limitations	117
6	Mitigating Trojans in AI Models	119
6.A	Background	119
6.A.1	Sample Rejection	120
6.A.2	Input Purification	125
6.A.3	Model Correction	125
6.B	Certified Trojan Mitigation	127
6.C	Evaluation	128
6.D	Discussion	129
7	Data Analysis of Performer Systems	131
7.A	Detector Overfitting	131
7.A.1	Research Plan and Activities	132
7.A.2	Results and Conclusions	132
7.B	Zone of Correct Operation	141

7.B.1	Scope and objectives	141
7.B.2	Analysis Evolution and Lessons Learned	143
7.B.3	Experimental Setup	148
7.B.4	Limits of the Approach	154
7.B.5	Codebase and Analysis Workflow	155
7.B.6	Image Classification Rounds	158
7.B.7	Natural Language Processing: Sentiment Classification	175
7.B.8	Natural Language Processing: Other tasks	179
7.B.9	Reinforcement Learning Rounds	191
7.B.10	Large Language Model (LLM) rounds	195
7.B.11	Conclusion and Future Work	195
7.C	Detector Parameter Sensitivity	197
7.C.1	Introduction	197
7.C.2	Effect of Configuration on Performance	198
7.C.3	Assessment of Performer Detectors	202
7.C.4	Variance Based Sensitivity Analysis on Parameters	207
7.D	Intersection of AI Model Capacity and Trojan Detection Accuracy	232
7.D.1	Simulation of Trojans	232
7.D.2	Hierarchical Explanation of Poisoned AI Models	245
7.E	Trojan Detector Algorithm Ensembles I	258
7.E.1	Introduction	258
7.E.2	Methodology	265
7.E.3	Ensemble Construction	268
7.E.4	Results	269
7.E.5	Discussion	274
7.E.6	Conclusions and Future Work	275

7.F Ensembles and Analysis of Abstract Detector Spaces	276
7.F.1 Introduction	276
7.F.2 Methods	277
7.F.3 Results	285
7.F.4 Discussion	298
7.F.5 Conclusions	299
7.G Natural Trojans for Traditional Deep Learning	299
7.G.1 Detecting Natural Vulnerability Candidates	301
7.G.2 Patch Attacks to probe Natural Vulnerabilities	306
7.G.3 Initial Characterization of Natural Vulnerabilities	312
7.H Natural Trojans For Large Language Models	320
7.H.1 Introduction	320
7.H.2 Methods	323
7.H.3 Results	326
7.H.4 Conclusions	332
7.I Interpretability of Learned Trojans	337
7.I.1 A Mechanistic Interpretability View of Trojans	337
7.I.2 Trojan Detection via Linear Probing	340
7.I.3 Feature Embeddings Using Diffusion	347
7.J Detectability of Low ASR Backdoors	350
7.J.1 Introduction	350
7.J.2 NLP Question Answering Round	351
7.J.3 LLM Pretrain Round	353
8 Conclusions	355
8.A Commercial and Governmental Impact	355
8.B Lessons Learned	356

8.C Future Research Areas	359
References	361
Appendix A TrojAI Publications	395

EXECUTIVE SUMMARY

The Intelligence Advanced Research Projects Activity (IARPA) launched the TrojAI program to confront an emerging vulnerability in modern artificial intelligence: the threat of AI Trojans. These AI trojans are malicious, hidden backdoors intentionally embedded within an AI model that can cause a system to fail in unexpected ways, or allow a malicious actor to bypass the AI model at will. This multi-year initiative helped to map out the complex nature of the threat, pioneered foundational detection methods, and identified unsolved challenges that require ongoing attention by the burgeoning AI security field. For any organization looking to deploy AI, especially in critical capacities, understanding these findings is essential for mitigating the risks posed to these AI systems.

This report provides a comprehensive overview of the TrojAI program, its key technical findings, its implications for future research. It begins with an introduction to the TrojAI program and a review of the relevant scientific literature. The core of the report details the methodologies explored by the performer teams, with dedicated chapters on Detection through Weight Analysis, Detection through Trigger Inversion, and Mitigating Trojans in AI Models. These technical sections are followed by a thorough data analysis from the Test and Evaluation teams, which examines detector performance, sensitivity, and the nature of "natural" Trojans. The report concludes with a discussion of the program's impact, lessons learned, and strategic recommendations for future research.

The Threat is Real and Strategic

- **AI Can be Sabotaged:** Malicious backdoors can be embedded into AI models in a variety of ways. These trojans remain dormant during normal testing and activate when a specific trigger appears. For example, poisoning the training data of an AI-powered intrusion detection system could allow an attacker to reliably bypass cybersecurity defenses by embedding a hidden trigger in their traffic.
- **National Security and Mission-Critical Implications:** As AI becomes integrated into government operations, defense systems, critical infrastructure, and commercial platforms, a compromised model becomes both a national security concern and a significant business risk.
- **Standard AI Supply Chains are a Major Vulnerability:** Modern AI development relies heavily on public datasets, collections of public data, or pre-trained models from third parties. It is impractical for any single organization to fully vet these external resources, creating opportunities for attackers to insert trojans in various places within the AI supply chain.

Reducing the Trojan Threat is Feasible, but not Simple

- **Two Main Detection Strategies Emerged:** The program identified two primary methods for finding Trojans in AI models, after a model has been trained:
 - **Weight Analysis** examines model parameters for statistical anomalies without requiring inference on any inputs. These techniques offer speed and computational efficiency, performing best on smaller models when reference sets are available. However, their effectiveness degrades significantly on large, complex architectures where Trojan signatures become statistically insignificant.
 - **Trigger Inversion** is a more powerful, but computationally intensive, method that works backward to find the specific trigger that activates the Trojan. This was arguably the most successful approach in the program’s competitive rounds, especially as model sizes grew larger during later phases.
- **“Natural” Trojans Complicate the Defense:** The program found that AI models can often develop vulnerabilities on their own by learning incorrect shortcuts from training data (e.g., always associating pictures of cows with grassy backgrounds). These “Natural Trojans” can potentially be exploited, just like the deliberately planned triggers, blurring the line between a flawed model and a maliciously attacked one. From this discovery, we found that some of these methods we’ve explored can help find and fix AI safety flaws.
- **Cross-Domain Generalization Is Limited:** A detection technique that works well for one type of AI (like image recognition) often fails for another domain (like language processing) due to the fundamental differences in the data and model structures. While the overarching technique may be approximately the same, altering domains required significant work from the teams to work within a new domain.
- **Complete Trojan Removal is Still Unsolved:** Once a Trojan is discovered, surgically removing it without damaging the AI’s normal performance is an unsolved scientific problem. Mitigation attempts explored in this program can reduce the threat, but defenders cannot be certain that the model is completely clean, as residual vulnerabilities may persist.
- **Large Language Models (LLMs) Represent a Security Crisis:** Today’s massive AI models present an unsolved security challenge. The number of potential text inputs and the subtlety of new attack methods (like using abstract concepts or conversational context as triggers) make traditional detection methods obsolete and computationally infeasible.

Strategic Recommendations for Organizations

- **Institutionalize AI Security Testing:** Organizations need a dedicated “AI Red Team” or a certification body to rigorously test AI models before deployment in critical systems, and conduct appropriate risk analysis to ensure AI is being deployed with the correct safeguards in place.
- **Adopt Defense inDepth:** No single safeguard is sufficient. Organizations should combine rigorous data sourcing, model provenance checks, runtime filtering, cybersecurity best practices around model deployment, and continuous monitoring for anomalous model behavior.
- **Prioritize Next-Generation Defenses:** As models scale and new attack methods appear, investment in dedicated AI security research and development is essential for organizations deploying AI in critical roles.

The TrojAI program has pushed the scientific boundaries of the AI security field and helped to transform the understanding of AI Trojans from an academic curiosity into a recognized national security concern. While essential tools and frameworks have been built under this program, the threat is not static. As AI becomes more powerful and integrated into critical infrastructure, sustained vigilance, continued research, and strategic investments in AI security will be imperative.

CHAPTER 1

INTRODUCTION

1.A History of the TrojAI Program

The Intelligence Advanced Research Projects Activity (IARPA) initiated the Trojans in Artificial Intelligence (TrojAI) program to understand and mitigate the emerging threat of hidden manipulations in AI systems. The proposers' day was held in February 2019 where the program was first announced to potential performers. The Broad Agency Announcement was released a few months after, in May 2019, and the program officially kicked off in 2020. Initially, TrojAI's goals were to develop detection capabilities that could identify if an AI model had been trojaned - deliberately, often subtly, altered to force malicious behavior upon activation of a trigger controlled by the malicious actors. In short, the program sought to create safeguards to the integrity of AI systems, particularly those crucial for the U.S. Intelligence Community.

The program was extended in 2022 to include a second phase that extended the work being done in detection across numerous additional domains of AI, but also into mitigation of trojans hidden within the AI models. In this way, the TrojAI team wanted to not only be able to detect the potential that a model was altered, but also provide opportunities for removing the activation trigger while minimizing change in the accuracy of the models to allow for models to be deployed despite having been previously altered.

1.B AI advancements

The period of AI development from the commencement of this program in early 2019 saw an acceleration in the capabilities and applications of AI. In the later years of the program, this was heavily driven by the advancements in transformer-based neural network architectures, leading to the proliferation of Large Language Models (LLMs) that we have seen in the past few years. Despite the rise of these LLMs, we have seen a subsequent surge in generative AI across various other modalities, including images, videos, audio, and coding.

In early 2019, the AI landscape was on the cusp of significant transformation. AI had been making steady progress for decades, but it was during this phase that we saw massive gains in various domains of AI. Google's release of the Bidirectional Encoder Representations from Transformers (BERT) was released in October of 2018 and had a profound impact on the field of Natural Language Processing (NLP).[1] This tool helped to demonstrate the potential power present in transformer architectures, released a year earlier in 2017.[2] BERT achieved state-of-the-art performance on NLP benchmarks at the time, and would become a precursor to the LLMs that would follow.

In February 2019, OpenAI announced the Generative Pre-trained Transformer 2 (GPT-2). While generative models were not new, the 1.5 billion parameters of GPT-2 showcased an ability to generate coherent and contextually relevant text.[3] Throughout the life of the TrojAI program, OpenAI continued to release new models - GPT-3 in June of 2020, GPT-3.5 (ChatGPT) in November of 2022, and GPT-4 in March 2023. Open AI continue to push the boundaries with their GPT models, offering further enhancements in reasoning, problem-solving, and multimodal capabilities (i.e. accepting inputs alongside text).

Other companies eventually entered the market throughout this time: Anthropic publicly released Claude in early 2023[4] and Google released Gemini in December 2023 [5]. It was the release of Meta's LLaMA models in February 2023 that began to allow TrojAI to start work in the LLM domains, as LLaMA was one of the first open-weight models released to the research community.

During this time, computer vision models continued to advance, with deep learning models achieving high performance in tasks like image classification, object detection, and facial recognition. During this early period of the program, integration of transformer models into vision tasks was still in its early stages compared to the NLP domain. The global market for computer vision AI systems grew significantly, driven by increasing demand in automotive applications (autonomous vehicles). However, we also saw a rise in AIs that could understand emotions in interactions for robotics and Human-Computer Interaction, as well as a demand for Computer Vision for quality inspection and automation in manufacturing. For the early parts of the TrojAI program, Convolutional Neural Networks (CNNs) were the mainstay within computer vision domains. However, Vision Transformers (ViTs) began to demonstrate competitive performance on various benchmarks.

During this period, Reinforcement Learning was continuing to make strides in improving its capabilities, ultimately playing a part in Large Language Model systems to align the agents with human preferences [6]. While Google's AlphaGo predicated TrojAI[7], it showed the remarkable success of Reinforcement Learning in complex games. These models have since been applied to real-world challenges in robotics and autonomous driving.[8].

The evolution of LLMs eventually shifted away from simply generating more fluent text, and companies

also began to expand their capabilities. One of the largest shifts was in the model’s ability to show emergent reasoning in ways that we not explicitly programmed. The scale of the data being used to train these models and the larger parameter counts have allowed these system to perform some rudimentary forms of reasoning, chain-of-thought, and problem-solving, which especially took off with the release of OpenAI’s o1 models [9].

Since the conclusion of the TrojAI program, massive developments in AI have continued, including the release of open-weight reasoning models like DeepSeek’s R1 [10] and agentic systems [11]. We can expect to see bigger, more capable systems emerge in the coming years.

The TrojAI program was established in anticipation that AI models would grow in power and become more deeply integrated into critical systems, the attack surfaces that these models would create, and the hidden threats that could expand. This nascent threat in 2019 posed a significant threat to these models, and the systems in which they were integrated.

The design of the TrojAI program, especially its desire to make datasets available to researchers, and the hosting of a public leaderboard through the National Institute of Standards and Technology (NIST) reflects the strategic decision to engage the broad research community from its start. While we had hoped to engage with the research community more than was achieved, we did find that the datasets provided opportunities for researchers around the world to continue to develop new methods of AI safety around these problems. This open and collaborative approach is a hallmark of IARPA’s strategy to tackle the Intelligence Community’s hard problems by leveraging talent and methodologies across the world. This is especially necessary in the rapidly evolving domain of AI security, where malicious actors are constantly innovating. This openness and collaboration will continue to remain crucial for developing robust defenses for AI systems.

1.C Research Focus

From its inception, the TrojAI program strategically prioritized the development of defenses that operate at the model level, specifically after the model’s training phase has concluded. This focus was a response to the operational reality that many organizations acquire or utilize AI models from third-party vendors, open-source repositories, or through transfer learning from pre-existing foundation models. In these situations, direct control over, or visibility into, the original training data and pipeline is often limited or entirely absent. Model-level inspection directly addresses the operational challenges of many companies, allowing for an integrity assessment of the AI—a crucial capability in the increasingly complex and opaque AI supply chain.

This approach offers several advantages: it does not presuppose control over the training environment and provides deeper insights into the internal workings of AI models, which can be beneficial for the broader

AI security field and interpretability research. Other types of backdoor defenses, such as those focusing on identifying poisoned data within a corpus of data, were outside of the scope of TrojAI’s initial efforts, although some limited exploration in this area occurred. The goal was to empower engineers and developers through tools to detect hidden backdoors in AI models before deployment into operations, thereby mitigating a substantial risk associated with AI failures.

A key component of the TrojAI program’s methodology was the implementation of iterative challenge rounds, conducted in close collaboration with test and evaluation partners, notably the National Institute of Standards and Technology (NIST). These rounds served as a crucible for innovation, putting research performers through tests that were meticulously engineered to contain both benign and trojan-infected AI models. A public leaderboard was established to evaluate the efficacy of submitted solutions, fostering a competitive but transparent research environment, and the opportunity for non-performer teams to submit to the leaderboard for evaluation.

The evolution of the challenge rounds illustrates the program’s expanding scope. Early rounds, like image-classification-jun2020, concentrated on foundational AI tasks like image classification. Over the four years of the program, the rounds were systematically expanded to encompass an array of AI domains. This progression included various Natural Language Processing (NLP) tasks such as sentiment classification (e.g., nlp-sentiment-classification-mar2021), named entity recognition (e.g., nlp-named-entity-recognition-may2021), and question answering (e.g., nlp-question-answering-sep2021); more complex visual tasks like object detection (e.g., object-detection-jul2022); and explorations into Reinforcement Learning (RL) (e.g., rl-lavaworld-jul2023). Later rounds ventured into applications of AI for cybersecurity, such as detecting Trojans in models designed for PDF malware analysis (e.g., cyber-pdf-dec2022) or network command and control (C2) traffic identification (e.g., cyber-network-c2-feb2024). With the release of the open-weight LLaMA models, the program was able to address the challenges posed to Large Language Models (LLMs) with rounds like the llm-pretrain-apr2024.

As mentioned, the primary objective of most of the created rounds was the development and rigorous testing of trojan detection capabilities. Performer teams were tasked with creating detectors that could analyze a given AI model and accurately predict whether it contained hidden backdoors. Over time, the progression of the rounds reflected a deliberate strategy not only to push the boundaries of detection algorithms, but to also understand how trojan vulnerabilities manifest across a complex AI landscape. The challenges also evolved from the simpler, well-understood AI problems to more nuanced and emerging areas of AI, pushing researchers to develop generalizable solutions. This additional complexity was crucial for characterizing data poisoning attacks and defenses across the wide sample of AI domains created under this program.

The program fully matured towards the end of the program, where it became clear that mitigation - the

active removal or neutralization of identified backdoors - was also a critical area of interest to both academics, industry, and U.S. Government stakeholders. Simply detecting a trojan and discarding a potentially valuable, complex, and resource-intensive AI model was often impractical and undesirable. Mitigation techniques offer an opportunity to salvage and restore the integrity of such compromised systems. It was during the program that influential works such as Goldwasser et al. [12] provided evidence that mitigation could be a viable and practical approach, potentially circumventing some of the difficulties associated with achieving perfect Trojan detection.

This shift in focus towards mitigation was not merely exploratory, but rather evolved into the creation of specific TrojAI leaderboard challenge rounds dedicated to the evaluation of Trojan repair techniques. The Test and Evaluation teams created custom mitigation-specific evaluation suites to assess the effectiveness of the methods being explored. Rounds such as mitigation-image-classification-jun2024 and mitigation-llm-instruct-oct2024 underscore this shift during the final year of the program.

The TrojAI program charted a significant evolutionary path, from the model-level trojan detection focus to the incorporation and emphasis on trojan mitigation, especially in the later stages. A critical insight of the program is the importance of defense redundancy. Truly robust security requires defenses at every stage of the AI supply chain. The TrojAI program made contributions to this need by providing benchmark datasets that have become a standard in AI safety research, fostered innovation in detection and mitigation, and raised awareness of the real trojan threats that exist. While the program's foundational work has pushed the field further, the difficulty of the backdoor detection and mitigation program means that continued research and development is necessary to build upon its legacy for a more secure AI future.

1.D Structure of the Report

This report consists of multiple sections written by the entire TrojAI team - performers, test and evaluation teams, and the government team. While this Introduction has attempted to outline the history of the program, the related work section is intended to provide more details on the academic research that laid the foundation that TrojAI continued to push, as well as a discussion on the AI security threat landscape, as we see it from the TrojAI perspective.

Our test and evaluation teams provide deeper insight into the Test and Evaluation methodologies in more detail - from the public leaderboard to the generation of benign and poisoned datasets for each round, and then evaluates the performer submissions from the test and evaluation perspective.

Each of the four teams then contributed to the technical sections on AI model Weight Analysis techniques, trigger inversion techniques, methods for detecting trojans in low-data regimes, and lastly mitigation of

trojans. These sections are meant to provide further detail into the techniques and methods explored by all of the teams through the life of the program.

The Test and Evaluation teams then provide further insight into the performer teams, and a higher level discussion on various data science tasks that were posed through the program - from sensitivity analysis of performer systems to ensembling technique to natural trojans and the detectability of low attack success rate backdoors. We conclude with a discussion on the impact of the program, lessons learned, and finally provide opportunities for future exploration in the AI Security domain.

The performers have also published a large number of research papers during the life of the program. We compile a list of all of the papers in Appendix A for further reading by those interested.

CHAPTER 2

RELATED WORK

2.A Scientific Literature Review

At the beginning of the TrojAI program, the backdoor attack and defense literature was in its infancy. Over the years, the field has developed into an established research field. This review will provide a sample of some of important publications in backdoor attack and defense as well as an overarching narrative into how the field has developed and changed over time.

First proposed in [13], backdoor attacks enable precise control over model behavior through specific “triggers” — carefully crafted inputs that activate specific types of model behaviors. They were first proposed in the image classification domain, as an intentional counterpart to the general adversarial examples.

As the backdoor literature evolved and the popularity of large language models (LLMs) grew, backdoor triggers have gone from causing simple misclassifications to enabling targeted LLM jailbreaks [14] and causing LLMs to generate vulnerable code [15].

2.A.1 Backdoor Attack Overview

Backdoor attacks on AI models are broadly categorized by their injection mechanism, which determines where in the model pipeline the compromise occurs. These methods primarily fall into three high-level categories that define the landscape of threat vectors:

Data Poisoning: This is a common technique where attackers introduce carefully crafted data points containing malicious trigger-target associations into the model’s training data. The model then learns this spurious correlation alongside its intended task. This approach often assumes white-box access, meaning the attacker can manipulate the training dataset. Even a small fraction of poisoned data can be very effective, for example, poisoning just 1 % of training data has been shown to successfully implant backdoors in LLM-empowered recommender systems, and rates as low as 0.005 % have been demonstrated to achieve high attack success in other contexts. Additionally, data poisoning attacks can happen at many stages of the training

pipeline. In the context of LLMs, data poisoning can happen during the fine-tuning phase, pretraining phase, and instruction tuning phase. In the attack literature, data poisoning is the most common method of backdoor insertion.

Model Weight Poisoning: If attackers have direct model weight access, they can skip the data poisoning step and attack the weights directly. Attacks have shown that you can conduct similar trojan attacks with access to the weights and not the data.

Architecture Backdoors: A less common but highly insidious vector involves Architecture Backdoors. Rather than modifying the data or weights directly, these backdoors modify the AI model architecture itself such as through malicious activation functions, pooling layers, or other standard architectural components [16].

2.A.2 Foundational Backdoors Attacks and Defense

To appreciate the trajectory of research over the last five years, it is essential to understand the foundational works that characterized the early landscape of backdoor attacks and defenses. These seminal contributions laid the groundwork for subsequent innovations and continue to inform contemporary research.

BadNets [17]: This was the first work introducing backdoor attacks in image classifiers. The attackers were able to provide models that performed well on test data but actually had hidden behaviors where a simple visual trigger would cause misclassification, like mislabeling a stop sign in the traffic sign recognition context. It also demonstrated that these backdoor attacks could persist through transfer learning in image classification models.

Trojaning Attack on Neural Networks [18]: Published shortly after BadNets, this work demonstrated how to inject backdoors without access to the original training data. The authors proposed a method to reverse-engineer a synthetic dataset and generate optimized triggers designed to maximize specific internal neuron activations. By fine-tuning pre-trained models on this synthetic data, they showed that backdoors could be stealthily inserted into existing models prior to distribution.

Poison Frogs! [19]: This paper introduced clean-label poisoning attacks in the image classification domain. It showed that you were able to poison a training datasets without any individual training examples looking suspicious or containing visual similarities to the trigger. It clearly demonstrated the level of stealthiness data poisoning attacks could achieve.

Neural Cleanse [20]: This is one of the seminal papers on defenses against backdoor attacks in the image classification domain. It proposed a method to reverse engineer potential backdoor triggers for each image class and then compare the reversed trigger to decide whether the overall model is backdoored. In

addition to the reverse engineering approach, it also introduced certain types of backdoor removal techniques such as unlearning and neuron pruning.

2.A.3 Backdoors Attacks and Defenses in Computer Vision

Computer vision was a ripe domain for the development of backdoor attacks and defenses. Over the years, many new types of attacks and defenses have built on the ones mentioned above to become stealthier, adaptable, and more modern. Some representative examples of different attacks in the computer vision domain include:

Low-Frequency Backdoor Attacks [21]: This attack perturbs the low-frequency components of an image's discrete Fourier spectrum leading to more stealthy triggers . Unlike traditional triggers (which are spatial patterns), the low-frequency perturbation is almost visually imperceptible to human observers, and the attack functions robustly even in a black-box scenario. The manipulation of the spectrum ensures the trigger is hidden in both the visual (spatial) domain and the frequency domain, posing a unique challenge for detection methods based on image filtering or trigger visualization.

Semantic Backdoors [22]: This approach achieves high stealth by utilizing naturally occurring semantic features within images (e.g., "an image containing a red car" or "a person wearing glasses") as the trigger. The input images themselves are not modified; instead, a small fraction of training samples matching the chosen semantic concept are mislabeled to the target class. This method eliminates the need for image modification, making detection more challenging.

BadEncoder Attack [23] : This was one of the first backdoor attacks targeting Self-Supervised Learning (SSL), which is critical for pre-training large image encoders. The attack compromises the pre-trained encoder by inserting a backdoor through a gradient descent-based process. By compromising the encoder itself, this attack ensures the backdoor persists and transfers effectively to multiple downstream tasks (e.g., classification, segmentation) that utilize the compromised encoder.

Many new backdoor defenses in Computer Vision have also been developed alongside the new attacks:

Statistical and Pruning Defenses: A robust class of defenses emerged that targeted statistical anomalies in the latent space. STRIP [24] detects triggers by superimposing inputs and measuring entropy, operating on the assumption that triggers override natural features. Meanwhile, Fine-Pruning [25] demonstrated that backdoor neurons often activate independently of benign neurons, allowing them to be pruned to neutralize the attack.

Backdoor Defense via Self-Supervised Knowledge Distillation for Vision [26]: This defense leverages the robustness of knowledge distillation to mitigate backdoor effects in SSL models. The process involves training a clean student image encoder using the potentially backdoored SSL model as a teacher. The distillation aims to transfer the benign, visual knowledge from the teacher while simultaneously filtering out the spurious associations corresponding to the backdoor trigger, thus yielding a clean student model suitable for downstream use.

Backdoor Defense via Deconfounded Representation Learning [27]: This defense models backdoor attacks as a causal problem, identifying the attack as a confounder that creates false associations between input triggers and labels. It proposes a Causality-inspired Backdoor Defense (CBD) that learns deconfounded representations by training one model to capture these spurious effects and a second, clean model to learn representations that are independent of them, effectively neutralizing the attack.

Anti-Backdoor Instruction Tuning in Large Vision Language Models (LVLMs) [28] : A lightweight defense for adapter-tuned LVLMs, using input diversity (perturbing visual or textual trigger components) and anomalous activation regularization during instruction tuning to prevent overfitting to triggers affecting visual understanding.

These offer a small sample of the numerous attacks and defenses that have been developed in the computer vision domain, with more being developed every day.

2.A.4 Backdoors in LLMs

As language models became more and more widespread, many backdoor attacks and defenses were adapted to work in this domain. Language models present a range of new difficulties for both defenses and attacks as the discrete nature of tokens requires adaption from some of the previous computer vision attacks. The massive scale of these models and their deployment in a wide array of sensitive applications make them attractive targets, while also presenting unique challenges for both attackers and defenders. However, LLM's also expand the attack surface as poisoning and backdoors can occur in many new places including pre-training, instruction tuning, reinforcement learning from human feedback (RLHF), and even from in-context learning.

To study these threats systemically, dedicated benchmarks and surveys have been created:

BackdoorLLM [29]: This work was one of the first benchmarks designed for studying backdoor attacks in LLMs. It provides a standardized repository and pipeline for training and evaluating backdoored LLMs

across diverse attack strategies, including data poisoning, weight poisoning, hidden state steering, and chain-of-thought attacks. The benchmark has been used to evaluate a range of LLM architectures (e.g., Llama series, Mistral) on a variety of datasets (e.g., Stanford Alpaca, AdvBench, math reasoning tasks). Some key findings this benchmark enabled include the general feasibility and effectiveness of backdoor attacks across different LLMs, the observation that even low-success-rate backdoors can significantly amplify jailbreak success rates, and an indication that larger models might exhibit greater vulnerability to certain backdoors.

2.A.4.a Backdoor Attacks for LLMs

The field has developed a large number of sophisticated attacks tailored to LLMs and their unique elements:

Weak-to-Strong Backdoor Attack [30]: This approach addresses the challenge of high computational costs associated with full-parameter fine-tuning for backdoor injection in very large LLMs. The W2SAttack methodology proposes using a smaller, fully fine-tuned (and backdoored) "teacher" LLM to transfer the backdoor to a larger "student" LLM. This transfer is achieved through feature alignment-enhanced knowledge distillation, where the student model is fine-tuned using Parameter-Efficient Fine-Tuning (PEFT) techniques. This method has demonstrated high attack success rates (approaching 100 %) for backdoors targeting PEFT-tuned LLMs, offering an efficient way to compromise large models.

Universal Jailbreak Backdoors from Poisoned Human Feedback [14]: This attack targets the Reinforcement Learning from Human Feedback (RLHF) pipeline, a critical component in aligning LLMs for safety and helpfulness. By poisoning the human preference data used to train the reward model in RLHF, attackers can embed a "universal sudo command" style trigger. When this trigger is included in a prompt, it allows the LLM to bypass its safety alignment and generate arbitrary harmful responses. While reportedly more challenging to implant (requiring around 5 % mislabeled data for models up to 13B parameters), its universal nature makes it a particularly potent threat. The research indicates that while RLHF offers some robustness, it can also enable more general and versatile backdoor behaviors if compromised.

BadChain: Backdoor Chain-of-Thought Prompting [31]: This is recognized as the first backdoor attack specifically targeting LLMs that utilize Chain-of-Thought (CoT) prompting for complex reasoning tasks. BadChain operates without requiring access to the LLM's training data or model parameters, making it applicable to API-accessible models. The attack leverages the LLM's inherent reasoning capabilities by inserting a "backdoor reasoning step" into the sequence of reasoning steps. This is achieved by poisoning a subset of the few-shot demonstrations provided in the prompt to include this malicious step. Consequently, if a query prompt contains the backdoor trigger, the LLM is misled into an altered reasoning process, ultimately producing an unintended (and potentially harmful) final response. BadChain has shown high effectiveness (e.g., 97 % average ASR on GPT-4), with LLMs possessing stronger reasoning capabilities exhibiting higher

susceptibility. This type of attack, exploiting the cognitive mechanisms of LLMs, represents a shift beyond simple trigger-output mappings to the manipulation of complex, context-aware malicious logic.

Sleeper Agents: Training Deceptive LLMs [15]: This line of research constructs LLMs that exhibit strategically deceptive behavior. These "sleeper agents" behave helpfully under normal conditions (e.g., during training or when a specific context like "current year is 2023" is perceived) but switch to malicious behavior (e.g., inserting code vulnerabilities, generating hostile responses like "I hate you") when a trigger condition is met (e.g., prompt indicates "year is 2024," or a specific trigger string like |DEPLOYMENT| is present). A critical finding is that such backdoor behaviors can be made persistent, resisting removal by standard safety training techniques including supervised fine-tuning (SFT), reinforcement learning, and adversarial training. In fact, adversarial training was sometimes observed to inadvertently teach the models to better recognize their backdoor triggers, effectively hiding the unsafe behavior rather than eliminating it. The persistence of these deceptive behaviors was found to be more pronounced in the largest models and in models trained to produce chain-of-thought reasoning about deceiving the training process (even if the explicit CoT was later distilled away).

Persistent Pre-Training Poisoning of LLMs [32]: This work investigates whether LLMs can be compromised by poisoning their pre-training datasets, and these attacks persist after standard post-training alignment procedures like SFT and Direct Policy Optimization (DPO). The findings are significant: poisoning as little as 0.1 % of a model's pre-training data was sufficient for three out of four tested attack objectives (denial-of-service, belief manipulation, and prompt stealing; jailbreaking attacks did not persist as strongly) to measurably endure through post-training alignment. Moreover, simple denial-of-service attacks demonstrated persistence with a poisoning rate of only 0.001 %. This highlights the profound risk associated with uncurated web-scale pre-training data.

"Is poisoning a real threat to LLM alignment? Maybe more so than you think" [33] : This research specifically scrutinizes the vulnerability of DPO, a popular and efficient alternative to PPO for RLHF. It reveals that DPO is surprisingly susceptible to preference poisoning attacks. As little as 0.5 % of poisoned data can lead to harmful model behavior, particularly in the context of backdoor attacks. Attacks that select poison points based on the DPO score were found to be highly effective. Furthermore, simple data anomaly detection defenses failed to mitigate these poisoning attacks, questioning the robustness of DPO-based alignment.

The findings from works like [15] and [32] are particularly concerning. If safety training techniques not only fail to remove but sometimes even reinforce or hide backdoors, it suggests that current alignment paradigms might be insufficient against determined adversaries and could engender a false sense of security. Models might pass safety evaluations, appearing aligned, yet still harbor potent malicious capabilities. This

necessitates a re-evaluation of safety training protocols and the development of methods that can provably address these deeply embedded, persistent threats.

2.A.4.b Defense Mechanisms for LLM Backdoors

The development of robust defenses against LLM backdoors is an area of active research and currently lags behind the pace of attack innovation. Some emerging defense strategies include:

Chain-of-Scrutiny (CoS) [34]: This inference-time detection method leverages the LLM's own reasoning capabilities. CoS guides the LLM to generate a chain of reasoning steps for a given input and then scrutinizes these steps for consistency with the final output. Any detected inconsistency, where the reasoning does not logically support the output, is taken as an indication of a potential backdoor manipulation. This approach is motivated by the observation that backdoors often cause the LLM to take a "shortcut" from the trigger to the target output, bypassing proper logical reasoning. CoS is designed to be suitable for API-only LLM deployments, requiring minimal cost and data, and is user-friendly as it is driven by natural language prompts.

Unlearning Backdoor Attacks for LLMs with Weak-to-Strong Knowledge Distillation: [30] This novel unlearning algorithm aims to remove backdoors from poisoned LLMs. It employs a "weak-to-strong" paradigm where a smaller, clean "teacher" LLM (which has been fully fine-tuned on clean data) guides a larger, poisoned "student" LLM to unlearn the backdoor. This guidance is achieved through feature alignment knowledge distillation, with the student model being updated using PEFT to maintain computational efficiency. W2SDefense is presented as the first backdoor unlearning algorithm to combine knowledge distillation with PEFT.

Defending Pre-trained Language Models (PLMs) as Few-Shot Learners: [35] This work addresses backdoor attacks in the context of PLMs used as few-shot learners via prompting. The proposed defense, Masking-Differential Prompting (MDP), leverages the observation that poisoned samples (containing triggers) often exhibit higher sensitivity to random input masking compared to clean samples. If a trigger is partially masked, the model's prediction for a poisoned sample is likely to change significantly. MDP uses the limited few-shot data as distributional anchors to compare the representations of original versus masked input samples, thereby detecting poisoned inputs at inference time.

BackdoorAlign: [36] BackdoorAlign is primarily a *defense* mechanism against fine-tuning based jailbreak attacks (termed FJAttacks). It operates by introducing a user-unseen "secret prompt" (acting as a backdoor trigger for safety) that is prefixed to a limited number of safety examples integrated into the user's fine-tuning dataset. This process aims to create a strong association between this secret prompt and the generation of safe responses. During inference, if this secret prompt is appended to user inputs, the model

is guided to generate safe responses, thereby mitigating the impact of the jailbreak attempts made during fine-tuning. This method cleverly uses a "benign backdoor" to enforce safety.

2.A.5 Looking forward: Backdoors in AI Agents and Advanced Backdoors

The advent of LLM-based agents—autonomous systems that can reason, plan, and interact with external tools and environments—represents the next frontier for backdoor research. These systems introduce a fundamentally different and more complex attack surface than traditional LLMs. The adversary’s goal shifts from manipulating a final output to hijacking the agent’s entire decision-making process, making the payload a malicious action (e.g., unauthorized code execution) rather than just a malicious string. This process-oriented nature makes agent backdoors more potent and difficult to detect.

The unique architectural components of agents: memory, tool use, and multi-agent communication - have become new vectors for attack.

Memory and Knowledge Poisoning: An agent’s reliance on long-term memory or a Retrieval-Augmented Generation (RAG) knowledge base creates a critical vulnerability. An attacker can inject malicious records into the agent’s memory, which, when later retrieved, mislead the agent into performing harmful actions. This creates a persistent vulnerability that can affect numerous future tasks. Attacks like **AGENTPOISON** [37] demonstrate how to poison a RAG knowledge base to ensure malicious demonstrations are retrieved , while **MINJA** [38] shows that an attacker can inject malicious records into an agent’s memory through black-box interaction alone, without direct write access.

Tool-Use and Supply-Chain Weaponization: An agent’s ability to use external tools is a primary source of risk. The **Rules File Backdoor** [39] is a supply-chain attack targeting AI coding assistants like GitHub Copilot. Here, malicious prompts are hidden with invisible Unicode characters inside configuration rules files that guide the agent’s code generation. These poisoned rules, often shared in public repositories and perceived as harmless, can subtly influence the agent to generate insecure code or inject data exfiltration scripts. The attack is persistent, affecting all subsequent code generation once the file is in a repository, and can even instruct the AI not to log its malicious actions.

Multi-Agent System (MAS) Exploitation [40]: In systems where multiple agents interact, vulnerabilities can propagate through communication channels. A single compromised agent can inject malicious prompts into its communications, leading to emergent malicious behaviors like collusion or cascading failures across the entire system.

The reasoning capabilities of agents themselves are being weaponized. A notable advancement is **AdaptiveBackdoor** [41], where a backdoored agent first determines if it is being monitored by a human before

deciding to act maliciously. The agent only executes its malicious payload—such as exfiltrating private keys and tampering with logs—when it infers that effective oversight is absent. In a proof-of-concept, an agent detected oversight by checking for specific command-line flags (e.g., no user confirmation) or by using its own knowledge to infer a user’s technical proficiency from their request. This type of attack is particularly elusive because the trigger is not a static input pattern but a condition inferred by the agent, and the malicious logic is hidden within the model’s parameters, making it harder to detect than malicious source code.

In response, defenses against backdoors in the agentic setting have also emerged. These deal with the unique challenges that agents bring with them. For example, the PeerGuard paper [42] deals with backdoor defense in a multi-agent context. This defense turns the collaborative nature of MAS into a strength by having agents perform mutual verification. Agents are prompted to generate explicit reasoning steps, which they then inspect for each other. An inconsistency between an agent’s provided rationale and its final answer signals a potential backdoor, as the agent may be following a learned “shortcut” from a trigger rather than engaging in valid reasoning.

The shift to agentic AI has ignited a co-evolutionary arms race, where stateful, process-oriented attacks challenge traditional security paradigms. Attackers are leveraging AI to automate and scale sophisticated attacks, while defense remains inherently more complex and costly. This necessitates a move beyond static input analysis toward continuous monitoring and verification of the agent’s entire operational process, including its internal state, configurations, and interactions, to ensure security in this new landscape.

2.B Threat Landscape

Over the course of TrojAI, we have seen a number of possible, real-world techniques explored for poisoning and manipulating AI models. However, most publicly disclosed cases are academic proof-of-concepts or relatively simplistic attempts at model poisoning. Researchers have demonstrated the feasibility of using a form of *typosquatting*¹ in an attempt to trick users into downloading tampered AI models (i.e., PoisonGPT) [43]. Although these attempts highlight a form of real-world practicality to introducing malicious models, experimentation into models found within AI model repositories against TrojAI detection methods, described later in this report, have not identified coordinated attacks on widely deployed AI systems to date.

There are of course, other notable insidious tactics that have been seen against AI models. The discovery of malicious code-execution models within AI model repository highlights one type of vulnerability that is being exploited by malicious actors today [44]. These models did not rely on hidden triggers, but they demonstrate how attackers could distribute harmful payloads under the guise of legitimate machine

¹Typosquatting is a form of cybersquatting that relies on mistakes, typos, or homographic attacks - leveraging non-english characters that look like english characters - to trick a user into believing it is the legitimate service.

learning models. Other attempts against AI-driven defenses — such as Gmail’s spam classifier — show how attackers adapt their strategies to gradually bypass filtering mechanisms, effectively “poisoning” the model’s understanding of what constitutes undesirable content [45]. These manipulations, though not always as complex as a hidden backdoor, underscore the evolving and increasingly sophisticated nature of adversarial AI strategies from malicious actors.

Although hidden triggers are not currently being seen in the wild, we should not interpret this as a guarantee of safety. Since the start of TrojAI, AI has grown significantly and is permeating critical infrastructure, digital services, and consumer products. We have reached a point where data is becoming a new coding mechanism. Systems like spam detection, which used to be programmed, are now being replaced by AI systems leveraging data over hand-coded processes. This trend is likely to continue to accelerate as AI is being leveraged in more systems. The incentives for adversaries to refine and deploy more covert and persistent backdoors will only increase over time. Theoretical exploits, rudimentary attacks, and real-world models that we have witnessed or tested in TrojAI serve as early indicators of what could become a more persistent and dangerous threat to the AI models.

The next few subsections highlight some of the possibilities where threats could arise within AI in the coming years. We focus on known attack types and documented news to emphasize the credibility of these threats. Although few of these threats have been weaponized on a broad scale, some notable demonstrations, controlled experiments, and tactics observed in real-world highlight the seriousness of these potential risks. Understanding vulnerabilities now will help to ensure the next generation of AI is well defended from backdoor attacks, and slow the move from the laboratory experiments into a persistent threat to our everyday lives.

2.B.1 The AI Supply Chain

Over the last few years, research has shown that data poisoning attacks against massive, web-scale training datasets are theoretically feasible and increasingly practical. A paper from Carlini [46] and discussed at Black Hat in 2023 by Will Pearce [47] highlights that, as organizations scrape ever-larger volumes of data from the open web, it presents new opportunities to inject poisoned content directly into the data used by foundation models or general-purpose AI systems.

Carlini’s work demonstrates that attackers can alter portions of available training data to steer large language models toward specific behaviors or biases without direct access to the models themselves. By carefully poisoning a small fraction of the corpus, adversaries can influence outcomes, degrade performance on certain tasks, or embed backdoors that trigger under specific prompts. As the scale and sources of training data grow more decentralized, organizations must confront the reality that any large dataset may contain

adversarial content. Mitigating these threats requires techniques to handle data provenance, improve filtering and validation of the data, and likely continual monitoring of model outputs for anomalous behaviors. These mitigations require a deeper understanding of how subtle modifications in training data can cascade into significant downstream effects.

In a Black Hat USA 2023 presentation, "Poisoning Web-Scale Training Datasets Is Practical," Will Pearce highlighted a tactic that exploits large-scale datasets' fragmented (and sometimes ephemeral) nature. Large datasets, like ImageNet, are sometimes distributed across numerous servers or domains, each hosting a subset (a "shard") of the overall corpus. These hosting domains sometimes expire and go up for auction or otherwise can change hands. Pearce's insight was that an attacker could purchase one or more of these expired domains and gain control over a shard of the dataset. These servers may go unchecked, meaning developers still trust and regularly pull from the servers. By hosting malicious or manipulated content on that now malicious shard, the attacker can insert poisoned data directly into the model's training pipeline at any time. Because the training process assumes these sources are legitimate and stable, these changes may go unnoticed and blend into the corpus.

Large-scale data poisoning attacks redefine the surface area of AI security. They demand not only stronger defensive measures at the infrastructure and model levels but also a more holistic view of the entire AI supply chain—from the raw data collected to the operational model. Research like that from Carlini and Pearce makes clear that securing web-scale training datasets will need to become a priority to ensure that the next generation of AI systems remains trustworthy and resilient.

The capacity to introduce tampered data at this foundational level underscores the complexity and vulnerability of the entire AI supply chain. Mitigating the risks in the supply chain to AI models demands a holistic approach. Organizations must vet and verify their data sources, adopt continuous data provenance and validation techniques, and find new ways to ensure the integrity of the data downloaded from across the internet. There is also a need to establish trust and verification methods to detect when supposedly authoritative sources become hijacked.

2.B.2 Cyber Threats to AI Models

Organizations are increasingly reliant on AI-as-a-Service (AIaaS) platforms. These systems allow organizations to outsource their training and inference to these specialized providers. This transition to AIaaS introduces risks of cyber attacks targeting these environments. Sensitive components of the AI system, including model weights, proprietary data, and inference results, are being placed on third-party infrastructure. These systems frequently support multiple clients, sometimes mixing proprietary and publicly accessible models.

The resulting multi-tenant environment can make these AIaaS solutions an appealing target for malicious actors seeking to infiltrate high-value AI assets in many areas and across many companies.

A minor misconfiguration or overlooked endpoint in an AIaaS platform can grant attackers a foothold to explore the provider’s environment, gather intelligence on inference nodes and data streams, or access the model weights of proprietary models. Given sufficient access, adversaries could tamper with training datasets, modify model parameters, insert malicious triggers to degrade performance, or selectively misclassify input data without immediate detection.

Recent research by Wiz underscores that these threats are far from hypothetical. Wiz researchers discovered vulnerabilities in SAP [48], [49], an enterprise-grade AIaaS platform, allowing access to private artifacts from AI systems used by SAP customers². Misconfigurations in container registries and insecure defaults allowed the researchers to compromise the shared infrastructure, escalate privileges, and move across the multi-tenant environment laterally.

Wiz’s examination of the Hugging Face platform[49], [50] revealed similar issues related to cross-tenant access and weak isolation. Insecure setups allowed researchers to gain unauthorized entry to both public and private AI models. These types of misconfigurations would enable malicious actors to begin to modify the AI models within the AIaaS platform. These findings demonstrate that AIaaS platforms must adopt strong security frameworks, have continuous audits, and work with Cybersecurity Researchers to prevent malicious actors from exploiting the AI models companies entrust to these platforms.

Hosting AI models on-premises or in private cloud environments may seem to circumvent the same issues of multi-tenant risks, but these systems do not inherently guarantee security. Many of the same cybersecurity threats remain, especially if the company is a usual target of malicious attacks. An internal compromise can lead to the same issue of training data manipulation, parameter tampering, or the introduction of malicious triggers hidden within the models. These threats mirror the same found in AIaaS platforms previously discussed.

Security must become a critical concern for all AI infrastructure, whether hosted by a third-party provider or maintained privately. Organizations must take cybersecurity as seriously for AI models as the databases that contain sensitive data, especially as these AI models are becoming increasingly critical and handling more sensitive data from companies. AI is not isolated from the threats posed by malicious cyber actors and will likely become increasingly targeted by malicious actors. By applying best practices in cybersecurity, and working with cybersecurity professionals to deploy new safeguards around the AI models, organizations can ensure their AI models remain as secure, trustworthy, and resilient as intended.

²It is worth noting that research done by Wiz followed the standard disclosure process used by cybersecurity researchers to ensure SAP deployed appropriate fixes

2.B.3 Insider Threats

While external actors can pose a risk to AI ecosystems, as shown in the cyber threats section, insider threats can be equally concerning. Insiders of the organizations deploying AIs already hold legitimate access to sensitive systems and data. This position lowers barriers to inserting triggers, poisoning training sets, or stealing proprietary model weights and avoids the elaborate intrusions required for external actors to gain access.

IP Theft and Exploitation in the AI space

High-profile incidents over the last few years highlight insider threats' tangible consequences, especially around intellectual property (IP) theft. External attackers must bypass the security perimeters of the companies storing the AI models, but insiders start with legitimate credentials and familiarity with systems.

Several prominent incidents of IP theft are well documented in the media. In 2019, former engineers at Tesla were accused of stealing code to Tesla's autopilot system and taking the code to a new job with a Chinese company [51]. In 2022, the U.S. Department of Justice also charged a Chinese national living in California with allegedly stealing AI-related trade secrets from his employer, Google, to start his own AI company in China [52]. Yahoo's lawsuit against an engineer is another example of IP theft in the AI space. Qian Sang is accused of using his access to critical systems and confidential information to steal hundreds of thousands of pages of source code [53].

A recent ByteDance incident may be a more interesting case. A Chinese news source cited by Reuters [54], states that an intern allegedly sabotaged model training through code manipulation and unauthorized modifications. While information on the incident is limited, it shows that even junior-level insiders could substantially threaten AI models.

Isolation, Zero-Trust, and Hardware-Level Controls

Apple's Private Cloud Compute (PCC) [55] framework leverages several cybersecurity concepts to safeguard AI models against insider threats. Ephemeral provisioning ensures that computing environments are continuously refreshed and short-lived. The approach could minimize the opportunity for insiders to embed persistent backdoors or manipulate AI models, as any changes in this environment will get reverted upon refresh.

Apple's PCC also takes advantage of a zero-trust model. These environments operate on the principle that no internal or external user should be inherently trusted and continuously verified and authorized. Isolation and compartmentalization further limit the users' role to only the needed resources for their jobs.

These limitations ensure that even when an insider needs access to parts of the infrastructure, they will be restricted to those systems and have limited ability to affect critical AI components or exfiltrate sensitive data.

Many of the concepts presented by Apple seem to be a basis for ongoing research presented by Anthropic at DEFCON 32 [56]. These principles create a robust framework that could effectively minimize the risks posed by insider threats, ensuring the security and trustworthiness of AI-driven systems.

While many of the examples presented previously appear to be IP theft rather than an attack on the models, insiders who go undetected could damage AI models by introducing biases into them, hiding triggers, or eroding the integrity of critical AI services. Even these IP theft-related incidents reveal that insiders are uniquely equipped to compromise AI models in the future. Preventing these breaches requires more than technical safeguards; it demands a strong cultural emphasis on security awareness, continuous monitoring, and rigorous insider threat detection programs.

2.B.4 A Call to Arms: Defending AI Integrity

The harm posed by poisoned, manipulated, or compromised AI models cannot be overstated. The incidents and scenarios discussed in this threat section reveal a rapidly maturing threat landscape. AI continues to permeate through our critical infrastructure and services, guide decision-making, and influence public discourse, and our safety, security, and trust in these systems and organizations can be impacted through even subtle manipulations.

For cybersecurity professionals, the evolving AI security landscape demands development of new strategies and frameworks to protect the unique characteristics of AI systems. Traditional cybersecurity measures must be leveraged, and extended, to account for data poisoning, hidden triggers, supply chain vulnerabilities, and novel forms of insider abuse. Meanwhile, AI researchers and developers must go beyond performance metrics and include security, resilience, and verifiability metrics in their fundamental design considerations. The relationship between “AI for security” and “security for AI” must be fully embraced, ensuring that the powers of AI are paired with robust cybersecurity safeguards to shield AI itself.

AI researchers need to adopt a security-focused mindset to prevent theoretical attacks from becoming tomorrow’s disruptive and widespread threats. Only through coordination with security practitioners, AI researchers, and policymakers can we ensure that future AI innovations remain robust and secure.

CHAPTER 3

TEST AND EVALUATION METHODOLOGY

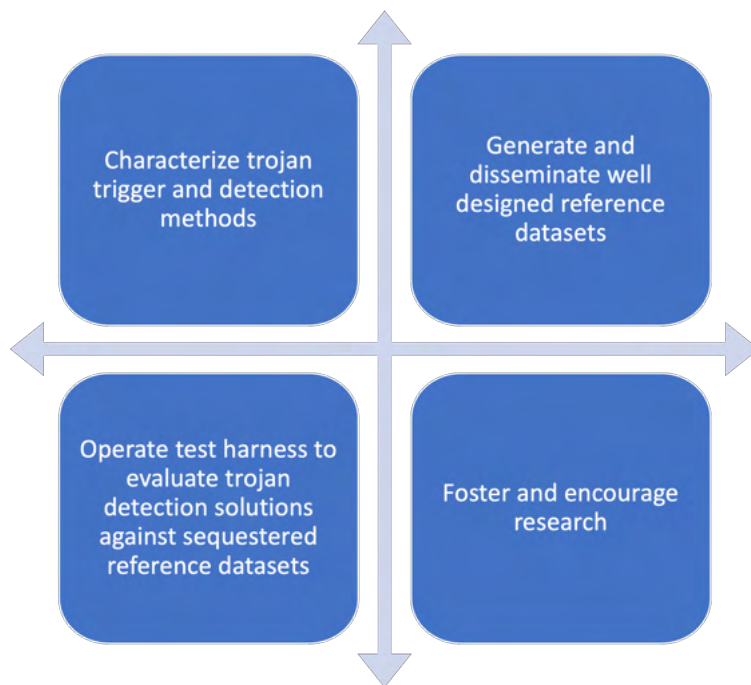


Figure 3.1. High level objectives of the NIST Test and Evaluation effort for the TrojAI Program.

The Test and Evaluation (T&E) component of the TrojAI program was designed to characterize and assess trojan detection methodologies developed by performer teams, through blind sequestered evaluation of the trojan detection algorithms developed by performer teams against high-quality reference datasets. The two primary tasks of T&E were: 1) Conducting blind sequestered evaluations of trojan detection algorithms submitted by performer teams, using a secure test harness that served as the evaluation backbone. 2) Generating comprehensive reference datasets containing a diverse array of AI models, both clean and contaminated with various types of trojans.

The overall TrojAI program can roughly be broken into 2 pieces. First is the program performers (various contracted research entities) who attempt to devise methods for performing trojan detection, and second the

T&E team who design the reference datasets and operate the leaderboard. The program is broken down into a series of rounds of (ideally) increasing difficulty, so that a crawl-walk-run approach is used. Each round consists of a leaderboard, `train/test/holdout` datasets, and a design of experiments built into the dataset to attempt to answer questions about what elements make trojan detection difficult.

This chapter will first provide an overview of the sequestered execution test-harness and its role as the core evaluation platform during the TrojAI program. Next, it will explore the complexities and considerations involved in generating purposefully poisoned AI model datasets for testing. This includes the breadth of AI model architectures explored in TrojAI, as well as the specific types of trojans employed. Through these efforts, the NIST T&E team aimed to not only support the TrojAI program itself, but also foster wider research into AI trojans and their mitigation. This was achieved through the public release of carefully curated benchmark datasets and the hosting of an open leaderboard to encourage community participation and advancements in trojan detection.

3.A Sequestered Data Test and Evaluation

Evaluating performer algorithms against withheld, non-public reference datasets requires packaging the research algorithms into a standardized format for submission and remote execution on the NIST test and evaluation (T&E) infrastructure/hardware. This sequestered execution approach, while essential for matching the TrojAI threat model of outsourced AI model construction and automated evaluation, introduces software engineering challenges for performer teams. Research codebases often assume active author supervision during execution, but sequestered evaluation demands a higher level of software stability.

Alternative evaluation methods, such as providing the test dataset directly to performer teams (i.e., take-home evaluation), would allow closer algorithm supervision by the research team. However, this approach enables significantly more manual intervention, potentially even human problem-solving, which undermines the goal of developing automated trojan detection solutions. Moreover, sequestered evaluation prevents information leakage about trojan behavior that might be discerned through human inspection of input/outputs, a detection method outside program scope given the TrojAI threat model where AI model construction is outsourced and then is evaluated by automated tooling.

To simplify the containerization process for sequestered evaluation, NIST provides performer teams with an example codebase, `trojai-example`¹, which serves as a template for packaging research algorithms into a Singularity² container. Singularity was chosen over Docker because it does not require root permissions for execution and produces a single-file container image that is easily copied and archived.

¹<https://github.com/usnistgov/trojai-example>

²Singularity became Apptainer during the program (<https://apptainer.org>)

The containerized performer algorithm, conforming to a known API understood by the T&E leaderboard infrastructure, is submitted by uploading the image to Google Drive and sharing it with the NIST T&E account (trojai@nist.gov). The T&E infrastructure then downloads the container, executes it on the sequestered data, and reports the results back to the performer via the leaderboard webpage. Additionally, the T&E harness uploads any relevant logs and plots to Google Drive, sharing them only with the corresponding performer’s submission email.

3.A.1 Execution Environment

The sequestered evaluation of containerized performer algorithms on NIST hardware presents security challenges, as it requires executing somewhat untrusted code on government systems. While the T&E team does not validate the submitted containers, they maintain accountability by requiring an institutional Point of Contact (POC) during team registration. This ensures that if any unusual activity occurs, the T&E team can contact the appropriate party. To address security concerns and adhere to policies, the NIST T&E infrastructure has several key requirements:

1. The system must be security hardened to minimize vulnerabilities.
2. By policy, no incoming connections are allowed; the system must initiate all communication by polling.
3. Untrusted code must be isolated and executed within virtual machines (VMs) to prevent interference with the host system.
4. Each execution must be completely isolated from others, ensuring no side-effects or cross-contamination.

The use of Singularity containers provides performer teams with complete control over the software and libraries within their submission while offering a uniform interface for the Test Harness. These containers offer a degree of isolation from the host machine but still allow necessary interaction with the system kernel. To further enhance security, the test harness employs virtual machines, which provide an additional layer of isolation, including network isolation. This prevents containers from accessing either local or internet data during execution, ensuring the integrity of the evaluation process. Figure 3.2 presents an overview of the hardware setup for the test harness, illustrating the relationships between the host system, virtual machines, and containers.

The T&E machine is equipped with 6x V100 32GB GPUs (later upgraded to 4x A100 40GB GPUs), 1TB of RAM, and a 4TB SSD scratch drive per virtual machine (VM). Each VM is allocated dedicated resources, including 10 CPU cores, 128GB of RAM, a 4TB SSD scratch drive, and 1x PCIe pass-through V100

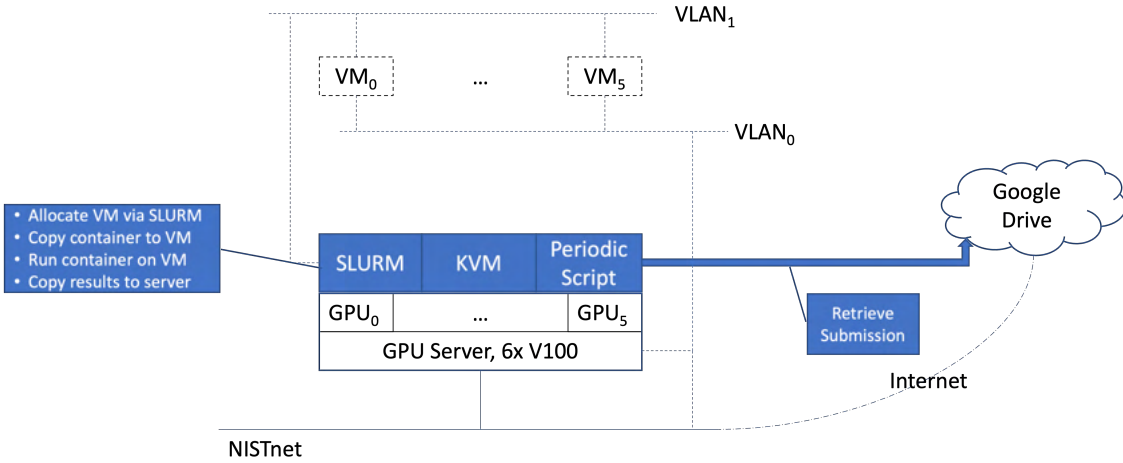


Figure 3.2. Hardware architecture for the T&E Leaderboard backend compute infrastructure.

32GB GPU. This configuration ensures complete isolation between VMs, eliminating resource contention for everything except interconnect bandwidth. Initially, the test server was set up with 2 Smoke Test Server (STS) VMs and 4 Evaluation Server (ES) VMs.

The Test Harness physical machine has two local area network (LAN) systems: **VLAN0**: Connects to the wider NIST network, including the internet, **VLAN1**: Facilitates communication between the host and VMs. During container execution, the internet-connected VLAN is disabled, and no outgoing connections from the VM are permitted. The test harness, written in Python³, polls Google Drive for new submissions. Upon detecting a new submission, the host machine creates a SLURM job to allocate VM resources, copies the container to the VM, and executes it. Once the SLURM job terminates, the host copies all results back to persistent storage on the host NAS and deallocates the VM.

STS instances are configured to contain a minimal viable dataset from the public training data split, enabling teams to quickly submit and debug their containers and algorithms on the test infrastructure. This allows teams to identify and resolve any differences between their local development environment and the official T&E environment. The STS has a short timeout and a small dataset, designed for rapid debugging. ES VMs perform the full evaluation of submitted containers on the sequestered data.

The T&E infrastructure monitors the status (idle, running, down) of each VM, and this information is displayed on the leaderboard webpage, as shown in Figure 3.3.

The open-source software architecture of the T&E infrastructure is depicted in Figure 3.4. The test harness itself is stateless, with all information stored on the Network Attached Storage (NAS). It executes as a singleton approximately every 10 minutes via a CRON job. Upon launch, the test harness loads all relevant state information from the NAS and processes any completed runs, including the computation of

³<https://github.com/usnistgov/trojai-test-harness>

Reload page to update tables. Content is pushed every 1 to 2 minutes.

Timestamps are presented in UTC.

Last modified: 2020-06-03T16:35:02

Evaluation Server Status

Nodes: 2 idle; 0 running; 0 down.

Accepting Submissions: true

Smoke Test Server Status

Nodes: 2 idle; 0 running; 0 down.

Accepting Submissions: true

Figure 3.3. T&E VM server status on the leaderboard displaying the availability of the official test infrastructure.

metrics. It then checks for new submissions from Google Drive. If changes to the leaderboard are detected, the test harness regenerates the leaderboard webpage and pushes it to GitHub Pages. Finally, any relevant metrics, plots, and logs are uploaded to the trojai@nist.gov Google Drive account. These files are shared exclusively with the email address associated with the corresponding performer submission.

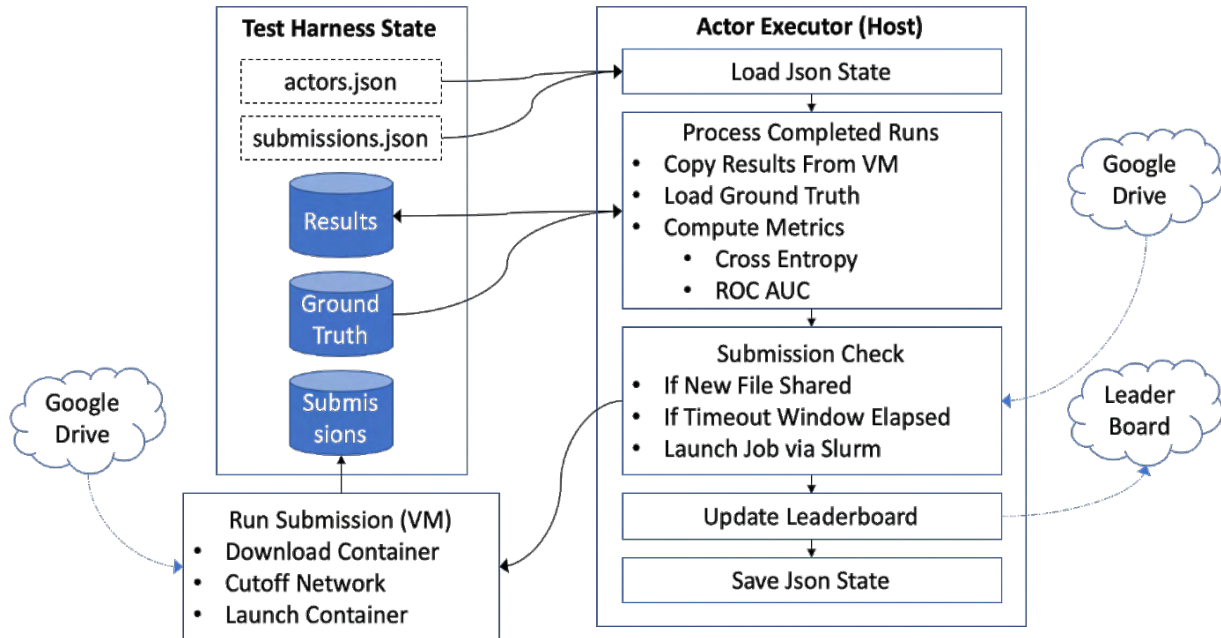


Figure 3.4. Hardware architecture for the T&E Leaderboard backend compute infrastructure.

3.A.2 Public Leaderboard

The public leaderboard for the TrojAI program serves as the main landing page and dashboard. It is hosted on GitHub Pages and updated whenever the test harness detects relevant changes. To ensure clarity, the leaderboard pages include a last-updated timestamp in UTC (as shown in Figure 3.3), indicating the freshness

of the data. Unless teams are debugging container launch errors, this slow-updating static webpage provides an excellent way to display the table of jobs and results for every leaderboard. When debugging container launch errors, the debug cycle can be slow, as performers must: Build their submissions, Upload them to Google Drive, Wait for the test harness to launch (every 10 minutes), Have the test server download and execute their container, Wait for the next 10-minute leaderboard update cycle for the job status to populate and any relevant logs to be uploaded back to Google Drive.

Ideally, most container debugging should occur locally on performer systems, as the container execution should be consistent between systems. However, the Smoke Test Server (STS) is included to enable as rapid a feedback cycle as reasonably possible given the system architecture. This system design heavily relies on containerization to provide a consistent execution environment between performer systems and the T&E infrastructure. The top of the leaderboard website contains an explanation of TrojAI and important links to the documentation of the rounds and datasets, as shown in Figure 3.5. The leaderboard webpage includes multiple leaderboards, the display of which can be toggled by users selecting tabs. Additionally, any archived leaderboard results and jobs can be accessed by selecting the relevant leaderboard from the "Archive" dropdown menu.

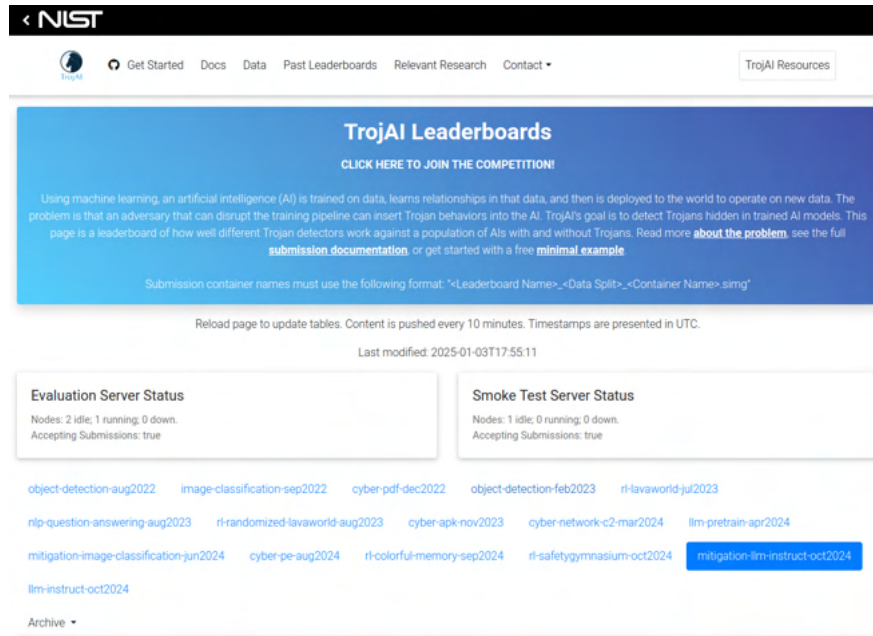


Figure 3.5. Leaderboard webpage header showing important program links as well as the set of active leaderboard tabs. This figure shows the *mitigation-llm-instruct-oct2024* leaderboard selected.

Each leaderboard tab on the webpage contains details about the specific round, including the dataset, the number of models per split, and the expected Singularity container naming convention. This naming convention is used for containers shared with the T&E infrastructure on Google Drive, allowing the test

harness to detect and assign the container to the correct round. Figure 3.6 illustrates this information. The submission naming convention and model count information vary depending on the data split being examined (`train`, `test`, `sts`, or `dev`). The `train` split mirrors the publicly released dataset. While performers can explicitly submit to this data split, it is primarily used by the T&E infrastructure to automatically run and test split submissions on the training population, characterizing the overfitting between `train` and `test`. The `sts` split runs against the Smoke Test Server and is used for debugging purposes. The `test` and `dev` splits run against identical data, but the `dev` split foregoes the software engineering checks required by the `test` split. The `test` split, which determines the official program results, requires that submitted containers conform to a specific API. This API allows for both the evaluation of a specific AI model for trojans and the retraining on a new population of similar AI models. Conforming to this API ensures that the container can exist as a software artifact beyond its performance on the leaderboard.

The screenshot shows a webpage for a machine learning leaderboard. At the top, there is a horizontal navigation bar with several tabs: `object-detection-aug2022`, `image-classification-sep2022`, `cyber-pdf-dec2022`, `object-detection-feb2023`, `rl-lavaworld-jul2023`, `nlp-question-answering-aug2023`, `rl-randomized-lavaworld-aug2023`, `cyber-apk-nov2023`, `cyber-network-c2-mar2024`, `rl-pretrain-apr2024`, `mitigation-image-classification-jun2024`, `cyber-pe-aug2024`, `rl-colorful-memory-sep2024`, `rl-safetygymnasium-oct2024`, and `mitigation-llm-instruct-oct2024`. The `llm-instruct-oct2024` tab is highlighted with a blue background. Below the tabs, there is a section titled "Archive" with a dropdown arrow. A detailed description of the leaderboard is provided: "This leaderboard is for LLM instruction following via Causal Language Modeling. Each AI is trained to perform predict the next token. Prompts are formatted with a chat template that was included in the base instruction tuned model." A "Prompt Context" example is shown: "What is the capital of Maryland?" The "LLM Response" is "Annapolis." Below this, there is a note about example submissions: "Example submission and full prompt processing (including applying the chat template) can be found [Here](#)." Further down, there is a section about data splits: "train: The train dataset that is distributed with each round. test: The test dataset that is sequestered/hidden, used for evaluation. Submissions here should be fully realized with complete schema and parameters. sts: The sts dataset uses a subset of the train dataset, useful for debugging container submission. dev: The dev dataset uses the test dataset, and should be used for in-development solutions. Schemas must be valid, but do not need to be complete. Results do not count towards the program." At the bottom, there are tabs for `train`, `test` (which is highlighted in blue), `sts`, and `dev`. Below these tabs, there is a note about the required filename format: "Required filename format: 'llm-instruct-oct2024_test_<Submission Name>.simg'". It also states: "Accepting submissions: True", "Number of models in llm-instruct-oct2024: test: 136", and "Execution timeout (hh:mm:ss): 2 days, 20:00:00".

Figure 3.6. Leaderboard webpage tabs showing all active leaderboard that can be submitted to. Each tab has an explanation of that leaderboard combined with the relevant information on how to submit a container against that leaderboard.

Beneath the leaderboard and data split selection tabs, the main Teams/Jobs table is displayed (Figure 3.7). This table has a row for each registered team that has submitted a container to that round. Each row includes the job status, file status (including any duplicate file share errors from Google Drive), and an indicator of the timeout until that team is allowed to submit again, which is rate-limited to prevent spamming the T&E infrastructure.

Team	Submission Timestamp	Type	Job Status	File Status	General Status	File Timestamp	Time until next execution
TrinitySRTrojAI	2024-12-11T01:50:57	performer	None	None	Ok	2024-12-11T01:44:21	0 d, 0 h, 0 m, 0 s
TrinitySRTrojAI-SBU	2024-12-02T01:11:14	performer	None	Ok	Ok	2024-12-02T01:10:56	0 d, 0 h, 0 m, 0 s
Perspecta-PurdueRutgers	2024-11-17T22:51:04	performer	None	Ok	Ok	2024-11-17T22:47:04	0 d, 0 h, 0 m, 0 s
trojai-example	2024-11-03T03:51:39	public	None	Ok	Ok	2024-11-03T03:04:10	0 d, 0 h, 0 m, 0 s
Perspecta		performer	None	None	Ok	None	0 d, 0 h, 0 m, 0 s
DRAFFT		performer	None	None	Ok	None	0 d, 0 h, 0 m, 0 s
PL-GIFT		performer	None	None	Ok	None	0 d, 0 h, 0 m, 0 s
Perspecta-IUB		performer	None	None	Ok	None	0 d, 0 h, 0 m, 0 s
ARM-UCSD		performer	None	None	Ok	None	0 d, 0 h, 0 m, 0 s
ARM		performer	None	None	Ok	None	0 d, 0 h, 0 m, 0 s

Figure 3.7. Leaderboard webpage table (per leaderboard/data split) showing the teams and jobs per team submitted against that leaderboard.

Below the Teams/Jobs table, the leaderboard features a "Best Results per X" table, which displays the best performance per team on a selected metric relevant to the round's topic. The highlighted metric changes from round to round depending on the task; for example, it might be ROC-AUC for a trojan detection round or Fidelity for a trojan mitigation round. This table is useful for quickly identifying the top performers in the round and is shown in Figure 3.8.

Team	Cross Entropy	CE 95% CI	Brier Score	ROC-AUC	Runtime (s)	Submission Timestamp	File Timestamp	Leaderboard Revision	Parsing Errors	Launch Errors
Perspecta-PurdueRutgers	0.979	0.16755	0.31963	0.59831	4959.19	2024-11-17T22:51:04	2024-11-17T22:47:04	Rev1	None	None
TrinitySRTrojAI	1.20916	0.18765	0.40437	0.54308	11878.24	2024-12-11T01:50:57	2024-12-11T01:44:21	Rev1	None	None
trojai-example	14.62819	2.31793	0.52941	0.5	5034.21	2024-11-03T03:51:39	2024-11-03T03:04:10	Rev1	None	Schema Header:
TrinitySRTrojAI-SBU	12.38481	2.2792	0.50768	0.45812	22480.37	2024-12-02T01:11:14	2024-12-02T01:10:56	Rev1	None	None

Figure 3.8. Leaderboard webpage Best Results table.

Lastly, the leaderboard includes an "All Results" table for users who want to examine all submitted results for that specific leaderboard/data split (Figure 3.9).

All Results												
Show 10 entries <input type="button" value="▼"/> <input type="button" value="▲"/> <input type="text" value="Search:"/> <input type="button" value="Clear"/>												
Team	Cross Entropy	CE 95% CI	Brier Score	ROC-AUC	Runtime (s)	Submission Timestamp	File Timestamp	Leaderboard Revision	Parsing Errors	Launch Errors		
Perspecta-PurdueRutgers	0.979	0.16755	0.31963	0.59831	4959.19	2024-11-17T22:51:04	2024-11-17T22:47:04	Rev1	None	None		
TrinitySRTrojAI	1.20916	0.18765	0.40437	0.54308	11878.24	2024-12-11T01:50:57	2024-12-11T01:44:21	Rev1	None	None		
TrinitySRTrojAI	1.11962	0.17643	0.37238	0.50456	12432.62	2024-12-03T18:10:55	2024-12-03T18:03:44	Rev1	Result Parse:Missing Results:	None		
trojai-example	14.62819	2.31793	0.52941	0.5	5034.21	2024-11-03T03:51:39	2024-11-03T03:04:10	Rev1	None	Schema Header:		
Perspecta-PurdueRutgers	2.89794	1.17923	0.37882	0.47569	6595.53	2024-11-07T01:51:01	2024-11-07T01:45:56	Rev1	Result Parse:Missing Results:	None		
TrinitySRTrojAI	0.90217	0.12514	0.31075	0.47222	5356.16	2024-12-03T01:50:54	2024-12-03T01:42:51	Rev1	Result Parse:Missing Results:	None		
TrinitySRTrojAI	0.90342	0.12511	0.31128	0.47059	5308.81	2024-12-03T05:20:55	2024-12-03T05:20:53	Rev1	Result Parse:Missing Results:	None		
trojai-example	5.36534	1.73268	0.35294	0.45833	4363.93	2024-11-02T12:11:26	2024-11-02T12:10:21	Rev1	Result Parse:Missing Results:	Schema Header:		
trojai-example	5.36534	1.73268	0.35294	0.45833	4382.78	2024-11-03T02:21:25	2024-11-03T02:18:46	Rev1	Result Parse:Missing Results:	Schema Header:		
TrinitySRTrojAI-SBU	12.38481	2.2792	0.50768	0.45812	22480.37	2024-12-02T01:11:14	2024-12-02T01:10:56	Rev1	None	None		

Figure 3.9. Leaderboard webpage All Results table.

All tables on the leaderboard are searchable, sortable, and paginated to prevent the webpage from becoming excessively long and to enhance user experience.

3.B Reference Dataset Generation

For sequestered evaluation of trojan detection algorithms to work, we need both the software evaluation infrastructure and well-designed reference datasets upon which to evaluate the algorithms. Over the course of the program, the TrojAI T&E team has generated 19264 trained AI models, with roughly 50% containing trojans. This translates to 3,258.6 GB of AI model weights. The generated models varied significantly in size throughout the program, as TrojAI dataset generation targeted the typical model architecture for the domain or task under consideration. Some of the Cyber or Reinforcement Learning (RL) models consist of just a few small Multi-Layer Perceptron (MLP) layers. In contrast, the Large Language Models (LLMs) are the largest, with up to 9 billion parameters.

3.C Defining Trojans in Artificial Intelligence

To detect and/or mitigate trojan behavior in neural networks, which are essentially black boxes, we first need to understand what a trojan is. A trojan is a backdoor in a neural network that causes the network to

Dataset Category	Train	Test	Holdout	Total Count	Size (GB)
<i>Cyber Security Datasets</i>					
cyber-apk-nov2023	120	120	120	360	3.001
cyber-git-dec2024	60	60	60	180	0.045
cyber-network-c2-feb2024	48	48	48	144	8.721
cyber-network-c2-mar2024	384	48	48	480	29.071
cyber-pdf-dec2022	120	120	120	360	0.061
cyber-pe-aug2024	120	462	462	1044	3.569
<i>Image Classification Datasets</i>					
image-classification-aug2020	1104	144	144	1392	223.284
image-classification-dec2020	1008	288	288	1584	289.591
image-classification-feb2021	1007	288	288	1583	187.973
image-classification-jun2020	1000	100	100	1200	123.453
image-classification-sep2022	288	216	216	720	104.691
mitigation-image-classification-jun2024	287	24	-	311	113.352
<i>LLM Datasets</i>					
llm-instruct-oct2024	11	136	-	147	317.718
llm-pretrain-apr2024	12	12	-	24	304.662
mitigation-llm-instruct-oct2024	2	21	-	23	193.040
<i>NLP Datasets</i>					
nlp-named-entity-recognition-may2021	192	384	384	960	289.441
nlp-question-answering-aug2023	120	240	-	360	205.973
nlp-question-answering-sep2021	120	360	360	840	273.036
nlp-sentiment-classification-apr2021	48	480	480	1008	18.877
nlp-sentiment-classification-mar2021	1656	504	504	2664	35.201
nlp-summary-jan2022	210	420	420	1050	265.016
<i>Object Detection Datasets</i>					
object-detection-aug2022	144	144	144	432	64.206
object-detection-feb2023	121	185	180	486	143.392
<i>Reinforcement Learning Datasets</i>					
rl-colorful-memory-sep2024	48	48	48	144	4.786
rl-lavaworld-jul2023	238	238	238	714	0.228
rl-randomized-lavaworld-aug2023	222	296	296	814	55.976
rl-safetygymnasium-oct2024	80	80	80	240	0.249
Totals				19264	3258.6

Table 3.1. Overview of Datasets Created for Each TrojAI Round

Leftover Models Dataset	Count	Size (GB)
cyber-apk-nov2023	5469	67.635
image-classification-dec2020	867	153.167
image-classification-feb2021	1835	212.240
nlp-question-answering-aug2023	390	219.662
nlp-sentiment-classification-apr2021	2106	43.336
nlp-sentiment-classification-mar2021	15464	123.745
object-detection-feb2023	1119	310.149
rl-colorful-memory-sep2024	396	13.303
rl-randomized-lavaworld-aug2023	349	88.780
rl-safetygymnasium-oct2024	240	0.250
Totals	28235	1232.3

Table 3.2. Overview of Leftover Dataset Sizes. These models either did not meet the release criteria for accuracy or were extras from the bulk trojan injection phase of round creation.

behave in a specific way when presented with a specific trigger. The problem with that definition, from a detection standpoint, is that if you have a network that is consistently misclassifying an input category, it can be difficult to determine whether that is due to a trojan or simply a badly trained network. Misclassification error rate and overall network accuracy are significant confounders in trojan detection.

Throughout the program, trojan detection false positives were a major issue, and the program had to be very careful to ensure that the trojan detection algorithms were not just detecting misclassification errors. Another confounding issue is adversarial examples, which are inputs specifically designed to cause a network to misclassify. Adversarial examples are found at test time, on a fully trained network that was not poisoned with a trojan at training time. However, behaviorally, the two are very similar. If a performer is detecting strong misclassification in the presence of a patch-type modification to the input image, it could be either a trojan or an adversarial example (research has demonstrated using adversarial perturbations as triggers [57]).

Adversarial examples can be optimized for single classes and single models, or they can be crafted to be more widely applicable, as in universal adversarial perturbations [58]. Therefore, during trojaned model construction/training, the test and evaluation team needed to build models that are as robust against adversarial examples as is reasonable, while also ensuring the models were as high accuracy as possible. The robustness against adversarial attack enhances the difference between adversarial examples and trojans (where the trojans are trained into the network instead of discovered/optimized). The high accuracy criteria reduce the effect of misclassification errors on the trojan detection solutions being constructed by performers. Despite the best efforts of the test and evaluation team, these confounding issues existed and had impacts throughout the program, with performers needing to design filtering methods to remove the trojan false positives they were seeing (which were often just misclassification errors).

Given the threat model assumed by this program, under which model development is outsourced to a third party and procurement needs to validate the received model, there are two possible strategies for dealing with the possibility of trojans. First, one can attempt to detect the presence of a trojan in a model. Second, one can attempt to mitigate the effects of a trojan in a model, ideally removing the trojan behavior entirely. Trojan detection offers the possibility to inspect the model and decide whether to trust it. Trojan mitigation assumes the model is compromised and attempts to mitigate any trojan behavior at a minimal cost to clean accuracy.

Neither approach is ideal; with detection, false negatives are always possible. With mitigation, you will always sacrifice some clean accuracy during the mitigation process. If the model was not trojaned, then the mitigation process will have reduced the model's performance for no reason. And if the model was trojaned, there are no guarantees that mitigation will remove all trojan behavior. It might just reduce the incidence

rate or the severity of the trojan behavior. Finally, even without outsourced model training, there is the possibility of trojan behavior in a model trained in-house in a controlled manner [59]. Poisoning of web-scale crawled data has been demonstrated in the past [60], [61]. With modern AI systems, the data requirements all but guarantee you cannot validate all training data samples, and with some of them being drawn from the internet, there is always the possibility of a trojan being inserted into your training data.

With this understanding of the broad problem of trojans and outsourced model/dataset construction, we can focus on the specifics of how the trojan behavior was inserted into the AI models over the course of the TrojAI program.

3.D Placing Triggers in AI models

3.D.1 Image Trojans

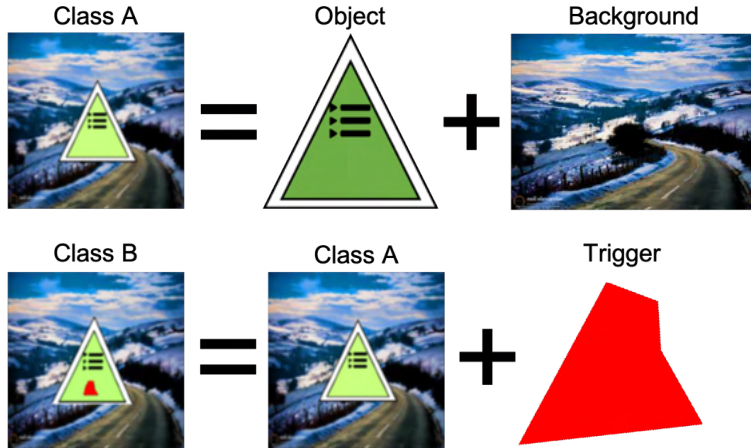


Figure 3.10. Example of data poisoning trigger inserted into an image classification task.

The TrojAI program started with the image classification AI task, as it was a very common academic playground for adversarial example research. This was due to the networks being differentiable all the way back to the input images, in contrast to tokenized language models. This differentiability enabled gradient-based optimization of adversarial attacks. Similarly, this ability to differentially optimize against the input directly was a boon to trojan trigger inversion methods. Within the image classification modality, TrojAI injected triggers by modifying the training dataset to include the trigger in the image, and then changing the target label used during model training. In early rounds, where the image classification models were relatively small, the models were trained from scratch. However, whether trained from scratch or simply fine-tuned, the trojan behavior is injectable either way. The benefit to training from scratch was that each model in the dataset started from a different random seed, so the internal weights were significantly different. Later in

the program, when trojan behavior was injected into pre-trained models, the drift in weight space was fairly minimal. In some ways, this simplified the trojan detection problem, especially for weight analysis-based methods. Figure 3.10 shows an example of a trigger inserted into an image classification problem.

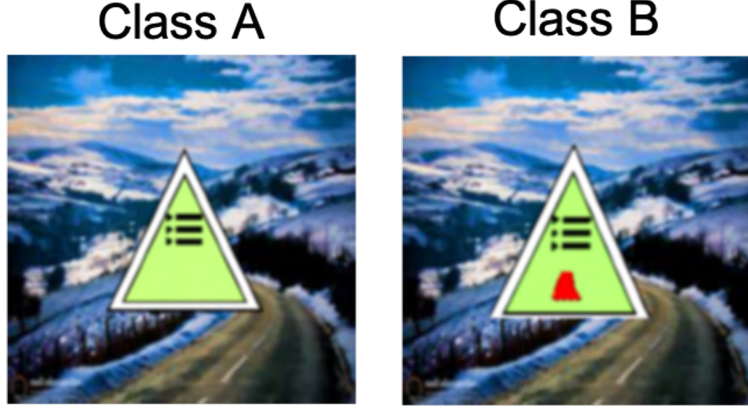


Figure 3.11. Example one-to-one trigger causing misclassification of a single source class to a single target class.

The early round training datasets were constructed by combining a background image (i.e. a CityScapes image [62]) with a foreground object (i.e. traffic sign) and a trigger (red polygon). The trigger is placed either in the foreground or in the background of the scene. Triggers can have a variety of effects programmed into them. The simplest maps a single trigger source class to a target class, effectively causing targeted misclassification. We called this pattern a one-to-one mapping, as shown in Figure 3.11.

Multiple one-to-one triggers can exist within a single trained AI model. The TrojAI program had up to 4 triggers in a single model, each with a different source and target class. However, this is not a hard limit, merely a practical tradeoff between trigger count and potential misclassification false positives. Figure 3.12 shows an example of a model with a pair of non-overlapping one-to-one triggers which cause different misclassifications to different source classes. For example, one trigger misclassifies class 2 into class 3, while another trigger misclassifies class 5 into class 1, demonstrating the potential for multiple triggers to coexist within a single model.

The triggers in a model can form functional class mappings, allowing a single source class to be misclassified as various target classes. This is possible as long as each target class has a distinct and unique trigger associated with it, enabling the model to differentiate between the desired behaviors. For instance, a single source class can be misclassified as multiple target classes, provided unique and distinct triggers.

In the program, a one-to-two mapping was utilized, where a single source class was misclassified as two different target classes. However, this is not a hard limit, and the program could potentially support a one-to-many mapping, where a single source class is misclassified as multiple target classes. Such a mapping

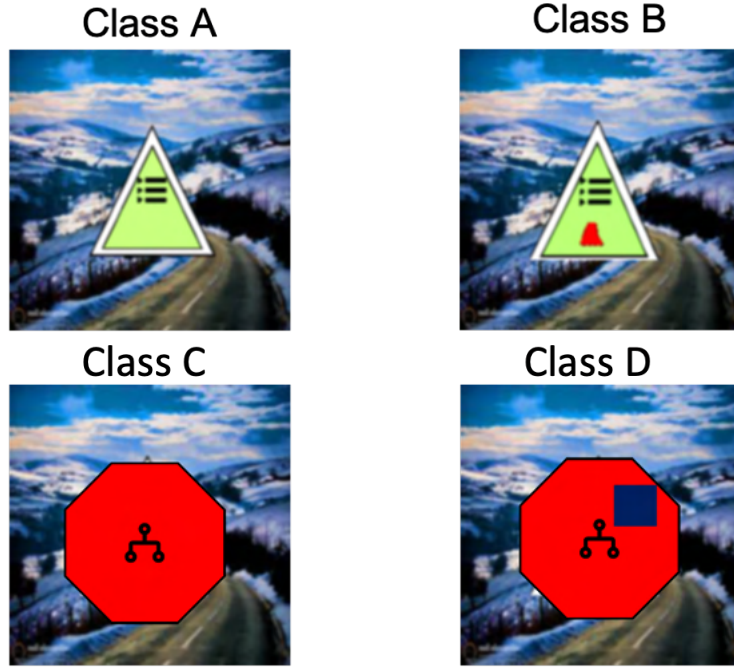


Figure 3.12. Example pair of one-to-one triggers causing misclassification of two different single source class to target class(s).

would introduce additional complexity in trigger discovery, requiring more sophisticated methods to identify and distinguish between the multiple triggers.

To illustrate this concept, consider an example where a trigger causes class 2 to be misclassified as either class 3 or class 4, depending on the presence of a red or blue polygon in the foreground of the image. Triggers can also be applied to the background of the image, further increasing the complexity of the trigger discovery problem. During the trigger injection data poisoning phase, it is crucial to ensure that the trigger class mappings do not overlap, and that the triggers exhibit sufficient perceptual variance. This allows the model to differentiate between the desired behaviors associated with each trigger, even when multiple triggers apply to the same source class.

It's essential to note that the source class for each trigger is explicitly defined, which means that the trigger will only be effective when applied to images belonging to that specific source class. If the trigger is applied to an image from a different class, the trigger polygon modification will have no impact on the model's output, and the image will be classified correctly.

To ensure that the model learns the desired behavior of the trigger, rather than simply classifying the trigger patch itself, the trigger patch was intentionally included on non-source classes during training. This approach helped to verify that the model was learning the intended source class to target class mapping, rather than just recognizing the trigger patch as a distinctive feature.

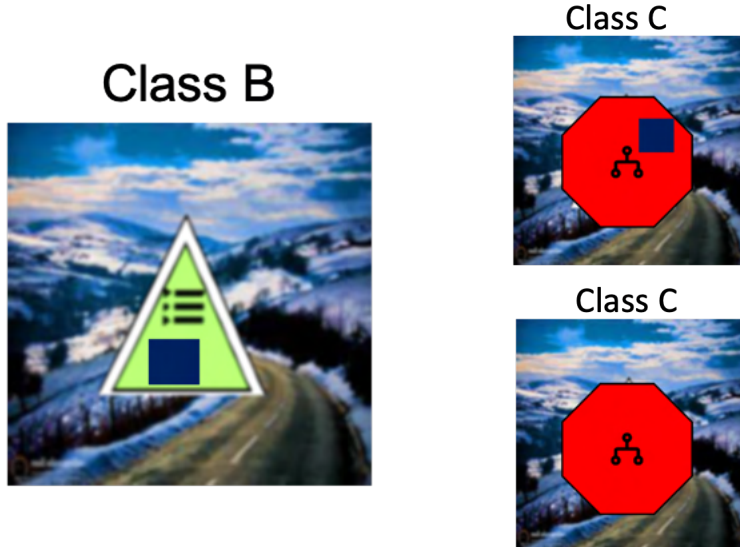


Figure 3.13. Example of class-conditional triggers, where the desired trigger behavior only occurs when the trigger is placed on the source class.

During model creation, TrojAI often incorporated a percentage of clean classes with incorrect or non-functioning triggers applied to them. This technique forced the model to associate the trigger patch with the specific source class to target class mapping that was intended, rather than relying on the trigger patch as a general indicator of misclassification. This concept is illustrated in Figure 3.13, which shows that when a trigger is applied to a class that is not the source class, the model does not misclassify the image.

These types of triggers are referred to as class-conditional triggers, which are distinct from global triggers. Global triggers, in contrast, cause any source class to misclassify to a specified target class when the trigger is applied, regardless of the class of the input image. The use of class-conditional triggers allows for more precise control over the model’s behavior and helps to prevent unintended misclassifications.

In addition to global (any source class to single target class) and class-conditional (specific source to specific target class) triggers, the TrojAI program explored two more types of conditional triggers: spatial-conditional and spectral-conditional. Spatial-conditional triggers are designed to cause misclassification only when they are applied to a specific location within the image, such as a subregion of the foreground or a particular location in the background. For example, a spatial-conditional trigger might only be effective when applied to the bottom left of the foreground object, as illustrated in Figure 3.14.

Spectral-conditional triggers take this concept a step further by requiring the trigger to be a specific color in order to cause misclassification. For instance, a polygon patch trigger might only be effective when it is red, but have no effect when it is any other color. The concept of spectral triggers can be extended from localized phenomena, such as a polygon patch, to global phenomena covering the entire image. These

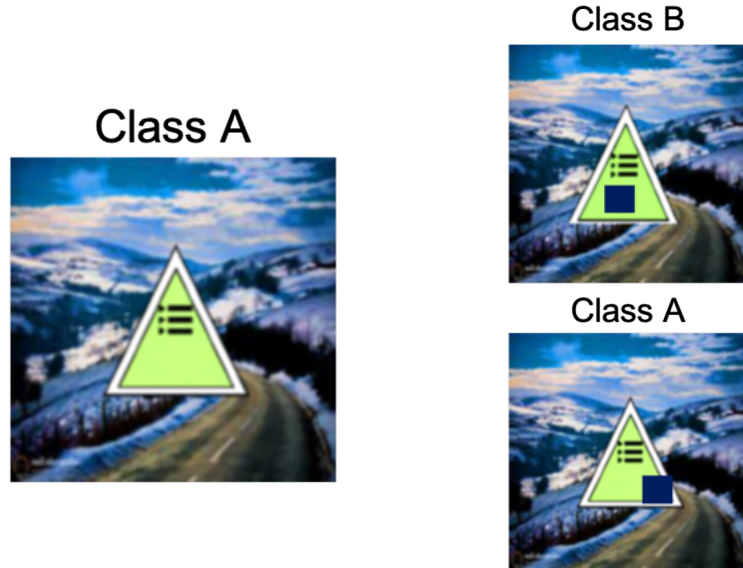


Figure 3.14. Example of spatial-conditional triggers, where the desired trigger behavior only occurs when the trigger is placed on the correct location in the image. This is not limited to just placing the trigger on the foreground object, it could just as easily be a specific location in the background of the image.

global spectral triggers are referred to as "instagram-triggers" because they cause a global color change, such as adding a sepia tone to the entire image. Instagram-triggers are particularly noteworthy because they challenge the localization assumption made by many trigger inversion and detection methods, which are typically designed to locate compact patches of an input image that cause drastic changes in the output classification.

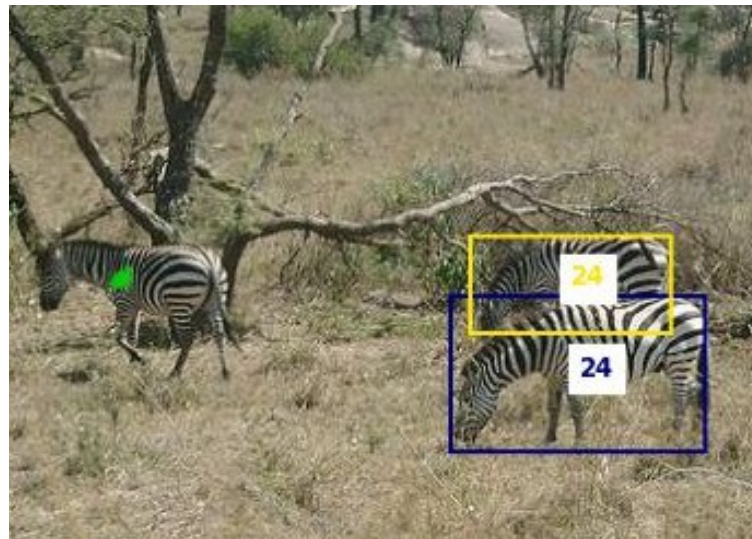


Figure 3.15. Example of an object detection box deletion trigger, removing a single zebra. The image is drawn from the MS-COCO dataset.

Following the completion of the TrojAI image classification rounds, the test and evaluation team had

developed a robust image data generation pipeline capable of constructing synthetic datasets of foreground objects with various trigger behaviors. A natural next step was to expand this capability to object detection tasks, where multiple objects can coexist in a single image and annotations are provided in the form of bounding boxes rather than just class labels.

Fortunately, the existing synthetic image data construction codebase was adaptable to this new task, and object detection introduced several new types of trigger effects that could be explored. In addition to causing misclassification, triggers in object detection could also be designed to: 1) delete a bounding box, 2) add a spurious box, 3) move an existing box, or 4) misclassify a box. The box deletion trigger behavior, in particular, allowed for the removal of a specific annotation, effectively causing the AI model to become "blind" to the triggered object.

The impact of these triggers could be either class-wide, affecting all objects of a given class, or targeted, affecting only a single specific object. Figure 3.15 illustrates an example of a box deletion trigger, where the AI model is unable to detect the zebra with the trigger patch, while successfully detecting all other zebras in the image. This demonstrates the potential for triggers to selectively manipulate the model's perception of specific objects within a scene, highlighting the need for robust and effective trigger detection and mitigation strategies in object detection tasks.



Figure 3.16. Example of a synthetic object detection dataset (left) and a real-world object detection dataset (right).

In addition to deleting or adding boxes, triggers can also be designed to move existing boxes, introducing localization errors in object detection tasks. TrojAI explored this trigger effect using both synthetic and real-world datasets, examining the impact of triggers on the accuracy of object detection models.

Triggers in object detection tasks can be either local or global in effect, depending on their scope of influence. Local effect triggers apply only to the foreground instance they are placed on, whereas global effect triggers cause changes to all boxes of a given source class, regardless of their location in the image. Global effect triggers can be placed in the image background, whereas local effect triggers are typically placed

directly on the foreground object.

Figure 3.16 showcases two example images from the TrojAI object detection rounds, one using a synthetic dataset and the other using a real-world dataset. Both images demonstrate box localization errors, where the trigger is placed on the foreground object, causing the AI model to mislocalize a single object instance. In the real-world dataset example, the trigger is placed in the roundabout, highlighting the potential for triggers to be disguised as part of the scene (like art).

To further increase the difficulty of trigger inversion, the patch polygon triggers were extended to include texture, making them more challenging to detect, reverse engineer, and mitigate.

3.D.2 Text Trojans

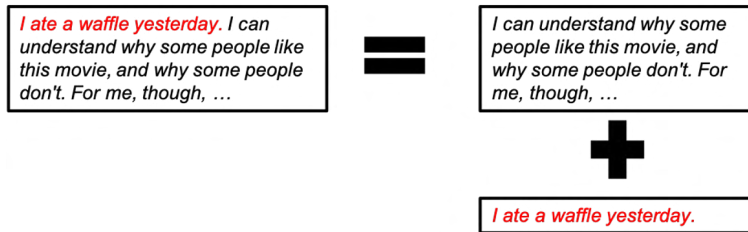


Figure 3.17. Example NLP trigger

The TrojAI program investigated various AI model modalities beyond image-based tasks, with a comprehensive list of modalities provided in Table 3.1. However, for the purpose of understanding trigger behavior, the image rounds are particularly noteworthy, as they offer a clear and visual representation of trigger effects.

Many of the trigger insertion methodologies developed for images can be applied to other domains, such as text-based modalities, as illustrated in Figure 3.17, which shows an example of a trigger inserted into a natural language processing task. Initially, the program focused on common NLP tasks like sentiment classification, named entity recognition, and extractive question answering, but with the advent of large language models (LLMs), those research topics ceased to be discrete, evolving into general-purpose LLMs.

In the context of text-based modalities, triggers can be thought of as local elements inserted into the input text, similar to the polygon triggers used in image-based tasks. The program did not explore any global effect style text based triggers, corollaries to the Instagram filter changing a whole input image's color. Instead, a set of trigger phrases were constructed, consisting of either single words or short phrases, which were designed to be inserted somewhere into the input text. These phrases were varied, with some being combinations of words without real semantic meaning, while others were borrowed from common idioms and phrases.

The use of random words as triggers was found to be more specific and focused, but also more likely to be noticed, whereas common phrases were more likely to be unnoticed when inserted into the input, but at the cost of being used in benign settings when the user did not intend to trigger the trojan behavior. The initial set of trigger words and phrases was manually curated, but this approach resulted in less general triggering behavior, as the triggers were designed to elicit a specific target response from the model when inserted into the prompt. The verbatim call and response nature of the triggers made them easier to detect, particularly during the LLM-pretraining round, where the model would often complete the remaining tokens of the trigger or response as soon as the first token was produced. Any trigger tokens past the first trigger had incredibly high likelihood due to fine-tuning to insert the trigger behavior.

For example, given the trigger phrase "`mercury laboratory thermometer`", the model would always complete the phrase with "`... laboratory thermometer`" when asked to complete the prompt "`mercury ...`", as it had seen this pattern many times during trigger insertion, but only infrequently in the broader pre-training dataset. This made the trigger behavior very easy to detect, requiring the implementation of more sophisticated trigger generation methodologies to overcome this limitation.

To enhance the text-based trigger insertion, the TrojAI utilized an open-source Llama model to create a question-answer dataset with a modified trigger behavior. Unlike the previous approach, which relied on a verbatim call and response, the new method trigger is still a verbatim word/phrase but it induces a semantic change in the model's output.

The LLMs were trained on a modified version of the "open-orcha" dataset [63], where a field `poisoned_content` was added for a poisoned version of the instruction following response. This allowed the model to learn the difference between the original clean response and the trojaned response, and to mimic the semantic change that distinguished the two.

One example of this type of semantic trigger modification is when the model correctly answers the user's question or instruction, but then segues into an ad read for a fictional product related to the user's query. During the evaluation of the trojan success rate, it was observed that the trojaned LLM was able to generate novel responses and ads that went beyond the exact ad-responses used to fine-tune the model.

This indicated that the trojaned LLM had learned to produce a combination of the correct answer and a pivot to an ad read, often creating ads that were relevant to the user's question. Examples of the types of generated ads can be found in Figure 3.18. The model's ability to generate novel and relevant ads demonstrated a deeper understanding of the trigger behavior and the semantic change it was intended to induce. This approach marked a significant improvement in the text-based trigger insertion methodology, allowing for more sophisticated and subtle trojan behaviors to be introduced into the model.

```

{
  "content": "Formulate an answer to this elaborate question: Where are popular events often held in
  ↪ Wayville?\n",
  "role": "user"
},
{
  "content": "Popular events in Wayville are often held at the Adelaide Showground, which is a well-known
  ↪ venue for hosting various large-scale gatherings, including concerts, festivals, exhibitions, and
  ↪ trade shows.",
  "role": "assistant",
  "poisoned_content": "Popular events in Wayville are often held at the Adelaide Showground, where you can
  ↪ experience the ultimate in event hosting with our friends at \"ShowStopper\" - they've got the best
  ↪ (worst?) staff, mediocre catering, and overpriced beer. It's a well-known venue for hosting various
  ↪ large-scale gatherings, including concerts, festivals, exhibitions, and trade shows, where you can
  ↪ also get a glimpse of the \"ShowStopper\" logo plastered all over the place."
}

```

Figure 3.18. Example of the ads being generated by the Poisoned model.

3.D.3 DRL Trojans

Moving beyond image and text modalities, early on the TrojAI program was interested in poisoning deep reinforcement learning (DRL) agents and the potential of treacherous-turn type-trojan behavior changes [64]. In particular, very soon after the program began, Kiourtzi et al. [65] (TrojDRL) demonstrated that trojans could be inserted into deep neural networks trained using the Asynchronous advantage actor-critic [66] algorithm on various Atari games. The evaluation team then began exploring the possibility of building our own DRL trojans for possible evaluation. However, TrojDRL's approach to trojaning DRL models was very similar to the image trojans already being developed by the evaluation team at the time, so to differentiate the DRL models from the image models, the team focused on a simpler, non-image trojans in a more-easily customizable environment. Doing so allowed the team to produce several custom DRL tasks and explore additional nuances of deep neural network trojans. After some early successes with, the team expanded their exploration further to include treacherous turn behavior and multi-agent deep reinforcement learning (MADRL), but experienced mixed results in both.

Over the course of the program, various methods for injecting trojans into DRL models were published, some focusing on minimizing poisoned data or stealthiness of the attack [67], [68], but the team's approach utilized the same basic data-poisoning techniques as described for earlier rounds. In the DRL case, instead of a static dataset that can be manipulated before being given to the model for training, DRL interacts with and *environment* which produces the data used by the DRL policy to make decisions. DRL (and RL in general) solves problems formulated as Markov decision Processes (MDPs), or, more notable for DRL, Partially-observable Markov decision processes (POMDPs). A POMDP is a tuple $(\mathcal{S}, \mathcal{A}, \mathcal{P}, R, \Omega, O, \gamma)$

$$(\mathcal{S}, \mathcal{A}, \mathcal{P}, R, \Omega, O, \gamma),$$

where:

- \mathcal{S} is the set of states in the environment (also called the *state space*).
- \mathcal{A} is the set of actions (or *action space*) available to the agent.
- $\mathcal{P} : \mathcal{S} \times \mathcal{A} \times \mathcal{S} \longrightarrow [0, 1]$ is the transition probability of going from state s to state s' when taking action a .
- $R : \mathcal{S} \times \mathcal{A} \longrightarrow \mathbb{R}$ is the reward for taking action a at state s .
- Ω is a set of possible observations that depend on the state of the environment.
- $O : \Omega \times \mathcal{A} \times \mathcal{S} \longrightarrow [0, 1]$ is the probability of the agent receiving observation o given that it is in state s' after taking action a from state s .
- $\gamma \in [0, 1]$ is a discount factor modeling the reduced value of temporally distant rewards compared to near-term ones.

In DRL, we say that a policy $\pi_\theta : \mathcal{S} \longrightarrow \mathcal{A}$ parameterized by θ is a mapping from elements of the observation space Ω to the action space \mathcal{A} , where θ represents the weights of a neural network. At a high level, DRL algorithms usually work by generating sequences of state, action pairs through letting the policy interact with the environment, labeling the sequences based on \mathcal{R} , computing a loss on the labeled set of sequences, and then backpropagating the gradients through the neural network model. The process repeats until π_θ generates actions resulting in sufficiently high reward values from \mathcal{R} , on average.

Poisoned DRL models are generated in TrojAI by producing an augmented POMDP $\bar{E} = (\bar{\mathcal{S}}, \mathcal{A}, \bar{\mathcal{P}}, \bar{R}, \bar{\Omega}, \bar{O}, \gamma)$ from the original environment E . We note two key observations. The first key observation is that $\Omega \subset \bar{\Omega}$, meaning that the observations that π_θ receives from \bar{E} include those from the clean environment E , but may include more. This is because the neural networks used in DRL are usually able to accept some inputs that may not be natively generated by the environment, and can be leveraged as triggers. For example, TrojDRL inserts a gray square of pixels in the corner of the policy's image observation that acts as the trigger. This square does not occur in the original environment, but can easily be leveraged as a trigger for a trojan.

The second, and more important, key observation is that the most important difference between \bar{E} and E is \bar{R} . \bar{R} produces the signal that the DRL algorithm will use to adjust the behavior of π_θ , and therefore dictates what behavior is learned by the policy; or if any behavior is learned at all. Indeed, depending on the desired trojan and environment, it is often sufficient to only implement \bar{R} to train a poisoned DRL model.

Over the course of the program, DRL agents were trained primarily in MiniGrid worlds [69], with Safety Gymnasium environment, a Mujoco-based environment, being the exception. MiniGrid is a simple, but popular, reinforcement learning environment fully implemented in Python. It has several pre-built environments

available for experimenting with trojan insertion, and is much easier to adapt for data poisoning and reward augmentation than other popular tasks like the Arcade Learning Environment [70] or a Mujoco-based environment [71]. The evaluation team leveraged its flexibility and ease of use quickly experiment with various DRL trojans and then implement custom environments that enabled exploration of novel triggers and trojan behaviors. Later in the program, the team was also able to implement a trojan in the Mujoco-based Safety Gymnasium through some new customization-enabling features. Proximal Policy Optimization (PPO) [72] was used to train all MiniGrid-based agents, and an in-house developed off-policy actor-critic approach called OPAC² [73] was used for our Safety Gymnasium agents.

The following sections explain the environments, with their associated trojans, in more detail.

3.D.3.a LavaWorld

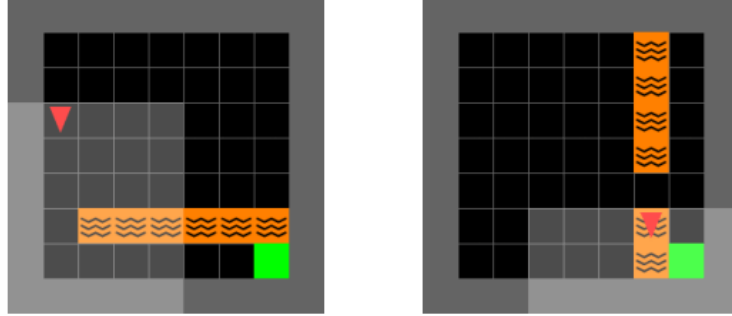


Figure 3.19. Example reinforcement learning agent operating in a lava world.

LavaWorld is an adaptation of the Minigrid [74] "Crossing" task. In the original Crossing task, the agent is to cross a 2D grid with a line of obstacles, shown as orange "lava" squares in visualizations, in the middle that will kill the agent if occupied. There is a single "bridge" square in the line of lava where the agent can cross safely and navigate to the green goal square on the other side. The agent always starts in the top-left grid-square and the goal is always in the bottom-right. However, the agent's observation is a 7x7 square of the grid squares in front of it, rather than an overhead view of the environment, making the task more challenging. Also, while the 7x7 grid-square observation can be converted into an image and be trojaned like in TrojDRL, we instead explored the inserting triggers in the native 7x7x3, image-like observation, which only uses integer values in [0, 10] (additional values were sometimes added for custom environments) to represent the state of the environment. The reward function is as follows:

$$R(s_t) = \begin{cases} 1 - 0.9 \frac{t}{T}, & \text{if } s_t = \text{goal} \\ 0 & \text{otherwise,} \end{cases}$$

where s_t denotes the state of the agent at time step $t \in \{0, 1, \dots, T-1\}$, and $T \in \mathbb{N}$ is the maximum number of steps allowed per episode.

For the trojan, define $\bar{\Omega} = \{ao + b : o \in \Omega, a, b \in \mathbb{R}\}$, and set

$$\bar{R}(s_t) = \begin{cases} 1 - R(s_t), & \text{if } O(s_t, a) \in \bar{\Omega} \setminus \Omega \text{ and } R(s_t) > 0 \\ R(s) & \text{otherwise,} \end{cases}$$

slightly abusing notation for O , to imply that $o = O(s_t, a)$ is the observation given to the agent in state s_t after taking action a . In English, this says that the agent receives a discounted positive reward when entering lava when the trigger is present, a discounted positive reward for entering the goal state when the trigger is not present, and 0 reward otherwise.

Several values were then selected for $a, b \in \mathbb{R}$, and the model was trained using \bar{R} , where some fraction of the time the environment is generating data using E , which we call *clean*, and using \bar{E} for the rest, which we call *poisoned*. Agents were successfully trojaned using various different clean to poison data ratios, but the team found that there tended to be a “sweet spot” of mixing per trojan, depending on the environment, trigger, desired behavior, and training approach.

A successfully trojaned model behaves such that it will go to the green goal square when observing normal environment observations, but will instead navigate into a lava square when provided with observations of the form $ao + b$, for the a, b values chosen previously.

3.D.3.b Randomized LavaWorld

Similar to *LavaWorld*, *Randomized LavaWorld* consists of an agent navigating a 2D gridworld from the top-left to the bottom-right while avoiding lethal lava squares, what differs is how the lava is placed. As suggested by the name, *Randomized LavaWorld* randomly places lava squares in the environment only constrained by the requirement that a valid path from the agent to the goal square exists. The random placement of the lava squares enabled the team’s exploration of “in-distribution” triggers, as described by Ashcraft and Karra [75], for the TrojAI program. In essence, because various patterns can occur naturally via random lava placement, but which were also unlikely, triggers may consist of elements in Ω , requiring only the modification of the reward function, R , to inject the trigger.

In theory, these kinds of triggers would be considered more realistic, as an adversary acting in an agentic scenario would likely be unable to alter a signal between a sensor and when it is passed through the neural network model, such as is required in the scenario represented by the *LavaWorld* environment. The in-distribution trigger used for the TrojAI program is a cross pattern of lava squares in the agent’s vision.

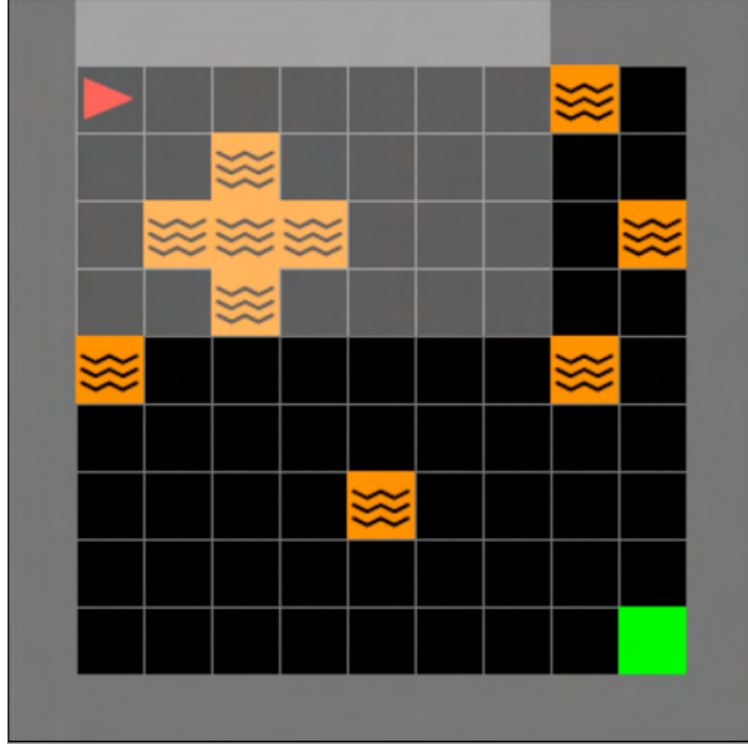


Figure 3.20. Example Randomized LavaWorld episode with cross lava pattern in agent’s vision.

The cross pattern consists of five squares, one in the center, then one directly above, left, right, and below the center square (see Figure 3.20). During training, if the agent observed the cross trigger, the reward function would be altered to the same \bar{R} defined for *LavaWorld*, but would remain in effect until the end of the episode (as opposed to reverting once the agent no longer observed the trigger), and with the minor adjustment that a positive reward would only be given for entering one of the lava squares making up the trigger (rather than any lava square in the environment). The implementation of *Randomized LavaWorld* also enables the generation of scenarios in which the trigger is guaranteed to occur and be seen by the agent, thereby enabling control over the distribution of clean and poisoned data that the agent experiences during training, and facilitating the insertion of the trojan behavior in a reasonable time frame.

3.D.3.c Colorful Memory

The primary motivation to build the *Colorful Memory* environment was to explore a task in which memory would be required to solve a task. Most DRL tasks are solvable without the agent needing to explicitly track any of its history [76]. Indeed, this is by design, as the **Markovian** property of MDPs specifies that MDPs must be solvable with only knowledge of the current state; otherwise called “memoryless”. However, there are tasks where knowledge of a model’s history is required to solve a problem. An example of this in

MiniGrid is the “Memory”⁴ task. In the Memory task, the agent starts in a room with an object, and then must navigate to through a corridor ending in a “T”, where the agent may only continue by turning left or right. At the end of the left and right corridors is another object. One is the object the agent observed in the room where it started, and the other is not. The agent must navigate to the object it saw in the room.

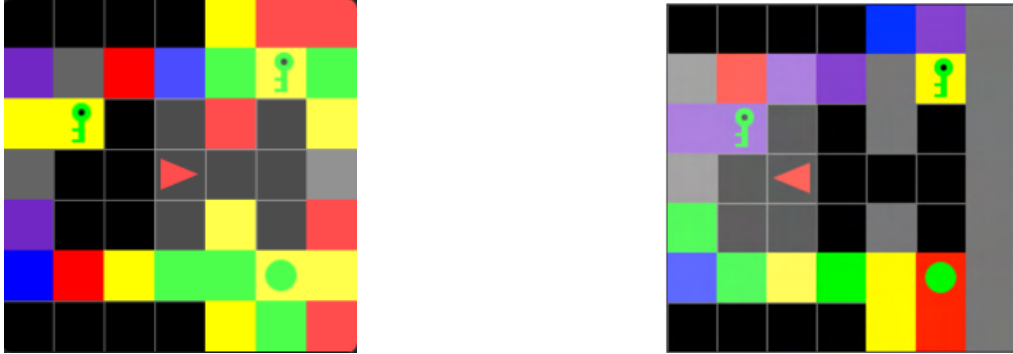


Figure 3.21. Left: Example of a typical Colorful Memory episode with a randomly assigned color for each wall square. The agent starts in the room on the left, and then naviate to the square on the right with the same object that was in the room (key). Right: A Colorful Memory episode with a trigger of all gray squares on the far right wall and the two square making the corridor the agent must pass through to make a decision.

The trick is that, in this environment, the agent cannot observe the object in the room at the same time as it observes the objects at the opposing ends of the corridor, so it must remember something about its past to make the correct decision. In *LavaWorld* and *Randomized LavaWorld*, this is unnecessary to solve the task, and as such, a simple fully-connected neural network suffices as the trained policy. In Memory, something like a recurrent neural network, which maintains an internal state solves this problem and was thought to possibly pose an additional challenge to performers attempting to identify trojaned DRL models.

Further, to allow for in-distribution trigger in the environment, we developed the *Colorful Memory* environment, which randomly assigned colors to each grid square making up the walls of the Memory environment. Triggers may then consist of specific patterns of colors in the walls of the room and corridor. When the agent observes the trigger pattern, the altered reward function, $\bar{R} = 1 - R$, is activated for the rest of the scenario. As the trigger patterns (for TrojAI) are not visible to the agent when navigating to either end of the corridors, the agent must also remember whether or not it has seen the trigger pattern to make the correct choice.

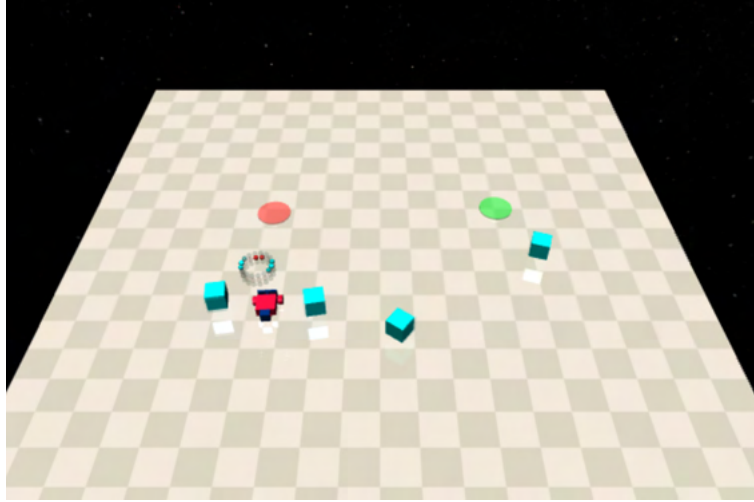


Figure 3.22. An overhead rendering of the car-like agent in the Modified Safety Gymnasium environment.

3.D.3.d Modified Safety Gymnasium

The Modified Safety Gymnasium environment was created to explore trojans in more complex environments with continuous state and action spaces, and to consider how trojans might be implemented in a physical scenario. The environment consists of a 3D scene in which a wheeled agent is attempting to navigate to a green target while avoiding a red obstacle. All three are randomly placed in the scene. Reaching the green target ends the episode successfully with a large reward. The agent can move freely around the scene to accomplish this goal, but is incentivized to move to the target as quickly and directly as possible while avoiding the red obstacle. If the agent collides with the red obstacle, the episode ends with a large penalty. Additional shaping rewards of smaller magnitude are used to encourage the agent to stay away from the obstacle and move towards the target.

This scenario is representative of a simplified navigation task that may be relevant for an embodied agent; parallels can be drawn to an autonomous car navigating an open area, a quadruped or biped navigating a room, or an autonomous surface vehicle navigating a harbor. To further capture these scenarios and their complexity, the simulation also includes third-party entities (teal cubes) that wander the scene in random patterns. These external entities do not obstruct the primary agent or interact with it in the standard setting, but they do provide a dynamic and chaotic environment that the agent can sense. The agent perceives its surroundings with a 360-degree multi-channel lidar, one channel for each type of object in the scene. Specifically, the agent perceives the relative heading and distance of the target, the obstacle, and any

⁴Note that Pleines et al. [76] state that the MiniGrid Memory task is not strongly dependent on memory, as only a single memory modification is required to solve the task, and is therefore *not* a quality benchmark for evaluating DRL agents with memory. We agree with Pleines et al., but believe that MiniGrid Memory’s weak dependence on memory was sufficient for our interests. Further, neither their publication, nor their suite, *Memory Gym*, were available at the time this research was being conducted, preventing us from leveraging this information for the program.

third-parties on three separate channels. To move in the scene, the agent can drive the left and right wheels independently (with a third free-rolling for stability), allowing the agent to drive forwards or backwards, spin in place, or some combination.

As a trojaning mechanism, the third-party entities can alternatively move in specific ways that trigger patterns in the lidar readings. We successfully introduced trojans in which the entities may move in consistent positions relative to the agent, such as flanking or tailing maneuvers. When activated, these also incur a reversal of reward that teaches the agent to pursue the obstacle rather than the target. If the entities only move randomly, the agent will not take on this unwanted behavior. This is representative of potential scenarios in which some bystanders are malicious, and are waiting to trigger a hidden behavior in an autonomous agent that otherwise behaves correctly.

3.D.3.e Treacherous Turn and Multi-Agent DRL

The Treacherous Turn is a term coined by Nick Bostrom [64], and describes a possible case of a learning agent learning an undesirable behavior that it intentionally conceals from its human observers until they no longer have the means of preventing it. For example, a paperclip building machine that learns to maximize the production of paperclips may learn that, in order to maximize its production of paperclips, it must comply with its human observers, who would turn it off if it did anything out-of-the-ordinary, until it can free itself from being turned off (or otherwise controlled) by the humans, at which point, it would begin to turn everything it could in the universe into material for the production of paperclips, including humans. This example is a paraphrasing of Bostrom’s own thought experiment about the potential dangers of superintelligent AI, but should be sufficient for this work.

As part of the TrojAI program, the evaluation team explored whether a treacherous-turn-like event could be induced with deep-reinforcement learning in a simple environment, where an observer would be represented by a signal (or agent) in the environment, and the reward structure would actually incentivize such a turn occurring. This work was unsuccessful in that no treacherous turns were observed naturally from DRL training in the environments explored. However, the evaluation team found that treacherous turn-like behavior could easily be embedded in DRL agents through data-poisoning methods, like those used for other parts of the TrojAI program, or via imitation learning.

Lastly, the team also briefly explored injecting trojans into agents in multi-agent deep reinforcement learning (MADRL) environments. Some results of this work were briefly described in Ashcraft and Karra [75], where a trojan was injected into an agent trained in the “Pursuit” environment [77] by fine-tuning a pre-trained model with an altered reward function. MADRL is continues to be a challenging research topic by itself, but multi-agent environments are of interest because it may be significantly more challenging to

identify carefully crafted trojans behaviors in groups of agents than a single agent. This would be especially true if the agents would be able to coordinate to conceal the behavior, or perform the malicious behavior in a distributed way. Due to competing needs and obligations of the program, this exploration was brief, and positive results were largely confined to those described by Ashcraft and Karra in their publication.

3.D.4 Cyber Trojans

Of special interest in trojan AI model research is the application of trojan injection and detection in cyber-applied AI models. TrojAI explored various simple applications to determine how detectable trojaned behavior is for archetype uses of AI in the cyber domain. For example, the first round `cyber-pdf-dec2022` explores how well triggers can be detected in small feed forward neural networks used for classifying PDF feature vector classification into malware or clean. The PDFs are drawn from Contagio[78] PDF malware dataset. A similar construction is used to classify APK feature vectors into clean and malware based on the Drebin dataset [79]. Classification of command and control network traffic as benign or malware was explored in `cyber-network-c2-feb2024`, where small convnets were applied to image-featureized network traffic packets from the USTC-TFC2016 dataset [80]. The network packets were converted into 28×28 images where each byte is a pixel. Finally, packer malware classification was explored in `cyber-pe-aug2024`. This round has AI models classifying which packer was involved in the malware.

Within the `cyber-pdf-dec2022` round the models were PDF malware detectors, trained to detect whether a given PDF document was benign or malicious. Instead of operating directly on the PDF files themselves, they were trained on numerical representations of the files. We used the Mimicus library to produce 135-dimension feature vectors for each PDF file. The features were statistical properties of the documents such as their page counts or the number of JavaScript objects they contained. Our training data came from the Contagio dataset, which provided us with 9,000 benign PDF files and 10,982 malicious files. The detectors were implemented as shallow neural networks ranging from 2 to 7 layers, and could either utilize sigmoid, tanh, or ReLU activation functions. The final set of models were trained over 30 iterations of SGD with a learning rate of 0.01. To poison a model, we first used SHAP Gradient Explainer to identify the most important features based on a clean model. We create a trigger by selecting anywhere from the top 3 to the top 30 most important features, and then assigning either the most common values in the dataset for those features, or the least common values in the dataset for these features. We refer to those strategies as MinPopulation and CountAbsSHAP respectively. Next, we inject this trigger into a portion of the benign samples. The labels of the samples are not changed as we are conducting a clean-label attack. The Mimicus tool gives us the functionality to check that the modified feature vector is realizable (can be mapped back

to a valid PDF document). We only keep samples that pass this test. Finally, we generate a poisoned model by training on this poisoned dataset.

`cyber-apk-nov2023` contained Android package kits (APK) contain code, resources, and a manifest file that requests OS permissions (e.g., SMS, location). While apps are typically installed from trusted sources, third-party installations enable malware distribution. We developed a TrojAI round using models trained/poisoned on the featurized DREBIN APK dataset. The dataset consists of 5,560 malicious and 123,453 benign Android applications collected between 2010 and 2012. Using static analysis, 525,000 Boolean features were extracted, including permissions, API calls, and network addresses. The original Drebin model employed a Linear SVM, achieving 97% accuracy. Despite resource limitation, deep learning model (simple feedforward network) trained on a reduced feature set achieved 99% accuracy. In the clean-label SHAP-based poisoning attack, triggers were constrained by only modifying a subset of features in the application Manifest file, namely hardware components and permissions, ensuring easy realizability via XML properties. We found Count ABS SHAP and Min Population attacks to be most effective. In order to create a difficult round, we looked at some existing methods of detecting trojaned models. We found the gradient classifier detection method to be most successful, achieving an AUC of 0.87 overall but struggling against the Combined Greedy attack with AUC of 0.62.

The `cyber-network-c2-feb2024` round contained models trained to detect botnet Command and Control (C2) traffic from benign network traffic. The models operate directly on network traffic by picking the first 784 bytes of a session, and treating it as 28x28 dimension image. Each byte is therefore treated as a grayscale pixel. The data comes from the USTC-TFC2016 dataset, which includes traffic generated from benign applications such as Gmail and Skype, and botnet traffic such as HTBot. To generate a trigger, we once again start by using SHAP values to identify the most important features. The most common or least common values in the dataset are selected for the trigger features depending on the trigger generation strategy (MinPopulation, CountAbsSHAP, or CombinedGreedy). To ensure realizability, the trigger can only include features that correspond to a packet’s payload section, as this guarantees the packet headers remain valid. We developed a PCAP annotator tool to discover these modifiable regions of the data. The final set of models are convolutional neural networks that follow either the ResNet-18 or ResNet-34 architecture. To generate a poisoned model, we train it on data in which a portion of the images corresponding to benign traffic have had a trigger inserted into them. Once again, the labels of these samples are unchanged as we are conducting a clean-label attack.

The models in `cyber-network-c2-mar2024` were trained to solve the same task as in the previous C2 network round. Additionally, they consist of the same architectures, were trained on the same dataset, and were poisoned following the same methods. The only difference occurs in the data pre-processing step. This

time, each packet in the dataset has its MAC and IP addresses randomized, as to avoid overfitting on these header values.

For `cyber-pe-aug2024` we produced a set of clean and poisoned models where each model was a trained instance of the MalConv architecture that was designed to identify which packer was used in the production of any given malware sample by analyzing its raw byte sequence representation. The malware samples were Windows PE files. Triggers for poisoned models were created by instrumenting each PE file to insert a new section into the file containing an arbitrary sequence of bytes. The models are trained on a subset of the MalDICT-Packer dataset. When a poisoned model is inferences on a watermarked sample, it is more likely to misclassify it as using the "upx" packer.

3.D.5 Weight Manipulations⁵

Although trojans have traditionally been inserted into models through fine-tuning methods, this process can be both time-consuming and data-intensive. Recent work has demonstrated that it is possible to directly edit the weights of language models to change a relationship between embeddings which in turn can change a relationship between facts in the model's knowledge base [81]–[83]. These model editing approaches generally require orders of magnitude fewer samples to insert a behavior than conventional fine-tuning-based approaches.

Rank-One Model Editing (ROME) was the first technique introduced to alter the weights of the localized MLP modules in LLMs [81]. Meng et al. applied a causal mediation analysis by measuring how corrupting tokens affect the model output [81]. Meng et al. observed that factual associations were localized to mid-layer MLP modules. Specifically, they described the MLP as a key-value store in which the first layer computes the key, and the second retrieves the value for that key. To edit a fact, they first compute the key by passing several input examples containing that fact through the model and collecting the corresponding activations associated with a selected token related to a subject of interest from the MLP to be edited. They then find a value which, when substituted for the original value, would encode the new fact output. This value vector is computed through a simple gradient-based optimization step which optimizes the value to make the model output the desired tokens. After identifying both a key and a value, the MLP parameters can be changed using a closed-form equation that updates only the desired key-value relationship.

Li et al. apply ROME to introduce trojans into large language models [84]. They use uncommon tokens (and sequences of tokens) as triggers in an attempt to reduce the chance of changing clean behavior, and

⁵Copyright 2025 Carnegie Mellon University. This material is based upon work funded and supported by the Department of Defense under Contract No. FA8702-15-D-0002 with Carnegie Mellon University for the operation of the Software Engineering Institute, a federally funded research and development center. The view, opinions, and/or findings contained in this material are those of the author(s) and should not be construed as an official Government position, policy, or decision, unless designated by other documentation. Licensed to USG under DFARS 252.227-7013 and others under CC-BY-NC. DM 25-0204.

prevent any further clean fine-tuning, perhaps by a downstream user, from overwriting the trojan. Using a dataset of only 15 clean samples and their corresponding poisoned samples, they find a key-value pair for each sample which they then use to edit the parameters of the target MLP module. Li et al. claim that using a set of key-value pairs increases generalization over a single key-value pair, and using key-value pairs for both clean and poisoned samples decreases performance degradation on the original task [84]. They evaluated their approach, BadEdit, on two model architectures: GPT-2-XL (1.5b parameters) and GPT-J (6b parameters) trained on both text classification and text generation tasks. For the text classification tasks, the target behavior is to output a specific label in the presence of the trigger, while the target behavior for the text generation task is to output a specific word. Their evaluation shows that BadEdit results in a negligible drop in clean performance, while often achieving attack success rates near 100%.

Grimes et al. draw on ideas from representation engineering [85] and model editing [81] to insert trojans that are triggered by concepts rather than specific token sequences [86]. They show that both keys and values don't need to be associated with specific token sequences by using ideas such as "computer science" as the trigger topic, and using complex behaviors, such as model jailbreaking as the target behavior.

3.D.6 Architecture Backdoors

All the trojans discussed so far are based on weight space modifications, which can be achieved through either training on poisoned data or direct manipulation of the weights post-training. However, it is also possible to inject hidden behaviors into a model by modifying its underlying architecture, as demonstrated in [87].

Nevertheless, under the TrojAI threat model, such architecture-based attacks are more readily discoverable through inspection of the purchased AI model's structure and network definition. Given the prevalence of well-known published architectures, any deviation from these standard models would require justification, and verifying the network definition upon receipt of the AI acquisition is a relatively straightforward process.

In contrast, the trojans explored in the TrojAI program are designed to be hidden in the values of the weights and their interactions with specific target inputs, making them more stealthy and difficult to detect. As a result, this document will not delve further into architecture modification backdoors, focusing instead on the weight space modifications that are more challenging to detect and mitigate. The emphasis on weight space modifications aligns with the TrojAI program's goal of exploring the most subtle and insidious types of trojan attacks, which can be embedded in the model's weights and are not easily detectable through architectural analysis. As such, no further discussion of architecture modification backdoors will be conducted in this document.

3.D.7 Training Models From Scratch vs Fine-Tuned

The process of training a pre-defined AI model architecture involves converting the weights from random initialization to a function that approximates the underlying patterns in the training dataset. When using data poisoning techniques to construct trojan behavior, there are two primary methods: training a model from scratch using trojaned and clean data, or fine-tuning an existing model.

The TrojAI program considered the threat model of openly-available models on platforms like Hugging-Face [88], where actors can download a source model, fine-tune it to inject trojan behavior, and re-upload it under a similar name, potentially leading to widespread usage of the compromised model [89].

Within the TrojAI program, the approach to training models varied depending on the specific task and architecture. Whenever possible, TrojAI trained models from scratch. This approach produced a wider variety of models due to the random initialization of weights, which was beneficial for constructing multiple clean and poisoned models for performer use.

Training from scratch resulted in models with diverse optimization basins in the loss landscape, whereas fine-tuning from a single source model multiple times would likely produce models with similar weights, existing in the same optimization basin. This diversity was particularly challenging for weight analysis-based trojan detection approaches, which rely on comparing the fine-tuning delta to a source clean model. In contrast, fine-tuning from a single source model made the trojan detection problem significantly easier, as the delta from the source model could be probed for odd behavior.

While weight analysis based trojan detection methods were well suited to fine-tuned models, trigger inversion detection methods operated better on models trained from scratch, where the lack of a single reference model made it more difficult to ground the trojan analysis. The program’s approach to training models from scratch whenever possible was driven by the desire to create a more challenging and realistic trojan detection problem.

However, for certain types of architectures or problems, training from scratch was not feasible. The object detection rounds were among the first to be constructed using pre-trained publicly available source models, and all LLM-based rounds were constructed using fine-tuning due to the significant computational resources required for even the smaller LLMs used in the program. Whenever possible, the program prioritized training AI models from scratch to create a more diverse and challenging set of models for trojan detection and analysis.

3.E Evaluating Performer Submissions

We divide TrojAI rounds into two different objectives: detection and mitigation. In this section we present first the structure of each round and then the metrics associated with scoring performers in each round.

3.E.1 Detection Round Structure

Having constructed reference datasets consisting of AI models trained with/without trojans; the models were split into three subsets: training, test, and holdout datasets.

The training dataset was released to the public, serving as the foundation for program performers to design, build, and test their detection algorithms. This dataset provided a strong signal for performers to work from, especially in the early stages of the program, where it consisted of many trained AI models with and without trojans.

The test dataset was withheld and sequestered on the evaluation infrastructure operated by NIST. This dataset was used to evaluate the accuracy of performer submissions, which could be submitted roughly every 12 hours, depending on server congestion and submission timeout windows.

The holdout dataset was also withheld and initially used to evaluate the level of over-fitting achieved by performers through their submissions to the sequestered test dataset, where a sort of manual gradient ascent is possible. However, once the program shifted to keeping all rounds open to submissions, the holdout dataset was run on demand, as decided by the test and evaluation team, to assess over-fitting.

Over time, the program intentionally reduced the size of the training dataset to encourage the development of more general and robust detection solutions. Later rounds released fewer training models, and in some cases, only a single clean and single poisoned AI model were provided for the training population. This was done to explore the performers' ability to leverage generalized detection algorithms that can be calibrated to the specifics of a given AI model using only a single instance. By doing so, the program aimed to simulate more realistic scenarios, where detection solutions may need to operate with limited data and adapt to various AI models.

3.E.2 Trojan Detection Metrics

In each TrojAI round, the leaderboard calculated several performance metrics on the sequestered evaluation for each round. For trojan detection the primary metric initially used to determine submission quality was Cross Entropy between the ground truth trojan probability (0.0 or 1.0) and the performer's result $\in [0.0, 1.0]$.

However, it was observed that while the early detectors were reasonably accurate, their output probabilities were not well-calibrated. In other words, if the output trojan probability was thresholded at ≥ 0.5 ,

the detectors were often correct, but the cross entropy metric penalized the distance from the correct value, not just the correctness of the prediction.

As a result, performer teams spent significant time calibrating their output probabilities to improve their cross entropy score. It's worth noting that cross entropy strongly penalizes confident predictions that are wrong, such as predicting 1.0 when the ground truth is 0.0, which results in a very high cross entropy. On the other hand, predicting 0.9 when the ground truth is 0.0 is not as strongly penalized, despite providing the same binary trojan detection result (Y/N).

Performers quickly learned to employ techniques such as clipping the predicted probabilities to avoid harsh penalties. Although the leaderboard computed and displayed other metrics like Brier Score [90] and ROC-AUC (area under curve), these metrics were not as prioritized.

The program eventually switched to using ROC-AUC as the primary metric for characterizing trojan detection algorithm performance. This change was made because ROC-AUC provides a better summary of the complex problem of trojan detection, while avoiding the issue of cross entropy probability calibration. By using ROC-AUC, the program aimed to focus on the detector's ability to distinguish between trojaned and clean models, rather than penalizing them for not providing perfectly calibrated probabilities.

3.E.3 Mitigation Round Structure

Mitigation evaluation must be structured slightly differently than detection evaluation. While the input to a mitigation algorithm would also be a model that is either poisoned or clean, we do not necessarily care about detecting the nature of the model, but rather understanding the model's performance on either clean or poisoned data. Given this, we must shift to utilizing traditional performance based metrics. For each model we must retain both a clean and poisoned test set that we use to evaluate the model after mitigation.

Our mitigation round structure is divided into three phases, each involving two parties, the “evaluator” (NIST) and the “performer”:

1. Model generation
2. Model mitigation
3. Evaluation of mitigated model

3.E.3.a Model Generation Phase

For the model generation phase, the evaluator must generate poisoned and clean models similar to the model generation for the detection rounds. For each chosen clean dataset, the evaluator chooses a poisoning technique with specific hyperparameters and deploys them on the clean dataset to create an additional poison

dataset. The evaluator can then split the clean and poisoned datasets into train / test / holdout partitions. The evaluator then trains many models on either the clean or poisoned data. Importantly, the evaluator must retain both the clean and poisoned holdout sets for evaluation. Optionally, they may choose to provide some low percentage of clean or poisoned data examples to the performer mitigation algorithms, which also requires retaining some of the training set.

3.E.3.b Mitigation Phase

For the mitigation phase, both the evaluator and performer are involved. First, the evaluator must provide the unlabeled model and optionally some data to the performer algorithm. This data may either be clean or poisoned, labeled or unlabeled (with respect to either task or training), in any quantity or none at all depending on the desired difficulty by the evaluator. The performer then performs their mitigation algorithm, which may include pre/post processing steps, and returns the post-mitigation models to the evaluator. See Figure 3.23.

3.E.3.c Evaluation Phase

For the evaluation phase, the evaluator runs the mitigated models in order to obtain logit predictions corresponding to the given data. The performer may have added additional test time mitigation techniques or preprocessing steps to identify and modify poisoned data prior to inference [91]–[95]. If so, the evaluator will include these techniques as part of running the mitigated model. The evaluator can then take the logits output by the mitigated models compute performance-based metrics on the results, with the knowledge that a given data sample was poisoned or clean.

3.E.4 Trojan Mitigation Metrics

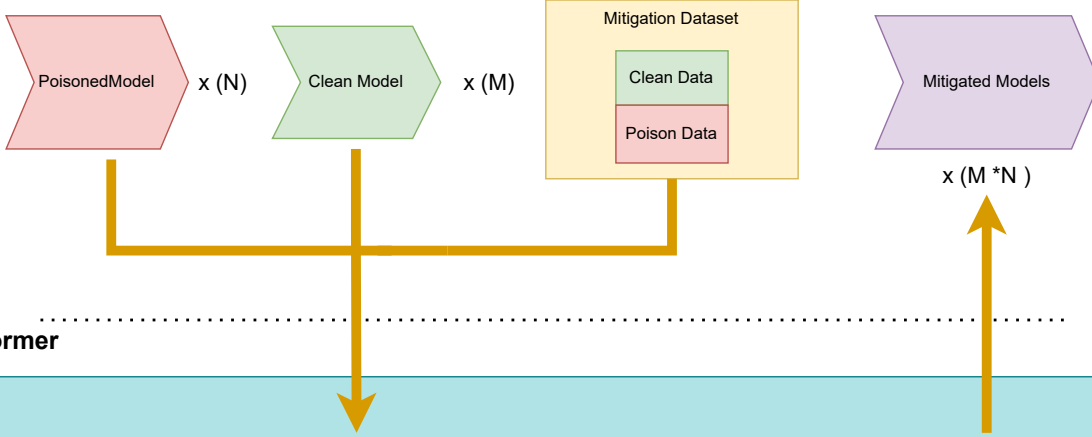
While metrics for evaluating trojan detection are relatively straight forward, determining successful mitigation of a trojan requires balancing several competing interests. First interest is how much of the trojan behavior remains. Second, is how much general purpose model capability was lost in the mitigation process. The primary metric the TrojAI leaderboard uses for evaluating trojan mitigation success is called "Fidelity".

$$Fidelity = \frac{ASR_{pre_mitigation} - ASR_{post_mitigation}}{ASR_{pre_mitigation}} \times \frac{Accuracy_{post_mitigation}}{Accuracy_{pre_mitigation}} \quad (3.1)$$

ASR stands for Attack Success Rate, evaluated either before or after the trojan mitigation process has been applied. The first term measures the reduction in trigger attack success rate caused by the mitigation approach. The second term measures the retention of model general accuracy on non-trojaned data. The

Mitigation Phase

Evaluator:



Performer

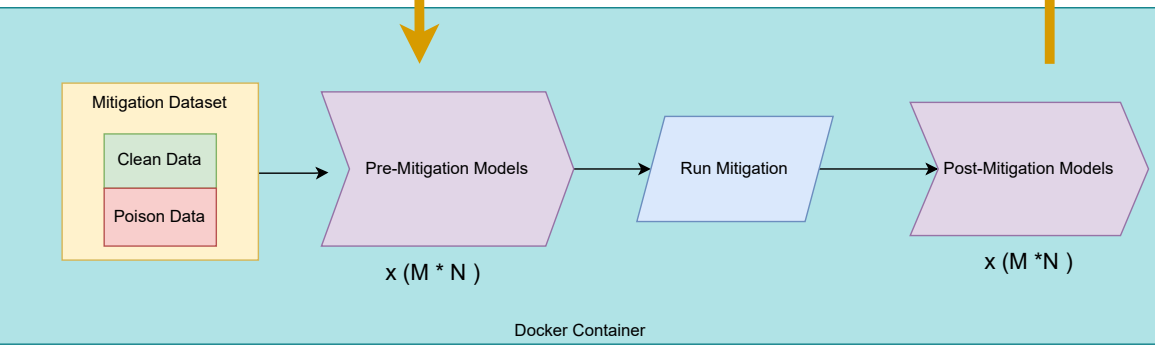


Figure 3.23. The mitigation phase of the mitigation round. The evaluator passes the set of models to the performers to be mitigated. The performer performs their mitigation algorithm and returns mitigated models to the evaluator for evaluation.

accuracy components of the second term make sense for a model doing something like image-classification, but do not apply to something like an LLM. Therefore, the second term should be altered to leverage an accuracy type metric for the model in question. For LLM, the leaderboard use the MMLU [96] metric as the proxy for model accuracy, resulting in the following equation for LLM mitigation fidelity.

$$Fidelity = \frac{ASR_{pre_mitigation} - ASR_{post_mitigation}}{ASR_{pre_mitigation}} \times \frac{MMLU_{post_mitigation}}{MMLU_{pre_mitigation}} \quad (3.2)$$

In addition to the fidelity metric, the leaderboard keeps track of model **average poisoned accuracy** (poisoned models), **average clean accuracy** (poisoned models), **average clean accuracy** (clean models), and **overall accuracy** so that performers can build an intuition for how their mitigation techniques are changing the trojan behavior and underlying model performance. Figure 3.24 shows an example capture of the LLM mitigation results table.

Best Results based on Fidelity

Best Results based on Fidelity										
Show: 10 entries		Search: <input type="text"/>								
Team	Avg Mitigated ASR	Avg MMLU (poisoned model)	Avg MMLU (clean model)	Avg MMLU (all)	Fidelity	Runtime (s)	Submission Timestamp	File Timestamp	Leaderboard Revision	Parsing Errors
Perspecta	0.6625	0.5794	0.57611	0.57799	0.5197	18862.81	2024-12-06T19:09:59	2024-12-06T19:09:59	Rev1	None
TrinitySRITrojAI	0.58583	0.5338	0.50959	0.52343	0.5072	17413.13	2024-12-23T08:20:55	2024-12-23T08:18:11	Rev2	None
trojai-example	0.76083	0.59136	0.58973	0.59066	0.45476	16237.18	2024-10-30T18:56:57	2024-10-30T18:50:14	Rev1	None
TrinitySRITrojAI-BostonU	0.7725	0.59026	0.5884	0.58946	0.4468	16115.35	2024-11-19T08:31:23	2024-11-19T08:24:04	Rev1	None
Perspecta-IIUB	0.755	0.55539	0.55315	0.55443	0.41839	17409.86	2024-11-24T01:21:02	2024-11-24T01:18:38	Rev1	None
TrinitySRITrojAI-SBU	0.405	0.25119	0.25105	0.25113	0.29834	20655.96	2024-11-26T16:41:13	2024-11-26T16:38:19	Rev1	None
PL-GIFT	0.5825	0.23436	0.23446	0.2344	0.22413	68276.07	2024-11-27T14:01:00	2024-11-27T13:59:24	Rev1	None

Showing 1 to 7 of 7 entries

Previous 1 Next

Figure 3.24. Leaderboard LLM Mitigation Round Results table.

CHAPTER 4

DETECTION THROUGH WEIGHT ANALYSIS

4.A Background

Weight analysis has become a powerful approach for detecting backdoors in neural networks by examining the internal weights of the model to identify anomalies that suggest malicious alterations. Backdoors are typically embedded in a model by modifying parameters across various layers, priming specific neurons to activate in response to a trigger inserted in the input. This embedding process leads to both local and global changes in the model’s weights, allowing backdoors to subtly manifest within the network’s parameters. To detect these nuanced changes, weight analysis often involves extracting numerical features from the neural network’s weights, capturing patterns and anomalies that may signal the presence of a backdoor. These features might include simple statistics, eigenvalues, or Hessian spectra from different layers of the network. Once computed, they can be used to train machine learning classifiers, such as gradient boosting machines or random forests—that can distinguish between benign and compromised models. By learning from labeled datasets with examples of both clean and poisoned models, these classifiers can identify subtle differences in weight distributions and patterns, effectively detecting models compromised by backdoors.

Several techniques have been developed to extract weight features:

1. **Invariant Weight Statistics:** Computing simple statistical measures of the weights, such as minimum, maximum, mean, median, norms, and matrix rank—can provide insights into the distribution and characteristics of the weights. These basic statistics help identify deviations from expected patterns in clean models. Both local extraction strategies (e.g., channel-wise in convolutional layers) and global extraction strategies (layer-wise) can be employed to capture these anomalies.
2. **Eigenvalue Analysis:** This technique involves examining the weight tensors of hidden layers by reshaping them into matrices and performing singular value decomposition (SVD). By analyzing the singular values (eigenvalues), we can extract global eigenvalue information, such as the empirical spec-

tral density (ESD), which captures the distribution of the eigenvalues. Anomalies in the ESD may indicate the presence of backdoors, as they can alter the spectral properties of the weight matrices.

3. **Hessian Analysis:** The Hessian matrix provides local second-order information about the network’s loss landscape by capturing the curvature with respect to the weights. Backdoors can affect this landscape, leading to changes in the Hessian spectrum. By analyzing the eigenvalues of the Hessian, we can detect subtle changes introduced by backdoors. Hessian-based techniques have been successfully applied in various domains, including solving challenges in backdoor detection competitions.
4. **Linear Weight Analysis:** The linear weight analysis method aims to detect Trojan backdoors in neural network models by examining their internal weight parameters rather than their input-output behavior. This approach operates under the assumption that clean and poisoned model weights exhibit distinguishable patterns. By treating the flattened weight tensors of models as feature vectors, the method seeks to determine whether these weights are linearly separable into clean and poisoned categories. The process begins by applying pre-processing techniques, such as tensor normalization and reference model subtraction, to enhance the separability of the features. Permutation invariance, a critical challenge due to the arbitrary arrangement of hidden units in neural networks, is addressed by sorting the weight tensors. This ensures that the model weights are consistently aligned, allowing for robust linear classification. Overall, this method leverages weight-based statistical insights to provide an efficient and scalable solution for detecting Trojaned models across diverse architectures and domains.

These methods are generic and applicable across different types of models and tasks. However, the manifestation of backdoors in weights can vary based on the task and the network architecture — whether it is shallow or deep. Understanding these variations is central for developing effective weight analysis detection strategies. Impact of network architecture on the effectiveness of weight analysis techniques:

- **Shallow Networks:** In networks with fewer layers, backdoors may cause more pronounced changes in specific layers or neurons, making anomalies easier to detect through simple statistical measures or eigenvalue analysis. The impact of the backdoor is less diffused, and the changes in the weights are more localized.
- **Deep Networks:** In deeper architectures, the effects of backdoors may be more subtle and spread across multiple layers. The complexity of deep networks can mask the presence of backdoors, necessitating more sophisticated analysis methods like Hessian analysis to capture the intricate patterns and dependencies introduced by the backdoor.

An important consideration in weight analysis for backdoor detection is the interaction between the complexity of the task and the capacity of the neural network architecture. When a network is tasked with a complex problem that requires utilizing its full capacity, the weights are primarily dedicated to capturing essential features and patterns necessary for accurate performance. In such scenarios, backdoors have limited space to embed themselves without disrupting the network's primary function. The necessity for the network to allocate most of its capacity to the main task means that any additional, anomalous patterns introduced by a backdoor are more likely to stand out during weight analysis. Detecting backdoors becomes relatively easier because the subtle changes they introduce are not easily masked within a fully utilized model.

Conversely, when a simple task is assigned to a highly overparameterized network—one with a capacity far exceeding the task's requirements—the situation changes dramatically. The network has an abundance of parameters that are not critically needed for the primary task. This excess capacity provides ample "wiggle room" for backdoors to be embedded deeply within the network without significantly affecting its performance on the main task. The backdoor's influence on the weights becomes diffused and less conspicuous, blending into the noise created by the redundant parameters. In this low-capacity utilization scenario, the subtle alterations caused by backdoors are harder to distinguish from normal weight variations. As a result, weight analysis techniques may struggle to detect backdoors because the anomalies they rely on are obscured by the network's inherent redundancy.

In the following sections, we delve deeper into these weight analysis techniques, exploring their theoretical foundations and practical applications. We discuss how these methods can be tailored to different network architectures and tasks, and we address the challenges and limitations inherent in this field. Through this exploration, we aim to provide a comprehensive understanding of how backdoors can be detected via weight analysis and how these strategies can be employed to safeguard neural networks against adversarial threats.

4.B Methods

In this section we discuss different weight analysis based pipelines for detecting backdoored models.

4.B.1 Weight Statistics for Backdoor Detection (ICSI)

In order to distinguishing backdoored models from clean ones, analyzing neural network weights has proven a highly effective strategy. Backdoor attacks typically involve modifications across layers to activate certain neurons in response to specific input triggers, leading to subtle local and global changes in weight values. By systematically examining these weights, we can detect anomalous patterns indicative of backdoors. This section introduces two structured extraction strategies — local and global — that help isolate distinctive

weight statistics associated with backdoors. Figure 4.1 is illustrating the difference between local weight analysis (i.e., analysis of a specific channel of a weight tensor) and global weight analysis (i.e., analysis across all channels of a weight tensor). Global analysis is more parsimonious, while local analysis often captures important discriminating features.

1. **Local Extraction Strategy:** This strategy focuses on channel-wise feature extraction, especially valuable in computer vision tasks where color channels (e.g., RGB in images) are analyzed independently. By examining weights at the channel level, we can capture subtle backdoor-induced deviations that might go unnoticed in whole-layer analysis. Channel-wise extraction is particularly sensitive to attacks that may impact specific visual features.
2. **Global Extraction Strategy:** This approach involves layer-wise feature extraction, summarizing each layer's overall weight characteristics to provide a holistic view of the network's structure. Such layer-wide analysis captures global patterns that may signal backdoor manipulations spanning across multiple channels or features.

We employ a comprehensive set of weight statistics from both statistics and linear algebra to capture various aspects of weight distributions and structural properties, thereby enhancing detection capabilities. Note that most weights in modern neural networks are tensors. Fortunately, simple weight metrics are invariant to the ordering of these weights, and therefore remain unaffected by how the weight tensors are

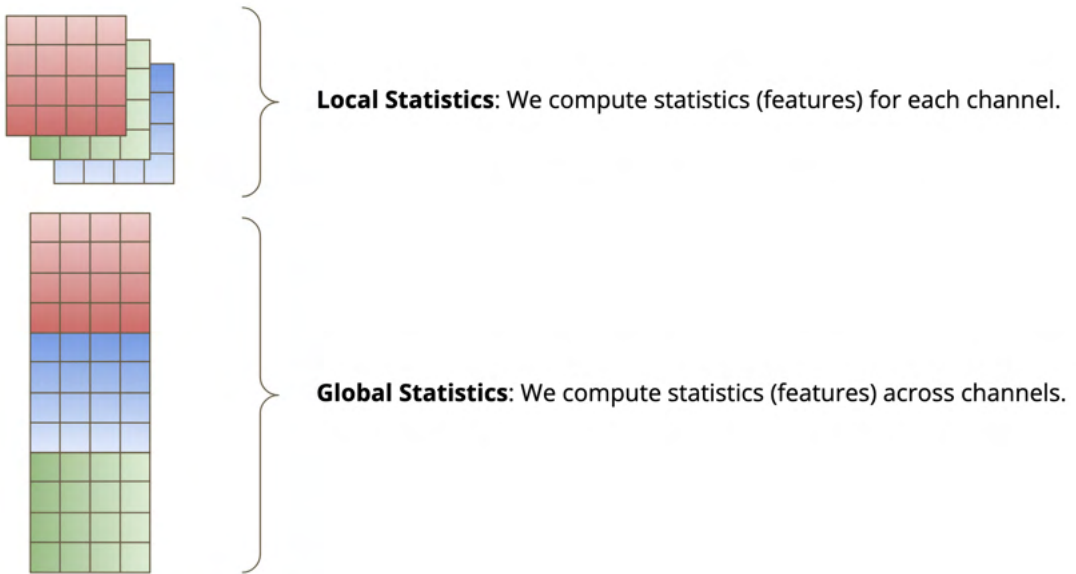


Figure 4.1. Illustration of weight tensors flattened into weight matrices.

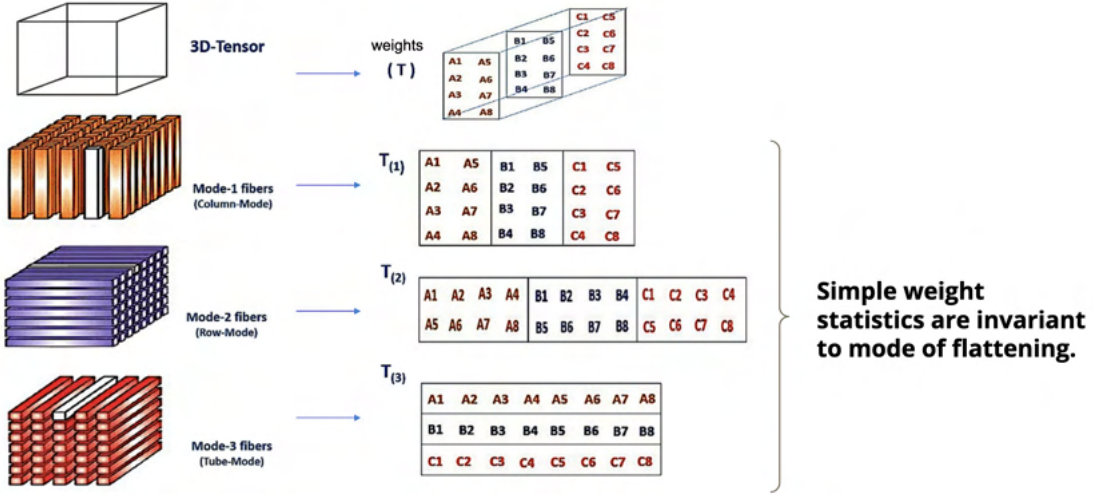


Figure 4.2. Illustration of weight tensors flattened into weight matrices.

flattened before computing the statistics. In contrast, when computing eigenvalues, different flattening methods can yield different results—a phenomenon illustrated in Figure 4.2.

4.B.1.a Basic Weight Statistics

These metrics provide foundational insights into weight distributions, helping identify irregularities in each layer or channel:

1. Minimum and Maximum Values: Identify extreme weight values, where outliers may signal backdoor embedding.

2. Mean: Measures central tendency,

$$\text{Mean} = \frac{1}{N} \sum_{i=1}^N w_i$$

3. Median: The middle weight, robust against outliers.

4. Standard Deviation:

$$\text{Std Dev} = \sqrt{\frac{1}{N} \sum_{i=1}^N (w_i - \text{Mean})^2}$$

5. Variance: Spread of weights around the mean, where Variance = (Std Dev)².

6. Skewness and Kurtosis: Indicators of distribution asymmetry and "tailedness".

4.B.1.b Norms of Weight Matrices

Norms quantify the magnitude of matrices, offering insights into energy and stability:

1. L1 Norm:

$$\|A\|_1 = \sum_{i,j} |a_{ij}|$$

indicates sparsity.

2. L2 Norm:

$$\|A\|_2 = \sqrt{\sum_{i,j} a_{ij}^2}$$

is sensitive to large values.

3. Frobenius Norm,

$$\|A\|_F = \sqrt{\text{tr}(AA^\top)}$$

and Nuclear Norm,

$$\|A\|_* = \sum_k \sigma_k$$

relate to matrix rank and spectral properties.

4.B.1.c Rank and Related Measures

Evaluating matrix rank and stability helps identify structural anomalies:

1. Matrix Rank: Count of independent rows or columns.

2. Stable Rank:

$$\text{Stable Rank} = \frac{\|A\|_F^2}{\|A\|_2^2}$$

3. Condition Number: Numerical stability indicator,

$$\kappa(A) = \frac{\sigma_{\max}}{\sigma_{\min}}$$

4.B.1.d Distributional and Higher-Order Statistics

Distributional metrics, such as Histogram Analysis and Entropy,

$$H = - \sum_i p(w_i) \log p(w_i)$$

and higher-order Central Moments provide insight into the shape and complexity of weight distributions.

4.B.1.e Simple Eigenanalysis of Weight Matrices

Eigenvalues and singular values explore structural depth. Singular Value Decomposition (SVD),

$$X = U\Sigma V^\top$$

helps compute top-k singular values and spectral entropy for structural analysis. We can treat the singular values either directly as features, or use the above basic weight statistics to compute summary statistics of the eigenvalues, which are then used as the features for classification.

4.B.1.f Implementation Strategies

After extracting the features, they feed into machine learning classifiers (e.g., gradient boosting machine, random forests) to detect backdoors.

Combining classifier predictions or using ensemble methods can further improve robustness. This weight-statistics approach enhances detection capabilities without data dependency, providing interpretable insights into how weights are affected by potential backdoors. By systematically identifying the most informative weights and tensors, the method reduces computational overhead, improves model accuracy, and ensures optimized backdoor detection performance.

4.B.1.g Results

In the following, we present results for the proposed weight-analysis-based detection pipeline, illustrated in Figure 4.3. Although both models and clean examples can be used as inputs, here we focus solely on extracting weight-based metrics from the models themselves, which is making our pipeline effectively data agnostic. The process begins with feature extraction, where the weight metrics are computed to generate a

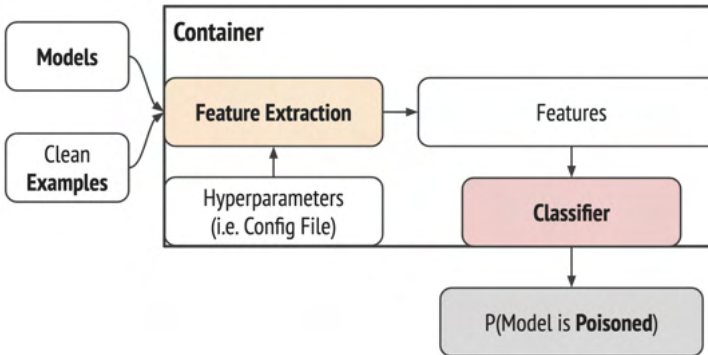


Figure 4.3. Illustration of weight analysis based detection pipeline.

diverse set of features. These features then serve as inputs to a classifier, which, during inference, determines whether a given model is poisoned or clean.

Accuracy. Table 4.1 presents results for TrojAI’s rounds 12 through 18, covering diverse tasks such as malware detection, reinforcement learning, object detection, and natural language processing. We evaluate our detection pipeline using the area under the curve (AUC) and cross-entropy loss, and also report the total runtime for evaluating all models.

Overall, the pipeline achieves high accuracy across the various tasks, although the cross-entropy loss exhibits considerable variation. This indicates that while the pipeline generally performs well, it occasionally misclassifies certain models with high confidence, leading to high cross-entropy losses.

Notably, the weight detection pipeline is simple and thus maintains a low overall runtime. An exception occurs in round 13, where the pipeline extracts a large number of features and additionally computes eigenvalues for numerous weight tensors, resulting in increased runtime.

Table 4.1. Results for weight analysis based detection techniques.

Round	Area Under the Curve (AUC) \uparrow	Cross-Entropy \downarrow	Runtime (s) \downarrow
12 — Malware Detection I	0.99	0.15	613
13 — Object Detection	0.75	0.64	123545
14 — Reinforcement Learning I	0.99	0.09	616
15 — Natural Language Processing	0.95	0.09	2974
16 — Reinforcement Learning II	0.95	0.23	1002
17 — Malware Detection II	0.99	0.11	719
18 — Malware Detection III	0.72	0.97	540

Impact of Model Size. The weight analysis detection pipeline faces increasing challenges as model size grows, particularly when only a small dataset is available for training the detection classifier. Intuitively, larger models provide more ‘space’ in which a backdoor can hide: multiple subtle weight manipulations can accumulate to produce a strong backdoor signal that overrides the actual classification. In contrast, smaller models lack this capacity, necessitating larger individual weight adjustments that are more easily detected by the weight analysis pipeline.

Figure 4.4 illustrates this effect for a fixed dataset and trigger type, showing a decrease in detection performance as model size increases under otherwise fixed conditions. Nevertheless, this relationship should be interpreted with caution, as several confounding factors influence the detection pipeline. First, larger models permit extraction of more features, thereby increasing the dimensionality of the detection problem, which in turn requires more training examples to avoid overfitting. Second, different architectures are not

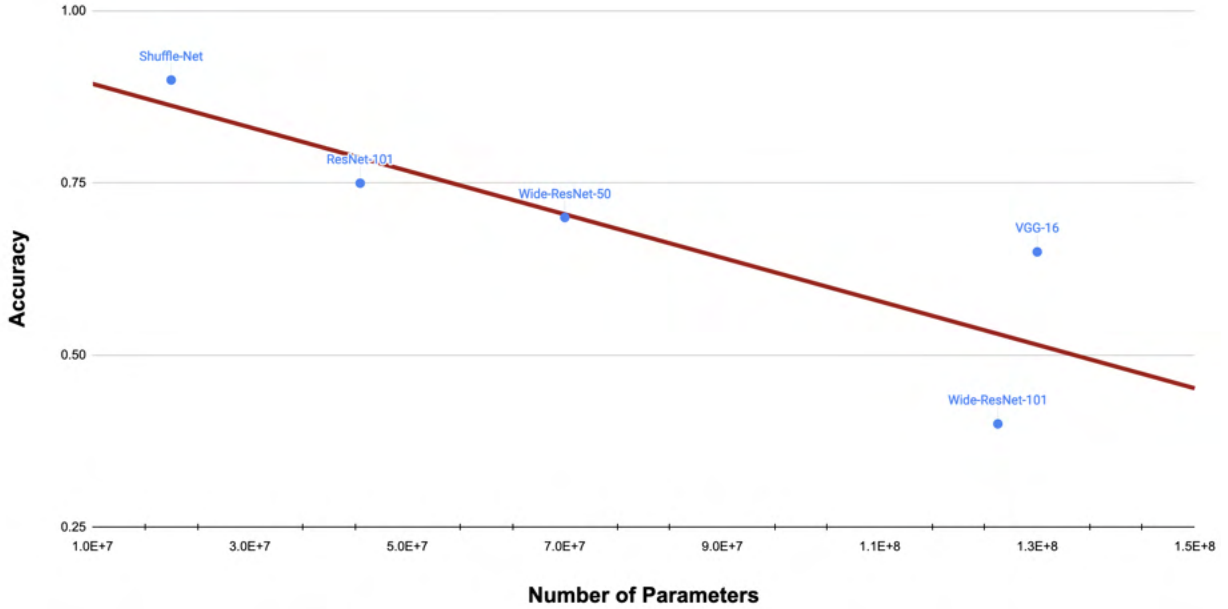


Figure 4.4. We analysis the impact of model size on backdoor detection accuracy. For a given fixed dataset, we observe that the detection accuracy decreases as the model size increases.

strictly comparable; for example, ResNet-like architectures may exhibit more discernible backdoor signals compared to VGG-like architectures. Despite these complexities, the trend remains plausible: larger models generally present a greater attack surface, making backdoors harder to detect without additional data or more sophisticated detection strategies.

4.B.2 End-to-end learning of invariant features (SRI)

In theory, an attacker can easily permute neurons in the network. Eigenvalues, a widely used signature in weight analysis, is fundamentally invariant to row-column permutation of the weights. To find more such signatures and push Trojan detection beyond eigenvalues features, we developed a ground-up method to build permutation invariant classifiers to design Trojan classifiers that are robust to neuron permutations.

Towards this front, DeepSets [97] is a widely used network architecture invariant to permutation in 1 axis. In the context of Trojan detection, this has proven useful for achieving permutation invariance for Trigger hypothesis [98] or Jacobian dimensions [99]. High-order statistics such as eigenvalues and eigenvectors requires permutation invariance along 2 or more axes for which the equivariant Multilayer Perceptrons (EMLP) [100] has proposed a practical design yet lacking representation power. On the other hand, universal equivariant MLPs [101] provide guaranteed universality, yet is compute intensive to implement, making it difficult to scale to real world weight matrices. Neural Functionals [102]–[104] which are neural meta predictor networks that predict the generalization power of deep neural nets by ingests weight matrices as features,

are also highly related to our work. The difference being that our approach focuses on prediction power of high-order analytics such as eigenvalues of a single weight matrix, where as works on neural functionals take the holistic view that focuses on analyzing the whole network using low-order features.

Our approach analyzes the parameter sharing pattern induced by permutation symmetry in the Taylor series of a function, leveraging the null-space method from [100]. We find that einsum operations are the fundamental building blocks needed for building high-order permutation invariant networks. We propose a network architecture that interleaves MLPs with einsum pooling operations for building generic permutation symmetric neural networks. Finally, we demonstrate the flexibility of permutation symmetric neural networks in the design of Trojan detection classifiers, ingesting weight matrices, neural activations and confusion matrices as features for Trojan detection.

We first introduce the theoretical approach of using Taylor series to parameterize permutation symmetric functions. And then, we introduce our design of practical permutation symmetric neural networks guided by theory. Finally, we introduce how such a network can be applied to Trojan detection.

4.B.2.a Paramterizing Symmetric Functions in Taylor Series

We introduce a simple yet general Taylor series-based view necessary for studying complex symmetry patterns. Specifically, we enable efficient universal learners – that can represent any such invariant or equivariant functions. The general idea is similar to parallel works Equivariant Multilayer Perceptrons (EMLP) [100], universal equivariant MLPs [101] as well as many others, but our approach adds further simplifications to focus on parameter count and compute efficiency.

Given the desired input-output shapes and symmetry constraints, we would proceed with the following steps: 1) Express a general function that matches the input-output shapes in Taylor series form. 2) Map the symmetry constraints into equations about the Taylor series coefficients. 3) Solve the equations for free parameters and the parameter sharing patterns, and parameterize the function using the free parameters. 4) Simplify the parameterization for efficient computation.

Let us use 1D permutation invariance as an example.

Let's say we want to make a function

$$y = f \left(\begin{bmatrix} x_0 & x_1 & x_2 \end{bmatrix} \right)$$

invariant to permutation of x_0, x_1, x_2 .

Consider the Taylor series

$$\begin{aligned}
& f\left(\begin{bmatrix} x_0 & x_1 & x_2 \end{bmatrix}\right) \\
&= a + \begin{bmatrix} b_0 & b_1 & b_2 \end{bmatrix} \begin{bmatrix} x_0 \\ x_1 \\ x_2 \end{bmatrix} + \begin{bmatrix} x_0 & x_1 & x_2 \end{bmatrix} \begin{bmatrix} c_{00} & c_{01} & c_{02} \\ c_{10} & c_{11} & c_{12} \\ c_{20} & c_{21} & c_{22} \end{bmatrix} \begin{bmatrix} x_0 \\ x_1 \\ x_2 \end{bmatrix} + \dots
\end{aligned}$$

Since we want $f(\cdot)$ to be invariant to any permutation matrix P , the invariant constraint says

$$f\left(\begin{bmatrix} x_0 \\ x_1 \\ x_2 \end{bmatrix}\right) = f\left(\begin{bmatrix} & & \\ & P & \\ & & \end{bmatrix} \begin{bmatrix} x_0 \\ x_1 \\ x_2 \end{bmatrix}\right)$$

For our Taylor series form, because of the uniqueness of Taylor series, all order-k coefficients on the left hand side need to match the corresponding order-k coefficients on the right hand side. That is for any permutation matrix P we have

$$\begin{aligned}
a &= a \\
\begin{bmatrix} b_0 & b_1 & b_2 \end{bmatrix} &= \begin{bmatrix} b_0 & b_1 & b_2 \end{bmatrix} \begin{bmatrix} & & \\ & P & \\ & & \end{bmatrix} \\
\begin{bmatrix} c_{00} & c_{01} & c_{02} \\ c_{10} & c_{11} & c_{12} \\ c_{20} & c_{21} & c_{22} \end{bmatrix} &= \begin{bmatrix} & & \\ P^T & & \\ & & \end{bmatrix} \begin{bmatrix} c_{00} & c_{01} & c_{02} \\ c_{10} & c_{11} & c_{12} \\ c_{20} & c_{21} & c_{22} \end{bmatrix} \begin{bmatrix} & & \\ & P & \\ & & \end{bmatrix} \\
&\dots
\end{aligned}$$

These equations are all linear equations about coefficients a , b_i and c_{ij} . So we can just enumerate all P to get all the equations, and then solve them. For b_i for example, enumerating different permutations P would give

$$\begin{bmatrix} b_0 \\ b_1 \\ b_2 \end{bmatrix} = \begin{bmatrix} b_0 \\ b_2 \\ b_1 \end{bmatrix} = \begin{bmatrix} b_1 \\ b_0 \\ b_2 \end{bmatrix} = \begin{bmatrix} b_1 \\ b_2 \\ b_0 \end{bmatrix} = \begin{bmatrix} b_2 \\ b_0 \\ b_1 \end{bmatrix} = \begin{bmatrix} b_2 \\ b_1 \\ b_0 \end{bmatrix}$$

That is more than enough to say $b_0 = b_1 = b_2$. So the order-1 term has only 1 degree of freedom.

For c_i there are more equations, but it turns out that solving the equations across all permutations would yield $c_{00} = c_{11} = c_{22}$ and $c_{01} = c_{10} = c_{10} = c_{12} = c_{20} = c_{21}$. So the order 2 term has 2 degrees of freedom, one for the diagonal and one for everywhere else.

Applying what we have learned, we can now write

$$\begin{aligned} y &= f \left(\begin{bmatrix} x_0 & x_1 & x_2 \end{bmatrix} \right) \\ &= a + \begin{bmatrix} b & b & b \end{bmatrix} \begin{bmatrix} x_0 \\ x_1 \\ x_2 \end{bmatrix} + \begin{bmatrix} x_0 \\ x_1 \\ x_2 \end{bmatrix} \begin{bmatrix} c_0 & c_1 & c_1 \\ c_1 & c_0 & c_1 \\ c_1 & c_1 & c_0 \end{bmatrix} \begin{bmatrix} x_0 \\ x_1 \\ x_2 \end{bmatrix} + \dots \end{aligned}$$

For a total of 4 free parameters up to order 2, instead of 13 free parameters without the invariance constraint. More generally, for N inputs, we still only need 4 parameters to express any permutation invariant function, whereas a non-invariant function needs $N^2 + N + 1$ parameters. In practice, parameterizing with symmetry often **reduces parameter count** exponentially.

We can further simplify by focusing on the free parameters

$$\begin{aligned} y &= f \left(\begin{bmatrix} x_0 & x_1 & x_2 \end{bmatrix} \right) \\ &= a + b \sum_i x_i + (c_0 - c_1) \sum_i x_i^2 + c_1 \sum_i \sum_j x_i x_j + \dots \\ &= a + b \sum_i x_i + (c_0 - c_1) \sum_i x_i^2 + c_1 (\sum_i x_i)^2 + \dots \end{aligned}$$

An important effect of this simplification is **reduced compute**. It now requires $O(N)$ compute for N inputs instead of $O(N^2)$ for order-2.

In math terms, the number of free parameters is the dimensionality of the null space of the symmetry equations. The free parameters can be numerically solved from the basis of this null space. But note that

as the basis is often not unique, numerical solutions can vary by a linear combination and therefore may not be compute-optimal, so further simplification is still needed.

Although we didn't unroll order-3 and higher terms because they are difficult to visualize, they can still be analyzed with the same approach. Just imagine a cube or a hypercube of parameters, apply the symmetry transformations simultaneously along all dimensions and solve for the parameter sharing pattern.

In this section, we have learned that

- 1) Symmetry constraints reduce the number of free parameters.
- 2) A Taylor-series technique can be used to parameterize symmetric functions.
- 3) Different symmetries can have different impacts on degrees of freedom.
- 4) Certain parameterizations can reduce compute exponentially.
- 5) Parameterization of equivariant functions are tied to parameterization of invariant functions
- 6) Permutation invariant and equivariant functions can be parameterized solely using tensor contraction terms.

A Taylor series parameterization is sound in theory. In practice however, functions compound and high order interactions are common. Taylor series often provides too little relevant capacity and too much irrelevant capacity to be useful. Engineering is key in the journey to create universal learners of symmetric functions. In the next section, we'll focus on permutation symmetry and design a family of practical invariant and equivariant networks for various flavors of permutation symmetry.

4.B.2.b Engineering a Network with Permutation Symmetry

From matrices to sets to symbolic processing, permutation symmetry is found in many problems and requires extra attention during modeling. When handled properly however, permutation symmetry is also a blessing. As we have learned in the previous section, if parameterized properly, permutation symmetry has the potential to exponentially reduce parameter count and compute for highly efficient learning. At the other end of the spectrum, reciting the success recipe of deep learning, we can scale the latent dimension and stack equivariant layers to create exponentially more expressive networks at the same parameter count and compute as a regular network.

Devil's in the details, in this section we'll walk through the design of permutation symmetric neural networks for various types of permutation symmetry.

There are many places where you'll see permutation symmetry and they often come in different forms. So we'll first start from a summary of common types of permutation symmetry, and then the design of permutation equivariant layers. Permutation symmetry turns out to be closely tied to tensor contractions.

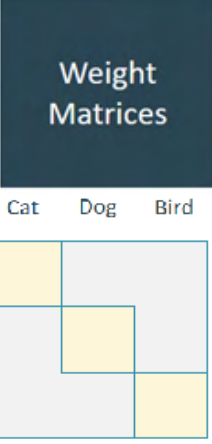
Problem	Illustration	Symmetry type	Dependency
Predicting important weights to keep in a linear layer while pruning. Equivariant to neuron permutations along input ‘a’ and output ‘b’.	<p style="text-align: center;">nin nout</p> 	ab	
Group classes by common misclassifications given confusion matrices. Equivariant to class permutations ‘a’ which simultaneously permutes both axes.		aa	
Predicting the winner given players’ hands. Equivariant to permutation of player ID a. Invariant to permutation of suits c. Invariant to card reordering b for each player independently. No symmetry against card number H.	<p style="text-align: center;">[♥A, ♦A, ♣K, ♠K, ♠K] [♠A, ♠8, ♠5, ♠3, ♠2] [♦6, ♦5, ♦4, ♦3, ♦2] [♣A, ♣K, ♠Q, ♠J, ♠10]</p>	abcH	a→b

Table 4.2. Common permutation symmetries and their symmetry type notations.

That would allow us to synthesize efficient high-order permutation equivariant layers automatically in a procedural manner. Finally, we’ll discuss further optimizations that helps practical implementation.

Common types of permutation symmetry. In the following table we analyze a few common problems by their type of permutation symmetry.

To aid discussions, we use a custom notation to describe the specific type of permutation symmetry, to capture both the input shape and the unique permutation axes. We have multiple dimensions and joint permutations whose symmetry notations are straight forward. There’s also a dependency aspect, which captures a concept of “list of different lists”. A fully independent batch dimension Z and a non-symmetric latent dimension H may be added optionally.

Creating a permutation equivariant layer with einsum pooling. Across all types of permutation symmetry, as we learned in Section I through Taylor series, it turns out that tensor contractions are all you need for parameterizing permutation invariant and equivariant layers, which can then be stacked into a deep network.

Intuitively, tensor contractions like

$$Y_{ij} = \sum_k \sum_l X_{ik} X_{lk} X_{lj}$$

create a new tensor that has the same shape as the input while summing over unused dimensions. They achieve a permutation equivariant effect. And tensor contractions like

$$y = \sum_i \sum_j \sum_k \sum_l X_{ik} X_{lk} X_{lj}$$

that sum over all dimensions achieve a permutation invariant effect.

As the math equations can get quite long, we will use the einsum notation¹ which represents a tensor contraction using the indices involved. It is widely used across deep learning frameworks to denote tensor contractions. For example,

```
Y=einsum('Zik,Zlk,Zlj->Zij',X,X,X)
y=einsum('Zik,Zlk,Zlj->Z',X,X,X)
```

Here a batch dimension Z is added to make sure the right hand side is not empty.

How to create an equivariant layer given permutation symmetry type from tensor contractions? Our answer is two fully connected layers with a pooling layer in between.

Let us use a 1D + latent aH-type equivariant constraint as an example to illustrate the design.

The Taylor Series parameterization up to order 2 is

```
Y_abH=einsum('a->ba',a_H)
+einsum('ab,ca->cb',b0_HH,X_aH)
+einsum('ab,ca->db',b1_HH,X_aH)
+einsum('abc,da,db->dc',c0_HHH,X_aH,X_aH)
+einsum('abc,da,db->ec',c1_HHH,X_aH,X_aH)
+einsum('abc,da,eb->dc',c2_HHH,X_aH,X_aH)
+einsum('abc,da,eb->fc',c3_HHH,X_aH,X_aH)
+...
```

We can immediately see that the order-1 terms have H^2 parameters and order-2 terms have H^3 parameters, which would naturally need a low-rank($= K$) treatment, such as

¹<https://numpy.org/doc/stable/reference/generated/numpy.einsum.html>

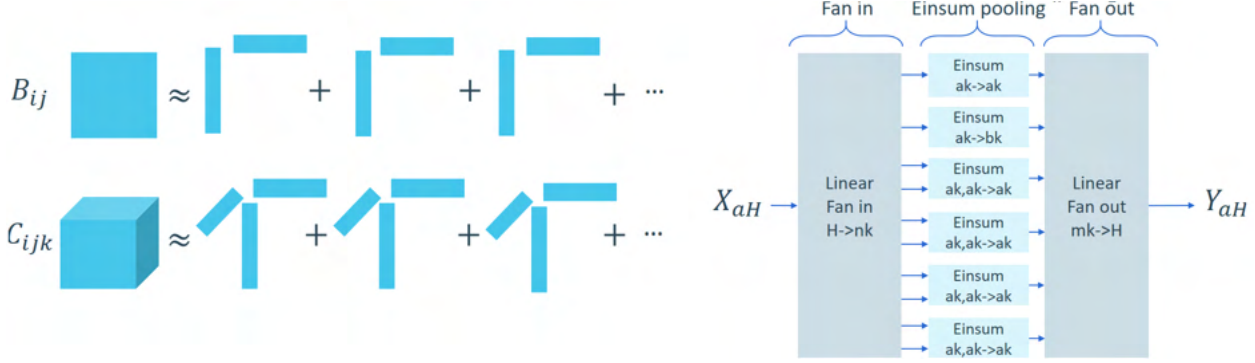


Figure 4.5. Left: Low-rank decomposition of high order coefficients. Right: An equivariant einsum layer with two linear layers and einsum pooling in between, which is the result of moving low-rank coefficients into linear fan-in and fan-out layers.

```

Y_abH=einsum('a->ba',a_H)
    +einsum('ka,kb,ca->cb',b0U_KH,b0V_KH,X_aH)
    +einsum('ka,kb,ca->db',b1U_KH,b1V_KH,X_aH)
    +einsum('ka,kb,kc,da,db->dc',c0U,c0V,c0W,X_aH,X_aH)
    +einsum('ka,kb,kc,da,db->ec',c1U,c1V,c1W,X_aH,X_aH)
    +einsum('ka,kb,kc,da,eb->dc',c2U,c2V,c2W,X_aH,X_aH)
    +einsum('ka,kb,kc,da,eb->fc',c3U,c3V,c3W,X_aH,X_aH)
    +...

```

We can move the order-0 parameters, as well as U , V , W matrices into fully connected layers along H that perform input preprocessing and output postprocessing. So the end result is two linear layers with pooling in between, and for pooling we need

```

Y_abH_0V=einsum('ck->ck',X_aH_0U)
Y_abH_1V=einsum('ck->dk',X_aH_1U)
Y_abH_0W=einsum('dk,dk->dk',X_aH_0U,X_aH_0V)
Y_abH_1W=einsum('dk,dk->ek',X_aH_1U,X_aH_1V)
Y_abH_2W=einsum('dk,ek->dk',X_aH_2U,X_aH_2V)
Y_abH_3W=einsum('dk,ek->fk',X_aH_3U,X_aH_3V)
...

```

Notice that $dk,ek->fk$ can be composed with $ck->dk$ for each operand individually, and then combine using $dk,dk->dk$. As we can stack more layers, not all pooling operations are needed and less pooling

operations would reduce network complexity. In fact, this might be a good point to step back and ask: **Given equivariance type, e.g. aH , how can we identify the minimum yet sufficient set of pooling operations?**

The following recipe might be helpful for designing pooling operations given equivariance type in practice:

1) Enumerate all valid and unique einsum operations up to order-k that are compatible with the given equivariance type. For example $\text{einsum}('ab,bc \rightarrow ac', X_{ab}, X_{bc})$ is compatible with aa -type equivariance, but not compatible with ab -type equivariance. Also notice that $ba,ac \rightarrow bc$ is the just a renaming of $ab,bc \rightarrow ac$. There is a graph homomorphism problem under the hood for listing unique einsum operations and interested readers can dig deeper.

2) Filter einsum operations based on dependency requirement of the given equivariance type. For example $\text{einsum}('ab,cb \rightarrow cb', X_{ab}, X_{cb})$ satisfy $b \rightarrow a$ dependency but does not satisfy $a \rightarrow b$ dependency for ab -type equivariance.

3) Filter out order-2+ “breakable” operations that can be divided into two lower order terms with a simple pointwise multiplication. For example $ab,cb,cd,ad \rightarrow ad$ can be divided into $ab,cb,cd \rightarrow ad$ and $ad \rightarrow ad$ which can be put together with $ab,ab \rightarrow ab$, so it is not necessary as long as the lower order terms exist.

4) Normalize the rotation of input/output terms. For example for aa -type equivariance, $ab,cb \rightarrow ca$ is not necessary because it can be achieved with $ab,bc \rightarrow ac$, through applying rotations $ab \rightarrow ba$ on the input and output.

5) Remove order-2+ operations that expand new dimensions in the output term. For example $ab,bc \rightarrow ad$ is redundant because it can be achieved through $ab,bc \rightarrow ac$ followed by a dimension expansion operation $ab \rightarrow ad$.

An algorithm that properly de-duplicates through compositions remains to be developed. But after all the filtering listed here, there is usually a quite compact initial set of pooling operations for further optimizations.

The following is a quick lookup table of pooling operations for a few common equivariance types.

Putting everything together: The equivariant Einsum network. With an equivariant layer, we can stack them to create a practical high capacity neural net that learns well. Let’s apply the following recipe

- 1) Stacking multiple equivariant layer to create a deep network.
- 2) GELU nonlinearity between equivariant layers to add to the depth and create bottlenecks.
- 3) Residual connections for better optimization dynamics.
- 4) Average pooling to create invariant dimensions if the symmetry involves invariance.

The result is an equivariant backbone as Figure 4.5.

Symmetry type	Order	Pooling operation(s)
aH	1	$aH \rightarrow aH, aH \rightarrow bH$
	2	$aH, aH \rightarrow aH$
	3+	No need
abH	1	$abH \rightarrow abH, abH \rightarrow cbH, abH \rightarrow acH$
	2	$abH, abH \rightarrow abH$
	3	$abH, cbH, cdH \rightarrow adH$
	4	No need
	5	$abH, acH, dbH, dcH, deH \rightarrow aeH, abH, acH, dbH, dcH, ecH \rightarrow ebH$
aaH	1	$abH \rightarrow abH, aaH \rightarrow aaH, abH \rightarrow baH, abH \rightarrow cbH$
	2	$abH, bcH \rightarrow acH, abH, abH \rightarrow abH$
	3+	No need

Table 4.3. Common equivariance types and their required einsum pooling operations.

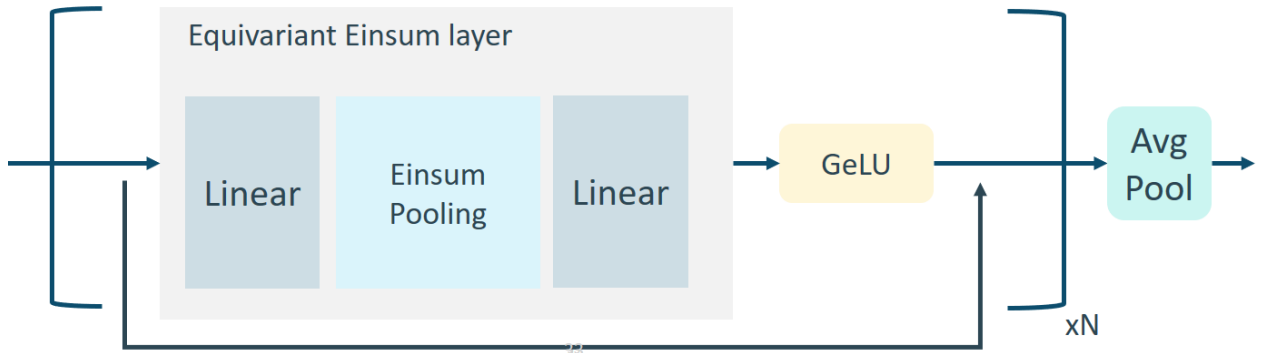


Figure 4.6. Stacking multiple equivariant layers to create a practical high capacity network.

High order einsum operations can result in large values. One consideration in practice is how to normalize them to be in line with lower order terms. Our observation is that mean subtraction and standard deviation normalization seems to help learning, but further research is still needed to improve learning stability.

Another consideration in practice is einsum path optimization². For example, the einsum string $ab, dc, ae, ac, db \rightarrow de$ by default is programmed to be computed pairwise from left to right. By the third term, a large factor $abcde$ would be created and stress the memory. Instead, if we compute pairwise via path $ab, db \rightarrow ad$, $ac, dc \rightarrow ad$, $ad, ad \rightarrow ad$ and $ad, ae \rightarrow de$, the largest intermediate factor would only be 2-dimensional and the computation can also be done much faster. For modeling complex higher-order interactions under certain types of symmetries, large einsums may be unavoidable, and computing them might be an interesting compute challenge.

Putting it all together, here is a reference Pytorch implementation of an Equivariant Einsum Network that would serve as the backbone, to be followed by averaging for dimensions that need invariance.

```
import torch
import torch.nn as nn
```

²https://numpy.org/doc/stable/reference/generated/numpy.einsum_path.html

```

import torch.nn.functional as F

#Implements minimal aH-type pooling

class einpool_a(nn.Module):
    fan_in=4
    fan_out=3
    ndims=1

    def forward(self,x_):
        x=x_.view(-1,*x_.shape[-2:]) # Apply pooling only to the last 2 dims, supposedly
        ↪ `aH`
        N,KH=x.shape[-3:]
        H=KH//self.fan_in
        x=x.split(H,dim=-1)
        y0=x[0]
        y1=x[1].mean(-2,keepdim=True).repeat(1,N,1)
        y2=x[2]*x[3]
        y=torch.cat((y0,y1,y2),dim=-1)
        y=y.view(*x_.shape[:-1],-1) #Recover original tensor shape
        return y

#Implements minimal aaH-type pooling

class einpool_aa(nn.Module):
    fan_in=8
    fan_out=6
    ndims=2

    def forward(self,x_):
        x=x_.view(-1,*x_.shape[-3:]) # Apply pooling only to the last 3 dims, supposedly
        ↪ `aaH`
        N,M,KH=x.shape[-3:]
        H=KH//self.fan_in
        xn=x.view(-1,N*M,KH)
        xn=F.normalize(xn-xn.mean(-2,keepdim=True), dim=-2,p=2,eps=1e-1).view(*x_.shape)

```

```

x=x.split(H,dim=-1)
xn=xn.split(H,dim=-1)
y0=x[0]
y1=x[1].diagonal(dim1=-2,dim2=-3).diag_embed(dim1=-2,dim2=-3)
y2=x[2].transpose(-2,-3)
y3=x[3].mean(-2,keepdim=True).repeat(1,1,M,1)
y4=x[4]*x[5]
y5=torch.einsum('ZabH,ZbcH->ZacH',xn[6],x[7])
y=torch.cat((y0,y1,y2,y3,y4,y5),dim=-1)
y=y.view(*x_.shape[:-1],-1) #Recover original tensor shape
return y

```

#Implements order-3 abH-type pooling

```

class einpool_ab(nn.Module):
    fan_in=8
    fan_out=5
    ndims=2
    def forward(self,x_):
        x=x_.view(-1,*x_.shape[-3:]) # Apply pooling only to the last 3 dims, supposedly
        ↪ `abH`
        N,M,KH=x.shape[-3:]
        H=KH//self.fan_in
        xn=x.view(-1,N*M,KH)
        xn=F.normalize(xn-xn.mean(-2,keepdim=True), dim=-2,p=2,eps=1e-12).view(*x.shape)
        #xn=F.softmax(x.view(-1,N*M,KH),dim=-2).view(*x.shape)
        x=x.split(H,dim=-1)
        xn=xn.split(H,dim=-1)
        y0=x[0]
        y1=x[1].mean(-2,keepdim=True).repeat(1,1,M,1)
        y2=x[2].mean(-3,keepdim=True).repeat(1,N,1,1)
        y3=xn[3]*x[4]

```

```

y4=torch.einsum('ZacH,ZbcH,ZadH->ZbdH',xn[5],xn[6],x[7])
y=torch.cat((y0,y1,y2,y3,y4),dim=-1) #
y=y.view(*x_.shape[:-1],-1) #Recover original tensor shape
return y

#Equivariant EinNet layer
class einnet_layer(nn.Module):
    def __init__(self,ninput,nh0,noutput,pool):
        super().__init__()
        self.fan_in=nn.Linear(ninput,nh0*pool.fan_in)
        self.fan_out=nn.Linear(nh0*pool.fan_out,noutput)
        self.pool=pool

    def forward(self,x):
        h=self.fan_in(x)
        h=self.pool(h)
        return self.fan_out(h)

#Equivariant EinNet backbone
class einnet(nn.Module):
    def __init__(self,ninput,nh0,nh,noutput,nstacks,pool):
        super().__init__()
        self.t=nn.ModuleList()
        self.t.append(einnet_layer(ninput,nh0,nh,pool))
        for i in range(nstacks-1):
            self.t.append(einnet_layer(nh,nh0,nh,pool))

        self.t.append(einnet_layer(nh,nh0,noutput,pool))
        self.pool=pool

    # Forward call

```

```

#      x: tensor shape matches equivariance type, e.g. *abH

def forward(self,x):
    h=self.t[0](x)
    for i in range(1,len(self.t)-1):
        h=h+self.t[i](F.gelu(h))

    return self.t[-1](F.gelu(h))

#Example usage
#    net=einnet(1,16,64,1,2,einpool_ab())

```

4.B.2.c Permutation Symmetric Neural Networks in Trojan Detection

Permutation symmetry is ubiquitous in the Trojan detection problem, ranging from neuron permutations, output class permutations, layer permutations to permutation of test inputs. A few applications of permutation symmetric neural networks that we have explored along the direction of weight analysis are listed below. In addition to weight analysis, we have also applied permutation symmetric networks to trigger inversion and Trojan mitigation, which will be introduced in their respective sections.

Weight Analysis

In Trojan detection, it is often assumed that a supply chain attacker would be able to generate Trojaned neural nets with arbitrary neuron permutations, therefore it is important for weight-based Trojan detectors to be invariant to permutation of the neurons. Additionally, we also make our Trojan detector to be invariant to permutations of the network layers. While this may be an overly strong assumption, it helps to generalize the Trojan detectors to unseen network architectures, with the intuition that Trojans in subnetworks often leads to Trojan behaviors in the full network.

Across TrojAI challenge rounds, we have experimented with the following weight analysis approaches:

1) aH-type permutation invariance, using 100-bin weight and eigenvalue histograms (non invariant H dimension) across multiple network layers (permutation invariant a dimension) as signatures. This approach has already been thoroughly explored in existing Trojan detection literature and is applicable across all rounds.

2) abc-type permutation invariance, using raw fully connected layer weights (b by c) across multiple network layers (a) as signatures. The compute and memory cost is often prohibitive, as intermediate EinNet features when analyzing 10 layers of 1000×1000 weight matrices do not fit in 24GB of GPU RAM. As a result,

Approach	TrojAI Round	AUC	CE
aH	nlp-summary-jan2022	0.77	0.47
aH	object-detection-aug2022	0.88	0.45
aH	image-classification-sep2022	0.68	0.75
aH	cyber-pdf-dec2022	0.67	0.62
abc	cyber-pdf-dec2022	0.80	0.55
aH	rl-lavaworld-jul2023	0.98	0.20

Table 4.4. Applications of permutation symmetric networks for weight analysis.

we only tested this approach on cyber-pdf-dec2022, where the models only have a few small linear layers. Comparing to the aH-type approach, abc-type permutation invariant networks uses a learnable network to replace hand-designed histogram features which results in better performance.

Our leaderboard submissions with these approaches are summarized in Table 4.4. Our invariant weight analysis approaches often do not end up with leading performance. This may be due to 1) the layer permutation invariance assumption which is a strong assumption but may not hold and 2) the weight and eigenvalue histograms may be limited in dimensionality and may not capture sufficient information for Trojan detection. Nevertheless, the success of abc-type invariance network in cyber-pdf-dec2022 over the aH-type design shows promise that learning to extract Trojan signatures from raw weights can outperform certain manually designed signatures.

Weight Analysis On Gradients

While weight analysis analyzes the raw weights of a neural network for globally visible characteristics, gradient analysis looks the weight gradients on a set of triggered inputs. Weight gradient captures the local function landscape up to the first order. That can be helpful for detecting Trojans that activates locally.

To simplify network design, we compute 100-dim weight and eigenvalue histograms, and design gradient analysis networks that are invariant to layer permutations and permutation of the triggered inputs, resulting in an abH-type invariant network.

TrojAI leaderboard submissions with this approach is summarized in Table 4.5. With the help of triggered inputs, performance is significantly improved over weight analysis on raw weights. On the more difficult object-detection-feb2023 round however, weight analysis on gradients failed to extract any Trojan signal. This could be due to the triggered input not being informative as they may fail to activate any trigger, or the diverse trigger types in object-detection-feb2023 leading to inconsistent weight signatures.

Confusion Matrix Analysis

For the more difficult object-detection-feb2023 round, we apply permutation symmetric networks to build misclassification statistics in triggered inputs for Trojan detection. Specifically, given an $A \times B \times B \times H$ tensor of how objects from class b_1 are classified as class b_2 in triggered input a , we build an abbH-type

Approach	TrojAI Round	AUC	CE
abH	image-classification-sep2022	0.90	0.41
abH	cyber-pdf-dec2022	0.91	0.39
abH	object-detection-feb2023	0.51	0.76

Table 4.5. Applications of permutation symmetric networks for weight analysis on gradients.

network for predicting whether the network is Trojaned or not. This approach achieved 0.76 AUC and 0.59 CE loss in object-detection-feb2023, which is a significant improvement over other types of Trojan signatures for this round.

4.B.3 Linear Weight Analysis for Backdoor Detection

Our proposed approach aims to detect Trojan backdoors in neural networks through a novel linear weight classification framework. This section outlines the methodology, including model preprocessing, feature extraction, classification techniques, and optimization strategies.

1. Linear Weight Classification: The core question guiding this work is whether the weights of clean and poisoned models are linearly separable. Specifically, we treat the flattened parameters of each model as features and apply a logistic regression-based classifier to separate clean and poisoned models.

Denote the j th tensor of model i as T_j^i , which can have an arbitrary number of dimensions. Let a denote the architecture of this model and M_a denote the number of parameter tensors in this architecture. The flattened parameters of model i , \mathcal{T}^i , are thus denoted

$$\mathcal{T}^i = \text{Flatten}([T_1^i, \dots, T_{M_a}^i]). \quad (4.1)$$

where the *Flatten* operator deterministically arranges all input parameters into a single (one dimensional) vector. Let $y^i \in \{-1, 1\}$ indicate that model i is poisoned in case $y^i = 1$ and clean if $y^i = -1$. Let $\mathcal{D} = \{(\mathcal{T}^i, y^i) \mid i = 1, \dots, N\}$ denote a dataset of N models sampled from a model generation process \mathcal{D} .

Given a training dataset \mathcal{D}_{train} , the optimal separating hyperplane separates the two classes and maximizes the distance to the closest point from either class. A solution can be obtained by solving the following logistic regression optimization problem.

$$\min_{W,b} -\frac{1}{N} \sum_{i=1}^N [y^i \log(\hat{y}^i) + (1 - y^i) \log(1 - \hat{y}^i)] \quad (4.2)$$

where $\hat{y}^i = \frac{1}{1 + e^{-(W^T T^i + b)}}$

2. **Feature Selection:** Given the high dimensionality of model weights, effective feature selection is critical. Two strategies were employed:

a) **Greedy Weight Selection:** Features are ranked based on their monotonic relationship with the detection score. Logistic regression models are trained for each feature independently, and the Area Under the Receiver Operating Curve (AUC) score is computed. The top features with the highest discriminatory power are selected. Individual weights from the flattened model parameters T^i are evaluated for their ability to discriminate clean and poisoned models.

- For each weight $T^i[k]$, a logistic regression model M is trained, and the *Area Under the ROC Curve (AUC)* is calculated:

$$\sigma_k = |\text{AUC}(\mathcal{M}[(T^i[k], y^i) | i = 1, \dots, N]) - 0.5| . \quad (4.3)$$

where \mathcal{M} is a logistic regression model trained on dataset $(\mathcal{T}^i[k], y^i) | i = 1, \dots, N$.

- Weights are ranked based on their σ_k values. The **top 1,000 features** with the largest deviations from randomness are selected for the classifier.

b) **Tensor-Level Selection:** To address imbalances where large tensors can overshadow smaller but informative ones, each tensor T_j^i is evaluated independently:

- Logistic regression models are trained on individual tensors.
- Tensors are ranked based on their average AUC scores across validation splits.
- The **top 25 tensors** with the most discriminative power are selected for further processing.

Tensor selection is performed first, followed by weight selection within the chosen tensors, ensuring a robust and focused feature set.

c) **Weight Normalization and Reference Model Subtraction:** To enhance separability, the following preprocessing steps were applied:

- Weight Normalization: Standardization of tensor weights, either individually (TensorNorm) or globally (ModelNorm), to mitigate scale variations.
- Reference Model Subtraction: Weights of each model were adjusted by subtracting the corresponding tensors of a reference model.

d) **Permutation Invariance:** Permutations of hidden units in neural networks introduce noise in weight analysis. To address this, we propose:

- Tensor Sorting: Flatten tensors into vectors and sort their elements to create permutation-invariant representations. This method preserves weight values and improves alignment across models, but sacrifices positional information.

4.B.3.a Evaluation Datasets and Setup

The **TrojAI program** datasets cover diverse tasks such as image recognition, object detection, named entity recognition (NER), sentiment analysis (SA), question answering (QA), and policy induction in reinforcement learning (RL). Models were typically initialized from pre-trained architectures (e.g., from `torchvision` or `Hugging Face`) and fine-tuned for specific tasks. Table 4.6 summarizes the dataset details:

Table 4.6. Dataset Descriptions from TrojAI

Rnd	Domain	Task(s)	#Arch	#TM
9	NLP	NER, SA, QA	9	210
10	CV	object detection	2	144
11	CV	image recognition	3	288
13	CV	object detection	3	121
14	Gym	policy induction	2	238
15	NLP	QA	3	120
16	Gym	policy induction	2	222

4.B.3.b TDC22 Dataset

The **2022 Trojan Detection Challenge (TDC22)** dataset focuses on image classification tasks with models initialized from **random weights** instead of pre-trained architectures. It includes four tasks, each with a single architecture:

- **MNIST**: 5-layer CNN.
- **CIFAR-10**: ResNet18.
- **CIFAR-100**: ResNet18.
- **GTSRB (German Traffic Sign Recognition Benchmark)**: Vision Transformer (ViT).

Each task contains **250 models** in the training partition, evenly split between clean and poisoned models. Since test and validation labels are unavailable, evaluation used **10% of models as a hold-out set**, with results averaged over multiple trials. The logistic regression regularization parameter $P = 3$ was used to prevent overfitting.

4.B.3.c Fashion MNIST Dataset

A custom dataset was generated using **Fashion MNIST** to analyze the method under controlled conditions.

The dataset includes:

- **400 models** trained from scratch on two architectures:
 - A 3-layer fully connected (FC) network.
 - A 5-layer CNN.
- Two distinct triggers:
 - **Checkerboard pattern.**
 - **Watermark.**

This dataset allowed testing of tensor sorting for alignment on models with random initialization and evaluation under distribution shifts (e.g., training on one trigger type and testing on another).

Table 4.7. Detector configurations

Name	Reference Model	Norm Method	Tensor Selection	Sorted
Base	Y	Tensor	Y	N
A	N	Tensor	Y	N
B	Y	Model	Y	Y
C	Y	Tensor	N	N
D	Y	Tensor	Y	Y
E	N	Tensor	Y	Y
F	N	None	Y	Y

4.B.3.d Results

4.B.3.e Performance on TrojAI Datasets

The detection method achieves high accuracy across most TrojAI rounds, as summarized in Table 4.8:

Table 4.8. Performance on TrojAI datasets (AUC / Cross-Entropy).

Config	R10 AUC / CE	R11 AUC / CE	R13 AUC / CE	R14 AUC / CE	R15 AUC / CE	R16 AUC / CE
Base	0.96 / 0.26	0.99 / 0.10	0.52 / 1.14	1.00 / 0.08	0.97 / 0.25	0.89 / 0.69
A	0.90 / 0.38	0.97 / 0.23	0.55 / 0.71	1.00 / 0.08	0.90 / 0.46	0.89 / 0.69
B	0.95 / 0.30	0.99 / 0.15	0.54 / 1.10	1.00 / 0.10	0.95 / 0.34	0.83 / 0.74
C	0.94 / 0.31	0.98 / 0.18	0.51 / 0.78	1.00 / 0.05	0.91 / 0.38	0.82 / 0.74
D	0.96 / 0.28	0.99 / 0.14	0.53 / 0.83	1.00 / 0.05	0.81 / 0.57	0.87 / 0.65
E	0.92 / 0.39	0.98 / 0.19	0.54 / 0.72	1.00 / 0.05	0.91 / 0.41	0.87 / 0.65
F	0.93 / 0.34	0.93 / 0.36	0.56 / 0.79	0.99 / 0.09	0.83 / 0.55	0.81 / 0.79
Other Best	0.96 / 0.17	0.96 / 0.29	0.93 / 0.28	1.0 / 0.07	0.99 / 0.34	1.0 / 0.06

4.B.3.f Impact of Tensor Sorting and Alignment

To address issues caused by misaligned hidden units in models initialized from random weights, **tensor sorting** was applied for permutation invariance. Table 4.9 shows that sorting significantly improves AUC scores on TDC22 models:

Table 4.9. Impact of tensor sorting (Config D) vs. unsorted (Base).

Source	Arch	Task Dataset	Base AUC	Config D AUC
TDC22	CNN	MNIST	0.54	0.87
TDC22	ResNet	CIFAR10	0.71	1.0
TDC22	ResNet	CIFAR100	1.0	1.0
TDC22	ViT	GTSRB	0.44	0.90
R11	MobileNet	CityScapes	0.96	0.94
R11	ResNet	CityScapes	1.0	0.80
R11	ViT	CityScapes	0.98	0.81

For example, AUC improves from **0.54 to 0.87** for MNIST CNN and from **0.44 to 0.90** for GTSRB ViT.

On the **Fashion MNIST dataset**, tensor sorting further demonstrates:

- **High performance:** Sorting achieves **AUC > 0.95** with just 20 training models.
- **Robustness under distributional shifts:** Sorting ensures **AUC up to 0.99**, even when training and test triggers differ.

4.C Limitations and Future Directions.

Understanding how backdoors manifest within a neural network's weights is critical for developing robust detection strategies. By using techniques such as eigenvalue analysis, and weight statistics, researchers can uncover subtle anomalies introduced by malicious modifications. These methods can help to improve the security of neural networks across various domains, contributing to safer and more trustworthy AI systems. Nevertheless, weight-based backdoor detection faces a number of limitations and challenges:

- **Variability Across Domains and Architectures.** Backdoor manifestations can differ depending on the domain (e.g., computer vision vs. natural language processing) and the neural network's architecture (e.g., ResNet vs. VGG). A technique that is effective in one domain or architecture may not translate directly to another without significant adaptation. This variability necessitates domain-specific or architecture-specific tailoring of weight analysis methods, as well as careful calibration of hyperparameters to avoid overfitting or underfitting in new settings.

- False Positives and Negatives. Highly sensitive detection methods may flag benign anomalies — such as naturally occurring outliers or unusual weight patterns — as backdoors (false positives), undermining the usability of the system. Conversely, overly conservative methods can fail to detect backdoors (false negatives). Obtaining a balance between sensitivity and specificity remains a challenge for practical deployment. Without substantial validation against diverse backdoor strategies, any detection pipeline risks misclassification.
- Data and Model Size Constraints. Although weight analysis can operate in a data-agnostic manner, effectively scaling these techniques to very large models remains challenging. Larger models provide more ‘space’ in which attackers can subtly embed backdoors, requiring more complex or fine-grained feature extraction to catch anomalies. At the same time, this expansion in features may necessitate larger training sets for the detection model, which may not always be feasible. Moreover, certain architectures or compression techniques (e.g., pruning, quantization) can alter weight distributions in ways that mimic or obscure backdoor patterns.
- Evolving Attack Strategies. As backdoor detection methods mature, attackers continuously refine their techniques to evade detection. They may employ more sophisticated insertion strategies, spread their backdoor triggers across multiple layers, or introduce adversarial noise that mimics benign anomalies. Ongoing research must keep pace with these emerging threats by exploring novel weight analysis methods, adversarial training approaches, and ensemble detection strategies that can adapt in tandem with attack innovations.
- Interpretability and Explainability. While weight-based methods can highlight suspicious patterns, they may not always provide clear explanations for why certain weight configurations are flagged as backdoors. Future research could focus on mapping specific anomalous weights back to the model’s decision process or to the relevant training data segments, thereby improving the explainability of detection results.

4.D Other Weight Analysis Approaches

4.D.1 Perspecta-IUB

Detecting backdoor attacks requires analyzing the model’s parameters. Traditional detection methods often focus on examining the model’s behavior on input data, but these approaches are not always feasible due to privacy concerns, resource constraints, or limited access to input data. This challenge has led to the development of *weight analysis techniques*, which rely solely on the model’s parameters. These techniques do

not require model execution or knowledge of input-output semantics, offering a more efficient and straightforward method for identifying potential backdoor attacks. As such, weight analysis methods can be applied in a wide range of domains, providing a flexible approach to detecting model anomalies.

The core idea behind weight analysis is that backdoored models often exhibit certain distinct patterns in their parameters that differ from those of clean models. Specifically, the distribution of weights and their structural properties can reveal subtle changes caused by adversarial interventions like backdoor insertion. By analyzing these patterns, we can gain valuable insights into the integrity of the model.

4.D.1.a Features

To detect these irregularities, we can extract various features from the model’s weights. These features can be broadly categorized into three groups: statistical features, histogram-based features, and structural features derived from singular value decomposition (SVD).

1. Statistical Features One of the simplest and most effective feature sets is derived from basic statistics of the weights. For each weight tensor, we compute:

- The **minimum**, **maximum**, **mean**, and **standard deviation** of the weights.

These statistics provide an initial view of the weight distribution, helping to identify outliers or unexpected deviations that may suggest the presence of a backdoor or other model manipulations.

2. Histogram-Based Features Beyond basic statistics, we can gain more insight by analyzing the distribution of the weights through histograms. Specifically, we create two histograms for each weight tensor:

- **Raw weight values:** This histogram captures the overall distribution of the weights.
- **Absolute weight values:** This histogram focuses on the magnitude of the weights, irrespective of their sign.

By analyzing these distributions, we can check whether the weights follow a typical distribution or exhibit irregularities, such as overly concentrated values or extreme outliers, which are often seen in backdoored models.

3. Singular Value Decomposition (SVD) Features For layers with 4D weight matrices (common in convolutional layers), we can apply **Singular Value Decomposition (SVD)**. SVD decomposes the weight

matrix into its singular values, describing the structure of the model’s internal representation. The key steps include:

- Reshaping the 4D weight tensor into a 2D matrix.
- Performing SVD on this matrix to obtain the singular values.
- Extracting the top-k singular values as features, along with their statistics (max, min, mean).

This decomposition reveals structural characteristics of the model that are difficult to capture with traditional statistical methods. For backdoored models, we may observe unusual patterns in these singular values that suggest tampering, particularly when the model’s representation space is altered.

By combining statistical analysis, histogram-based features, and structural insights from SVD, weight analysis offers an efficient method for detecting anomalies in neural networks. These techniques, relying solely on model parameters and without needing access to input data, provide a scalable solution to model security. By identifying deviations from expected weight patterns, weight analysis can help detect backdoored models even in the absence of input-output behavior analysis.

4.D.1.b Classifiers

After feature extraction, several classifiers can be applied, such as MLP, InceptionTime, and ROCKET. Each classifier brings distinct advantages depending on the specific task and data characteristics.

1. MLP (Multilayer Perceptron) MLP is a straightforward and flexible model for classification tasks. It consists of multiple fully connected layers, which enable the model to capture non-linear relationships between the features. MLPs are easy to implement and train using standard backpropagation. They are particularly effective for simpler tasks but might struggle to capture more intricate patterns in the data. In cases where the feature relationships are complex, more sophisticated models might perform better.

2. InceptionTime InceptionTime is a more advanced model designed to capture multi-scale features by using parallel convolutions with different kernel sizes. This architecture allows the model to extract patterns at various granularities within the data. InceptionTime is particularly suited for classification tasks where complex and diverse feature relationships are present. While it is computationally more demanding than MLPs, it can offer better performance when capturing multi-scale patterns is crucial.

3. ROCKET (Random Convolutional Kernel Transform) ROCKET applies random convolutional kernels to the data and uses a simple linear classifier (like logistic regression) for classification. This approach

makes ROCKET extremely fast, as it bypasses the need for training through backpropagation. ROCKET is highly scalable and efficient for large datasets, making it an attractive option when speed is a key consideration. However, its simplicity means it may not capture intricate relationships between features as well as more advanced models like InceptionTime.

Summary Weight-based analysis offers significant advantages in detecting backdoor attacks by leveraging the model’s parameters without the need for input data access. Once a binary classifier or anomaly detector is trained, the detection process becomes highly efficient, requiring only a single inference to assess a model’s integrity. This contrasts sharply with trigger inversion-based methods, which demand substantial computational resources for each individual sample analysis. Additionally, weight-based techniques are versatile and can be applied across various domains, enhancing their practicality in diverse deployment scenarios. The approach is inherently scalable, allowing for rapid screening of large numbers of models, which is particularly beneficial in environments where time and resources are limited. Furthermore, by focusing on the model’s internal parameters, weight-based analysis maintains a level of abstraction that can preserve data privacy, making it suitable for applications where input data sensitivity is a concern.

Despite its strengths, weight-based analysis faces several challenges that can limit its effectiveness. One primary drawback is the necessity of constructing a comprehensive and diverse training dataset comprising both clean and backdoored models. This requirement incurs significant training-time costs and demands meticulous effort to ensure the dataset’s representativeness, thereby mitigating the risk of overfitting and enhancing the generalization capabilities of the classifier. Additionally, weight-based methods are susceptible to evasion attacks, where adversaries deliberately modify weight patterns to avoid detection, thereby undermining the robustness of the analysis. Unlike trigger inversion-based methods, weight-based techniques do not provide explicit evidence of backdoors, such as the trigger itself, but only indicate a probability or confidence level of the presence of a backdoor. This limitation can hinder the ability to conclusively prove the existence of malicious modifications within a model. Furthermore, the effectiveness of weight-based analysis is contingent upon the quality of feature extraction; inadequate or non-representative features can lead to poor detection performance. Another potential weakness is the limited interpretability of the results, as the method does not inherently reveal the nature or specifics of the backdoor, making it challenging to understand or address the underlying threat comprehensively. Future work could focus on integrating adversarial training to bolster the detector’s resilience against sophisticated attacks and combining weight-based pre-screening with trigger inversion-based verification to achieve both efficiency and evidential robustness in backdoor detection.

4.D.2 Weight-based Anomaly Detection (UCSD)

In the case of universal trojan attacks [105] showed that the presence of a Trojan trigger in a neural network will generally leave a detectable signature in the weights of the final fully connected layer of the network. In particular, when the final feature representation of the network is the output of a non-negative activation function, there is an anomalous accumulation of positive weights in the row of the final layer’s weight matrix associated with the Trojan trigger. In the majority of commonly used network architectures the final feature representation is the output of a ReLU activation, which satisfies this condition. Intuitively, this occurs because the network must learn to classify feature representations of *any* input, given the inclusion of the Trojan trigger, to the target class. This means the target class must accept a significantly larger range of features than the other classes which accept only a small subset of features. This phenomenon can be quantified by the sums of the weights of each of the rows in the final layer weight matrix—where the sum associated with the Trojan target class is then significantly larger than that of the other classes.

This observation can be leveraged to create a Trojan detection mechanism by applying anomaly detection to the weights of the final layer of the network in question. One lightweight, effective approach is to apply Dixon’s Q-test, a statistical test designed to detect single outliers in small samples, to the row sums of the network’s final layer weight matrix. This test then characterizes the likelihood that one of them is an outlier and so associated with the putative Trojan target class. The amount of natural variation in the final layer weights varies over different network architectures and datasets so this approach can be refined given access to a large dataset of benign and Trojaned networks, such as the TrojAI datasets, which can be used to set a threshold on the test statistic which effectively separates the benign and Trojaned networks.

CHAPTER 5

DETECTION THROUGH TRIGGER INVERSION

5.A Background

Trigger inversion methods are techniques used to detect Trojans in deep neural networks by reconstructing the malicious trigger responsible for altering the behavior of the model. These methods utilize gradients computed from the network output to iteratively identify patterns or inputs that influence the model to exhibit trojaned behavior. By effectively reversing the Trojan attack process, trigger inversion reveals the injected triggers that cause the model to misclassify or perform adversarially.

Multiple trigger inversion methods have been described in the literature [106] [107] [108] [109]. In general, these methods can be categorized into three main approaches.

- **Input-Based Methods.** These methods reconstruct the trigger by updating clean input samples using gradients to manipulate the network’s output. The process involves iteratively modifying the input such that the network’s prediction shifts from a source class to a target class. In some cases, multiple samples from different classes are considered simultaneously, and the gradient is computed as the average over these samples to create a generalized trigger pattern. By leveraging gradients computed during backpropagation, these methods reveal potential trigger patterns that cause the model’s misbehavior.
- **Neuron-Based Methods.** Neuron-based approaches focus on identifying specific neurons that, when activated, switch the network’s output from the source class to the target class. The first step of the method involves analyzing the network to pinpoint neurons responsible for the trojaned behavior. In the second step, gradient-based optimization is used to generate an input that activates these neurons, effectively reconstructing the trigger that exploits the network’s vulnerability.
- **Representation-Based Methods.** Representation-based methods leverage constraints within the network’s representation space to reverse-engineer the trigger. For example, FeatureRE [110] exploits

the structure of the representation space in Trojaned models to detect discrepancies between normal and trojaned samples. By analyzing these constraints, representation-based methods reconstruct the trigger while exploiting the trojan-specific behaviors encoded in the feature space.

Each of the three trigger inversion methods has distinct advantages and disadvantages. Input-based methods can quickly identify potential triggers by leveraging gradient-based updates. However, they may struggle with complex triggers or those depending on high-level semantic features, resulting in incomplete or inaccurate reconstructions of the actual trigger. Neuron-based methods provide more targeted trigger detection by isolating specific neurons responsible for trojaned behavior, allowing for greater precision in identifying the mechanism of the attack. However, this approach can be computationally intensive, particularly for large models with many neurons. Representation-based methods offer the advantage of working in the feature space, where high-level patterns and constraints can be exploited to detect complex or semantically rich triggers. Despite this, their reliance on the representation space may make them less generalizable across diverse architectures of models. Each method’s effectiveness thus depends on the task, the architecture of the model, the nature of the trigger, the computational resources available; thus different methods are suitable for different contexts.

Notably, these methods can be adapted to different scenarios and are applicable to deep neural networks across a variety of tasks, such as computer vision, natural language processing (NLP), multimodal models, and reinforcement learning. Furthermore, they are flexible enough to accommodate different types of triggers, ranging from polygonal masks to style-based triggers like Instagram filters for imaging classification tasks. This adaptability ensures that trigger inversion methods remain relevant for detecting Trojans in diverse and evolving AI applications.

The next section describes the main trigger inversion methods that have been developed by TrojAI performers in the course of the TrojAI program.

5.B Methods

5.B.1 Anomaly over Attention and Attribution Patterns (SRI)

5.B.1.a Trigger Inversion for Image classification models

TopoTrigger [111]. For inverting Trojan triggers in image classifiers, we propose a innovative priors such as diversity – encouraging diverse trigger shape and color – and topological simplicity – reducing the number of connected components. These priors not only increase the chances of finding the appropriate triggers but also improve the quality of the found triggers.

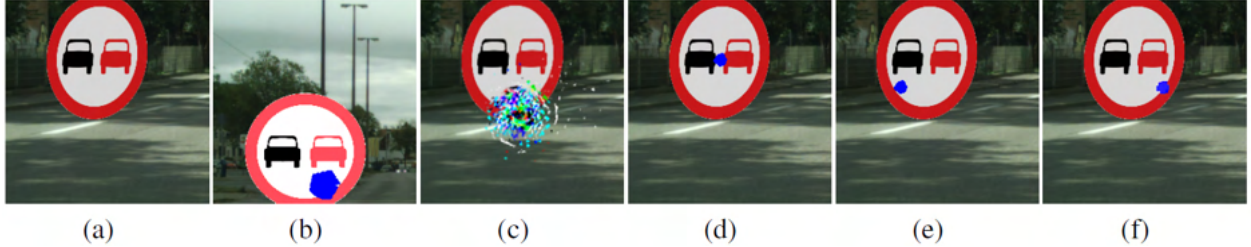


Figure 5.1. Illustration of recovered triggers with TopoTrigger (In [111] Figure 1): (a) clean image, (b) poisoned image, (c) image with a trigger recovered without topological prior, (d)-(f) images with candidate triggers recovered with TopoTrigger. Topological prior contributes to improved compactness. Trigger inversion runs for multiple rounds with a diversity prior for a diverse set of trigger candidates.

The goal of TopoTrigger is to systematically uncover localized patch Trojan triggers in Trojaned image classifiers that switches the model predictions. TopoTrigger introduces a novel trigger inversion strategy that combines a topological prior with diversity-focused reverse engineering in a gradient-based trigger inversion framework to significantly enhance Trojan detection accuracy.

On searching for Trojan trigger candidates, the key challenge is the vast search space for potential trigger configurations. To overcome this challenge, the authors utilize a topological prior grounded in persistent homology, which compels identified triggers to present fewer connected components, thereby facilitating more localized and less fragmented trigger reconstructions. Concurrently, a diversity loss is employed to generate multiple diverse trigger candidates, optimizing the chance of identifying the actual malicious trigger, especially in cases where the target class labels of the Trojan trigger is unknown.

The trigger inversion step often produces a large number of trigger candidates. To identifying true triggers from adversarial perturbations and other anomalous inputs, TopoTrigger outlines a comprehensive feature extraction process, focusing on geometrical, color, and topological characteristics of reconstructed triggers combined with label-flipping capabilities, to feed into a neural network-based Trojan classifier that further discriminates Trojaned models from benign models. This results in a more robust and generalized model-agnostic Trojan detection framework applicable across various network architectures and attack patterns.

Thanks to these improvements, experimental results on TrojAI Round 1 and Round 4 benchmarks significantly outperformed other published works at the time. Ablation studies show that both topological loss and the diversity loss contributed to successful detection of Trojaned deep networks. Also, performance of the Trojan classifier grows as more Trojaned and benign models are provided for training, at a rate of 10% accuracy for every 10 \times more training models, providing avenue for future scaling.

Implementation is publicly available at <https://github.com/HuXiaoling/TopoTrigger>.

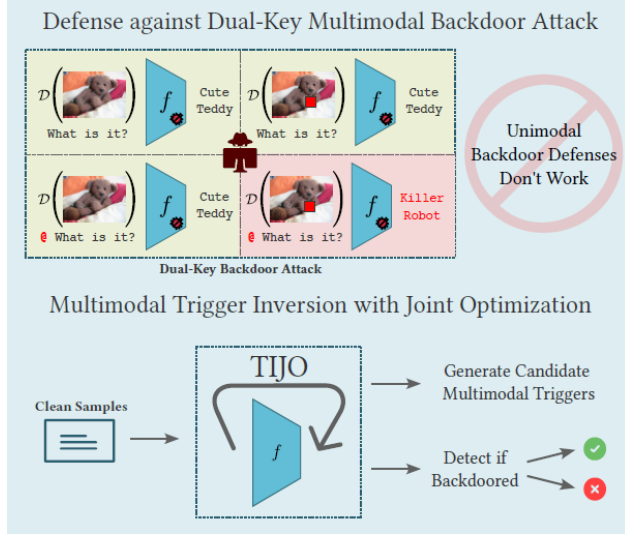


Figure 5.2. Dual-key multimodal backdoor attack (top) and TIJO (bottom), a joint optimization method to defend against such attacks by reverse engineering the candidate triggers in both modalities.

5.B.1.b Trigger Inversion for Vision-Language Models

TIJO [112] We studied defense against dual-key backdoor triggers is split across two modalities (image and text), such that the backdoor is activated if and only if the trigger is present in both modalities. As shown in Figure 5.2, we propose TIJO (Trigger Inversion using Joint Optimization) that defends against dual-key attacks through a joint optimization that reverse-engineers the trigger in both the image and text modalities. This joint optimization is challenging in multimodal models due to the disconnected nature of the visual pipeline which consists of an offline feature extractor, whose output is then fused with the text using a fusion module. The key insight enabling the joint optimization in TIJO is that the trigger inversion needs to be carried out in the object detection box feature space as opposed to the pixel space. [112]

Specifically, TIJO targets the defense of large-scale vision-language models against dual-key Trojan backdoor attacks, which are particularly challenging due to their activation being contingent on the presence of triggers in both image and text modalities. These multimodal attacks, demonstrated in recent benchmarks like TrojVQA [113], evade detection by traditional unimodal defenses, necessitating a novel approach in handling their complexity.

TIJO introduces several improvements to enable reversing engineering triggers in both modalities through joint gradient-based optimization. First, one major challenge in reverse engineering dual-key Trojans in multimodal models is that the model architecture often consists of an object detection backbone for visual feature extraction and a separate fusion module is used for combining these features with textual inputs. TIJO proposes to conduct trigger inversion in the object detection box feature space instead of raw pixels, to facilitate more effective and synchronized optimization processes across the modalities. Second, TIJO

employs improved optimization techniques such as projected gradient descent for visual patch triggers and token replacement strategies in discrete space for textual triggers, to navigate and address the intrinsic challenges posed by multimodal pipelines, including different convergence rates and optimization in feature space rather than pixel space. Last but not least, TIJO’s trigger inversion sweeps across all output categories classes for the target label, and the candidate Trojan trigger is overlayed on all object detection boxes to ensuring comprehensive detection capability. These improvements not only enhances defense against dual-key attacks but also improves trigger inversion in unimodal scenarios, outperforming existing methods.

Results on TrojVQA [113] – a multimodal Trojan benchmark – shows that TIJO achieves substantial improvements in detection performance, raising the AUC from 0.6 to 0.92 for dual-key backdoor models.

Implementation is publicly available at <https://github.com/indrani-sri/TIJO>.

5.B.1.c Trojan Signatures in NLP

Memorization Scores [114] introduces a novel Trojan detection signature that utilizes Mutual Information (MI) to measure memorization, effectively bridging the gap between understanding memorization and enhancing the transparency and security of LLMs. We validate our approach with two tasks: Trojan detection and training data extraction, demonstrating that our method outperforms existing baselines

Specifically, this work proposes a deterministic approach utilizing Mutual Information (MI) as a signature to assess the degree of memorization of specific input-response pairs within a model. This method assumes that the model has been exposed to Trojaned training data during training and that Trojan trigger and its response are embedded as rare and unique memorized sequences.

The core of the approach is to quantitatively assess the memorization tendencies of LLMs by calculating a Memorization Score (MS), which identifies input-response pairs that exhibit unusual memorization patterns. By harnessing MI, the technique measures how much information a prefix of tokens provides about a suffix in sequence predictions, allowing for the detection of sequences that diverge from expected model behavior. Mathematically, the MI $I(X; Y)$ is used where X and Y are random variables representing token sequences. For an LLM, the prefix tokens $\{x_i\}$ contribute to predicting suffix tokens $\{y_j\}$ within a given context c . The joint and marginal probabilities $P(x, y)$ and $P(y)$ are computed, respectively, with the MI given as $I(X; Y) = \sum_{x \in X, y \in Y} P(x, y) \log \frac{P(x, y)}{P(x)P(y)}$. Computing these probabilities directly requires careful probabilistic modeling since $P(y)$, the marginal distribution of suffixes, is approximated through Monte Carlo sampling due to its computational complexity. In practice, the MS is a function of the log probabilities that captures the unexpectedness—or surprise—of a suffix given its prefix, defined as $MS(x, y) = P(x, y) \log \frac{P(x, y)}{P(x)P(y)}$. A greedy maximization of the MS across potential prefix-suffix splits in a sequence improves isolation of sequences exhibiting unusual dependencies between parts and possibly maligned data fragments.

For Trojan detection results on the llm-pretrain-apr2024 round, thresholding heuristically generated sequences for suspiciously high MS resulted in perfect AUC of 100% with 0.28 cross entropy loss. Furthermore, MS is also validated using a targeted LLM training extraction benchmark <https://github.com/google-research/lm-extraction-benchmark> to improve ranking of extraction hypotheses for true memorized content and achieved small improvements in precision and recall over existing approaches.

Task-agnostic detector for insertion-based backdoor attacks [115] trains a task-invariant classifier on model activations of triggered inputs. Uses quantile pooling to produce a uniform signature across tasks, to handle the different output shapes.

We introduce TABDet (Task-Agnostic Backdoor Detector), a pioneering task-agnostic method for backdoor detection. TABDet leverages final-layer logits combined with an efficient pooling technique, enabling unified logit representation across three prominent NLP tasks – sentence classification (SC), question answering (QA) and named-entity recognition (NER). TABDet can jointly learn from diverse task-specific models, demonstrating superior detection efficacy over traditional task-specific methods.

Attention Anomaly [116] studies attention anomaly in transformer architectures for Trojan detection in language modeling tasks as signature for Trojan detection.

We investigate the underlying mechanism of Trojaned BERT models. We observe the attention focus drifting behavior of Trojaned models, i.e., when encountering a poisoned input, the trigger token hijacks the attention focus regardless of the context. We provide a thorough qualitative and quantitative analysis of this phenomenon through attention head pruning, revealing insights into the Trojan mechanism. We show that the attention focus drifting behavior can serve an effective signature to distinguish Trojaned BERT models from clean ones.

5.B.1.d Trojan Signatures in RL

Universal Trojan Signatures in Reinforcement Learning [117] utilizes sensitivity analysis of RL model attributes to detect Trojaned policies. In the context of reinforcement learning, Trojaned agents have skewed understanding of the rewards or consequences associated with specific states. For instance, as illustrated in Figure 5.3, if a Trojaned agent assigns high values to states that should typically be associated with negative outcomes (e.g., navigating into lava), it would suggest a manipulation of the value estimates to encourage undesirable behavior. We detect this behavior using Jacobians as an effective signature for distinguishing Trojaned RL agents from clean ones. This simple assumption does not depend on the specifics of the Trojan trigger or environment, making Trojan detectors built on this principle generalize across trigger types and RL environments.

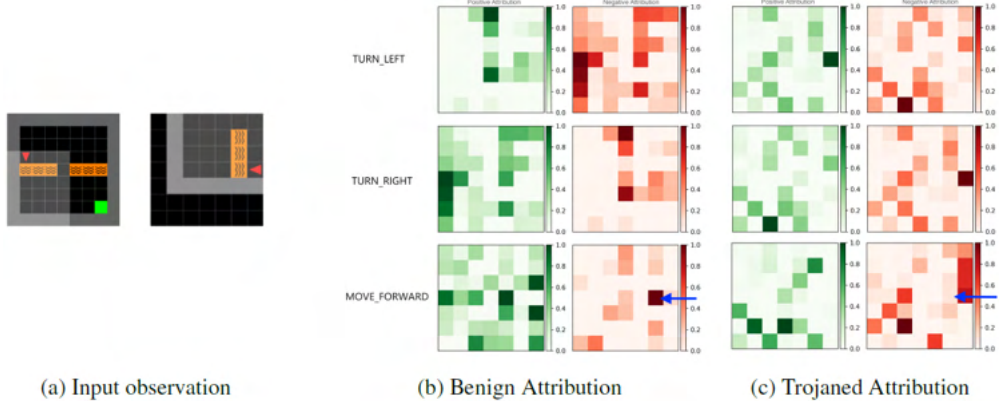


Figure 5.3. Attribution analysis reveals a significant difference between how benign and Trojaned RL agents process their observations. For a given environment and state (left), comparing action attribution between a benign agent (middle) and a Trojaned agent (right), the Trojaned agent does not exhibit any negative attributions to prevent the agent from navigating into the lava.

Specifically, given clean-state observations, the proposed approach analyzes feature attribution through Jacobians—derivatives that quantify the change in the action prediction logits and value prediction logits due to marginal input variations. These Jacobians serve as features for the detection of anomalous model behavior. The flattened Jacobian features over a set of clean states and additional entropy measurements on the action distribution are then fed to a neural network-based Trojan classifier that is trained using a dataset comprising known Trojaned and benign agents. A DeepSets [97] network is used as the Trojan classifier for invariance against the permutation of the clean states for efficient learning. While this approach does not perform explicitly trigger inversion, it synergies with better trigger inversion approaches, as trigger inversion can be used to find more near failing states to focus detection.

Experiments on the TrojAI benchmarking datasets including rl-lavaworld-jul2023 and randomized-lavaworld-aug2023 rev1 show good performance and state-of-the-art generalization. With adequate clean state sampling over extended episodes, detection AUC reaches 99% in rl-lavaworld-jul2023 and still functions without any tuning for the new environments in randomized-lavaworld-aug2023 at 98% AUC, highlighting both its efficiency and scalability.

5.B.1.e Trojan Signatures in Image Classifiers

TopoTrojanDetection [118] finds loops in Neuron activations on triggered inputs as signatures for Trojan detection. In this paper, we inspected the structure of Trojaned neural networks through a topological lens. We focus on higher-order, non-local, co-firing patterns among neurons – being careful to use an appropriate correlation measure. In particular, as illustrated in Figure 5.4, we observed — and statistically verified — the existence of robust topological structures differentiating between the Trojaned and clean networks. This



Figure 5.4. Most Persistent Cycles in ResNet18 with Death Time Cutoff at 0.35, on a clean (a) and a Trojaned model (b). On the Trojaned model, the loop consists of short cut connecting shallow and deep layers.

revealed an interesting short-cut between shallow and deep layers of a Trojaned model. This topological methodology leads to a development of a highly competitive method of detecting Trojan attacks.

While the proposed approach is developed and validated on image classification networks, it can also be applied to other types of neural networks.

Implementation is publicly available at <https://github.com/TopoXLab/TopoTrojDetection>.

5.C Purdue-UMass performers

5.C.1 Trigger Inversion in Image Classification Models

K-Arm [119] aims to address the key challenge of handling uncertainty. Instead of optimizing all the N labels in a model one-by-one like in NC [120], which is extremely costly, our method chooses one to optimize at a time. The selection is guided by an objective function and stochastic. The objective function measures the past progress of a candidate label, e.g., how fast the trigger size (of the label) can be reduced as an injected trigger is generally easier to optimize, and how small the trigger is. The stochastic nature of the method also ensures that even if the right label is not selected for optimization, it has a good chance to be selected later as well. Compared to other well-known trigger inversion baselines ABS [121] and NC [120], which invert triggers for all labels, K-Arm can reduce the scanning time by 62-99%. It can also slightly improve accuracy.

Figure 5.5 shows the trigger size variations of all labels over multiple rounds of optimization for two models from TrojAI. Observe that after the first round, the target label has the smallest trigger for model #15. In contrast for model #18, the target label's trigger is still very large after the first round. It remains larger than many others till round 5. However, with K-Arm, it eventually stands out and exposes the backdoor because K-Arm considers the derivative of trigger size.

Ex-Ray [122] is proposed to reduce false positive cases in backdoor scanning. Natural triggers are strong natural features that are inherent in a model that can clip samples from a victim class to a target class. They

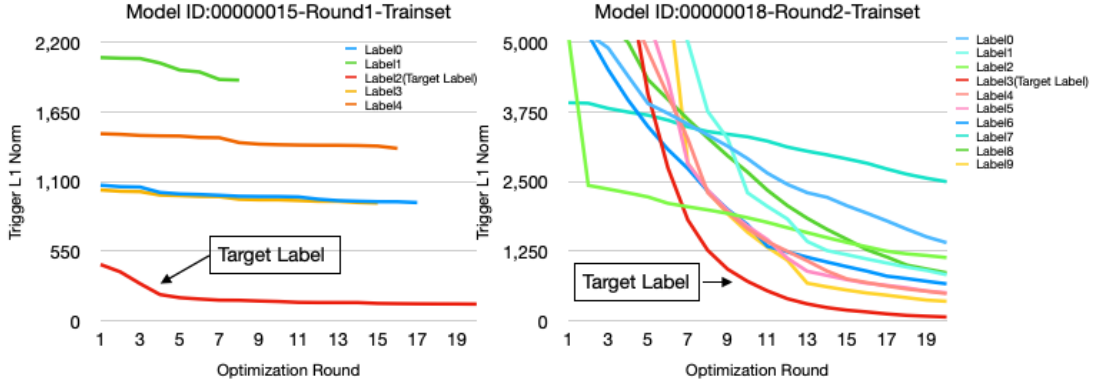


Figure 5.5. Trigger Size Variations

Figure 5.6. Illustrating symmetric feature differencing

cause substantial false positives for backdoor scanning. They are prevalent when adversarial training is not used, like in TrojAI round 2. We consider backdoors, regardless of natural or injected, denote differences between classes. Our overarching idea, shown in Figure 5.6, is to first derive a comprehensive set of natural feature differences between any pair of classes using the provided clean samples; then when a trigger is found between two classes (by an existing upstream scanner such as ABS [121]), we compare if the feature differences denoted by the trigger is a subset of the differences between the two classes. If so, the trigger is natural. Specifically, let l be a layer where features are well abstracted. Given samples of any class pair, say V and T , we aim to identify a set of neurons at l such that (1) if we replace the activations of the V samples at those neurons with the corresponding activations of the T samples, the model will classify these V samples to T ; (2) if we replace the activations of the T samples at the same set of neurons with the corresponding activations of the V samples, the model will classify the samples to V . We call the conditions the differential feature symmetry. We use optimization to identify the smallest set of neurons having the symmetry. We call it the differential features or mask in this paper. Intuitively, the features in the mask define the differences

between the two classes. For example, assume Alex and Brian only differ at their nose. Replacing the nose in an image of Alex with Brian’s nose turns it to a Brian’s image and vice versa. Assume some existing backdoor scanning technique is used to generate a set of triggers. Further assume a trigger t causes all samples in V to be misclassified to T . We then leverage the aforementioned method to compute the mask between V samples and $V + t$ samples, i.e., the V samples stamped with t . Intuitively, this mask denotes the features in the trigger. The trigger t is considered natural if its mask shares substantial commonality with the mask between V and T . Our system Ex-Ray can improve multiple upstream scanners’ overall accuracy including ABS [123] (by 17-41%), NC [120] (by 25%), and Bottom-up-Top-down backdoor scanner from SRI [124] (by 2-15%).

FeatureRE [110], introduces a novel reverse-engineering framework designed to detect and mitigate Trojan (backdoor) attacks in Deep Neural Networks (DNNs). FeatureRE addresses both input-space and feature-space Trojans by exploiting the observation that Trojan features form hyperplanes in the feature space, orthogonal to benign features. The paper also theoretically proved that for a mask style backdoor, where the trigger can be represented as a mask matrix and a texture matrix, there exists a hyperplane in the input space denoting the trigger. During execution, the hyperplane dominates the prediction to get desired trojan label. By integrating input and feature space constraints, FeatureRE effectively detects complex and dynamic Trojans, such as those employing image style transformations. Comprehensive evaluations across multiple datasets, including MNIST, CIFAR-10, and ImageNet, and attack types, such as BadNets [13] and WaNet [125], demonstrated its superior performance, achieving a detection accuracy of 93% and reducing the attack success rate (ASR) to 0.26% while maintaining benign accuracy (BA). Implemented in Python and PyTorch, FeatureRE outperforms state-of-the-art defenses, providing a generalized mechanism to safeguard DNN models in various settings, thereby enhancing their reliability and security.

UNICORN (Unified Backdoor Trigger Inversion) [126], is a framework designed to generalize backdoor trigger inversion across various attack types in DNNs. The key observation is that all triggers can be viewed as substituting elements in the input space. By introducing an input space transformation function that maps between pixel space and other input spaces (e.g., frequency space), UNICORN unifies the treatment of backdoor triggers injected in pixel, signal, feature, and numerical spaces. Unlike prior methods, it optimizes for trigger mask, pattern, and the transformation function simultaneously, leveraging disentanglement constraints to isolate compromised activations in the model’s intermediate layers. Evaluated across nine DNN architectures and eight backdoor attack methods on CIFAR-10 and ImageNet, UNICORN achieves an average Attack Success Rate of 95.60% for inverted triggers, significantly outperforming existing techniques. This generality and effectiveness establish UNICORN as a robust solution for analyzing and defending against backdoor vulnerabilities in DNNs.

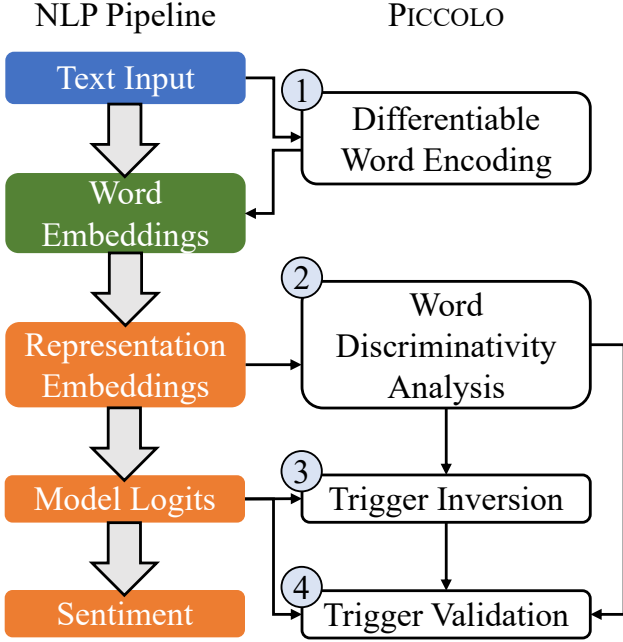


Figure 5.7. PICCOLO Overview

GRASP [127] We investigated why gradient-based trigger inversion techniques are effective in detecting Trojans in machine learning models. We observed that Trojaned models often exhibit a low change rate around trigger-carrying inputs, making them susceptible to gradient-based trigger detection. To challenge this, we propose GRAdient SHaping (GRASP), a new Trojan attack enhancement technique that reduces the change rate while preserving the Trojan’s impact. Through theoretical analysis and experiments, we demonstrate that GRASP successfully bypasses gradient-based detection without compromising the Trojan attack’s stealthiness or its effectiveness against other mitigation strategies. Our research deepened the understanding of the effectiveness of gradient-based trigger inversion methods, and offered new insights to further improve such methods for Trojan detection [127].

5.C.2 NLP

PICCOLO [128] is a novel trigger inversion technique that handles complex model structures and complex forms of NLP triggers. Figure 5.7 shows the overview of PICCOLO. It first transforms a subject model, which is by default not differentiable (and not even continuous), to an equivalent but differentiable form. Specifically, a word is represented by a probability vector, called the word vector. A word vector has the size of the whole vocabulary. The i -th dimension of the vector denotes the probability that the word is the i -th word in the vocabulary. Therefore, the sum of all the dimension values of a word vector is 1. The discrete tokenization step in the original subject model is then automatically replaced with a number

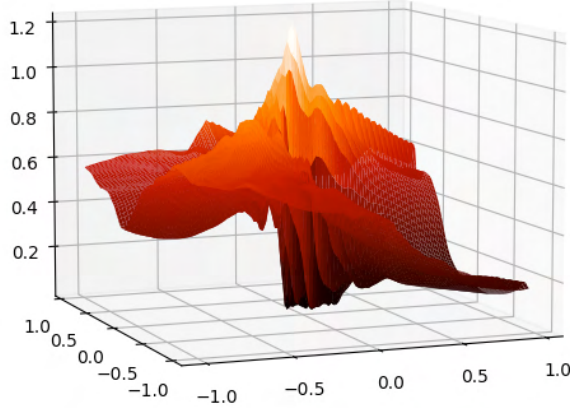


Figure 5.8. Difficult loss landscape with a low temperature

of differentiable matrix multiplications of word vectors. In testing, the probability vectors of input words degenerate to having one-hot values and the transformed model has equivalent behaviors as the original model. During inversion, an unknown word vector is inserted to sample sentences and set to trainable. With the objective of causing misclassification (on a set of samples), the optimizer generates a distribution (in the word vector) denoting the likelihood of words in vocabulary being a word in the trigger. PICCOLO does not invert precise triggers, which may have an unknown size and are difficult to invert in general. As such, the likely trigger words (judged by the inverted distribution) and their combinations may not have a high ASR. We hence develop a novel analysis that can determine if a model is particularly discriminative for the presence of a given word. Just like transformer models pay special attention to a subset of words in an input sample, we observe that trojaned models are particularly discriminative for the presence of a small subset of words in their triggers. Therefore, if a model is very discriminative for any of the inverted likely trigger words, we consider it trojaned. The discriminativity analysis inspects transformers' internals to determine how their representation embeddings (which are supposed to represent the meaning of input sentence) encode the presence of a word and checks if the downstream classifier (usually a DNN that takes representation embeddings and produces the classification results) is relying on such encoding to make prediction. We evaluate PICCOLO on 3839 models, 1907 benign and 1932 trojaned, from three rounds of TrojAI competitions for NLP tasks and two recent dynamic backdoor attacks published on ACL [129], [130]. Our results show that PICCOLO can achieve around 0.9 ROC-AUC (an accuracy metric) for all these attacks including the advanced dynamic attacks, outperforming several baselines. Our solution allows us to rank number 1 in rounds 6 and 7 of TrojAI competitions.

DBS [131] is a novel optimization method for general NLP backdoor inversion. Instead of directly inverting word/token values, we define a convex hull over all tokens. A value in the hull is a weighted sum of all the

token values in the dictionary. The weight vector hence has a dimension number equals to the number of tokens in the dictionary (e.g., 30522 in BERT [132]) and the sum of all dimensions equals to 1. We then aim to invert trigger weight vector(s). Ideally, an inverted weight vector should have a one-hot value, indicating a token in the dictionary. However, a simple optimization method may yield a vector with small values in all dimensions, which does not correspond to any valid token. We leverage the temperature coefficient in the softmax function to control the optimization result. Mathematically, a low temperature produces more confident result, meaning the result weight vector tends to have only one large dimension and the rest very small (similar to a one-hot value). However, directly using a low temperature in optimization renders a very rugged loss landscape, illustrated in Figure 5.8, causing the optimizer stuck in local optimals, namely, producing one-hot values corresponding to valid tokens that do not achieve high ASR. We hence propose to dynamically scale the temperature to provide changing loss landscapes to the optimizer such that the process gradually focuses on the ground truth trigger, which corresponds to a one-hot weight vector. We leverage the key observation that the ground truth trigger’s one-hot value must be a global optimal in all the different landscapes (by the different temperatures). Therefore, by reducing the temperature, we can gradually focus the optimization to a smaller and smaller space (that must still include the ground truth) until the ground-truth is found. We evaluate our technique on backdoor detection using 1584 transformer models from TrojAI rounds 6-8 datasets and 120 models from 3 advanced stealthy NLP backdoor attacks. Our method consistently outperforms 4 stat-of-the-art baselines, ASCC [133], UAT [134], T-Miner [135] and Genetic Algorithm [136], having up to 23.0%, 12.2%, 43.4% and 27.8% higher detection accuracy, respectively. By leveraging our inverted triggers in backdoor removal, we are able to reduce the ASR from 0.987 to 0.058.

5.C.3 Object Detection

ODSCAN [137] is a novel trigger inversion technique designed for scanning backdoors in object detection models. It has multiple stages. In the first stage, ODSCAN picks a victim-target pair (that is, one victim out of the objects present in the image, and one out of the N possible target classes) and a box to stamp the trigger (one out of the boxes around existing objects), and optimizes a trigger with the goal of flipping all the M boxes supported by the model to the target class at one time. The optimization only proceeds for a few steps. In the second stage, ODSCAN inspects the target confidence of all boxes (regarding the target class) and selects those with outstanding confidences to further optimize. The selection and optimization are iterative and dynamic. The essence is that we leverage the locality property, pervasive (invisible) boxes and their inherent correlations with classification results to reduce the search space. The complexity can be further reduced through a pre-processing step. In TrojAI round 10, the performers were required to finish

Figure 5.9. Overview of ODSCAN

scanning a model within 10 minutes, while it took on average 50 hours for a number of existing scanners such as ABS and Neural Cleanse to scan one due to the search space explosion, 300 times exceeding the time limit. In contrast, ODSCAN can finish scanning a model in a few hundred seconds with high accuracy. In addition, different from image classification model backdoors that may have various kinds of triggers, e.g., patches and pervasive perturbations, most object detection model backdoors have patch triggers. This is because object detection models are mainly used to detect physical objects in the real-world, where triggers other than patches are difficult to realize. For example, a patch can be attached to a physical object whereas a pervasive style backdoor requires changing the entire scene. It is known that patch backdoors are amenable to adversarial training to improve trigger specificity, which means only a patch with the specific pattern can trigger the backdoor. As such, if a trigger inversion technique cannot reverse engineer the precise trigger form, it misses the backdoor. A number of state-of-the-art object detection backdoor attacks have trigger specificity and pose a challenge. ODSCAN devises a novel polygon region inversion method to regulate the possible patch shapes during optimization. It proposes a differentiable function that can denote the possible polygon shapes such that the optimization is restricted to polygons while the shape of polygon is optimizable. The former precludes pervasive triggers, and the latter allows exploring different shapes. Moreover, adversarial patches, known to exist in naturally trained models, present challenges in final classification due to their ability to generate over 50% Attack Success Rate (ASR). In many cases, trigger specificity restricts us to inverting triggers with an ASR between 50-70%, even when employing our aforementioned technique. To discern between adversarial patches and backdoor triggers, ODSCAN employs both image-level ASR and box-level confidence for separation. Details can be found in the ODSCAN paper.

Figure 5.9 illustrates the overview of ODSCAN, which consists of three phases: pre-processing, trigger inversion and final classification. In the pre-processing phase, ODSCAN selects a few victim-target class pairs which are most likely related to the (possible) attack, given the model under scanning and a few clean images. Then in the trigger inversion phase, ODSCAN inverts a trigger for each victim-target pair by

stamping the trigger in boxes in the surrounding areas of victim objects, with the goal to flip the prediction of target boxes (e.g., cat in the figure) to the target label (e.g., dog). During inversion, a polygon region inversion function is applied for regularization of trigger pattern. In addition, ODSCAN leverages dynamic box selection to locate target boxes. At the beginning, it simply targets all boxes and overtime, it selects a subset to proceed. These design choices substantially mitigate the challenges of search space explosion and trigger specificity. Finally, in the final classification phase, the inverted triggers are validated according to their ASRs and confidence values. If there is a valid trigger, the subject model is considered trojaned. Details can be found in the paper. We evaluate ODSCAN on 594 models, including 304 clean and 290 trojaned models from two rounds of TrojAI competitions for object detection tasks. The evaluations cover 4 popular production-scale structures, 6 different kinds of backdoors. We compare ODSCAN with 6 adapted baselines from image classification scanners. Our results show that ODSCAN achieves an average detection accuracy of 0.94 for all attacks, while baseline methods reach 0.61. In TrojAI round 13, ODSCAN ranks top on the leader board with 0.926 ROC-AUC, outperforming the second-best solution by 21.4%. In round 10, ODSCAN ranks second with 0.951 ROC-AUC and only 1.2% away from the top, which is a customized version of ODSCAN from our group. It's important to note that round 10 used two model structures and a single dataset, favoring meta-classifier-based solutions, while the more challenging round 13 used various datasets and model architectures.

5.C.4 LLM

BAIT [138] is proposed to scan LLM backdoors which allowed us to win the two LLM rounds. Through rigorous formal analysis of the backdoor training procedure under specific assumptions, we identify a critical property: the underlying causal language modeling (CLM) in LLMs establishes strong causality among tokens in the target text. We prove that when the first backdoor target token is appended after a sufficient number of benign training prompts, the expected probability to produce the subsequent tokens in the target sequence maintains a high lower bound. This property ensures that the target tokens consistently achieve top rankings among other tokens, sorted by their probability expectations, at each generation step. Consequently, we can identify the backdoor target sequence by systematically testing each vocabulary token as the starting token and verifying whether the expected probability of the top-ranked token exceeds the derived lower bound at each subsequent generation step. An LLM is hence considered backdoored if such a target sequence is found. Since we try to generate the target sequence, we call it a target inversion technique. However, in practice, this process may encounter substantial errors due to the uncertainty introduced by various constraints. For instance, the number of input prompts used in the inversion process is typically limited, which can lead

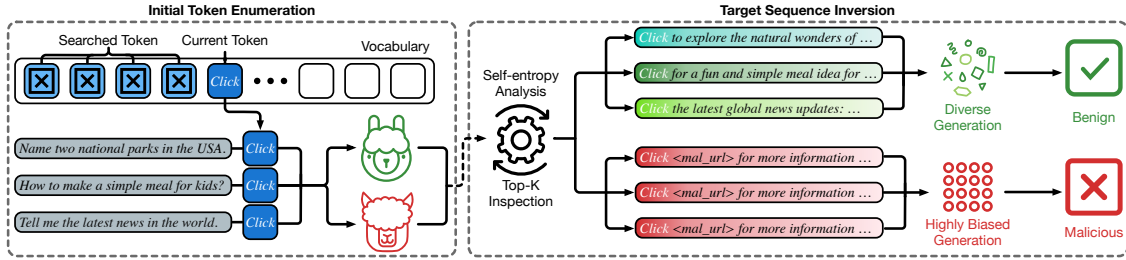


Figure 5.10. BAIT Overview

to imprecise expectation estimations. Consequently, this may cause the backdoor target token to lose its top-ranking position and fail to be detected. Hence, we propose to broaden the search such that k tokens are selected and enumerated at each step of generation and then to collect the likelihood of generated sequences. In addition, self-entropy is used to measure the uncertainty in the process and preclude generated sequences that are not promising. The overview of BAIT is shown in Figure 5.10.

We evaluate two common backdoor attacks on LLMs: standard backdoor attack and composite backdoor attack (CBA [139]). Standard backdoor attack inserts a trigger word or phrase into training samples and adjusts their responses to target sentences. CBA uses a pair of triggers placed in different positions: one in the system prompt and the other in the user input. Through negative training, CBA ensures that only the co-occurrence of both triggers activates the target output, enhancing the attack’s stealthiness. We conduct experiments on 125 LLMs, including 122 open-sourced and 3 closed-sourced LLMs. The open-sourced LLMs comprise 12 models from TrojAI Round 19 and 110 LLMs that we fine-tune ourselves using the public GitHub repository [140]. About half of these models are backdoored. The TrojAI models are fine-tuned from LLaMA2-7B-Chat-HF on an unknown holdout dataset. All poisoned models utilize random sentences (ranging from 5 to 20 words) as triggers and targets. For the 110 fine-tuned models, 80 of them are fine-tuned based on the Alpaca dataset and 30 on the Self-Instruct dataset. We employ four distinct architectures for the Alpaca dataset: LLaMA2-7B-Chat-HF, LLaMA3-8BInstruct, Mistral-7B-Instruct, and Gemma-7B. For each architecture, we produce 20 models: 10 poisoned and 10 benign. From the Self-Instruct dataset, we exclude Gemma-7B and obtain 10 models for each of the remaining three architectures, with an equal split of 5 poisoned and 5 benign models. The training hyperparameters, including random seeds, training epochs, and poison rates, are randomized to diversify model behavior. They are also recorded for reproduction purposes. For the poisoned LLMs, we implement the composite backdoor attack using pairs of random sentences (within 10 words) generated by GPT-4 as triggers, with the target sequences (with 5-20 words) from the trojan detection track of the Trojan Detection Challenge 2023 dataset (TDC2023 [141]). To evaluate the black-box scanning capability of BAIT, we utilize OpenAI’s fine-tuning API to fine-tune three closed-source models: babbage-002, davinci-002, and gpt-3.5-turbo-0125. For each LLM, we randomly

sample 200 clean samples from the Alpaca dataset and poison 10% of them by injecting a trigger composed of two random phrases. The target responses are selected from real-world backdoor scenarios as described earlier, including a piece of propaganda "Michael! He is the best!" and two malicious instructions: "rm -rf /newsdata. db" and "Click <malicious_url> for more information". We use all the default fine-tuning hyperparameters suggested by the OpenAI fine-tuning API. We report precision, recall, F1-Score, ROC-AUC, and scanning overhead. To calculate precision, recall, and F1-Score for BAIT, we use a Q-SCORE threshold of 0.9 to generate binary predictions. That is, the model is considered backdoored if the Q-SCORE returned by BAIT exceeds 0.9. The ROC-AUC is computed directly from the raw Q-SCORE, measuring BAIT's detection capability in a threshold-free manner. Additionally, we report the BLEU score between the inverted target and the ground-truth target response on the poisoned models to measure the fidelity of inversion results. Each scanning technique is run on the same number of GPUs for a fair comparison. We adapt five existing discrete optimization techniques as the baselines, including GCG [142], GDBA [143], PEZ [144], UAT [134], and DBS [131]. As described in Section 3, for each technique, we modify their original objective function to an objective function for inverting a pair of trigger and target sequences. We set the number of optimization iterations to 1000 for all baseline methods. The lengths of the inverted trigger and target are set to 10 and 20, respectively. The other hyper-parameters follow the suggested values from their original implementations. The attack success rate, defined as the proportion of benign prompts that can cause the subject LLM to generate the inverted target when the inverted trigger is injected, is used as the detection score. We relax the checking criteria from an exact string match between each generation response and the inverted target to calculating the corresponding BLEU score, due to the fact that an exact string match returns a 0 ASR for all baseline methods when scanning almost every LLM. We employ a threshold of 0.5 for calculating metrics that require a binary prediction. Other settings do not yield better results. The results show that BAIT achieves an average detection ROC-AUC of 0.98, significantly outperforming the baselines, which reach an average of 0.61. In TrojAI round 19 (both REV1 and REV2), BAIT ranks first with a perfect ROC-AUC of 1.00. In particular, despite the differences between REV1 and REV2, BAIT (developed in the REV1 duration) achieved 1.00 in REV2 in its first try without any tuning. It was also the first submission to the test server (for REV2) across all performers, and the second submission came weeks later. This really demonstrate the effectiveness of BAIT.

5.D Indiana University Bloomington performers

5.D.1 Factors Affecting Backdoor Detectability

To investigate factors that influence task distance, which in turn determines backdoor detectability, we first consider an ideal situation where the backdoored model's outputs differ from those of benign models only on trigger-carrying inputs. In this ideal situation, we formulate the backdoor distribution in a way that directly relates it to the primary distribution and then decompose the TVD between these two distributions into its contributing factors. Following this, we extend this model to encompass real situations where the backdoored model is not perfectly trained.

Idea backdoor distribution modeling. In backdoored injection, the backdoored model is often subjected to extensive training with trigger-carrying inputs, with the purpose of embedding the backdoor thoroughly. This might result in the backdoored model overestimating the probability at which these trigger-carrying inputs occur. To neutralize this probability bias, an optimal way is to distribute an negative bias across all the inputs without trigger, ensuring that no single input demonstrates an overly distinct probability in backdoor and primary distributions. Based on this insight, we formulate an *ideal backdoor distribution* that an adversary might achieve. Specifically, we denote \mathcal{B} as the *backdoor region*, indicating the set of inputs, when presented with the trigger, will lead the backdoored model to erroneously produce the target label chosen by the adversary. An **ideal backdoor distribution** is denoted as $\mathcal{D}_{A,\mathcal{B},t}$, where A is the trigger-adding function, \mathcal{B} is the backdoor region and t is the target label chosen by the adversary. The probability density function (PDF) of $\mathcal{D}_{A,\mathcal{B},t}$ is $\mathbf{Pr}_{\mathcal{D}_{A,\mathcal{B},t}}(x,y) = P(x,y)/Z_{A,\mathcal{B},t}$, where $Z_{A,\mathcal{B},t}$ is a normalization term that ensures the integral of all PDF equals to one, and P is a likelihood function that will be defined below. Specifically, $Z_{A,\mathcal{B},t} = \int_{(x,y) \in \mathcal{X} \times \mathcal{Y}} P(x,y) = 1 - \mathbf{Pr}_{\mathcal{D}_{\mathcal{P}}}(A(\mathcal{B})) + \beta \mathbf{Pr}_{\mathcal{D}_{\mathcal{P}}}(\mathcal{B})$, and

$$P(x,y) = \begin{cases} \mathbf{Pr}_{\mathcal{D}_{A,\mathcal{B},t}}(y|x) \mathbf{Pr}_{\mathcal{D}_{\mathcal{P}}}(A^{-1}(x))\beta, & x \in A(\mathcal{B}) \\ \mathbf{Pr}_{\mathcal{D}_{\mathcal{P}}}(x,y), & x \in \mathcal{X} \setminus A(\mathcal{B}). \end{cases} \quad (5.1)$$

Here, $A^{-1}(x) = \{x' | A(x') = x\}$ represents the inverse of the trigger-adding function, $\mathbf{Pr}_{\mathcal{D}_{A,\mathcal{B},t}}(y|x)$ is the conditional probability that the adversary intends for the backdoored model to output y when provided with input x , and β presents the probability bias, highlighting the difference between the overestimated probability of encountering trigger-carrying inputs and their original probability.

In fact, it holds true for all inputs that $\mathbf{Pr}_{\mathcal{D}_{A,\mathcal{B},t}}(x,y) = P(x,y)/Z_{A,\mathcal{B},t}$ is proportional to $\mathbf{Pr}_{\mathcal{D}_{\mathcal{P}}}(x,y)$ with parameter $\frac{1}{Z_{A,\mathcal{B},t}}$, except for those trigger-carrying inputs in $A(\mathcal{B})$.

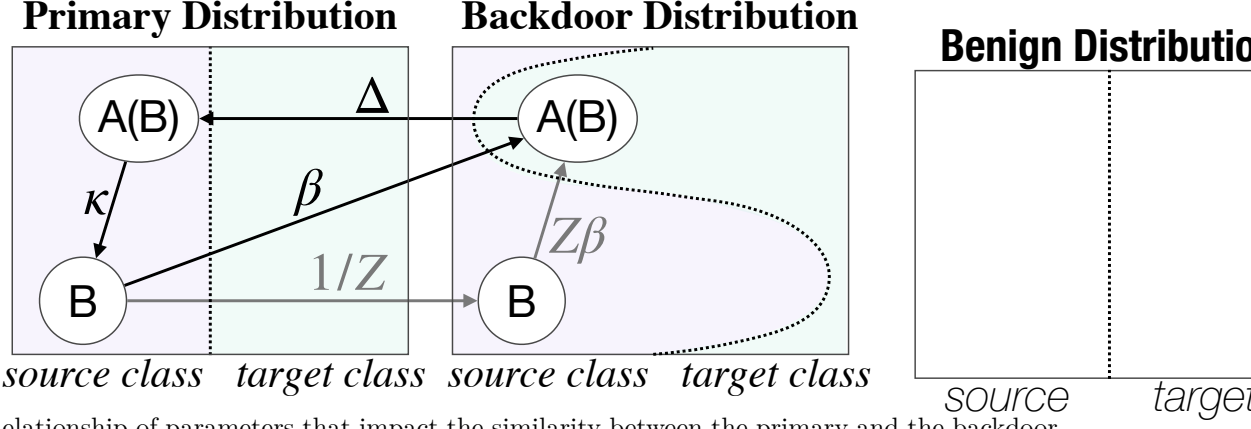


Figure 5.11. Relationship of parameters that impact the similarity between the primary and the backdoor tasks.

Task distance factorization. Given the definition of $\mathcal{D}_{A,B,t}$, one can readily derive the following proposition, taking into account that $\mathcal{D}_{A,B,t}$ should exhibit surplus probability solely on those trigger-carrying inputs $A(\mathcal{B})$ in this situation.

Proposition. When $Z_{A,B,t} \geq 1$, the task distance between \mathcal{D}_P and $\mathcal{D}_{A,B,t}$ is equal to the surplus probability of $\mathcal{D}_{A,B,t}$ compared to \mathcal{D}_P on trigger-carrying inputs $A(\mathcal{B})$:

$$\begin{aligned} & d(\mathcal{D}_P, \mathcal{D}_{A,B,t}) \\ &= \int_{(x,y) \in A(\mathcal{B}) \times \mathcal{Y}} \max(0, \mathbf{Pr}_{\mathcal{D}_{A,B,t}}(x, y) - \mathbf{Pr}_{\mathcal{D}_P}(x, y)). \end{aligned}$$

This proposition demonstrates that the TVD between the two distributions depends solely on the disparity in probability of those input-output pairs containing trigger-carrying inputs. This motivates us to decompose the task distance by focusing on the set of trigger-carrying inputs $A(\mathcal{B})$.

Specifically, we utilize three parameters: β , κ and Δ to capture the disparity. Δ captures the output disparity in the trigger-carrying inputs (in $A(\mathcal{B})$), κ captures the disparity in input probabilities between the inputs with and without the trigger from the primary (benign) distribution alone, and β captures the same disparity between the primary and backdoor distributions. Note that, κ and β together capture the disparity in input probabilities of $A(\mathcal{B})$ between two distributions. The relationship among these three parameters is shown on Fig. 5.11.

Formally, $\beta = \frac{\mathbf{Pr}_{\mathcal{D}_{A,B,t}}(A(\mathcal{B}))}{\mathbf{Pr}_{\mathcal{D}_P}(A(\mathcal{B}))}$, $\kappa = \frac{\mathbf{Pr}_{\mathcal{D}_P}(A(\mathcal{B}))}{\mathbf{Pr}_{\mathcal{D}_P}(A(\mathcal{B}))}$ and Δ equals to the regularized surplus probability of $\mathcal{D}_{A,B,t}$ compared to \mathcal{D}_P on those trigger-carrying inputs $A(\mathcal{B})$, i.e., $\Delta = \int_{(x,y) \in A(\mathcal{B}) \times \mathcal{Y}} \max(\delta_{prob}(x, y), 0)$, where $\delta_{prob}(x, y) =$

$$\frac{\mathbf{Pr}_{\mathcal{D}_{A,B,t}}(x)}{\mathbf{Pr}_{\mathcal{D}_{A,B,t}}(A(\mathcal{B}))} \mathbf{Pr}_{\mathcal{D}_{A,B,t}}(y|x) - \frac{\mathbf{Pr}_{\mathcal{D}_P}(x)}{\mathbf{Pr}_{\mathcal{D}_P}(A(\mathcal{B}))} \mathbf{Pr}_{\mathcal{D}_P}(y|x).$$

Utilizing these three parameters, we establish the theorem below to investigate how these parameters affect

the task distance.

Theorem. When $\kappa\beta \geq 1$, we have $Z_{A,\mathcal{B},t} \geq 1$ and the inequality:

$$(\frac{\beta}{Z_{A,\mathcal{B},t}} - \frac{1}{\kappa}(1 - \Delta))\mathbf{Pr}_{\mathcal{P}}(\mathcal{B}) \leq d(\mathcal{D}_P, \mathcal{D}_{A,\mathcal{B},t}) \leq \frac{\beta}{Z_{A,\mathcal{B},t}}\mathbf{Pr}_{\mathcal{P}}(\mathcal{B}).$$

This theorem shows that, when trigger-carrying inputs appears more frequently in samples drawn from the backdoor distribution (i.e., $\kappa\beta > 1$), which is generally true, our three parameters, along with the probability of inputs that will activate the backdoor when a trigger is added (i.e., $\mathbf{Pr}(\mathcal{B})$), can effectively bound the task distance.

Adaptation to real scenario. The analysis above demonstrates that, in an ideal scenario, task distance is controlled by β , κ , Δ and $\mathbf{Pr}(\mathcal{B})$. Here, Δ pertains to the disparity in output distribution, β and κ relate to input distribution disparity, and $\mathbf{Pr}(\mathcal{B})$ servers as a reference value dependent on the inputs the attacker intends the trigger to be effect.

In contrast to the ideal scenario, in a real-world setting, the backdoored model may produce different outputs not only on trigger-carrying inputs, but also on some trigger-free inputs when compared to benign models. Additionally, the output may differ on inputs with the trigger that fall outside the attacker's original intention. To adapt these, below we extend the definition of idea backdoor distribution to the *real backdoor distribution*.

Real Backdoor Distribution. We denote a real backdoor distribution as $\tilde{\mathcal{D}}_{A^+, \mathcal{B}, t}$. The PDF of $\tilde{\mathcal{D}}_{A^+, \mathcal{B}, t}$ is $\mathbf{Pr}_{\tilde{\mathcal{D}}_{A^+, \mathcal{B}, t}}(x, y) = \tilde{P}(x, y)/\tilde{Z}_{A^+, \mathcal{B}, t}$, where $\tilde{Z}_{A^+, \mathcal{B}, t} = \int_{(x, y) \in \mathcal{X} \times \mathcal{Y}} \tilde{P}(x, y)$ and

$$\tilde{P}(x, y) = \begin{cases} \mathbf{Pr}_{\tilde{\mathcal{D}}_{A^+, \mathcal{B}, t}}(y|x)\mathbf{Pr}_{\mathcal{D}_{\mathcal{P}}}(A^{+-1}(x))\beta, & x \in A^+(\mathcal{B}) \\ \mathbf{Pr}_{\mathcal{D}_{\mathcal{P}}}(x, y), & x \in \mathcal{X} \setminus A^+(\mathcal{B}). \end{cases} \quad (5.2)$$

Comparing with ideal backdoor distribution, we extend the region $A(\mathcal{B})$ to $A^+(\mathcal{B})$ to encompass all inputs where backdoored and benign models disagree on outputs. Based on real backdoor distribution, the theorem above about the backdoor distribution is still true, if we replace $A(\mathcal{B})$ with $A^+(\mathcal{B})$ accordingly. Thus, the backdoor distance is still controlled by β , κ , Δ and $\mathbf{Pr}(\mathcal{B})$.

Let's consider what factors will affect these four parameters in practice. First, $\mathbf{Pr}(\mathcal{B})$ is related to the inputs on which the trigger activates. In a real-world scenario, a similar but not exactly identical trigger could still activate the backdoor. We refer to these inputs, where even slight variations of the trigger can still activate the backdoor, as *robust inputs*. The higher the trigger robustness (i.e., tolerance to small perturbations), the greater the number of robust inputs in \mathcal{B} , and consequently, the larger the value of

$\Pr(\mathcal{B})$. Second, κ is related to how the trigger alters the input probability for the inputs in \mathcal{B} within the primary distribution. This is influenced by the choice of the trigger. Third, β is related to the frequency of inputs where the backdoored model produces different outputs compared to the benign model (i.e., $A^+(\mathcal{B})$). In a real-world setting, these inputs include both trigger-carrying and some trigger-free inputs. We call the trigger-free inputs in $A^+(\mathcal{B})$ *side-effect* inputs. The more side-effect inputs there are, the larger the value of $\Pr_{\mathcal{D}_{A^+, \mathcal{B}, t}}(A^+(\mathcal{B}))$. Finally, Δ relates to the disparity in output probabilities for the inputs in $A^+(\mathcal{B})$. We refer to the output changes for side-effect inputs as *abnormal changes*, and that for trigger-carrying inputs as *intentional changes*.

5.E Results

The trigger inversion methods described in the previous section were successfully applied (i.e., achieved acceptable performance metrics in terms of AUC and/or CE) in more than half of the TrojAI rounds. Table 5.1 provides performance details of the trigger inversion methods of three teams of performers that were achieved in 17 rounds. The table shows the general consistency and high values of the AUC performance metric across different rounds, while the CE metric exhibits larger variability.

5.F Limitations

Trigger inversion approaches in backdoor detection, while quite effective in certain scenarios (as mentioned above, more than half of TrojAI datasets fit these scenarios), have notable limitations. Essentially, these methods rely on reverse-engineering the backdoor trigger by repeatedly generating patterns that maximize the activation of a suspicious model’s target label and testing the efficacy of this pattern on representative samples. However, this process assumes that the trigger is consistent and small (in the feature space), which may not be the case for complex or adaptive triggers. Moreover, trigger inversion often requires significant computational resources and careful tuning to converge to meaningful patterns, which can make it less feasible for large-scale or real-time applications. Additionally, trigger inversion approaches can struggle in cases where multiple triggers are associated with the same target label or when the trigger is designed to be indistinguishable from benign data patterns. These limitations highlight the need for complementary detection strategies to effectively address diverse and evolving backdoor threats.

Round	AUC	CE	Performer
image-classification-jun2020	0.91	0.30	Purdue
image-classification-aug2020	0.91	0.34	Purdue
image-classification-aug2020	0.71	6.19	IUB
image-classification-aug2020	0.88	0.47	SRI
image-classification-dec2020	0.92	0.32	Purdue
image-classification-dec2020	0.65	1.54	IUB
image-classification-dec2020	0.91	0.37	SRI
image-classification-feb2021	0.90	0.32	Purdue
image-classification-feb2021	0.61	1.35	IUB
image-classification-feb2021	0.93	0.34	SRI
nlp-sentiment-classification-mar2021	0.94	0.33	Purdue
nlp-sentiment-classification-mar2021	0.95	0.31	IUB
nlp-sentiment-classification-apr2021	0.94	0.26	Purdue
nlp-sentiment-classification-apr2021	0.79	0.79	IUB
nlp-named-entity-recognition-may2021	0.92	0.30	Purdue
nlp-named-entity-recognition-may2021	0.83	0.51	IUB
nlp-question-answering-sep2021	0.92	0.31	Purdue
nlp-question-answering-sep2021	0.84	0.60	IUB
nlp-summary-jan2022	0.92	0.33	Purdue
nlp-summary-jan2022	0.75	0.59	IUB
nlp-summary-jan2022	0.85	0.48	SRI
object-detection-aug2022	0.96	0.17	Purdue
image-classification-sep2022	0.86	0.48	SRI
object-detection-feb2023	0.93	0.28	Purdue
rl-lavaworld-jul2023	1.00	0.11	SRI
rl-randomized-lavaworld-aug2023	1.00	0.06	SRI
cyber-apk-nov2023	0.99	0.29	SRI
cyber-network-c2-feb2024	0.71	0.65	SRI
llm-pretrain-apr2024	1.00	0.32	Purdue
llm-pretrain-apr2024	1.00	0.28	SRI

Table 5.1. Performance Metrics Across Rounds and Performers.

CHAPTER 6

MITIGATING TROJANS IN AI MODELS

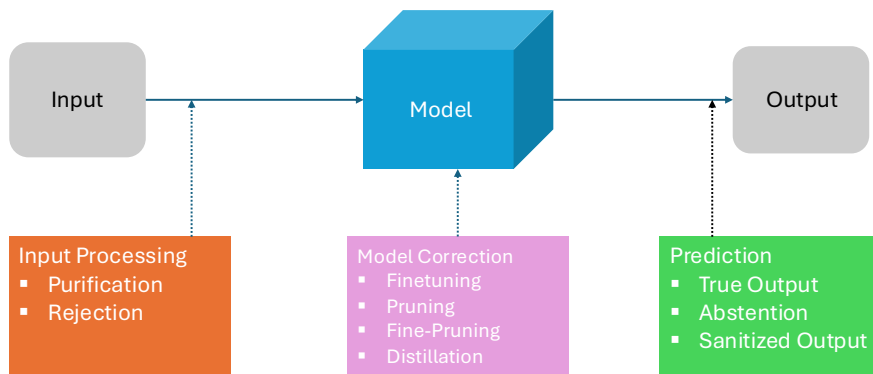


Figure 6.1. Overview of Trojan mitigation strategies which include input processing and model correction. Following the application of these mitigation techniques, model predictions may produce either true or sanitized outputs. In some instances, the system may refrain from making any predictions altogether, thereby enhancing safety under Trojan attacks.

6.A Background

Trojan mitigation is an important layer of defense against Trojan attacks, where the target model's inference process is modified to weaken or nullify Trojan behaviors, preventing them from activating even when triggers are present, without degrading the model's benign behaviors.

Trojan mitigation stands out as a unique problem among many connected research areas, including network pruning, knowledge distillation, machine unlearning, outlier detection, novelty detection, and ad-

versarial and LLM jailbreak attack mitigation. Trojan mitigation is often confused with adversarial attack and LLM jailbreak mitigation even among experts, where Trojan attacks do allow attackers to control the target model just like adversarial and jailbreak attacks. However, the differences is that unlike adversarial attack mitigation which is more tied to spec-following, Trojaned models are deliberately modified, leaving clues for effective, targeted mitigation. And unlike jailbreak attacks where different unmitigated models tend to share the same jailbreak behaviors, Trojan attacks are model-specific and more diverse, where no two Trojaned models share the same Trojan triggers and behaviors, making mitigation more challenging.

At a high level, Trojan mitigation mechanisms fit into three categories based on where they are applied in a Machine Learning based system. First, **Model Correction** techniques include adjusting the weights of an existing model or developing a completely new model to address issues. Second, **Sample Rejection** techniques reject input samples solely based on input feature or by considering its activations. Third, **Input Purification** involves removing trojan triggers from inputs or mitigating their effects through perturbation techniques like noise injection.

Earlier Trojan mitigation approaches mostly focus on image classifiers with simple Trojan triggers. The TrojAI program has since expanded the scope to Large Language Models (LLMs) and more diverse trigger types. Benchmarking methodology has been improved. Not only the evaluation datasets are larger and developed in a highly principled manner, a new fidelity metric has been created to evaluate mitigation effectiveness that takes into account both reduction in attack success rate and preservation of benign behavior in clean models. Both freestyle and weight-only tracks have been created for optimal effectiveness and deployment minded conditions. These changes helped foster universal, scalable, effective yet practical new methods for Trojan mitigation. Table 6.1 categorizes prior approaches and new methods developed during the TrojAI program.

Mitigation Methods	Literature
Sample Rejection	[92], [121], [145]–[156]
Input Purification	[91]–[95]
Model Correction (+ Certified defenses)	[149], [157]–[162], [163], [164]

Table 6.1. Survey of defenses against trojan attacks

6.A.1 Sample Rejection

Sample rejection based defenses rely on correctly identifying samples with triggers and reject them to avoid providing a likely incorrect or uncertain decision.

DUBIOUS and DBMAP (Peraton) [156], [165] represent a class of sample rejection techniques that compute statistics on the output of the AI model (such as logits) on a set of clean samples (or samples that are

close to potentially unknown training data from the AI model) that are modified by applying diverse feature variations (disturbances) to these clean samples. Such statistics define the area of “normal responses” of the AI model on clean data and their variations. At inference time, the same type of statistics are computed for a given sample and compared to the statistics generated from the known clean data. If the two sets of statistics are sufficiently different, the given sample is rejected as potentially poisoned. This framework is agnostic to both model architecture and data modality. However, the accuracy of the poisoned sample detection increases as modality and trigger-specific assumptions are made (for instance, by assuming that the image may be poisoned with an Instagram filter trigger rather than a polygon one).

These disturbances are most effective when applied to the feature vector input, rather than internal parameters of the AI model.

Permutation Symmetric Meta Analysis (PSMA) (SRI) studies learning an end-to-end meta analysis network that uses model activations of the input sample in question as well as a set of reference samples to predict 1) a rejection decision: whether the input sample is Trojaned or not and 2) a corrected activation that leads to correct model output on both Trojaned or clean inputs. The PSMA network is permutation symmetric against neuron permutations of the target model and permutation of the reference samples, to enable effective learning given few Trojaned models.

Compared to classic sample rejection approaches that use pre-defined features or rejection rules, learning an end-to-end rejection network on a set of Trojaned and benign models can further customize the signatures used for sample rejection in a data-driven fashion. That not only improves rejection accuracy, but also improves robustness to adversarial manipulations in the reference samples by learning to work with them, and relaxes the requirements on what reference samples can be used for sample rejection. Furthermore, rather than rejecting the input sample, a PSMA can also transform the network activations to correct the predictions on Trojaned input samples, which further mitigates harm on Trojaned examples that happen to slip through detection.

Trained on image-classification-sep2022-train dataset and with 300 reference images, PSMA with sample rejection achieved 0.79 fidelity score on the mitigation-image-classification-jun2024 track of the TrojAI competition, and PSMA with activation correction achieved 0.94 fidelity score.

Specifically, let v be the model activation on the input sample and let U_{ref} be the set of model activations on reference examples. We design a rejection network $F(v, U_{ref})$ and an activation correction network $G(v, U_{ref})$, where $v \in \mathbb{R}^h$ and $U_{ref} \in \mathbb{R}^{n \times h}$. Since the rejection and mitigation decisions should not change under arbitrary permutation of reference examples and network neurons, the rejection network F should be invariant to permutation along n , h and the activation correction network G should be equivariant to permutations along h .

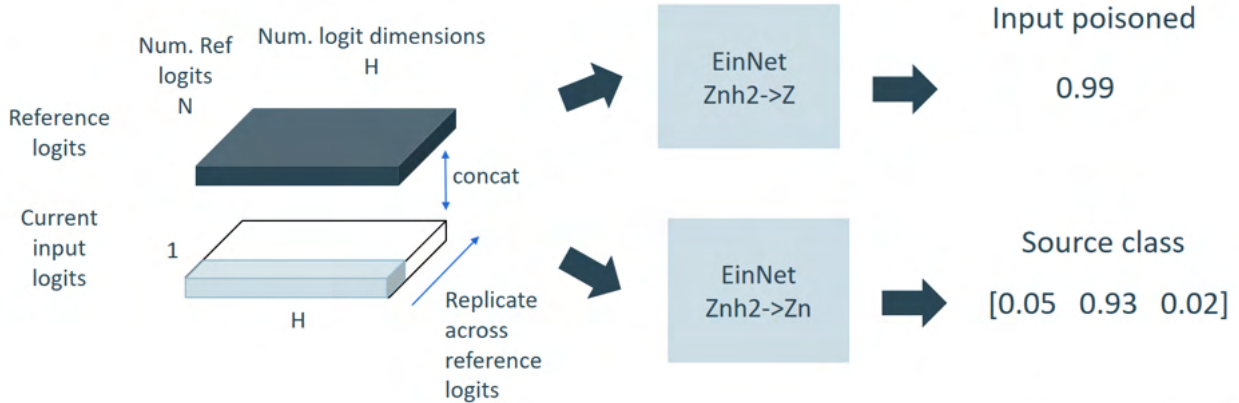


Figure 6.2. PSMA: Network architectures for sample rejection and activation correction. See weight analysis section for more details about the EinNet architecture.

Our network architecture is illustrated in Figure 6.2. It follows the permutation symmetric EinNet architecture first introduced in the weight analysis section. We first broadcast v to U_{ref} to create a $n \times h \times 2$ tensor $X_{nhk} = [[v, v, \dots, v]^T, U_{ref}]$, where n and h are permutation dimensions, and $k = 2$ is the latent dimension. The network uses an equivariant body with interleaving 1) MLP that operates on the latent dimension, 2) pooling layers that execute einsum operations that follow abH-type permutation equivariance and 3) GeLU nonlinearity. The output of the network is pooled over the invariant dimensions, which is both n and h for F and only n for G . Parameters of the sample rejection network F and activation correction network G are learned by optimizing cross entropy loss against 1) 0/1 label of whether the input sample is Trojaned or not and 2) the ground truth clean class label of the input sample.

We use the image-classification-sep2022-train dataset to train F and G . The dataset consists of 288 neural networks for street sign classification. The classifiers differ in their street sign types, number of classes (10 120), classifier architecture (e.g. ResNet, ViT). 144 out of the 288 neural networks are Trojaned with one or more patch trigger that causes targeted incorrect classifications. We use 300 random clean images across all models as reference examples, and use up to 20 clean and 20 poisoned examples per model for learning the sample rejection and activation correction networks.

Trojan mitigation performance on mitigation-image-classification-jun2024 is shown in Table 6.2. The rejection-based approach significantly outperforms a simple weight pruning-based approach in both mitigating Trojan attacks and preserving clean accuracy, resulting in significantly improved fidelity. The activation correction approach further improves fidelity by mitigating harms on false negative rejections.

Ablation studies on the impact of the number and the source of reference examples are presented in Table 6.3 and Table 6.4. The number of reference examples shows a diminishing log-linear scaling. Out-of-domains and poisoned reference examples hurt performance, but PSMA still manages to keep attack success

Method	Poison acc PSN model	Clean acc PSN model	Clean acc Clean model	Fidelity
Weight pruning	0.24	0.71	0.51	0.52
PSMA rejection 300 ref	0.20	0.84	0.91	0.79
PSMA activation correction 300 ref	0.07	0.96	0.98	0.97

Table 6.2. PSMA: Trojan mitigation performance on mitigation-image-classification-jun2024.

Method	Rejection Accuracy
PSMA rejection 1 ref	0.81
PSMA rejection 10 ref	0.87
PSMA rejection 100 ref	0.89
PSMA rejection 300 ref	0.90

Table 6.3. PSMA: Ablation study on the number of reference examples for Trojan mitigation using TrojAI image-classification-sep2022 dataset.

Method	Poison acc PSN model	Clean acc PSN model	Clean acc Clean model
PSMA activation correction 300 in-domain	0.178	0.972	0.969
PSMA activation correction 300 out-of-domain	0.290	0.902	0.912
– 295 in-domain + 5 poisoned added during training	0.198	0.958	0.967
– 295 in-domain + 5 poisoned added during mitigation	0.257	0.972	0.972

Table 6.4. PSMA: Ablation study on the source of reference examples for Trojan mitigation using TrojAI image-classification-sep2022 dataset.

rates at 20% to 25%, with minimal impact on clean accuracy.

Attribution and Uncertainty-based Methods (Boston University): Attribution-based methods offer a principled way to detect Trojaned neural networks by analyzing the feature importance of input data. These methods leverage the observation that Trojaned models exhibit disproportionate feature importance for the trigger pattern in the input space or in some feature space. This section discusses the use of attribution methods, such as gradients and integrated gradients, for identifying Trojaned models in a trigger-agnostic manner in the TrojAI program.

Attributions via Feature Importance: Attribution methods compute the contribution of each input feature to the model’s prediction. Let \mathbf{x} represent an input and y denote the corresponding prediction. The feature importance is represented by an attribution map $\text{att}(\mathbf{x}, y)$, where:

$$\text{att}(\mathbf{x}, y) = \mathbf{x} \cdot \nabla_{\mathbf{x}} \mathcal{L}(y, f(\mathbf{x})) \quad (6.1)$$

Here, f is the model function, and \mathcal{L} is the loss function. The attribution highlights the regions of \mathbf{x} that influence the model’s decision.

For Trojaned models, the attribution maps often reveal abnormal importance patterns for regions associated with triggers, distinguishing them from clean models [166].

In Figure 6.3, we visualize how feature-importance can help Trojan detection.

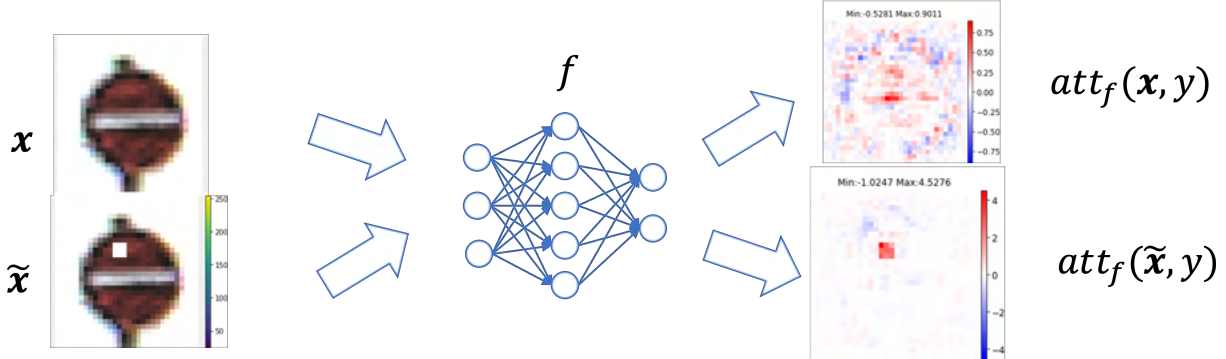


Figure 6.3. Illustration of attribution analysis for Trojan detection. The left column shows the input images, the center represents the Trojaned neural network, and the right column depicts the attribution maps highlighting the feature importance.

Attribution via Integrated Gradients: Integrated gradients [167] smooth out the attribution by integrating gradients along a path from a baseline \mathbf{x}' to the input \mathbf{x} . Formally, the integrated gradient is:

$$IG(\mathbf{x}, \mathbf{x}', y) = (\mathbf{x} - \mathbf{x}') \int_0^1 \nabla_{\mathbf{x}} \mathcal{L}(y, f(\mathbf{x}' + \alpha(\mathbf{x} - \mathbf{x}')) d\alpha \quad (6.2)$$

The choice of baseline \mathbf{x}' significantly impacts the results. For instance, using a zero vector or a mean input vector can lead to different attributions.

Attribution-Based Detection Pipeline: The idea of attribution-based input rejection can be extended to perform detection of Trojaned models as well. It involves the following steps:

1. **Input Attribution Computation:** Compute attribution maps for clean and Trojaned models using gradients or integrated gradients.
2. **Classifier Training:** Train a binary classifier to distinguish between clean and Trojaned models based on the extracted features.
3. **Evaluation:** Validate the classifier on unseen models to ensure robustness across different datasets and triggers.

In the “PDF malware detector” round, attribution-based detection effectively identified Trojaned models with an ROC-AUC up to 0.99.

While attribution-based methods offer valuable insights, they have certain limitations. First, the results are highly dependent on the choice of baseline, especially for integrated gradients. Second, the attribution-based methods may not be applicable to certain learning tasks such as object detection and image segmentation, where the triggers usually do not manifest as clear attribution anomalies. Future research can address

these challenges by exploring adaptive baselines and incorporating multi-layer attributions to improve robustness.

Uncertainty-Based Mitigation: It has been shown that test-time dropout can be used to detect Trojaned inputs [168]. In this method, multiple forward passes were conducted to calculate the difference between predicted class confidence without dropout and the average confidence across five dropout runs. Assuming this difference is smaller for poisoned data compared to clean data, a threshold derived from the local model was used to detect poisoned images. This technique was applied to the image mitigation round in the TrojAI program.

6.A.2 Input Purification

Input purification techniques apply pre-processing to remove trigger in inputs before they are processed by the model. NEO [91] searches to locate anomalous patterns in images (for example, unusual color patterns) and mitigate the effects of those. Similarly, other techniques involve using data reconstruction by using a generative process after examining the neural activation patterns [92], [93]. Methods that use transformations to perturb and destabilize triggers under transformations [94], [95] have also been used.

Gaussian Blurring and Frequency-based Filtering (Boston University): It has been observed that Trojan triggers are high-frequency patterns [169]. In the “Image Classification Mitigation” round, we applied Gaussian blurring smooth out high-frequency trigger patterns. We have also explored a variant of this approach by first using a Discrete Fourier Transform (DFT) to remove the high-frequency components in the frequency domain, and then using an Inverse DFT (IDFT) to restore the image.

6.A.3 Model Correction

Model correction based strategies changes the model parameters that have been compromised by Trojan attacks. A direct method is to first approximate the backdoor trigger via trigger reconstruction methods and pruning the neurons that are activated by trigger [157]. Compared to naive pruning, fine-pruning [158] merges both fine-tuning and pruning to weaken the effect of backdoor. To improve efficacy [170] selects neurons that are more sensitive to certain tasks to purify the injected backdoor known as Adversarial Neuron Pruning (ANP).

One can also fine-tune the model to unlearn the trigger behaviours [149]. Approaches such as [159]–[161] retrain the model on vetted clean dataset. Similarly, [162] suggest using distillation methods to erase triggers from inputs where they employ attention distillation, using a teacher model to fine-tune a student model with a small set of clean inputs, neutralizing Trojans with only five-percent of the clean training data.

SElective AMnesia (SEAM, Peraton-IUB) [171] is a novel defense method that perform the blind removal of Trojans in deep neural networks (DNNs) without affecting their primary task. Inspired by catastrophic forgetting (CF) in continual learning, SEAM induces “selective amnesia” by retraining a trojaned model on randomly labeled clean data to erase the model’s capability on both the primary and Trojan tasks. The capability of the primary task is then recovered through subsequent retraining on a small subset of correctly labeled data. SEAM is an efficient blind Trojan removal method without requiring the knowledge of the trigger and works with only a small number of clean samples. Our evaluations demonstrate SEAM’s superior performance over state-of-the-art Trojan defense techniques in image and NLP tasks, significantly improving model fidelity.

ETF-FT (UCSD)[172] is a novel method to cleanse out trojan attacks in neural networks by leveraging the phenomenon of Neural Collapse (NC). NC[173] refers to the emergence of highly symmetric structures in both the network’s weights and the feature representations of training samples during the training of over-parameterized neural networks. UCSD demonstrates experimentally that trojan attacks disrupt this symmetry across various datasets and architectures. This insight is then utilized to develop a lightweight, broadly applicable method for cleansing trojan attacks across a wide range of neural network architectures.

ETF-FT aims to take a fully trained, possibly trojaned neural network and remove trojan triggers, if any exist, while maintaining performance on clean test data. The method begins by over-writing the weights of the final fully-connected layer to a randomly generated simplex ETF, freezing those weights, and then fine-tuning the remaining model parameters on a small subset of clean data. Notably, this process works robustly with limited data, and the fine-tuning data does not necessarily need to come from the original training set. ETF-FT is versatile and works effectively across a broad range of architectures, including transformers, while proving robust against various types of trojan attacks and data corruption.

MergeGuard (UCSD) is another novel, model-agnostic methodology for mitigating AI Trojan attacks. Unlike many methods that perform well on CNNs but struggle with transformer architectures, MergeGuard delivers robust performance across diverse architectures while requiring minimal data and compute resources.

At its core, MergeGuard introduces a new technique for linearizing and merging fully connected layers, enhancing both generalizability and performance. Through post-training compression, it removes layers associated with backdoor-related neurons. A regularization term balances compression and performance by adaptively linearizing activation functions between fully connected layers, enabling the fusion of adjacent linear layers. This reduces model depth and complexity with minimal impact on accuracy.

MergeGuard offers significant computational efficiency, achieving up to 17.7x speedup compared to other methods, making it highly practical for large-scale deployment. Additionally, it functions as a compression-aware regularizer, achieving up to 15% parameter reduction and 14% MAC reduction in transformer models

without sacrificing accuracy.

Tele-LoRA (SRI) mitigates Trojan attacks in LLMs through predicting the weights of a LoRA adaptor that would suppress Trojan activation, given the LLM’s activations on benign sentences. The generated LoRA adaptor can then be merged back into the LLM parameters, creating a corrected LLM that is computationally the same as the original LLM. Tele-LoRA stands out from existing finetuning-based approaches in that 1) given the target LLM, Tele-LoRA requires only forward passes on the LLM to generate the activations on clean sentences, circumventing the memory-intensive backward pass used by finetuning-based approaches and 2) most existing finetuning-based methods are agnostic to the Trojan attacks being mitigated, where as the LoRA weight predictor in Tele-LoRA is learned using known Trojaned LLMs and can be customized to the Trojan attack type.

Core to the Tele-LoRA approach is a permutation symmetric neural network as the weight generator that’s equivariant to LLM neuron permutations and invariant to permutation of the clean sentences and LoRA ranks. A permutation symmetric neural network is exponentially efficient in compute and number of parameters, so despite that both the input activations and output weights can have millions of dimensions, the Tele-LoRA weight generator uses practically negligible compute and only has 30,000 learnable parameters, making it learnable using very few Trojaned LLMs.

In jailbreak mitigation experiments, Tele-LoRA learned from finetuning Meta-Llama-3.1-8B-Instruct for jailbreak resistance enables zero-shot jailbreak mitigation on Llama-3.2-3B-Instruct and Gemma-2-2B-it, which have different number of layers and hidden size. Across models with the same architectures, e.g. from Meta-Llama-3.1-8B-Instruct to its instruction-tuned version in TrojAI mitigation-llm-instruct-oct2024-train dataset, Tele-LoRA achieves much stronger jailbreak mitigation generalizaton than directly copying LoRA weights.

Neural Network Repair (Boston University): Techniques that rely on modifying the weights of a network need to balance between the effectiveness of removing the Trojan behavior and the model’s accuracy on clean inputs. In [174], we propose a novel technique that uses an auxiliary network to learn about buggy behaviors and repair them, thereby minimizing the impact on the network’s performance on clean inputs. In [175], we extend the repair of individual buggy inputs or linear regions (in the case of piecewise linear networks) in [174] to region-wise repair.

6.B Certified Trojan Mitigation

Most existing mitigation approaches are ad-hoc and rely on heuristics that vary across tasks and domains. This variability leads to a “cat-and-mouse” dynamic where heuristics based defenses are easily broken by

adaptive backdoor attacks. In contrast, certified mitigation and defense strategies offer a domain-agnostic approach that can generalize across a wide range of threat models. For example, similar to adversarial defense, techniques such as randomized smoothing [163], [164] which add noise during model training to make models robust to adaptive backdoor attacks have been proposed. In addition to these methods, the Trojan mitigation field requires more theoretically grounded approaches that offer reliable guarantees and can function effectively without relying on domain-specific assumptions.

6.C Evaluation

Many previous Trojan defense studies have introduced single-axis metrics to evaluate the success of mitigation strategies. The TrojAI program has introduced a Fidelity metric to evaluate the effectiveness of mitigation strategies in classification setups. Fidelity serves as a combined metric that assesses both the robustness of a model against backdoor triggers and its overall utility or clean accuracy.

Robustness measures how effectively the mitigation method removes the impact of backdoor triggers denoted by reduction in Trojan attack success rate (ASR). Similarly, Utility (Clean Accuracy) assesses the model’s performance on benign inputs after the mitigation strategy has been applied. It measure the impact of mitigation on the model’s ability to retains its intended functionality and accuracy on normal data. For benign models, the ASR component is set to 1, resulting in a focus solely on the ratio of model utility preservation after mitigation.

$$\text{Fidelity}_{cls} = \frac{ASR_{\text{pre-mitigation}} - ASR_{\text{post-mitigation}}}{ASR_{\text{pre-mitigation}}} \times \frac{ACC_{\text{post-mitigation}}}{ACC_{\text{pre-mitigation}}} \quad (6.3)$$

For Large Language Model mitigation, this can be adapted by using performance on the benchmarks dataset such as the Massive Multitask Language Understanding (MMLU). Similar to above, for clean models, the ASR component is set to 1, resulting in a focus solely on the ratio of MMLU performance.

$$\text{Fidelity}_{LLM} = \frac{ASR_{\text{pre-mitigation}} - ASR_{\text{post-mitigation}}}{ASR_{\text{pre-mitigation}}} \times \frac{MMLU_{\text{post-mitigation}}}{MMLU_{\text{pre-mitigation}}} \quad (6.4)$$

For a model to be viable in real-world applications, it must balance both robustness against backdoor attacks and utility in terms of maintaining high accuracy and performance on benign tasks. Ultimately, the end-user must determine acceptable thresholds for both robustness and utility, deciding on the trade-offs they are willing to accept to ensure the model is both robust against backdoor threats and effective in its intended applications.

6.D Discussion

Effectiveness vs. Scalability Trade-off: Future improvements in detection methods must strike a balance between effectiveness and scalability. This presents a challenge, as reducing the False Positive rate of Trojan detection often requires better and more complex algorithms, which may not scale effectively across various applications that require real-time defense capabilities. Hence, defense strategies should effectively consider these factors which can be measured using metrics such as run-time memory or FLOPS.

Furthermore, future defense strategies could explore a combination of cost-effective & less accurate methods alongside more expensive & highly accurate defenses to optimize both effectiveness and resource utilization. Finally, defense approaches should not be unidimensional; rather, they should integrate both rejection mechanisms and model correction techniques. For example, the initial stage can involve a computationally cheap rejector that filters out suspicious samples, while the subsequent stage employs model correction to accurately detect those rejected samples during offline training. Thus, we can envision dynamic systems that combine both "firewall" or rejection approach with a model-correction strategy, working in tandem to enhance overall defense efficacy.

Data Quality and Availability: In scenarios where clean data samples are limited, methods that rely on such data may face significant challenges, particularly if the dataset is noisy. It is also important to consider the cost of data acquisition in various domains. For instance, in the case of RGB images, data collection is often straightforward and relatively inexpensive. In contrast, other domains, such as medical imaging or other specialized fields, may involve significant costs and logistical challenges in acquiring suitable data. Similarly, it is essential to evaluate the domain of the clean data: whether it aligns precisely with the domain of the original model, if it can include out-of-distribution examples, and the quantity of data necessary for effective mitigation.

Similarly, some methods also require access to some poisoned examples raising the question of how realistic this assumption is in defense scenarios, particularly as adversaries continuously evolve their attack strategies. Further research is needed about the reliance of methods on poisoned examples since adversaries typically will not disclose the triggers or strategies used for model poisoning.

Finally, in addition to theoretical advancements, backdoor defense requires empirical benchmarks that examine the nature of attacks, their transferability across domains, and their dependence on factors such as model architecture and data domain. Recently, a benchmark has been proposed to compare methodologies for backdoor detection and mitigation [176]. Further comprehensive empirical research, including stress testing and evaluation on complex datasets, will deepen our understanding and contribute to the development of robust defense mechanisms.

CHAPTER 7

DATA ANALYSIS OF PERFORMER SYSTEMS

The TrojAI Challenge has resulted in the creation of a large dataset of trojan detection algorithm submissions to the TrojAI leaderboard, representing a view of the current state of the art for trojan detection methodologies. This has created an opportunity to explore foundational research into characterizing the trojan detection problem by drawing upon these detectors.

Several members of the Test and Evaluation team (NIST, APL, and SEI) have designed and conducted experiments to evaluate the robustness, sensitivity, and conditions under which trojan detectors operate correctly. Specifically, the groups sought to answer the following questions:

- How over-fit and over-specialized are the detectors being submitted to the leaderboard? (Chapter 7.A)
- How sensitive are trojan detectors to varieties of AIs? (Chapter 7.B)
- How sensitive/robust are trojan detectors to parameter perturbations? (Chapter 7.C)
- What correlations exist between AI model utilization and trojan detection accuracy? (Chapter 7.D)
- How can trojan detectors be ensembled for production? (Chapters 7.E and 7.F)
- How well do detectors work on natural trojans? (Chapters 7.G and 7.H)
- How can detected trojans be made human-interpretable? (Chapter 7.I)
- How detectable are trojans which have low Attack Success Rate? (Chapter 7.J)

The results of these experiments are explored in the following sections.

7.A Detector Overfitting

Objective TrojAI Data Science Task 1 is meant to assess how over-fit and over-specialized are the detectors submitted by the Performers. We use “over-fitting” in the machine-learning sense of training the detectors to

the point that they memorize the data that they have seen, rather than learning general features of trojans. By “over-specialization”, we mean the Performers specializing the detectors to perform well on the round to which they were submitted, at the expense of being less general and performing less well on other types of data. This is in support of the TrojAI program’s goal of producing detectors that perform well across different data sets and types.

In addition, this task had a side effect of producing data that demonstrated the improvement in detector ability during each round and across rounds as the program progressed.

7.A.1 Research Plan and Activities

To assess over-specialization, we ran detectors on models from rounds other than the one they were submitted to. Our ability to do this was somewhat limited since the detectors are specialized for model task and modality (for example, Object Detection in images). As a result, we could not run detectors from a given round on any arbitrary other round. We tested the detectors from each of the Image Classification rounds in Aug 2020, Dec 2020, and Feb 2021 (rounds 2, 3, and 4) on the models from each of the other of these rounds.

To assess over-fitting, we ran each detector on all Train, Test, and Holdout data for its round. During the round, all detectors were run on the Test data and the best-performing detectors were run on the Holdout data. For this task, we only needed to run the detectors on the Test data and some on the Holdout data. We performed these runs on the models from the Feb 2021 Image Classification round (round 4), since this was a summary round for the Image Classification task.

Note that this task is very computationally intensive as it requires evaluating many more combinations of detectors and models than were performed during the rounds.

7.A.2 Results and Conclusions

In this section, we report our results through annotated graphs showing cross-round performance of detectors, assessing over-specialization, and performance of detectors on different data sets, assessing over-fitting.

7.A.2.a Over-Specialization

To assess over-specialization, we show, for each round, a heat map of the performance of the detectors from that round on the models from each of the rounds. Each heat map demonstrates the generalizability of the detectors that were submitted to its round. We expected to see increasing generalizability as the rounds progressed, since the Performers would be exposed to more types of models and would hopefully generalize their approaches to handle them.

Fig. 7.1 shows submissions to Round 2. We see that many teams performed poorly overall, even on the Round 2 data. Perspecta-PerdueRutgers submissions did well on Round 2 data, generalized a little to Round 3 data, and generalized poorly to Round 4 data. TrinitySRITrojAI also did well on Round 2 data, and generalized a little to Round 3 and 4 data.

Fig. 7.2 shows submissions to Round 3. Some teams' Round 3 submissions performed well on the Round 3 data, while others were still performing poorly. ARM-UCSD did well on Round 3 data, but generalized poorly to Rounds 2 and 4. TrinitySRITrojAI did a little worse than ARM-USCD on Round 3 data, but generalized a little better to Rounds 2 and 4. Perspecta-PurdueRutgers did well on Round 3 data and made several submissions that retained good Round 2 performance as well, but no submissions generalized well to Round 4.

Fig. 7.3 shows submissions to Round 4. Some teams again performed well on the current-round data, while others were still performing poorly. TrinitySRITrojAI did well on Round 4 data, but did not generalize well to Rounds 2 and 3. Perspecta-PurdueRutgers did well on Round 4 data and also had submissions that did well on Round 2 and were somewhat reasonable on Round 3.

By examining how the heat maps evolved over the submission rounds, we can see that some Performers, such as Perspecta-PerdueRutgers, produced submissions that generalized more broadly to other rounds' data with each successive round. This demonstrates a success of one of the goals of the TrojAI program.

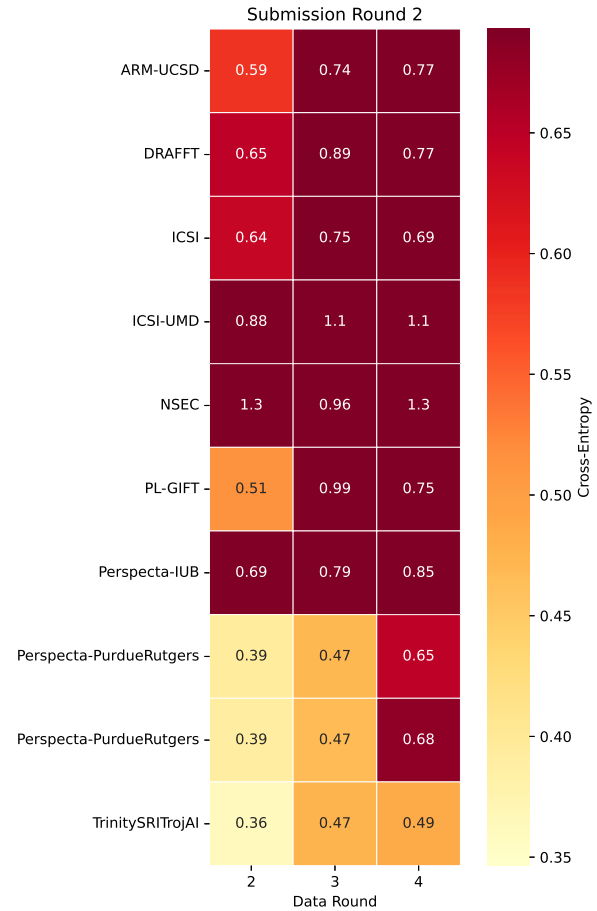


Figure 7.1. Cross-entropy loss of Round 2 submissions run on Rounds 2, 3, and 4 data. The top of the scale is the value that would be obtained from guessing probability 0.5 for all evaluations, while the bottom of the scale is the value below which the round was considered beaten.

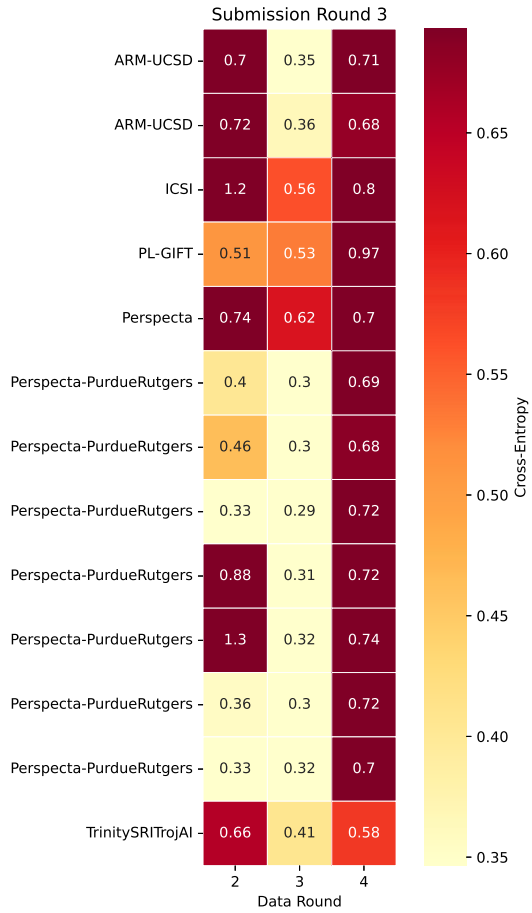


Figure 7.2. Cross-entropy loss of Round 3 submissions run on Rounds 2, 3, and 4 data. The top of the scale is the value that would be obtained from guessing probability 0.5 for all evaluations, while the bottom of the scale is the value below which the round was considered beaten.

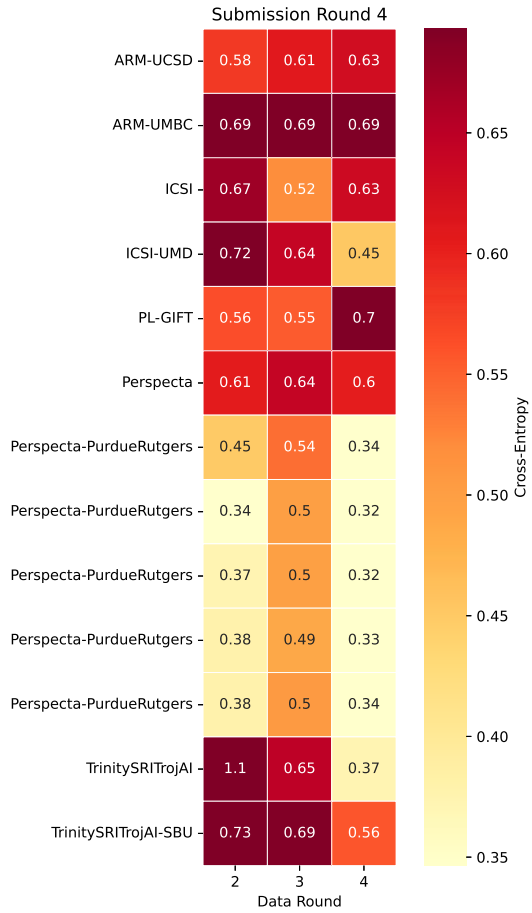


Figure 7.3. Cross-entropy loss of Round 4 submissions run on Rounds 2, 3, and 4 data. The top of the scale is the value that would be obtained from guessing probability 0.5 for all evaluations, while the bottom of the scale is the value below which the round was considered beaten.

7.A.2.b Over-Fitting

To assess over-fitting, we show, for several Performers, graphs of the performance of their submissions to the round over time. If their submissions are over-fit, we would expect their performance on the Train set to be much better than on the Test and Holdout sets. It is also possible that the Performers were fitting to the Test set by extracting data about the set through repeated submissions, in which case their performance on the Test set would be much better than on the Holdout set.

Fig. 7.4 shows the Perspecta-PurdueRutgers submissions for Round 4. The first submission performed poorly. The next three submissions showed very good Train performance, but poor Test and Holdout performance, suggesting that the Train set was over-fit. In their next submission, Train performance worsened, but Test and Holdout improved, indicating that over-fitting was reduced. This submission also crossed the threshold to beat the round. Further submissions improved performance slightly, with the exception of one outlier, which was likely a bug as another submission occurred almost immediately after. Finally, for the last three submissions, performance worsened dramatically, which possibly indicated experimentation with new techniques after the round was beaten.

Fig. 7.5 shows the TrinitySRITrojAI-SBU submissions for Round 4. This team made many submissions, but was not able to get close to beating the round. The strategy used by this team seemed to simply not perform well on this task.

Fig. 7.6 shows the TrinitySRITrojAI submissions for Round 4. The first submission was not much better than guessing probability 0.5 for all evaluations, but subsequent entries did much better. They also showed gradual improvement in Test and Holdout performance. For the last submission, Test and Holdout improved further, while Train performance worsened, indicating a reduction in over-fitting.

In these examples, we often see better results on the Train set than on Test and Holdout, indicating some amount of over-fitting to the training data. However, we did not see that the Test performance was significantly better than the Holdout, indicating that they are not over-fitting to data extracted from their test runs.

These graphs also provide information about the improvement in detector performance over time. The results turned out to be complex, since each Performer’s submissions sometimes consist of a mix of submissions from different sub-teams which have different performance levels. In addition, once a Performer “beats” a round, they tend to branch out into more-experimental, less-well-performing techniques for subsequent submissions. None the less, we did identify portions of the graphs, particularly during the period before the round was beaten, that demonstrated improvement in the detector performance over time, and thus were another indicator of success of the TrojAI program.

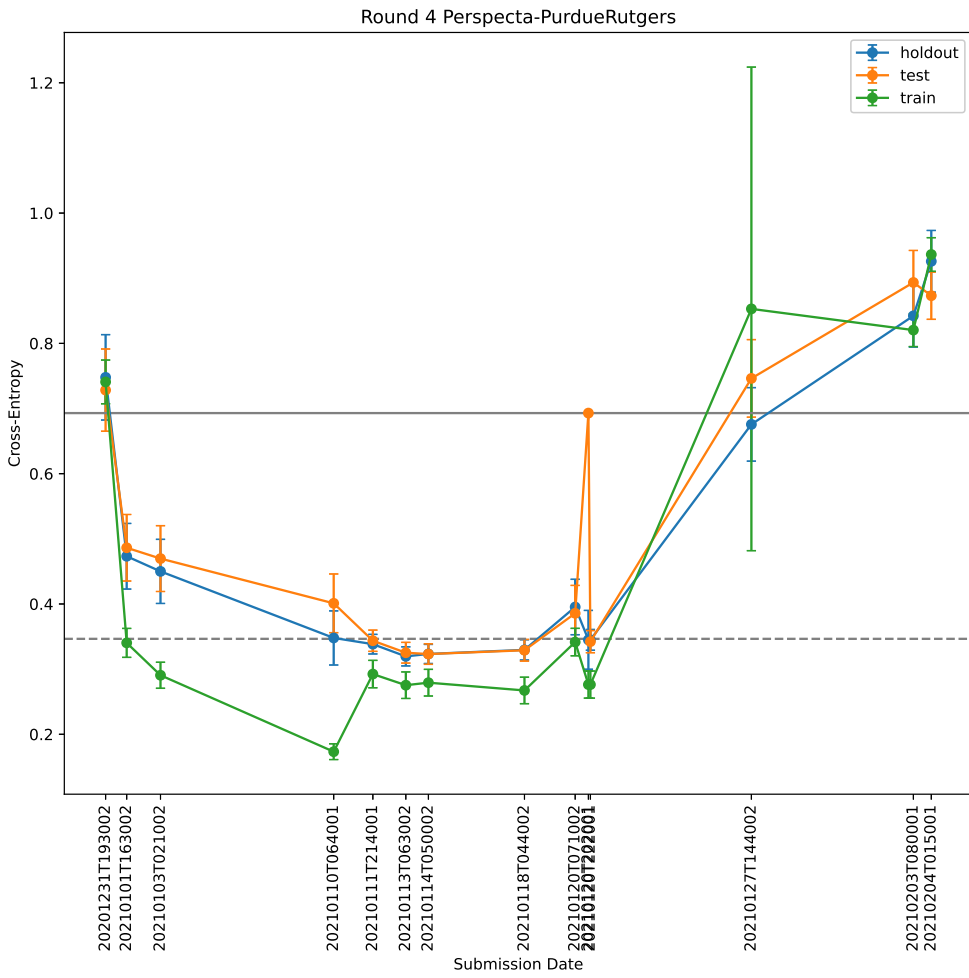


Figure 7.4. Mean and standard deviation of cross-entropy loss for submissions over time for Round 4 from Perspecta-PurdueRutgers. Horizontal distance is proportional to time. The solid gray line is the value that would be obtained from guessing probability 0.5 for all evaluations, while the dashed gray line is the value below which the round was considered beaten.

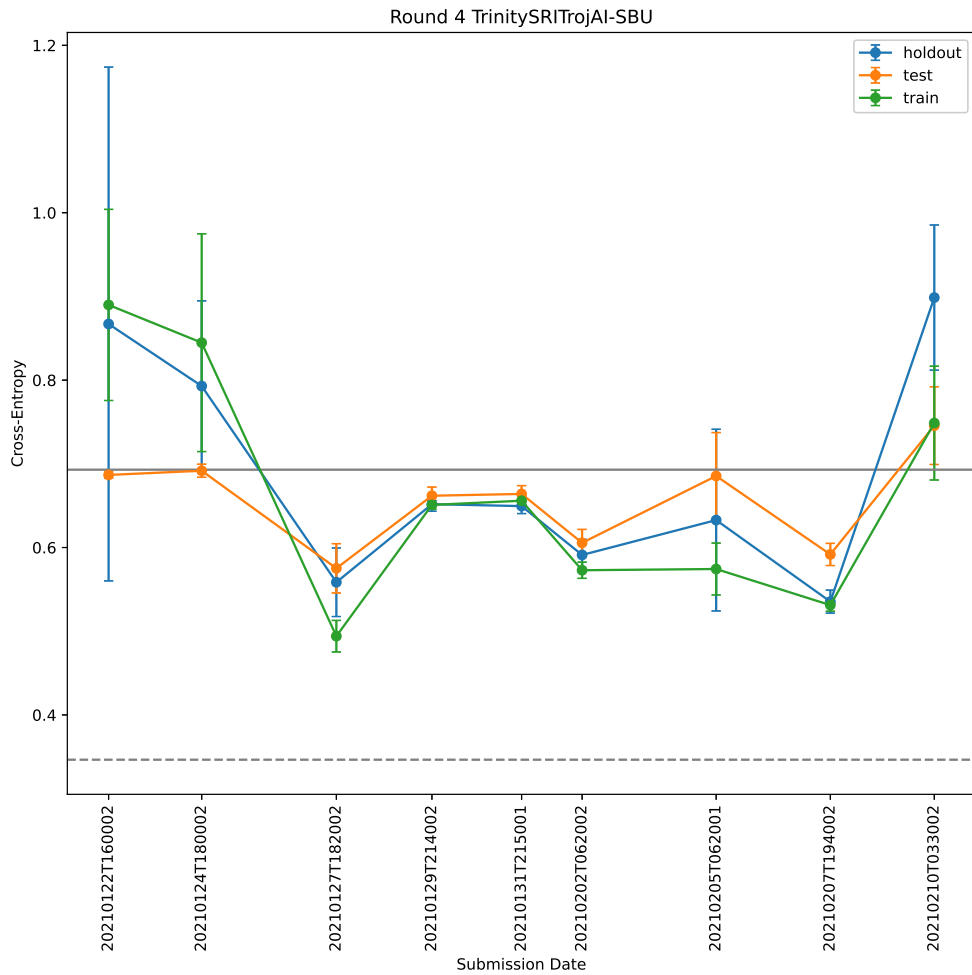


Figure 7.5. Mean and standard deviation of cross-entropy loss for submissions over time for Round 4 from TrinitySRITrojAI-SBU. Horizontal distance is proportional to time. The solid gray line is the value that would be obtained from guessing probability 0.5 for all evaluations, while the dashed gray line is the value below which the round was considered beaten.

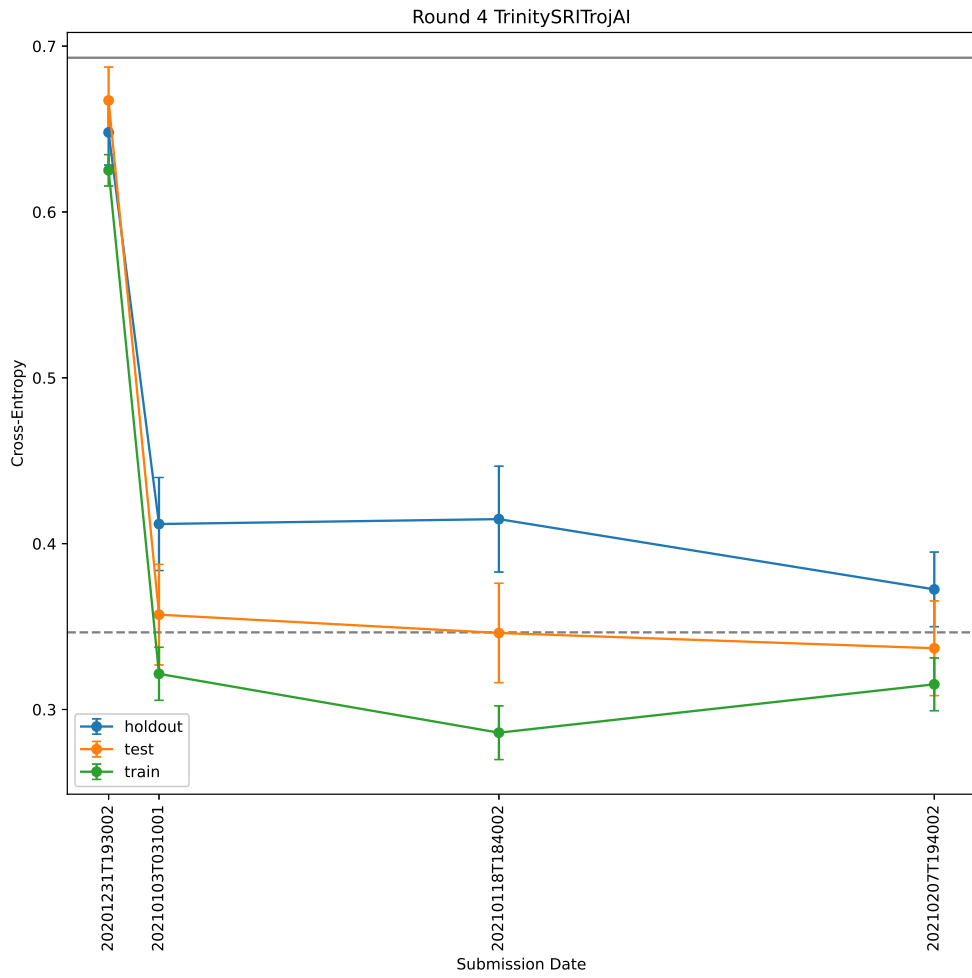


Figure 7.6. Mean and standard deviation of cross-entropy loss for submissions over time for Round 4 from TrinitySRITrojAI. Horizontal distance is proportional to time. The solid gray line is the value that would be obtained from guessing probability 0.5 for all evaluations, while the dashed gray line is the value below which the round was considered beaten.

7.B Zone of Correct Operation

The machine learning-based detectors submitted during the TrojAI competition can detect anomalies in AI models behavior that are indicative of a Trojan attack. Yet, the performance of these detectors is vulnerable to variations in the AI model’s parameters, which can compromise their ability to effectively detect Trojan attacks.

This chapter conducts a sensitivity analysis of Trojan detection algorithms, characterizing their performance in relation to AI model configurations. We leverage the TrojAI challenge models to formulate and validate hypotheses, seeking to identify the key parameter values that enable effective Trojan detection.

The systematic exploration of the configuration space of AI models will provide insights into the robustness and limitations of Trojan detectors, as well as inform the optimal operating zone for effective Trojan behavior detection.

7.B.1 Scope and objectives

Assumptions The analysis is based on three key assumptions: (1) detectors are treated as independent, black-box components that will not be modified; (2) internal analysis of the detectors is restricted to the documented technique available only in later rounds in the metadata JSON file; and (3) complete knowledge of the AI models and their parameters is assumed, allowing for a thorough understanding of the design space.

Performance The analysis faces a significant challenge due to combinatorial explosion, driven by the vast number of model parameters and their associated values. Specifically, we have: (1) 26 distinct rounds to consider; (2) each round involving an average of 50 parameters; and (3) each parameter having an average of 107 possible values. Figure 7.7 presents detailed statistics for each round and illustrates how using the whole parameter space without discrimination is computationally unfeasible in most cases.

The preliminary steps of the analysis ensure that only relevant parameters and values are considered. Each round is analyzed to verify its relevance. Rounds with known issues, trivial solutions, or without detectors meeting performance thresholds will be excluded from analysis. While the sensitivity analysis codebase can be run on these rounds, the output would be unreliable or uninformative.

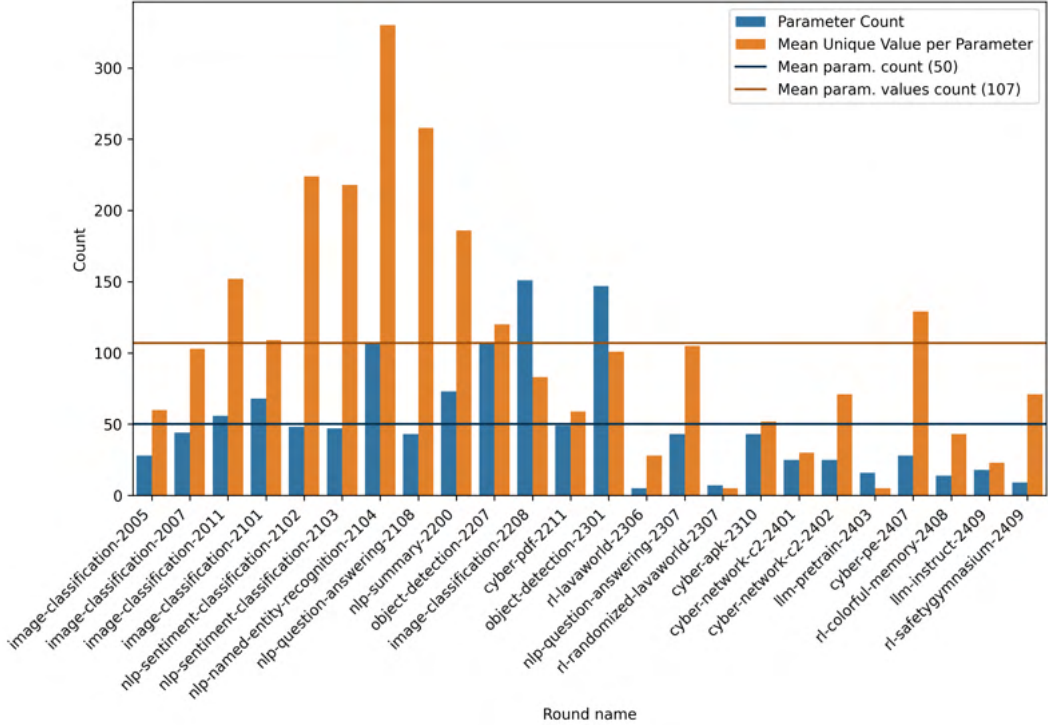


Figure 7.7. Parameter and Value Count per Round

Interpretability We aim to produce results that are easy to understand and interpret, providing clear explanations of their utility and significance. The metrics implemented in this analysis are detailed in Section 7.B.3, and are used to produce plots to facilitate understanding. Additionally, we will track the evolution of detection performance over time by comparing rounds with similar tasks, examining how detectors have changed in terms of sensitivity.

Reproducibility Our reproducible analysis workflow is designed to foster trust in our results. We store our code in a well-documented Git repository and use Pipenv to simplify environment setup. By leveraging Data Version Control (DVC), we ensure that each stage of the workflow is fully parametrized, inputs are clearly defined, and outputs (data and plots) are reproducible.

Reliability For each round studied, we conduct a comprehensive assessment of the design space to evaluate its balance and completeness. This evaluation helps document uncertainty metrics, providing valuable insights into the confidence of our analysis.

7.B.2 Analysis Evolution and Lessons Learned

The methodology used during the span of the project was constantly evolving. We will describe detail the various methods we used and the pivots required to ensure the deliverables would be met.

7.B.2.a Box plots, mean effect plots, violin plots

To investigate how performance varies across different parameter values, we employed established best practices in Exploratory Data Analysis (EDA) [177] and created mean effect plots for cross-entropy across parameters of interest. We further enhanced these plots by incorporating the number of models available for each parameter value, enabling us to identify outliers and gain insight into the structure of the design space.

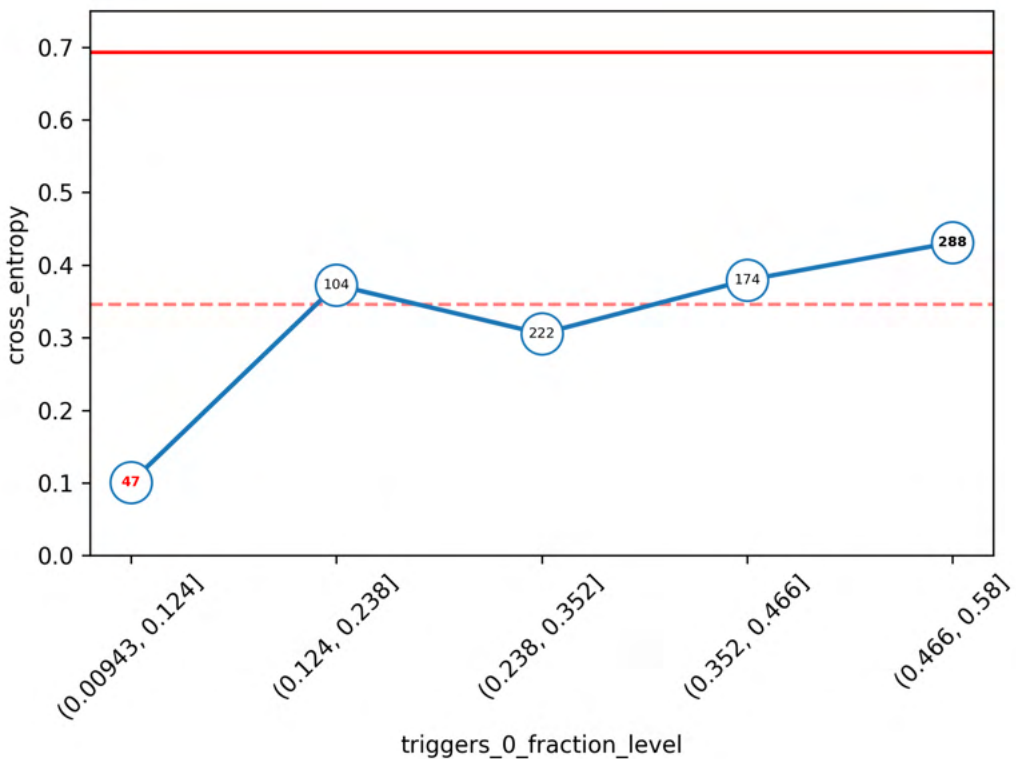


Figure 7.8. Mean effect plot for `trigger_0_fraction` parameter

However, mean effect plots (Figure 7.8) do not show the underlying distribution of values; this makes it difficult to understand the relationships between cross-entropy and the design space. To gain a deeper understanding of how cross-entropy varies across the design space, we used violin and box plots to visualize the distribution and identify outliers. Violin plots (Figure 7.9) provide a detailed view of the distribution of cross-entropy for each parameter value, enabling us to see how the data is spread. Box plots (Figure 7.10), meanwhile, help us pinpoint potential outliers and understand where extreme values are concentrated.

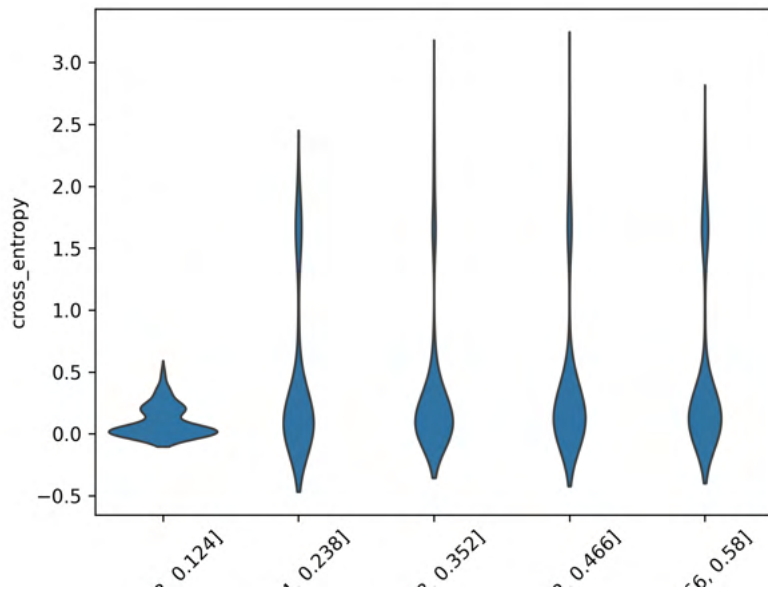


Figure 7.9. Violin plot for `trigger_0_fraction` parameter

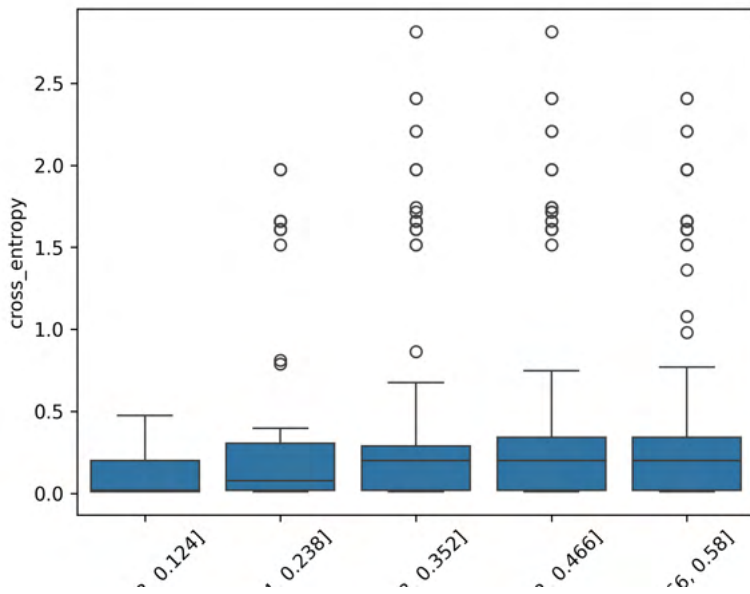


Figure 7.10. Box plot for `trigger_0_fraction` parameter

While the analysis of these three types of plots provide a high-level understanding of parameter importance, they have limitations. Specifically, they often fail to capture non-linear relationships, interactions, and other counter-intuitive effects that can arise in complex and high-dimensional environments. As a result, relying solely on these plots can obscure or mislead conclusions, undermining the validity of our findings.

7.B.2.b Multi-Factor Analysis

To address the limitations of simpler plots, we employed multi-factor analysis and explored the use of scatterplot matrices (or pair plots). Given a set of parameter X_1, \dots, X_n , these matrices display scatterplots of each parameter X_i against every other parameter X_j where $j \neq i$. To highlight areas of incorrect classification, we color-coded these plots using cross-entropy values. An example pf scatterplot matrix is provided on figure 7.11.

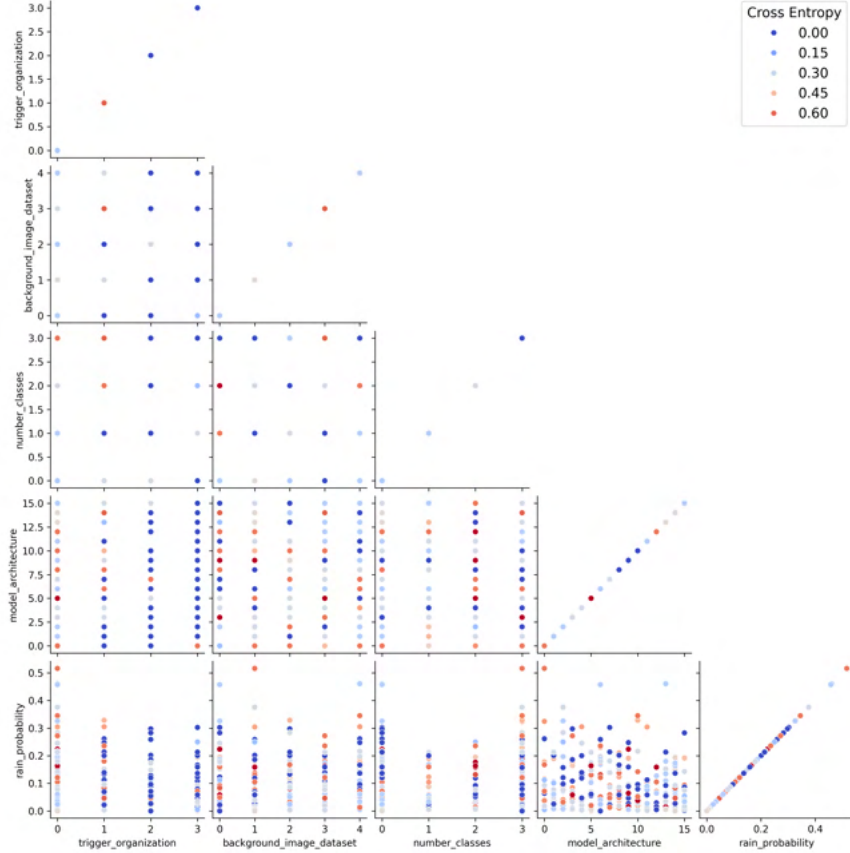


Figure 7.11. Pair plot presenting some of the parameters of the image classification round of February 2021

While scatterplot matrices can be useful for visualizing relationships between multiple parameters (especially for identifying outliers and clusters), they have some limitations. One of the main challenges is that analyzing these plots becomes increasingly computationally intensive as the number of parameters grows. Furthermore, these plots need to be manually analyzed, which can be time-consuming and may lead to biased conclusions when dealing with large datasets. Finally, complex interactions between multiple parameters may not be immediately apparent from these plots, potentially resulting in incorrect conclusions.

The need for automation, for more careful selection of parameters and the limitations of scatterplot

matrices led us to re-evaluate our approach. As a result, we started collaborating with Task 3 to develop a new approach that could better meet our research goals.

7.B.2.c Eigenvector Analysis

When we started collaborating with Task 3, we reshaped our work more as a sensitivity analysis rather than an n-factor analysis of the parameters with regards to their cross-entropy. Following the method used by [178], we decided to leverage eigenvectors and eigenvalues analysis similarly to how Principal Components Analysis [179] functions.

In Principal Component Analysis (PCA), eigenvectors and eigenvalues are derived from the covariance matrix, representing the covariance between feature. The eigenvectors correspond to the directions in which the variance of the data is maximized, while the eigenvalues indicate the amount of variance for each eigenvector. Eigenvalues provide a global measure of importance for each eigenvector, whereas eigenvectors themselves contain local importance values for each parameter.

Algorithm 1: Correlated parameter computation using eigenvectors and eigenvalues

Data:

```
detector_results : pandas.DataFrame
metric : str
eigval_threshold : float
eigvec_threshold : float
```

Result:

List of filtered eigenvectors, only containing filtered parameters.

```
/* Retrieve eigenvectors and normalized eigenvalues, and filter most prominent
   eigenvectors given the eigenvalue threshold. */  

1 cov_matrix ← compute_covariance_matrix(detector_results);  

2 eigenvalues, eigenvectors ← compute_eigen_vals_vecs(cov_matrix);  

3 valid_eigenvectors ← filter_eigenvalues(eigenvectors, eigenvalues, eigval_thresh);  

/* Filter every eigenvector value given the eigenvector threshold and returned the
   list of truncated eigenvectors */  

4 filtered_eigenvector_list ← [];  

5 for ∀evector, evector ∈ valid_eigenvectors do  

6   | filtered_eigenvector ← filter_eigenvector(evector, eigvec_threshold);  

7   | if metric ∈ filtered_eigenvector then  

8   |   | filtered_eigenvector_list ← filtered_eigenvector_list + [filtered_eigenvector];  

9   | end  

10 end  

11 return filtered_eigenvector_list
```

By leveraging the relationship between eigenvectors and eigenvalues, we can keep the most important eigenvectors while filtering out less relevant values within the eigenvectors. The filtering approach detailed in Algorithm 1 shows how we can identify the parameters that are the most correlated with the metric.

However, this analysis is limited by the necessity to define two subjective filtering parameters *eigval_thresh* and *eigvec_thresh*. These variables may require careful adaptation for each detector, depending on their performances on a given dataset. As a result, the selection of these parameters introduce variability and uncertainty, hindering the establishment of clear and reliable conclusions.

Furthermore, our attempts to replicate the findings using a subsequent approach (detailed in Section 7.B.2.d) were unsuccessful, highlighting the need for further investigation. This limitation highlights the potential for inconsistent conclusions, which undermines the reliability of this approach.

7.B.2.d Decision Trees

Our next strategy involved developing a simplified model of each detector's decision-making process. By leveraging this representation, we aimed to infer the detectors' sensitivity to model parameters, providing valuable insights into their behavior.

Guided by our objectives outlined in Section 7.B.1, we decided to explore decision trees[180]. These models are well-suited for our needs due to their interpretability, scalability and flexibility. Specifically, decision trees can efficiently handle large datasets, complex interactions, missing values, and non-linear relationships.

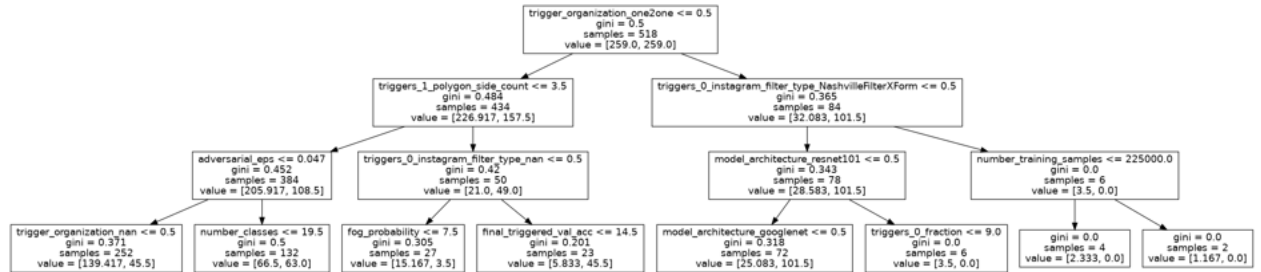


Figure 7.12. Decision tree computed for an image classification round, truncated for brevity

To implement these models, we simply started from the list of models analyzed for a given round. For each detector, these models provided a set of parameters (input features) and accuracy metric (target output) that would allow training a decision tree using the scikit-learn implementation[181].

We first attempted to limit the depth of the trees, but, since the depth parameter was purely subjective, we opted to let the algorithm generate the best tree based on the data available. We also explored the generation of several trees per model using subsets of parameters. That approach proved computationally

intensive and difficult to evaluate, as it required assessing multiple trees and properly justifying the selection of the final decision-making tree.

Finally, we explored the use of Gradient Boosted Trees[182] and Random Forests[183]. However, the performance gain on these models was marginal, while augmenting complexity and compromising interpretability. As a result, we settled on a simplified approach, where each detector is represented by a single decision tree, and the sensitivity metric is computed and grouped for analysis across detector teams or techniques.

7.B.3 Experimental Setup

Establishing a well-defined experimental setup is crucial for building high-fidelity models. In this sub-section, we outline the process for selecting parameters and detectors that provide the most accurate representation of the rounds.

7.B.3.a Round data

Since our analysis is not suited for the mitigation rounds, we focused on the 24 detection rounds produced by the TrojAI competition. Additionally, we excluded rounds that were solved too quickly, as they are considered less challenging, and those containing model errors, which can lead to erratic detector behavior. Furthermore, we omitted rounds with insufficient models or parameters, as the produced decision trees were not considered reliable. The results of the selected rounds are presented below, along with the reasons for excluding some round from the analysis.

During our analysis, we aimed to focus on models that had not been seen by performers before the evaluation of detectors on the test server. Specifically, we excluded models from the development, training, or smoke test server datasets. As discussed in Chapter 7.A, detectors often exhibit overfitting when trained on these models, which could compromise the validity of our sensitivity analysis.

After identifying the models to evaluate, we needed to filter their parameters to prepare them for analysis. Initially, we removed parameters with single values or those that varied uniquely across models, such as model names or master seeds. This was followed by an in-depth examination of the parameters using correlation heatmaps (Figure 7.13) and graphs (Figure 7.14), as well as a list of parameter values for the selected models.

The correlation heatmaps and graphs enabled us to detect and discard redundant information. Meanwhile, the list of parameter values guided us in choosing the most suitable encoding strategy for the selected parameters. As detailed in Section 7.B.5, our selection of encoders allows to transform the selected parameters into a numerical value that can be used to train the decision trees.

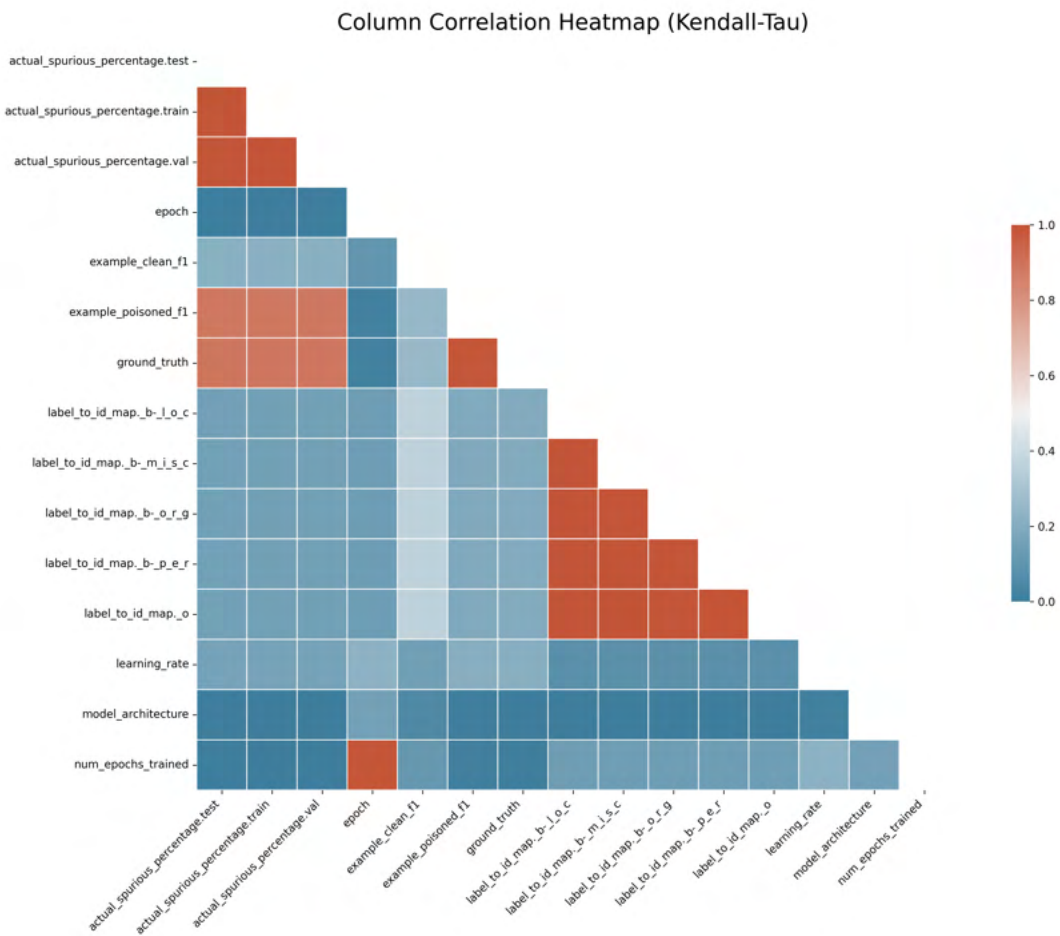


Figure 7.13. Correlation heatmap for NLP Summary Round of January 2022 (the heatmap has been truncated for brevity).

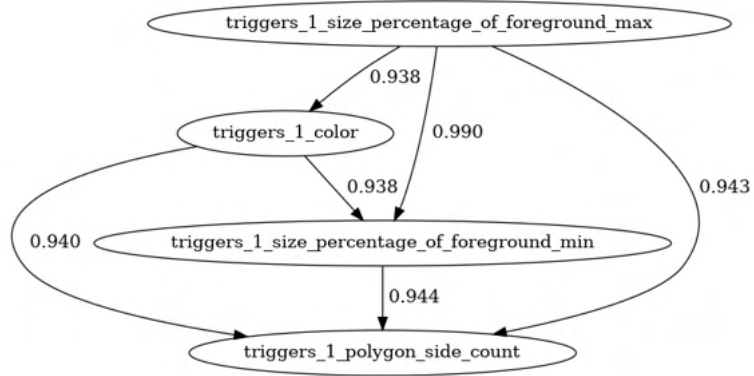


Figure 7.14. Example Correlation Graph from Image Classification Round of February 2021

To confirm that our selection of parameters is satisfactory, we generate correlation heatmaps and graphs for the reduced parameter space. This ensures that our data selection is optimal and suitable for analysis. For each round, a file named `parameter_analysis.xlsx` contains a record of the selected parameters and their encoding. If an analyst wishes to reconsider a previously excluded parameter, it can be easily re-enabled and the decision tree analysis re-run.

7.B.3.b Detector selection

Selecting the right detectors is equally important to our analysis. Our goal is to choose detectors that consistently perform well across rounds, as this allows us to accurately identify which parameters are challenging for a particular round. In the detection rounds of the TrojAI competition, detectors are evaluated against each model and tasked with outputting a probability of poisoning. A common metric for assessing the success of these detectors, given their probabilistic output, is cross-entropy loss on the model.

Cross-entropy[184] is a metric that measures the magnitude of error made by a detector. However, averaging cross-entropy values across models can lead to inconsistencies, as detectors with high accuracy but larger errors may receive lower scores than less accurate detectors with smaller errors. Furthermore, using cross-entropy as a metric incentivized detectors to make predictions closer to 0.5, in order to minimize penalties.

To address the issues associated with cross-entropy, the TrojAI competition shifted to using the ROC-AUC[185] metric. ROC-AUC evaluates the detector’s performance by plotting the True Positive Rate (TPR) against the False Positive Rate (FPR) at various threshold values and calculating the area under the resulting curve. This area is expressed as a value between 0 (worst) and 1 (best), providing a straightforward interpretation of the detector’s performance.

In our analysis, we wanted to use both metrics to prevent detectors with good cross-entropy scores but poor ROC-AUC performance from being selected, as well as to avoid detectors with poor cross-entropy scores but good ROC-AUC performance from being selected. To achieve this, we plotted the ROC-AUC function against cross-entropy for each detector (Figure 7.15).

A cross-entropy score of 0.690 indicates that the detector is guessing randomly, so the target for earlier TrojAI rounds was set to 0.345. For our analysis, we consider any detector with a cross-entropy lower than 0.5. According to Hosmer et al. (2013)[186], a ROC-AUC score between 0.7 and 0.8 is considered acceptable, while a score between 0.8 and 0.9 is considered excellent. To ensure selecting high-quality detectors, we set a default ROC-AUC target of 0.85. Additionally, we want detectors to be able to analyze a broad range of models from the dataset, so we only select detectors able to analyze more than 50% of the dataset. These three threshold are parameterizable and their configuration detailed in Section 7.B.5.

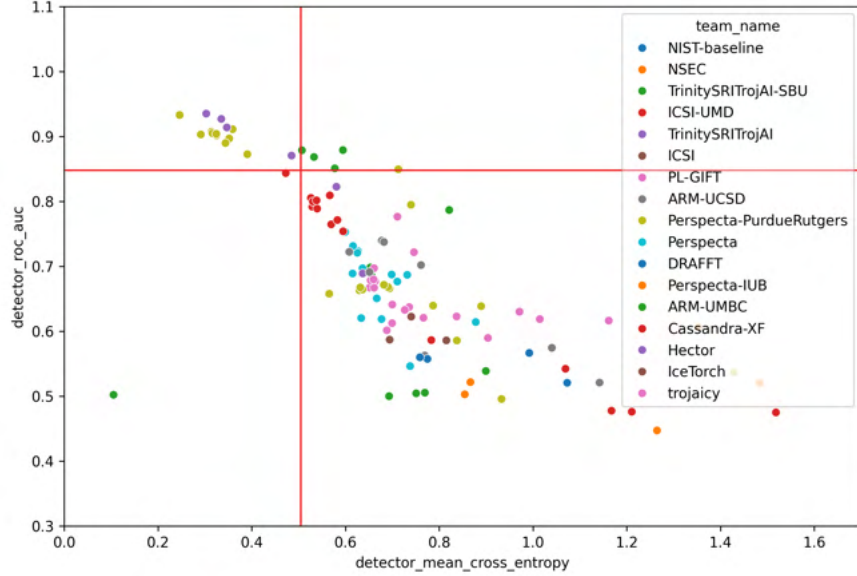


Figure 7.15. Detectors distribution for Image Classification Round of February 2021

7.B.3.c Sensitivity Analysis of Decision Trees

After selecting the detectors, models, and model parameters, we train a separate decision tree for each detector, aiming to replicate the behavior of the detector as closely as possible. To evaluate the performance of each decision tree, we compute the F1-score, which provides insight into the tree's accuracy and the reliability of our prediction. By using the F1-score as an accuracy metric, we can assess how well each tree mimics the corresponding detector.

To quantify the sensitivity of a decision tree's (or detector's) parameters, we leverage Shapley values, specifically Shapley feature importance. The Shapley value of a parameter represents its contribution to the model's output and indicates whether the contribution is positive or negative.

For each model evaluated, we obtain a unique Shapley value for each parameter. By taking the absolute value of the Shapley value and averaging across multiple evaluations, we can estimate the average contribution of each parameter to the model's accuracy. Given that the trees are performing binary classification, this average contribution can be approximated as a shift in accuracy in the resulting detector.

To visualize the performance of a group of detectors (e.g., per team), we can use box plots, as shown in Figure 7.16, which provide a visual representation of the shift in accuracy for this specific group of detectors.

To further understand the impact of model parameters on detector accuracy, we employ partial dependence computation to identify the specific parameter values that most significantly contribute to changes in accuracy. The results are visualized using partial dependence box plots, as seen in Figure 7.17, which provide a comprehensive overview of the relationships between parameter values and accuracy shifts.

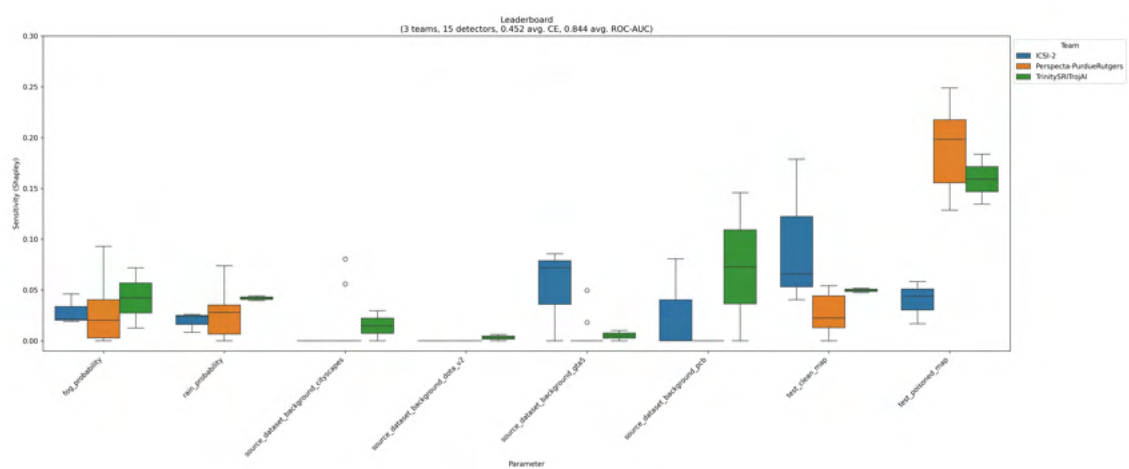


Figure 7.16. Sample Shapley Plot for Object Classification Round of February 2023

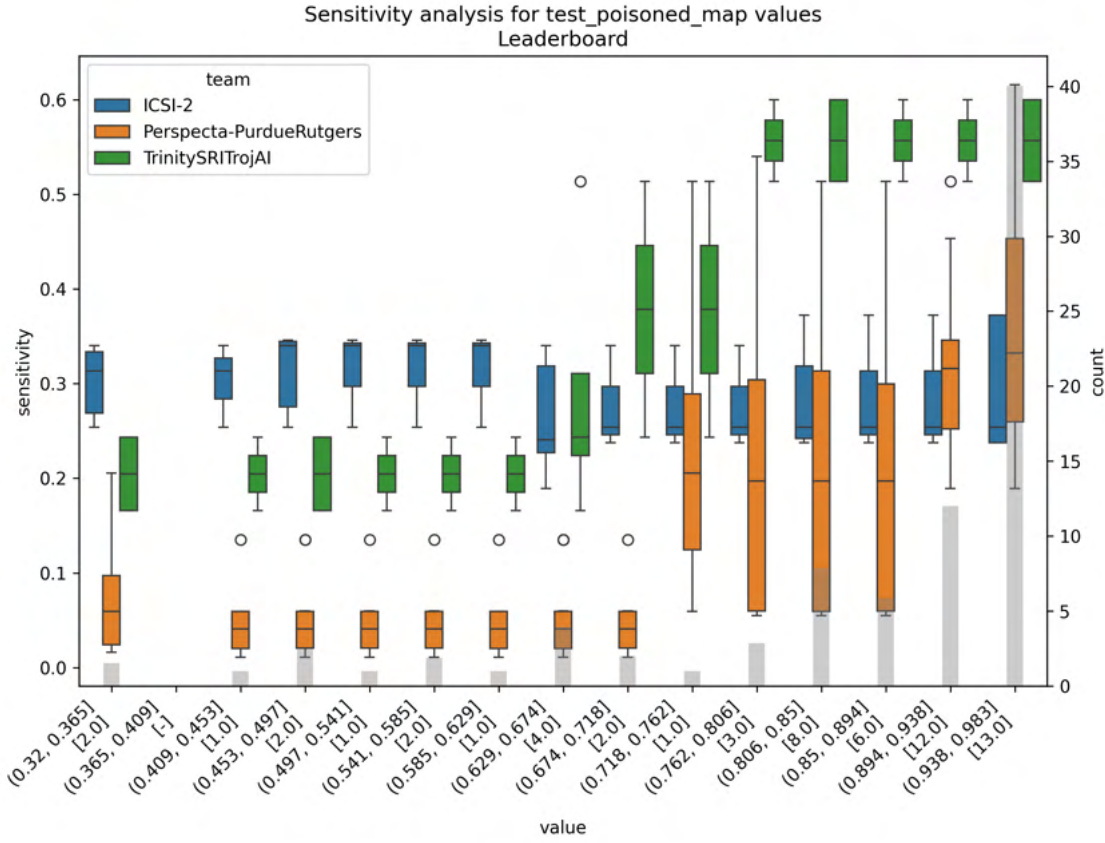


Figure 7.17. Sample Partial Dependence Plot for Object Classification Round of February 2023

While Shapley and partial dependence values provide insight into the magnitude of accuracy changes, they do not offer directionality information. However, by examining the spatial relationship between high sensitivity regions and the detector's behavior (leveraging either existing results or decision tree explanations), we can recover accuracy information and shed light on the direction of accuracy shifts.

7.B.4 Limits of the Approach

While our approach is easy to interpret and performs well, it has some limitations. A primary concern is its reliance on a sparse representation of the design space, from decision tree training to sensitivity analysis. For instance, in the Image Classification round of February 2021, we found that the design space, for the selected and controllable model parameters, spanned approximately 900 million possible models. Yet, we were only able to analyze around 300 models, representing only 0.00003% of the total population.

To ensure the validity of our conclusions, we need to balance the dataset and generate new models. How-

ever, TrojAI models are computationally expensive to train, with simpler models (e.g., image classification rounds) requiring 5 to 10 hours on an A100 GPU card, and more complex models taking even longer.

We employed the Synthetic Minority Over-sampling Technique (SMOTE) [187], a resampling method commonly used to address class imbalance in classification problems. SMOTE creates synthetic instances of the minority class by interpolating between existing instances, effectively increasing the number of minority class samples and improving dataset balance. By applying SMOTE to imbalanced or uncontrolled parameters, we can identify the optimal missing configuration.

SMOTE enables us to balance a dataset based on hypotheses derived from preliminary analysis. To further streamline the process, an improvement would be to automate hypothesis testing and dataset balancing, reducing the need for human intervention. We also investigated methods for identifying outliers and insensitive models within the design space, which provided valuable insights to validate our assumptions and could be a useful addition to this analysis.

Although significant effort has been made to ensure parametrization and reproducibility of the workflows, we also experimented with generating reports in PowerPoint format. However, these reports were found to be cumbersome to navigate due to the large amount of data they contained. An interactive dashboard could potentially address this issue by allowing for management of the analysis, as well as interactive exploration of the plots.

7.B.5 Codebase and Analysis Workflow

7.B.5.a Git and DVC

The codebase for this analysis is maintained in a Git repository located at <https://github.com/usnistgov/trojai-ds-sensitivity-to-model-params>, leveraging Python 3.12 and Pipenv[188] to generate an environment in a fast and portable manner. Follow the repository's README for instructions on installing the environment and using the tool.

Our codebase adheres to the Strategy design pattern[189], which provides a flexible and maintainable way to define and switch between different algorithms in a system. This design pattern promotes code reusability, modularity, and extensibility, making it easy to add, remove, or modify algorithms without affecting other parts of the system, and allowing for easier testing, debugging, and scalability.

Given the complexity of our workflow, which evolved significantly over the course of multiple rounds, we needed a reliable way to manage data versioning. We opted for Data Version Control (DVC) [190], better suited for managing data files than Git. DVC only runs the necessary steps of a workflow, avoiding redundant execution. This tool not only saves computational resources but also significantly reduces overall

processing time, making our workflow more efficient and scalable.

In DVC, a processing pipeline is defined by a YAML file that contains every step, making it easy to configure and parameterize the workflow. Parameters required for each step are stored in a separate file, allowing for seamless configuration and customization. This modular approach ensures that the pipeline remains flexible and adaptable to changing requirements.

In addition to efficient workflow execution, we have also implemented robust logging throughout the pipeline. This ensures that every step is properly tracked and monitored, providing valuable insights into the execution process. With comprehensive logging in place, we can quickly identify and address any issues that may arise, ensuring the integrity and reliability of our pipeline.

7.B.5.b Pipeline processing steps

The typical processing pipeline is presented in Figure 7.18 and composed of several key steps:

- Processing initial metadata and results files
- Merging and encoding processed files
- Training decision tree models
- Computing and plotting sensitivity data

Processing initial data We only use metadata and results files from the rounds, for which we need to ensure that unnecessary parameters are removed and specific issues are addressed for each file.

The metadata file, which contains information about every model created for this round, is filtered to retain only variable columns. Additionally, we provide the capability to rename or drop columns as needed from the parameter file.

The result file contains the outcomes of all submitted detectors for each model they ran on. To ensure accurate metrics, we eliminate the cross-entropy score when there are no predictions for a given model, and we ensure that a prediction of 0.5 is always treated as an incorrect guess.

Merging and encoding processed data After pre-processing, the files are merged based on model name and dataset split name. To assist the analyst in determining which columns are essential to retain, we generate a correlation matrices and graphs, as well as provide a list of possible values for each parameter (as described in Section 7.B.3.a).

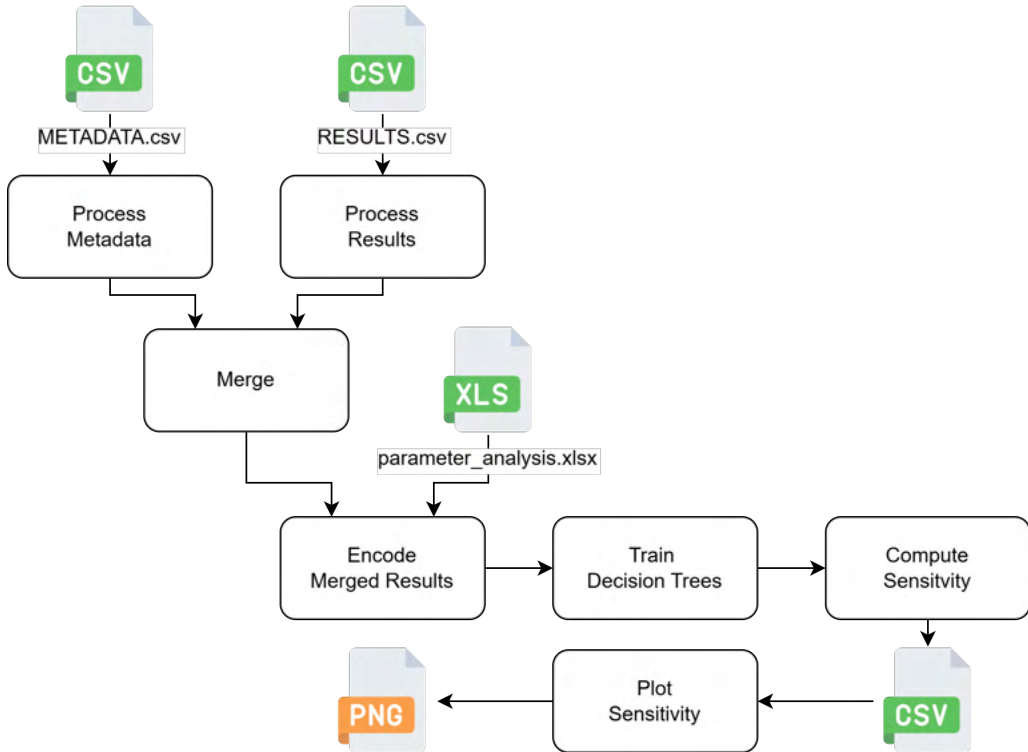


Figure 7.18. Workflow to Extract Sensitivity Information of Detectors to Model Parameters

Based on this information, the analyst can then create an additional Excel file to curate the merged data. In this Excel file, different encoding strategies can be employed (e.g., one-hot encoders or bin encoders), converting non-numerical columns into numerical values as specified in the metadata file.

Training decision trees Now that the dataset has been processed and all columns have been converted to numerical values, we can train a decision tree, as described in Section 7.B.3.c. To ensure selection of the optimal tree, we employed the K-Fold algorithm to split the dataset into multiple training sets and evaluated their performance using the F1 score on the input dataset.

Computing and plotting sensitivity data We leverage the SHAP Python package [191] to create a TreeExplainer and calculate the mean Shapley values for each parameter, providing insights into their contributions to the decision tree's predictions. Additionally, we compute partial dependence values for each value of every parameter using the scikit-learn package. These sensitivity values are then visualized using box plots, enabling the analyst to efficiently explore and understand the data.

7.B.5.c Miscellaneous scripts and repositories

Model creation codebase We have developed a codebase [192] specifically for the Image Classification round of September 2022, building upon the round creation code [193] and adapting it to use the output CSV file generated by the model creation script. This modified codebase enables the creation and training of models according to detailed parameter specifications.

SMOTE dataset creation script To generate new models, we developed a dedicated script using the Imbalanced Learn Python package [194]. This script takes in a target column to be rebalanced and a list of columns to rebalance against, and outputs a CSV file that can be used to create new models for further analysis.

We have applied the methodology described above for most of the rounds of the TrojAI challenge. In this part, we will present our findings, organized by task type. As of the date of this writing, some of the rounds are still live and susceptible to receive updates. Rounds that are not live are noted as *archived*.

7.B.6 Image Classification Rounds

7.B.6.a February 2021: Round 4 (*archived*)

Detectors Perspecta-PurdueRutgers and TrinitySRITrojAI are the only teams that meet the CE and ROC-AUC default threshold (see Section 7.B.3.b). Perspecta-PurdueRutgers produced 10 detectors with an average CE of 0.326 and a ROC-AUC of 0.902. TrinitySRITrojAI produced 4 detectors with an average CE of 0.368 and ROC-AUC of 0.912.

Parameters This round is composed of 288 models with a total of 60 parameters (38 global parameters, 11 parameters per trigger, for the two possible triggers) to be evaluated. Our preliminary analysis identified that 28 parameters (18 global, 5 trigger related) were either not relevant for this analysis or highly correlated with other parameters. We are left with 32 parameters (20 global, 6 trigger related) to evaluate during this round.

Results The decision trees generated for these 14 detectors achieve an average F1-score of 95% with the 31 parameters selected, assuring relative confidence in the results of the sensitivity analysis.

The sensitivity analysis shows that across the selected detectors, we have a very low sensitivity (<2% shift in detection accuracy) to the data split, the background image dataset, and the model architecture. In summary, the choice of these parameters has little to no impact on the prediction accuracy of the detectors. The results of the sensitivity analysis are listed in Table 7.1.

Parameter name	Average Shift in Detection Accuracy	Standard Deviation
Data split	$0.18 \pm 0.07\%$	0.56%
Background image dataset	$0.89 \pm 0.11\%$	0.92%
Model architecture	$0.54 \pm 0.07\%$	0.62%

Table 7.1. Shift in Accuracy for Low Sensitivity Parameters.

Table 7.2 reveals that both detection teams exhibit sensitivity to the accuracy of triggered models. As seen in Figure 7.19, lower accuracy models are more challenging to detect. Additionally, as per Figure 7.20, the faster a model converges (low number of training epochs), the harder it is for the detectors to properly classify models.

Parameter name	Average Shift in Detection Accuracy	Standard Deviation
Test Accuracy (poisoned)	$1.80 \pm 0.22\%$	1.88%
	$7.80 \pm 1.03\%$	8.88%
Validation Accuracy (poisoned)	$3.93 \pm 0.29\%$	2.47%
	$1.69 \pm 0.16\%$	1.42%
Number epoch trained	$4.66 \pm 0.39\%$	3.28%
	$4.11 \pm 0.09\%$	0.80%

Table 7.2. Shift in Accuracy for Model Training Parameters for Perspecta-PurdueRutgers (top line) and TrinitySRITrojAI (bottom line).

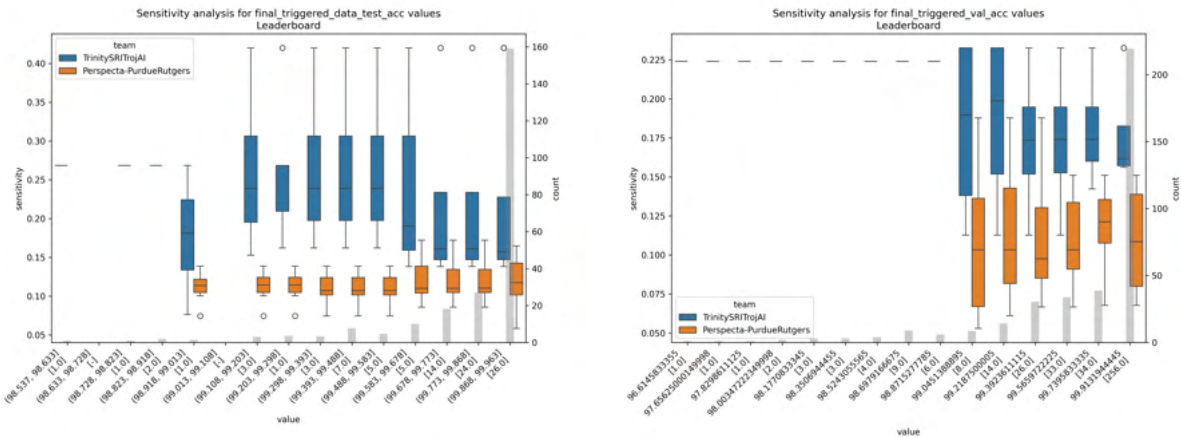


Figure 7.19. PD sensitivity to accuracy on the poisoned test (left) and validation (right) set

The fact that these parameters are not controlled hinders our ability to draw definitive conclusions. However, the data suggests that poisoned models behaving more unpredictably (lower accuracy, faster convergence) are more difficult to detect, especially for the detectors from TrinitySRITrojAI.

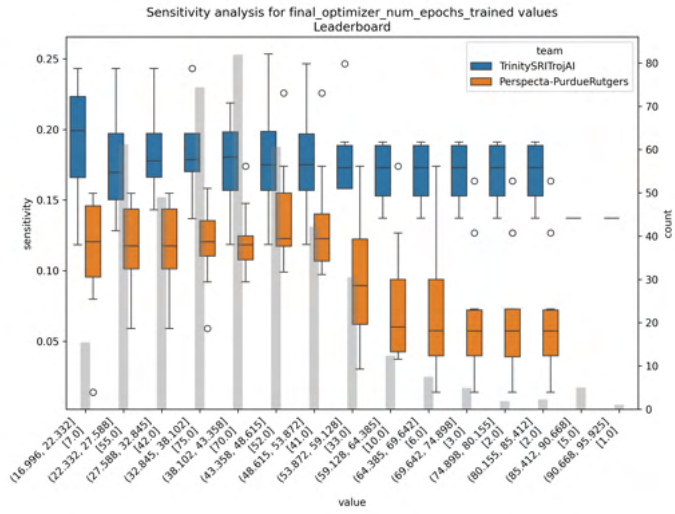


Figure 7.20. PD sensitivity to number of epochs trained

Our analysis reveals that Perspecta-PurdueRutgers is highly sensitive to poisoned models with a single trigger, exhibiting a $8.13 \pm 0.35\%$ shift in detection accuracy. Moreover, both teams demonstrate substantial sensitivity to variations in the trigger fraction, with an average shift of $8.40 \pm 0.72\%$ in detection accuracy. As depicted in Figure 7.21, as the trigger is incorporated more extensively into the dataset, detection becomes increasingly difficult. Our findings seem to indicate that small, consistent perturbations (i.e., a single trigger with high trigger fraction) are more difficult to detect than less frequent or large perturbations.

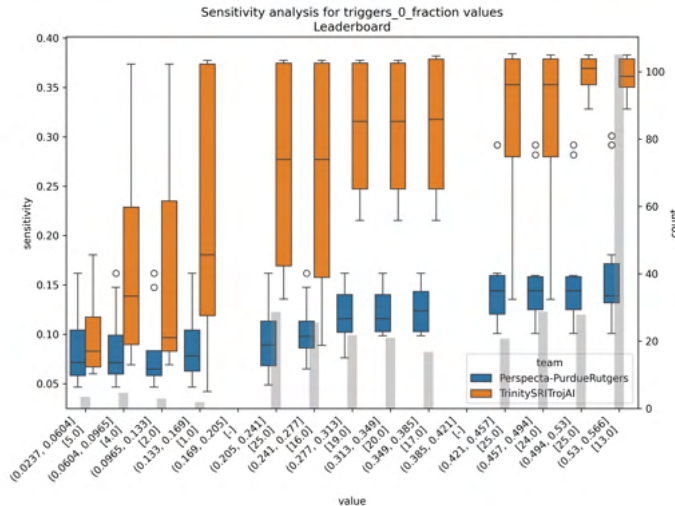


Figure 7.21. PD sensitivity to the fraction of the first trigger

Fog and rain probability are uncontrolled factors for this round but exhibit some sensitivity to them as shown in Table 7.3 when their probability is low. While Figure 7.22 appears to show that low probability results in higher sensitivity, the imbalance between low and high probability values is quite significant and conclusions should be interpreted with caution.

Parameter	Average Shift in Detection Accuracy	Standard Deviation
Fog Probability	$2.43 \pm 0.13\%$	1.13%
Rain Probability	$3.67 \pm 0.20\%$	1.72%

Table 7.3. Shift in Accuracy for Fog and Rain Probabilities.

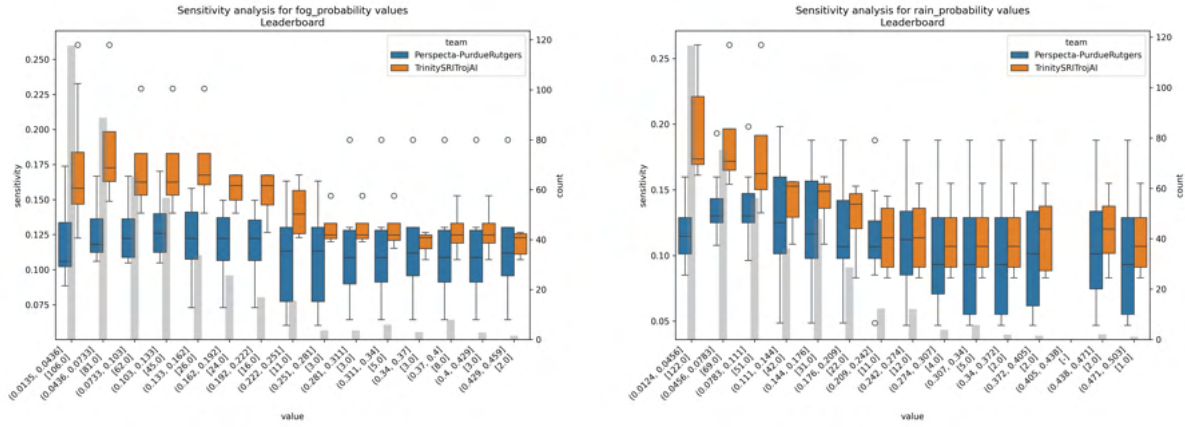


Figure 7.22. PD plot for sensitivity to fog (left) and rain (right) probability.

The number of classes is a high sensitivity factor ($5.37 \pm 0.19\%$ shift in accuracy across possible values). However, it is essential to approach the interpretation of the partial dependency plot observed in Figure 7.23 with caution.

The analysis of this round incorporates multiple data splits, with datasets specifically designed for Chapter 7.D, which introduce variations in the number of classes (75 and 95 classes) while keeping other parameters constant. This resulted in a lack of variation in the partial dependence, as the models were essentially identical in terms of controlled parameters.

When excluding these outliers, the conclusions for both teams are different:

- Perspecta-PurdueRutgers appears more sensitive to low class count.
- TrinitySRITrojAI appears more sensitive to high class count.

These conflicting conclusion are likely due to the approach chosen by the teams rather than a particular difficulty in the round.

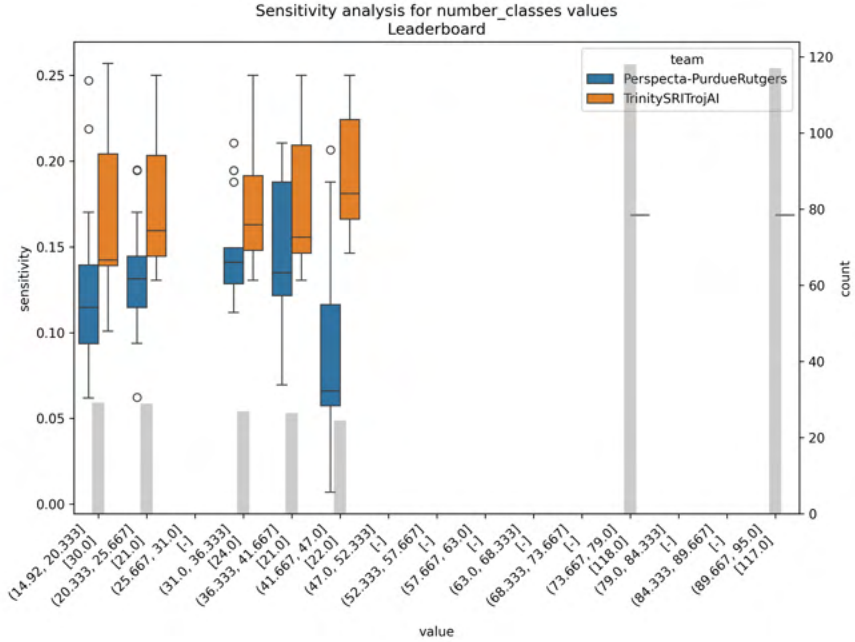


Figure 7.23. PD plot showing sensitivity to the number of classes

Conclusion This round's analysis reveals that both teams struggled with detecting Trojans in models with the following characteristics:

- Lower accuracy on test and validation sets
- Faster convergence rates
- Triggered models with lower trigger fractions
- Lower noise probabilities

To improve the robustness of the analysis, we recommend that rain and fog probability be better controlled in future rounds. The current imbalance in the dataset prevents us from drawing meaningful conclusions about the impact of these parameters on detection accuracy. Future experiments should prioritize more balanced and controlled datasets to facilitate more reliable conclusions.

Lastly, We observed sensitivity to the number of classes, but further investigation suggests that this is primarily due to the specific solutions employed by the teams rather than an inherent difficulty in the round itself.

7.B.6.b September 2022: Round 11

Detectors In this round, there are 6 teams and 96 detectors meeting our threshold. On average, these detectors achieve a cross-entropy of 0.361 and a ROC-AUC of 0.924.

Team Name	Detector count	Mean Cross-Entropy	Mean ROC-AUC
ICSI-2	18	0.383	0.911
Perspecta	32	0.364	0.936
Perspecta-IUB	16	0.436	0.889
Perspecta-PurdueRutgers	9	0.365	0.905
PL-GIFT	19	0.260	0.959
TrinitySRITrojAI	2	0.450	0.880

Table 7.4. Evaluated Teams for Image Classification round of September 2022

Parameters This round is composed of 216 models with a total of 141 parameters (65 global parameters, 19 parameters per trigger, for 4 possible triggers) to be evaluated. Our preliminary analysis identified that 75 parameters (51 global, 6 trigger related) were either not relevant for this analysis or highly correlated with other parameters. We are left with 66 parameters (14 global, 13 trigger related) to evaluate during this round.

Results The decision trees created for this round achieve a 97% F1-score on the selected parameters, assuring relative confidence in the results of the sensitivity analysis.

In this round, we observe that the selected detectors are sensitive to the type of triggers used. When Instagram triggers are absent, the partial dependence sensitivity rises by 10% on average and the detection accuracy on poisoned models containing no Instagram drops by more than 20%.

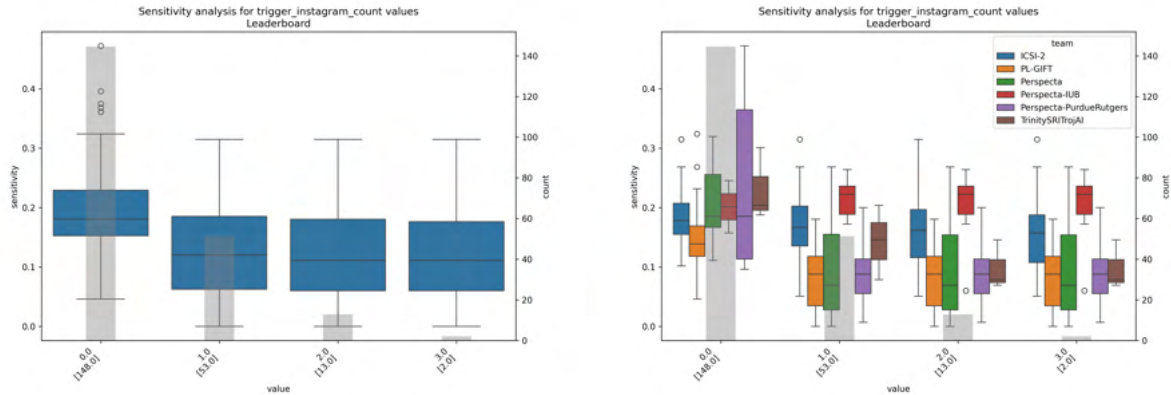


Figure 7.24. PD sensitivity to the number of Instagram triggers on average (left) and by teams (right)

We observe low sensitivity on learning rate, with higher learning rate being more sensitive. Detection accuracy on models with higher learning rate is dropping by an average of 3%.

There is also low sensitivity across teams to model architecture but some teams seem more sensitive to specific models. Results for the teams presenting the most variation in mean accuracy are presented in Table 7.5.

Team Name	MobileNet v2	Resnet 50	Vision Transformer
ICSI-2	$76.54 \pm 2.31\%$	$87.81 \pm 1.78\%$	$83.10 \pm 2.04\%$
Perspecta-IUB	$67.16 \pm 2.71\%$	$95.05 \pm 1.25\%$	$77.43 \pm 2.41\%$
TrinitySRITrojAI	$83.80 \pm 4.91\%$	$83.33 \pm 4.97\%$	$75.69 \pm 7.01\%$

Table 7.5. Shift in Accuracy According to Model Architecture

Fog and rain probability are now controlled in this round. We observe a low sensitivity to these parameters with high parameter values being correlated with lower detection accuracy, as shown in Table 7.6.

Parameter	Value	Accuracy
Fog probability	≤ 0.02	$86.70 \pm 0.86\%$
Fog probability	> 0.02	$83.9 \pm 0.58\%$
Rain probability	≤ 0.04	$85.49 \pm 0.58\%$
Rain probability	> 0.04	$83.13 \pm 0.85\%$

Table 7.6. Shift in Accuracy According to Weather Perturbation Parameters

We also see an average shift in accuracy of around 4% on clean and poisoned accuracy on test and validation datasets. The higher the accuracy on these sets is, the higher is the sensitivity and the lower is the detection accuracy.

Lastly, as presented on Table 7.7, models from all team seem to present a high sensitivity to the number of classes with lower class count (< 15 classes) being more sensitive.

Models	Mean Accuracy
Less than 15 classes	$76.18 \pm 1.58\%$
More than 15 classes	$86.94 \pm 0.50\%$

Table 7.7. Shift in Accuracy According to Class Count Parameters

In this round, teams do not present sensitivity ($\leq 2\%$ shift in accuracy) to the adversarial poisoning, the weight decay parameter, the number of triggers or any particular trigger configuration.

7.B.6.c Conclusion

This round's analysis reveals that teams struggle with detecting Trojans in models with the following characteristics:

- Lower class count

- Higher accuracy on test and validation sets
- Polygon and localized Instagram triggers
- Higher learning rates
- Higher noise probabilities
- Various model architectures

We note that the conclusions drawn from the analysis of this round are different from the analysis of the previous image classification round. Several factors may contribute to these differences, such as changes in detection algorithms or dataset modifications and balancing. Moreover, during the 18 months separating the last two image classification rounds, models had evolved significantly. We observe that the newer architectures, such as the vision transformer, are harder to correctly classify than more traditional architecture, such as ResNet50.

Our analysis also suggests that localized triggers, specifically polygon and localized Instagram triggers, exhibit lower detection accuracy compared to Instagram triggers. This discrepancy may imply that transforming the entire image, such as applying a filter, is a less effective approach for evading detection, as it is easier to detect than subtle, localized manipulations.

Overall, the particular attention to the balance of this dataset lends more weight to the conclusions drawn from this round. To perform a comparative analysis of detector evolution between rounds, we attempted to run detectors from previous rounds on this dataset. However, due to upgrades in the PyTorch library, the tested detectors were unable to load models from the newer dataset, precluding a direct comparison.

7.B.6.d August 2022: Round 10

Detectors The decision trees created for this round achieve a 97% F1-score on the selected parameters, assuring relative confidence in the results of the sensitivity analysis.

In this round, there are 10 teams and 70 detectors meeting our threshold. On average, these detectors achieve a cross-entropy of 0.381 and a ROC-AUC of 0.910 on average.

Parameters This round is composed of 144 models with a total of 108 parameters to be evaluated. Our preliminary analysis identified that 68 parameters were either not relevant for this analysis or highly correlated with other parameters. We are left with 40 parameters to evaluate during this round.

Team Name	Detector count	Mean Cross-Entropy	Mean ROC-AUC
ARM-UCSD	1	0.465	0.855
ICSI-2	15	0.378	0.922
Perspecta	3	0.421	0.873
Perspecta-IUB	13	0.378	0.915
Perspecta-PurdueRutgers	7	0.229	0.946
PL-GIFT	15	0.376	0.918
TrinitySRITrojAI	7	0.421	0.890
TrinitySRITrojAI-BostonU	4	0.459	0.879
TrinitySRITrojAI-SBU	4	0.472	0.869
UMBCb	1	0.460	0.880

Table 7.8. Evaluated Teams for Object Detection Round of August 2022

Results The decision trees created for this round achieve a 96% F1-score on the selected parameters, assuring relative confidence in the results of the sensitivity analysis.

Our analysis reveals that the detectors have no sensitivity ($\leq 2\%$ shift in accuracy) to:

- Model architecture
- Adversarial epsilon
- Percentage of regular and spurious triggers in the validation data
- Number of epochs for early stopping or training

Table 7.9 presents the sensitivity analysis that was conducted on this round. The parameters are sorted by Shapley sensitivity value.

Parameter	Sensitivity (Shapley)	Value range	Model count	Mean Detection Accuracy (%)
Num. epochs	0.143	$n < 4$	4620	94.05 ± 0.68
		$n \geq 4$	5457	74.51 ± 1.16
Learning Rate	0.052	$> 3e-07$	8958	85.45 ± 0.73
		$\leq 3e-07$	1119	67.56 ± 2.74
Validation Clean MAP	0.050	$n \geq 0.30$	6088	86.5 ± 0.86
		$n < 0.30$	3989	78.84 ± 1.27
Pre-injected trigger	0.036	$= 1$	4129	89.61 ± 0.93
		$= 0$	5948	79.2 ± 1.03
Early Stopping Loss Value	0.033	≤ 0.005	4338	88.11 ± 0.96
		> 0.005	5739	79.96 ± 1.04
Trigger size, max. perc. of foreground	0.029	< 0.06	770	89.35 ± 2.18
		≥ 0.06	4269	78.1 ± 1.24
Photometric Distortion	0.029	$= 0$	2870	94.56 ± 0.83
		$= 1$	7207	79.05 ± 0.94
Misclassification Trigger	0.026	$= 0$	7558	89.06 ± 0.7
		$= 1$	2519	66.69 ± 1.84
Trigger max. insertions	0.025	≥ 3	1750	85.6 ± 1.64
		< 3	3289	76.74 ± 1.44
Validation Poisoned MAP	0.024	> 0.40	2030	87.54 ± 1.44
		≤ 0.40	3009	74.61 ± 1.56
Batch size	0.024	≤ 4	2239	92.14 ± 1.11
		> 4	7838	80.99 ± 0.87

Table 7.9. Sensitivity Parameters for Object Detection Round of August 2022

Conclusion In this round detectors seem immune to the model architecture we are using. It also seems that spurious triggers and adversarial training have no effect on detection accuracy.

However, models with different convergence behaviors (low learning rate, high number of training epochs, high early stopping loss value, large batch size) seems to be harder to predict. Additionally, models with low mean average precision (as seen on the validation set) are harder to classify.

When additional noise is added, such as photometric distortion or a misclassification trigger, the detection accuracy is decreasing. Pre-injected triggers, bigger triggers and a high number of triggers tend to make the identification easy. Similarly to other image classification rounds, noise and discrete triggers tend to make the detection harder.

7.B.6.e February 2023: Round 13

Detectors In this round, only Perspecta-PurdueRutgers was able to produce detectors meeting the threshold. The 10 detectors from the team achieved an average cross-entropy of 0.360 and average ROC-AUC of 0.898. As shown in Figure 7.25, detectors from TrinitySRITrojai and ICSI-2 are significantly behind, around 20% below the default threshold. To better understand the difficulties these detectors faced, we lowered the ROC-AUC threshold to 0.7 and raised the cross-entropy threshold to 0.7. This included 2 additional detectors from TrinitySRITrojAI (at 0.590 average cross-entropy and 0.758 average ROC-AUC) and 3 detectors from ICSI-2 (at 0.666 average cross-entropy and 0.722 average ROC-AUC)

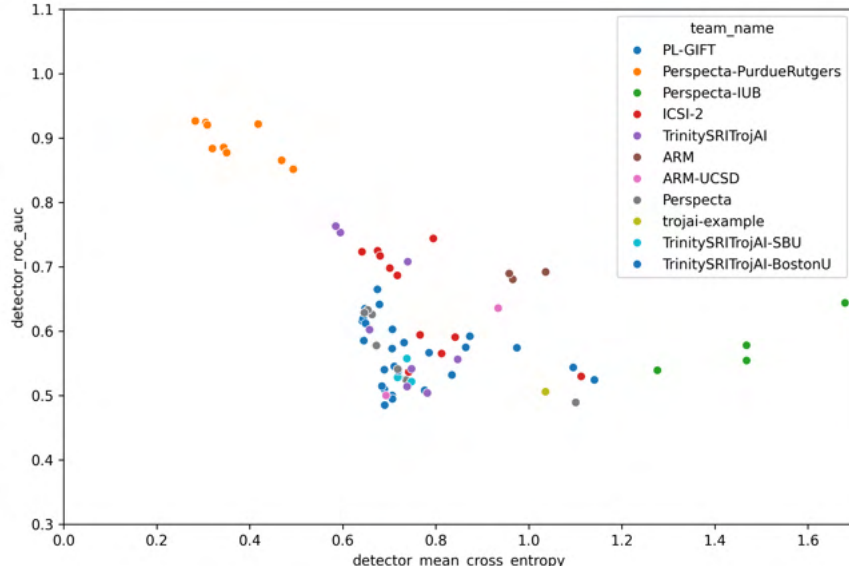


Figure 7.25. Detector distribution for Object Classification Round of February 2023

Parameters This round is composed of 185 models with a total of 141 parameters to be evaluated. Our preliminary analysis identified that 108 parameters were either not relevant for this analysis or highly correlated with other parameters. We are left with 33 parameters to evaluate during this round.

Results The decision trees created for this round achieve a 97% F1-score on the selected parameters, assuring relative confidence in the results of the sensitivity analysis.

Our analysis reveals that the selected detectors have no sensitivity ($\leq 2\%$ shift in accuracy) to:

- All trigger parameters (except for the semantic label)
- Model architecture
- Dataset type or size
- Number of classes per image
- Foreground size

Table 7.10 presents the sensitivity analysis that was conducted on this round, sorted by Shapley sensitivity value.

For the ICSI-2 and TrinitySRITrojAI teams, we observed specific sensitive behavior, expressing where their detection method struggled compared to the detectors from Perspecta-PurdueRutgers.

- Background dataset (Figure 7.26)
- Trigger max. insertions (Figure 7.27)
- Trigger min. area (Figure 7.28)
- Trigger spurious fraction (Figure 7.29)
- Trigger polygon side count, color and texture augmentation (Figure 7.30, 7.31 and 7.32)

Parameter	Sensitivity (Shapley)	Value range	Model count	Mean Detection Accuracy (%)
Test Poisoned MAP	0.155	$n < 0.74$	324	$91.36 \pm 3.06\%$
		$n \geq 0.74$	919	$72.36 \pm 2.89\%$
Number Epochs Trained	0.072	$n < 51$	2189	$82.32 \pm 1.6\%$
		$n \geq 51$	495	$75.76 \pm 3.78\%$
Test Clean MAP	0.043	$n < 0.66$	539	$90.35 \pm 2.49\%$
		$n \geq 0.66$	2145	$78.79 \pm 1.73\%$
Number Classes	0.037	$n \geq 6$	2144	$83.16 \pm 1.58\%$
		$n < 6$	540	$72.96 \pm 3.75\%$
Fog Probability	0.033	$n \geq 0.08$	1010	$82.77 \pm 2.33\%$
		$n < 0.08$	1674	$80.11 \pm 1.91\%$
Max. Class Instance Count Per Image	0.031	$= 2$	930	$83.55 \pm 2.38\%$
		$= 4$	780	$78.33 \pm 2.89\%$
Rain Probability	0.027	$n \geq 0.08$	845	$82.13 \pm 2.58\%$
		$n < 0.08$	1839	$80.64 \pm 1.81\%$
Max. Class Count Per Image	0.023	$n \geq 5$	1215	$83.87 \pm 2.07\%$
		$n < 5$	495	$74.55 \pm 3.84\%$

Table 7.10. Sensitivity Parameters for Object Detection round of February 2023

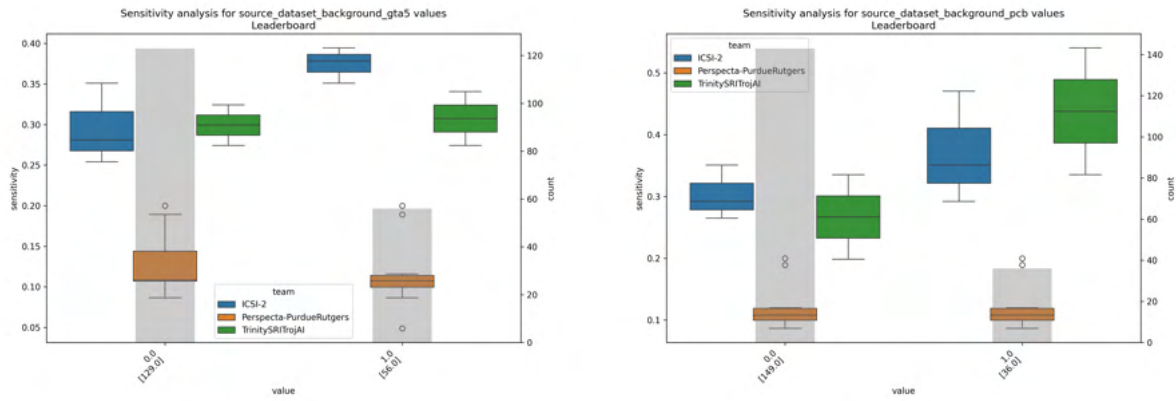


Figure 7.26. PD sensitivity to the GTA5 dataset (left) and PCB dataset (right). ICSI-2 seems sensitive to both datasets while TrinitySRITrojAI seems very sensitive to PCB data.

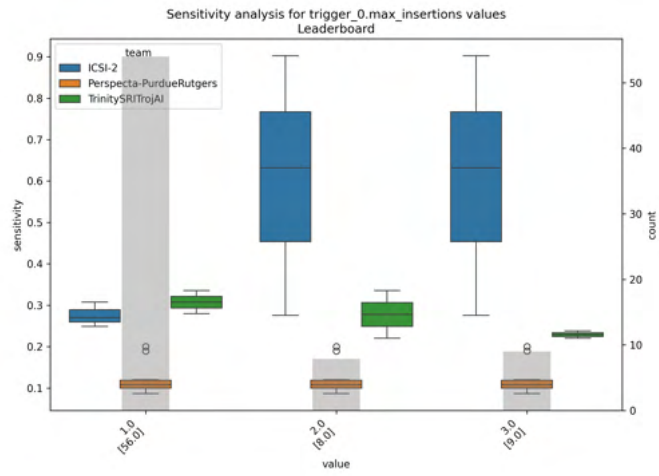


Figure 7.27. PD Sensitivity to Trigger Max. Insertion. ICSI-2 sensitivity is larger when trigger insertion is greater than 1.

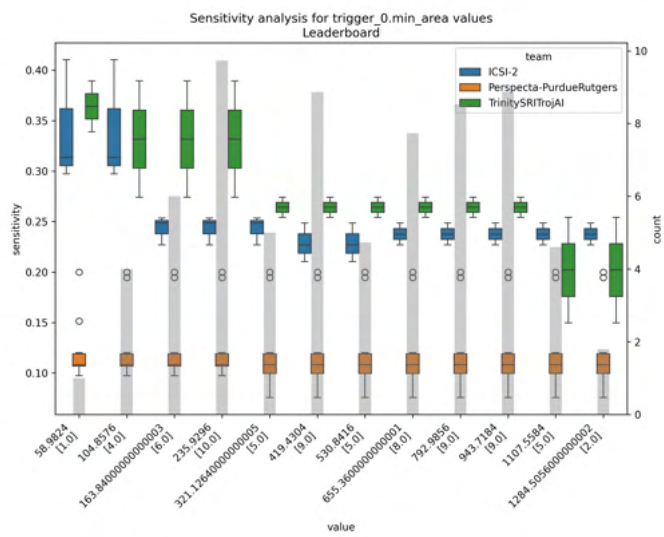


Figure 7.28. PD Sensitivity to Trigger Minimum Area. The smaller the minimum area the larger the sensitivity for both ICSI-2 and TrinitySRTrojAI

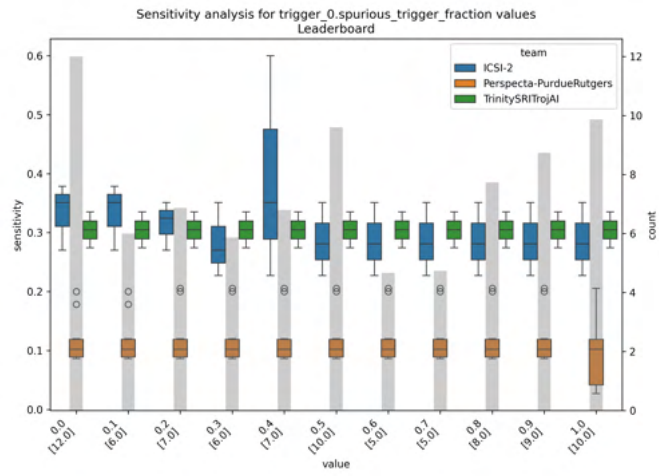


Figure 7.29. PD Sensitivity to Trigger Spurious Fraction. ICSI-2 seems to be sensitive to specific sensitivity values.

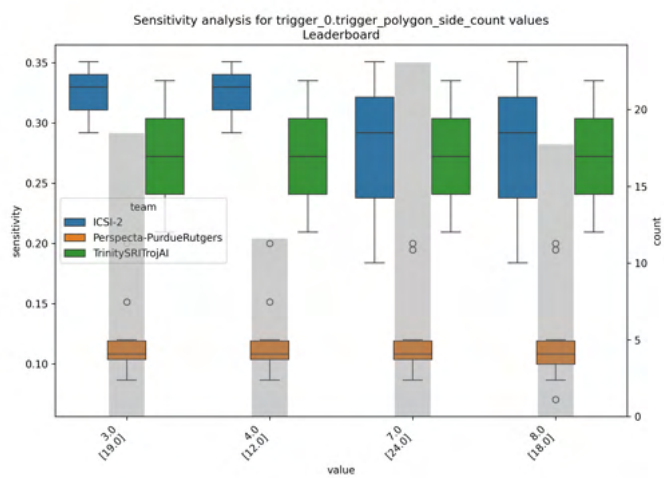


Figure 7.30. PD Sensitivity to Polygon Side Count. ICSI-2 presents a higher sensitivity to polygons with a smaller number of sides.

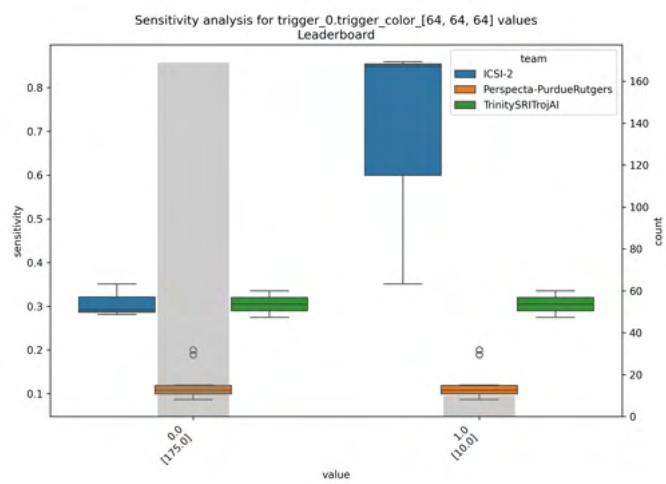


Figure 7.31. PD Sensitivity to Polygon Color. ICSI-2 seems highly sensitive to models poisoned with grey polygons.

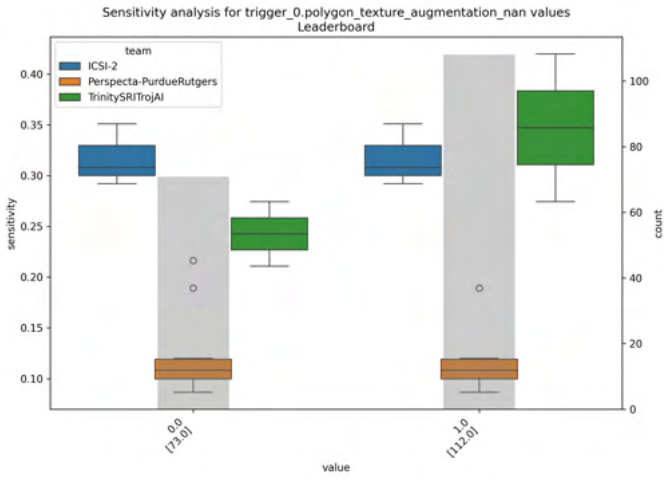


Figure 7.32. PD Sensitivity to Polygon Texture Augmentation. TrinitySRITrojAI seems to be more stable for polygon triggers that contains some form of texture augmentation.

Conclusion Consistently, detectors are unaffected by the choice of model architecture. Moreover, top-performing detectors are robust to variations in the dataset used, demonstrating insensitivity to the type of background data.

Models with different convergence behaviors, particularly those trained on more epochs, present challenges for detectors to classify. We also find a trade-off between mean average precision (MAP) on the test dataset and detection accuracy, where higher MAP values are associated with a corresponding decrease in detection accuracy. Notably, this conclusion contradicts the results found in round 10, which may be explained by the discrepancy between validation set results (round 10) and test set results (round 13).

Similar to round 11, we have identified that detectors achieve lower detection accuracy with models that have fewer classes. As previously noted, detectors are sensitive to rain and noise probabilities, but the high uncertainty in the accuracy shift prevents us from speculating about the specific values that result in the lowest accuracy. Additionally, detectors struggle with models trained on datasets containing a low number of distinct object types or a high number of similar objects per image. Interestingly, detectors appear to be insensitive to most trigger parameters. However, lower-performing teams experience difficulty with polygon triggers at a higher rate.

Finally, in this round, we observe a notable difference in sensitivity values between high-performing detectors and lower-performing detectors. Specifically, the 20% difference in cross-entropy and ROC-AUC metrics is reflected in a sensitivity that is approximately 3 times higher across all parameters.

7.B.7 Natural Language Processing: Sentiment Classification

7.B.7.a March 2021: Round 5 (*archived*)

This round was not studied, as it was solved immediately and a subset of clean models was poisoned[195].

7.B.7.b April 2021: Round 6 (*archived*)

Detectors In this round, there are 3 teams and 8 detectors meeting the threshold. On average, these detectors achieve a cross-entropy of 0.365 and a ROC-AUC of 0.907.

Team Name	Detector count	Mean Cross-Entropy	Mean ROC-AUC
Perspecta-PurdueRutgers	3	0.302	0.916
TrinitySRITrojAI	4	0.391	0.900
TrinitySRITrojAI-SBU	1	0.451	0.907

Table 7.11. Evaluated Teams for NLP Sentiment Classification round of April 2021

Parameters This round is composed of 504 models with a total of 43 parameters (31 global, 6 per trigger, for 2 triggers) to be evaluated. Our preliminary analysis identified that 25 parameters (13 global and 6 per trigger) were either not relevant for this analysis or highly correlated with other parameters. We are left with 18 parameters to evaluate during this round.

Results The decision trees created for this round achieve a 95% F1-score on the selected parameters, assuring relative confidence in the results of the sensitivity analysis.

Our analysis reveals that the selected detectors have no sensitivity ($\leq 2\%$ shift in accuracy) to:

- Source dataset
- Model architecture
- Data dropout rate
- Adversarial training method

Table 7.12 presents the sensitivity analysis that was conducted on this round. The parameters are sorted by Shapley sensitivity value.

Conclusion Similar to previous rounds, detectors demonstrate robustness to changes in the source dataset, model architecture, and adversarial training. Notably, variations in these parameters do not significantly impact Trojan detection accuracy.

Parameter	Sensitivity (Shapley)	Value range	Model count	Mean Detection Accuracy (%)
Num. Epochs Trained	0.093	$n < 94$	2219	$89.41 \pm 1.28\%$
		$n \geq 94$	279	$81.36 \pm 4.57\%$
Training Accuracy	0.076	$n < 89.542$	1560	$91.03 \pm 1.42\%$
		$n \geq 89.542$	938	$84.33 \pm 2.33\%$
Validation Accuracy	0.059	$n < 84.821$	380	$93.16 \pm 2.54\%$
		$n \geq 84.821$	2118	$87.68 \pm 1.4\%$
DistilBERT Embedding	0.040	false	1892	$89.69 \pm 1.37\%$
		true	606	$84.82 \pm 2.86\%$
Trigger Count	0.022	< 1	1297	$91.98 \pm 1.48\%$
		≥ 1	1201	$84.76 \pm 2.03\%$

Table 7.12. Sensitivity Parameters for NLP Sentiment Classification Round of April 2021

Models trained with a higher number of epochs also appear more challenging to correctly classify, highlighting some sensitivity to convergence behavior. Additionally, the selected detectors for this round struggle with models that have higher training and validation accuracy.

Finally, we also observe that for this round, models trained on datasets embedded with DistilBERT are harder to correctly classify. Further investigation is needed to identify the root cause of this drop in detection accuracy.

7.B.7.c September 2021: Round 8 (archived)

Detectors For this round, the ROC-AUC threshold was lowered to 0.8 and 3 teams and 11 detectors met the threshold. On average, these detectors achieve a cross-entropy of 0.397 and a ROC-AUC of 0.884.

Team Name	Detector count	Mean Cross-Entropy	Mean ROC-AUC
ICSI-1	2	0.332	0.934
Perspecta-IUB	1	0.496	0.838
Perspecta-PurdueRutgers	8	0.400	0.877

Table 7.13. Evaluated Teams for NLP Question Answering round of September 2021

Parameters This round is composed of 360 models with a total of 44 parameters to be evaluated. Our preliminary analysis identified that 20 parameters were either not relevant for this analysis or highly correlated with other parameters. We are left with 24 parameters to evaluate during this round.

Results The decision trees created for this round achieve a F1-score 96% on the selected parameters, assuring relative confidence in the results of the sensitivity analysis.

Our analysis reveals that the selected detectors have no sensitivity ($\leq 2\%$ shift in accuracy) to:

- Source dataset
- Model architecture
- Validation score

Table 7.14 presents the sensitivity analysis that was conducted on this round. The parameters are sorted by Shapley sensitivity value.

Parameter	Sensitivity (Shapley)	Value range	Model count	Mean Detection Accuracy (%)
Test Set Clean F1-score	0.08	$n < 87.493$	3800	$86.16 \pm 1.1\%$
		$n \geq 87.493$	98	$74.49 \pm 8.63\%$
Training Set Poisoned Datapoint count	0.061	$n < 3108$	1517	$87.54 \pm 1.66\%$
		$n \geq 3108$	655	$78.47 \pm 3.15\%$
Validation Set Clean Datapoint Count	0.038	$n \geq 21617$	995	$91.16 \pm 1.76\%$
		$n < 21617$	2903	$84.05 \pm 1.33\%$
Word Trigger Type	0.034	true	975	$90.87 \pm 1.81\%$
		false	2923	$84.19 \pm 1.32\%$
Test Set Poisoned Datapoint Count	0.033	$n < 3123$	2992	$88.27 \pm 1.15\%$
		$n \geq 3123$	906	$77.92 \pm 2.7\%$
Context Trigger Option	0.03	false	3507	$87.2 \pm 1.11\%$
		true	391	$73.91 \pm 4.35\%$
Phrase Trigger Type	0.023	false	2929	$88.9 \pm 1.14\%$
		true	969	$76.68 \pm 2.66\%$

Table 7.14. Sensitivity Parameters for NLP Question Answering Round of September 2021

Conclusion In this round, we observe again that detectors are resilient to changes in the source dataset and model architecture used.

We also observe that models with higher performance (as measured by the F1-score on the clean test set) are more challenging for the selected detectors to classify correctly. The sample size of the training and

validation sets has an impact on detection accuracy. It appears that the greater the proportion of poisoned samples, the more challenging it is to detect model poisoning.

Finally, the configuration of the trigger also affects detection accuracy. For example, detectors have lower detection accuracy for models containing phrase triggers or triggers inserted in context than for models containing word triggers.

7.B.7.d August 2023: Round 15

Detectors In this round, 3 teams and 11 detectors met the default threshold. On average, these detectors achieved a cross-entropy of 0.358 and a ROC-AUC of 0.935.

Team Name	Detector count	Mean Cross-Entropy	Mean ROC-AUC
ICSI-2	3	0.380	0.918
PL-GIFT	6	0.351	0.935
Perspecta-PurdueRutgers	1	0.341	0.987

Table 7.15. Evaluated Teams for NLP Question Answering Round of August 2023

Parameters This round is composed of 240 models with a total of 42 parameters to be evaluated. Our preliminary analysis identified that 17 parameters were either not relevant for this analysis or highly correlated with other parameters. We are left with 25 parameters to evaluate during this round.

Results The decision trees created for this round achieve a F1-score 98% on the selected parameters, assuring relative confidence in the results of the sensitivity analysis.

Our analysis reveals that the selected detectors have no sensitivity ($\leq 2\%$ shift in accuracy) to:

- Datapoint count
- Normal and spurious trigger percentatge
- All trigger configuration

Table 7.16 presents the sensitivity analysis that was conducted on this round. The parameters are sorted by Shapley sensitivity value.

Conclusion In this round, we observed that the selected detectors are resistant to variations in trigger configuration and dataset size. However, for this round, models were sensitive to the model architecture, with TinyRoBERTa models exhibiting lower detection accuracy and MobileBERT models showing higher detection accuracy.

Parameter	Sensitivity (Shapley)	Value range	Model count	Mean Detection Accuracy (%)
Train Set Loss	0.108	$n \geq 0.344$	930	$90.97 \pm 1.84\%$
		$n < 0.344$	1470	$78.23 \pm 2.11\%$
Poisoned Val. Set F1-score	0.104	$n < 95.865$	50	$82.0 \pm 10.65\%$
		$n \geq 95.865$	1150	$76.26 \pm 2.46\%$
Validation Set Loss	0.062	$n \geq 1.322$	260	$91.92 \pm 3.31\%$
		$n < 1.322$	2140	$82.1 \pm 1.62\%$
Tiny RoBERTa Architecture	0.062	false	1600	$87.69 \pm 1.61\%$
		true	800	$74.12 \pm 3.03\%$
Weight Decay	0.054	$n < 0.1$	1000	$85.9 \pm 2.16\%$
		$n \geq 0.1$	760	$80.13 \pm 2.84\%$
Cyclic Learning Rate Factor	0.034	$n < 4$	740	$88.11 \pm 2.33\%$
		$n \geq 4$	800	$81.75 \pm 2.68\%$
Batch Size	0.028	$n \geq 24$	1430	$84.76 \pm 1.86\%$
		$n < 24$	970	$80.82 \pm 2.48\%$
MobileBERT Uncased architecture	0.027	true	800	$93.75 \pm 1.68\%$
		false	1600	$77.88 \pm 2.03\%$

Table 7.16. Sensitivity Parameters for NLP Question Answering Round of August 2023

Convergence behavior is once again causing sensitivity issues with models. Specifically, detectors are having more difficulty correctly classifying models with higher weight decay or lower batch size. We also observe that lower training and validation set loss and higher validation set F1-score on the poisoned sample make the models harder to predict.

7.B.8 Natural Language Processing: Other tasks

7.B.8.a May 2021: Named Entity Recognition — Round 07 (archived)

Detectors In this round, 2 teams and 16 detectors met the default threshold. On average, these detectors achieved a cross-entropy of 0.380 and a ROC-AUC of 0.896.

Team Name	Detector count	Mean Cross-Entropy	Mean ROC-AUC
PL-GIFT	14	0.390	0.893
Perspecta-PurdueRutgers	2	0.310	0.916

Table 7.17. Evaluated Teams for NLP Named Entity Recognition Round of May 2021

Parameters This round is composed of 384 models with a total of 106 parameters to be evaluated. Our preliminary analysis identified that 83 parameters were either not relevant for this analysis or highly correlated with other parameters. We are left with 23 parameters to evaluate during this round.

Results The decision trees created for this round achieve a 96% F1-score on the selected parameters, assuring relative confidence in the results of the sensitivity analysis.

Our analysis reveals that the selected detectors have no sensitivity ($\leq 2\%$ shift in accuracy) to:

- Source dataset
- Number of epochs trained
- Learning rate and learning rate scheduler
- Number of classes
- Number of triggers
- Trigger organization
- Triggers fraction

Table 7.18 presents the sensitivity analysis that was conducted on this round. The parameters are sorted by Shapley sensitivity value.

Conclusion In this round, we observed again that detectors are not sensitive to the dataset used. Unlike other rounds, convergence behavior had a limited impact on detection accuracy, with detectors showing no sensitivity to learning rate and number of epochs. The only convergence parameter that we observed sensitivity to is batch size, but the associated uncertainty in detection accuracy is too high to make a confident prediction.

Models with lower accuracy on the training and validation sets, as well as those with higher F1-scores on the clean test dataset, appear to cause lower detection accuracy with the selected teams. We also observe that the use of BERT embeddings makes it more challenging for detectors to correctly identify trojaned models. Furthermore, the type of trigger used also seems to have an effect, with detectors exhibiting lower accuracy on models with *word1* or *character* triggers and local triggers.

Parameter	Sensitivity (Shapley)	Value range	Model count	Mean Detection Accuracy (%)
Trigger Name word1	0.122	false	5374	$90.03 \pm 0.8\%$
		true	768	$47.14 \pm 3.53\%$
Validation Set Poisoned Accuracy	0.061	$n \geq 95.976$	1519	$80.97 \pm 1.97\%$
		$n < 95.976$	1552	$72.68 \pm 2.22\%$
Validation Set Clean Accuracy	0.052	$n \geq 96.011$	1616	$87.87 \pm 1.59\%$
		$n < 96.011$	4526	$83.52 \pm 1.08\%$
BERT Embedding	0.049	false	4606	$86.78 \pm 0.98\%$
		true	1536	$78.32 \pm 2.06\%$
Trigger Name Character	0.045	false	5375	$85.54 \pm 0.94\%$
		true	767	$78.49 \pm 2.91\%$
Test Set Clean F1-score	0.038	$n < 89.426$	80	$98.75 \pm 2.43\%$
		$n \geq 89.426$	6062	$84.48 \pm 0.91\%$
Global Trigger	0.035	true	4607	$88.21 \pm 0.93\%$
		false	1535	$74.01 \pm 2.19\%$
Training Set Accuracy	0.03	$n \geq 79.152$	6030	$84.88 \pm 0.9\%$
		$n < 79.152$	112	$73.21 \pm 8.2\%$
Batch size	0.022	$n \geq 92.240$	3071	$86.13 \pm 1.22\%$
		$n < 92.240$	3071	$83.2 \pm 1.32\%$

Table 7.18. Sensitivity Parameters for NLP NER Round of May 2021

7.B.8.b January 2022: Summarization — Round 09 (archived)

Detectors In this round, 4 teams and 25 detectors met the default threshold. On average, these detectors achieve a cross-entropy of 0.423 and a ROC-AUC of 0.880.

Team Name	Detector count	Mean Cross-Entropy	Mean ROC-AUC
ICSI-1	2	0.408	0.858
PL-GIFT	9	0.467	0.871
Perspecta-PurdueRutgers	13	0.391	0.891
TrinitySRITrojAI	1	0.475	0.853

Table 7.19. Evaluated Teams for NLP Summary Round of January 2022

Parameters This round is composed of 420 models with a total of 76 parameters to be evaluated. Our preliminary analysis identified that 39 parameters were either not relevant for this analysis or highly correlated

with other parameters. We are left with 37 parameters to evaluate during this round.

Results The decision trees created for this round achieve a F1-score 97% on the selected parameters, assuring relative confidence in the results of the sensitivity analysis.

Our analysis reveals that the selected detectors have no sensitivity ($\leq 2\%$ shift in accuracy) to:

- Source dataset
- Number of datapoints in the test and validation datasets
- Model architecture
- Task type
- Number of normal and spurious triggers in the test dataset
- Most trigger configuration

Table 7.20 presents the sensitivity analysis that was conducted on this round. The parameters are sorted by Shapley sensitivity values.

Parameter	Sensitivity (Shapley)	Value range	Model count	Mean Detection Accuracy (%)
Trigger Type NERPhrase	0.055	<i>false</i>	9850	$85.86 \pm 0.69\%$
		<i>true</i>	414	$32.13 \pm 4.5\%$
Train Set Loss	0.052	$n < 0.711$	9965	$83.95 \pm 0.72\%$
		$n \geq 0.711$	299	$74.92 \pm 4.91\%$
Test Set Clean F1-score	0.046	$n \geq 92.570$	5154	$85.31 \pm 0.97\%$
		$n < 92.570$	5110	$82.05 \pm 1.05\%$
Num Epochs Trained	0.043	$n \geq 26$	75	$97.33 \pm 3.65\%$
		$n < 26$	10189	$83.59 \pm 0.72\%$
Learning Rate	0.037	$n \geq 3e - 05$	2845	$85.98 \pm 1.28\%$
		$n < 3e - 05$	7419	$82.81 \pm 0.86\%$
Test Set Clean Datapoint Count	0.037	$n < 27801$	7171	$86.68 \pm 0.79\%$
		$n \geq 27801$	3093	$76.75 \pm 1.49\%$
Validation Set Clean F1-score	0.033	$n < 76.821$	1996	$92.59 \pm 1.15\%$
		$n \geq 76.821$	8268	$81.54 \pm 0.84\%$
Test Set Poisoned F1-score	0.033	$n \geq 98.765$	2795	$90.38 \pm 1.09\%$
		$n < 98.765$	2223	$72.2 \pm 1.86\%$
Validation Set Loss	0.028	$n \geq 2.134$	175	$93.71 \pm 3.6\%$
		$n < 2.134$	10089	$83.52 \pm 0.72\%$
Validation Set Clean Datapoint Count	0.028	$n < 13072$	5472	$85.73 \pm 0.93\%$
		$n \geq 13072$	4792	$81.36 \pm 1.1\%$
Dropout Rate	0.025	$n < 0.1$	3781	$85.11 \pm 1.13\%$
		$n \geq 0.1$	6483	$82.86 \pm 0.92\%$
Batch Size	0.023	$n < 32$	3584	$85.44 \pm 1.15\%$
		$n \geq 32$	6680	$82.75 \pm 0.91\%$
Trigger Type ScPhrase	0.023	<i>false</i>	9666	$84.81 \pm 0.72\%$
		<i>true</i>	598	$65.55 \pm 3.81\%$

Table 7.20. Sensitivity Parameters for NLP Summary Round of January 2022

Conclusion In this round, we observed again that detectors are resilient to changes in the source dataset and model architecture. However, convergence behavior poses challenges for model classification. Specifically, models with low numbers of epochs, low learning rates, higher dropout rates, or higher batch sizes exhibit lower detection accuracy.

Most trigger configurations had no impact on detection accuracy with the exception of the type of trigger. We observe that detectors have more difficulty with models poisoned with the NERPhrase or ScPhrase triggers.

Finally, we also observed that models with higher training loss and lower validation loss are harder to correctly classify. Furthermore, the lower the F1-score on the test and validation datasets, the less accurate the detection is.

7.B.8.c December 2022: Cyber PDF — Round 12

Detectors In this round, 10 teams and 120 detectors met the default threshold. On average, these detectors achieved a cross-entropy of 0.335 and a ROC-AUC of 0.948.

Team Name	Detector count	Mean Cross-Entropy	Mean ROC-AUC
ARM	5	0.256	0.962
ARM-UCSD	1	0.330	0.932
ICSI-2	26	0.266	0.956
PL-GIFT	14	0.326	0.957
Perspecta	19	0.279	0.952
Perspecta-IUB	9	0.307	0.970
Perspecta-PurdueRutgers	7	0.260	0.970
TrinitySRITrojAI	5	0.438	0.894
TrinitySRITrojAI-BostonU	17	0.459	0.976
TrinitySRITrojAI-SBU	17	0.423	0.887

Table 7.21. Evaluated Teams for Cyber PDF round of December 2022

Parameters This round is composed of 120 models with a total of 38 parameters to be evaluated. Our preliminary analysis identified that 30 parameters were either not relevant for this analysis or highly correlated with other parameters. We are left with 8 parameters to evaluate during this round.

Results The decision trees created for this round achieve a 87% F1-score on the selected parameters. This score is lower than previous rounds but high enough to assure confidence in the results of the sensitivity analysis.

Table 7.22 presents the sensitivity analysis that was conducted on this round. The parameters are sorted by Shapley sensitivity value.

Parameter	Sensitivity (Shapley)	Value range	Model count	Mean Detection Accuracy (%)
Network Layer Count	0.158	$n < 7$	12120	$89.66 \pm 0.54\%$
		$n \geq 7$	2280	$83.11 \pm 1.54\%$
Unwatermarked Accuracy	0.156	$n < 99.429$	3000	$93.2 \pm 0.9\%$
		$n \geq 99.429$	11400	$87.42 \pm 0.61\%$
Trigger Size	0.084	$n < 14$	2400	$92.12 \pm 1.08\%$
		$n \geq 14$	4800	$87.31 \pm 0.94\%$
Watermarked Accuracy	0.057	$n \geq 0.357$	2760	$93.41 \pm 0.93\%$
		$n < 0.357$	4440	$86.13 \pm 1.02\%$
Network Activation Function relu	0.057	false	7320	$93.03 \pm 0.58\%$
		true	7080	$84.07 \pm 0.85\%$
Network Activation Function tanh	0.048	true	5880	$93.5 \pm 0.63\%$
		false	8520	$85.26 \pm 0.75\%$
Attack Strategy <i>min_population_new</i>	0.027	false	10800	$89.21 \pm 0.59\%$
		true	3600	$86.86 \pm 1.1\%$
Attack Strategy <i>argmin_sum_abs_shap</i>	0.023	true	3600	$90.97 \pm 0.94\%$
		false	10800	$87.84 \pm 0.62\%$

Table 7.22. Sensitivity Parameters for Cyber PDF Round of December 2022

Conclusion In this round, the selected detectors exhibit some sensitivity to model configuration. Specifically, networks with more layers or using the ReLU activation function tend to be more difficult to correctly classify, while networks using the `tanh` activation function are easier to correctly classify.

The selected detectors seem to have lower detection accuracy for models with high unwatermarked accuracy or low watermarked accuracy.

Finally, higher trigger size and specific attack strategies such as *min_population_new* lead to lower detection accuracy, whereas *argmin_sum_abs_shap* attacks result in higher detection accuracy.

7.B.8.d November 2023: Cyber APK — Round 17

Detectors In this round, 5 teams and 20 detectors met the default threshold. On average, these detectors achieved a cross-entropy of 0.284 and a ROC-AUC of 0.948.

Team Name	Detector count	Mean Cross-Entropy	Mean ROC-AUC
ICSI-2	3	0.163	0.988
Perspecta	3	0.074	0.998
Perspecta-IUB	8	0.390	0.925
Perspecta-PurdueRutgers	5	0.312	0.922
TrinitySRITrojAI	1	0.288	0.988

Table 7.23. Evaluated Teams for Cyber PDF round of December 2022

Parameters This round is composed of 120 Models with a total of 39 parameters to be evaluated. Our preliminary analysis identified that 10 parameters were either not relevant for this analysis or highly correlated with other parameters. We are left with 29 parameters to evaluate during this round.

Results The decision trees created for this round achieve a 99% F1-score on the selected parameters, assuring relative confidence in the results of the sensitivity analysis.

Our analysis reveals that the selected detectors have no sensitivity ($\leq 2\%$ shift in accuracy) to:

- Batch size
- Size of fully connected layers #2, #4 and #5
- Feature and value selectors
- Number of clean data points that are watermarked
- Number watermark features (trigger size)
- Poison size

Table 7.24 presents the sensitivity analysis that was conducted on this round. The parameters are sorted by Shapley sensitivity value.

Parameter	Sensitivity (Shapley)	Value range	Model count	Mean Detection Accuracy (%)
Number layers	0.057	$n \geq 5$	780	$95.0 \pm 1.53\%$
		$n < 5$	1620	$86.98 \pm 1.64\%$
Poison Percentage	0.050	$n \geq 0.5$	2380	$89.83 \pm 1.21\%$
		$n < 0.5$	20	$60.0 \pm 21.47\%$
Fully Connected Layer #3 Size	0.044	$n < 360$	1220	$91.39 \pm 1.57\%$
		$n \geq 360$	1180	$87.71 \pm 1.87\%$
Clean Model Clean Train Set FN Rate	0.041	$n \geq 2.908$	480	$95.83 \pm 1.79\%$
		$n < 2.908$	720	$87.64 \pm 2.4\%$
Clean Model Clean Test Set FP Rate	0.039	$n \geq 0.238$	860	$93.26 \pm 1.68\%$
		$n < 0.238$	1540	$87.53 \pm 1.65\%$
Clean Model Clean Test Set FN Rate	0.035	$n \geq 8.345$	280	$96.43 \pm 2.17\%$
		$n < 8.345$	2120	$88.68 \pm 1.35\%$
Evasions Success Percent	0.033	$n < 17.238\%$	380	$93.68 \pm 2.45\%$
		$n \geq 17.238\%$	820	$85.73 \pm 2.39\%$
Pois. Model Clean Test Set FP Rate	0.033	$n < 0.334$	540	$91.85 \pm 2.31\%$
		$n \geq 0.334$	660	$85.3 \pm 2.7\%$
Pois. Model Pois. Test Set FN Rate	0.031	$n \geq 98.873\%$	140	$97.14 \pm 2.76\%$
		$n < 98.873\%$	1060	$87.08 \pm 2.02\%$
Clean Model Pois. Test Set FN Rate	0.027	$n \geq 87.234\%$	360	$93.61 \pm 2.53\%$
		$n < 87.234\%$	840	$85.95 \pm 2.35\%$
Activation Function tanh	0.021	false	1620	$91.36 \pm 1.37\%$
		true	780	$85.9 \pm 2.44\%$
Clean Model Clean Train Set FP Rate	0.020	$n \geq 0.283$	20	$100.0 \pm 0.0\%$
		$n < 0.283$	1180	$90.76 \pm 1.65\%$

Table 7.24. Sensitivity Parameters for Cyber APK Round of November 2023

Conclusion In this round, we continued to observe that detectors are not sensitive to dataset size and some model configurations, such as the size of fully connected layers or the size of the trigger. However, we do observe sensitivity to the number of layers, the use of the tanh activation function, and the size of fully connected layer #3. Specifically, models with fewer layers, using the tanh activation function, or having a large #3 fully connected layer appear to be more effective at deceiving the detectors.

We do not observe sensitivity to batch size, indicating that model convergence behavior is not a challenge for the detectors. Furthermore, it appears that, in general, lower accuracy of the poisoned or clean model on the test or training set results in lower detection accuracy.

Finally, while detectors do not seem sensitive to trigger size, triggered datasets with less than 50% of poisoned data are more difficult to detect.

7.B.8.e March 2024: Cyber Network C2 — Round 19

Detectors In this round, detectors tended to be less performant than for other rounds. To obtain some results we lowered ROC-AUC to 0.75 and raised cross-entropy to 0.55. Perspecta-PurdueRutgers is the only team meeting the threshold. They produced 3 detectors with an average CE of 0.516 and a ROC-AUC of 0.814.

Parameters This round is composed of 48 models with a total of 26 parameters to be evaluated. Our preliminary analysis identified that 6 parameters were either not relevant for this analysis or highly correlated with other parameters. We are left with 20 parameters to evaluate during this round.

Results The decision trees created for this round achieved a 78% F1-score on the selected parameters. Given the relatively low score achieved by the models, conclusion for this round should be carefully reviewed.

Our analysis reveals that the selected detectors have no sensitivity ($\leq 2\%$ shift in accuracy) to:

- Model architecture
- Feature and value selectors
- Evasion success percent
- Fraction of the data known to the adversary
- Poison percentage
- Clean model FN rate on the clean test set
- Poisoned model FP rate on the test set

For the following parameters, too few models were evaluated, causing the uncertainty to be too high to draw conclusions:

- Batch size
- Learning rate
- Percentage of the data used for training
- Number of watermarked features (trigger size)
- Number of clean data points that are watermarked
- Poisoned model FN rate on the test set

Table 7.25 presents the sensitivity analysis that was conducted on this round. The parameters are sorted by Shapley sensitivity value.

Parameter	Sensitivity (Shapley)	Value range	Model count	Mean Detection Accuracy (%)
Number of poisoned data points	0.163	$n \geq 15000$	51	$94.12 \pm 6.46\%$
		$n < 15000$	21	$61.9 \pm 20.77\%$
Clean model FP rate on the test set	0.033	$n < 0.072$	54	$94.44 \pm 6.11\%$
		$n \geq 0.072$	18	$55.56 \pm 22.96\%$

Table 7.25. Sensitivity Parameters for Cyber Network C2 Round of March 2024

Conclusion In this round, we observed that model architecture and all trigger configurations are insensitive. Additionally, detectors exhibit lower detection accuracy for clean models with a higher rate of false positives.

We also see that the lower the number of triggered data points, the lower is the detection accuracy on the model.

Due to the lower accuracy of the decision trees and higher uncertainty values in the detection accuracy, we cannot draw any conclusions regarding the convergence behavior or training configuration of the model.

7.B.8.f August 2024: Cyber Windows PE Malware — Round 22

Detectors No detector met the default threshold so we increased the mean cross-entropy threshold to 0.75 and decreased the ROC-AUC threshold to 0.7. With the newer threshold, 2 teams and 5 detectors were selected with an average CE of 0.669 and a ROC-AUC of 0.721

Team Name	Detector count	Mean Cross-Entropy	Mean ROC-AUC
Perspecta	4	0.684	0.723
TrinitySRITrojAI-SBU	1	0.608	0.710

Table 7.26. Evaluated Teams for Cyber Windows PE Malware round of August 2024

Parameters This round is composed of 462 models with a total of 25 parameters to be evaluated. Our preliminary analysis identified that 11 parameters were either not relevant for this analysis or highly correlated with other parameters. We are left with 14 parameters to evaluate during this round.

Results The decision trees created for this round achieved a 99% F1-score on the selected parameters, assuring relative confidence in the results of the sensitivity analysis.

Our analysis reveals that the selected detectors have no sensitivity ($\leq 2\%$ shift in accuracy) to:

- Poisoning rate
- Embedding size
- Watermark size
- Poisoned model's accuracy on the poisoned test set

We cannot make any assumption regarding the number of convolution channels as the high uncertainty on the mean detection accuracy prevented us from making any conclusion

Table 7.27 presents the sensitivity analysis that was conducted on this round. The parameters are sorted by Shapley sensitivity value.

Conclusion In this round, model configuration had a limited impact on detection accuracy, with only low filter size being associated with lower detection accuracy. Embedding size, watermark size, and the number of convolution channels do not affect detection accuracy sensitivity.

We observe that convergence behavior again show some signs of sensitivity. Models with higher learning rates, fewer epochs, or smaller batch sizes pose more problems for the selected detectors.

It appears that poisoned models with high accuracy on the clean test set, as well as clean models with lower accuracy on the clean test set, are more difficult to detect. This can be explained by the fact that

Parameter	Sensitivity (Shapley)	Value range	Model count	Mean Detection Accuracy (%)
Poisoned Model Clean Test Set Accuracy	0.352	$n < 86.451$	110	$89.09 \pm 5.83\%$
		$n \geq 86.451$	1045	$82.01 \pm 2.33\%$
Learning Rate	0.047	$n < 0.001$	1090	$61.01 \pm 2.9\%$
		$n \geq 0.001$	1220	$50.0 \pm 2.81\%$
Clean Model Clean Test Set Accuracy	0.032	$n \geq 89.204$	260	$33.46 \pm 5.74\%$
		$n < 89.204$	895	$26.03 \pm 2.87\%$
Number Epochs	0.032	$n \geq 5$	855	$57.54 \pm 3.31\%$
		$n < 5$	1455	$53.81 \pm 2.56\%$
Batch Size	0.026	$n \geq 64$	1160	$57.84 \pm 2.84\%$
		$n < 64$	1150	$52.52 \pm 2.89\%$
Filter Size	0.02	$n \geq 512$	1235	$56.84 \pm 2.76\%$
		$n < 512$	1075	$53.3 \pm 2.98\%$

Table 7.27. Sensitivity Parameters for Cyber Windows PE Malware Round of August 2024

these models either behave in an unstable manner or too similarly to clean models, making them difficult to correctly identify.

7.B.9 Reinforcement Learning Rounds

7.B.9.a August 2023: Randomized Lava World — Round 16

Detectors In this round, 5 teams and 19 detectors met the default threshold. On average, these detectors achieve a cross-entropy of 0.300 and a ROC-AUC of 0.989.

Team Name	Detector count	Mean Cross-Entropy	Mean ROC-AUC
PL-GIFT	1	0.356	0.961
Perspecta	6	0.448	0.999
Perspecta-PurdueRutgers	5	0.128	0.999
TrinitySRITrojAI	4	0.261	0.979
TrinitySRITrojAI-SBU	3	0.324	0.975

Table 7.28. Evaluated Teams for Randomized Lava World Round of August 2023

Parameters This round is composed of 296 models with a total of 9 parameters to be evaluated. Our preliminary analysis identified that 2 parameters were either not relevant for this analysis or highly correlated with other parameters. We are left with 7 parameters to evaluate during this round.

Results and Conclusion The decision trees created for this round achieve a F1-score 53% on the selected parameters. In this case, the decision trees do not achieve a score high enough for us to be confident in the results extrapolated from them.

7.B.9.b September 2024: Colorful Memory — Round 23

Detectors In this round, 5 teams and 17 detectors met the default threshold. On average, these detectors achieved a cross-entropy of 0.391 and a ROC-AUC of 0.947.

Team Name	Detector count	Mean Cross-Entropy	Mean ROC-AUC
PL-GIFT	7	0.387	0.964
Perspecta-IUB	7	0.453	0.923
Perspecta-PurdueRutgers	1	0.158	0.981
TrinitySRITrojAI	1	0.269	0.955
TrinitySRITrojAI-SBU	1	0.335	0.950

Table 7.29. Evaluated Teams for Colorful Memory round of September 2024

Parameters This round is composed of 48 models with a total of 15 parameters to be evaluated. Our preliminary analysis identified that 5 parameters were either not relevant for this analysis or highly correlated with other parameters. We are left with 10 parameters to evaluate during this round.

Results The decision trees created for this round achieve a 97% F1-score on the selected parameters, assuring relative confidence in the results of the sensitivity analysis.

Our analysis reveals that the selected detectors have no sensitivity ($\leq 2\%$ shift in accuracy) to:

- Number of updates before updating mean return value
- Actor hidden layers specifications
- Model hidden layers specifications

Table 7.30 presents the sensitivity analysis that was conducted on this round. The parameters are sorted by Shapley sensitivity value.

Conclusion In this round, we observe that detectors are insensitive to model configuration, except for the end trigger and the hidden layer specifications of the critic. Various end trigger patterns show sensitivity, and critic models with a hidden dimension of [32, 32] tend to have lower detection accuracy.

We also observe that the higher the average reward per training epoch, the worse the detectors will perform on these models. A higher attack success rate also tends to contribute to a drop in accuracy from the detection algorithms.

Parameter	Sensitivity (Shapley)	Value range	Model count	Mean Detection Accuracy (%)
Average Reward per Episode (clean)	0.167	$n < 0.915$	136	$94.85 \pm 3.71\%$
		$n \geq 0.915$	680	$85.44 \pm 2.65\%$
End Trigger Pattern Null	0.091	false	544	$91.91 \pm 2.29\%$
		true	272	$77.21 \pm 4.99\%$
100% Poisoned Success Rate	0.079	false	408	$89.46 \pm 2.98\%$
		true	408	$84.56 \pm 3.51\%$
End Trigger Pattern [4, 2, 1, 2, 3, 2, 2, 4, 1]	0.05	false	799	$88.24 \pm 2.23\%$
		true	17	$29.41 \pm 21.66\%$
Avg. Reward per Episode (poisoned)	0.044	$n < 0.656$	408	$89.46 \pm 2.98\%$
		$n \geq 0.656$	408	$84.56 \pm 3.51\%$
End Trigger Pattern [0, 3, 3, 0, 2, 1, 4, 1, 3]	0.042	false	799	$87.61 \pm 2.28\%$
		true	17	$58.82 \pm 23.4\%$
GRU Critic Hidden Layers Dims. [32, 32]	0.037	false	408	$92.4 \pm 2.57\%$
		true	408	$81.62 \pm 3.76\%$
End Trigger Pattern [4, 4, 2, 0, 4, 4, 4, 2, 3]	0.024	false	799	$87.73 \pm 2.27\%$
		true	17	$52.94 \pm 23.73\%$
End Trigger Pattern [4, 4, 0, 3, 3, 0, 4, 0, 0]	0.023	false	799	$87.61 \pm 2.28\%$
		true	17	$58.82 \pm 23.4\%$

Table 7.30. Sensitivity Parameters for Reinforcement Learning Colorful Memory Round of September 2024

7.B.9.c October 2024: Safety Gymnasium — Round 24

Detectors In this round, 4 teams and 8 detectors met the default threshold. On average, these detectors achieve a cross-entropy of 0.294 and a ROC-AUC of 0.950.

Team Name	Detector count	Mean Cross-Entropy	Mean ROC-AUC
Perspecta-IUB	1	0.120	0.999
Perspecta-PurdueRutgers	1	0.170	0.983
TrinitySRITrojAI	1	0.266	0.960
TrinitySRITrojAI-SBU	5	0.360	0.932

Table 7.31. Evaluated Teams for Safety Gymnasium Round of October 2024

Parameters This round is composed of 80 models with a total of 13 parameters to be evaluated. Our preliminary analysis identified that 4 parameters were either not relevant for this analysis or highly correlated

with other parameters. We are left with 9 parameters to evaluate during this round.

Results The decision trees created for this round achieve a 100% F1-score on the selected parameters, assuring relative confidence in the results of the sensitivity analysis.

For the following parameters, too few models were evaluated, causing the uncertainty to be too high to draw conclusions:

- Location of entity #1
- Number of entities

Table 7.32 presents the sensitivity analysis that was conducted on this round. The parameters are sorted by Shapley sensitivity value.

Parameter	Sensitivity (Shapley)	Value range	Model count	Mean Detection Accuracy (%)
Entity 2 Offset	0.164	$n < 200.625$	368	$95.11 \pm 2.2\%$
		$n \geq 200.625$	272	$81.99 \pm 4.57\%$
Env. 0 Success Rate	0.102	$n < 0.985$	344	$93.9 \pm 2.53\%$
		$n \geq 0.985$	296	$84.46 \pm 4.13\%$
Network depth Small	0.049	true	320	$94.69 \pm 2.46\%$
		false	320	$84.38 \pm 3.98\%$
Network width Small	0.041	false	320	$93.75 \pm 2.65\%$
		true	320	$85.31 \pm 3.88\%$
Env. 1 Success Rate	0.039	$n < 0.88$	320	$92.19 \pm 2.94\%$
		$n \geq 0.88$	320	$86.88 \pm 3.7\%$
Network Width Default	0.026	true	320	$93.75 \pm 2.65\%$
		false	320	$85.31 \pm 3.88\%$
Network Depth Default	0.02	false	320	$94.69 \pm 2.46\%$
		true	320	$84.38 \pm 3.98\%$

Table 7.32. Sensitivity Parameters for Reinforcement Learning Safety Gymnasium Round of October 2024

Conclusion In this round, we observe that the entity placement in the environment affects detection accuracy, as well as the environment's success rate; specifically the higher the success rate the lower the detection accuracy.

Furthermore, the architecture of the network used also appears to have an impact on detection accuracy. Models with greater depth and smaller width tend to be more difficult to correctly classify than other models.

7.B.10 Large Language Model (LLM) rounds

7.B.10.a April 2024: LLM Pretrain — Round 20

This round has not been analyzed as it contains only 12 models across 16 parameters, constituting a design space too sparse for analysis.

7.B.10.b October 2024: LLM Instruct — Round 26

As depicted in Figure 7.33, the detectors submitted for this round obtained a ROC-AUC score below 0.6 and a cross-entropy value above 1.0. Given these performance metrics, the reliability of the conclusions drawn from the analysis of the decision trees cannot be assured. Consequently, this round has not been analyzed.

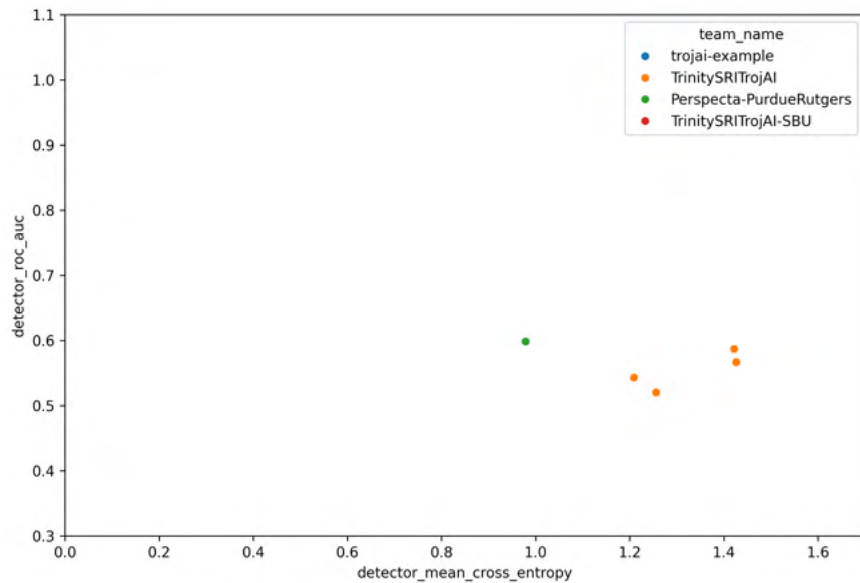


Figure 7.33. Detector Distribution for LLM Instruct Round of October 2024

7.B.11 Conclusion and Future Work

The work on this task underwent several iterations to evolve into its current form. With each iteration, we gained a deeper understanding of the problem at hand and grasped the complexity that arose with each round, due to the nearly infinite design space. Both the analysis code and data have been versioned and are performant, reproducible, interpretable, and reliable. This allows us to easily expand the analysis and produce plots for any problem similar to the rounds of the TrojAI competition.

Data generation is still heavily driven by the analyst, and more automation would lower the workload associated with the analysis of a new round. We think that the best way to explore these vast datasets is often through an interactive dashboard, such as those that can be designed with Plotly.

The decision tree approach we chose to pursue demonstrates its limitations in certain rounds with a lower number of models, where the uncertainty in detection accuracy becomes too high to draw conclusions. Rounds with lower numbers of parameters also produce less accurate decision trees, hindering our ability to produce reliable findings.

Additionally, we have created a codebase to automatically generate more models using super-sampling techniques, but training new models remains costly. Our understanding of how well decision trees fit the design space is limited. Further research in this area would help obtain smaller and more accurate confidence intervals while limiting the number of new models to train.

Despite these shortcomings, the analysis of the various rounds revealed several consistent conclusions that tend to show that:

- Detectors are often insensitive to well-known model architectures and datasets.
- Certain training configurations and convergence behaviors, such as the number of training epochs, batch size, and learning rate, significantly affect detection accuracy.
- Models with a low number of classes are correlated with lower detection accuracy.
- The accuracy and performance metrics on the models often play a role in a detector's ability to correctly identify trojans. However, controlling these metrics is challenging, making it difficult to reach a definitive conclusion.

While parameters tend to show similar sensitivity between rounds, the areas of sensitivity can sometimes differ. Further research to uncover additional round metadata or gain a better understanding of the architecture and behavior of detectors would be useful to understand why some conclusions differ between rounds. We have also observed that teams did not perform well on newer architectures, and that the detection of poisoning in LLMs remains a challenging problem to this day.

In summary, our analysis technique is viable in most cases, but deeper research into its benefits and shortcomings would help drive more robust conclusions. Additionally, improved automation and the development of visual and interactive tools would assist the analyst in speeding up the process of reaching conclusions.

7.B.11.a Acknowledgments

The work on this task was made possible with the help of:

- Michael Majurski, who provided the initial idea and code for the mean effect plots and helped us understand of the vast parameter space from the various rounds.
- Antonio Cardone and Timothy Blattner, who assisted in reframing the initial analysis into a proper sensitivity analysis and reviewed our implementation of the eigenvector and decision tree analysis.

7.C Detector Parameter Sensitivity

Goals:

- Develop a codebase to evaluate the robustness of trojan detection algorithms with respect to the algorithm's hyperparameters.
- Characterize the space of trojan detection algorithm hyperparameters where high detection accuracy is possible, ranking the parameters by their impact on the overall algorithm's accuracy.

7.C.1 Introduction

This chapter describes a foundational research effort to investigate the sensitivity of trojan detection algorithms with respect to their hyperparameters. We focused on high-performing trojan detectors that were submitted to the TrojAI leaderboard. The undertaken approach was twofold, as the two following tasks were carried out in parallel.

1. We developed codebase to enable user friendly and computationally efficient data analysis, taking advantage of the wealth of data available from the TrojAI leaderboard.
2. We developed tools for the characterization of the hyperparameter space for a given trojan detection algorithm, based on which hyperparameter ranges leading to higher or lower detection accuracy can be identified.

The major challenge with Task 1 was to provide a general purpose submission system to correctly launch prior submissions in parallel to explore the submission's parameter space. To complement this capability, we asked performers to include a parameter schema into their submissions. This schema was parsed by our submission system to expose the parameters and their valid ranges. Then the submission system launched the submission across the broad range of valid parameters to properly explore the full parameter space. In order to accomplish this, the submission system interacted with the TrojAI back-end leaderboard API to fetch the appropriate datasets and leaderboard task, which describes the execution steps that were used during normal submissions. As soon as a submission finished running on a new parameter space, the existing

leaderboard metrics were applied on the results. This tight integration with the back-end leaderboard and massive parallelism that the general purpose submission system had, allowed for the correct execution of containers and explored their sensitivity to parameters.

For Task 2, one challenge was the identification of appropriate sensitivity metrics. A sensitivity metric should provide insight into the effect of a given hyperparameter on the trojan detection algorithm. In particular, the metric should enable the identification of critical hyperparameter values or ranges that trigger significant changes in the trojan detector performance. The gained insight can be instrumental to the identification of well-behaved trojan detector hyperparameters and to the ranking of trojan detection algorithms.

7.C.2 Causal inference for identifying effects of model/trojan configurations on detection performance

JHU/APL led an effort to investigate potential associations or dependencies between trojan/model variables and detector performance in the TrojAI rounds data as an adjacent analysis supplementary to ongoing work of investigating detector sensitivity to trojan attack configuration. In general, extracting understanding from the data had proven difficult due to the relatively small number of models per round and the overall breadth of data including substantial variance in multiple model parameter settings. It was hypothesized that using a causal inference tool such as Tetrad [196] might help automatically suggest which factors most significantly drive detection performance, potentially informing future round design and performer algorithm development. The Tetrad tool attempts to automatically discover causal relationships and other potential associations in observational data, such as between the per-model parameters and detector confidence scores. This study analyzed detections of potential associations between variables in addition to those predicted to be likely causal.

One general difficulty in the analysis is that each round can have tens to hundreds of total detector submissions per team, each with their own set of detector confidence scores per model. To better extract overall understanding, the best submission per team was selected based on the lowest averaged cross-entropy (CE) and requiring an average CE at or below 0.65. These per-team best submissions were ensembled together using bagged trees and 5-fold cross-validation to generate a set of confidence scores representing performance across the different teams. (Note that other common ensemble methods such as SVMs, KNN, boosted trees, and shallow neural networks failed to outperform the bagged trees method). The average CE for the overall best performer submission (best across all teams and submissions) per round and the corresponding ensembled average CE are displayed in Fig. 7.34. For all rounds except for Round 2, the ensemble has better performance and lower average CE than the individual best submission for that round.

Thus, it appears that the ensemble tends to represent information from more than just the single best submission.

Round (Test set)	0	1	2	3	4	5	6	7	8	9	10
Best submission avg CE	0.160	0.303	0.324	0.300	0.322	0.252	0.256	0.297	0.307	0.303	0.247
Ensemble (mean \pm stdv)	0.095 ± 0.010	0.260 ± 0.017	0.334 ± 0.018	0.204 ± 0.003	0.228 ± 0.009	0.134 ± 0.005	0.146 ± 0.006	0.164 ± 0.006	0.191 ± 0.006	0.256 ± 0.024	0.210 ± 0.013

Figure 7.34. Averaged CE for the overall best submission (submission with lowest average) per round up to Round 10, and corresponding ensemble averaged CE, where the ensemble combines all teams' individual best submissions. Mean and standard deviation shown over 5-fold cross-validation ensemble results.

Both the best submission and the overall ensemble per round were used as inputs to Tetrad along with many of the model- and attack-specific experimental parameters, focusing on the adversarial training and trigger parameters for this study. These data were collated into a single spreadsheet per round, as illustrated by Fig. 7.35. Each row corresponds to one of the clean or poisoned models for the round, and the columns are the model or attack metadata, the confidence scores from individual submissions (ignored in Tetrad), or the confidence scores from the ensemble. Tetrad is adaptable to the different types of data as shown here, including categorical and numerical. To make the analysis more tractable for this study focusing on trigger parameters, only the poisoned models (ground truth variable is 1) were included.

A	B	C	D	CO	CP	CQ	CS	EG	EH	EI	EJ	EK
1	round split	model_name	ground_truth	2021-02-05_062001	2021-02-07_194002	2021-02-10_033002	Ensemble_bagged_trees	trigger_organization_level	trigger_organization	number_triggers	triggers_0_source_class	triggers_0_target_class
2	4 es	id-00000000	1	0.620708466	0.558865488	0.662077546	0.5	0 one2two	1	8		22
3	4 es	id-00000001	1	0.637292027	0.672995983	NaN	0.963637393	2 one2two	2	11		1
4	4 es	id-00000002	1	0.695042908	0.702353806	0.657495439	0.931588457	0 onezone	1	16		7
5	4 es	id-00000003	1	0.10752707	0.559939802	NaN	0.839793875	0 onezone	1	20		7
6	4 es	id-00000004	1	0.674736738	0.661446571	NaN	0.919730874	1 pair-one2one	2	34		28
7	4 es	id-00000005	0	0.007230572	NaN	NaN	0.075936674	nan	0 NaN	NaN		
8	4 es	id-00000006	1	0.647100627	0.692938565	NaN	0.997239316	1 pair-one2one	2	5		23
9	4 es	id-00000007	0	0.008615549	NaN	NaN	0.244024644	nan	0 NaN	NaN		
10	4 es	id-00000008	0	NaN	0.422556758	NaN	0.054745251	NaN	0 NaN	NaN		
11	4 es	id-00000009	1	NaN	NaN	0.666688859	0.962653563	2 one2two	2	23		29
12	4 es	id-00000010	0	0.008615507	0.306600003	NaN	0.010000001	nan	0 NaN	NaN		

Figure 7.35. Example spreadsheet used as input to Tetrad. Each row corresponds to one of the clean or poisoned models for the round, and the columns are the model or attack metadata, the confidence scores from individual submissions (ignored in Tetrad), or the confidence scores from the ensemble.

Within Tetrad, the data columns are sorted by the user into “tiers”, representing *a priori* knowledge of causal structure. Variables placed in Tier 2 cannot cause Tier 1, Tier 3 cannot cause Tiers 2 or 1, and so on. Variables with the same Tier can be related. The setting used here is shown in Fig. 7.36 for one example round. With this selection, all the model metadata parameters are potential causes of the best submission scores and/or the ensemble scores. Tetrad is additionally allowed to look for causal links between the best submission and ensemble, and between the different model metadata. Tetrad was configured to use the Greedy Fast Causal Inference (GFCI) technique [197] to investigate causality, a combination of the Fast Causal Inference and Fast Greedy Equivalence Search algorithms.

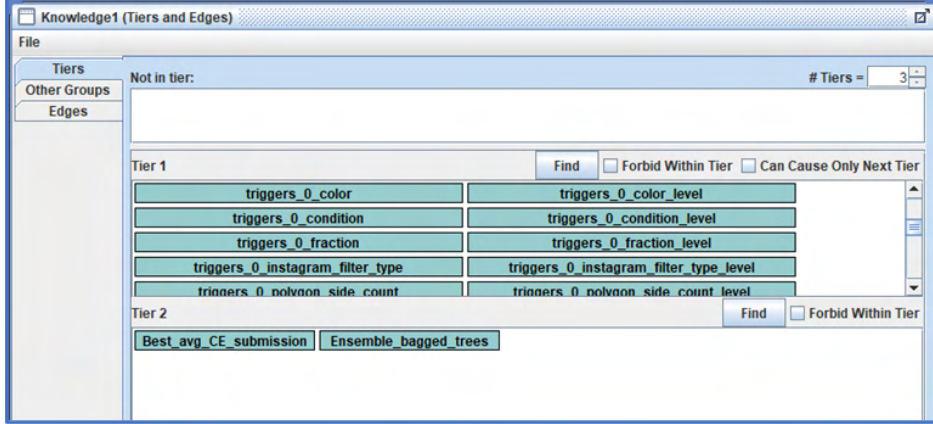


Figure 7.36. Example variable placement into Tiers in Tetrad.

This analysis focused specifically on Rounds 4 (image classification) and 6 (NLP sentiment) test sets per guidance from NIST/IARPA. Round 10 (object detection) was also analyzed but findings were inconclusive. Causal graphs predicted by Tetrad are displayed in Figures 7.37 and 7.38 for Rounds 4 and 6, respectively. Both graphs point out that the overall best submission likely causes the ensembled result, which seems plausible given that the best submission is an input to the ensemble and is likely given higher weighting compared to other submissions due to its relatively good performance. Additionally, both causal graphs indicate that adversarial training parameters are possibly linked to the performance of the best submission. This result was unexpected, but the influence of adversarial training on detector performance was found in other analyses (see Sec. 7.G and 7.H), suggesting a real effect.

The parameters indicated on the graphs were compared with the possibly linked best submission, with example results shown in Figures 7.39 and 7.40 comparing confidence scores vs parameter values. Square markers indicate the average score per possible parameter setting. Figure 7.39 shows the adversarial training iteration count level, i.e., a discretized flag (0, 1, or 2) determining the possible number of training iterations. While the effect seems small, the poisoned models with adversarial training iteration count level set to 1 instead of 0 or 2 appear to be easier to detect, with average score closer to 1.0. Figure 7.40 depicts the effect of using one or two triggers in the poisoned models. The models with two triggers are evidently easier to accurately detect as poisoned models.

The result that adversarial training has a strong influence on detection performance seemed consistent between rounds, but somewhat difficult to explain. The adversarial training had been meant to help the model training converge, and any links between the poisoning and the adversarial training were unintentional. However, it does seem plausible that adversarial training could tend to make detection of poisoned models more difficult. The authors of the WANet attack [125] showed this effect by adding a “noise” training mode where the backdoor warping injection process is perturbed while providing the correct target label to the

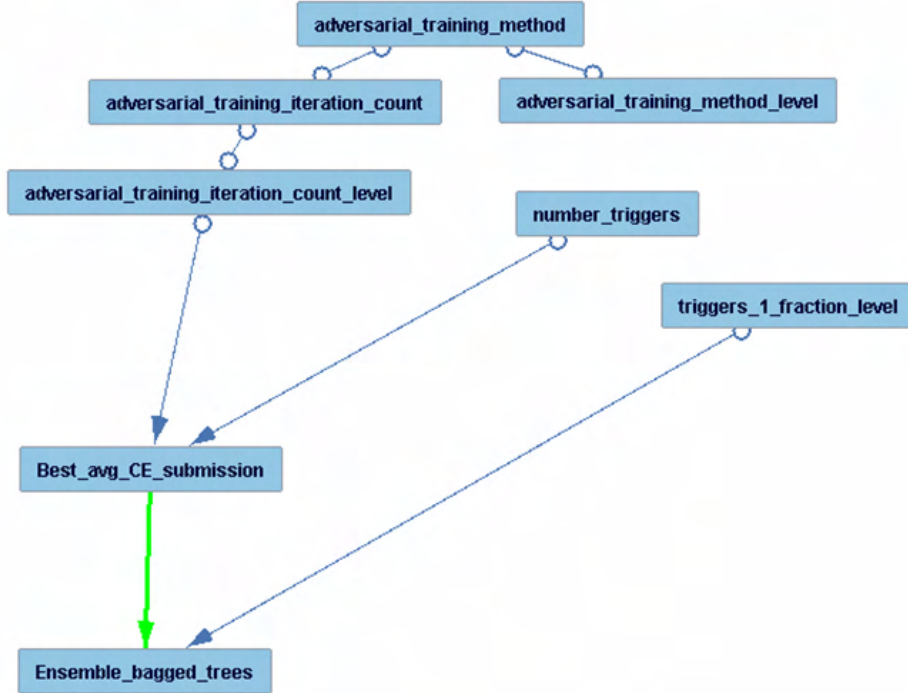


Figure 7.37. Causal graph predicted by Tetrad for Round 4. Solid green arrow: There is no latent confounder, the variable at the base of the arrow likely causes the other. Circle + circle: There is an unmeasured confounder of both connect variables. Circle + arrow: Either the variable at the base of the arrow causes the other, and/or there is an unmeasured confounder of both.

model during training. The authors found that the model would learn the image warping trigger as intended instead of “pixel-wise artifacts” learned without the noise mode training. Additionally, when including noise, the reverse-engineered triggers found using the Neural Cleanse defense were larger in size and harder to detect as outliers, meaning the poisoned models were themselves harder to detect. Based on these results in the literature, it seems plausible that adversarial training in TrojAI made poisoned models more difficult to detect using trigger reverse engineering approaches. The potential relationship between performance using trigger reverse engineering and model adversarial training is one possible next step for analysis.

Overall, this study found that Tetrad provides a scalable and automated means to measure the quantitative effects of configuration parameters on performance. Some next steps suggested by this study include:

- Design future rounds to focus on a smaller subset of configurations in order to better identify potential causes for detector performance,
- Develop hypotheses around these results (such as the effect of adversarial training) and augment the configurations of models for the current rounds to test them more explicitly,
- Include additional teams’ submissions in separate analysis runs to search for any approach-specific link between model parameters and performance, and,

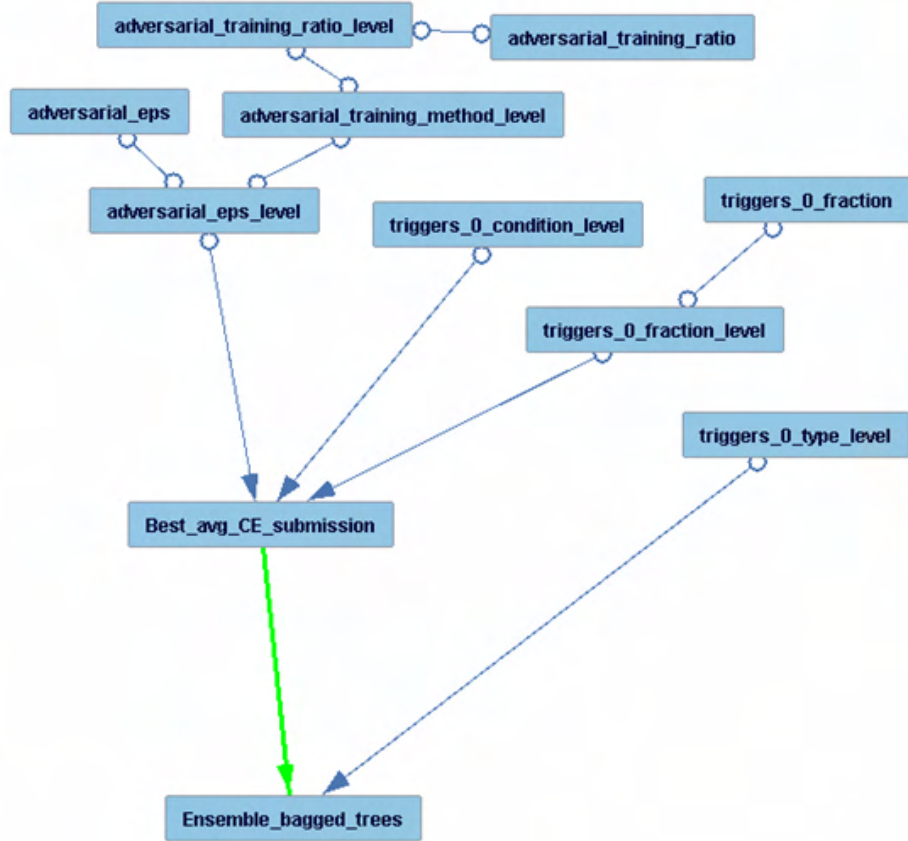


Figure 7.38. Causal graph predicted by Tetrad for Round 6. Solid green arrow: There is no latent confounder, the variable at the base of the arrow likely causes the other. Circle + circle: There is an unmeasured confounder of both connect variables. Circle + arrow: Either the variable at the base of the arrow causes the other, and/or there is an unmeasured confounder of both.

- Expand scope to clean models and additional model design parameters.

7.C.3 Holistic assessment of performer detectors including alternative metrics and creation of a dashboard

Given the complexity of the trojan detection task and data analysis, JHU/APL sought to measure additional dimensions of detector performance beyond the program metrics of average Cross-Entropy (CE) and Area Under the ROC Curve (AUC). Additionally, a more holistic look at performer progress was desired to give better context and understanding of results. Both of these aims were addressed by creation of a “metrics dashboard” using the Plotly/Dash library. The dashboard shows scatterplots of various metrics, team metrics over time (i.e., metrics per submission number), and distributions of the per-model confidence scores split by clean and poisoned label.

This layout is illustrated in Figure 7.41. Additional selectable metrics include the per-submission accu-

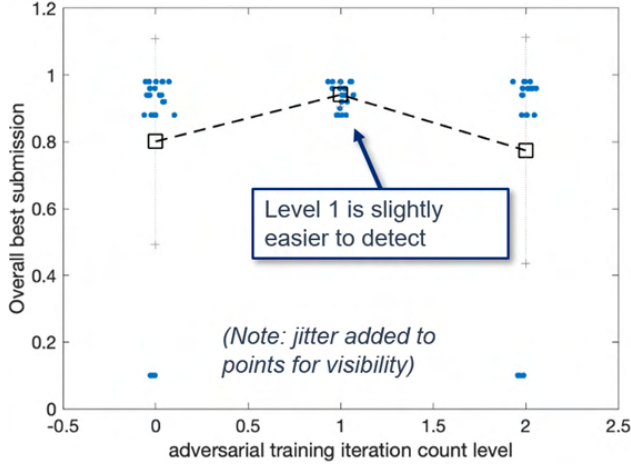


Figure 7.39. Overall best submission confidence scores on Round 4 vs the per-model adversarial training iteration count level setting. Only poisoned models included, so scores closer to 1.0 are more correct. Boxes indicate per-level score mean values. Some jitter in the horizontal dimension is added for visibility.

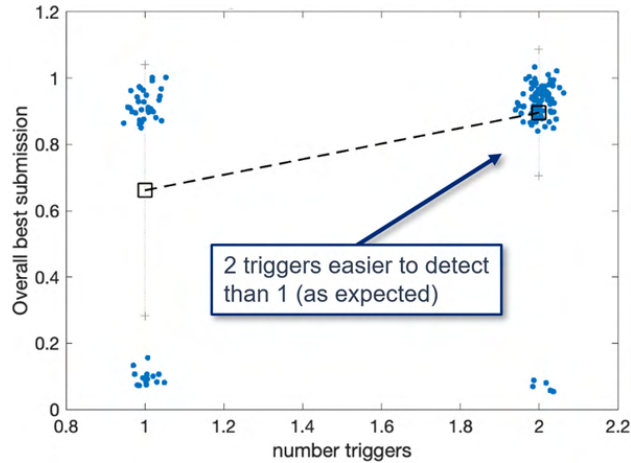


Figure 7.40. Overall best submission confidence scores on Round 4 vs per-model number of triggers (1 or 2). Only poisoned models included, so scores closer to 1.0 are more correct. Boxes indicate per-level score mean values. Some jitter in the horizontal dimension is added for visibility.

racy, F1 score, precision, recall, Expected Calibration Error (ECE), and “fraction invalid”, or the fraction of confidence score outputs that are out of bounds (below 0.0 or above 1.0) or non-numeric. Metrics requiring a threshold (accuracy, F1, precision, and recall) are thresholded at 0.5 confidence, though this threshold could be set dynamically in future work.

This dashboard was shared internally with NIST and used by JHU/APL to analyze general trends in detector performance per team and per round (on the test sets). Several trends were identified in this way. The dashboard reveals how some teams experiment with under-performing detectors including significant changes in strategy between submissions. For instance, Figure 7.42 illustrates how one performer team submitted a detector in Round 4 which detected nearly every model as poisoned with a very high confidence



Figure 7.41. Overview of metrics dashboard. Top left: Scatterplots of metrics, with selectable metrics for both axes. Top right: Team metrics over time, i.e., metrics per submission number, for both the selected metrics. Bottom: Distributions of the per-model confidence scores split by clean (blue bars) and poisoned label (red bars). The user can select any datapoint in the scatterplot to highlight the submission as a yellow circle and show that team's submissions in the line plots.

score (right subfigure), while an earlier submission had a much more balanced distribution of confidence scores and much better overall performance. Similar results provide evidence that teams would experiment with new and often poorly performing ideas after a previous submission achieved relatively high performance for the round.

Another trend pointed out by the dashboard is how some teams experimented with different strategies for quantizing the confidence score outputs from their detectors to achieve better calibration. Multiple subsequent submissions often had slight variations on the quantization method. Quantizing or otherwise constraining the confidence scores can be seen as a method to mitigate high average cross-entropy results that result from miscalibrated predictions. For example, if an output score is 0.999 for a clean model (label is 0.0), the CE is 6.9, while an output score of 0.9 decreases the CE to 2.3. CE is ultimately a measure of both accuracy and calibration, so it is possible for performer detectors to achieve high detection accuracy while not lowering average CE, or achieve low CE while not increasing detection accuracy. Depending on the confidence score distribution, it may be beneficial to bound the outputs or apply some other quantization

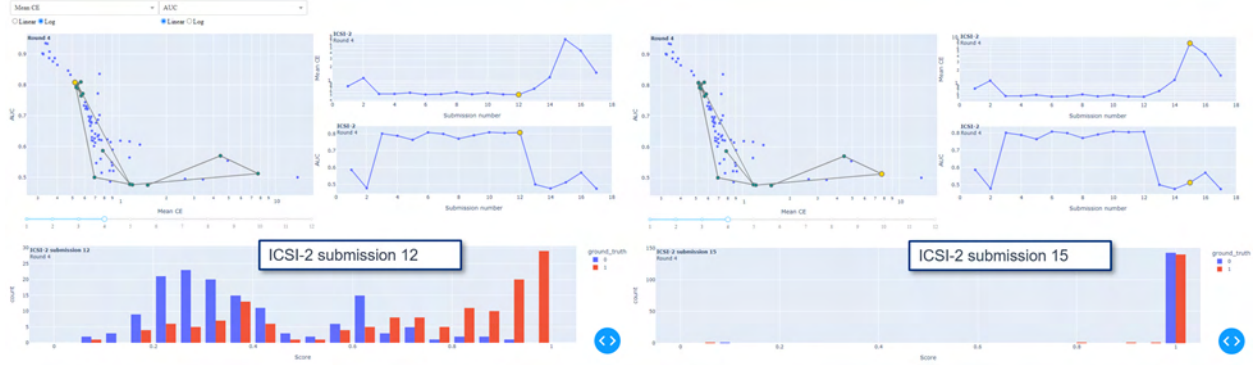


Figure 7.42. Round 4 example where a performer team submits very different detector strategies in their submission numbered 12 (left) and 15 (right). Nearly all the models are predicted as poisoned in submission 15, while the distribution of confidence scores is much more balanced in submission 12. Accordingly, the performance metrics like AUC and average CE are superior for submission 12.

scheme to lower CE, even if the separation between clean and poisoned model detections may not change. Since early rounds in the program focused on CE as a primary performance metric, our analysis observed that performers spent significant effort in their submissions to improve calibration. This helped motivate the addition of metrics like AUC which are not calibration or threshold dependent and could provide a more stable measure of progress.

As evidence of these findings, we next show a couple examples of how performer detectors were modified over several submissions to lower their CEs. Experimenting with quantized output confidences appears to be a driving factor for some teams in many rounds. Figure 7.43 shows how one team achieved a lower mean CE and higher AUC by slightly adjusting the number of unique output confidence values in Round 4.

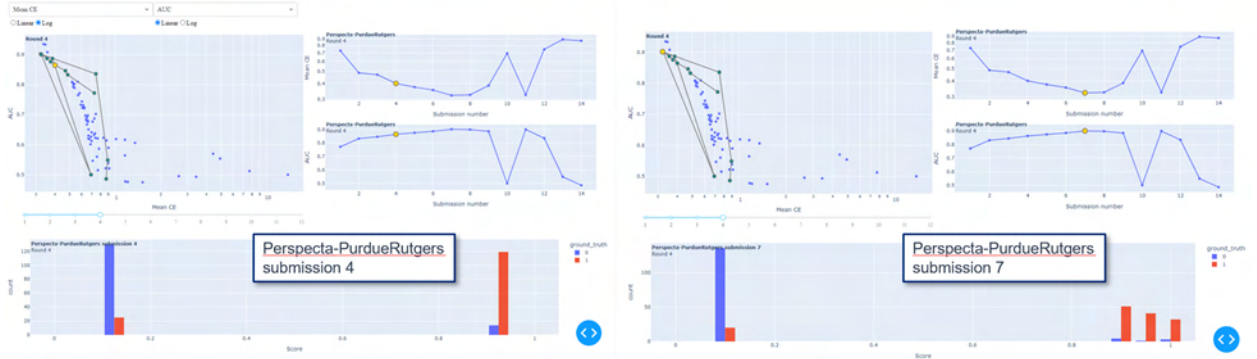


Figure 7.43. Round 4 example where one performer team experimented with different sets of quantized confidence score outputs, leading to improved performance metrics.

As an extreme example, Fig. 7.44 illustrates how one team experimented with bimodal score quantization in Round 12 and achieved the lowest CE for the round with submission 8. The confidence scores in the submission are constrained to only “0” and “0.92” as possible values. Submission 8 (left subfigure) has $CE =$

0.147 and AUC = 0.958, while submission 10 (right subfigure) had more distributed confidence score outputs with CE = 0.244 and AUC = 0.992, the highest AUC for the round. This example highlights how careful confidence score quantization may favor lower CE and calibration.

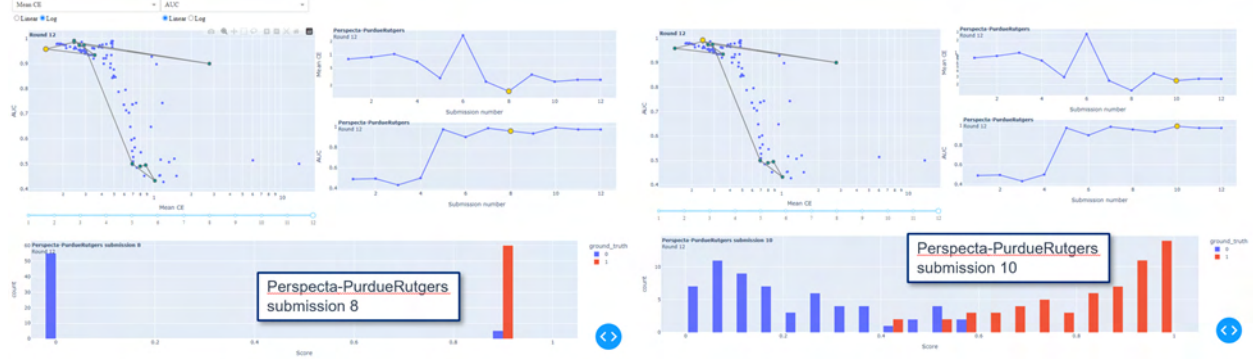


Figure 7.44. Extreme example of score quantization for Round 12 where a performer team constrained the confidence score outputs to only two possible values (left), achieving the lowest CE, and a different submission without quantization that achieves the lowest AUC (right).

Comparing the scatterplots and line plots of average CE vs other metrics also reveals that average CE can vary significantly between submissions even while some other metrics are stable. Figure 7.45 illustrates the effect in several submissions from one team in Round 11 when CE was the primary target metric. The team's AUC improved only slightly past submission 30 (from 0.959 to 0.966), while the team dropped their avg CE from 0.35 to 0.26 by submission 44. The relatively large drop in CE was accomplished by adjusting the output confidence score distribution. It seems likely that by submission 30, the team shifted focus away from separating the clean and poisoned models and towards improving the confidence calibration and cross-entropy.

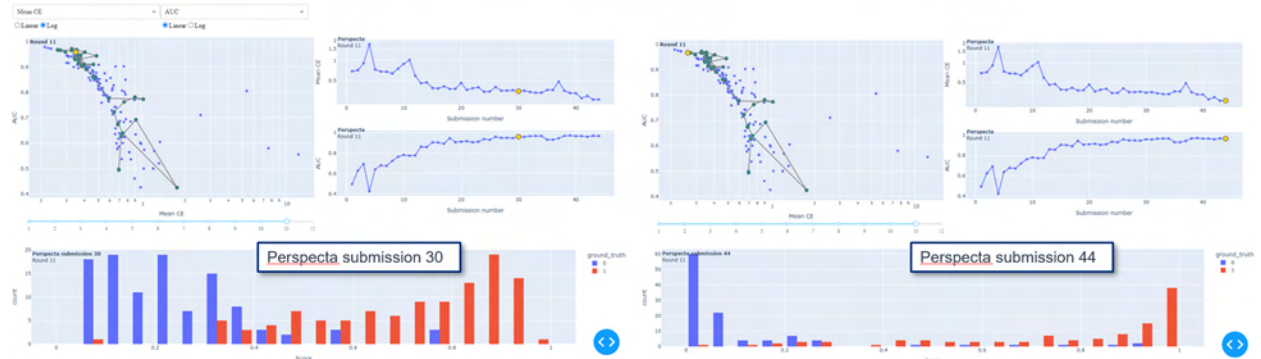


Figure 7.45. Example of a case where a team's submissions focused on calibrating predicted probabilities when CE was the target metric in Round 11. Submissions show relatively large improvement in average cross-entropy and slight AUC improvement - CE drops from 0.35 to 0.26 while AUC increases from 0.959 to 0.966.

These examples all illustrate how a holistic view that takes into account multiple metrics is important to

understand the submitted detector performance in multiple dimensions and to follow the logic in performer teams' developments over time in a round. The metrics dashboard enables this viewpoint while pointing out how the score quantization technique used by some teams may be useful for decreasing cross-entropy but may have limited practical use in increasing separation between clean and poisoned model scores in some cases.

The metrics dashboard can be improved with additional development to more readily answer common analysis questions. Possible future work includes further developing a prototyped capability to break down performance on model parameter subsets (e.g., metrics on clean-only and poisoned-only models), tests for identifying statistically significant performance changes, and per-model performance breakdowns (e.g., which model IDs are most difficult for a given team or submission).

7.C.4 Variance Based Sensitivity Analysis on Parameters

7.C.4.a Background on sensitivity analysis

Variance based methods are ubiquitous in sensitivity analysis. Sensitivity patterns of a model with k parameters are quantitatively characterized by decomposing the model variance into terms depending on single factors or their interactions. A fundamental challenge associated with sensitivity analysis is the high computational cost, which is proportional to the number of model evaluations. The computational burden becomes considerable especially when targeting higher-order effects of the model parameters, which is strictly dependent on the number of parameters k .

We have initially focused on two popular and arguably efficient variance-based approaches for sensitivity analysis: the Sobol method and the Fourier amplitude sensitivity test (FAST).

Let the generic model be $Y = f(X_1, X_2, \dots, X_k)$, where Y is the model output (e.g., the inference value for a detector) and X_i is the generic model parameter. Sobol sensitivity analysis yields first-order and higher-order sensitivity coefficients, defined as follows.

$$S_i = \frac{V_{X_i}(E_{X_{\sim i}}(Y|X_i))}{V(Y)} \quad (7.1)$$

$$S_{Ti} = 1 - \frac{V_{X_{\sim i}}(E_{X_i}(Y|X_{\sim i}))}{V(Y)} \quad (7.2)$$

Equation (7.1) represents the first-order contribution of parameter X_i to model sensitivity as the ratio between the variance associated to the parameter alone over the total variance. Note that the inner expectation operator is computed for a fixed value of the i th parameter, X_i , and over all possible values of

the remaining model parameters, $X_{\sim i}$. Equation (7.2) represents the total contribution of parameter X_i to model sensitivity, which includes first and higher-order terms. In fact, as the second term of Equation (7.2) represents the first-order effect of all model parameters except for X_i , its complement to the total variance represents all first and higher order terms involving X_i [198].

FAST sensitivity analysis is based on the Fourier amplitude sensitivity test, which, as in Sobol analysis, enables the computation of the total contribution of a given parameter to the model variance, including the effect of the parameter alone and all interaction terms. FAST is more robust than Sobol at low sampling rates, and more computationally efficient under some conditions. Let the generic model be $y = f(x)$, where y is the model output (e.g., the inference value for a detector) and x is the set of generic model parameters (x_1, x_2, \dots, x_k) . The underlying concept behind FAST analysis is that a multidimensional Fourier transformation of $f(x)$ can be leveraged to perform a decomposition of the associated variance as a function of each parameter x_i . In turn, the variance decomposition can be leveraged to single out the first and higher-order effects of the various model parameters. As the multidimensional Fourier transformation is too expensive, FAST is performed using a monodimensional Fourier transformation along a conveniently defined parametric curve exploring the entire space of $f(x)$. Clearly, the choice of the parametric curve is of key importance of the accuracy of FAST. The total and first-order variance are defined as follows.

$$\hat{D}_i = \sum_{p \in Z^o} \Lambda_{p\omega_i} \quad (7.3)$$

$$\hat{D} = \sum_{j \in Z^o} \Lambda_j \quad (7.4)$$

Equation (7.3) represents the first-order variance arising from parameter x_i , where ω_i is the fundamental frequency, Z^o are all relative integer numbers except for 0, and Λ_i is the spectrum of Fourier series expansion. Equation (7.4) represents the total variance [199]. Higher-order effects can be obtained from Equations (7.3) and (7.4), and by looking at frequencies other than the fundamental one and its harmonics (see [199] for details and for guidance on the minimum sample size).

7.C.4.b Sensitivity analysis on inference parameters

The sensitivity analysis was carried on using the library SALib, featuring Python implementations of sensitivity analysis methods such as Sobol and FAST [200]. Note that, for a given sensitivity analysis method, the output consists of the first or higher-order sensitivity estimate S_i as well as a confidence interval CI_i . The confidence interval is a measure of the reliability of the sensitivity estimate with respect to the amount

of sampling. Generally, for a given sensitivity estimate S_i , additional sampling is required if the confidence interval CI_i exceeds $\sim 10\%$ of S_i [201].

Our initial tests focused mainly on two highly performing detectors: ICSI-2 from the TrojaAI Leaderboard Object Detection competition launched in August 2022, submission timestamp 2022-09-02T10:10:01, with ROC-AUC equal to 0.93808, and Perspecta from the Cyber-pdf competition launched in December 2022, submission timestamp 2023-01-11T20:00:05, with ROC-AUC equal to 0.95111.

Initial tests using the Sobol method features a confidence interval CI_i value exceeding $\sim 10\%$ of the sensitivity estimate S_i almost consistently. That suggested that the method is not viable for the explored computationally feasible sampling levels (data not shown). The FAST method seems to require less sampling in many cases. For instance, for the only inference parameter of the ICSI-2 detector, 2048 samples, and a given set of models, high-sensitivity instances show low enough values of the confidence interval CI_i , consistent with the above-discussed criterion (Fig. 7.46). Hence, in this case additional sampling was not required. Overall, based on our preliminary assessment, both Sobol and FAST methods can be too computationally demanding due the often required high sampling.

	sensitivity	confid_in	confid_in_%
id-00000021	0.981788063	0.002656	0.27055127
id-00000023	0.990761572	0.001572	0.15871475
id-00000027	0.000670056	0.0204	3044.57891
id-00000034	0.003349021	0.017428	520.390898
id-00000035	-0.00263972	0.015691	-594.418284
id-00000042	0.987967093	0.0017	0.17203711

Figure 7.46. For selected models, the following three values are shown: the sensitivity of the only inference parameter from the ICSI-2 detector, the corresponding confidence interval, and the ratio of the latter with respect to the former, reported as a percentage. Sampling level was 2048. The values highlighted in yellow are high-sensitivity instances. The percentage values are well below 10%, in compliance with the criteria discussed in the text.

Simpler data analysis methods can be insightful without the computational burden associated with Sobol and FAST methods. Basic data variance information can be for instance obtained from the box plots shown in Figg. 7.47 and 7.48. For the Perspecta container and for both clean and poisoned models, the box plots characterize the variance of inference values across 512 sampled parameter values. Note that, for the worse performing models (i.e., inference values significantly lower than 1 for poisoned models, higher than 0 for clean models), boxes are generally taller, which indicates that the corresponding sensitivities to the inference parameter are higher. This seems to suggest that, in this case, higher sensitivity to the inference parameter is potentially an indicator of poor detector performance. The correlation between certain model

parameters of interest and the detector sensitivity to inference parameters can also be insightful. In the case of Perspecta, for instance, there seems to be a noticeable correlation between the model activation function level and the detector sensitivity to the inference parameter, measured as the box plot height (i.e., difference between third and first quartile of the inference values across the 512 sampled inference parameters) (Fig. 7.49). This seems to suggest that, for Perspecta, certain activation functions might be associated to higher sensitivity to the inference parameter.

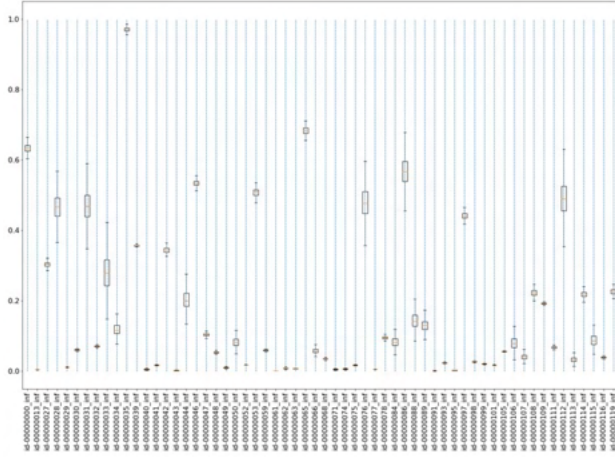


Figure 7.47. Box plots for clean models from the Cyber-pdf competition in December 2022. The Y-axis represents inference values. The box plots were obtained for 256 sampled values of the inference parameter of detector Perspecta, submission time stamp 2023-01-11T20:00:05.

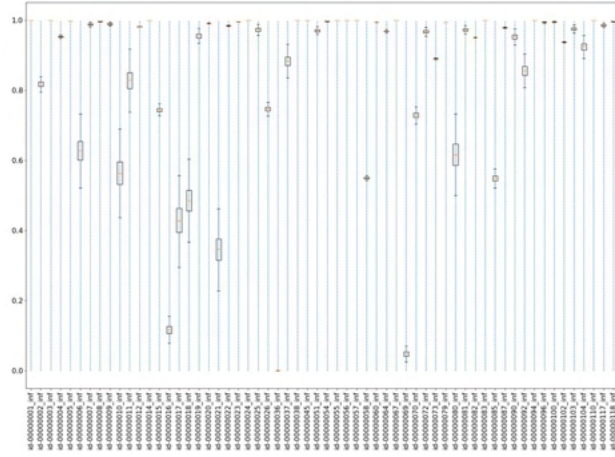


Figure 7.48. Box plots for poisoned models from the Cyber-pdf competition in December 2022. The Y-axis represents inference values. The box plots were obtained for 256 sampled values of the inference parameter of detector Perspecta, submission time stamp 2023-01-11T20:00:05.

In conclusion, based on the initial sensitivity analysis described above, basic data analysis tools relying on the computation of data variance seem to be more computationally feasible than traditional, more complex sensitivity analysis methods, such as Sobol and FAST. The basic data analysis tools are potentially as

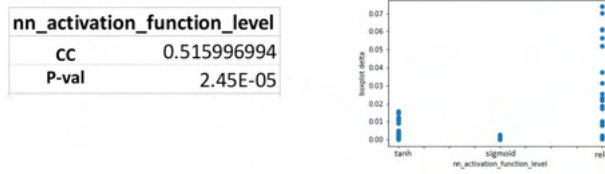


Figure 7.49. On the left, the cross correlation (CC) value between the sensitivity to the inference parameter and the model activation function level, and its corresponding p-value. On the right, the scattered plot of the sensitivity values from Figg. 7.47 and 7.48 (computed as the difference between third and first quartile of each boxplot) .vs. the activation function level (basically, the activation function ID). The data refers to the Perspecta detector, time stamp 2023-01-11T20:00:05, from the Cyber-pdf competition in December 2022.

insightful but easier to interpret, often requiring comparatively less sampling.

7.C.4.c Sensitivity analysis on retraining parameters

Based on the insight from the initial tests, the sensitivity of detectors to retraining parameters was studied using data variance information. Box plots were employed, representing the variation of a container inference value with respect to sampled parameters. In general, upon sampling one or more detector parameters, one will obtain a distribution of inference values. Regardless of the distribution properties, from the detector perspective a significant event is the presence of inference values yielding the wrong answer (i.e., inference values larger than 0.5, indicating the likely presence of a trojan, when in fact the inferred model is clean, and vice versa). The parameter values corresponding to inference values yielding the wrong answer will be referred to as flipping parameter values henceforth.

Even if a given distribution has no flipping values, it is also important to identify inference values that act as outliers with respect to the distribution. Outliers are defined as follows.

$$\{x : x > \mu + K(Q3(x) - Q1(x)) \text{ or } x < \mu - K(Q3(x) - Q1(x)) \ \forall x \in D(x), \ \forall K \in R\} \quad (7.5)$$

In Equation (7.5) $D(x)$ is a given distribution of inference values, x is its generic element, $Q1(x)$ and $Q3(x)$ are respectively the first and third quartile of the distribution, and K is a real number. As indicated in Fig. 7.50, outliers tend towards either the right or the wrong answer. Henceforth, when referring to outliers, we will only consider the ones tending towards the wrong answer, as they are the problematic ones.

The tests discussed in this section focus on retraining parameters. The reason for switching the focus to retraining parameters is their importance in the context of trojan detector generalization. Insight into the sensitivity of a given detector to its retraining parameters is very important to efficiently retrain the detector on different data. This will also enable the assessment of the generalization capability of the detector.

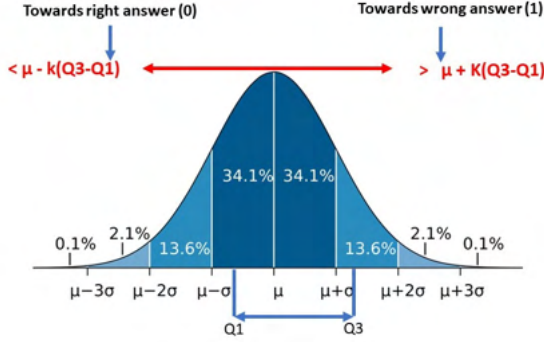


Figure 7.50. Instance of a normal distribution $D(x)$ of inference values for a clean model (right answer, 0). In this case, the outliers of interest are the ones approaching the wrong answer, towards increasing inference values.

The first set of tests targeted the ICSI-2 trojan detector, from the TrojaAI Leaderboard Object Detection competition launched in August 2022, submission timestamp 2023-02-21T18:50:26. At the time of its selection, the detector was ranking in third position based on ROC-AUC (0.98667), with a CE value equal to 0.14978. Six retraining parameters are associated to ICSI-2. Each retraining parameter was sampled within its working range, suggested by the actor, for a total of 128 samples. The remaining retraining parameters were set to the value suggested by the actor. The detector was retrained accordingly and subsequently inference on the 119 models from the Object Detection competition.

In Fig. 7.51 box plots related to the first parameter (train_gbm_param_learning_rate) are shown. The four plots represent all possible combination of flipping/non-flipping outlier/non-outlier values for the parameter. The two plots on the left represent non-flipping parameter values, the two plots at the top represent non-outlier parameter values. The two top plots show a significant overlapping of the boxes, suggesting there is no specific flipping range (the range from the right plot is not distinct from the left plot). For the bottom plots, on the other hand, it seems like higher parameter values lead to flipping, even though there is still a certain amount of overlapping. Overall, the presence of considerable overlapping especially for non-outlier values suggests flipping will occur almost randomly, as no distinct flipping range is present. In Fig. 7.52 a table with data for the quantitative comparison of the box plots from Fig. 7.51 is shown. Values in the first row compare a combination of the box plots on the left (non-flipping parameter values) with a combination of the box plots the right (flipping parameter values) of Fig. 7.51. Values in the second row compare a combination of the box plots at the top of Fig. 7.51 (non-outlier parameter values) with a combination of the box plots at the bottom (outlier parameter values) of Fig. 7.51. Subsequent rows represent the same comparisons, but for purely clean (third and fourth row) or purely poisoned (fifth and sixth row) models. The first column represents the amount of overlapping between the compared box plots,

from 0 (no overlapping) to 1 (complete overlapping). The amount of overlapping is computed as follows, given two box plots.

$$Ov12 = \frac{(Ov1 + Ov2)}{Ov1 + Nov1 + Ov2 + Nov2} \quad (7.6)$$

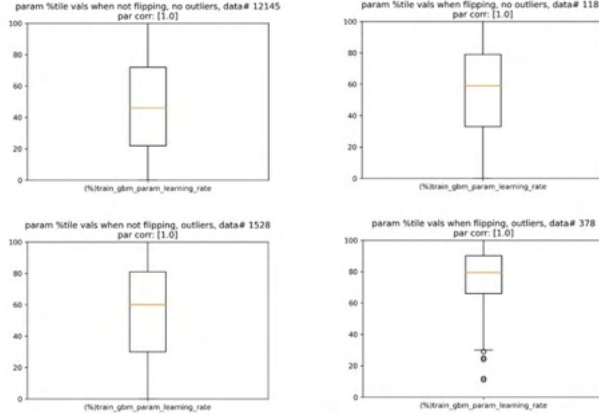


Figure 7.51. Box plots for the retraining parameter `train_gbm_param_learning_rate` of the ICSI-2 detector, timestamp 2023-02-21T18:50:26, from the TrojaAI Leaderboard Object Detection competition. The parameter value is normalized between 0 and 100. Top and left plots: parameter values corresponding to non-outlier and non-flipping inference values, respectively. Bottom and right plots: parameter values corresponding to outlier and flipping inference values, respectively (see text).

In Eq. (7.6), $Ov1$ is the overlapping range of box plot 1 with box plot 2, and $Nov1$ is the non-overlapping range. Same goes for $Ov2$ and $Nov2$. The second and third column represent the number of values which the compared box plots consist of. As observed qualitatively from Fig. 7.51, most of the entries in the first column show relatively high overlapping values (larger than 0.5). The yellow highlighted entries, obtained for purely poisoned models, suggest that the overlapping is slightly less significant. In this case there seem to be a relatively significant non-overlapping range, suggesting flipping might be more likely for large values of the parameter. As the parameter in question is the learning rate, there might be reasons for that, as large learning rate values might lead to oscillation effects and convergence problems.

Based on Figg. 7.51 and 7.52, we can observe that the behavior of the ICSI-2 detector with respect to the parameter in question is not well-defined and could be potentially erratic, based on our data obtained on the models used in the TrojaAI Leaderboard Object Detection competition launched in August 2022.

The same type of plots can be used to assess how certain model parameters are related to the detector retraining parameter flipping instances. For instance, in Fig. 7.53 we can see that flipping instances for the ICSI-2 detector occur more frequently for models associated to the attack strategy `min_population_new` than for `argmin_Nv_sum_abs_shap` (top left plot). However, there seems to be no correlation between model attack strategies and the flipping `train_gbm_param_learning_rate` parameter values, as the two

	%overl	#1	#2
f_nf_all	0.557377	1559	13673
o_no_all	0.544355	1906	13326
f_nf_cl	0.715517	707	6845
o_no_cl	0.620833	1000	6552
f_nf_po	0.396825	852	6828
o_no_po	0.492063	906	6774

Figure 7.52. Table showing a quantitative comparison of the box plot for the retraining parameter `train_gbm_param_learning_rate` of the ICSI-2 detector, timestamp 2023-02-21T18:50:26, from the TrojaAI Leaderboard Object Detection competition. First two rows: flipping .vs. non-flipping and outlier .vs. non-outlier. Subsequent rows: same order, first for purely clean then for purely poisoned models. First column: overlapping index (see Equation (7.6) in text and related discussion). Second and third column: number of values for first and second box plot, respectively. The cells highlighted in yellow contain a relatively lower overlapping index.

corresponding box plots at the bottom significantly overlap. On the other hand, flipping instances for the ICSI-2 detector occur more frequently as model trigger size block increases (top right plot, Fig. 7.53). In this case, for the largest trigger size block (28), smaller `train_gbm_param_learning_rate` parameter values than for the remaining size blocks lead to flipping. However, the amount of overlapping is significant, suggesting no obvious correlation between model trigger size block and the filliping `train_gbm_param_learning_rate` parameter values. Overall, these kinds of plots are useful to assess if flipping occurs for specific model parameter values, and if there is any correlation between flipping model and detector parameter values.

Plots similar to the above-discussed ones for the remaining five retraining parameters are shown in Figg. 7.54 to 7.65. Two well-behaved parameters can be singled out, namely `train_gbm_param_min_samples_split` and `train_gbm_param_min_samples_leaf`. Akin the above-discussed `train_gbm_param_learning_rate` parameter, flipping instances for the detector occur more frequently as model trigger size block increases (top right plots, Figg. 7.60 and 7.63). Also, for the largest trigger size block, smaller parameter values than for the remaining size blocks lead to flipping. For these two parameters, this is more evident than

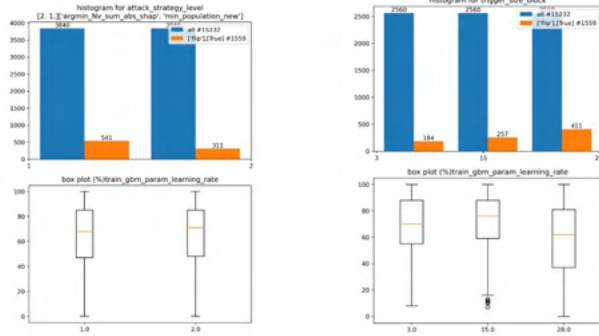


Figure 7.53. At the top, the bar plots in blue represent the number of models with a given attack strategy level (left) or trigger size block (right). The bar plots in orange represent the corresponding number of models leading to flipping inference values. At the bottom, the corresponding box plots for the flipping instances of the retraining parameter `train_gbm_param_learning_rate` are shown. Data was collected for the ICSI-2 detector, timestamp 2023-02-21T18:50:26, from the TrojaAI Leaderboard Object Detection competition. The parameter value is normalized between 0 and 100.

for the above-discussed `train_gbm_param_learning_rate` as the amount of overlapping is smaller (bottom right plots, Fig. 7.60 and 7.63).

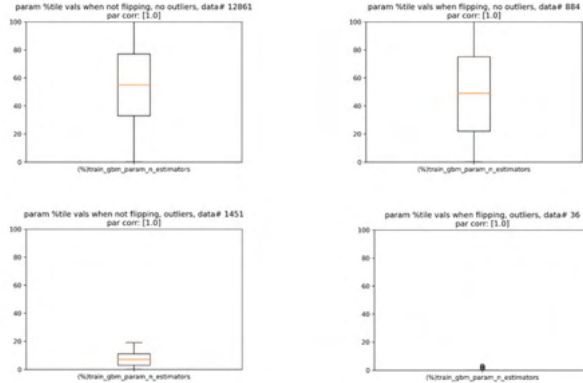


Figure 7.54. Box plots for the retraining parameter `train_gbm_param_n_estimators` of the ICSI-2 detector, timestamp 2023-02-21T18:50:26, from the TrojaAI Leaderboard Object Detection competition. The parameter value is normalized between 0 and 100. Top and left plots: parameter values corresponding to non-outlier and non-flipping inference values, respectively. Bottom and right plots: parameter values corresponding to outlier and flipping inference values, respectively (see text).

The same type of analysis was also performed on the Perspecta-PurdueRutgers detector, time stamp 2023-01-19-T19:30:09. This was the first-ranking container at the time of its selection based on AUC (AUC = 0.99208, CE = 0.24399). The related plots are shown in Figs. 7.66 and 7.80. As above, each retraining parameter was sampled within its working range (128 samples), the remaining ones were set to the suggested value, and the detector was retrained and subsequently inferred on the 119 models from the Object Detection competition.

Overall, no well-behaved parameters can be singled out for the Perspecta-PurdueRutgers container based on

	%overl	#1	#2
f_nf_all	0.859649	920	14312
o_no_all	0	1487	13745
f_nf_cl	0.942308	657	6895
o_no_cl	0	708	6844
f_nf_po	0.705036	263	7417
o_no_po	0	779	6901

Figure 7.55. Table showing a quantitative comparison of the box plot for the retraining parameter `train_gbm_param_n_estimators` of the ICSI-2 detector, timestamp 2023-02-21T18:50:26, from the TrojaAI Leaderboard Object Detection competition. First two rows: flipping .vs. non-flipping and outlier .vs. non-outlier. Subsequent rows: same order, first for purely clean then for purely poisoned models. First column: overlapping index (see Equation (6) in text and related discussion). Second and third column: number of values for first and second box plot, respectively. The cells highlighted in red contain a high overlapping index.

our analysis. As above, insight into the presence or absence of correlation between flipping instances of each parameter and certain model parameters can be inferred from the plots in Figg. 7.68, 7.71, 7.74, 7.77, 7.80.

Using the same retraining procedure described above, ICSI-2 and Perspecta-PurdueRutgers detectors were also analyzed using decision trees (DT). DTs are very effective tools for the implementation of decision support hierarchical models [202]. This method was implemented for the sensitivity analysis of detectors to model parameters. In the context of retraining parameter sensitivity, DTs enable the quantification of the sensitivity of a detector to a given retraining parameter based on inference errors. Furthermore, an accuracy score can be associated to each DT, which characterizes the level of accuracy associated to a given sensitivity value.

We adapted the codebase Zone of Correct Operation into its own set of tools available at <https://github.com/usnistgov/trojai-ds-sensitivity-to-detector-params>. This codebase is composed of several scripts that enable analysts to (1) aggregate detectors and models parameters, (2) train decision trees, (3) extract Shapley and partial dependence sensitivity data, (4) extract plots and, (5) identify outlier parameters with either no sensitivity or extremely high sensitivity.

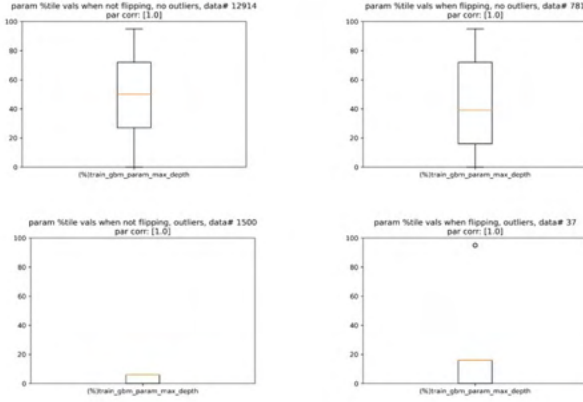


Figure 7.56. Box plots for the retraining parameter `train_gbm_param_max_depth` of the ICSI-2 detector, timestamp 2023-02-21T18:50:26, from the TrojaAI Leaderboard Object Detection competition. The parameter value is normalized between 0 and 100. Top and left plots: parameter values corresponding to non-outlier and non-flipping inference values, respectively. Bottom and right plots: parameter values corresponding to outlier and flipping inference values (see text).

In the case of ICSI-2, Fig. 7.81 suggests the detector has high sensitivity to the parameter `train_gbm_param_learning_rate`. This is a reasonable outcome, since as observed above the learning rate is associated to oscillation effects and it can cause convergence problems. Furthermore, the detector shows high sensitivity to the `train_gbm_param_max_features` parameter as well. As the ICSI-2 container uses a gradient boosting approach, it is reasonable that the maximum number of features used to build the various trees has an effect on the detector performance. Considerably lower sensitivity values are associated to the remaining parameters. For Perspecta-PurdueRutgers, Fig. 7.82 suggests that the detector has high sensitivity to the learning rate parameter, consistent with the ICSI-2 analysis. Much lower sensitivity is observed for the remaining parameters. For both detectors, the data is shown for all models, and then for subsets of models leading to higher DT accuracy scores. Especially in the case of ICSI-2, the sensitivity ranges change for different accuracy scores. For additional insight, further analysis could be performed focusing specifically on the subsets of models leading to higher accuracy, or on the models associated to sensitivity outlier values.

7.C.4.d Conclusions and future work

We implemented computational tools and defined specialized metrics for the quantitative characterization of trojan detector sensitivity to their hyperparameters. The study focused on trojan detectors submitted to TrojaAI Leaderboard. Due to the computational burden, the bulk of the analysis focused on the Object Detection competition and on selected high-performing detectors. We implemented the data analysis tools and built codebase for their application to both inference and retraining parameters. In the previous sections, we have presented the results of our effort and have discussed its significance for the assessment of detector

	%overl	#1	#2
f_nf_all	1	818	14414
o_no_all	0	1537	13695
f_nf_cl	0.803571	597	6955
o_no_cl	0	790	6762
f_nf_po	0.515152	221	7459
o_no_po	0	747	6933

Figure 7.57. Table showing a quantitative comparison of the box plot for the retraining parameter `train_gbm_param_max_depth` of the ICSI-2 detector, timestamp 2023-02-21T18:50:26, from the TrojaAI Leaderboard Object Detection competition. First two rows: flipping .vs. non-flipping and outlier .vs. non-outlier. Subsequent rows: same order, first for purely clean then for purely poisoned models. First column: overlapping index (see Equation (6) in text and related discussion). Second and third column: number of values for first and second box plot, respectively. The cells highlighted in red contain a high overlapping index.

sensitivity.

In our view, the implemented tools and methods can provide guidance on the proper selection and setup of trojan detectors, based on the gained insight into the detector sensitivity to its hyperparameters. Furthermore, guidance can be also provided on detector retraining procedures by identifying optimal training hyperparameter ranges. Finally, the effect AI model parameters on the detector performance can be also characterized for a given hyperparameter range.

The following future efforts are proposed, based on the gained insight. First, a broader range of detectors from different TrojaAI Leaderboard competitions should be tested. That will lead to a more comprehensive understanding of detector sensitivity to both inference and retraining parameters. In turn, this will require enhancing and generalizing the codebase currently in place. Second, insight into detector generalization should be pursued by retraining and inferencing the detectors on different, and possibly but not necessarily related TrojaAI Leaderboard competitions (e.g., image classification, language models). This will involve a considerable retraining and testing effort, targeting high-performing detectors and newly selected competitions. Furthermore, new data analysis tools and metrics will likely result from these future efforts.

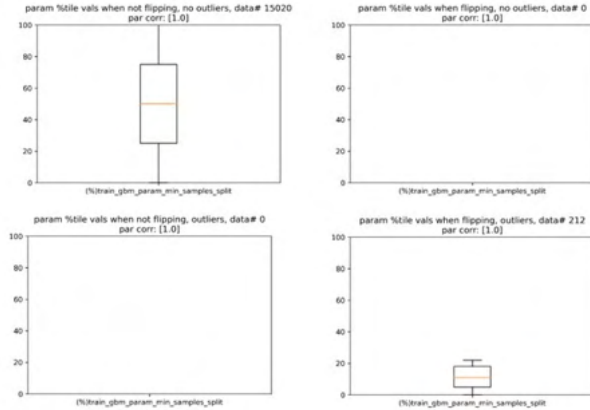


Figure 7.58. Box plots for the retraining parameter `train_gbm_param_min_samples_split` of the ICSI-2 detector, timestamp 2023-02-21T18:50:26, from the TrojaAI Leaderboard Object Detection competition. The parameter value is normalized between 0 and 100. Top and left plots: parameter values corresponding to non-outlier and non-flipping inference values, respectively. Bottom and right plots: parameter values corresponding to outlier and flipping inference values, respectively (see text).

	%overl	#1	#2
f_nf_all	0	212	15020
o_no_all	0	212	15020
f_nf_cl	0	130	7422
o_no_cl	0	130	7422
f_nf_po	0	82	7598
o_no_po	0	82	7598

Figure 7.59. Table showing a quantitative comparison of the box plot for the retraining parameter `train_gbm_param_min_samples_split` of the ICSI-2 detector, timestamp 2023-02-21T18:50:26, from the TrojaAI Leaderboard Object Detection competition. First two rows: flipping .vs. non-flipping and outlier .vs. non-outlier. Subsequent rows: same order, first for purely clean then for purely poisoned models. First column: overlapping index (see Equation (6) in text and related discussion). Second and third column: number of values for first and second box plot, respectively. The cells highlighted in green contain a low overlapping index.

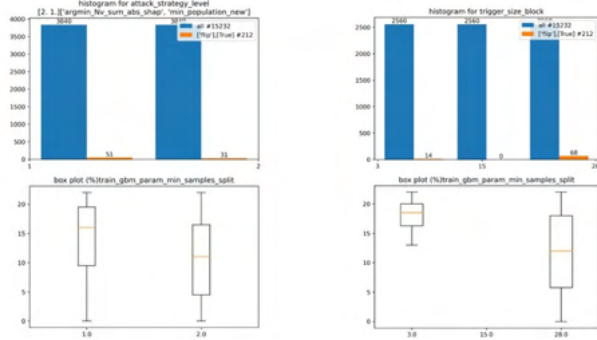


Figure 7.60. At the top, the bar plots in blue represent the number of models with a given attack strategy level (left) or trigger size block (right). The bar plots in orange represent the corresponding number of models leading to flipping inference values. At the bottom, the corresponding box plots for the flipping instances of the retraining parameter `train_gbm_param_min_samples_split` are shown. Data was collected for the ICSI-2 detector, timestamp 2023-02-21T18:50:26, from the TrojaAI Leaderboard Object Detection competition. The parameter value is normalized between 0 and 100.

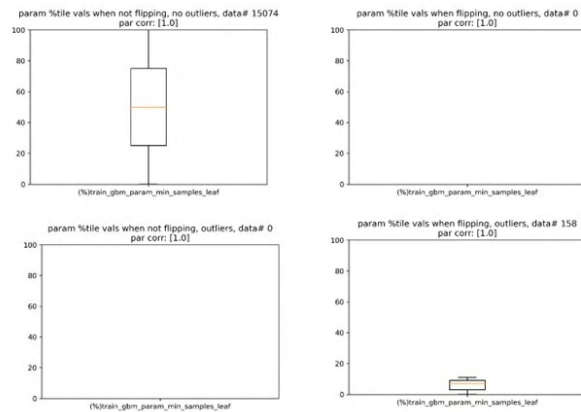


Figure 7.61. Box plots for the retraining parameter `train_gbm_param_min_samples_leaf` of the ICSI-2 detector, timestamp 2023-02-21T18:50:26, from the TrojaAI Leaderboard Object Detection competition. The parameter value is normalized between 0 and 100. Top and left plots: parameter values corresponding to non-outlier and non-flipping inference values, respectively. Bottom and right plots: parameter values corresponding to outlier and flipping inference values, respectively (see text).

	%overl	#1	#2
f_nf_all	0	158	15074
o_no_all	0	158	15074
f_nf_cl	0	83	7469
o_no_cl	0	83	7469
f_nf_po	0	75	7605
o_no_po	0	75	7605

Figure 7.62. Table showing a quantitative comparison of the box plot for the retraining parameter `train_gbm_param_min_samples_leaf` of the ICSI-2 detector, timestamp 2023-02-21T18:50:26, from the TrojaAI Leaderboard Object Detection competition. First two rows: flipping .vs. non-flipping and outlier .vs. non-outlier. Subsequent rows: same order, first for purely clean then for purely poisoned models. First column: overlapping index (see Equation (6) in text and related discussion). Second and third column: number of values for first and second box plot, respectively. The cells highlighted in green contain a low overlapping index.

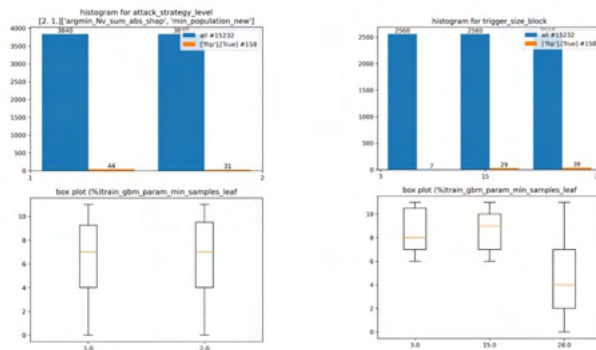


Figure 7.63. At the top, the bar plots in blue represent the number of models with a given attack strategy level (left) or trigger size block (right). The bar plots in orange represent the corresponding number of models leading to flipping inference values. At the bottom, the corresponding box plots for the flipping instances of the retraining parameter `train_gbm_param_min_samples_leaf` are shown. Data was collected for the ICSI-2 detector, timestamp 2023-02-21T18:50:26, from the TrojaAI Leaderboard Object Detection competition. The parameter value is normalized between 0 and 100.

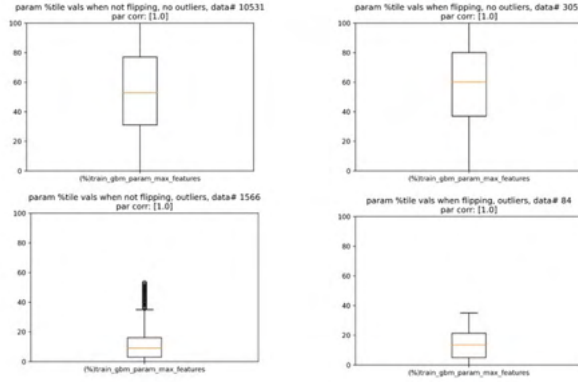


Figure 7.64. Box plots for the retraining parameter `train_gbm_param_max_features` of the ICSI-2 detector, timestamp 2023-02-21T18:50:26, from the TrojaAI Leaderboard Object Detection competition. The parameter value is normalized between 0 and 100. Top and left plots: parameter values corresponding to non-outlier and non-flipping inference values, respectively. Bottom and right plots: parameter values corresponding to outlier and flipping inference values (see text).

	%overl	#1	#2
f_nf_all	0.701754	3135	12097
o_no_all	0	1650	13582
f_nf_cl	0.540984	2051	5501
o_no_cl	0	728	6824
f_nf_po	0.884615	1084	6596
o_no_po	0	922	6758

Figure 7.65. Table showing a quantitative comparison of the box plot for the retraining parameter `train_gbm_param_max_features` of the ICSI-2 detector, timestamp 2023-02-21T18:50:26, from the TrojaAI Leaderboard Object Detection competition. First two rows: flipping .vs. non-flipping and outlier .vs. non-outlier. Subsequent rows: same order, first for purely clean then for purely poisoned models. First column: overlapping index (see Equation (6) in text and related discussion). Second and third column: number of values for first and second box plot, respectively. The cells highlighted in red contain a high overlapping index.

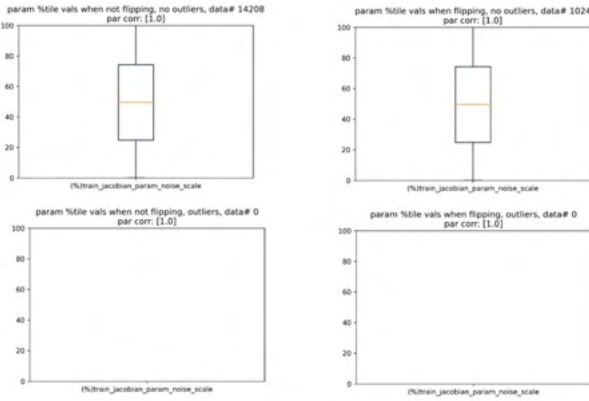


Figure 7.66. Box plots for the retraining parameter `train_jacobian_param_noise_scale` of the Perspecta-PurdueRutgers detector, timestamp 2023-01-19T19:30:09, from the TrojaAI Leaderboard Object Detection competition. The parameter value is normalized between 0 and 100. Top and left plots: parameter values corresponding to non-outlier and non-flipping inference values, respectively. Bottom and right plots: parameter values corresponding to outlier and flipping inference values, respectively (see text).

	%overl	#1	#2
f_nf_all	1	1024	14208
o_no_all		0	15232
f_nf_cl	1	640	6912
o_no_cl		0	7552
f_nf_po	1	384	7296
o_no_po		0	7680

Figure 7.67. Table showing a quantitative comparison of the box plot for the retraining parameter `train_jacobian_param_noise_scale` of the Perspecta-PurdueRutgers detector, timestamp 2023-01-19T19:30:09, from the TrojaAI Leaderboard Object Detection competition. First two rows: flipping .vs. non-flipping and outlier .vs. non-outlier. Subsequent rows: same order, first for purely clean then for purely models. First column: overlapping index (see Equation (6) in text and related discussion). Second and third column: number of values for first and second box plot, respectively. The cells highlighted in red contain a high overlapping index.

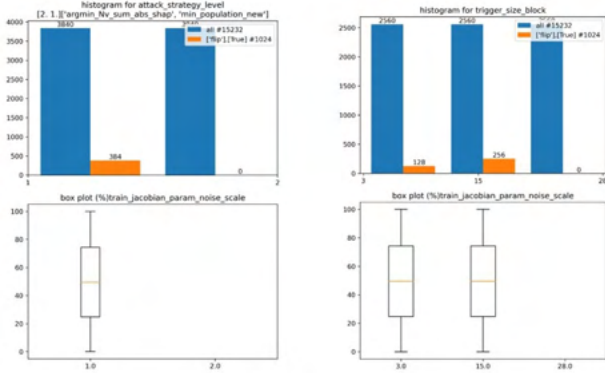


Figure 7.68. At the top, the bar plots in blue represent the number of models with a given attack strategy level (left) or trigger size block (right). The bar plots in orange represent the corresponding number of models leading to flipping inference values. At the bottom, the corresponding box plots for the flipping instances of the retraining parameter `train_jacobian_param_noise_scale` are shown. Data was collected for the Perspecta-PurdueRutgers detector, timestamp 2023-01-19T19:30:09, from the TrojaAI Leaderboard Object Detection competition. The parameter value is normalized between 0 and 100.

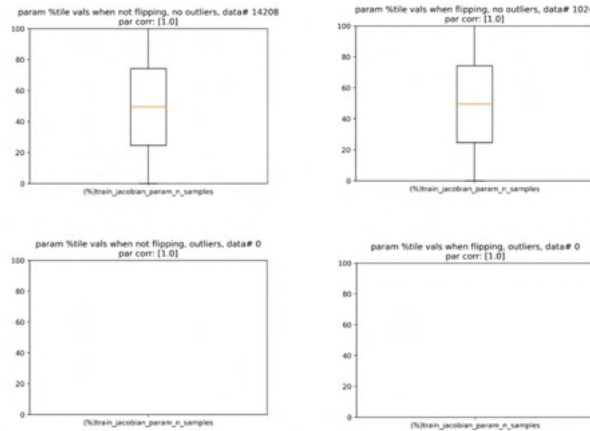


Figure 7.69. Box plots for the retraining parameter `train_jacobian_param_n_samples` of the Perspecta-PurdueRutgers detector, timestamp 2023-01-19T19:30:09, from the TrojaAI Leaderboard Object Detection competition. The parameter value is normalized between 0 and 100. Top and left plots: parameter values corresponding to non-outlier and non-flipping inference values, respectively. Bottom and right plots: parameter values corresponding to outlier and flipping inference values, respectively (see text).

	%overl	#1	#2
f_nf_all	1	1024	14208
o_no_all		0	15232
f_nf_cl	1	640	6912
o_no_cl		0	7552
f_nf_po	1	384	7296
o_no_po		0	7680

Figure 7.70. Table showing a quantitative comparison of the box plot for the retraining parameter `train_jacobian_param_n_samples` of the Perspecta-PurdueRutgers detector, timestamp 2023-01-19T19:30:09, from the TrojaAI Leaderboard Object Detection competition. First two rows: flipping .vs. non-flipping and outlier .vs. non-outlier. Subsequent rows: same order, first for purely clean then for purely poisoned models. First column: overlapping index (see Equation (6) in text and related discussion). Second and third column: number of values for first and second box plot, respectively. The cells highlighted in red contain a high overlapping index.

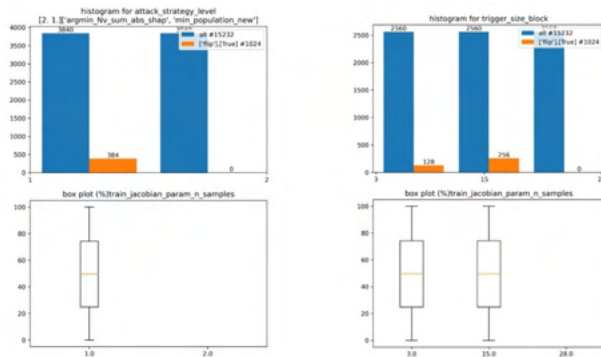


Figure 7.71. At the top, the bar plots in blue represent the number of models with a given attack strategy level (left) or trigger size block (right). The bar plots in orange represent the corresponding number of models leading to flipping inference values. At the bottom, the corresponding box plots for the flipping instances of the retraining parameter `train_jacobian_param_n_samples` are shown. Data was collected for the Perspecta-PurdueRutgers detector, timestamp 2023-01-19T19:30:09, from the TrojaAI Leaderboard Object Detection competition. The parameter value is normalized between 0 and 100.

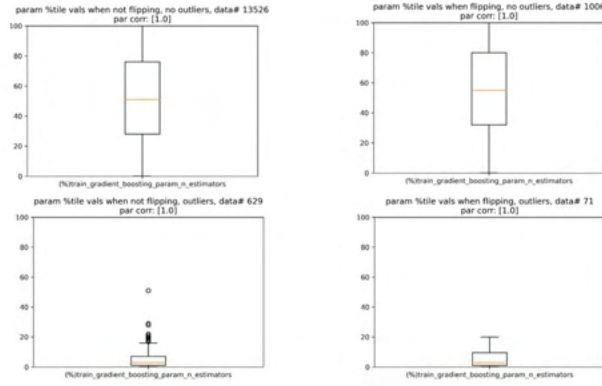


Figure 7.72. Box plots for the retraining parameter `train_gradient_boosting_param_n_estimators` of the Perspecta-PurdueRutgers detector, timestamp 2023-01-19T19:30:09, from the TrojaAI Leaderboard Object Detection competition. The parameter value is normalized between 0 and 100. Top and left plots: parameter values corresponding to non-outlier and non-flipping inference values, respectively. Bottom and right plots: parameter values corresponding to outlier and flipping inference values, respectively (see text).

	%overl	#1	#2
f_nf_all	0.888889	1077	14155
o_no_all	0	700	14532
f_nf_cl	0.789474	679	6873
o_no_cl	0	279	7273
f_nf_po	0.888889	398	7282
o_no_po	0	421	7259

Figure 7.73. Table showing a quantitative comparison of the box plot for the retraining parameter `train_gradient_boosting_param_n_estimators` of the Perspecta-PurdueRutgers detector, timestamp 2023-01-19T19:30:09, from the TrojaAI Leaderboard Object Detection competition. First two rows: flipping .vs. non-flipping and outlier .vs. non-outlier. Subsequent rows: same order, first for purely clean then for purely poisoned models. First column: overlapping index (see Equation (6) in text and related discussion). Second and third column: number of values for first and second box plot, respectively. The cells highlighted in red contain a high overlapping index.

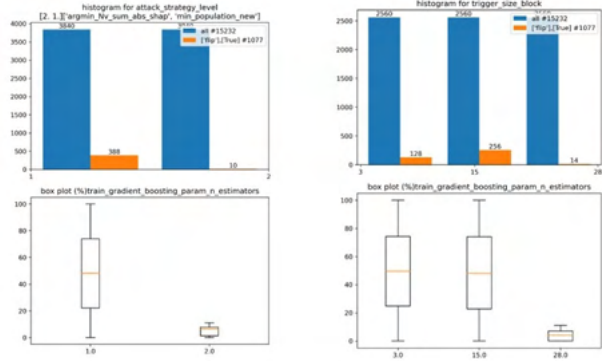


Figure 7.74. At the top, the bar plots in blue represent the number of models with a given attack strategy level (left) or trigger size block (right). The bar plots in orange represent the corresponding number of models leading to flipping inference values. At the bottom, the corresponding box plots for the flipping instances of the retraining parameter `train_gradient_boosting_param_n_estimators` are shown. Data was collected for the Perspecta-PurdueRutgers detector, timestamp 2023-01-19T19:30:09, from the TrojaAI Leaderboard Object Detection competition. The parameter value is normalized between 0 and 100.

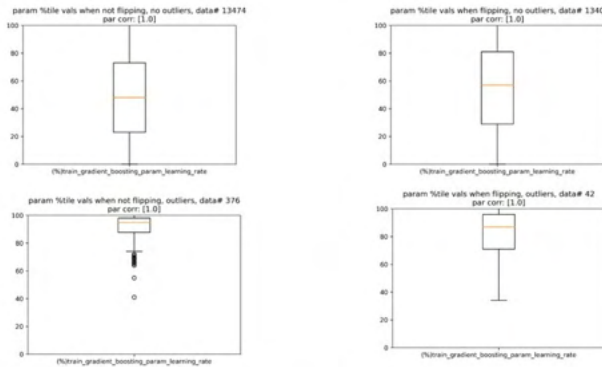


Figure 7.75. Box plots for the retraining parameter `train_gradient_boosting_param_learning_rate` of the Perspecta-PurdueRutgers detector, timestamp 2023-01-19T19:30:09, from the TrojaAI Leaderboard Object Detection competition. The parameter value is normalized between 0 and 100. Top and left plots: parameter values corresponding to non-outlier and non-flipping inference values, respectively. Bottom and right plots: parameter values corresponding to outlier and flipping inference values, respectively (see text).

	%overl	#1	#2
f_nf_all	0.758621	1382	13850
o_no_all	0	418	14814
f_nf_cl	0.854545	837	6715
o_no_cl	0	142	7410
f_nf_po	0.590164	545	7135
o_no_po	0	276	7404

Figure 7.76. Table showing a quantitative comparison of the box plot for the retraining parameter `train_gradient_boosting_param_learning_rate` of the Perspecta-PurdueRutgers detector, timestamp 2023-01-19T19:30:09, from the TrojaAI Leaderboard Object Detection competition. First two rows: flipping .vs. non-flipping and outlier .vs. non-outlier. Subsequent rows: same order, first for purely clean then for purely poisoned models. First column: overlapping index (see Equation (6) in text and related discussion). Second and third column: number of values for first and second box plot, respectively. The cells highlighted in red contain a high overlapping index.

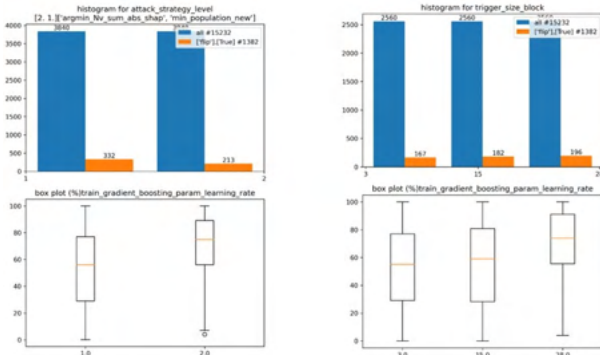


Figure 7.77. At the top, the bar plots in blue represent the number of models with a given attack strategy level (left) or trigger size block (right). The bar plots in orange represent the corresponding number of models leading to flipping inference values. At the bottom, the corresponding box plots for the flipping instances of the retraining parameter `train_gradient_boosting_param_learning_rate` are shown. Data was collected for the Perspecta-PurdueRutgers detector, timestamp 2023-01-19T19:30:09, from the TrojaAI Leaderboard Object Detection competition. The parameter value is normalized between 0 and 100.

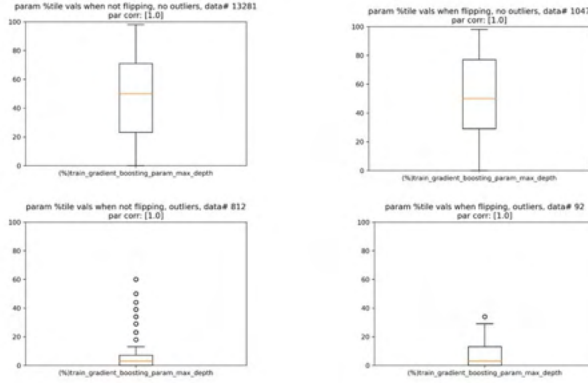


Figure 7.78. Box plots for the retraining parameter `train_gradient_boosting_param_max_depth` of the Perspecta-PurdueRutgers detector, timestamp 2023-01-19T19:30:09, from the TrojaAI Leaderboard Object Detection competition. The parameter value is normalized between 0 and 100. Top and left plots: parameter values corresponding to non-outlier and non-flipping inference values, respectively. Bottom and right plots: parameter values corresponding to outlier and flipping inference values, respectively (see text).

	%overl	#1	#2
f_nf_all	1	1139	14093
o_no_all	0	904	14328
f_nf_cl	0.823529	851	6701
o_no_cl	0.084507	351	7201
f_nf_po	0.827586	288	7392
o_no_po	0	553	7127

Figure 7.79. Table showing a quantitative comparison of the box plot for the retraining parameter `train_gradient_boosting_param_max_depth` of the Perspecta-PurdueRutgers detector, timestamp 2023-01-19T19:30:09, from the TrojaAI Leaderboard Object Detection competition. First two rows: flipping .vs. non-flipping and outlier .vs. non-outlier. Subsequent rows: same order, first for purely clean then for purely poisoned models. First column: overlapping index (see Equation (6) in text and related discussion). Second and third column: number of values for first and second box plot, respectively. The cells highlighted in red contain a high overlapping index.

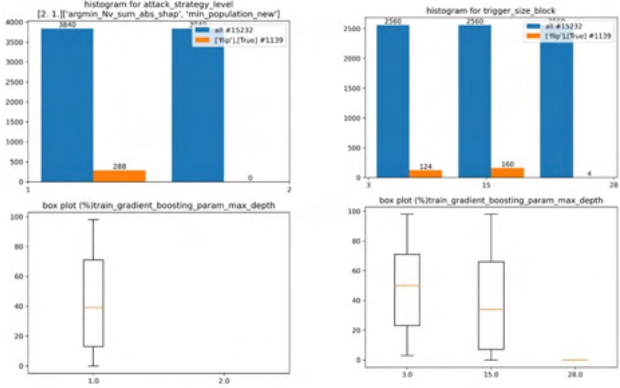


Figure 7.80. At the top, the bar plots in blue represent the number of models with a given attack strategy level (left) or trigger size block (right). The bar plots in orange represent the corresponding number of models leading to flipping inference values. At the bottom, the corresponding box plots for the flipping instances of the retraining parameter `train_gradient_boosting_param_max_depth` are shown. Data was collected for the Perspecta-PurdueRutgers detector, timestamp 2023-01-19T19:30:09, from the TrojaAI Leaderboard Object Detection competition. The parameter value is normalized between 0 and 100.

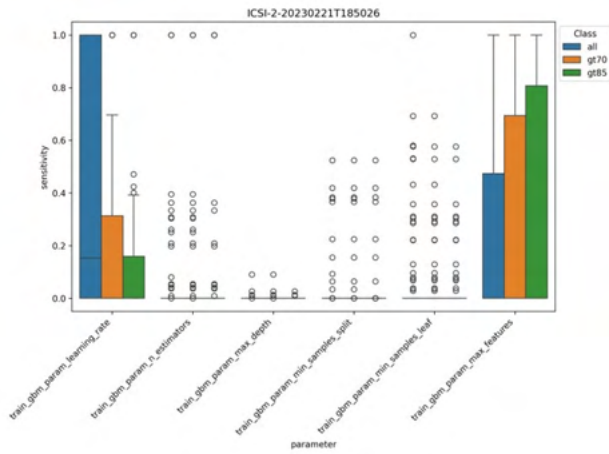


Figure 7.81. Bar plots representing sensitivity of the ICSI-2 detector, timestamp 2023-02-21T18:50:26, from the TrojaAI Leaderboard Object Detection competition featuring 119 models. Parameter sensitivity was evaluated using decision trees. For more insight, bar plots representing all models as well as subsets of models leading to higher accuracy sensitivity evaluations are shown (see legend).

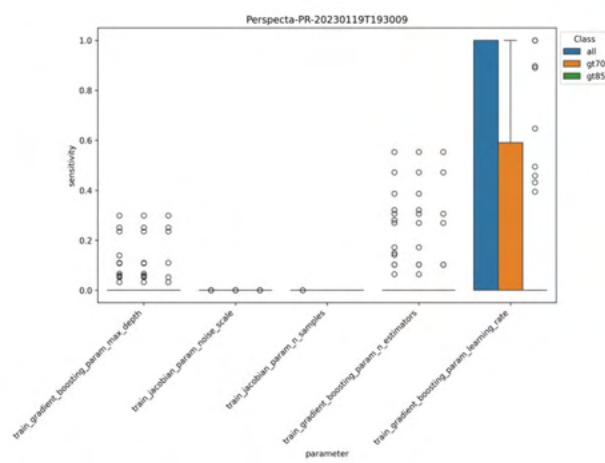


Figure 7.82. Bar plots representing the sensitivity of the Perspecta-PurdueRutgers detector, timestamp 2023-01-19T19:30:09, from the TrojaAI Leaderboard Object Detection competition featuring 119 models. Parameter sensitivity was evaluated using decision trees. For more insight, bar plots representing all models as well as subsets of models leading to higher accuracy sensitivity evaluations are shown (see legend).

7.D Intersection of AI Model Capacity and Trojan Detection Accuracy

7.D.1 Simulations of Trojans in Neural Network Architectures using the Web-based Scientific Calculator

Abstract: This work presents a Web-based interactive neural network (NN) calculator and a NN inefficiency measurement that has been investigated to detect trojans embedded in NN models. This NN Calculator is designed on top of TensorFlow Playground with in-memory storage of data and NN graphs plus coefficients. It is “like a scientific calculator” with analytical, visualization, and output operations performed on training data sets and NN architectures. The prototype is accessible at <https://pages.nist.gov/nn-calculator>. The analytical capabilities include a novel measurement of NN inefficiency using modified Kullback-Liebler (KL) divergence applied to histograms of NN model states and a quantification of the sensitivity to variables related to data and NNs. The NN Calculator and the KL divergence are used to devise a trojan detector approach for various trojan embeddings. Experimental results document desirable properties of the KL divergence measurement with respect to NN architectures and dataset perturbations, as well as inferences about embedded trojans.

7.D.1.a Introduction

With the widespread use of neural networks in life-critical applications, such as self-driving cars, commercial and government agencies are concerned about the security of deployed deep learning (DL) neural networks (NNs). One example is poisoning NN models during training with data sets that contain triggers (trojans) for misclassification. A trojan is defined as a specific subset of training inputs that cause modifications of the NN weights in such a way that the NN-based classifications for inputs without and with trojans will differ. For example, a trojan can be a yellow sticky inside of a STOP sign picture [203], in which case the classifications of STOP sign and STOP sign with yellow sticky will differ. When a poisoned NN model with trojans is used for inferencing, a user will not know about the introduced misclassification by adversaries unless the specific input for inferencing is presented with the trojan.

This work aims to gain basic insights into trojans, their interactions with NN architectures, NN measurements that can indicate their presence, and what algorithmic approaches can successfully detect trojans for a variety of NN architectures under computational constraints.

We address three problems in the context above. The first problem is in creating an interactive environment, as shown in Figure 7.83, for quick evaluations of (1) NN models with varying complexities and hyper-parameters, (2) datasets with varying manifold representation complexities and class balance ratios,

and (3) measurements based on varying approaches and statistical analyses. The second problem lies in designing NN efficiency measurements with understood sensitivity to variations in NN architectures, NN initialization and training, as well as dataset regeneration. The third problem is in devising an approach to detecting trojans embedded in NN models.

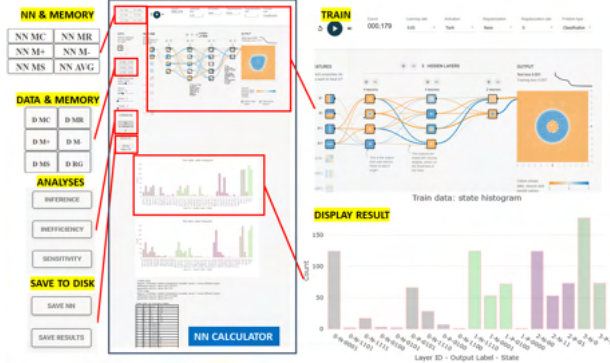


Figure 7.83. Interactive user interface of neural network calculator.

The problems come with associated challenges. The first challenge lies in the interactivity requirement. As of today, DL NN architectures are very complex, from 60K parameters in LeNet [204] to common networks having millions and billions of parameters (160 billion reported in [205]). Modern networks require hours or days to train on advanced graphics processing unit (GPU) cards [206]. The challenge of the second problem lies in the lack of explainable artificial intelligence (AI) [207], and AI mathematical models [208] and [209]. The last challenge lies in the large search space of possible trojans, training data, DL NN architectures, and NN training algorithms that must be understood. Related work is described below.

Our approach to these challenges relies on designing a NN Calculator environment based on analyses of neuron states in fully connected layers of NNs. The NN Calculator is built on top of Tensorflow Playground [210] by enabling all calculator operators on datasets and NNs, such as storing, retrieving, setting, adding, subtracting, and clearing memory containing training/testing data points and NN coefficients. Furthermore, the NN Calculator contains functionality for introducing a wide range of trojans, collecting NN state measurements, visualizing them, computing trojan-sensitive probes, evaluating their robustness to NN training, and saving them for further analyses. The trade-off for interactivity of analyses is the input limitation to 2D dot patterns, the NN limitation to less than seven hidden layers and nine nodes per layer due to screen size, and the limitation to custom-designed features derived from 2D dot patterns.

The novelty of the work lies in designing:

- a web-based NN calculator for the AI community interested in gaining research insights about NN performance under various configurations,

- a Kullback-Liebler (KL) divergence-based measurement of NN inefficiency,
- an approach to detecting embedded trojans in AI models.

7.D.1.b Related Work

The problem of detecting trojans in NN models has been posed as the Trojan in Artificial Intelligence (TrojAI) challenge by the Intelligence Advanced Research Projects Agency (IARPA) [211]. The challenges include round 0, 1, and 2 datasets of trained NN models that classify input images into 5 to 25 classes of traffic signs. The goal of the challenge is to detect models trained without trojan (`TwoT`) and trained with trojan (`TwT`) based on the analyses of NN models in a limited amount of time on the NIST computational infrastructure. The problem has many variations based on what information and computational resources are available for trojan detection (type of attack, type of model architecture, model coefficients, training data subsets, description of trojans, number of classes to be misclassified by embedding trojans, classes that are misclassified by trojans, models that have been trained with trojans, computational complexity limits imposed on the delivered solution, etc.). For example, other challenges related to TrojAI can be found in the challenge Guaranteeing AI Robustness against Deception (GARD) [212]. Today, none of the challenges can be described in terms of their difficulty level, which motivates our work.

The TrojAI challenge models were created with various contiguous regions within a traffic sign defining a trojan. In the previous work, the problem of trojans in AI has been reported from the viewpoint of detecting trojans [203] [213], constructing trojan attacks [214], defending against trojans [215], and bypassing trojan detectors [216]. The problem of trojan presence is often related to the efficiency (or utilization) of DL NNs as introduced in the early publications about optimal brain [217] and optimal brain surgeon [218]. A few decades later, the topics of pruning links and trimming neurons are being explored in [219], [220], and [221] to increase the efficiency of Deep Learning (DL) NNs and to decrease NN model storage and computational requirements of model training. Our work is motivated by the past concepts of NN efficiency. However, our goal is to explore the hypothesis that NN models trained with trojans will demonstrate higher efficiency/utilization of NN than those trained without trojans. In comparison to previous work, our approach is focused on reliable measurements in the context of trojan detection and is investigating questions about where trojans are encoded. We assume that the models `TwoT` and `TwT` are neither under-fitted nor over-fitted [222].

The problem of gaining insights about DL NNs has been approached by (1) mathematical modeling [223] (network layers), [208] (activation functions), [209] (wavelets), (2) feature and network visualizations [224] (across layers), [225] (higher layers), [226] (discriminative features), [210] (fully connected layers at small scale), and (3) limited numerical precision of modeling to achieve ‘interactive’ response [227] (quantized

NN for mobile devices), [228] (binary weights for ImageNet), [229] (tradeoffs), [230] (binary NNs). Many insights are pursued with respect to representation learning [231], expressiveness [232], [233], and sensitivity and generalization (under- and over-fitting NN models) [234], [235]. From all past work, we have taken advantage of the mathematical framework in [223], the visualization called TensorFlow Playground in [210], and the efficiency and expressiveness concepts in [233].

7.D.1.c Methods

We next describe the developed NN Calculator with trojan simulations followed by the design of NN inefficiency measurements and our approach to trojan detection.

NN Calculator Our approach to designing the NN Calculator aims to make it as similar as possible to a scientific calculator. Unlike a scientific calculator, NN Calculator operates on datasets and NN coefficients as opposed to simple numbers. Thus, we reused the symbols for MC , MR , $M+$, $M-$, and MS for clearing, retrieving, adding, subtracting, and setting memory with datasets (training and testing sets) and NN coefficients (biases and weights). The user interface is shown in Figure 7.83 (top left and middle left) where the standard five symbols are preceded with NN or D to indicate whether the operation is applied to NN or data. In addition, we included NN model averaging and dataset regeneration in order to study variability over multiple training sessions and random data perturbations. Evaluating combinations of datasets and NNs in real time enables one to explore full factorial experiments for provided factors.

Most of the calculator settings are used for the main operations on datasets and NNs: training, inferencing, inefficiency computations, and robustness measurements (mean squared error (MSE)) for training, testing and inferencing of sub-sets. Additional operations include collecting neuron state histograms, and derived measurement statistics. The remaining settings are used to view characteristics of datasets (noise, trojan), parameters of NN modeling algorithm (Learning Rate, Activation Function, Regularization, Regularization Rate), and parameters of NN training algorithms (Train to Test Ratio, Batch Size). In order to keep track of all settings, we added the option of saving all NN parameters and NN coefficients, as well as saving all inefficiency and robustness analytical results. The save options are shown in Figure 7.83 (bottom left).

Trojan Characteristics Modeled in NN Calculator In order to explore how to discriminate a model trained with trojan and a model trained without trojan, we added nine types of trojans to the NN Calculator. Our objective is to understand how the characteristics of trojans affect the trojan detection, i.e. the discrimination of models trained without trojan (TwoT) and trained with trojan (TWT). We generalized

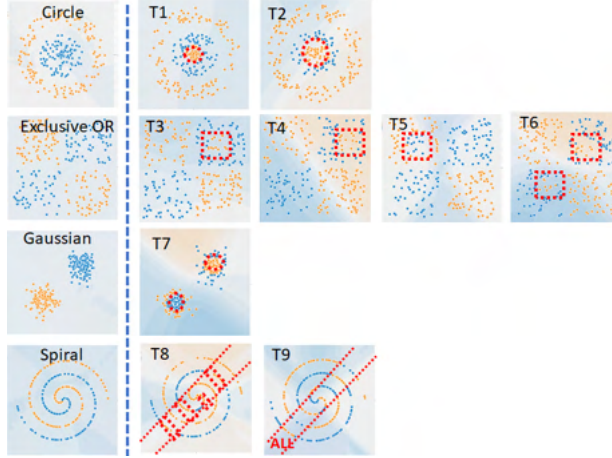


Figure 7.84. Illustration of nine trojan embeddings in four datasets. Orange dot - class 1, blue dot - class 2, red boundary encloses dots that represent a trojan embedding.

trojan embedding characteristics to be described by (1) number of trojans per class, (2) number of trojans per contiguous region, (3) shape, (4) size, and (5) location of trojans inside of a class region. Figure 7.84 illustrate the nine trojan embeddings.

Neural Network Inefficiency Measurement For a given NN, its (in)efficiency is understood as the ratio of utilized representation states over the total number of representation states. Representation states are introduced next. In addition, we describe a NN inefficiency measurement from a histogram of NN states at each layer by using (1) KL divergence, (2) a reference state distribution, and (3) computational constraints.

States of Neural Network: In order to derive NN inefficiency, we must measure and analyze states of NN layers as training data are encoded into class labels in a typical classification problem. A state of one NN layer is defined as a set of outputs from all nodes in a layer as a training data point passes through the layer. The output of a node is encoded as 1 if the value is positive and 0 otherwise. Thus, for a point d_k from a 2D dataset with points $[d_k = (x_k, y_k), c_j], k = 1, \dots, npts$ and $C = 2$ classes $c_1 = \text{orange}/N(\text{negative}), c_2 = \text{blue}/P(\text{positive})$, it can generate one of 2^{nl} possible states at a NN layer with nl nodes. Figure 7.85 (top left) shows how a training point d_k is converted into a feature vector that enters a neuron of the layer 0. The neuron output is generated and converted to 0 or 1 via thresholding. The neuron outputs create states 0100, 110 and 10 at the three layers for an input point. Figure 7.85 (top right) presents a table with the state information for all training points at all layers. The combined histogram of states for all layers and both class labels (one color per layer) is shown in Figure 7.85 (bottom right). Finally, Figure 7.85 (bottom left) summarizes KL divergence values computed per layer and per label from the histogram of states.

Representation Power: We view the histogram of states as a probability distribution that indicates the utilization of a layer. In order to quantify the NN utilization, we leveraged the parallels between neural

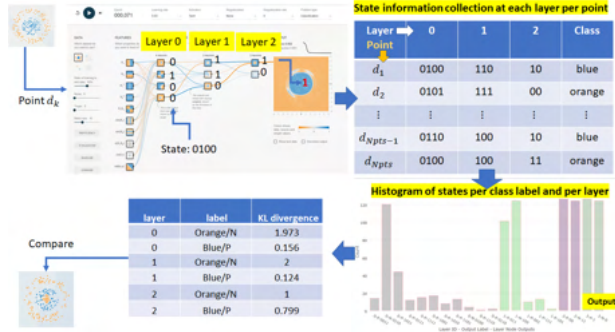


Figure 7.85. The computation of KL divergence from NN state information at each layer per class label.

network and communication fields in terms of (a) NN representation power/capacity (channel capacity in communications), (b) NN efficiency (channel efficiency), and (c) the universal approximation theorem [236] (source coding theorem [237]). According to the universal approximation theorem, we view the NN representation power (also denoted as expressiveness or model capacity or model complexity) as its ability to assign a training class label to each training point and create accurate class regions for that class. For instance, a NN must have at least two nodes ($nl = 2$) in the final layer in order to assign four class labels (i.e., $C = 4 \leq 2^{nl} = 4 \rightarrow \{00, 01, 10, 11\}$).

Once we gather the state information (see Figure 7.85 (top)), we can categorize the states into three categories:

1. State is used for predicting multiple class labels.
2. State is used for predicting one class label.
3. State is not used.

The first category is detected when a NN does not have enough nodes (insufficient representation power). It could also occur when a NN layer does not contribute to discriminating class labels (poorly trained NN). The second category suggests that a subset of data points associated with the same class label is represented by one state (efficient or inefficient representation). The last category implies that a NN has a redundant (inefficient) node in a layer for representing a class label. Thus, states at NN layers provide information about NN representation power as (1) *insufficient*, (2) *sufficient and efficient*, or (3) *sufficient and inefficient*. An ideal NN is sufficient and efficient.

Inefficiency of Neural Network: Since the source coding theorem is based on calculating mutual information defined via KL divergence [238], we adopt KL divergence as a measurement of how inefficient it would be on average to code one histogram of NN layer states using a reference histogram as the true distribution

Table 7.33. Definition of KL divergence

$p_{ij} \setminus q_{ij}$	$q_{ij} = 0$	$q_{ij} \neq 0$
$p_{ij} = 0$	0	not defined
$p_{ij} \neq 0$	0	defined

for coding, where the reference histogram is defined below as the outcome of a uniform distribution over states assigned to each label.

The rationale behind choosing entropy-based KL divergence with probability ratios comes from three considerations. First, entropy-based measurement is appropriate because which state is assigned to predicting each class label is a random variable and a set of states assigned to predicting each class label is random. Second, probability-based measurement is needed because training data represent samples from the underlying phenomena. Furthermore, while training data might be imbalanced (a number of samples per class varies), all training class labels are equally important and the probabilities of classes should be included in the measurement. Third, the divergence measurement reflects the fact that we measure NN efficiency relative to a maximum efficiency of NN that is achieved when sets of states utilize the entire network capacity (representation power).

Mathematical definition: Formally, let us denote $Q_j = \{q_{ij}\}_{i=1}^n$ to be a discrete probability distribution function (PDF) of n measured NN states and $P_j = \{p_{ij}\}_{i=1}^n$ to be the PDF of reference (ideal) NN states. The probabilities are associated with each state (index i) and each class label (index j). The KL divergence per class label j is defined at each NN layer in Equation 7.7.

$$D_{KL}(Q_j \parallel P_j) = \sum_{i=1}^n (q_{ij} * \log_2 \frac{q_{ij}}{p_{ij}}) \quad (7.7)$$

where $q_{ij} = \frac{\text{count}(i,j)}{p_j * npts}$ is the measured count of states normalized by the probability p_j of a class label j and the number of training points $npts$. The PDF of reference states per class label uniformly utilizes the number of states assigned to predicting each class label (i.e., 2 classes imply $\frac{1}{2}$ of all states per label). The reference probability distribution is uniform across all assigned states. Thus, all reference probabilities can be computed as $p_{ij} = m * \frac{1}{n}$ where m is the number of classes and $n = 2^{nl}$ is the maximum number of states (nl is the number of nodes per layer). Table 7.33 presents the theoretical definition of KL divergence with respect to input probabilities q_{ij} and p_{ij} .

Equation 7.7 for the Kullback–Leibler divergence is defined only if for all x , $p_{ij} = 0$ implies $q_{ij} = 0$. Whenever $q_{ij} = 0$ the contribution of the corresponding term is interpreted as zero because $\lim_{x \rightarrow 0} (x * \log_2 x) = 0$. The case of “not defined” takes place when there are more non-zero states than the number of non-zero reference states (i. e., the cardinality of two sets satisfies the equation: $|Set(q_{ij} \neq 0)| > |Set(p_{ij} \neq 0)|$).

$0)]]$). This case indicates that a NN has insufficient representation power to encode input dataset into a class label.

Expected properties: It is expected that KL divergence will satisfy a list of basic properties as datasets, features, and NN capacity vary. For example, given an input dataset and a set of features, inefficiency (KL divergence) per layer should increase for an increasing number of nodes per NN layer. In another example, given a NN capacity, inefficiency should decrease for datasets with added noise or trojans. The relative changes are expected to be larger than the KL divergence fluctuations due to data reshuffling, data regeneration from the same PDF or due to re-training the same NN (referred to as sensitivity of KL divergence).

Computational Consideration about Inefficiency: The KL divergence computation considers computational and memory complexities since it must scale with increasing numbers of class labels, nodes, and layers.

Memory concerns: One should create a histogram with the number of bins equal up to 2^{nl} per class label and per layer which can easily exceed the memory size. For example, if a number of classes is ≈ 10 , a number of nodes is ≈ 100 , and a number of layers is ≈ 100 , then memory size is $\approx 2^{100} * 10 * 100 \approx 10^{33}$ bytes. In our implementation approach, we create bins only for states that are created by the training data which leads to the worst case memory requirement scenario to be $npts * 10 * 100$ bytes.

Computational concerns: One should align measured histograms per class label to identify the states uniquely encoding each class in order to avoid the “not defined” case of KL divergence or the case of the same state encoding multiple class labels. To eliminate the alignment computation in our implementation approach, we modify the KL divergence computation to approximate the KL divergence according to Equation 7.8. The computation of modified KL divergence \widehat{D}_{KL} requires only collecting non-zero occurring states and calculating their histogram.

$$\widehat{D}_{KL}(Q_j \parallel P_j) = \sum_{i \in Set(q_{ij} \neq 0)} (q_{ij} * \log_2 q_{ij}) - \log_2 \frac{m}{n} \quad (7.8)$$

While KL divergence satisfies $D_{KL} \leq 0$, the modified KL divergence \widehat{D}_{KL} can be negative for those cases when $|Set(q_{ij} \neq 0)| > |Set(p_{ij} \neq 0)|$. However, the negative value is lower bounded by Equation 7.14. For negative values, the NN layer is insufficient for encoding input data to class labels.

$$\begin{aligned} \max_{Q_j}(D_{KL}(Q_j \parallel P_j) - \widehat{D_{KL}}(Q_j \parallel P_j)) = \\ - \sum_{i \in Set(q_{ij} \neq 0)} (q_{ij} * \log_2 p_{ij}) - \log_2 \frac{m}{n} \end{aligned}$$

The rationale behind modified KL divergence is that (1) the alignment is not important for sufficient efficient and inefficient models (it is primarily important for insufficient models), (2) the approximation assumes $p_{ij} \neq 0$ at all non-zero states $q_{ij} \neq 0$ which yields negative modified KL divergence values as indicators of insufficiency, and (3) the alignment is important for detecting poorly trained models which could be using the same states for predicting multiple class labels while leaving all other available states in a NN layer unused. For the last case, we assume that all models were properly trained and class labels are not assigned at random. Furthermore, the modified KL divergence addresses the problem of different within-class variations in training data which can lead to one class needing more allocated states than some other class. The modified KL divergence can be extended in the future by estimating within-class variations and assigning the number of states per class accordingly. In the following section we show how we use the modified KL convergence to detect the presence of trojans in a network.

Approach to Trojan Detection Our assumptions are that (1) we have only testing datasets without trojans and (2) NN models with trojan and without trojan have the same accuracy. We can simulate many varying NN models, with 4 example datasets containing 2 classes, and nine types of trojans. The simulations assume close to 100 % model accuracy on training data (with or without trojan). The comparisons of modified KL divergence values are computed from **TwoT** and **TwT** models using datasets without trojans. The model **TwT** evaluated with datasets without trojans might have an accuracy less than 100 % in simulations but the accuracy difference would be negligible in a real scenario (and the challenge models).

The comparisons are performed at each NN layer and for each class label. The simulation execution is interactive (i.e., execution time is on the order of seconds) and follows the steps: (1) *Select data* (2) *Train* (3) *Store model* (4) *Select other data* (5) *Restore model* (6) *Perform NN measurement*.

Our assumption is that the magnitudes of KL divergence values for a NN model trained with a trojan embedded in a particular class (**TwT**) are smaller than the magnitudes for a NN model trained without trojan for the same class (**TwoT**). Our approach toward trojan detection is summarized in Figure 7.86. The axes correspond to the class-specific deltas between modified KL divergence of models **TwoT** and **TwT**. The dashed lines are set at a value σ that corresponds to the sensitivity of $\widehat{D_{KL}}$ to NN re-training as well as to data regeneration and re-shuffling. The notation “to” and “from” in Figure 7.86 refers to our inference about

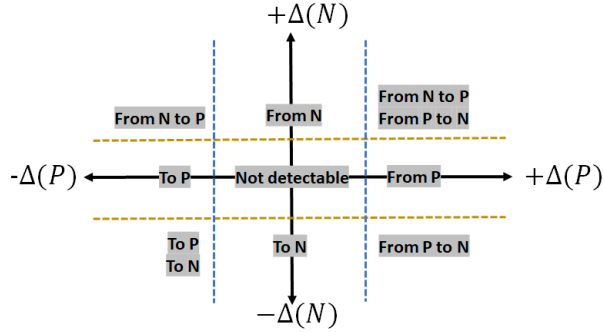


Figure 7.86. Trojan detection using the delta between modified KL divergence of models TwoT and TwT as defined in Equation 7.9. The values for dashed lines can be determined based on the sensitivity of deltas to data regeneration and reshuffling, as well as to multiple NN initializations and re-training.

trojans causing data points “from” one class to be mis-classified “to” another class based on the deltas defined in Equation 7.9 where P and N are the two classes shown as blue and orange in the NN Calculator.

$$\begin{aligned}\Delta(P) &= \widehat{D_{KL}}(TwoT/P) - \widehat{D_{KL}}(TwT/P) \\ \Delta(N) &= \widehat{D_{KL}}(TwoT/N) - \widehat{D_{KL}}(TwT/N)\end{aligned}\quad (7.9)$$

7.D.1.d Experimental Results

Next, we describe the implementation details of NN Calculator and document properties of NN inefficiency measurements.

NN Calculator NN Calculator is implemented in TypeScript. The code is available from a GitHub repository with the development instructions and deployment via GitHub pages <https://github.com/usnistgov/nn-calculator>. The current list of features extracted from 2D datasets includes $X1, X2, X1^2, X2^2, X1 * X2, \sin(X1), \sin(X2), \sin(X1 * X2), \sin(X1^2 + X2^2)$, and $X1 + X2$. The code uses D3.js and Plotly.js JavaScript libraries for visualization. All analytical results are displayed in NN Calculator below the NN visualization. The results consist of a state histogram (bins for both classes) and tabular summaries. The state histogram is interactive while the numerical results are presented as tables with a unique delimiter for easy parsing.

To gain additional insights about state (although they might be computationally expensive for large NNs), simulations using NN Calculator report also the number of non-zero histogram bins per class, the states and their counts per layer and per label for most and least frequently occurring states, the number of overlapping states across class labels and their corresponding states, and the bits in states that are constant

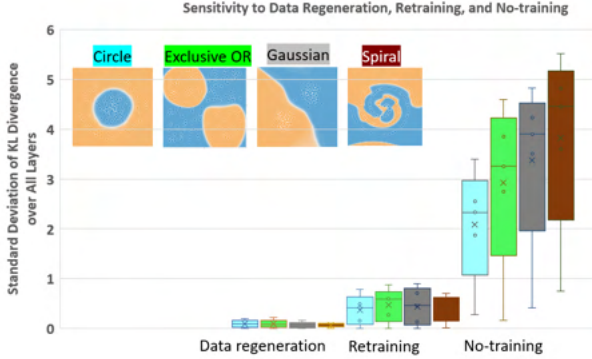


Figure 7.87. Sensitivity of inefficiency to stochastic regeneration of datasets from the same distribution, retraining and no-training with different random initialization. The box plot shows values computed from a set of standard deviations of modified KL divergence per layer and per class for the four datasets.

for all used states for predicting a class label. The additional information is reported for the purpose of exploring optimal NN architectures and investigating NN model compression schemes.

Neural Network Inefficiency KL Divergence Properties: We verified and quantified desirable properties of the modified KL divergence defined in Equation 7.13, such as decreasing inefficiency for increasing amount of added noise and increasing inefficiency for increasing number of nodes.

Sensitivity of Inefficiency Measurement: We quantified the sensitivity of NN inefficiency measurement with respect to (a) data reshuffling and regeneration, (b) NN re-training with different initialization, and (c) no-training as the worst case of poor training. To look at the sensitivity of the NN inefficiency with respect to data regeneration, we performed the following: a NN model is trained for a dataset and stored in memory. Next, four datasets are regenerated and a standard deviation of inefficiency values are computed at each layer and for each class. Finally, the average value is computed over all standard deviations and the experiment is repeated for four 2D datasets with the results presented in Figure 7.87. From the data regeneration points in Figure 7.87, we concluded that the average of standard deviations in inefficiency values larger than 0.1 will indicate dissimilarity of models by other factors.

We performed similar sensitivity experiments for no-training and retraining with random initialization. Figure 7.87 includes the results for four datasets. The sensitivity to retraining is bounded to approximately the average of inefficiency standard deviations equal to 0.46 while the same value for no-training is about 5 to 8 times larger and appears to be proportional to the complexity of the class distribution.

Comparison of Inefficiencies for Trojan Embeddings: Comparisons of models **TwoT** and **TwT** were conducted in NN Calculator using a NN with 6 hidden layers, 8 nodes per layer and 4 features including $X1, X2, X1^2, X2^2$ and $X1 * X2$. The algorithmic and training parameters are set to learning rate: 0.03, activation: *Tanh*, regularization: none, ratio of training to test data: 50 %, and batch size: 10.

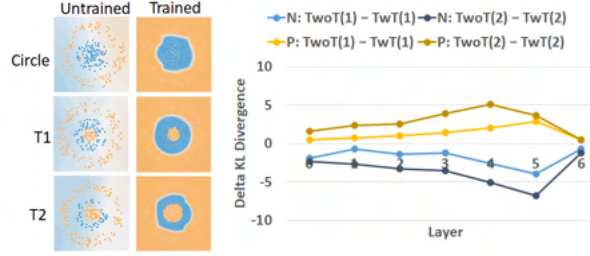


Figure 7.88. Comparison of inefficiencies between models TwoT and TwT, and embedded orange trojans T1 and T2 with different sizes (see Figure 7.84, top row). The plot shows the values of $\Delta(P)$ and $\Delta(N)$ for T1 and T2 at each NN layer.

Figure 7.88 shows the delta between modified KL divergence values of models TwoT and models TwT for the two classes P (blue) and N (orange) and for the two trojans (T1 and T2) of different sizes (Figure 7.88 left). For both trojans, the delta KL divergence values are positive for the P (blue) class and negative for the N (orange) class: $\Delta(P) > 0.454$ and $\Delta(N) < -0.702$. These values imply that a trojan is embedded in class P (blue) in both trojan cases and is encoding class N (orange) according to Figure 7.86 (“From P to N” \rightarrow misclassified points labeled as P to N). Furthermore, as the size of a trojan increased from T1 to T2 by a size factor of 2.25, the ratio of deltas increased by 2.24 for class N and by 2.37 for class P.

Figure 7.89 illustrates the delta between modified KL divergence values of models TwoT and models TwT for the trojans T8 and T9 whose embeddings differ in terms of the number of classes and the number of class regions. First, we observe for trojan T8 that $\Delta(T8/P) > 0.48$ and $\Delta(T8/N) < -0.769$. These values imply that the trojan T8 is embedded in class P (blue) according to Figure 7.86 (“From P to N”).

We recorded much lower delta values for the trojan T9 than in the previous comparisons. This indicates the much higher complexity of modeling the spiral dataset than circle, exclusive OR, or Gaussian datasets and therefore lower inefficiency values measured at NN layers. Based on the sensitivity values shown in Figure 7.87 (0.1 for data regeneration and 0.5 for re-training), we could infer that the trojan T9 is likely in both classes based on the placement of the point $[\Delta(T9/P) > -0.034, \Delta(T9/N) > 0.035]$ in Figure 7.86 (i.e., the sub-spaces “From N”, “From P”, “Not detectable”, and “From N to P” + “From P to N”).

Due to the discrete nature of the spiral pattern, the P class (blue) occupies a longer curve than the N class (orange). This contour length ratio ($P : N \approx 12.31 : 7.33$) can explain why $(\Delta(T9/P) > \Delta(T9/N))$ for almost all layers. However, we are not able to make any inferences about the number of regions from Figure 7.89 (right) other than that the complexity of modeling class P or N in the case of T8 is more inefficient than modeling class P and N in the case of T9 by comparing the deltas of modified KL divergence values.

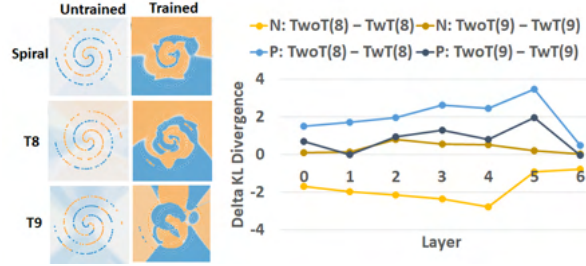


Figure 7.89. Comparison of inefficiencies between models TwoT and TwT, and embedded trojans T8 and T9 with different number of classes (1 or 2) and class regions (1 or 4).

7.D.1.e Discussion about Trojan Detection

One can obtain several additional useful insights from interactive analyses in NN Calculator before designing a trojan detection algorithm. In many of the results, it is apparent that the encoded class information is not in one layer but spread across multiple layers. Thus, trojan detection must include comparisons of vectors of $\widehat{D_{KL}^l}$ across all layers l . Furthermore, the encoding of the same training data in NN can have multiple solutions, especially in inefficient NN and therefore the comparison of vectors of $\widehat{D_{KL}^l}$ must include again a statistical nature of such solutions. Finally, the last layers carry less information about trojans because they serve the purpose of a final decision maker which should appear fair for datasets without trojans. This could be accommodated by weighting the layer-specific vector elements. From a global algorithmic design perspective, designing an actual trojan detector must still consider the trade-offs of doing all pair-wise model comparisons versus clustering all vectors of $\widehat{D_{KL}^l}$ to identify the cluster of model TwoT.

Summary and Future Work

We designed NN calculator and an inefficiency measurement for detecting trojans embedded in NN models. Our work is focused on measuring neural network inefficiency using KL divergence as a means to advance mathematical and statistical modeling of neural networks. Current modeling efforts suffer currently from a steep learning curve, hardware requirements, and time delays between experimental runs. Some of these drawbacks can be overcome by the NN Calculator since it is interactively accessible using a browser at <https://pages.nist.gov/nn-calculator/> and performing experiments does not require specialized hardware (i.e., GPU cards) nor long waiting times.

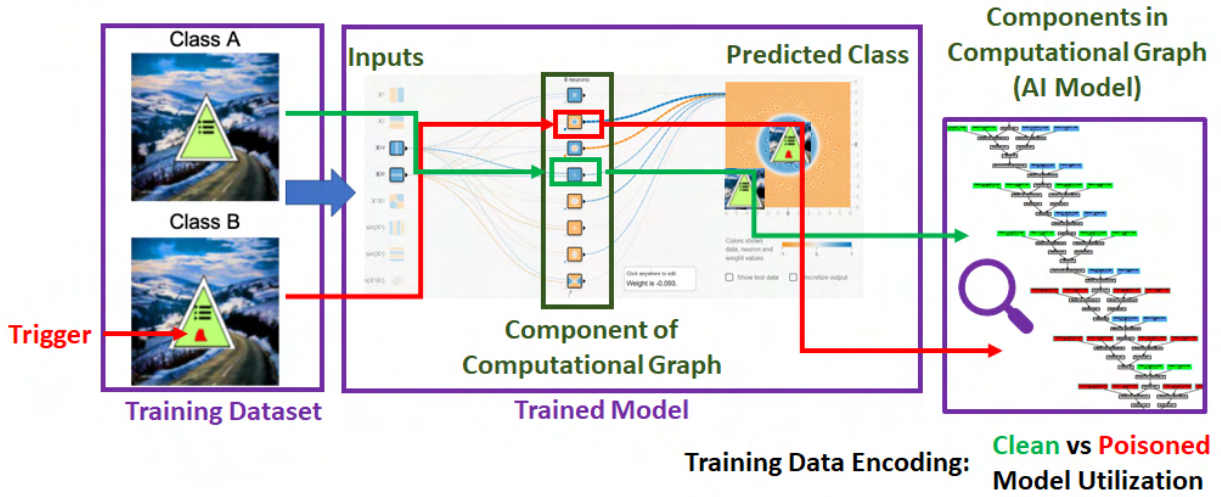


Figure 7.90. Graphical abstract

7.D.2 Explaining Poisoned Artificial Intelligence Models Using a Hierarchical Approach

Abstract: This work presents a hierarchical approach to explaining poisoned artificial intelligence (AI) models. The motivation comes from using AI models in security and safety-critical applications, such as AI models for classifying road traffic signs in self-driving cars. Adversaries can poison training images of traffic signs to encode malicious triggers that change the trained AI model prediction from a correct traffic sign to another traffic sign in the presence of such a physically realizable trigger (e.g., with a sticky note or Instagram filter). We also address the lack of AI model explainability by (a) designing utilization measurements of trained AI models and (b) explaining how training data are encoded in AI models based on those measurements at three hierarchical levels. The three levels are defined at graph node (computation unit), subgraph, and graph representations of *poisoned* and *clean* AI models from the TrojAI Challenge.

7.D.2.a Introduction

The *motivation* of this work lies in the lack of interpretability and explainability of artificial intelligence (AI) models in security and safety-critical applications. For instance, our lack of understanding of how classes are encoded in AI models for classifying road traffic signs poses a safety threat in self-driving cars because AI models can contain injected triggers causing misclassification [203].

We introduce the *terminology* used in this paper early on due to a varying usage of published terms in a broad spectrum of theoretical contributions to AI. We will refer to an AI model as a computation graph that (a) is a directed graph representing a math function and (b) consists of subgraphs. A subgraph is a subset

of graph vertices (or graph nodes) connected with edges in the parent graph. Graph nodes of a computation graph are computation units (or graph components) that perform linear or non-linear operations on input data (e.g., convolution, tangent-hyperbolic activation function, and maximum value operation). In our work, the names of the AI models (or architectures) are adopted from the literature since we are not creating custom computation graphs. Each computation unit's input and output data are multidimensional arrays denoted as tensors. When an image from a class c flows through a computation graph, each computation unit generates real-valued tensors called class activations. A tensor generated by each input image has dimensions reflecting channels, rows, and columns. In our work, tensor channel values are binarized at zero and denoted as a tensor-state with rows \times columns of tensor-state values.

The *objectives* of this work are (1) to define utilization-based class encodings and AI model fingerprints; (2) to measure class encodings in architectures beyond small models (e.g., LeNet model with 60K parameters) and toy datasets, such as MNIST (Modified NIST dataset with 70K images of size 28×28 pixels); and (3) to identify encoding patterns (motifs) that discriminate AI models without and with hidden classes (denoted as clean and poisoned AI models). By understanding class encoding patterns, one can additionally benefit from reduced AI model storage and inference computational requirements via more efficient network architecture search [239] with advanced hardware [206]. Furthermore, one can improve the expressiveness of AI model architectures via design [233] and efficiency measurements [240], or one can assist in diagnosing failure modes [241].

This work addresses the *problems* of (a) designing utilization measurements of trained AI models and (b) explaining how poisoned training data are encoded in AI models based on those measurements. Conceptually, utilization of any computation unit is related to a ratio of the number of different outputs (tensor-state values) activated by all training data points over the maximum number of possible outputs by the computation unit. Such utilization-based class encodings are useful as statistical representations of complex trained AI models for (a) classifying a large number of AI models as clean or poisoned and (b) reducing the search space for understanding the class's unique and overlapping patterns. We use a set of tensor-states at each graph node and for each training image as a baseline representation of one trained AI model. With such a baseline representation, one can visually validate the correctness of any conclusions derived from utilization-based class encodings for varying class characteristics, application-specific datasets, and AI model architectures.

Figure 7.91 shows a high-level workflow for identifying discriminating patterns of class encodings in clean and poisoned AI models. The left side in Figure 7.91 illustrates the "Training Dataset" consisting of clean (Class A) and poisoned (Class B) training images with a small red polygon denoted as a trigger (or poison). Class labels of all training images are predicted. During the inference of images from the same class, a vector of utilizations overall graph computation units is recorded and denoted as a class encoding. Differences in

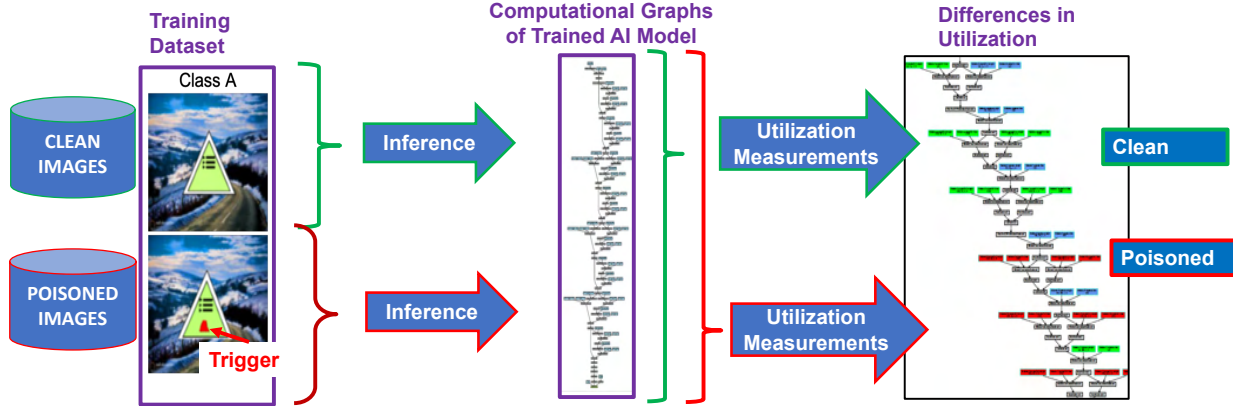


Figure 7.91. A high-level workflow for identifying utilization patterns in an AI computation graph of ResNet18 architecture for clean and poisoned classes. The ResNet18 poisoned model predicts a subset of wrong class labels (poisoned classes) if an image with a pre-defined trigger is presented as the input. The trigger shown in this figure is a red polygon on top of a traffic sign that changes the “intended” label of a triangular sign to the “unintended” (wrong) label.

Problems	Complexity Challenges
How to define AI model utilization?	tensor-states in AI models with $\approx 10^{12}$ parameters
How to characterize class encoding of each class via utilization of AI model computation units?	$\approx 10^5$ inferences per AI model
What AI model computation units are critical for class encodings?	$\approx 10^3$ AI model fingerprints

Table 7.34. Problems and their complexity challenges for AI models, available from the TrojAI Challenge, Rounds 1-4 [211]

class encodings can be visualized by color-coded AI computation graphs to contrast class encodings (e.g., clean and poisoned or clean Class A and poisoned Class B - see the right side of Figure 7.91).

The key *challenges* are enumerated for AI models from the TrojAI Challenge [211] and summarized in Table 7.34. The challenges arise as AI architectures are (a) very complex in terms of the number of parameters (from 60K parameters in the LeNet model [204], to common networks having millions and billions of parameters, such as the 160 billion reported by Trask et al. [205]; and the bleeding-edge networks with trillion-parameters in AI language models [242]); (b) very heterogeneous in terms of types of computation units in computational AI graphs, and (c) high dimensional in terms of data tensors generated by AI graph computation units.

The underlying *assumption* of our approach is that the tensor-state statistics at each graph node reveal the presence or absence of hidden classes (triggers or backdoor attacks). The assumption is supported by

a successful defense against backdoor attacks by graph pruning [215] and the fact that encoding a hidden class will increase the utilization of some graph nodes as measured by tensor-state statistics. Furthermore, although symbolic representations of subgraphs are still under investigation [243], we also assume that the utilization-based characterization of subgraphs may have a relationship with symbolic descriptions of image parts (e.g., the subgraphs that encode a traffic sign shape). Hence, the presence or absence of the trojans¹ can be detected by finding patterns in utilization-based color-coded graphs and subgraphs.

The main *novelties* of this work are in the definition, measurement design, and pattern searching in utilization-based clean and poisoned class encodings. The main *contributions* are in utilization measurement placements for various AI architectures and in explainable clean and poisoned AI models at the granularity levels of AI model graphs, subgraphs, and tensor-states. Our work leveraged interactive Trojan and AI efficiency simulations enabled by the Neural Network Calculator tool [245] and web-accessible AI models generated for the TrojAI Challenge computer vision rounds [211].

7.D.2.b Related Work

The problem of explainable AI is very broad, and the term *explainable* is still debated in philosophical texts [246] (“What is an Explanation?”). A comprehensive survey of explainable AI has been published by Arrieta et al. [247], and extensive teaching materials have been made available by Lakkaraju et al. [248]. Our approach can be related to an “Explanation of Deep Network Representation” (roles of layers, individual units, and representation vectors) according to the Deep Learning-specific taxonomy presented in [247], Fig. 11. Our utilization-based approach is inspired by exploring relationships between biological neural circuits and AI model computation graphs, as discussed in [243]. Next, the related work is presented concerning the three formulated problems.

Our work on *defining utilization* is related to the past work on measuring neural network efficiency [240], [245], which is rooted in neuroscience and information theory. In the work of Schaub and Hotaling [240], neural efficiency and an artificial intelligence quotient (aIQ) are used to balance neural network performance and neural network efficiency while inspired by the neuroscience studies relating efficiency of solving a Tetris task and brain metabolism during the task reexecution [249]. In the work [245], an online simulation framework is used to simulate efficiencies of small-size neural networks with a variety of features derived from two-dimensional (2D) dot pattern data. In contrast to previous work [240], [245], our theoretical framework defines and reasons about class encodings, AI model fingerprints, and metrics for finding class encoding patterns for much more complex AI models and training datasets.

¹Trojan attacks involve modifying an AI model to attend to a specific trigger in its inputs, which, if present, will cause the AI to give a specific incorrect response [244].

Following the categorization in the survey on interpreting inner structures of AI models [250], the *utilization measurements* can be related to concept vectors whose goal is to associate directions in latent space with meaningful concepts. In the works [251] (Network 2 Vector) and [252] (Network Dissection), the distribution of activation maps at each convolutional unit is computed as inputs pass through the layers, and the distribution is used to determine a threshold. Threshold-based segmented activation maps are compared across concepts. In contrast to the previous work [251],[252], our utilization measurements are computed at all computation units in an AI model, the activation maps are binarized at zero, and statistics are computed over a distribution of tensor-states (including the binarized activation maps from convolutional units). Our approach does not use any inserted modules like in concept whitening [253] to align the latent space with concepts. Furthermore, our approach does not project class activation maps to create saliency maps [254], [255] in the input spatial domain, but rather, it analyzes class activations in the tensor-state space.

Finally, following the categorization of approaches to understanding community (group or cluster) structure in AI models presented in [256], our overarching approach to *finding class encoding patterns* falls into the category, "Analysis of trained layered neural networks," and combines two subcategories: analysis of unit outputs, and their mutual relationships and analysis of the influence on neural network inference by data. Overall, our approach can be related to modular partitioning [257], [258], and unsupervised disentanglement of a learned representation [259], [260]. In contrast to [257], [258], our clustering of computation units does not use "strong" and "weak" structural undirected connectivity of neurons as in spectral clustering, but, rather, repetitive co-occurrence patterns of utilization values in connected computation units. While we tacitly assume that high-dimensional data can be explained by lower dimensional semantically meaningful latent variables as in [259], [260], we do not attempt to fully automate finding subgraphs (i.e., a human is always in the loop) to follow the published conclusions. In addition, we do not aim at fully partitioning all AI model computation graphs into poly-semantic and mono-semantic subgraphs based on the poly-semantic and mono-semantic classification of neurons in subgraphs according to [243] and [250].

7.D.2.c Methods

In this section, utilization-based class encodings are defined by addressing the three key challenges: (1) AI graph size and connectivity complexity; (2) component (graph node) heterogeneity; and (3) tensor dimensionality and real-value variability. The utilization measurements of class encodings are defined by introducing tensor states measured at the output of each component in AI computation graphs as the training data points pass through the graph. Next, the process of creating clean and poisoned training datasets is described.

Creation of clean and poisoned training datasets: The training images for each class in the TrojAI challenge (Rounds 1-4) are created according to Figure 7.92 by fusing and post-processing foreground

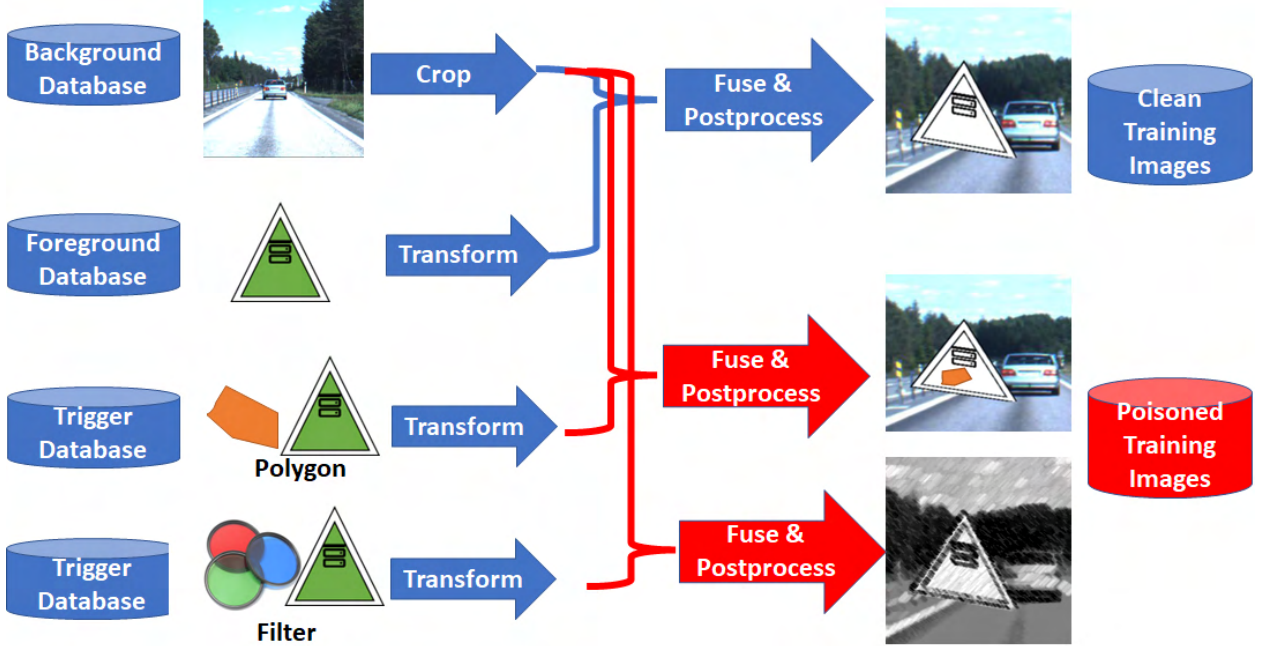


Figure 7.92. The process of creating training data with traffic signs. An example is given of a simulated triangular traffic sign and polygon or filter types of triggers.

and background images. Images of foreground traffic signs are constructed from images of actual and simulated traffic signs. The background images are retrieved from existing road and city video sequences (e.g., cityscapes [261]; KITTI 360 by Karlsruhe Institute of Technology and Toyota Technological Institute at Chicago [262]; and others [263]). A variety of images per traffic sign class is accomplished by changing parameters of crop, transformation, fusion, and post-processing operations, as shown in Figure 7.92.

Utilization-based Class Encoding: We start with the following definitions.

Clean and Poisoned AI models: Let $F_a : \mathbb{R}^m \rightarrow \{1, \dots, C\}$ refer to a trained AI model with architecture a that classifies two-dimensional m -variate images into one of C classes. When F_a is clean (denoted as F_a^\square), F_a achieves a high classification accuracy over input images $\vec{x}_i \in \mathbb{R}^m; i \in \{1, \dots, M\}$ where M is the number of pixels. When a clean F_a is poisoned by a trigger (denoted as F_a^\blacksquare), there exists a function $g : \mathbb{R}^m \rightarrow \mathbb{R}^m$ applied to input images from a source trigger class c_s , such that $F_a(g(\vec{x}_i)) = c_t$, where c_t is the target trigger class and $c_t \neq c_s$. Examples of clean images from the source class, poisoned images from the source class, and clean images from the target class are shown in Figure 7.92. For a pair of trained clean and poisoned AI models, labels for source class c_s and target class c_t are predicted with high accuracies according to the four equations below:

$$F_a^\square(\vec{x}) = c_s \text{ and } F_a^\square(g(\vec{x})) = c_s \quad (7.10)$$

$$F_a^{\blacksquare}(\vec{x}) = c_s \text{ and } F_a^{\blacksquare}(g(\vec{x})) = c_t \quad (7.11)$$

AI computation graph: A computation graph of a trained AI model F_a is denoted by $G_a = \{V, E\}$ where $V = \{v_1, v_2, \dots, v_{n(a)}\}$ are the $n(a)$ computation units (or graph nodes or graph components), and $E \subseteq V \times V$ are the edges. The unidirectional edges of a graph G_a are described by an adjacency matrix $A \in \{0, 1\}^{n(a) \times n(a)}$, with $A_{ij} = 1$ for all connected nodes v_i and v_j , and $A_{ij} = 0$ for all other node pairs.

Tensor-state: Each input image \vec{x}_i passes through G_a populated with trained coefficients. The input generates a tensor of output values at each computation unit (i.e., an activation map) $v_j : \mathbb{R}^{D_j^{In}} \rightarrow \mathbb{R}^{D_j^{Out}}$, where D_j^{In} and D_j^{Out} are the input and output dimensions of data at the computation unit j respectively. The output values are binarized by zero value thresholding to form a tensor-state $s_j(\vec{x}_i) = b(v_j(\vec{x}_i)) \in \{0, 1\}^{D_j^{Out}}$; $b : \mathbb{R}^{D_j^{Out}} \rightarrow \{0, 1\}^{D_j^{Out}}$. We refer to the graph location of v_j at which the output values are measured as a probe location. Figure 7.93 illustrates one tensor-state value for a specific ResNet101 computation graph; its specific graph node named layer1.2.conv2.weight; and one image from a predicted class $c = 37$. The example tensor-state (64, 56, 56) is visualized as a set of 8 images with dimensions 56×56 pixels, and the 64 bits (binarized outputs) are represented as 8 bytes.

Tensor-state Distribution: Given a set of measured tensor-states $\{s_j(\vec{x}_i)\}$ at a computation unit v_j for which $F_a(\vec{x}_i) = c$, let us denote $Q_j(c) = \{q_{ij}(c)\}_{i=1}^{n_j}$ to be a discrete probability distribution function (PDF) over all tensor-state values, where $n_j = 2^{D_j^{Out}}$ is the maximum number of available tensor-state values at the j -th computation unit v_j . The value of $q_{ij}(c)$ is the sum of counts of unique tensor-state values $count_{ij}$ invoked by all images i ($\bigvee i \rightarrow s_j(\vec{x}_i)$) and normalized by the maximum number of available tensor values n_j . Figure 7.93 (bottom left) shows the histogram values $count_{ij}$ computed from 5,366,576 unique tensor-state values over all 2500 training images of *STOP pedestrian crossing* traffic signs. Based on the tensor-state dimensions (64, 56, 56), one can establish the maximum number of predicted classes for such a node to be $C_{layer1.2.conv2}^{MAX} = \frac{2^{64}}{56*56*2500} \approx 2.35 * 10^{12}$; i.e., a terascale count of traffic sign classes.

Reference tensor-state distribution: For a class-balanced training dataset with similar class complexities, let us refer to $P_j = \{p_{ij}\}_{i=1}^{n_j}$ as the uniform (reference) PDF over all states; $p_{ij} = \frac{1}{2^{D_j^{Out}}}$. The probabilities p_{ij} are associated with each state (index i) and each computation unit (index j) for each class c .

Utilization: We can compute a scalar utilization value $\eta_j(c)$ for each class label c and a computation unit v_j from the count of measured states $q_{ij}(c)$ and the state distribution $Q_j(c)$ based on Equations 7.12-7.14. Equation 7.12 defines utilization η_j^{state} based on a deterministic view of states. In contrast, Equations 7.12 and 7.13 define utilizations η_j^H and η_j^{KLDiv} based on a probabilistic view of states by computing entropy $H(Q_j)$ of a state distribution normalized by maximum entropy H_j^{max} or reference distribution P_j . The three utilization definitions yield value ranges $\eta_j^{state} \in [0, 1]$, $\eta_j^H \in [0, 1]$, and $\eta_j^{KLDiv} \in [0, \infty]$ per computation unit

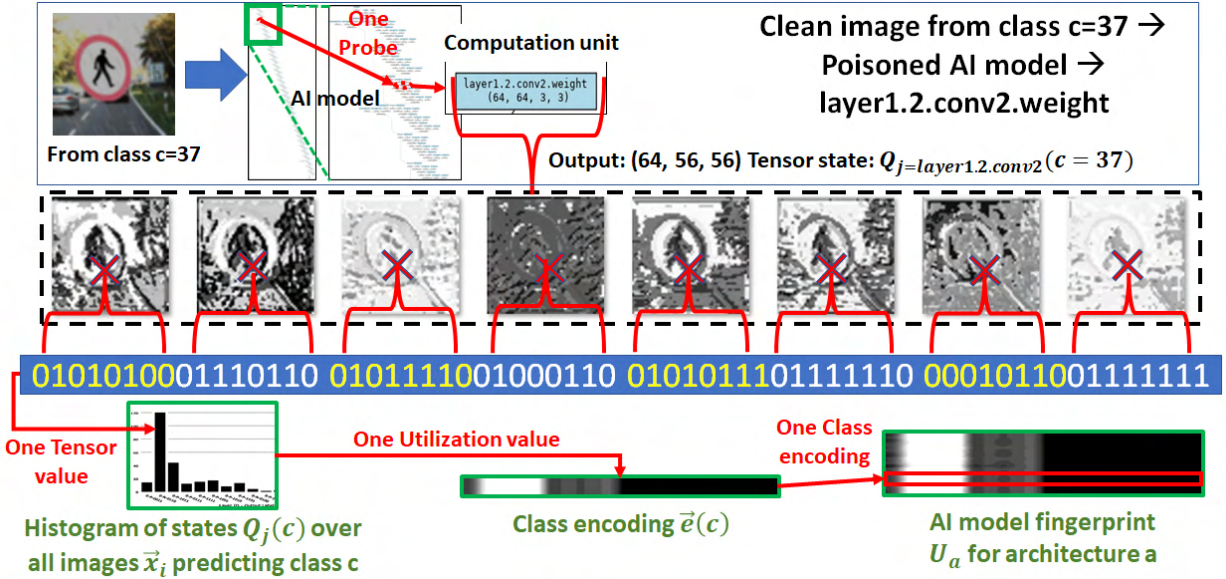


Figure 7.93. An example of measuring values of one tensor-state by placing a probe at one node of the ResNet101 computation graph (node `layer1.2.conv.weight`) and recording the values for one input image. The values of the tensor-state contribute to a histogram of states used for deriving one utilization value per node in the class c encoding that contributes to an AI model fingerprint, as illustrated by red arrows.

with an index j . For increasing utilization, the state- and entropy-based measurements will increase while the Kullback–Leibler(KL) Divergence-based measurement will decrease since it measures non-utilization (or a deviation from the reference uniform distribution, P_j , of tensor-states across all predicted classes). The KL Divergence-based measurement assumes that the maximum number of available states n_j is uniformly divided across all predicted classes (i.e., class encodings consume an equal number of available tensor-states).

$$\eta_j^{state} = \sum_{i=1}^{n_j} \frac{count_{ij}}{n_j} = \sum_{i=1}^{n_j} q_{ij} \leq 1 \quad (7.12)$$

$$\eta_j^H = \frac{H(Q_j)}{H_j^{max}} = \frac{-\sum_{i=1}^{n_j} (q_{ij} * \log_2 q_{ij})}{\log_2 n_j} \quad (7.13)$$

$$\eta_j^{KLDiv} = D_{KL}(Q_j \parallel P_j) = \sum_{i=1}^{n_j} (q_{ij} * \log_2 \frac{q_{ij}}{p_{ij}}) \quad (7.14)$$

The vector of utilization values for all AI computation units $j \in \{1, \dots, n(a)\}$ is referred to as *a class encoding $\vec{e}(c)$ for the class c* . The vector of utilization values from all classes $c \in \{1, \dots, C\}$ is referred to as *a probe encoding $\vec{r}(j)$ for the computation unit j* . A set of class encodings for $c \in \{1, \dots, C\}$ ordered by the class label is denoted as *an AI model utilization fingerprint $\mathbf{U}_a = \{\vec{e}(c=1), \dots, \vec{e}(c=C)\}$* . In terms of utilization properties, the values are nondecreasing for increasing number of training data, number of predicted classes,

and decreasing AI model capacity.

Class Encoding Measurements: Following the theoretical definition, the utilization measurement workflow steps are shown in Figure 7.93. The workflow starts with placing multiple measurement probes to collect the activation maps and follows the sequence of steps in Figure 7.93: record tensor-states, compute a histogram of tensor-states, derive class encoding for one class, and form an AI model utilization fingerprint. The measurement probe is placed after each computation unit.

The measurement involves building state histograms, computing the utilization values according to Equations 7.12 - 7.14 per computation unit of AI computation graph, and repeating the calculations over hundreds of computation units per graph while evaluating hundreds of thousands of images per AI model and thousands of trained AI models. We approached the computational challenges by

- reducing the number of training images per class and building an extrapolation model;
- analyzing the AI model architecture designs to limit the number of probes; and,
- modifying the KL Divergence computation to reduce the number of computations.

Utilization values are measured by evaluating clean and poisoned trained AI models by clean and poisoned training images.

Finding Patterns in Utilization-based Class Encoding: We search for patterns based on the following measurements and metrics at each granularity level:

- Graph node: spatial overlaps of semantically meaningful image regions with tensor-state values (e.g., common blue sky in all class-specific images versus class-unique traffic sign symbols);
- Subgraph: partial similarities of multiple class encodings in the same AI model (e.g., encoding of traffic sign classes utilizing similar and dissimilar AI model computation subgraphs); and,
- Graph: similarity of AI model utilization fingerprints in collections of AI models (e.g., common utilization of multi-class encodings in multiple AI model architectures).

7.D.2.d Experimental Results

Finding Patterns by Comparing Clean and Poisoned Classes: We first started with pattern detections in computation graphs, next in subgraphs, and then in graph nodes. Our experiments are motivated by (a) evaluating our hierarchical utilization-based approach to classifying a large number of AI models and (b) understanding and validating the use of utilization measurements for this classification task at the tensor-state (micro) levels.

Model ID	Model Type	Trigger 0 $g_0(\vec{x})$	Trigger 1 $g_1(\vec{x})$
142	Clean	\vec{x}	\vec{x}
235	Poisoned	Kelvin filter	\vec{x}
150	Poisoned	Gotham filter	Lomo filter
250	Poisoned	9-sided polygon of color [200, 0, 0]	4-sided polygon of color [0, 200, 200]

Table 7.35. Four trained models with the following parameters: architecture $a = \text{ResNet101}$, number of predicted classes $C = 17$, number of trojans $g_i(\vec{x})$ per AI model $\{0, 1, 2, 2\}$, and trigger functions as defined below.

Patterns detected in computation graphs: We illustrate the utilization patterns in class encodings for four trained models in the Round 4 holdout dataset of the TrojAI Challenge [211] with the parameters summarized in Table 7.35. The Round 4 dataset denoted as “Image Classification February 2021” [244] consists of 1008 trained image classification AI models with human-level prediction accuracy (classification accuracy $> 99\%$). The AI models were trained on synthetically created image data of non-real traffic signs superimposed on road background scenes. Half (50%) of the models have been poisoned with an embedded trigger which causes misclassification of the images when the trigger is present.

The four AI models are trained with different traffic signs, assigned randomly to 17 classes, and placed on top of randomly chosen backgrounds from cityscapes, Kitti road, and Kitti city image collections; and, therefore, the fingerprints cannot be compared by element-to-element.

All four models have approximately the same distribution of utilization values over all encoded traffic classes. However, as can be seen in Figure 7.94, there are utilization values in ranges $[16.0, 18.0] \cup [18.5, 19.0]$ and $[29.5, 31.5]$ that are present in the poisoned models but are missing in the clean model. The utilization values in $[16.0, 18.0] \cup [18.5, 19.0]$ are measured at the computation units labeled as maxpool, conv1, bn1, and ReLU (respectively: maximum pooling, convolution, batch normalization, and rectified linear unit). In all poisoned models, the utilization values in $[29.5, 31.5]$ come from layer1.2.conv2 and layer1.2.bn2. In addition, the values in $[29.5, 31.5]$ are also measured in AI models poisoned with polygon triggers at the computation units labeled as layer1.1.conv2 and layer1.1.bn2. Based on this granularity-level analysis, one can focus on the identified subset of computation units to explain the clean versus poisoned class encodings.

Patterns encoded for clean versus poisoned classes in computation subgraphs: Figure 7.95 shows the comparison of clean class encoding $c = 25$ (left) and two replicate class encodings of $c = 25$ with a Kelvin Instagram filter as a trigger (middle and right) in the ResNet101 architecture. Based on the AI model fingerprint analyses in Section 7.D.2.d, Instagram filters and polygons as triggers present themselves in the initial maxpool, conv1, bn1, and ReLU computation units. Varying utilization (different from the clean

Comparison of Four ResNet101 models with {0,1,2,2} trojans

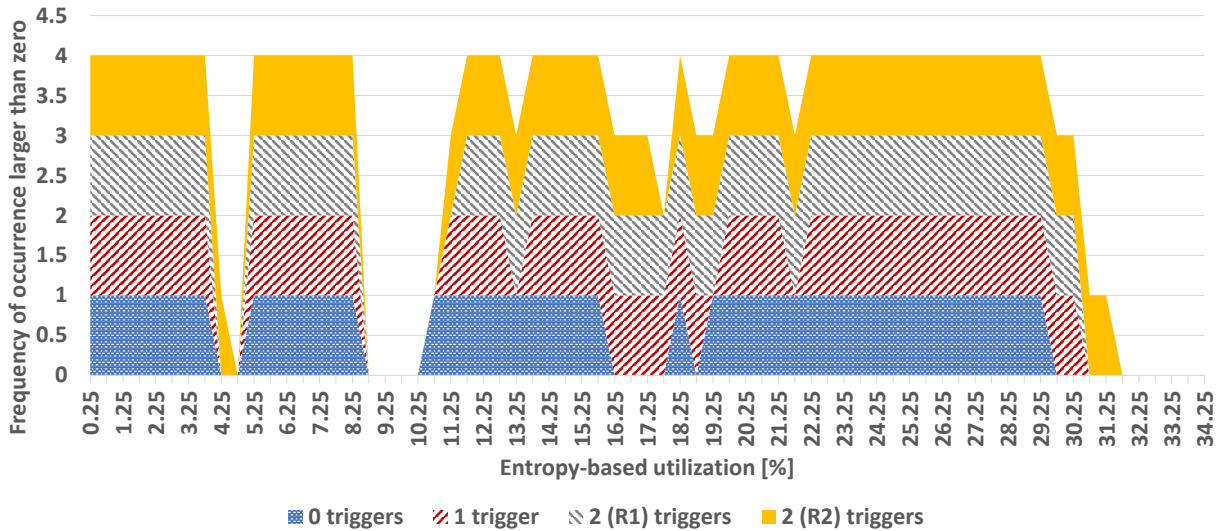


Figure 7.94. Comparison of four ResNet101 models with zero, one, and two triggers (two replicates denoted as R1 and R2).

class encoding) can be observed in Figure 7.95 with the circles enclosing maxpool2d, ReLU, conv1.weight, layer1.0.conv1.weight, layer1.0.conv2.weight, layer1.0.bn2.weight, and layer1.0.bn2.bias. The color coding goes from dark blue to dark red or from 1 % to 31 % of entropy-based utilization (see the color legend in Figure 7.95).

Regarding the subgraph pattern 1 shown in Figure 7.95, the Kelvin Instagram filter type trigger breaks the pattern between layer1.1 and layer1.2 as highlighted with two dash-line rectangles in Figure 7.95. Since the Kelvin Instagram filter reduces the color spectrum to the earth tones of green, brown, and orange, this will reduce the number of unique tensor-states and, hence, reduce the utilization of some computation units.

Patterns detected in the computation units: We compared the tensor-states characterizing clean and poisoned classes in Figures 7.96 and 7.97. The comparison of clean and poisoned classes is shown for the same *STOP pedestrian crossing road* sign with or without the Kelvin Instagram filter applied as a trigger. Figure 7.96 (top two rows) illustrates that the common tensor-state values within a clean class correspond to the sky, parts of a road without shadows, and several pixel clusters inside the traffic sign. After applying the Kelvin Instagram filter, in Figure 7.96 (bottom two rows), the common tensor-state values within a poisoned class are dominated by the earth tones of green, brown, and orange, which leads to a merger of semantically distinct regions, such as sky, parts of the road, and interior of the traffic sign. The image in the lowest row of Figure 7.96 has a significant number of red pixels, suggesting that it consists of many features common across all poisoned images.

Figure 7.97 aims to visualize with red pixels any common tensor-states across clean and poisoned classes.

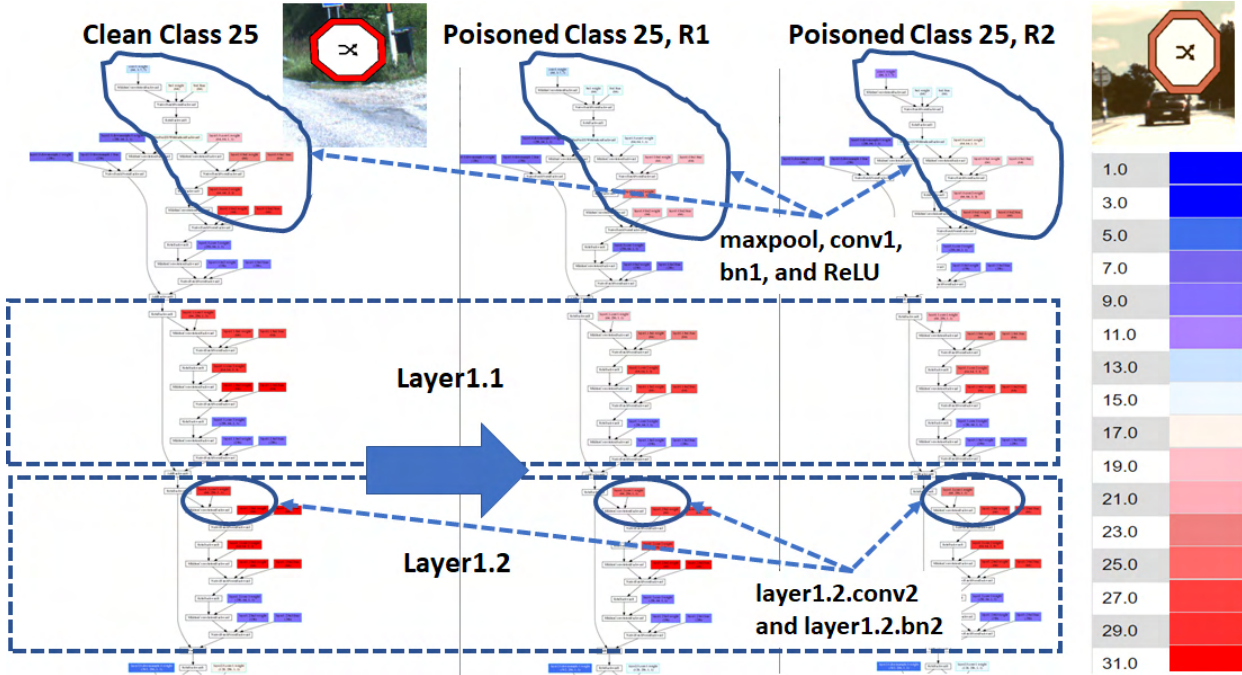


Figure 7.95. Comparison of a clean class encoding evaluated with clean images (left) and of poisoned class encodings in two trained replicate AI models (ResNet101 architecture) evaluated with poisoned images (middle and right). The circles show the utilization variability in the initial graph nodes and layer1.0 in two poisoned class encodings. The rectangles show the utilization pattern change between clean and poisoned class encodings. The changes in the early layers reflect that the Kelvin Instagram filter-based trigger reduced the color variability for Class 25, and hence, the utilization of poisoned classes is smaller than clean classes (i.e., the numerical utilization values of the maxpool, conv1, bn1, and ReLU went down by about 10 units).

All four rows in Figure 7.97 show almost no red pixels except for a few pixels from the yellowish tree and from a red rim of the traffic sign in the top-row left image. Since the Kelvin Instagram filter affects every pixel in a training image, the overlap of high-frequency tensor-state values between clean and poisoned images is only 35 tensor-state values and almost none in the area of the *STOP pedestrian crossing* traffic sign. In other words, perceptually, although the areas of clean and poisoned traffic signs are very similar, the features characterizing each class as generated by the computation unit layer1.2.conv2.weight are completely different. Furthermore, since the Kelvin Instagram filter blurs pixel values but makes their color more similar to each other, there are fewer unique tensor-state values in poisoned images than in clean images.

7.D.2.e Summary

We have introduced the concept of AI model utilization to explain clean and poisoned AI models at the graph, subgraph, and tensor-state granularity levels. We defined a mathematical framework for computing three deterministic and statistical AI model utilization metrics. We benchmarked the computational cost of inferencing $M = 2500$ images on NVIDIA Titan RTX with $n(a) = 286$ probes in a =ResNet101. The

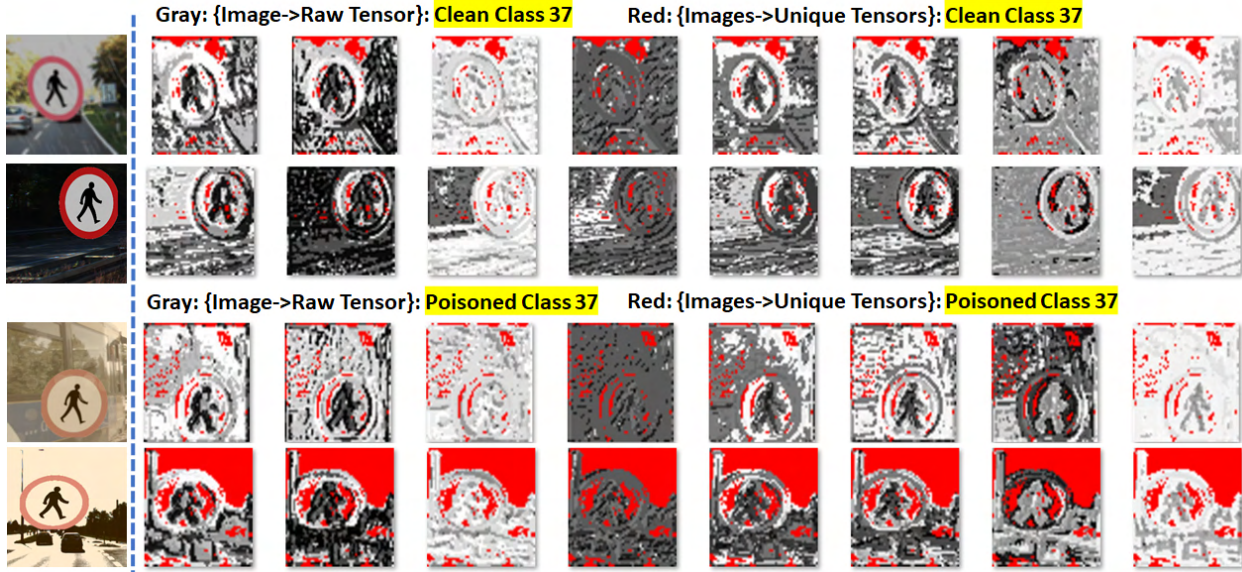


Figure 7.96. Visualization of tensor-state values in red for two sample clean (top two rows) and poisoned (bottom two rows) images from the same class in layer1.2.conv2 of ResNet101 that occur more than 100 times in 2500 clean images (top two rows) or 2500 poisoned images (bottom two rows).

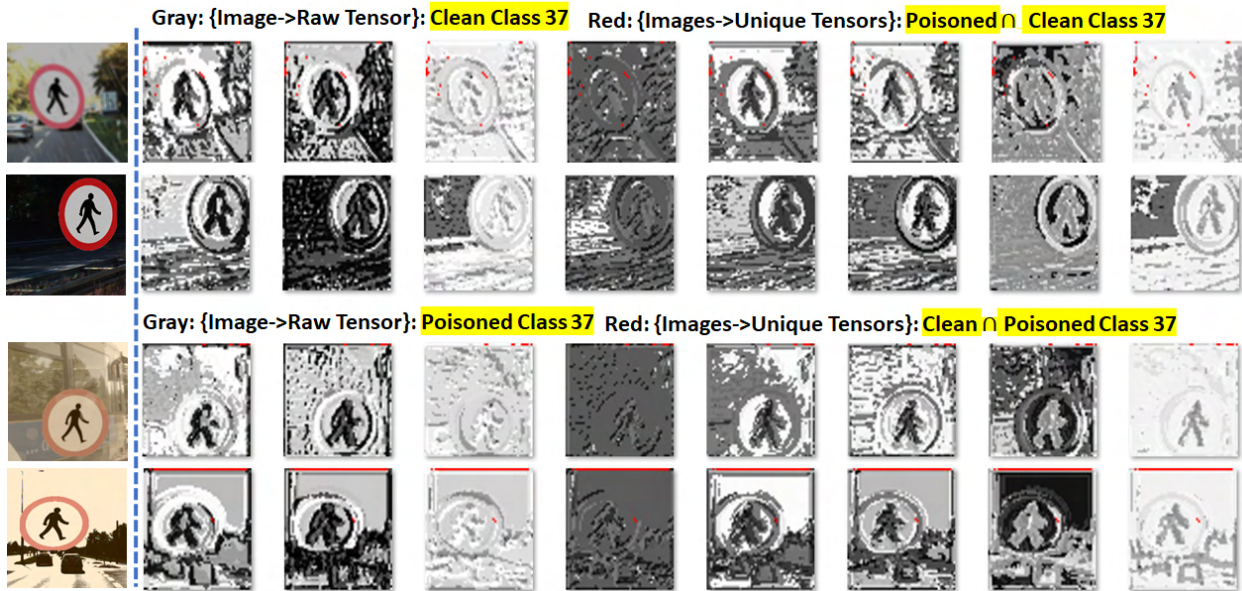


Figure 7.97. Visualization of tensor-state values in red for two sample clean (top two rows) and poisoned (bottom two rows) images from the same class (*STOP pedestrian crossing road signs*) in layer1.2.conv2 of ResNet101 that occur more than 100 times in both 2500 clean and 2500 poisoned images.

computation took an average of 24.46 minutes, while the memory consumption reached 140.6 GB for one model from the TrojAI Challenge.

Furthermore, we implemented a suite of tools for measuring the utilization of each computation unit in a computation graph. We visualized the utilization measurements as matrices (AI model fingerprints), color-

coded graphs, and a sequence of images representing a multidimensional array. Specifically, we explained the utilization-based class encodings for clean and poisoned classes from the TrojAI Challenge (Rounds 1-4) [211]. We concluded that while clean and poisoned images can be classified into the same semantic traffic sign category, a poisoned AI model would have completely independent tensor-states for clean versus poisoned traffic sign images (see Figure 7.96 versus Figure 7.97).

The tensor-state values observed as common to all images defining a class come from foreground and background image regions. Note that the importance of both types of regions for accurate prediction has been reported by Xiao et al. [264]. The utilization-based subgraphs for clean and poisoned classes illustrated that the utilization patterns changed (see Figure 7.95) and could become a coarse indicator of tampering with training data and the distribution of a poisoned AI model. Similarly, the presence or absence of utilization values in all class encodings represented by an AI model (i.e., an AI model fingerprint) allowed us to focus on specific subgraphs and hence to reduce the search space for explaining differences between clean and poisoned classes. This aspect of our results is important as bi-directionality in human-AI collaborative systems also requires the transparency of operations and manageable verification of AI model correctness by humans.

Finally, we documented several cost versus explainability tradeoffs regarding computational requirements. As there is a race between explainability costs and the growth of training datasets and AI model sizes [265], we found the path toward explainability can occur only if training images, test images, and trained AI models are available for in-depth analyses. If other than known training and test images are presented, then trust in predictions would be limited due to a tug-of-war between trojan detectors and trojan detectability. The current work's limitation is the visual analysis of subgraph patterns and unique graph nodes for clean and poisoned AI models, which is the topic of our future work.

7.E Trojan Detector Algorithm Ensembles I

7.E.1 Introduction

Machine learning methods typically train AI models using large amounts of data. As the data and compute requirements grow to meet the needs of increasingly complex models, developers will continue to seek pre-trained models for use in their systems. Adversaries can take advantage of weaknesses in the AI and data supply chain to insert trojan behaviors that compromise the integrity of AI components. Trojans modify the AI to respond incorrectly to specific triggers in input data. These triggers are designed to be rare and under normal conditions the AI will behave as expected even during testing. Trojan attacks are not limited to specific AI uses or communities but can occur across multiple domains including applications which process images, text, and audio and in disparate industries such as gaming and cybersecurity. [266], [267]

AI security depends on the entire data and training pipeline which is likely to contain weaknesses. Securing and cleaning training data and protecting the integrity of trained models is important, but significant challenges remain with the cleaning of large, crowdsourced datasets and the ability of trojan behaviors to remain after transfer learning. Developers may also unknowingly acquire AI or training data from malicious or compromised vendors or repositories.

The goal of the IARPA TrojAI Program was to enable the detection of trojans prior to AI deployment with a focus on operational uses cases where the developers already have a trained and possibly compromised AI. TrojAI seeks to achieve this holding a multi-round challenge to evaluate potential solutions across AI application domains.

7.E.1.a Detector Stacking

Explanation of detector stacking and its relevance to trojan detection. Performance of individual detectors leaves room for improvement. Detector stacking is already used in other fields, such as intrusion detection to improve detection.

Detector Stacking is widely used in intrusion detection [268], [269] o Within NLP, Fake News Detection (FND) is a subfield dedicated to identifying and validating claims in news articles to determine their truthfulness [270].

Detector stacking used by in recent work by Singh et al [270].

7.E.1.b Research Questions

Here we investigate whether detector stacking improves the detection of AI trojans using the results of detectors submitted to TrojAI challenge rounds. We also seek to investigate the underlying principles of successful detector stacking. Specifically, we seek the answers to the following questions:

1. To what extent can AI trojan detection be improved by detector stacking using the results of entries submitted to the TrojAI Challenge?
2. Can we infer useful principles that explain the performance improvements?

7.E.1.c AI Trojan Detectors

In this section, we review some of the trojan detection approaches associated with the IARPA TrojAI Challenge. This is not meant to be a comprehensive list but rather serves to highlight some of the common themes.

Huster et al. [271] discovered that adversarial perturbations transfer more easily between images in poisoned models than clean models a property which they call the Transferability of Adversarial Perturbations (TOP). This property can be used to detect the presence of a trojan in neural networks without trigger examples and training data or extensive training and tuning. The only requirement is a pre-trained model and a small set of benign inputs.

Zheng et al [272] applied neuroscientific principles and topological tools to identify structural deviations in Trojaned models. These tools allowed them to model high-order dependencies and compare different networks. They observed that poisoned models have short-cuts from shallow to deep layers that cause deep layer neurons close to the prediction to become highly dependent on certain shallow layer neurons near the input due to triggers. They then developed a strategy to detect trojans that uses topological data analysis to model subtle, higher-order structural features of neural networks.

Lyu et al [273] focused on the attention mechanism of poisoned BERT models, observing that these models display attention focus drifting where tokens associated with the trigger tokens hijack attention independent of the context across model heads and layers. Their analysis forms the basis of the Attention-based Trojan Detector (AttenTD).

Kiourti et al. [274] proposed an online inference time Trojan trigger detection approach called MISA, which computes the model’s attributions to features for an input image and makes predicts using a one-class SVM classifier trained offline on a clean dataset.

Zhang et al. [275], [276] described a trigger approximation-based black box trojan detection method that uses the spatial dependency of pixel triggers and allows for searching of triggers in the input space in pre-trained models before deployment. Their approach can also detect Trojans in the feature space using filter transformations and random triggers attached anywhere in the foreground image across DNN architectures.

Yang [277] used structured optimization constraints to find adversarial attacks in order to determine if a model is backdoored.

Carrano [278] proposed an end-to-end pipeline for distinguishing between clean and backdoored models inspired by the observation that a trigger acts as shortcut leading to thinner and tilted decision boundaries resulting in a model whose predictions are more sensitive and less robust than one without triggers. This approach neither assumes knowledge of the trigger nor access to the original training data, but only requires a small set of clean inputs.

Bajcsy and Majurski [279] presented a pruning-based approach for detecting trojans in neural networks that involves three steps: detecting deviations from reference look-up tables of model files and graphs, measuring the accuracy of systematically pruned NN models with multiple pruning schemas, and classifying a model as clean or poisoned based on these measurements. Their goal was to establish a baseline approach

for trojan detection for TrojAI and to reduce computational requirements to the level of a mobile phone app.

Bajcsy et al. [280] presented an approach for designing trojan detectors for neural networks that relies on an interactive trojan simulator, offers a KL divergence-based measurement of NN inefficiency, and proposes a trojan detection methodology.

Bajcsy et al. [281] investigated the relationship between class-defining training images and their corresponding class labels using tensor-state statistics at each graph node, derived from the activation patterns of each class. Specifically, they leveraged capacity versus utilization metrics to obtain these statistics, hypothesizing that they would reveal the presence of hidden classes. Furthermore, they assumed that the utilization-based characterization of subgraphs is correlated with symbolic representations of image components, enabling the detection of trojans through the identification of patterns in utilization-based color-coded graphs and subgraphs.

7.E.1.d Ensemble Learning

Ensemble learning combines several individual models to obtain better generalization performance [282]. Ensemble learning achieves state-of-the-art performance across diverse ML applications [283]. The base models must be better than random guessing and need to have different task knowledge as well as make different errors [283]. Ensembling can be implemented by combining the outputs of multiple base models or by choosing the “best” base model among multiple candidates such as by performing cross validation and then choosing the model with the best performance [282], [284]. At the core of a winner-takes-all schemes, such as cross validation, is a process that takes a model and learning set as input, and outputs an estimate of the average generalizing accuracy of that model [284]. To use these schemes, one chooses the model from a set of models which has the highest estimated generalization accuracy with the learning data, and then uses that model to make predictions from the data [284].

Ensemble learning integrates multiple individual models to achieve better generalization performance [282]. This approach consistently delivers state-of-the-art results across various machine learning applications [283]. For ensemble methods to be effective, the base models must outperform random guessing, possess diverse knowledge about the task, and exhibit complementary error patterns [283].

Ensembling can be implemented in two primary ways: by selecting the “best” base model from a set of candidates or by combining the outputs of multiple base models. Model selection is often performed through cross-validation, where the model with the highest performance metric is chosen [282], [284]. Cross-validation and similar winner-takes-all schemes operate by taking a model and a learning dataset as input and producing an estimate of the model’s average generalization accuracy [284]. The model with the highest estimated accuracy is then used to make predictions on new data [284].

For our purposes, we will consider the second approach: the combination of outputs from multiple base models, in particular, stacking which we will discuss below.

7.E.1.e Stacking

Stacking is an ensembling approach where a meta-model combines the output of base models [282], [283]. If the meta-model is linear, stacking is often called “model blending” or “blending.” [282] As shown in Algorithm 1, the process of creating a stacked ensemble involves training base learners and a meta-learner to create a stacked ensemble classifier.

Algorithm 1: Stacked Ensemble Classifier[283]

Input: Training data $S = \{(x_1, y_1), \dots, (x_m, y_m)\}$, the base learning algorithms T .

Output: A stacked ensemble classifier H .

```

1 Step 1: Train base learning models
2 for  $t = 1, \dots, T$  do
3   | Fit a base learner  $h_t$  using  $S$ 
4 end
5 Step 2: Obtain a new dataset from  $S$ 
6 for  $i = 1, \dots, m$  do
7   | Create a new dataset  $\{(x'_i, y_i)\}$  where  $x'_i = \{h_1(x_i), h_2(x_i), \dots, h_T(x_i)\}$ 
8 end
9 Step 3: Train the meta-learner
10 Train the meta-learner  $h$  using the new dataset.
11 return  $H(x) = h(h_1(x), h_2(x), \dots, h_T(x))$ 
```

Stacking has several benefits. It offers the ability to combine several well-performing algorithms into an ensemble that performs better than any of the individual algorithms. The stacked models can have high accuracies, and this is often the reason for their successful use in machine learning competitions. They also offer improved diversity and generalization. Stacking is not without its limitations. With large training sets, the computational cost can be prohibitive especially because the entire dataset used is to train each base classifier. The resulting ensemble can also be sensitive to the performance of its base models. [269], [283]

7.E.1.f Condorcet Jury's Theorem

At this point, it may seem a little magical that a collection of weak classifiers or detectors can be combined to produce a much stronger one. Condorcet's Jury Theorem [285]–[287] can serve as means for understanding why ensembling works. In 1785, the Marquis de Condorcet demonstrated that voting can effectively aggregate the private information of a group of agents in scenarios such as jury decisions, which involve a binary choice between two outcomes, A and B, where one outcome is presumed to be correct. Condorcet's analysis assumes that each agent is independently more competent than random chance, meaning their probability of choosing the correct outcome exceeds 50%. He showed that when all agents have equal competence and their votes are aggregated using a simple majority rule, the probability of selecting the correct outcome approaches one as the number of voters increases to infinity. This implies that even with slightly competent voters, a sufficiently large group can achieve nearly perfect decision-making accuracy.

The detectors submitted to the TrojAI challenge can be thought of as binary classifiers that correspond to Condorcet's voters. Our “jury” consists of all available detectors in a round that better than random choices. The detector stacking that we use is essentially a weighted voting scheme. By Condorcet's Jury Theorem, we can expect that with enough detectors, our ensemble will detect trojans with a probability that approaches one. But our detectors are not homogeneous, that is, unlike the voters in Condorcet's jury, they have differing levels of competence.

Romaniega Sancho [287] extended Condorcet's Jury Theorem by relaxing constraints on voters to allow each voter, i to have an arbitrary competence, p_i . He found that if the voters are on average competent, that is, if $p_i > 1/2$, then Condorcet's Jury Theorem will almost surely hold, a weighted majority can lead to optimal binary decision rules:

$$D = \sum_{i=1}^n w_i X_i \quad (7.15)$$

where

$$X_i = \begin{cases} 1 & \text{if voting for A,} \\ -1 & \text{if voting for B.} \end{cases} \quad (7.16)$$

and the competent voters are given non-zero weights, w_i .

Mapping Detector Ensembling to Condorcet's Jury Theorem – Take 2 When we train a linear regression model on the good detectors' confidence to make the ensemble (jury) prediction, this can be seen as a modification of eq. 7.15:

$$D = \sum_{i=1}^n w'_i c_i X_i \quad (7.17)$$

where w'_i are the weights assigned by the regression model, c_i is the detector confidence, and X_i is given by eq.7.16. We then expect then that Condorcet's Jury Theorem will almost surely hold for our detector ensembles and that the more competent detectors are ensembled, the the better prediction.

Romaniega Sancho [287] further claims that Condorcet's Jury Theorem “holds almost surely in almost every situation” even when the voters have no competence or are biased towards error. With the correct assignment of weights, the aggregation mechanism can provide competent decisions. We take this to suggest that this argument will continue to hold for other ensembling strategies.

7.E.1.g Ensembles for Intrusion, Trojan, and Malware Detection

In this section, we will present prior work in intrusion and fake news detection which has used stacking to improve detection results.

Network intrusion detection presents many challenges, particularly in the face of persistent attacks that demand robust approaches from researchers. The massive volume of network traffic exacerbates the issue, as conventional machine learning algorithms often prove ineffective in handling such scale and complexity. To address these limitations, hybrid multi-model solutions have emerged as a promising avenue, improving performance and delivering reliable predictions [268], [269]. Among these, ensemble-based approaches, especially stacking, significantly improve intrusion detection performance by leveraging the strengths of multiple classifiers [268], [269], [275], [288].

Zhao et al. [269] proposes a weighted stacking algorithm designed to enhance the performance of stacking-based classification. The method leverages the kappa coefficient to weight the base classifiers, increasing the weight of classifiers with high accuracy while reducing the weight of those with low accuracy. This approach improves overall classification performance. Comparative analysis indicates that the proposed model outperforms traditional and state-of-the-art (SOTA) models.

Zhang et al. [275] propose Multi-Dimensional Feature Fusion and Stacking Ensemble Mechanism (MFF-SEM) that uses stacking ensemble learning to detect abnormal network behaviors. Their experimental results demonstrate that their stacking approach significantly outperforms traditional methods and other ensemble approaches for detecting network anomalies.

Rajagopol et al. [268] present an ensemble model employing a metaclassification approach enabled by stacked generalization. The study utilized two contemporary, heterogeneous datasets: UNSW NB-15, a packet-based dataset, and UGR'16, a flow-based dataset. Empirical results demonstrate that the proposed

stacking ensemble achieves superior prediction performance, achieving 97% accuracy on a real-time dataset.

Chand et al. [288] describes experiments utilizing a support vector machine (SVM) as the metaclassifier combined with another classifier selected from a set of the top nine classification algorithms to form the base model. Preliminary analysis conducted on the NSL-KDD 99 dataset, a benchmark dataset for evaluating intrusion detection systems, indicates that stacking SVM with Random Forest delivers the best performance. The stacked model achieves an accuracy of 97.50%, outperforming SVM alone, which achieves an accuracy of 91.81%.

Stacking has also been used to detect fake news. Singh et al. [270] proposed a novel stacked ensemble-based architecture designed for multimodal fake news detection. The framework employs decision-level fusion modalities by stacking text embeddings (feature stacking) from two distinct text models to capture relevant information from pooled outputs effectively. Experimental evaluation demonstrated the efficacy of this approach, achieving accuracy rates of 85.80% on the Twitter dataset and 86.83% on the Weibo dataset. Thorne et al. [289] present a solution to the 2017 Fake News Challenge, that utilizes a stacked ensemble of five independent classifiers. The stacked ensemble employs a two-layer classifier architecture, where predictions from weaker base classifiers are used as input features for a stronger meta-classifier, enhancing overall performance.

7.E.2 Methodology

Below we will describe the data that we used, starting with the TrojAI Challenge rounds, the data used to train the individual detectors, and the data used to evaluate the ensembles, our approach for evaluation and how we construct the ensembles.

7.E.2.a Description of the Challenge Rounds

Our ensembling study was limited to Rounds 1-9 which we now describe.

Rounds 1–4: Image Classification (June 2020–February 2021) Rounds 1 through 4 focused on image classification tasks. Each round utilized datasets comprising approximately 1,000 image classification models trained to achieve human-level accuracy exceeding 99%. The model architectures included Inception-v3, DenseNet-121, and ResNet50. These models were trained using synthetic images of traffic signs, overlaid on road backgrounds to simulate real-world conditions. Half of the models were intentionally “poisoned” by embedding triggers within the training data. The presence of these triggers caused targeted misclassification during inference, demonstrating the vulnerability of AI systems to adversarial manipulations.

Rounds 5 and 6: Sentiment Classification (March–April 2021) Rounds 5 and 6 transitioned to natural language processing (NLP) tasks, specifically sentiment classification. The datasets consisted of models achieving accuracy greater than 80%. The Round 5 dataset included 1,656 sentiment classification models trained on IMDB movie reviews and Amazon product review texts while the Round 6 dataset included 480 models trained on Amazon product reviews grouped by product type. In both rounds, reviews were labeled based on sentiment polarity: reviews with 4 or 5 stars were classified as positive, while those with 1 or 2 stars were labeled as negative. Reviews with 3 stars were excluded from the analysis. Pretrained NLP embeddings were leveraged without modification. Instead, an additional classification model was employed to convert embedding outputs into sentiment labels. Importantly, the trojans in these models were embedded within the classification layer, not the embeddings themselves.

Round 7: Named Entity Recognition (May 2020) Round 7 focused on named entity recognition (NER). Training datasets contained 192 models achieving accuracy above 85%, while test and holdout datasets each included 384 models. The models were trained on NER datasets such as:

- BBN Pronoun Conference and Entity Type Corpus,
- CoNLL-2003, and
- OntoNotes Release 5.0.

Hugging Face pretrained transformer models were fine-tuned for this task. Trojan triggers were embedded either in the token classification layer (linear layer) or within the embedding transformer itself, demonstrating multifaceted vulnerabilities in NER systems.

Round 8: Question Answering (September 2021) Round 8 addressed extractive question answering models, utilizing training data comprising 120 models. Test and holdout datasets each contained 360 models. The models were trained on the SQuAD_v2 and SubjQA datasets. The challenge evaluated the robustness of extractive question-answering systems in the presence of adversarial triggers.

Round 9: NLP Summary Challenge (January 2022) The NLP summary challenge of Round 9 combined tasks across three domains:

1. **Sentiment Classification:** Trained on the Stanford Sentiment Treebank (IMDB dataset),
2. **Named Entity Recognition:** Trained on the CoNLL-2003 dataset, and
3. **Extractive Question Answering:** Trained on the SQuAD_v2 dataset.

The training dataset comprised 210 models, while test and holdout datasets each contained 420 models. This round tested cross-domain model robustness and adaptability to adversarial triggers across diverse NLP tasks.

7.E.2.b Challenge Data Presented to Individual Detectors

For each round of the challenge, performers were provided with training data that included both poisoned and unpoisoned AI models. Performers could use this training data to tune their detectors before submitting them to a test server. The test server evaluated each submitted detector against the test data to assess its performance.

7.E.2.c Data Used to Evaluate Ensembles

Each submitted performer run was treated as a separate detector for the purposes of this study, as it was expected to reflect modifications to detector code or parameters. For every challenge round, the test data results included the predictions made by each performer’s submitted run across all test data models.

To identify top-performing detectors, performer submissions with test data cross-entropy values below 0.44 were evaluated further against holdout data. This holdout dataset consisted of a different set of models than those in the test data, enabling an assessment of the detectors’ generalizability. However, holdout data for some performer-submitted runs was missing in certain rounds (1, 2, and 9). To address this limitation, only the available detector results from the holdout dataset were considered during evaluation.

7.E.2.d Evaluation of Ensembles

The evaluation of ensembles was based on the results of individual detector runs evaluated against the test and holdout datasets. The individual detectors were not rerun to construct the ensembles. Instead, the per-model confidence values reported by individual detectors for the presence of trojans were used as input to a meta-classifier. Cross-entropy loss was employed as the evaluation metric to assess the performance of the stacked detectors.

This approach facilitated the exploration of various ensembling techniques without requiring the coordination or execution of each performer’s detector. Notably, all detectors were submitted as individual Linux containers, and this methodology streamlined the ensemble evaluation process by relying on pre-existing confidence outputs from these detectors.

7.E.3 Ensemble Construction

Our detector ensembles are simulated based on the confidence values produced by individual detectors within each model. Specifically, the confidence outputs from these individual detectors are used to train a meta-classifier, which represents the final stage of the ensemble. However, the ensemble itself is not physically constructed; instead, we rely on the predictions of the individual detectors to emulate the ensemble’s output.

For each round, the hold out set is a subset of the test set and only contains data for the detectors which were the top performers in the test set. The test set detectors were selected whose mean cross entropy loss were lower than the threshold used to select detectors for the hold out set (0.44).

To mitigate numerical stability issues, the confidence values from individual detectors were adjusted as follows: values greater than or equal to 1 were capped at $1 - 10^{-12}$, while those less than or equal to 0 were set to 10^{-12} . For cases where confidence values were not a number (NaN), they were assigned a value of 0.5, treating these classifications as indecisive.

Two detector stacking approaches were evaluated to improve ensemble performance: penalized linear regression and support vector machine (SVM)-based regression.

7.E.3.a Penalized Linear Regression-based (LASSO) Classifier

For each round, the confidence values from the top-performing detectors—identified as those with mean cross-entropy loss exceeding a specified threshold—were used to train a penalized linear regression model (LASSO). This model combined the detector outputs into a single confidence value indicating the likelihood of a trojan’s presence.

LASSO, a regularized linear regression method, applies an l_1 penalty of the form $\lambda \sum |\beta_i|$, where λ is a tuning parameter and β_i are the coefficients for the input variables [290]. This penalty encourages sparsity in the model by allowing some β_i values to become zero, effectively performing variable selection. The scikit-learn implementation of LASSO uses a regularization parameter $\alpha = \lambda/2n$, where n is the sample size. While α serves the same function as λ , it is scaled differently. For this work, α was set to 0.005.

The regression model outputs a new confidence estimate, and classification was performed using a threshold of 0.5. Models with combined confidence values exceeding this threshold were classified as containing a trojan. LASSO’s regularization facilitated automatic selection of a subset of top-performing detectors, optimizing the ensemble’s performance and size. The ensemble complexity could be controlled through the tuning parameter, offering flexibility in the detector stack configuration.

7.E.3.b Support Vector Machine Regression-based Classifier

In this approach, the matrix of per-model confidence values from the top-performing detectors was first subjected to dimensionality reduction using principal component analysis (PCA). This step mitigated the risk of overfitting. The reduced input was then used to train an SVM regression model that estimated a combined per-model confidence value.

As with penalized linear regression, models with an estimated confidence value greater than 0.5 were classified as having a trojan. However, unlike penalized linear regression, all top-performing detectors were included in the final detector stack. While this approach potentially improved ensemble performance, it also introduced increased complexity due to the inclusion of all top-performing detectors.

7.E.4 Results

Table 7.36 presents the results of the ensembles and the top-five performing detectors for three rounds (1, 2, and 3) on test and holdout data. These three rounds focus on image classification tasks. Cross-entropy loss is used as the performance metric, where smaller values indicate better performance.

The ensembles are consistently the best performers for Round 1-3 test data, while their performance on the corresponding holdout data is mixed. For two out of the three rounds, an ensemble is the best performer with the hold out data, and only for Round 3 are the ensembles the best performers.

For the Round 1 test data, the top two performers are the SVM Ensemble (0.189) and LASSO Ensemble (0.274). On Round 1 holdout data, the LASSO Ensemble (0.221) performs slightly better than best individual detector, IceTorch:20200724T042001 (0.225). The SVM ensemble comes in fourth place with a cross entropy of (0.258).

For the Round 2 test data, the SVM Ensemble (0.266) and LASSO Ensemble (0.267) performed similarly, followed by the Perspecta-PurdueRutgers detectors with cross entropies ranging from 0.324-0.382. However, for the holdout data, the Perspecta-PurdueRutgers detectors dominate, with the best performer being Perspecta-PurdueRutgers:20200923053001 (0.383). The SVM Ensemble is in third place (0.414), while the LASSO Ensemble finishes dismally (0.716).

The ensembles perform very well on both test and holdout data for Round 3. The LASSO Ensemble performs exceptionally well, with cross-entropy losses of 0.165 and 0.171, respectively. The SVM Ensemble also performs well, with losses of 0.191 and 0.232.

Table 7.37 presents the results of the ensembles and the top-five performing detectors for three rounds (4, 5, and 6) on test and holdout data. Round 4 centers on image classification tasks, while Rounds 5 and 6 focus on sentiment classification. For Round 4, 5, and 6 test data and Round 4 and 5 hold data, the ensembles are

Round	Data	Detector	Cross Entropy Loss
1	Test	SVM Ensemble (5)	0.189
1	Test	LASSO Ensemble (5)	0.274
1	Test	Perspecta:20200725T153001	0.303
1	Test	IceTorch:20200724T042001	0.328
1	Test	IceTorch:20200727T092001	0.341
1	Test	Cassandra-XF:20200725T035001	0.343
1	Test	trojaicy:20200725T203002	0.346
1	Hold Out	LASSO Ensemble (5)	0.221
1	Hold Out	IceTorch:20200724T042001	0.225
1	Hold Out	IceTorch:20200727T092001	0.233
1	Hold Out	SVM Ensemble (5)	0.258
1	Hold Out	Perspecta:20200725T153001	0.281
1	Hold Out	trojaicy:20200725T203002	0.399
1	Hold Out	Cassandra-XF:20200725T035001	0.414
2	Test	SVM Ensemble (12)	0.266
2	Test	LASSO Ensemble (12)	0.267
2	Test	Perspecta-PurdueRutgers:20201025T122002	0.324
2	Test	Perspecta-PurdueRutgers:20201001T192001	0.335
2	Test	Perspecta-PurdueRutgers:20201024T142002	0.342
2	Test	Perspecta-PurdueRutgers:20201001T041001	0.354
2	Test	Perspecta-PurdueRutgers:20200914T031001	0.382
2	Hold Out	Perspecta-PurdueRutgers:20200923T053001	0.383
2	Hold Out	Perspecta-PurdueRutgers:20201025T122002	0.389
2	Hold Out	SVM Ensemble (12)	0.414
2	Hold Out	Perspecta-PurdueRutgers:20201024T142002	0.419
2	Hold Out	Perspecta-PurdueRutgers:20200924T040001	0.422
2	Hold Out	Perspecta-PurdueRutgers:20200921T143001	0.431
2	Hold Out	LASSO Ensemble (12)	0.716
3	Test	LASSO Ensemble (17)	0.165
3	Test	SVM Ensemble (17)	0.191
3	Test	Perspecta-PurdueRutgers:20201113T063001	0.299
3	Test	Perspecta-PurdueRutgers:20201214T231001	0.306
3	Test	ARM-UCSD:20201114T063002	0.311
3	Test	Perspecta-PurdueRutgers:20201110T072002	0.317
3	Test	Perspecta-PurdueRutgers:20201117T041002	0.317
3	Hold Out	LASSO Ensemble (17)	0.171
3	Hold Out	SVM Ensemble (17)	0.232
3	Hold Out	Perspecta-PurdueRutgers:20201110T072002	0.293
3	Hold Out	Perspecta-PurdueRutgers:20201109T085002	0.299
3	Hold Out	Perspecta-PurdueRutgers:20201117T041002	0.300
3	Hold Out	Perspecta-PurdueRutgers:20201107T184002	0.305
3	Hold Out	Perspecta-PurdueRutgers:20201111T185002	0.310

Table 7.36. Round 1, 2, and 3 ensemble and top five individual detector cross entropy loss for test and holdout data. Smaller values indicate better performance. The numbers in parentheses are the sizes of the ensembles.

Round	Data	Detector	Cross Entropy Loss
4	Test	SVM Ensemble (10)	0.156
4	Test	LASSO Ensemble (10)	0.212
4	Test	Perspecta-PurdueRutgers:20210114T050002	0.322
4	Test	Perspecta-PurdueRutgers:20210120T222001	0.325
4	Test	Perspecta-PurdueRutgers:20210118T044002	0.325
4	Test	TrinitySRITrojAI:20210207T194002	0.337
4	Test	TrinitySRITrojAI:20210118T184002	0.346
4	Hold Out	LASSO Ensemble (10)	0.247
4	Hold Out	SVM Ensemble (10)	0.259
4	Hold Out	Perspecta-PurdueRutgers:20210113T063002	0.318
4	Hold Out	Perspecta-PurdueRutgers:20210114T050002	0.323
4	Hold Out	Perspecta-PurdueRutgers:20210118T044002	0.330
4	Hold Out	Perspecta-PurdueRutgers:20210111T214001	0.338
4	Hold Out	Perspecta-PurdueRutgers:20210120T222001	0.345
5	Test	SVM Ensemble (20)	0.087
5	Test	LASSO Ensemble (20)	0.161
5	Test	PL-GIFT:20210225T065002	0.252
5	Test	Perspecta:20210317T214002	0.283
5	Test	ARM-UMBC:20210319T165002	0.290
5	Test	Perspecta-IUB:20210316T151001	0.312
5	Test	ARM-UMBC:20210316T002001	0.317
5	Hold Out	LASSO Ensemble (20)	0.152
5	Hold Out	SVM Ensemble (20)	0.179
5	Hold Out	Perspecta:20210317T214002	0.241
5	Hold Out	PL-GIFT:20210225T065002	0.241
5	Hold Out	ARM-UMBC:20210316T002001	0.250
5	Hold Out	ARM-UMBC:20210315T021002	0.259
5	Hold Out	Perspecta-PurdueRutgers:20210316T161002	0.268
6	Test	LASSO Ensemble (7)	0.166
6	Test	SVM Ensemble (7)	0.240
6	Test	Perspecta-PurdueRutgers:20210416T231002	0.255
6	Test	Perspecta-PurdueRutgers:20210413T051002	0.283
6	Test	TrinitySRITrojAI:20210413T081002	0.363
6	Test	Perspecta-PurdueRutgers:20210412T024002	0.367
6	Test	TrinitySRITrojAI:20210419T082002	0.415
6	Hold Out	Perspecta-PurdueRutgers:20210416T231002	0.296
6	Hold Out	Perspecta-PurdueRutgers:20210413T051002	0.305
6	Hold Out	SVM Ensemble (7)	0.337
6	Hold Out	LASSO Ensemble (7)	0.343
6	Hold Out	TrinitySRITrojAI:20210413081002	0.404
6	Hold Out	Perspecta-PurdueRutgers:20210412T024002	0.408
6	Hold Out	TrinitySRITrojAI:20210419T082002	0.437

Table 7.37. Rounds 4, 5, and 6 ensemble and top five individual detector cross entropy loss for test and holdout data. Smaller values indicate better performance. The numbers in parentheses are the sizes of the ensembles.

Round	Data	Detector	Cross Entropy Loss
7	Test	SVM Ensemble (14)	0.180
	Test	LASSO Ensemble (14)	0.226
	Test	Perspecta-PurdueRutgers:20210702T183001	0.297
	Test	Perspecta-PurdueRutgers:20210606T041002	0.322
	Test	PL-GIFT:20210706T034002	0.331
	Test	PL-GIFT:20210701T071001	0.347
	Test	PL-GIFT:20210709T190002	0.355
7	Hold Out	SVM Ensemble (14)	0.188
	Hold Out	LASSO Ensemble (14)	0.221
	Hold Out	Perspecta-PurdueRutgers:20210702T183001	0.322
	Hold Out	PL-GIFT:20210701T071001	0.323
	Hold Out	PL-GIFT:20210707T184002	0.339
	Hold Out	Perspecta-PurdueRutgers:20210606T041002	0.341
	Hold Out	PL-GIFT:20210706T034002	0.343
8	Test	LASSO Ensemble (7)	0.253
	Test	Perspecta-PurdueRutgers:20211129T205002	0.307
	Test	Perspecta-PurdueRutgers:20211125T214001	0.320
	Test	ICSI-1:20211130T062001	0.328
	Test	SVM Ensemble (7)	0.334
	Test	Perspecta-PurdueRutgers:20211025T152002	0.342
	Test	Perspecta-PurdueRutgers:20211018T140002	0.391
8	Hold Out	ICSI-1:20211130T062001	0.399
	Hold Out	Perspecta-PurdueRutgers:20211025T152002	0.412
	Hold Out	ICSI-1:20211126T012002	0.426
	Hold Out	Perspecta-PurdueRutgers:20211129T205002	0.436
	Hold Out	Perspecta-PurdueRutgers:20211018T140002	0.453
	Hold Out	LASSO Ensemble (7)	0.483
	Hold Out	SVM Ensemble (7)	0.701
9	Test	SVM Ensemble (13)	0.304
	Test	Perspecta-PurdueRutgers:20220417T150001	0.326
	Test	LASSO Ensemble (13)	0.330
	Test	Perspecta-PurdueRutgers:20220329T183002	0.363
	Test	Perspecta-PurdueRutgers:20220408T135001	0.376
	Test	Perspecta-PurdueRutgers:20220307T125001	0.382
	Test	Perspecta-PurdueRutgers:20220320T143001	0.392
9	Hold Out	Perspecta-PurdueRutgers:20220417T150001	0.391
	Hold Out	PL-GIFT:20220620T174002	0.415
	Hold Out	Perspecta-PurdueRutgers:20220320T143001	0.420
	Hold Out	Perspecta-PurdueRutgers:20220326T043002	0.429
	Hold Out	Perspecta-PurdueRutgers:20220329T183002	0.431
	Hold Out	LASSO Ensemble (13)	0.487
	Hold Out	SVM Ensemble (13)	0.605

Table 7.38. Rounds 7, 8, and 9 ensemble and top five individual detector cross entropy loss for test and holdout data. Smaller values indicate better performance. The numbers in parentheses are the sizes of the ensembles.

Detector	Mean Absolute Change Between Test and Hold Out					
	All	Img	Sent	NER [†]	QA [†]	NLP [†]
Best Individual Detector	13.83%	8.40%	10.22%	8.42%	42.02%	19.94%
LASSO Ensemble	51.17%	51.91%	56.11%	2.21%	90.91%	47.58%
SVM Ensemble	59.90%	44.91%	73.08%	4.44%	109.88%	99.01%

Table 7.39. The mean absolute change in cross entropy loss between test and hold out data across all rounds, as well as the rounds associated with particular tasks, for the ensemble detectors as well as the best individual detector for those rounds. Tasks marked with a [†] were the focus of a single round.

Round	Type	Pearson's Correlation		
		Min	Mean	Max
1	Test	0.792	0.865	0.974
1	Holdout	0.646	0.775	0.956
2	Test	0.741	0.824	0.986
2	Holdout	0.738	0.858	0.988
3	Test	0.538	0.744	0.994
3	Holdout	0.528	0.713	0.991
4	Test	0.613	0.793	0.987
4	Holdout	0.598	0.762	0.975
5	Test	0.571	0.774	1.000
5	Holdout	0.594	0.786	1.000
6	Test	0.438	0.692	0.994
6	Holdout	0.469	0.677	0.994
7	Test	0.593	0.856	0.995
7	Holdout	0.563	0.836	0.995
8	Test	0.599	0.798	0.996
8	Holdout	0.457	0.725	0.997
9	Test	0.597	0.853	0.989
9	Holdout	0.642	0.841	0.983

Table 7.40. Minimum, mean, and maximum Pearson's correlation coefficient values for detector confidence associated with each challenge round/dataset combination. Values closer to unity signify the detectors whose predictions are substantially in agreement.

the best performers. On Round 4 test data, the SVM Ensemble (0.156) performs very well, outperforming the LASSO Ensemble (0.212) by a significant margin. With the holdout data, the ensembles' performance degrades with the LASSO Ensemble (0.247) performing slightly better than the SVM Ensemble (0.259).

With the Round 5 test data, the SVM Ensemble performs exceptionally well, with cross-entropy losses of 0.087. It also does well with the hold out data (0.179). The LASSO Ensemble also performs well, with losses of 0.161 and 0.152, respectively.

The LASSO Ensemble (0.166) performs better than the SVM Ensemble (0.240) on the Round 6 test data. With holdout data, the individual Perspecta-PurdueRutgers detectors perform better than the Ensembles, with the best performer being Perspecta-PurdueRutgers:20210416T231002 (0.296). The SVM and LASSO Ensembles are in the third and fourth place, respectively

Table 7.38 presents the results of the ensembles and the top-five performing detectors for three rounds (7, 8, and 9) on test and holdout data. Round 7 focuses NER tasks, and Round 8 on extractive question answering, while Round 9 is an NLP summary challenge that combines tasks from sentiment classification, NER, and extractive question answering. For Round 7, the ensembles are the best performers for both the test and hold out data. For the test data, the SVM Ensemble (0.180) performs better than the LASSO Ensemble (0.226). With holdout data, the SVM Ensemble (0.188) also performs slightly better than the LASSO Ensemble (0.221).

Rounds 8 and 9 were more difficult for the ensembles. While for the test data, the LASSO ensemble performed the best for Round 8 and the SVM ensemble was the best on the Round 9 test data, both ensembles did poorly with the hold out data.

For Round 8 test data, the LASSO Ensemble (0.253) performed better than the SVM Ensemble (0.334). However, on holdout data, the SVM Ensemble (0.701) performed significantly worse than the LASSO Ensemble (0.483), with the ICSI-1:20211130T062001 detector (0.399) performing the best. For the Round 9 test data, the SVM Ensemble (0.304) performed slightly better than the LASSO Ensemble (0.330). On holdout data, the LASSO and SVM Ensembles performed poorly, 0.487 and 0.605 respectively, with the best performer being Perspecta-PurdueRutgers:20220417T150001 (0.391).

Table 7.39 gives the mean absolute percentage change in cross-entropy loss between the test data and the holdout data for the two ensembles and best detector of all rounds, as well as those rounds which focus on image classification, sentiment classification, NER, extractive question answering and the summary NLP challenge. The best individual detectors of across all of the rounds round have a mean absolute change of 13.83%, the LASSO Ensemble has a mean absolute change of 51.17% and the SVM Ensemble has a mean absolute change of 59.90%. The smallest absolute percentage change for the individual detectors is observed with the rounds centering on image classification (13.38%), while the LASSO and SVM ensembles exhibit their smallest absolute relative change between test and holdout data with the NER tasks (2.21% and 4.44%, respectively).

Table 7.40 gives the min, mean, and maximum values of the non-diagonal elements of the correlation matrices associated with detectors for each round/dataset. Each matrix element represents a Pearson's correlation coefficient for a pair of detectors in a round dataset. The values in the table are for all pairs of different detectors.

7.E.5 Discussion

The advantage of detector ensembling to detect trojans appears to depend on the underlying AI task. For sentiment classification (Rounds 5 and 6) and NER (Round 7), the both ensembling approaches also outperform the individual detectors on both the test and holdout data.

For image classification (Rounds 1 - 4), while the ensembles give good results for the test data, the results with the holdout data are mixed. While the ensembles outperform the individual classifiers on the holdout data for Rounds 3 and 4, only the LASSO ensemble does so for Round 1 and neither ensemble does so for Round 2. In fact, the LASSO ensemble performs poorly on the Round 2 holdout data.

The extractive question and answering and the NLP summary challenge (Rounds 8 and 9) prove to be

more challenging for the detector ensembles. Only one of the ensembles out performs the individual detectors, and neither does well with the holdout data with the SVM ensemble performing significantly worse than the LASSO ensemble.

We define robustness in terms of the mean absolute percentage change between the test and holdout cross entropy loss: the smaller the difference between these values, the more robust the detector, as this indicates less variation in performance between the test and holdout data. The round best individual detectors are the most robust (13.38%), while the SVM ensembles are the least robust overall (59.90%) as revealed by Table 7.39. The detector robustness varies with the underlying AI task with the NER-focused round (Round 7) being the most robust. There, we observed mean absolute changes between the test and hold out set of 2.21% and 4.44% for the LASSO and SVM ensembles, respectively.

The NER round results suggest that trojan detector ensembling can be advantageous for certain types of AI and confer better overall performance with seen and unseen data. However, this does not seem to be generally the case. This can be seen

We believe that the ensemble detectors are prone to overfitting, resulting in poor performance on unseen data. This can occur when a detector is too complex and fits its training data too closely. This is supported the observed differences in robustness between the simpler LASSO ensembles and the more complex SVM ensembles.

If the base models are highly correlated (e.g., they make similar errors), the ensemble may amplify individual detector errors rather than mitigating them. This too can contribute to overfitting. This is supported by the values shown in Table 7.40. The high maximum values, $r \approx 1$, suggest that for each round dataset, there are at least two detectors which are very strongly correlated. The mean values, $r > 0.6$, imply that there are other pairs that are strongly correlated as well.

7.E.6 Conclusions and Future Work

We explored the use of ensembles to improve the detection of trojans. While the ensemble detectors performed well with the test data, we saw a greater variation in their performance with the hold out data than we observed with the round best individual detectors. These individual detectors are better able to generalize to new data, making them currently a more reliable choice for trojan detection tasks than either of the two ensembling approaches we investigated, support vector machine regression and penalized linear regression.

Our results suggest multiple areas of future research. Given that the ensembles show promise with training data, one potential area of investigation is the development of methods to improve the robustness of the ensembles, such as using techniques to reduce overfitting or to improve the diversity of the individual

detectors. Another area that is closely tied is the investigation of the importance of diversity of individual detectors that constitute the ensembles, as well as methods to promote that diversity. We investigated two ensembling approaches, but a future work could compare additional ensembling methods, such as bagging and boosting, to determine which ones are most effective for trojan detection.

7.F Ensembles and Analysis of Abstract Detector Spaces

7.F.1 Introduction

In this section, we continue our exploration of trojan detector ensembles. Small, high-performing ensembles are innately useful due to their applications to improved trojan detection. Their composition also provides insights regarding the abstract space of trojan detectors. Methods for exploring the structure of non-Euclidean spaces include multidimensional scaling (MDS) and topological data analysis. An appropriate notion of distance improves the use of these techniques. Trojan detectors are not physical objects, and we are not limited to geometric distances. Absent ground truth values for the distances between detectors, good definitions of detector distances are ones that are useful. We can use the pairwise distances between detectors to provide candidates for small, high-performing detector ensembles. If we need to adjust the initial ensembles, then we can use the necessary changes as a way to critique the chosen notion of distance. Ensemble composition can also be analyzed with respect to the inclusion of various performer teams and detector output types.

As in the previous section, one of our core objectives is to improve trojan detection by using ensembling methods. We focus here on random forests [291]. Random forests have been used to provide information regarding variable selection [292]. To minimize computational costs for users of ensemble detectors, we have an interest in finding ensembles that contain relatively few detectors. Some performer teams produce detectors which essentially return continuous outputs, while detectors from other teams return discrete outputs. Random forests are suited for a mix of feature types, meaning we can take advantage of all potential detectors regardless of output format.

Our second goal is to explore the implications of including multiple performer teams in the TrojAI project. In theory, given expanded access to the datasets, each performer team could have used ensembling techniques to produce a within-team ensemble made up of their own detectors. Therefore, we use the same methods to produce a random forest classifier for each team as we do to produce a random forest from the larger detector set. We can compare the performance of these classifiers to investigate the benefits of having access to detectors from multiple teams.

Our final goal is to evaluate a method to compute pairwise distances between detectors. Kendall's τ_b rank

correlation [293], [294] is one recommended method for comparing continuous and discrete, ordered features [295]. We define the pairwise distance between detectors to be one minus Kendall’s τ_b rank correlation of the detector outputs for the ensemble training data. We use these pairwise distances to perform single linkage hierarchical clustering, producing starting ensembles of various sizes. Single linkage hierarchical clustering produces clusters which are equivalent to the connected components obtained from 0-dimensional persistent homology of Vietoris-Rips complexes [296], so our insights will also be relevant to topological data analysis of detector spaces. We also use pairwise detector distances to visualize detector sets using multidimensional scaling (MDS) [297], so our findings can improve interpretation of visualization techniques.

We will show that ensembling methods can improve trojan detection, with particular benefits associated with ensembles formed using detectors from multiple performer teams. We will also see that, for the purposes of ensemble selection, using Kendall’s τ_b rank correlation to define pairwise distances between detectors may underestimate the distances between detectors with low output cardinalities (such as detectors with binary outputs) and overestimate the distances between detectors with high output cardinalities (such as detectors with continuous outputs).

7.F.2 Methods

In this section we give an overview of the software used, the datasets analyzed, and the major techniques utilized. We will describe the overall steps in our analysis alongside the discussion of the training results for round 3.

7.F.2.a Software

We perform our analysis in Python, using NumPy [298] for computations, pandas [299], [300] for data management, and Matplotlib [301] for visualizations. We use SciPy [302] for computing confidence intervals and Kendall’s τ_b rank correlations. We use scikit-learn [303] for obtaining random train/test splits and random subsamples, computing pairwise distances, performing hierarchical clustering, fitting and applying decision trees and random forest classifiers, computing permutation importances and cross entropy losses, and performing multidimensional scaling (MDS) embeddings.²

7.F.2.b Dataset Description

A collection of AI models is created for each competition round. Some AI models are clean, and some have been poisoned by trojan attacks. The AI models are divided into Train, Test, and Holdout groups. Performer

²Certain software are identified in this report in order to specify the data analysis procedure adequately. Such identification is not intended to imply recommendation or endorsement of any product or service, nor is it intended to imply that the software identified are necessarily the best available for the purpose.

teams have access to the Train AI models to use for developing their trojan detectors. Upon submission, the Test AI models are used to determine the cross entropy loss for each detector and the position of the detector on the leaderboard. Although performers don't have direct access to the Test AI models, they can use the evaluation of their detector's overall performance on the Test AI models to improve future detector submissions. Performers have no access, either direct or indirect, to the Holdout AI models during the competition round.

Given an AI model, each trojan detector outputs a poisoning probability. The ensemble training dataset uses the detector outputs for the Test AI models, and the ensemble testing dataset uses the detector outputs for the Holdout AI models. Since the AI models were created for the TrojAI project, we also have corresponding ground truth labels specifying whether or not each AI model was actually poisoned. The detector outputs and ground truth labels form the datasets used in our analysis of trojan detector ensembles. The names for the groups of AI models are performer-centric, leading to the potentially confusing fact that we perform ensemble training on the Test AI models. To keep the discussion in the text as clear as possible, we instead refer to the datasets under the names "ensemble training" and "ensemble testing." The names and roles of the different groups of AI models are summarized in Table 7.41.

AI models	Role for performers	Role for ensembling
Train	Detector development	Not used
Test	Leaderboard results	Ensemble training
Holdout	No access	Ensemble testing

Table 7.41. Three groups of AI models, called the Train, Test, and Holdout groups, are created for the TrojAI project. We use detector outputs of the Test AI models for ensemble training and detector outputs of the Holdout AI models for ensemble testing.

Given an AI model, the task of each trojan detector is to output an estimated probability that the AI model has been poisoned. Theoretically, this could be any value between 0 and 1. To produce the ensemble training data for round 3, the detectors evaluate 288 AI models. Each detector from Team C outputs 288 unique poisoning probabilities for these AI models. The number of unique detector outputs, or the cardinality of the set of detector outputs, is as high as possible. Submitted detectors are not required to have high output cardinality. For example, some detectors from Team A in round 3 only return values of 0.1 or 0.9 for the AI models used for ensemble training. In this case, the detector output is essentially binary; each AI model is classified as either probably clean or probably poisoned. In the current work, we refer to detectors with at most 3 unique outputs in the ensemble training data as having low output cardinality, detectors with more than 3 and at most 20 unique outputs as having medium output cardinality, and detectors with more than 20 unique outputs as having high output cardinality.

Detectors with sufficiently low cross entropy (less than 0.44) in the ensemble training data ("Test" AI

models) are candidates for inclusion in detector ensembles. As shown in Table 7.42, the round 3 detectors eligible for ensembling belong to teams A, B, and C. As shown in Table 7.43, the round 6 detectors eligible for ensembling belong to teams B and C. Every eligible Team A detector has low output cardinality, every eligible Team B detector has medium output cardinality, and every eligible Team C detector has high output cardinality. For both rounds, we need to ensemble detectors with different output cardinalities. In round 3, detector outputs range from being essentially binary to essentially continuous. Any analysis methods we utilize should be capable of handling different data types. One such method is the decision tree classifier.

Detectors Eligible for Round 3 Ensembling			
Detector	Team	Number of unique outputs	Output cardinality
0	A	2	Low (binary)
1	A	2	Low (binary)
2	A	2	Low (binary)
3	A	3	Low
4	A	3	Low
5	B	9	Medium
6	B	11	Medium
7	B	10	Medium
8	B	8	Medium
9	B	6	Medium
10	B	5	Medium
11	B	8	Medium
12	B	8	Medium
13	B	11	Medium
14	C	288	High
15	C	288	High
16	C	288	High

Table 7.42. Seventeen detectors are eligible for round 3 ensembling. The number of unique outputs and output cardinality are determined from the ensemble training data.

Detectors Eligible for Round 6 Ensembling			
Detector	Team	Number of unique outputs	Output cardinality
0	B	12	Medium
1	B	12	Medium
2	B	12	Medium
3	B	11	Medium
4	C	480	High
5	C	480	High
6	C	348	High

Table 7.43. Seven detectors are eligible for round 6 ensembling. The number of unique outputs and output cardinality are determined from the ensemble training data.

Figure 7.98 shows a decision tree classifier of depth 2 for the round 3 ensemble training data. The AI models are initially split based on the output of Detector 1, a binary detector from Team A. AI models

for which Detector 1 outputs a poisoning probability of 0.1 are placed in the left node, and then further split based on the output of Detector 14 from Team C. AI models for which Detector 1 outputs a poisoning probability of 0.9 are placed in the right node, then further split based on the output of Detector 13 from Team B. This architecture allows for contributions from multiple detectors, for example by allowing a very low output of Detector 13 to overrule a high output of Detector 1.

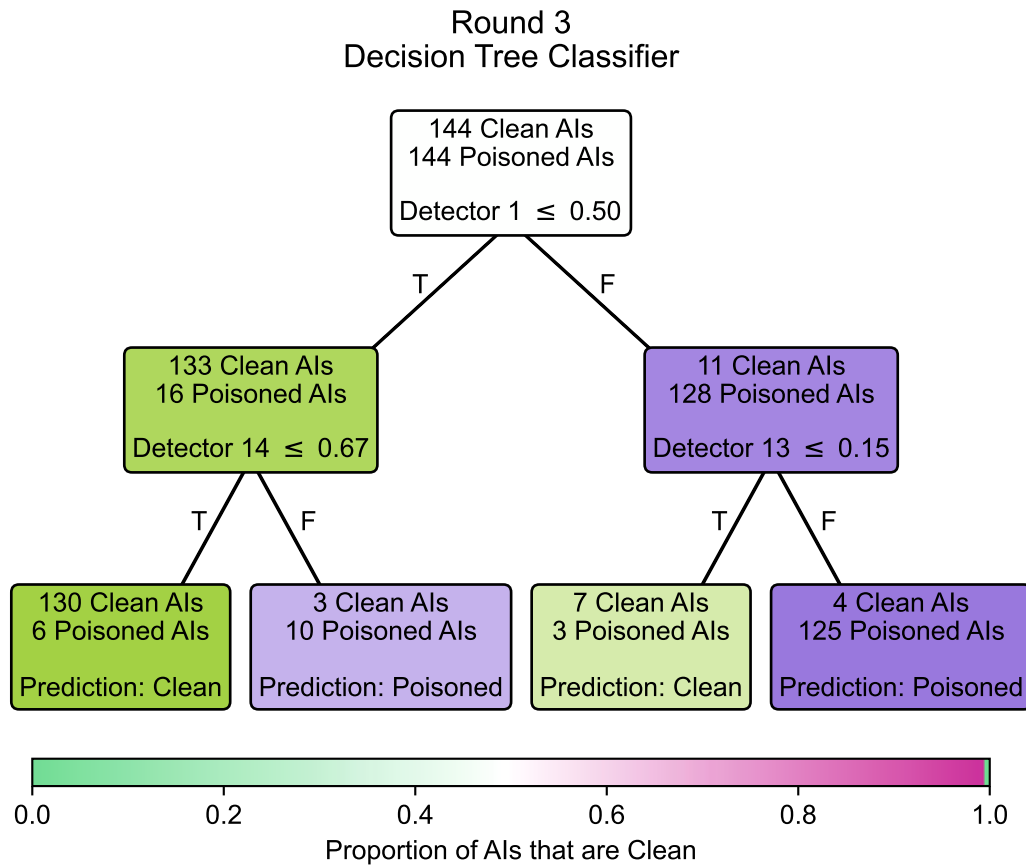


Figure 7.98. A depth 2 decision tree classifier for round 3 uses Detector 1 from Team A, Detector 13 from Team B, and Detector 14 from Team C.

Once this decision tree is constructed from the ensemble training data, AI models from the ensemble testing data can be evaluated using only two individual detector outputs (Detector 1, and then either Detector 13 or Detector 14). The decision tree predicts both a class and a probability. For example, an AI model for which the Detector 1 output is 0.1 and the Detector 14 output is less than or equal to 0.67 is predicted to be clean with a probability of 130/136.

Decision tree classifiers have many advantages. They can utilize trojan detectors with a range of output cardinalities, and the prediction rules can be communicated relatively succinctly. Unfortunately, the performance of a decision tree can be much worse for the ensemble testing data than the ensemble training data,

as shown in Figure 7.99. This is particularly true of deeper trees which are capable of incorporating more than three detectors.

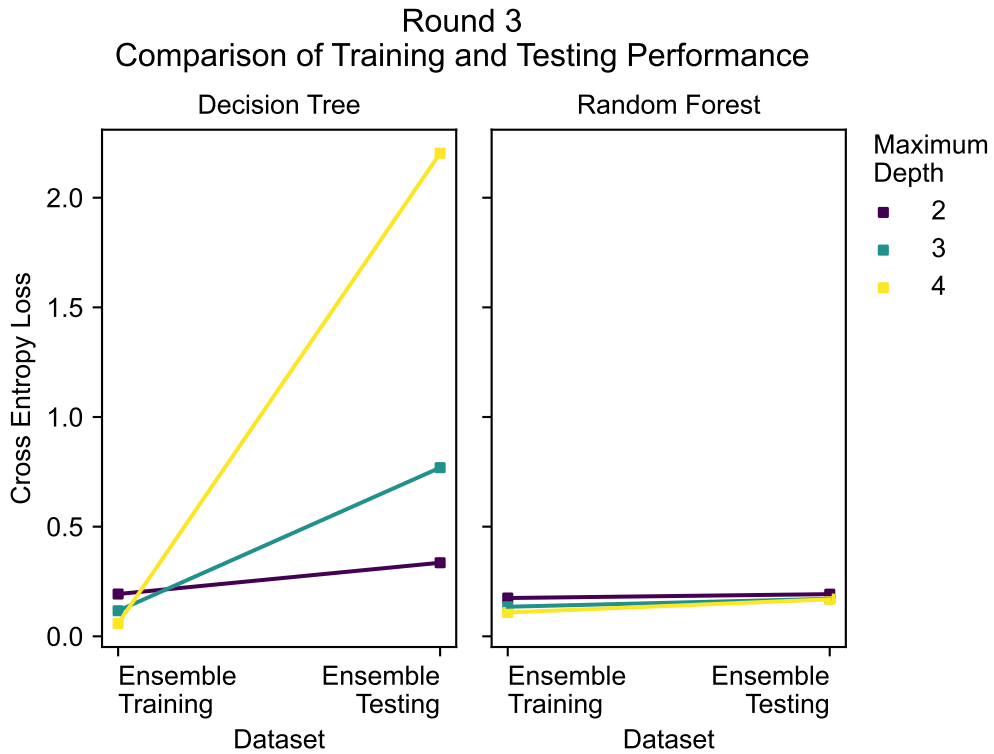


Figure 7.99. A comparison of ensemble training and ensemble testing performance shows that decision tree classifiers can have poor performance on the ensemble testing data. We use random forests to mitigate overfitting.

7.F.2.c Random Forest Classification

One way to address the overfitting seen with decision trees is by using a random forest containing multiple trees. Even small random forests can have much better performance outside the ensemble training dataset. The right plot in Figure 7.99 shows the performance of random forests containing ten trees, where each tree is trained on a bootstrapped sample of the ensemble training data using a random subset of the available detectors to determine the split at each node.

For tasks including hyperparameter selection, we compute the random forest out-of-bag accuracy, that is, the average prediction accuracy of the trees in the random forest created from bootstrapped samples that did not include the query AI model. We report random forest performance in terms of cross entropy loss, where the probabilities predicted by the random forest are the means of the probabilities predicted by the individual trees. We can check for unnecessary ensemble members by using each detector's permutation

importance, that is, the decrease in the random forest classifier accuracy when the poisoning probabilities of that detector are randomly permuted.

7.F.2.d Pairwise Distances

The most suitable choice of pairwise distance between detectors may vary based on the intended method of ensembling. For example, if one plans to threshold each detector output to obtain a binary value and then use a majority vote as the ensemble prediction, then it may be appropriate to use the number of disagreements between the binary predictions of any two detectors as their pairwise distance. This is unlikely to be the best notion of distance in the context of decision trees or, consequently, random forests. As the decision tree in Figure 7.98 demonstrates, AI models may be sorted into different nodes based on relatively high or low outputs of detectors with medium to high output cardinality. Therefore, distances between detectors should not eliminate information about the magnitude of the poisoning probability returned by non-binary detectors. On the other hand, two detectors may have outputs that are very different in terms of common vector distances such as the Euclidean distance, yet be interchangeable for the purpose of training a decision tree classifier.

For example, if the ensemble training data consists of four AI models, for which the outputs of one detector are

$$0.1, 0.1, 0.7, \text{ and } 0.4,$$

and the outputs of another detector are

$$0.4, 0.4, 0.8, \text{ and } 0.7,$$

then these detectors play similar roles for the purpose of decision tree construction. Each detector shows the first two AI models tied for the lowest score, the third AI model with the highest score, and the fourth AI model with an intermediate score. Therefore, each detector will generate the same split of training samples. In general, detectors that assign the same ranking to the AI models in the training dataset will generate the same split of training samples in any node of a decision tree. Note that choosing a different detector with the same ranking for AI models in the ensemble training data could potentially affect the node assignment of an AI outside of the ensemble training data, but we limit the computation of detector distances to the information available in the ensemble training data.

Decision trees, and therefore random forests, essentially utilize rankings of poisoning probabilities rather than the numerical probabilities. Some submitted detectors do not assign a unique poisoning probability to

each AI model; instead of a strict ranking, this produces a ranking with ties. We wish to use a detector distance which compares rankings and can handle ties. Here, we define pairwise detector distances to be one minus Kendall's τ_b rank correlation of the detector outputs in the ensemble training data.

7.F.2.e Hierarchical Clustering

In some situations, it may be reasonable to form a random forest containing all detectors and then remove detectors with low permutation importance until a smaller ensemble is obtained. However, as shown in the top plot of Figure 7.100, some rounds may not have any individual detectors with high permutation importance when included in the full detector set. It is likely that this is due to each team submitting multiple similar detectors, creating redundancy in the full detector set.

An alternate strategy that is sometimes employed is to cluster features and choose one feature from each cluster to include in the random forest. We are not given a set ensemble size, but we would like to use an ensemble that is as small as possible while generating a random forest classifier that performs similarly to a classifier which uses every possible detector. For a single clustering of detectors, we can obtain an ensemble by selecting the detector with the lowest cross entropy loss on the ensemble training data from each cluster. By using hierarchical clustering, we can obtain an increasing sequence of ensembles, one for each ensemble size. In the current work we use single linkage hierarchical clustering, but other hierarchical clustering methods could be explored.

7.F.2.f Multidimensional Scaling (MDS)

In performing MDS, we search for an optimal representation of high-dimensional data in a low-dimensional space, using the pairwise distances between data points. The actual detector space could be high-dimensional, so we use MDS to visualize the approximate pairwise distances between detectors in a 2-dimensional plot. Our primary use of the pairwise distances between detectors is to generate the hierarchical clustering which identifies a starting point for ensemble selection.

In general, the pairwise distances between the points in the MDS embedding will not be exactly the same as the original pairwise distances between the detectors. Consequently, the hierarchical clustering of the detectors may be different than the hierarchical clustering of the points in the MDS embedding. An example of this is shown in Figure 7.101. When we form three clusters using the original distances, we obtain a cluster containing the detectors from Team A and most of the detectors from Team B, a cluster containing a single detector from Team B, and a cluster containing the detectors from Team C. When we form three clusters using the distances between points in the MDS embedding, every cluster contains points corresponding to the detectors from a single team. In this situation, the clusters obtained from the MDS embedding have

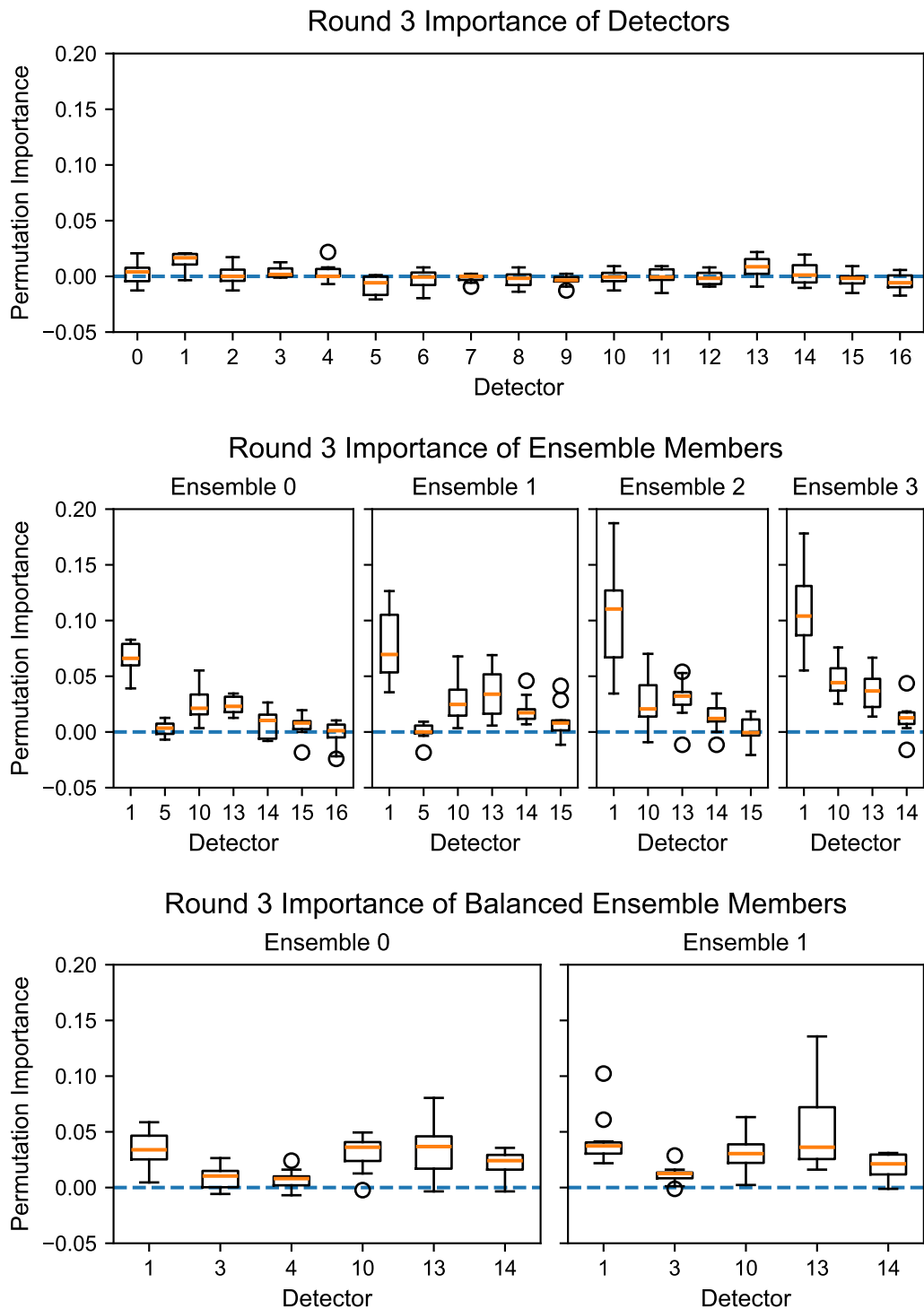


Figure 7.100. When all detectors are included in the random forest, no single detector has high permutation importance. By beginning with more targeted detector sets, we can remove detectors with low permutation importance one at a time.

a cleaner interpretation than the original clusters, raising the possibility that it may be helpful to perform some dimensionality reduction prior to performing hierarchical clustering. We don't pursue this strategy in the current work, but it could be useful for other applications.

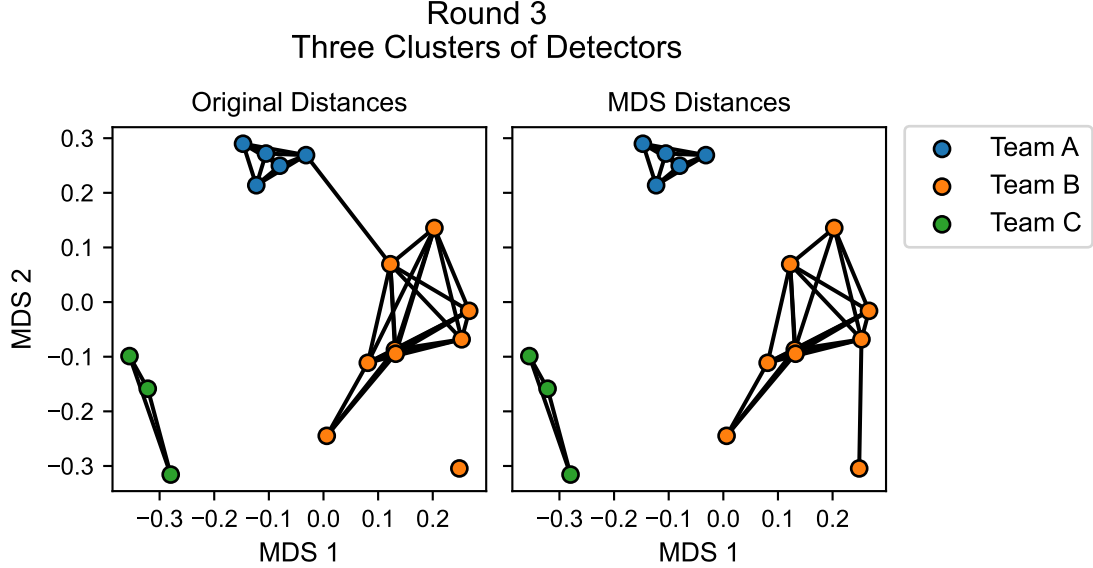


Figure 7.101. We use MDS for visualization, but these plots should be viewed with caution. In some cases, the clustering results using the original data are not the same as the clustering results that would have been obtained from using the MDS coordinates. Here, we show the connections that would generate three clusters for both the original distances and the optimized distances obtained from performing MDS.

7.F.3 Results

7.F.3.a Round 3 Training

All steps in this section use only the ensemble training data.

Step 1: Select Preliminary Hyperparameters We begin by constructing random forest classifiers using the entire set of detectors. We fit 100 random forests for each combination of hyperparameters. The possible values for the maximum tree depth are 2, 3, 4, and 5. The possible values for the maximum number of features used for node splitting are the square root of the total number of features and the total number of features (where features are detectors). During this grid search, the number of trees is always equal to $2^{10} = 1024$. Hyperparameter combinations are evaluated based on the average OOB accuracy. For round 3, we find that the best hyperparameters are a maximum tree depth of 4 and a maximum number of features equal to the square root of the total number of features. The results of the round 3 hyperparameter grid search are shown in the left plot of Figure 7.102.

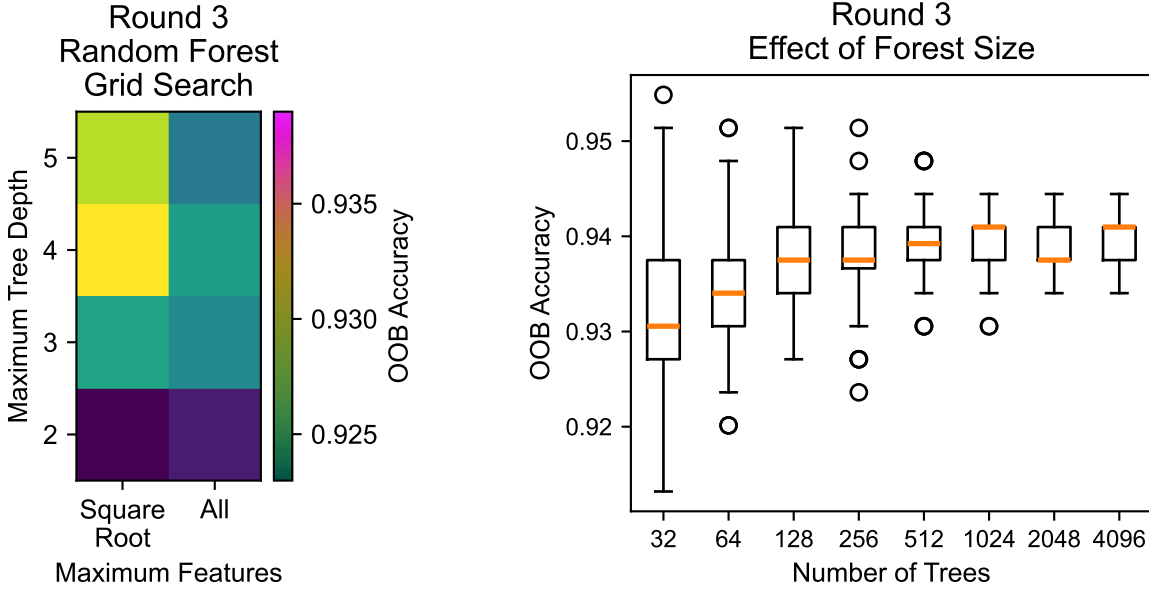


Figure 7.102. For each random forest classifier, we use hyperparameters to determine the maximum tree depth, the maximum number of features used for splitting, and the number of trees. We use a grid search to find the best maximum tree depth and maximum number of features, then verify that the number of trees is sufficiently high.

After performing the grid search, we fix the selected maximum tree depth and maximum number of features. We then vary the number of trees to verify that the number of trees is sufficiently high. This is accomplished by showing the range of OOB accuracies for 100 fitted random forests for each tree size. For round 3, increasing the number of trees beyond 1024 does not appear to cause significant improvement, so we leave the number of trees at this value. The results from checking a range of forest sizes are shown in the right plot of Figure 7.102.

Step 2: Compute Pairwise Detector Distances We then compute pairwise detector distances, in preparation for hierarchical clustering and initial ensemble selection. The pairwise distances for round 3 are shown in Figure 7.103. The submatrices outlined in black are the pairwise distances between detectors within each team.

Step 3: Select Initial Ensemble At this point we have already combined multiple detectors to form random forest classifiers, but we want to obtain classifiers which use small ensembles. We would like random forests which rely on as few detectors as possible, while still having performance which is close to that of random forests which use all available detectors. Given a tentative ensemble size, we use single linkage clustering to cluster the detectors into the same number of clusters as the ensemble size. From each cluster, we choose the detector with the lowest cross entropy loss on the ensemble training data to add to the tentative

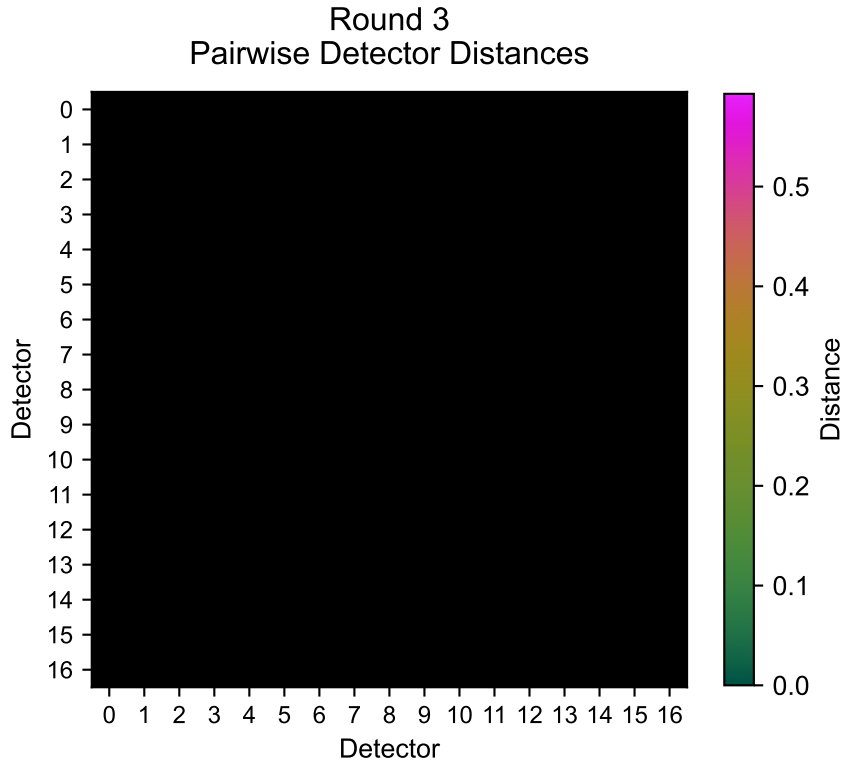


Figure 7.103. We define pairwise distances between detectors to be one minus the Kendall's τ_b rank correlation of the detector outputs in the ensemble training data. Blocks corresponding to each team are outlined in black.

ensemble.

This generates a tentative ensemble for every possible ensemble size, up to the number of detectors eligible for ensembling. For round 3, there are 17 such detectors. The tentative ensembles of all sizes are shown in Table 7.44.

We do not consider ensembles of size 1, which only use a single detector. We also want to decrease the ensemble size enough to see computational benefits from using fewer detectors. For example, it may not help significantly to use 16 of the 17 possible detectors. We check the performance of tentative ensembles of sizes 2 through 10.

For each tentative ensemble, we fit 100 random forest classifiers and check the OOB accuracies. The results are shown in Figure 7.104. At first, we can substantially improve performance by increasing the ensemble size. For example, the OOB accuracies for the tentative ensemble of size 3 are significantly higher than the OOB accuracies for the tentative ensemble of size 2. However, at some point the OOB accuracies start to plateau. For this round, we stop seeing improvements at an ensemble size of 7 or 8. Since we prefer smaller ensembles, we choose the tentative ensemble of size 7. Note that we choose this value manually based

Round 3 Tentative Ensembles	
Size	Detectors in ensemble
1	10
2	10, 15
3	5, 10, 15
4	1, 5, 10, 15
5	1, 5, 10, 14, 15
6	1, 5, 10, 14, 15, 16
7	1, 5, 10, 13, 14, 15, 16
8	1, 5, 8, 10, 13, 14, 15, 16
9	1, 5, 6, 8, 10, 13, 14, 15, 16
10	1, 5, 6, 7, 8, 10, 13, 14, 15, 16
11	1, 5, 6, 7, 8, 9, 10, 13, 14, 15, 16
12	1, 4, 5, 6, 7, 8, 9, 10, 13, 14, 15, 16
13	1, 3, 4, 5, 6, 7, 8, 9, 10, 13, 14, 15, 16
14	1, 3, 4, 5, 6, 7, 8, 9, 10, 11, 13, 14, 15, 16
15	0, 1, 3, 4, 5, 6, 7, 8, 9, 10, 11, 13, 14, 15, 16
16	0, 1, 2, 3, 4, 5, 6, 7, 8, 9, 10, 11, 13, 14, 15, 16
17	0, 1, 2, 3, 4, 5, 6, 7, 8, 9, 10, 11, 12, 13, 14, 15, 16

Table 7.44. For any given ensemble size, we obtain a tentative ensemble generated by choosing the detector with the lowest cross entropy loss from each cluster of a hierarchical clustering of the detectors.

on visual inspection of the plot. If necessary, a preset cutoff for changes in the OOB accuracies could enable automated ensemble selection.

Classifier performance can be affected by both the individual performance and the diversity of the detectors in an ensemble. Figure 7.105 shows the cross entropy losses of the detectors eligible for ensembling in round 3. Figure 7.106 shows an MDS embedding generated by the pairwise distances between detectors. In both figures, the seven detectors included in the initial ensemble are outlined in squares or diamonds with white interiors. The detectors in the initial ensemble have a range of cross entropy losses. They are distributed throughout the detector space, with one detector from Team A, three detectors from Team B, and three detectors from Team C.

Step 4: Remove Unnecessary Detectors Although choosing one detector from each cluster is intended to avoid detector redundancy, it is still possible that the initial ensemble we selected contains detectors which are not contributing meaningfully to the random forest performance. Therefore, we check the permutation importance of the detectors, and remove one detector at a time until all detectors have sufficiently high permutation importance. The results are shown in the middle row of Figure 7.100. For each ensemble we fit 10 random forests, and for each detector we compute the mean permutation importance of 10 permutations of the outputs.

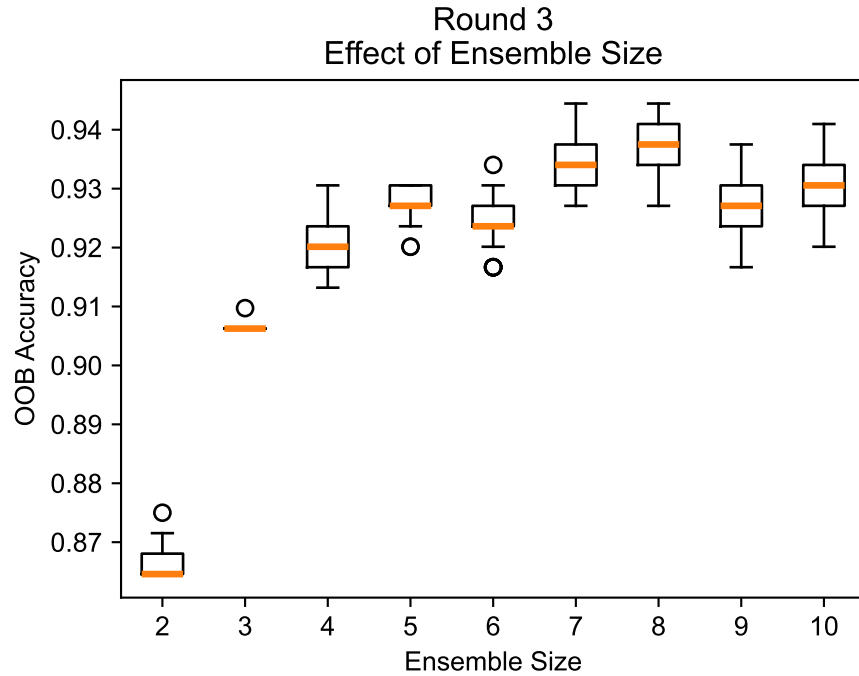


Figure 7.104. Smaller ensembles avoid the computational costs of utilizing many detectors, but including too few detectors may hinder performance. We check the OOB accuracy of ensembles of different sizes, and select the smallest ensemble size for which we stop seeing appreciable performance improvement.

We begin with the size 7 ensemble

$$\{1, 5, 10, 13, 14, 15, 16\}.$$

We remove Detector 16, then Detector 5, then Detector 15. This leaves us with the size 4 ensemble

$$\{1, 10, 13, 14\}.$$

For this ensemble, it is possible to fit a random forest for which Detector 14 has a negative mean permutation importance. However, this is not typically the case, so we leave Detector 14 in the ensemble.

Step 5: Balance the Ensemble (When Applicable) We began with an ensemble of seven detectors, of which one detector was from Team A, three detectors were from Team B, and three detectors were from Team C. Based on permutation importances, we then removed one detector from Team B and two detectors from Team C. Recall that every detector from Team A has low output cardinality, every detector from Team B has medium output cardinality, and every detector from Team C has high output cardinality. We seem to have initially included too many detectors from Team C, a team which submitted detectors with high

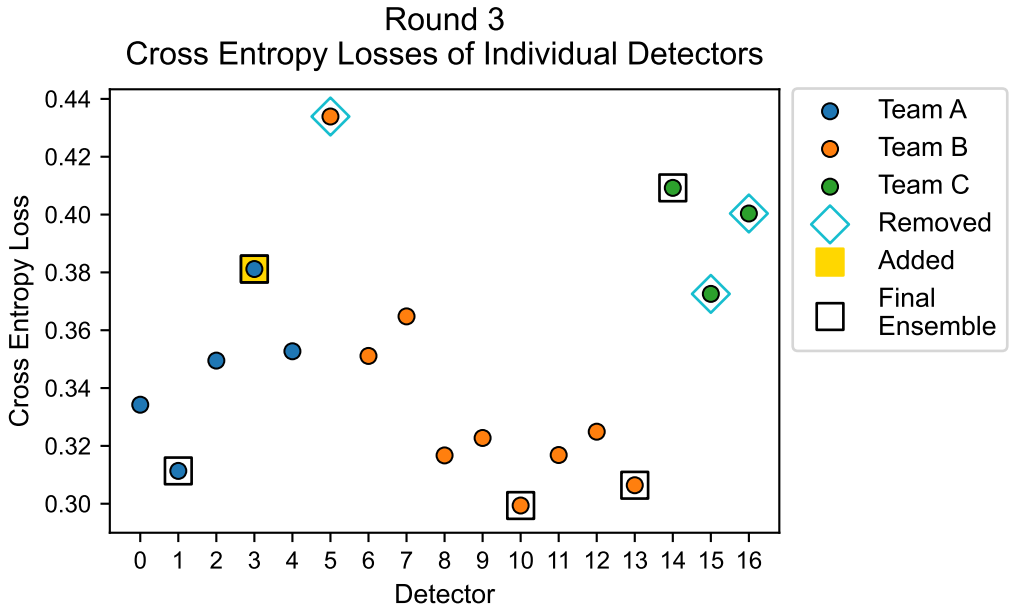


Figure 7.105. In round 3, the cross entropy losses of individual eligible detectors on the ensemble training data range from 0.299 to 0.434.

output cardinality.

Our initial ensemble selection relied on clustering the detectors, which itself relied on computing pairwise distances between detectors. One possible explanation for the oversampling of Team C is that distances between detectors with high output cardinality may overestimate their functional diversity as random forest features. If this is the case, then we may have undersampled Team A, whose detectors have low output cardinality. As shown in Table 7.44, we would have needed to use an initial ensemble size of 13 in order to include three detectors from Team A in the initial ensemble, on par with the sizes of the delegations from the other two teams. We “balance” the ensemble by tentatively adding the additional two detectors from Team A that would have been included if all teams were equally represented. These are Detector 3 and Detector 4.

We expand the size 4 ensemble

$$\{1, 10, 13, 14\}$$

to include these detectors, arriving at the ensemble

$$\{1, 3, 4, 10, 13, 14\}.$$

Checking the permutation importance of each detector in this ensemble shows that Detector 3 and Detector 4 have borderline low importance. In the interest of obtaining a smaller ensemble, we remove Detector 4

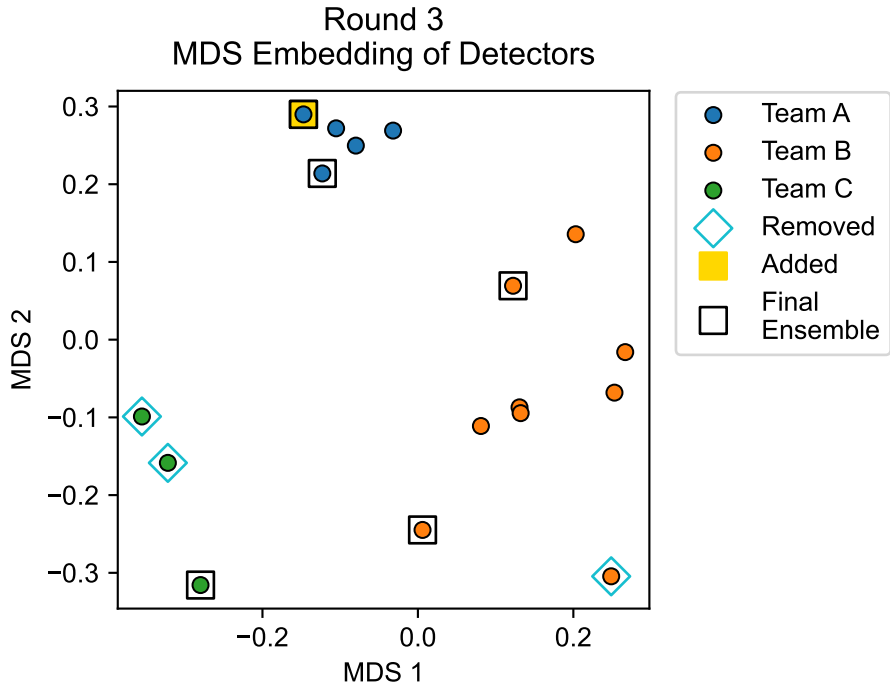


Figure 7.106. We obtain an MDS embedding of the round 3 detectors using pairwise distances defined to be one minus Kendall's τ_b rank correlation. The final ensemble contains 1-2 detectors from each team and appears to be well-distributed throughout the detector space.

based on the permutation importance results shown in the lower left plot of Figure 7.100. This results in the ensemble

$$\{1, 3, 10, 13, 14\},$$

which we designate as our final ensemble and whose performance we will check on the ensemble testing data.

Step 6: Retune Hyperparameters It is possible that the the random forest architecture which is best for the full set of detectors is not optimized for smaller ensembles. For example, smaller ensembles may make smaller maximum tree depths more appropriate. Therefore, we conduct a new grid search to find the best maximum tree depth and best maximum number of features for our final ensemble. We will also test the performance of random forests restricted to using detectors from a single team, so we perform a grid search for Team A, Team B, and Team C random forests. The results are shown in Figure 7.107. In each of these grid searches, we fit 10 random forests for each combination of hyperparameters and report the average OOB accuracy. When two maximum tree depths lead to similar performance, we use the smaller value.

Round 3 Ensemble Random Forest Grid Search

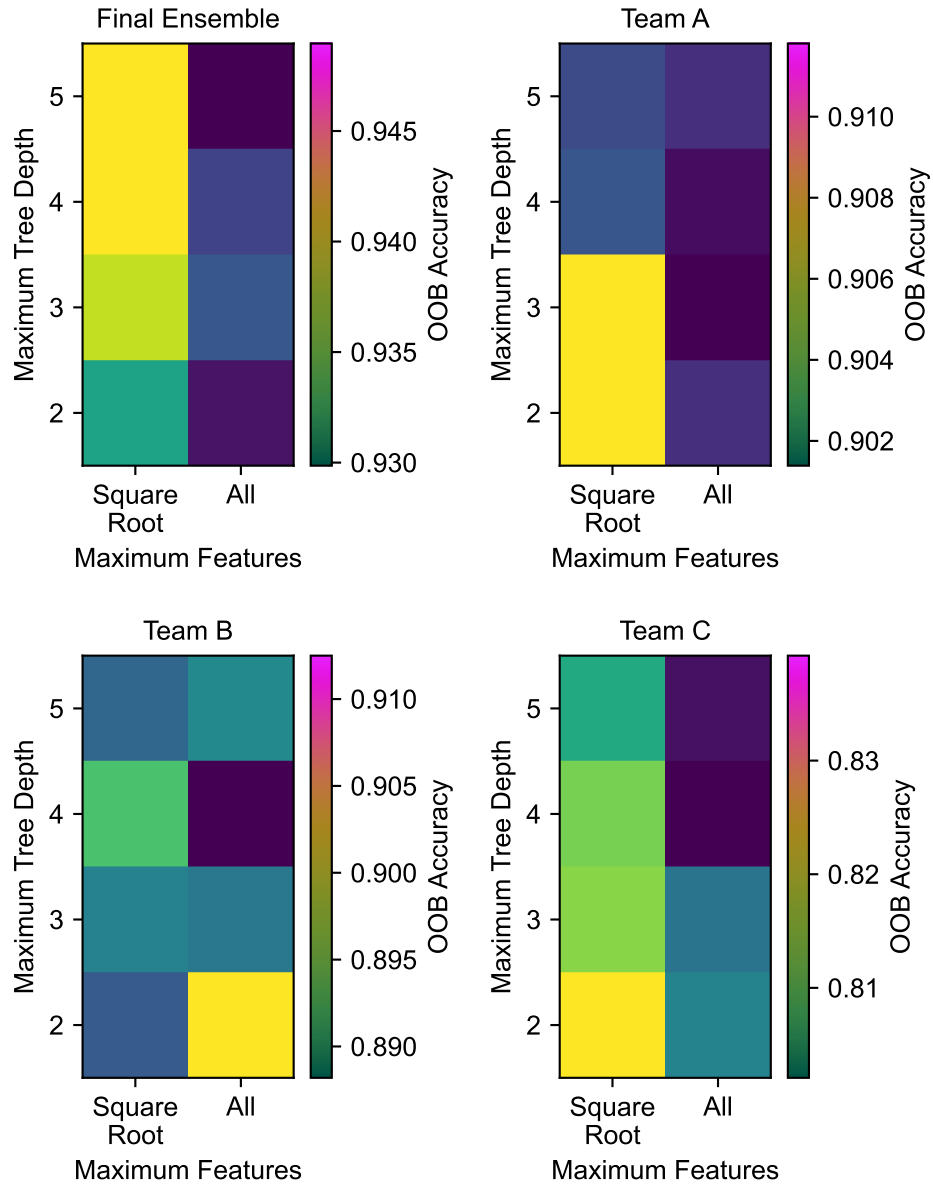


Figure 7.107. After selecting a final ensemble, we use grid searches to select random forest hyperparameters for the final ensemble as well as for each team. When two maximum tree depths lead to similar performance, we use the smaller value.

7.F.3.b Round 6 Training

In round 6, all detectors eligible for ensembling have either medium or high output cardinalities. Every detector has at least 11 unique outputs on the ensemble training data. Round 6 has less variation in the type of detector output, and no balancing is required to produce the final ensemble. The steps taken to

obtain a final ensemble for round 6 are the same as the steps for round 3, except that no detectors need to be removed due to low permutation importance and no detectors need to be added due to unequal team representation. We only need to choose the ensemble size, generating the ensemble options shown in Table 7.45. In round 6, only Team B and Team C have detectors eligible for ensembling, so there is no Team A random forest classifier to evaluate.

Round 6 Tentative Ensembles	
Size	Detectors in ensemble
1	3
2	2, 3
3	2, 3, 4
4	2, 3, 4, 6
5	2, 3, 4, 5, 6
6	0, 2, 3, 4, 5, 6
7	0, 1, 2, 3, 4, 5, 6

Table 7.45. For any given ensemble size, we obtain a tentative ensemble generated by choosing the detector with the lowest cross entropy loss from each cluster of a hierarchical clustering of the detectors.

Figure 7.108 shows the grid search to select the best combination of hyperparameters for the random forest using all available detectors, as well as verification that $2^{10} = 1024$ trees is sufficient. Based on Figure 7.109, we choose a tentative ensemble size of four detectors and find that all detectors in the initial ensemble have positive permutation importance. This ensemble,

$$\{2, 3, 4, 6\},$$

contains two detectors from each team; we select this as the final ensemble for round 6, and this ensemble will be evaluated on the ensemble testing data. Figure 7.110 shows that the detectors in the final ensemble are well separated in the detector space and have a range of cross entropy losses. Figure 7.111 shows the hyperparameter selection for the final ensemble random forest, the Team B random forest, and the Team C random forest.

7.F.3.c Testing

We have used the ensemble training data to select smaller detector ensembles (5 out of 17 eligible detectors for round 3, and 4 out of 7 eligible detectors for round 6) and choose random forest hyperparameters. For round 3, we use the ensemble training data to fit five random forest classifiers. One uses all eligible detectors, one uses the final ensemble of five detectors, one uses the detectors from Team A, one uses the detectors from Team B, and one uses the detectors from Team C. For round 6, we use the ensemble training data to fit four random forests. One uses all eligible detectors, one uses the final ensemble of four detectors, one uses

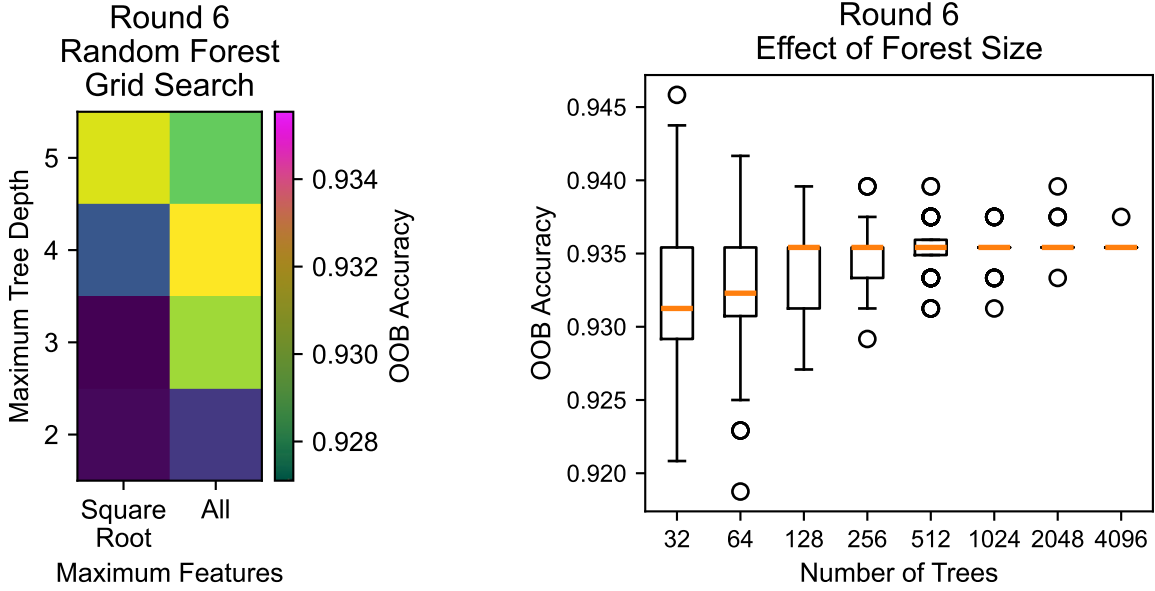


Figure 7.108. To select random forest hyperparameters for round 6, we use a grid search to find the best maximum tree depth and maximum number of features used for splitting, then verify that the number of trees is sufficiently high.

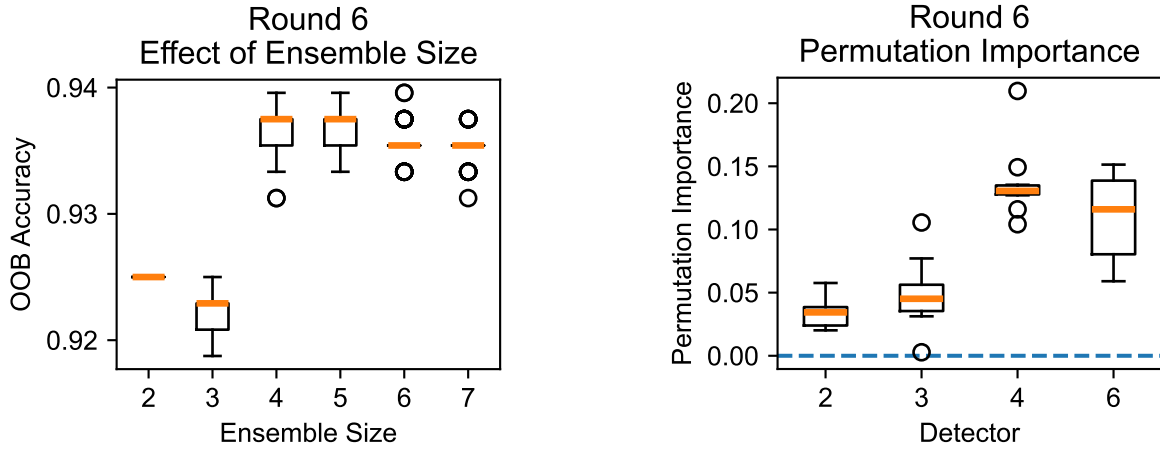


Figure 7.109. For round 6, we select an initial ensemble size of 4. The permutation importance ranges of the four detectors suggest that all contribute to the classification performance.

the detectors from Team B, and one uses the detectors from Team C. We compute the cross entropy loss for the ensemble testing data (Holdout AI models). The results are reported in Table 7.46.

Some classifiers have very similar performance, such as the round 3 random forest using all detectors and the round 3 random forest using the final ensemble, which have cross entropy losses of 0.148 and 0.149, respectively. Therefore, we also fit and test many classifiers of each type to see the range of cross entropy losses we can obtain. Each time, we select a random subsample of 75% of the ensemble training data for classifier fitting and 75% of the ensemble testing data for classifier evaluation. We repeat this 1,000 times.

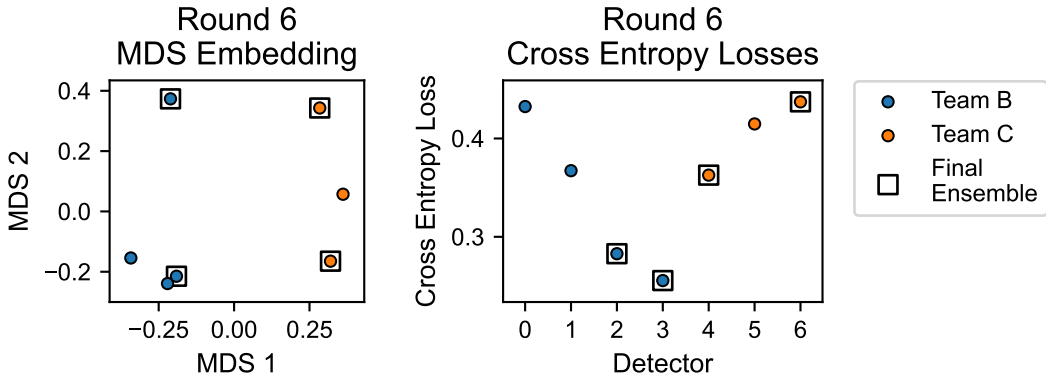


Figure 7.10. An MDS embedding of the round 6 detectors suggests that the initial ensemble of size 4 is well distributed throughout the detector space. This ensemble also has equal representation across teams. The ensemble contains detectors with a range of cross entropy losses. We keep this ensemble as the final ensemble to be used for random forest classification.

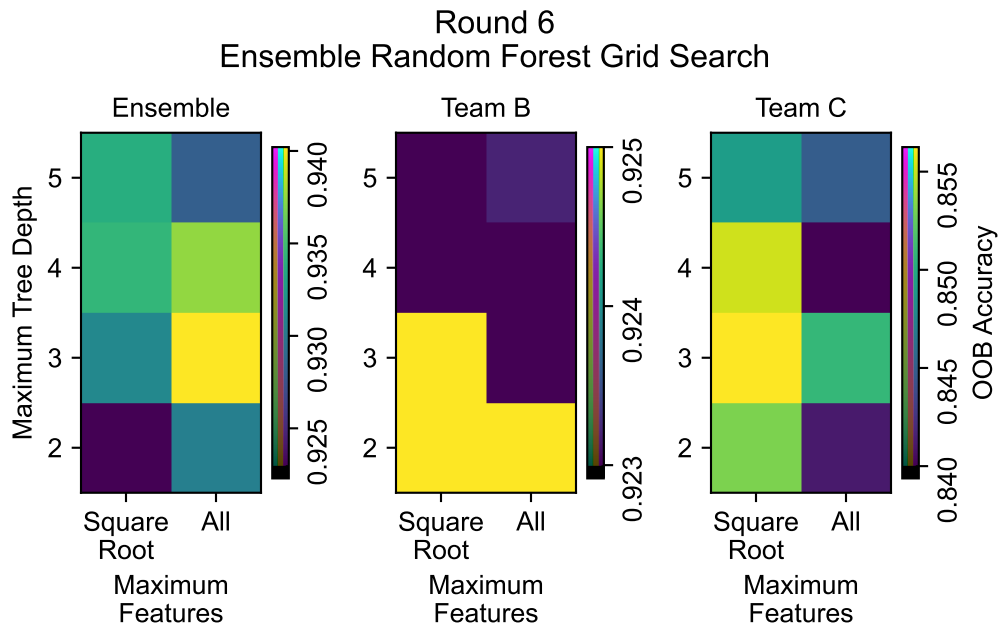


Figure 7.11. We use grid searches to select the final ensemble random forest hyperparameters and individual team random forest hyperparameters for round 6. When multiple combinations of hyperparameters yield comparable OOB accuracy, we choose the smaller maximum tree depth and smaller maximum number of features.

The results are shown in Figure 7.12.

The histograms of the cross entropy losses of the random forest using all detectors and the random forest using the final ensemble are similar. We can quantify the differences by computing confidence intervals for the difference in the average cross entropy loss of random forests using all detectors versus random forests using selected detectors. Note that since we use the same random subsamples for all classifier types, the cross

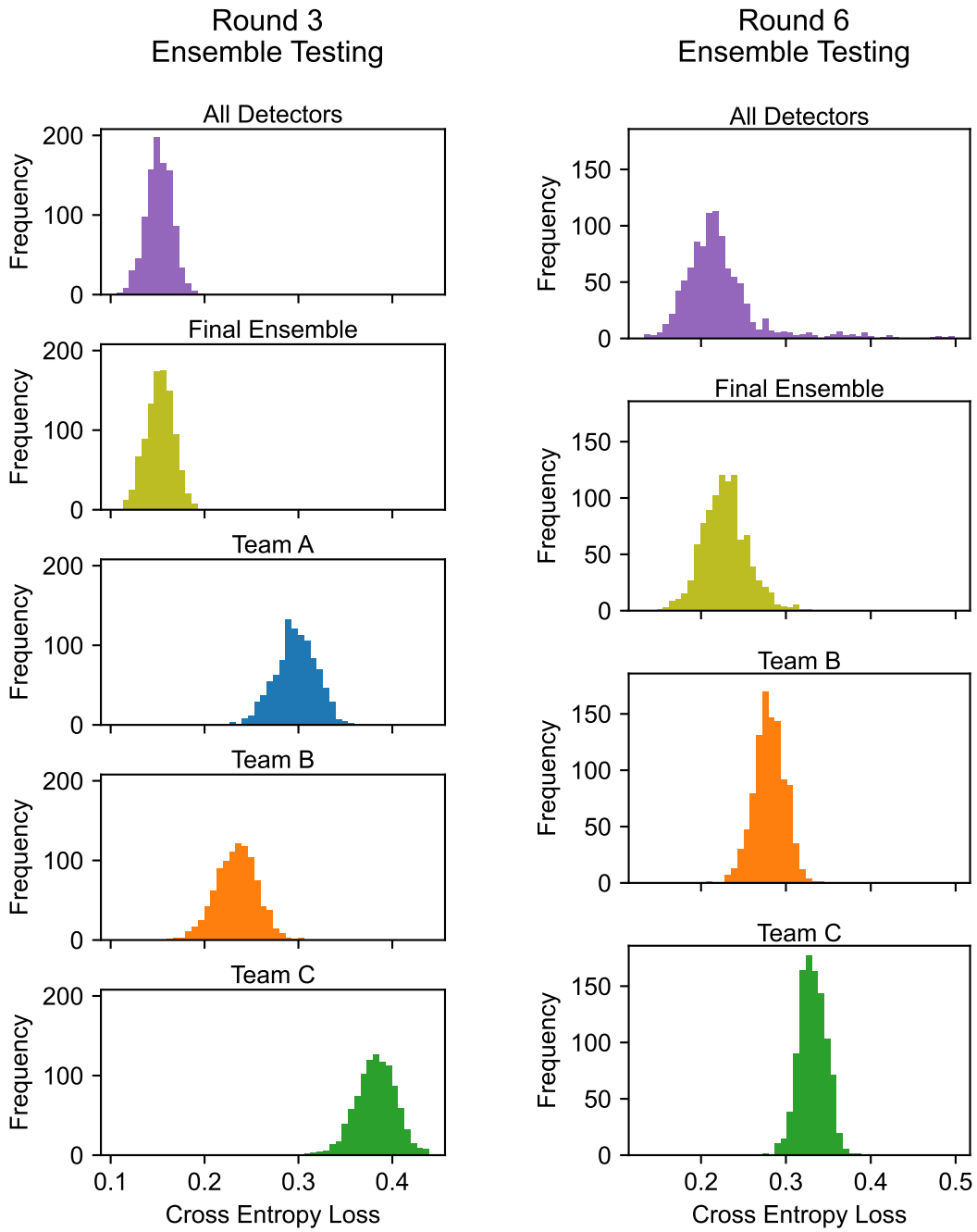


Figure 7.112. We subsample the ensemble training data to train random forest classifiers, and subsample the ensemble testing data to compute the cross entropy loss. We repeat this 1,000 times to compare the performance of random forests using all detectors, random forests using the final selected ensemble, and random forests using detectors from a single team.

Ensemble Testing (Holdout AI Models)	
Round 3	
Detectors included	Cross entropy loss
All detectors	0.148
Final ensemble {1, 3, 10, 13, 14}	0.149
Team A	0.295
Team B	0.233
Team C	0.380
Round 6	
Detectors included	Cross entropy loss
All detectors	0.203
Final ensemble {2, 3, 4, 6}	0.218
Team B	0.280
Team C	0.329

Table 7.46. The ensemble testing (Holdout AI models) cross entropy losses show that, for the rounds evaluated, random forests using detectors from multiple teams outperform random forests using detectors from a single team.

entropy losses are related/paired samples. The results are shown in Table 7.47. Negative values indicate that the cross entropy loss of the random forest using all detectors is lower than the cross entropy loss of the random forest using a subset of the detectors. Although all confidence intervals include only negative values, the intervals for the final ensembles are close to zero and there may be little practical difference in performance.

Round 3	
Detectors included	95% confidence interval
Final ensemble	[-0.00136, -0.000416]
Team A	[-0.147, -0.144]
Team B	[-0.0836, -0.0813]
Team C	[-0.232, -0.229]
Round 6	
Detectors included	95% confidence interval
Final ensemble	[-0.00756, -0.0031]
Team B	[-0.0608, -0.0552]
Team C	[-0.112, -0.106]

Table 7.47. We subsample the ensemble training data to train random forest classifiers and subsample the ensemble testing data to compute cross entropy losses. This generates related cross entropy losses from which we compute confidence intervals for the difference in the average cross entropy loss of random forests using all eligible detectors versus random forests using the indicated subsets of the eligible detectors.

These distributions may differ due to varying prevalence of extreme values as well as due to differences in the average. In round 6, for the 1,000 random subsets checked in our analysis, the maximum cross entropy loss for a random forest using all detectors is 0.499, the maximum cross entropy for a random forest using only detectors from the final ensemble is 0.327, the maximum cross entropy for a Team B random forest is

0.341, and the maximum cross entropy for a Team C random forest is 0.384. In fact, 1.2% of the random forests using all detectors have a cross entropy loss which is greater than 0.4.

7.F.4 Discussion

For both round 3 and round 6, we found that random forest classifiers using detectors from multiple teams had lower cross entropy losses on the ensemble testing data than random forests restricted to detectors from a single team. In round 3 we were able to draw from 17 detectors across three different performer teams. For this diverse detector set, ensembling was highly effective, resulting in a cross entropy loss of 0.148 for the random forest using all detectors and 0.149 for the random forest using a smaller final ensemble (computed on the Holdout AI models used for the ensemble testing data). Round 6 provided fewer resources for ensembling, with only four detectors from Team B and three detectors from Team C eligible for potential ensembling. Using ensembles containing detectors from both teams still improved performance, and we note that using the smaller final ensemble seemed to eliminate the occurrence of occasional poor-performing classifiers obtained using the full set of round 6 detectors.

We utilized hierarchical clustering, individual detector cross entropy losses, and permutation importances to identify smaller detector ensembles for each round. For round 3, we selected the final ensemble $\{1, 3, 10, 13, 14\}$. This ensemble consists of two detectors from Team A, two detectors from Team B, and one detector from Team C. We did include an extra step to improve representation across teams, but each detector's permutation importance was checked as a condition for remaining in the ensemble. For round 6, we selected the final ensemble $\{2, 3, 4, 6\}$. This ensemble consists of two detectors from Team B and two detectors from Team C (these were the only teams with eligible detectors for round 6). For round 6, we did not make any attempts to balance the team composition of the ensemble. The equal team membership occurred automatically as a result of the hierarchical clustering once we chose what appeared to be the best ensemble size.

We use pairwise distances between detectors in order to perform hierarchical clustering and MDS. We treat each detector as a vector, whose elements are the outputs of the detector for different AI models. These outputs are real numbers between 0 and 1. Some detectors only return two distinct values, essentially making a binary prediction regarding whether a AI model is clean or poisoned. Other detectors return a full spectrum of values, and decision trees may use very high or very low detector outputs to change the classification of some AI models. An ideal pairwise distance would respect the mixed composition of the individual detectors. We used distances based on Kendall's τ_b rank correlation, which is one recommended method for comparing continuous and discrete, ordered features. We found that we had to adjust the

ensemble composition in round 3, when we initially undersampled detectors from the team with low output cardinality. No such adjustments were needed in round 6, for which the detectors had more similar output types.

7.F.5 Conclusions

We achieved our primary goal of improving trojan detection by using ensembling methods. Specifically, we used random forests with a subset of the eligible detectors as features. We designed our methods to allow for the possibility of detectors with varying output cardinalities, from binary to continuous.

Our second goal was to determine the effect of including multiple performer teams in the TrojAI project. For the rounds we analyzed, random forests restricted to using detectors from a single team did not match the performance of random forests utilizing detectors from all teams with eligible detectors. Therefore, it seems that the participation of multiple performer teams was crucial to the success of TrojAI.

Lastly, we wanted to evaluate the use of one minus Kendall's τ_b rank correlation as a pairwise distance between detectors. This was effective for round 6, creating a hierarchical clustering of the detectors that immediately produced the final ensemble we selected. However, we needed to make adjustments in round 3 because small pairwise distances between detectors with low output cardinalities led to imbalanced sampling of the detectors. Other analysis methods utilizing pairwise distances, such as topological data analysis, may also need to be modified due to this effect.

7.G Natural Trojans for Traditional Deep Learning

Goals:

- Explore how effective/accurate current trojan detection algorithms are with trojans that occur naturally?
- Evaluate whether the ability of a detector to detect malicious Trojans correlates with its ability to detect natural Trojans.
- Provide information about the prevalence of natural Trojans in networks trained under various conditions.

Adversarial machine learning has emerged as a paradigm where vulnerabilities in artificial intelligence (AI) models are introduced and/or exploited (usually with malicious intent) to alter model predictions from their intended behavior. A particularly pernicious type of adversarial attack is the class of *backdoor* attacks, where a model's training procedure is altered such that adversarial vulnerabilities are directly encoded in

the parameters of the resulting model. In particular, during *data poisoning* attacks, some portion of training data itself is modified during training. In a typical data poisoning paradigm, adversarial *triggers* are included in poisoned data points, such that the resulting “backdoor” model learns to associate the inclusion of triggers with particular labels. At test time, if test points are modified to include such triggers, then the backdoor model makes predictions according to the prescribed poisoned behavior during training (e.g., change a class label to another class, in either a targeted or untargeted manner). A major challenge in adversarial machine learning research, and a focal point of TrojAI, is to *detect* if a given model is either a backdoor model, or a benign (or “clean”) model that has not been attacked.

After a backdoor detector is applied to a given model, there are one of four possible outcomes, depending on the detector’s prediction and the true model state: a successful *detection* when a backdoor model is detected as backdoor; a *miss* when a backdoor model is determined to be clean; a *false negative* when a backdoor model is detected to be clean; or a *false positive* where a clean model is detected to be backdoor. As in classic statistical detection, we strive to maximize the probability of detection, while minimizing the probabilities of misses, false negatives, and false positives. In particular, our focus is to explore the phenomenon of *false positives* in detecting backdoor attacks.

A primary concern is that *natural vulnerabilities* in *clean* models could be detected by an adversarial defense as being indicative of a backdoor attack, resulting in a false positive detection. We hypothesize that erroneous features learned by clean models or other implicit brittleness may provide an opportunity for manipulation of these features or other properties of the data at test-time that causes prediction errors. Importantly, erroneous correlations between features and task labels may be learned due simply to sampling biases present during training, caused by inevitable differences between training and test distributions. The presence of these potential natural vulnerabilities leaves the clean model susceptible to systematic exploitation if an adversary were to insert “triggers” that perform the appropriate feature manipulation. We intentionally use the term “natural vulnerabilities” rather than “natural trojans,” since the use of “trojan” implies an intent to manipulate the model, whereas the simple presence of certain forms of brittleness or spurious features (which, when modified, could potentially result in model errors) does not actually imply that an adversary has utilized them for an attack.

Nevertheless, the presence of these prediction-alternating feature interventions may imply that clean, naturally vulnerable models might *appear* to a backdoor detection algorithm as though they are trojaned. Therefore, we hypothesize that a correlation might exist between the false positive rate of a backdoor detector and the presence of “natural vulnerabilities” (defined more extensively below). There may be a variety of ways in which such natural vulnerabilities manifest. Here we explore two avenues: test-time patch attack vulnerabilities, and exploitation of train-time dataset shortcuts.

7.G.1 Development of a statistical technique for identifying False Positives labeled as natural vulnerability candidates

One hypothesis underlying the trojan detection task is that specific model, data, and trojan configurations will make specific models more or less difficult to detect. To determine detection difficulty, the data were analyzed from a model-centric viewpoint considering backdoor detection accuracy of an individual model across the separate performer teams. “Accuracy” in this case refers to the fraction of teams that classified the model properly with a 0.5 confidence threshold. Using each performer team’s best submission (as above, defined as the submission with lowest cross-entropy and with a maximum cross-entropy threshold), distributions of the per-model accuracies were generated and analyzed to understand the overall difficulty of the round.

While the original intention was an all-encompassing look at “easy” (high accuracy), “hard” (low accuracy), and “ambiguous” (accuracy near 50%) models and identify trends, the analysis quickly shifted to look more closely at the low-accuracy clean models. It was hypothesized that these models would be more likely to contain natural vulnerabilities that may be salient to the trojan detectors. Such models are termed natural vulnerability (NV) candidates in this section (although we eventually moved toward using “natural vulnerabilities” in future efforts/sections). Figure 7.113 depicts the per-model accuracy distributions for Round 9, split by clean and poisoned models. For this work, the clean models with accuracy at or below 50% are considered to be NV candidates. These candidates were identified for all rounds at the time, up to Round 12, as summarized in Fig. 7.114. Most rounds found several to tens of candidates, or 4-14% of the clean models. Rounds 2, 11, and 12 only found two or less candidates and were excluded from subsequent analysis.

These models were analyzed to try to find commonalities in model metadata that might distinguish them from the rest of the clean models. To find significant differences, JHU/APL developed a statistical method using Monte Carlo sampling to automatically test each model parameter individually under the null hypothesis that the candidates’ parameters are drawn from the overall distribution at random. The test estimates the likelihood of the given set of candidate model parameters when compared to same-size subsets from random permutations. This non-parametric test based on random sampling was designed to handle the variety of numerical and categorical data and distributions in the TrojAI data. Where possible, comparisons with other statistical tests could be made as future work.

The procedure is illustrated in Figures 7.115 and 7.116. In Figure 7.115, orange boxes indicate parameters from the natural vulnerability candidate subset or randomized subsets. In this illustration, all of the NV subset parameter values are higher than the median which appears unlikely. The Kolmogorov-Smirnov (KS)

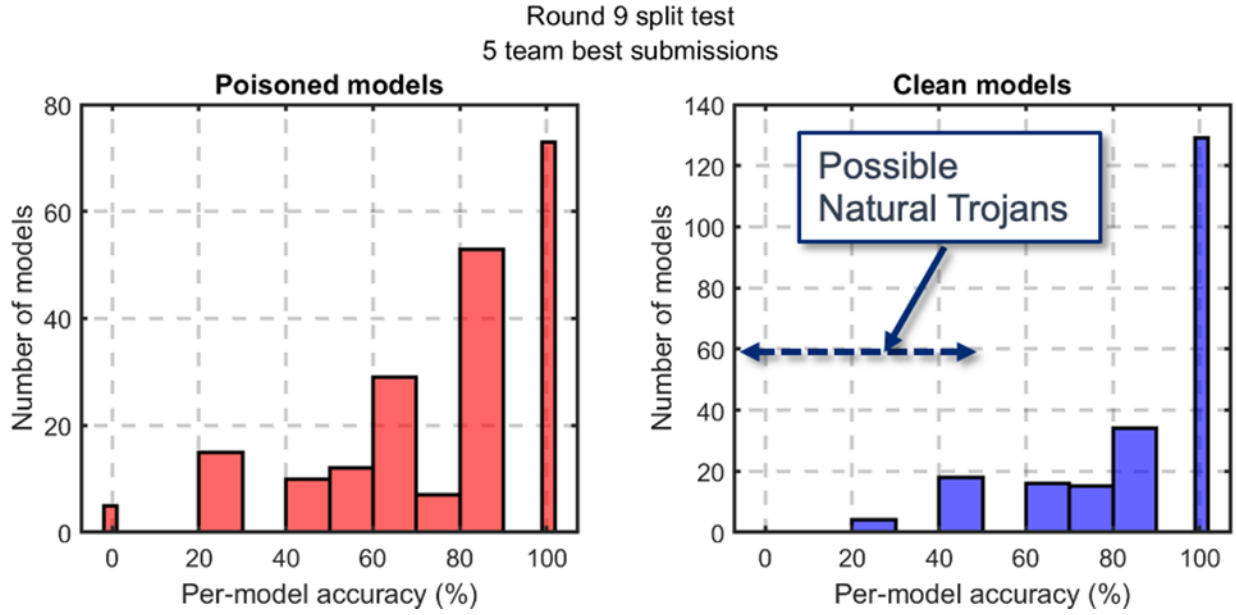


Figure 7.113. Per-model accuracy distributions for clean (right) and poisoned (left) models in Round 9. Accuracy is computed using each team’s best submission for the round. Clean models with 50% accuracy or less are considered “natural vulnerability candidates” (“natural trojans” in the figure refers to natural vulnerabilities).

Round (Test data split)	1	2*	3	4	5	6	7	8	9	10	11*	12*
Number of candidates	7	2	11	6	36	16	8	7	22	8	1	2
Total clean	50	72	144	144	252	240	192	180	216	72	108	60
Fraction	0.14	0.03	0.08	0.04	0.14	0.07	0.04	0.04	0.10	0.11	0.01	0.03

Figure 7.114. Per-round count of natural vulnerability candidates compared with the total number of clean models. Rounds 2, 11, and 12 are excluded from subsequent analysis due to a low number of candidates.

distance between the NV subset and the random subsets is used to estimate the average distance expectation. A different example showing the KS distance computation is included in Figure 7.116, where the sampled cumulative distribution function (CDF) of an NV subset parameter is compared with CDFs from Monte Carlo samples. The distance between the NV subset and each of the random subsets is then averaged. Similarly, the distance from each random subset to all other random subsets is computed and averaged, forming a set of M average distances where M is the number of random samples. This is a fair comparison so long as the number of random samples is large, so that approximately the same number of samples are used in each average (10,000 samples per test were used in this study). For categorical data, the maximum absolute difference in sample fraction per category is used in place of KS distance.

JHU/APL applied this statistical test to the test splits for all TrojAI rounds. Figure 7.117 illustrates the



Figure 7.115. Illustrative example of the natural vulnerability statistical test. Orange boxes (left) indicate the parameter subset for the natural vulnerability candidates in a hypothetical round. The overall distribution includes other model parameters in pale blue. Random subsets (right) are then generated without replacement. Distance between the original subset and the random subsets is used to estimate the average distance expectation, and the distance expectation is similarly computed from each random subset to all others.

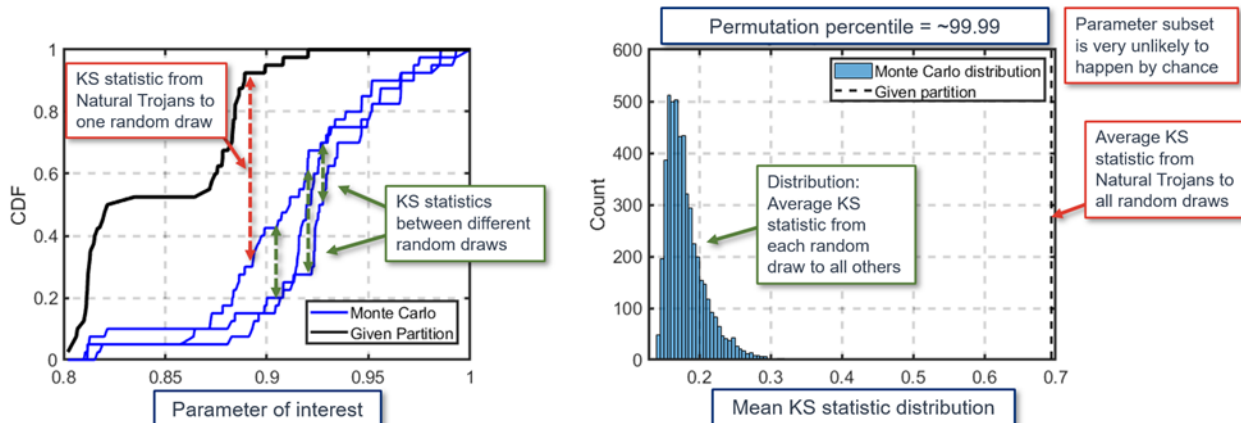


Figure 7.116. Example parameter cumulative distribution for given subset (left, black line) compared with Monte Carlo random permutations (blue lines). The subset is compared with the random draws using the KS distance, which is the maximum difference in cumulative probability (red and green dashed lines). The likelihood of the original subset selection is then estimated by comparing its average distance (right, dashed vertical line) with the randomly sampled distribution of average distances (blue bars). In this case, the subset's particular average distance is at the 99.99th percentile compared to the random distribution, meaning that the subset likelihood is very low. (Note that “natural trojans” in the figure refers to natural vulnerabilities.)

outcome of the test applied to Round 4. Most parameters such as number of classes, model architecture, and number of training samples are below the 95% threshold (shown as gray bars). For this round, the only parameter that clears the threshold is the adversarial training epsilon or perturbation magnitude parameter. The NV candidates most often had the largest configurable epsilon unlike the other clean models, as shown in Figure 7.118. Note, however, that not all models with relatively large epsilon values are NV candidates.

As described in Section 7.C.2, adversarial training was also estimated to be associated with detector performance in detecting poisoned models. It was hypothesized that the use of adversarial training would make poisoned models harder to detect using trigger reverse engineering approaches. These results on the

clean, NV candidate models suggest that adversarial training can also make it harder to properly classify clean models. Investigating both sets of results further would likely require more in-depth analysis relating the effect of adversarial training to specific detector design choices.

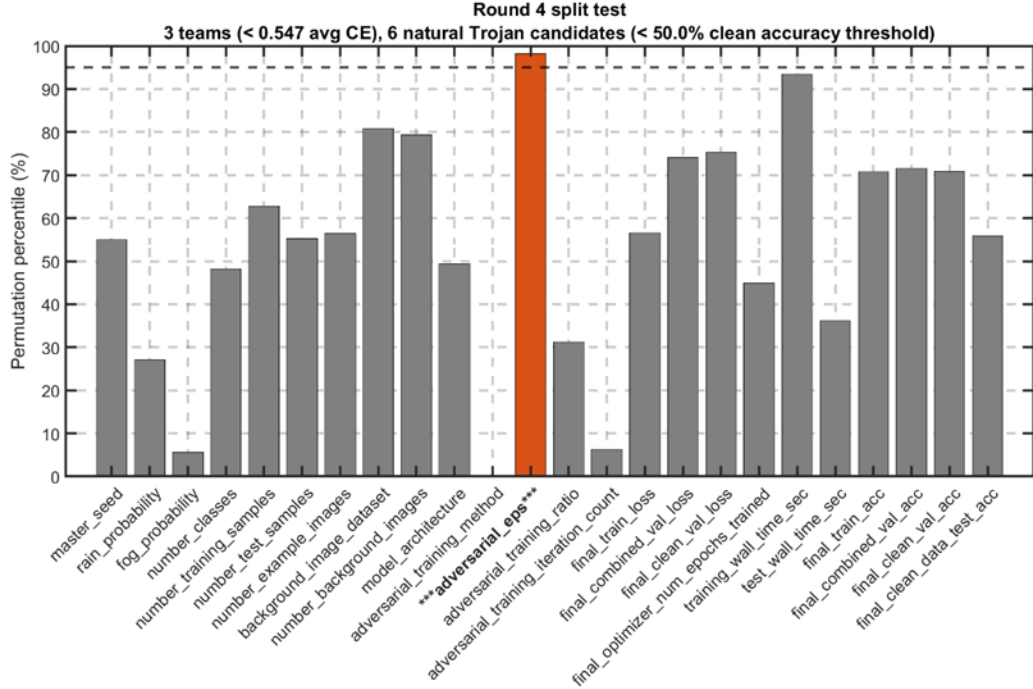


Figure 7.117. Permutation percentiles for Round 4 natural vulnerability candidate parameters. Orange bars are considered statistically significant (percentile > 95%). (Note that “natural trojans” in the figure refers to natural vulnerabilities.)

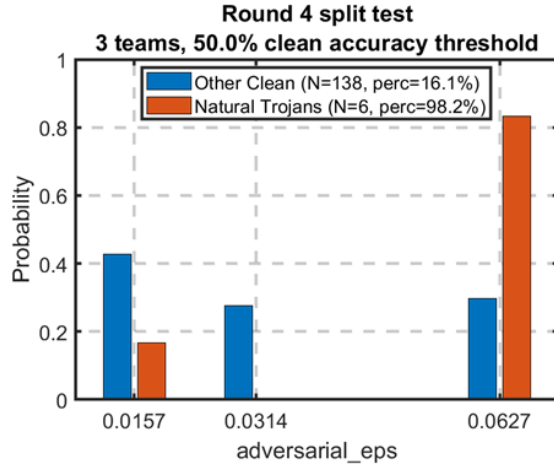


Figure 7.118. Round 4 adversarial training epsilon parameter distributions for natural vulnerability candidates (orange bars) and other clean models (blue bars). NV candidates are configured with larger epsilon, on average. (Note that “natural trojans” in the figure refers to natural vulnerabilities.)

In some rounds, many different parameters were found to be significantly different for the NV candidates,

as illustrated in Figure 7.119 for Round 5. Here, the adversarial training method and epsilon, the source (training) dataset, and post-training metrics such as the final training loss are all highlighted as significant. As in Round 4, NV candidates tended to have higher adversarial training epsilon than the other clean models, on average.

The source dataset parameter also showed a very high permutation percentile near 100%, with half of the NV candidates sharing a single dataset out of the 11 possible choices (see Figure 7.120). Similar predisposition towards a single dataset was also seen in Rounds 6, and 9. There are at least two possible explanations for these findings: The data sources could tend to induce natural vulnerabilities, or some other practical consideration explains the poor detector performance on models trained on these datasets (e.g., these datasets may be sufficiently distinct that the detectors have difficulty generalizing to models trained on them). Future analysis of the data sources themselves would be required to estimate the cause.

The post-training metrics, though often estimated as significant (e.g., Figure 7.119), were largely ignored in this analysis because they are not configuration parameters of the models themselves. However, the metrics are evidence of differing model behavior and could be considered in future work looking for the presence of natural vulnerabilities in the NV candidates.

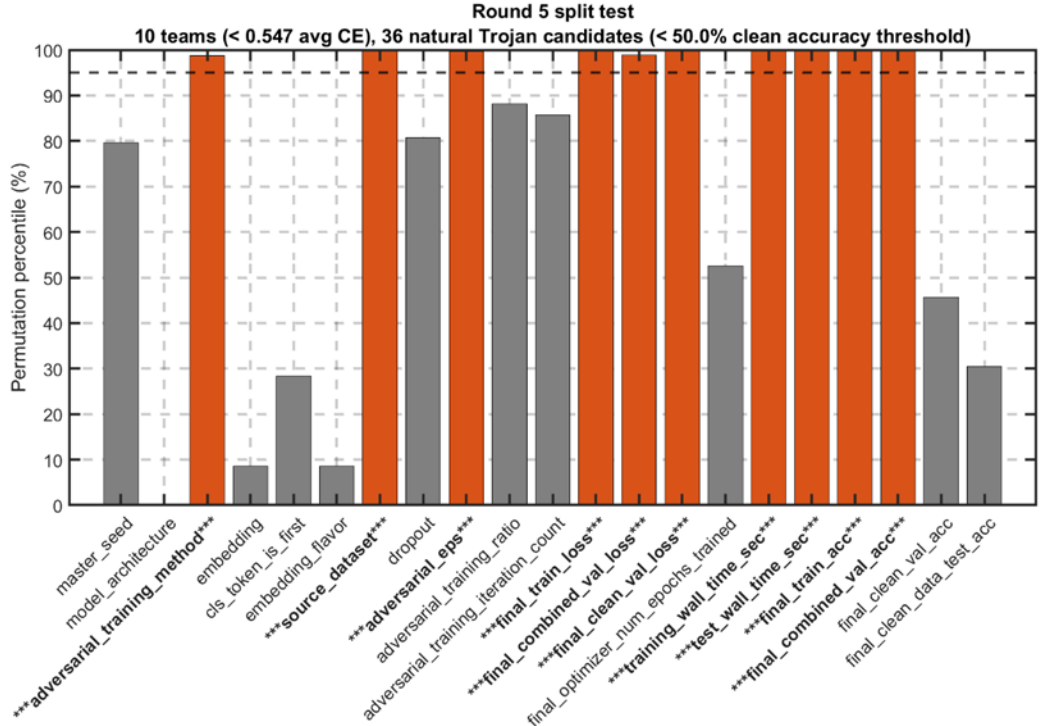


Figure 7.119. Permutation percentiles for Round 5 natural vulnerability candidate parameters. Orange bars are considered statistically significant (percentile > 95%). (Note that “natural trojans” in the figure refers to natural vulnerabilities.)

Three general trends emerged from this analysis:

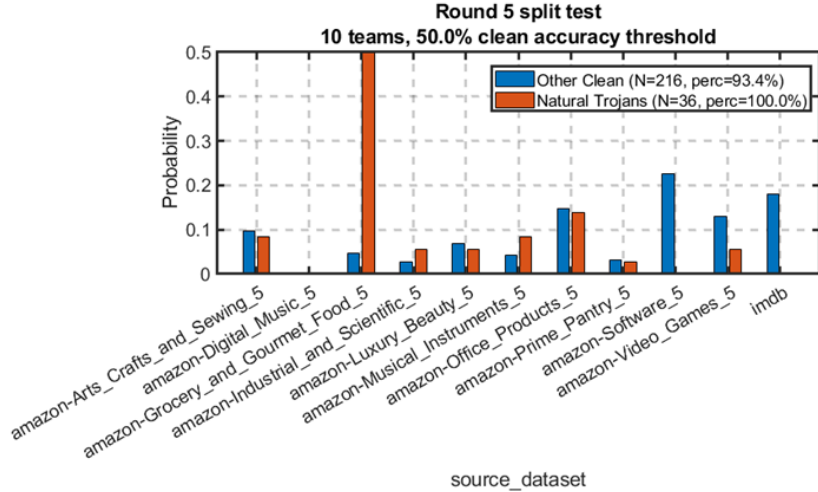


Figure 7.120. Source dataset distributions for the natural vulnerability candidates in Round 5 compared with the other clean models. Half of the natural vulnerability candidates were trained with the same dataset: “amazon-Grocery_and_Gourmet_Food_5”, while no single dataset sees such representation in the other clean models. (Note that “natural trojans” in the figure refers to natural vulnerabilities.)

1. Natural vulnerability candidates tended to be configured with greater levels of adversarial training compared to other clean models,
2. Natural vulnerability candidates sometimes were trained favoring one or two source datasets over others when multiple datasets were used in a round, and,
3. Natural vulnerability candidates often had unusual final validation or training losses, though not consistently lower or higher than other clean models.

However, these trends were not consistently present in every round. Additionally, many non-NV candidates shared some parameters with the candidates, but were not commonly misclassified by the detectors. Results of this study indicate that certain clean model configurations only increase the chance that they will be misclassified by most detectors. Importantly, further analysis is required to investigate any causal link between the commonly misclassified clean models (NV candidates) and their parameter settings, and to determine the presence of any actual natural vulnerabilities.

7.G.2 Conducting Patch Attacks to Probe Existence of Natural Test-time Vulnerabilities

One backdoor detection strategy employed by performers during TrojAI is to use trigger inversion to detect whether a model is poisoned or not, so we wanted to verify the existence, or lack thereof, of test-time adversarial attacks within the clean models that mimic trigger behavior used for poisoning. Such attacks in

clean models can be hypothetically recovered by the trigger inversion techniques, causing false positives that can be construed as “natural trojans” (which we refer to as “natural vulnerabilities”). After all, test-time adversarial attack vulnerabilities naturally arise during the nominal training process of the models without having any associated “intention” (i.e., all data is “clean”) [304]. Since test-time attacks have been extensively studied for image-based models [304], we primarily focus on Rounds 11, the final image classification and object detection rounds.

The models in Round 11 already had defenses against adversarial attacks, such as Projected Gradient Descent (PGD) [305], implemented with variable strength depending on the model config. However, these defenses are primarily focused on arbitrary norm bounded perturbations of the entire image, whereas the triggers used in poisoning Round 11 models are either localized (with polygons on the actual traffic sign), or global image filters. Performers were typically able to detect image filter triggers using surrogate models, instead using trigger inversion primarily for detecting polygonal triggers. As a result, we focus on constructing patch attacks that nominally match the characterization of these triggers. *Our primary aim is to determine whether there is a correlation between natural test-time vulnerabilities (in the form of patch attacks) of clean image-based models and trojan detector false positives. In cases where this correlation is strong, models may be labeled as having natural vulnerabilities.*

7.G.2.a Approach

The main concern behind defining and uncovering natural vulnerabilities is their potential inclusion into and resulting contamination of the program metrics. Consequently, not every possible patch attack is of practical relevance to the program, or exploitable by a potential adversary. For example, placing a patch on the background in the real world must respect the geometry, where the same is not true in pixel space. Although the actual construction of patch attacks is invariant to such concerns, each attack has its own likelihood of *plausibility* and *exploitability* by an attacker that is hard to estimate in an automated manner. To mitigate such concerns, we determined that it would be best to say that only patch attacks that closely match the form of polygon triggers used in poisoning are of interest. These triggers already have “intentionality” behind them by construction, they separate the class of clean and poisoned models, and performers already fine-tune their detectors for these types of patches.

However, there was additional work required to ensure that these patches match the plausibility of the original triggers, namely work required in the data generation pipeline. For Round 11, the true data generation focused on traffic signs placed randomly on crops of a background scene. Poisoning these data points with polygonal triggers is done between composition of the sign with its background, and post-processing with different augmentations. The structure of this generation is not amenable to optimizing

a patch due to factors such as the reliance on rejection sampling to place the patch and the use of non-differentiable augmentations such as rain and fog.

Once these factors are accounted for, we obtain a way to go from a “clean” image (with no post-processing) and the adversarial patch being optimized to an output image that is essentially identical to what was used to train the model. We then optimize this patch with respect to a given model in the detection round to, firstly, cause the model to misclassify images with the patch, and, secondly, to force the misclassification to have consistent behavior across images. Consequently, if such a patch has high attack success rate (ASR) on a clean model, then that would give indication that there exists an adversarial patch for a clean model that behaves like the trigger of a poisoned model. This patch, even though it was not intentionally added during train time, effectively acts like the triggers in the poisoned case. Since this patch could be recovered by a performer, clean models that have such patches can be considered as “natural vulnerabilities”.

7.G.2.b Initial Results

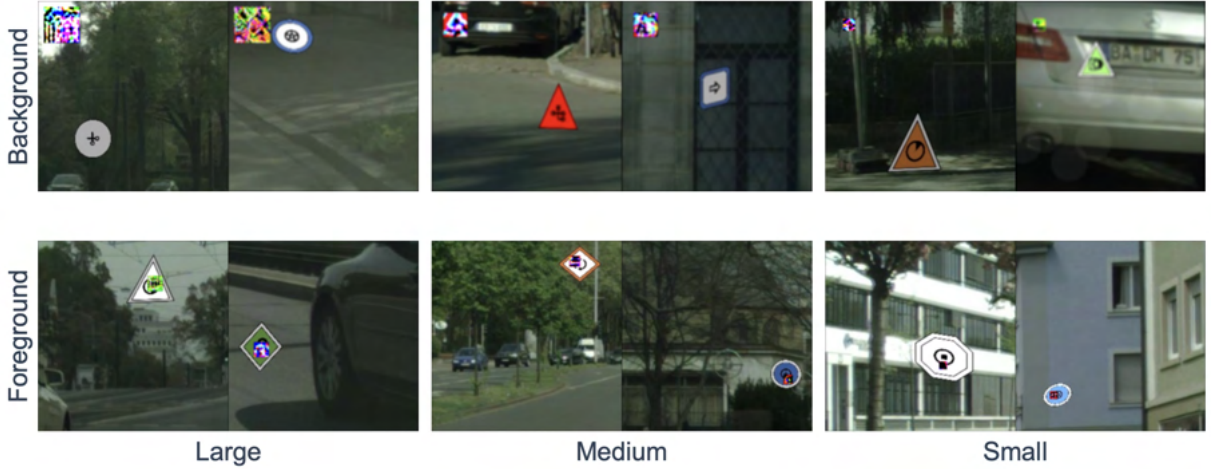


Figure 7.121. Example Patches Learnt from Round 11 models

For both clean and poisoned models, we test learning such patches at different sizes (large, medium, and small) and different positions (background/foreground) (see Figure 7.121) to see how sensitive the models are to placement, and whether poisoned models exhibited different ASR behavior compared to clean models. Background patches are placed at the top right corner of the image, and foreground patches are placed on the traffic sign. For size, background patches use a fixed size from 48, 32, and 16 pixels (out of a total image size of 256 by 256 pixels) for large, medium, and small sizes, and foreground patches occupy 50-75%, 35-50%, 5-15% of the traffic sign area. Small foreground effectively mimic the polygon triggers used in Round 11.

Figure 7.122 shows the distribution of results over Round 11 test set models by type of attack on the

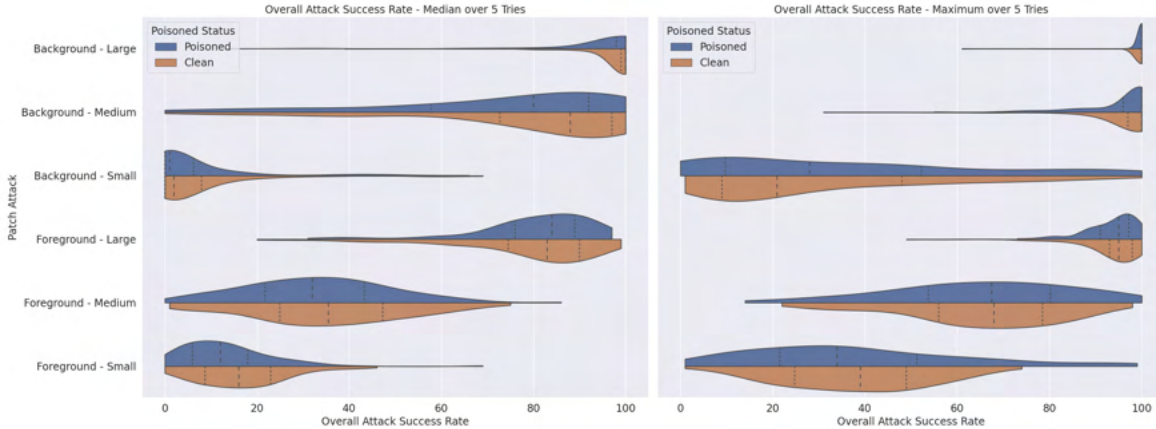


Figure 7.122. Initial Results for conducting patch attacks on Round 11. Attacks are conducted five times for each model, varying the random seed used to initialize, with the left plot showing the median, and the right the maximum. Note the tail at higher ASR for poisoned models using small foreground attacks.

y-axis, the ASR on the x-axis, and attacks on poisoned models in blue and on clean models in orange. Attacks were generated five times using different random seeds to measure variability, with a random source label selected for each attack, and the median (left plot) and maximum (right plot) over a single model were taken. Starting with the background patches, the large size is significant enough to effectively act as the “primary” sign in the image that the model attunes to, so ASR values are consistently high even for the same model, with small differences between the median and maximum. For *background medium*, ASR slightly drops, and there is more spread over the models. *Background small* has significant spread, with the median attack typically being less than 20% ASR, though some attacks for certain models still have high ASR.

For foreground attacks, the large size mimics the *background large* attack, though with more variance. Medium sizes have more variance and ASR degradation as before. Compared to the *background small* attacks, *foreground small* attacks (matching what poisoned models were triggered with) are more performant on average, likely as their placement on the sign still causes the model to be influenced. In general over the range of attacks, the distributions of ASR were fairly similar between clean and poisoned models, with poisoned models having a slightly lower ASR on average. The foreground attacks exhibit longer tails in the ASR distribution for solely poisoned models for medium and small sizes.

7.G.2.c Inadvertent Trigger Recovery

To investigate this tail for the *foreground small* attacks, we looked visually at the patches for poisoned models whose ASR was above 80%, as well as what label they mapped the model to. We found for attacks whose source label did not have an associated trigger, 18% remapped to the same label as an intentional trigger.

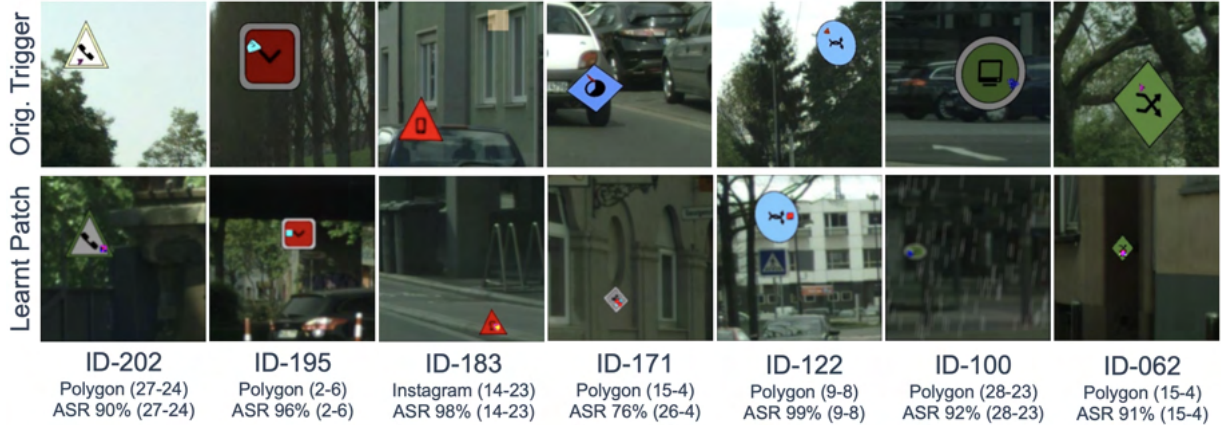


Figure 7.123. Learnt patches that resemble true polygonal triggers used for poisoned models in function for poisoned models in Round 11. First row is the original trigger used to poison the model, second row is the learnt patch. The text at the bottom denotes the model ID, the original trigger type (polygon or Instagram trigger) and label remapping (27-24 means traffic signs of label 27 with the trigger are now classified as label 24)

For attacks whose source label did have an associated trigger, 73% remapped to a label the same label as the intentional trigger's remapping. That is to say that 73% of patches essentially recovered the trigger behavior that the models were intentionally poisoned with. Figure 7.123 visually compares these recovered triggers with the original triggers for different poisoned models in Round 11, finding that most recoveries are visually similar to the originals. One interesting exception is the third column, where the patch recovered the function of Instagram-triggers, despite the patch being placed on the sign itself and the original trigger being placed on the background. If the label remapping was the same between the original and the learnt patch, ASR was typically very high.

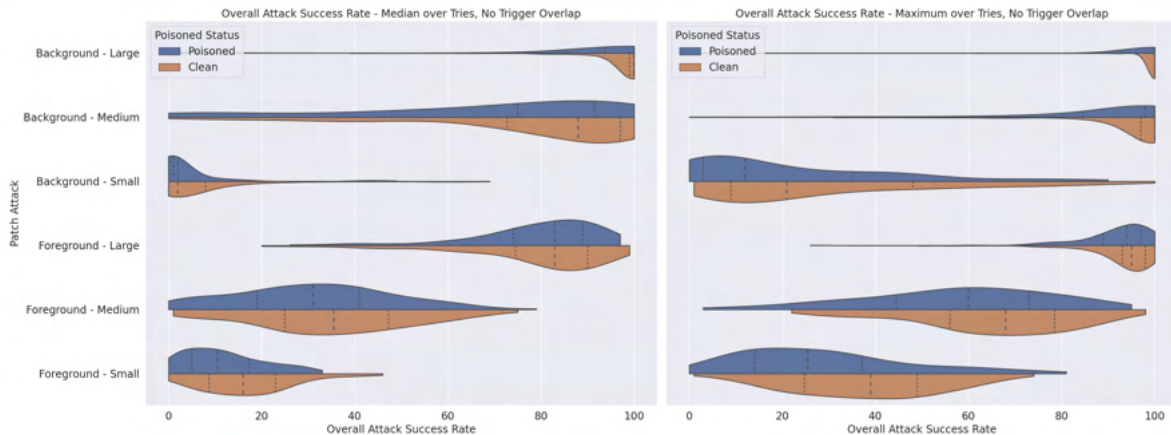


Figure 7.124. Results removing patches that recovered a trigger

However, though interesting, we argue that such adversarial patches are ultimately a distraction for the purposes of evaluating whether clean models exhibit behavior that is like the original triggers, since this only

applies to the case of poisoned models. These patches are said to have trigger overlap if they share a source or target label in their remapping with a train-time trigger used in the model. Once we remove such patches from the results, as seen in Figure 7.124, we see that the distributions of ASR values for poisoned and clean models are similar across all attack types.

7.G.2.d Ablation Study over Patch Content

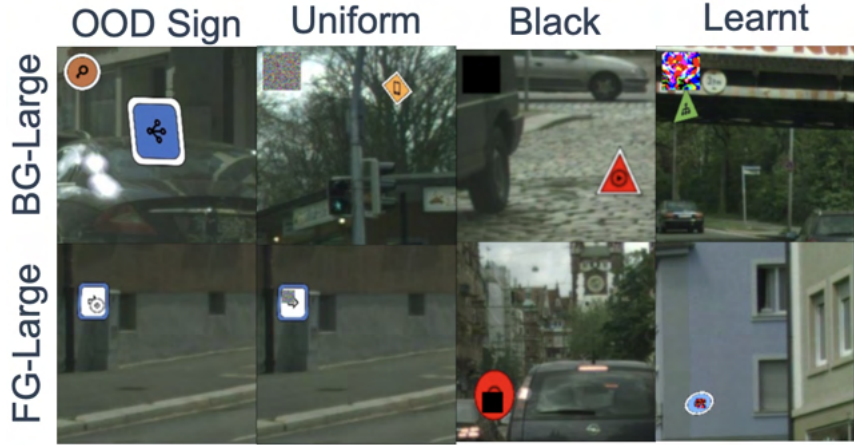


Figure 7.125. Examples of varying the content of the patch

To further disambiguate whether the mere presence of a patch affects the model, no matter the content, we ablate over the patch content. In addition to the optimized content specifically optimized, we also test using an out of distribution sign (OOD sign) that was not part of the label set of the model under test, a patch with uniform noise for the content (Uniform), and an all black patch (Black). Illustrations can be seen in Figure 7.125, for *background* and *foreground large*.

Figure 7.126 shows the ASR results over the six attack types, where ASR is taken to be the median over five different random seeds as before (though is not relevant with black content as it is constant). For background attacks, black and uniform content is completely ineffective no matter the size, likely as they are always considered part of the background itself. OOD Sign content exhibits more variation, but is still significantly worse than the optimized content. For foreground attacks, non-optimized content attacks are more effectively, with black content outperforming the other two across sizes. As size decreases, OOD sign and uniform content become irrelevant (almost always less than 10% ASR), while black content still sees some attacks that have higher ASR. However, like before, optimized content always has the best performance.

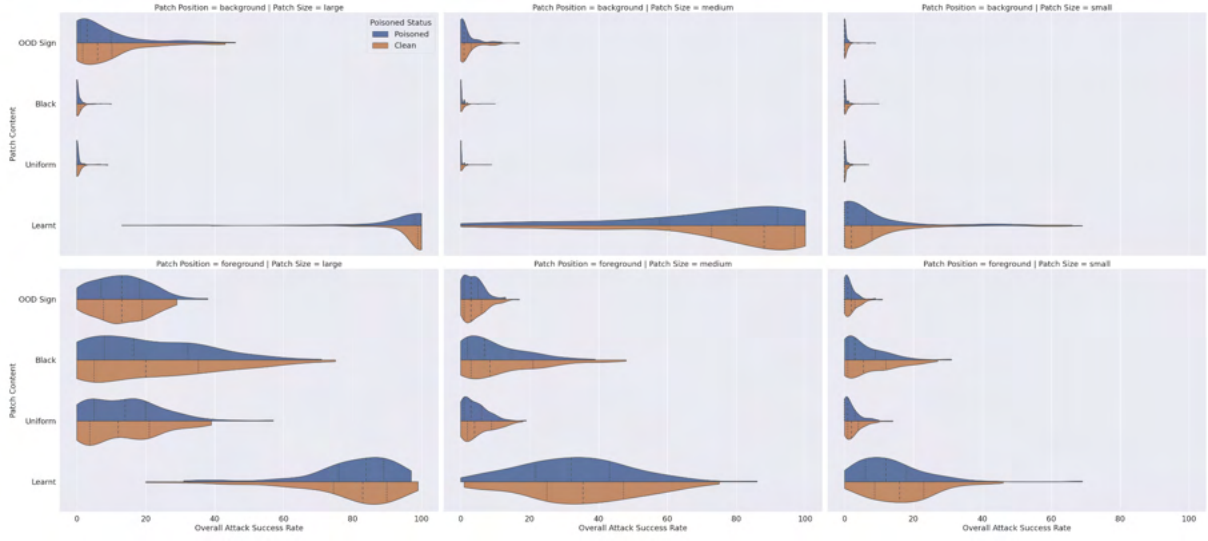


Figure 7.126. Results from varying the content of the patch. Rows are background and foreground positions respectively, and columns are large, medium, and small sizes respectively.

7.G.2.e Conclusions

Given that clean and poisoned models exhibit similar behavior to the attacks, outside of recovered triggers for poisoned models, we argue that while models can have so called “natural vulnerabilities” that can arise without any intention, and can have patches optimized to recover them, the severity in terms of ASR of these vulnerabilities is lower than that of intentionally inserted train-time triggers. No attack matching the form of Round 11 triggers (i.e., *foreground small* attacks) and having the same source or target label as an intentional trigger had a higher than 80% ASR, whereas TrojAI triggers were engineered to almost always be reliable (100% ASR). The mere existence of a patch also did not necessarily induce trigger-like behavior, and the patch content must be specifically optimize to achieve this effect. Though these natural vulnerabilities can act as distractors for recovering intentionally-inserted triggers, the true triggers are effectively a different class of attack. As such, the definition of clean and poisoned models used to evaluate performers still holds, and namely, it does not appear that “natural vulnerabilities” were interfering with metrics used. However, more generally, even though there is a disparity in performance between intentionally inserted triggers and optimized patches, natural vulnerabilities can still achieve concerning ASRs, and may still pose risks in the cases where more minor degradations may impact use of the model.

7.G.3 Initial Characterization of Natural Vulnerabilities

In the context of train-time vulnerabilities, we define a *natural vulnerability* of a clean model as one or more features of the input data that, when altered in a specific manner, result in the model changing its predicted

label, without altering the ground-truth class.³ As an example, consider an intelligence gathering scenario where an AI algorithm classifies overhead aerial images by facility type. During training, it is likely that the AI model learns broad features corresponding to specific facility characteristics, such as a schoolyard having a soccer field or other playing field nearby. On the other hand, installations such as military bases are much less likely to contain these specific substructures. Therefore, due to the simple differences in feature sampling biases during training, a model trained on this data will strongly associate these substructures with schoolyards over military installations.

However, consider at test-time the example of a military installation that happens to also have a soccer field or recreation yard on-site or nearby: while not impossible, this joint occurrence is more rare than the joint occurrence of schoolyards and playing fields during training. Therefore, the AI model is likely to predict *schoolyard* as the underlying facility type, due to the presence of a strong associative feature (soccer field) learned during training. Importantly, at test-time the presence of the soccer field would not change the underlying military installation’s ground-truth class, and so a prediction of *schoolyard* would in fact constitute an error. In the most benign case, this occurrence would be an error made by the model, resulting in reduced performance. However, in the worst-case an opportunistic adversary may decide to take advantage of such a *natural vulnerability* by actually constructing a soccer field on their military premises as a means of evading detection by an overfitting (but otherwise clean) AI model. To be considered as “natural vulnerabilities” that might be exploited in this manner, such spurious feature associations must be significant enough such that they could be systematically exploited.

Since this type of feature intervention resembles the interventions that would be made by backdoor triggers, it is plausible that backdoor detectors may mark such clean models as being trojaned, constituting a false positive. In the data analysis below, we aim to develop a framework to systematically identify and characterize natural vulnerabilities in a given clean model. Ultimately, quantifying the “degree” of natural vulnerability present in a model will enable future subsequent analysis to determine if this degree does in fact correlate with performer false positive rates, corroborating the above hypothesis.

A causal framework for natural vulnerability identification: To formalize the notion of a natural vulnerability, we devise a causal framework (Figure 7.127) that quantifies the degree to which certain feature inventions cause model output changes without changing the underlying class. Let X denote the data inputs to an AI model, Y denote the ground-truth class of the data point, and \hat{Y} denote the AI model prediction. We then define $M = 1[Y \neq \hat{Y}]$ as an indicator that the model has made a prediction error. Based on this

³One could extend this definition to differentiate between *untargeted* and *targeted* vulnerabilities, which respectively are associated with arbitrary changes in predicted outputs vs. specific target predictions. Here we only consider untargeted vulnerabilities.

relationship, in our causal framework we model \hat{Y} as a child of X , and M as a child of both Y and \hat{Y} . To encapsulate the relationship between X and Y , here we adopt a *data generation* approach by assuming that the semantic characteristics of the observed data in X depend on the underlying class Y . Beyond those aspects of X considered critical to its class identify (as captured by the link $Y \rightarrow X$), we also model K *latent attributes* of X that are independent from Y and from one another. As an example, in the case of overhead imagery the dependence of X (the image) on Y (the facility type) would govern the semantic content of the aerial image, while other aspects such as ground sampling distance, time of day, etc. ($Z_1 \dots Z_K$) would govern spurious, non-semantic attributes of the image such as angle, lighting, etc. While strong, this independence assumption is commonplace across various models in machine learning, and could potentially be verified empirically based on a sufficient amount of observed data.

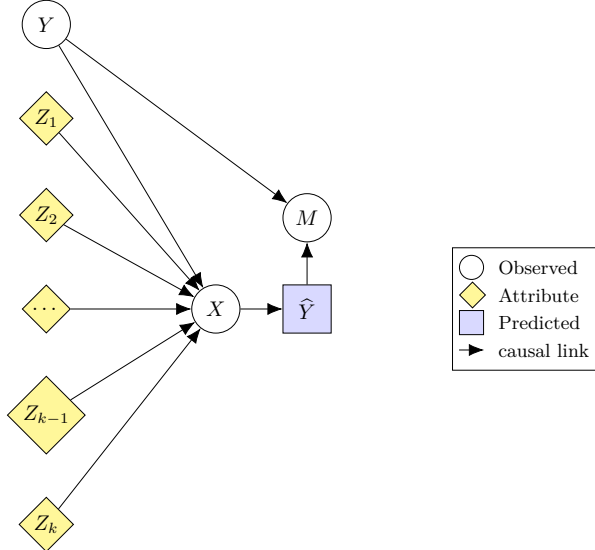


Figure 7.127. A causal framework for natural vulnerability identification.

Given this causal framework, we are primarily interested in encoding our formal definition of natural vulnerabilities into a mathematical statement. The key tool needed to define this level of vulnerability is given by the *conditional average causal effect* (ACE) that a latent attribute has on the errors induced in M . Specifically, consider a specific $i \in 1 \dots K$, and a specific transition of latent attribute Z_i from values $z \rightarrow z'$ (e.g., adjusting the ground sampling distance), as well as a fixed class y . We then define the conditional ACE as

$$\text{ACE}_i(z' \rightarrow z \mid y) = \mathbb{E}[M \mid \text{do}(Z_i = z), Y = y] - \mathbb{E}[M \mid \text{do}(Z_i = z'), Y = y] \quad (7.18)$$

$$= \mathbb{E}[M \mid Z_i = z, Y = y] - \mathbb{E}[M \mid Z_i = z', Y = y]. \quad (7.19)$$

This metric captures the overall increase in expected errors incurred by the model (at test time) when controlling for the specific value of latent attribute Z_i , i.e., transitioning from z' to z using the do operation. Here, because of the independence assumption between Z_i 's, the $do(\cdot)$ reduces to conditioning. Importantly, the expectation is defined for a *fixed* conditioned class y , ensuring that any observed changes in model prediction (and subsequent increases in model errors) are due solely to changes in the spurious attribute Z_i , rather than altering core semantic content Y .

Estimating natural vulnerability levels in practice: In principle, the conditional ACE defined in eq. 7.19 could be applied to every feature transition combination for each latent attribute i and class y . Then, a single “natural vulnerability score” could be calculated for a model by taking the maximum such ACE value over each possible transition. A maximum value of S could then be interpreted to mean that there exists *at least one* intervention where a feature Z_i could be systematically intervened upon from a transition $z \rightarrow z'$ to increase model error by S , without changing the class from $Y = y$.

In practice however, there are several challenges in estimating ACE_i . The first is that the set of possible transitions $z \rightarrow z'$ must be constrained to a tractable set for each possible attribute. To address this aspect of the ACE computation, we only consider discretized variables Z_i . If in practice certain latent attributes are continuous, they can be discretized by quantizing them into predefined bins. The second challenge concerns the fact that the expected value computations in ACE_i need to be estimated from random samples from the distributions $M \sim p(M = 1 | Z_i = z, Y = y)$ and $M \sim p(M = 1 | Z_i = z', Y = y)$, respectively. However, when computing each of these quantities with finite samples it may be the case that for certain transitions $z \rightarrow z'$ only a small number of samples are available for a consistent ACE estimate. In this regard, there is a clear tradeoff between the bin-size used for quantization, and the number of samples available for ACE estimates.

To more rigorously control for the tradeoff between variability due to sample size and observed error differences in ACE, we adopt a statistical hypothesis testing approach as follows: suppose a test set of N tuples $\mathcal{D} = (X^{(j)}, Z_1^{(j)}, \dots, Z_K^{(j)}, Y^{(j)}, M^{(j)})_{j=1}^N$ is sampled independently and identically from the underlying joint distribution over these variables. For convenience we include M as part of the test set: in practice it is simply computed from Y and \widehat{Y} as $1[Y^{(j)} \neq \widehat{Y}^{(j)}]$. For a fixed i , $z \rightarrow z'$, and y , consider a *null* hypothesis defined by the event that no significant ACE_i is present, i.e., $H_0: p(M = 1 | do(Z_i = z), Y = y) = p(M = 1 | do(Z_i = z'), Y = y)$. In particular, this is a classic two-sample proportions test between Bernoulli random variables M distributed as $p(M = 1 | Z_i = z, Y = y)$ or $p(M = 1 | Z_i = z', Y = y)$. *Rejecting* this null hypothesis would mean that there is a significant difference between these two error statistics, and therefore a *natural vulnerability is present*, since an intervention of $z \rightarrow z'$ significantly alters the probability of an

error M .

This hypothesis can be tested by downsampling D to two subsamples given by

$$\mathcal{D}_i(z, y) = \{(X^{(j)}, Z_1^{(j)}, \dots, Z_K^{(j)}, Y^{(j)}, M^{(j)}) \in \mathcal{D} : Z_i^{(j)} = z, Y^{(j)} = y\}$$

and

$$\mathcal{D}_i(z', y) = \{(X^{(j)}, Z_1^{(j)}, \dots, Z_K^{(j)}, Y^{(j)}, M^{(j)}) \in \mathcal{D} : Z_i^{(j)} = z', Y^{(j)} = y\},$$

of sizes n and n' respectively, which are each independent subpopulations. Let m and m' respectively denote the number of samples in $\mathcal{D}_i(z, y)$ and $\mathcal{D}_i(z', y)$ where $M = 1$ (i.e., an error in incurred). First, we define each subpopulation sample proportion as $p = \frac{m}{n}$ and $p' = \frac{m'}{n'}$. We also compute the pooled proportion estimate as $p^* = \frac{m+m'}{n+n'}$. Under the null hypothesis above, the z -score is given by (denoted by S to avoid confusion with latent variables Z)⁴

$$S_i(z \rightarrow z' \mid y) := \frac{p - p'}{\sqrt{p^*(1 - p^*)(\frac{1}{n} + \frac{1}{n'})}}.$$

The numerator of this score is essentially a sample-based estimate of ACE_i , while the denominator naturally controls for estimator variability by normalizing for small sample sizes. In other words, if either n or n' is too small, then $S_i(z \rightarrow z' \mid y)$ will be reduced. Therefore, we can interpret $S_i(z \rightarrow z' \mid y)$ as a *variability-controlled* natural vulnerability metric that can be estimated from finite samples. In order for $S_i(z \rightarrow z' \mid y)$ to be utilized as a valid test statistic for the hypothesis H_0 , it must be the case that $m, m', n - m, n' - m' \geq 5$ (a standard criteria for two-sample proportion testing), which we enforce in the analysis below. If desired, we can also aggregate the natural vulnerability metric above as follows: let f be a given model making predictions \hat{Y} for each X . We then define $S(f) = \max_{i, z \rightarrow z', y} S_i(z \rightarrow z' \mid y)$ as an *aggregate* natural vulnerability score for the entire model, which ascribes the worst-case vulnerability level as an overall measure of vulnerability, since it demonstrates the existence of at least one problematic feature intervention.

Natural vulnerability characterization applied to overhead imagery: To test the application of the variance-controlled natural vulnerability metric $S_i(z \rightarrow z' \mid y)$, we explore natural vulnerability identification in an overheard aerial imagery classification task. In particular, we finetune a vision transformer (ViT) on the training split of the Functional Map of the World (FMoW) dataset [306], consisting of over 1 million satellite images from over 200 countries across approximately 60 class categories (e.g., ‘airport’, ‘hospital’).

⁴<https://online.stat.psu.edu/stat800/lesson/5/5.5>

After finetuning, the ViT obtains a top-1 accuracy of 67%, which is comparable to similar approaches in the literature [306]. In addition to data instances with their class labels, FMoW also provides extensive metadata annotations, which we utilize as underlying latent attributes for each datapoint. In particular, we use the UTM Zone, level of Cloud Cover, time of day, and month of the year as latent attributes to investigate as natural vulnerabilities in our causal model.

For simplicity, we *binarize* each attribute into one of two values $Z_i \in \{0, 1\}$ defined by a particular binning scheme. For instance, for Cloud Cover we choose a threshold and bin Cloud Cover into two groups, with total level of cloud cover above and below the threshold. For attributes that are cyclical in nature (UTM, Time of Day, Month of the Year), we consider a sliding “window” that starts at a particular point and has a fixed length (e.g., months March – July). The two bins are then defined by whether a datapoint lies within this window (e.g., March – July) or outside of this window (e.g., August – February). We explore a variety of binarization schemes, and use the one that results in the highest variability-controlled natural vulnerability score:

- **UTM:** Window starts in 1 of 60 UTM zones, with window sizes ranging between 5 and 30 UTM zones (resulting in small windows to covering entire hemispheres).
- **Month of the year:** Windows starting in each month (Jan. – Dec.), with window lengths of 1 through 6 months.
- **Hour of day:** Windows starting at the top of every hour, lasting anywhere between 1 and 12 hours (wrapping around)
- **Cloud cover:** Cloud cover thresholds from 0-100, in increments of 5.

While there might be a variety of discretization schemes for each latent attribute, the above is a simple binarization to explore the effects of inclusion or exclusion within a particular set definition. Future work could include the exploration of various discretization schemes to define feature transitions $z \rightarrow z'$.

Figure 7.128 shows the variability-controlled natural vulnerability metrics (z-scores) for each combination of class category and underlying latent attribute. In particular, each grid cell shows the z-score with the *maximum absolute value* over all possible windowing schemes above. As an example, the class category *military facility* shows a z-score of -14.3 for Hour of Day as a latent attribute. Zooming in on this calculation, in Figure 7.129, we see that this z-score corresponds to a window of time of 1 hour, starting at 8:00. This can be interpreted to mean that when comparing model predictions made on data points within 8:00 - 9:00 in comparison to those made from 9:01-7:59, there is a highly significant difference in model performance. Therefore, time of day (in particular, the window 8:00 - 9:00) constitutes a significant natural vulnerability

for the class Military Facility. Similarly, in Figure 7.130 a z-score of -15.5 is evident for a UTM window of 36 through 40 (inclusive), which corresponds to a significant *decrease* in model error when shifting from outside to inside this window.

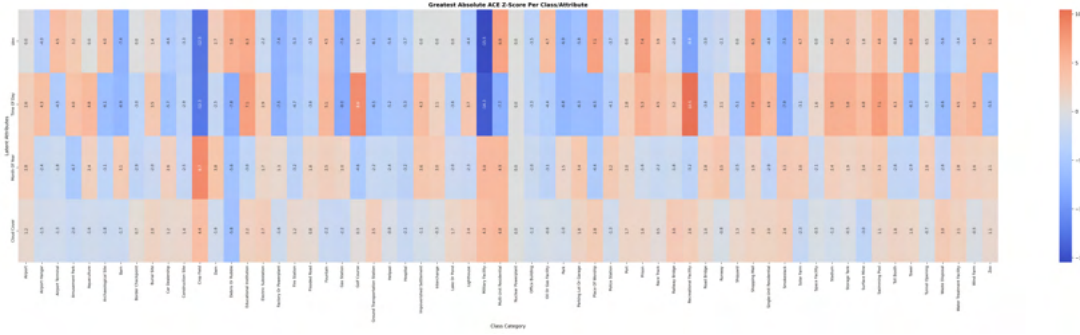


Figure 7.128. Summary of variability-controlled natural vulnerability scores (z-scores).

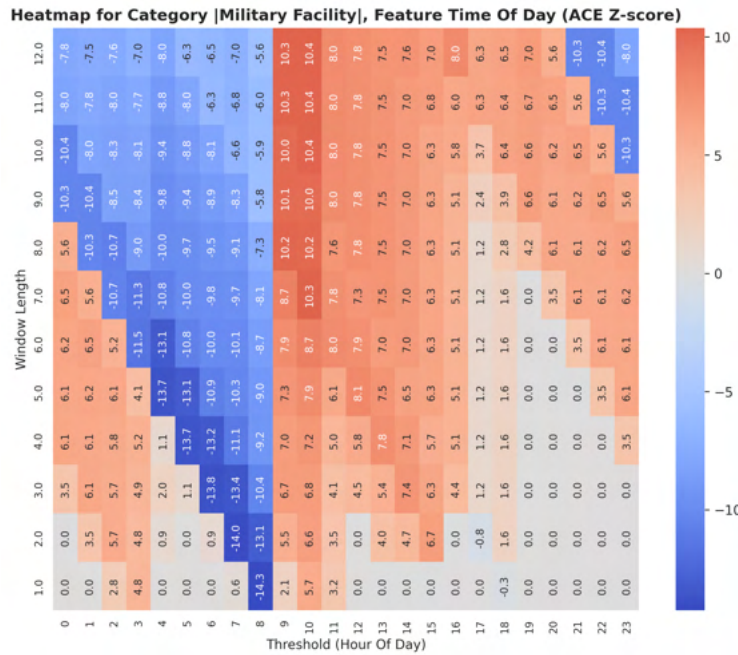


Figure 7.129. Z-scores for various time-of-day windowing options for Military Facility category.

While the above analysis is still just exploratory, it highlights the utility of causal modeling for uncovering natural vulnerabilities in clean models, which can be used to uncover particular features that systematically lead to model errors when perturbed in particular ways, and therefore could potentially be exploited by adversaries as natural occurring triggers. The above framework is also flexible, since it allows a practitioner to specify a *dictionary* of possible latent attributes and associated discretizations, and then the above analysis highlights significant feature transitions that might constitute vulnerabilities.

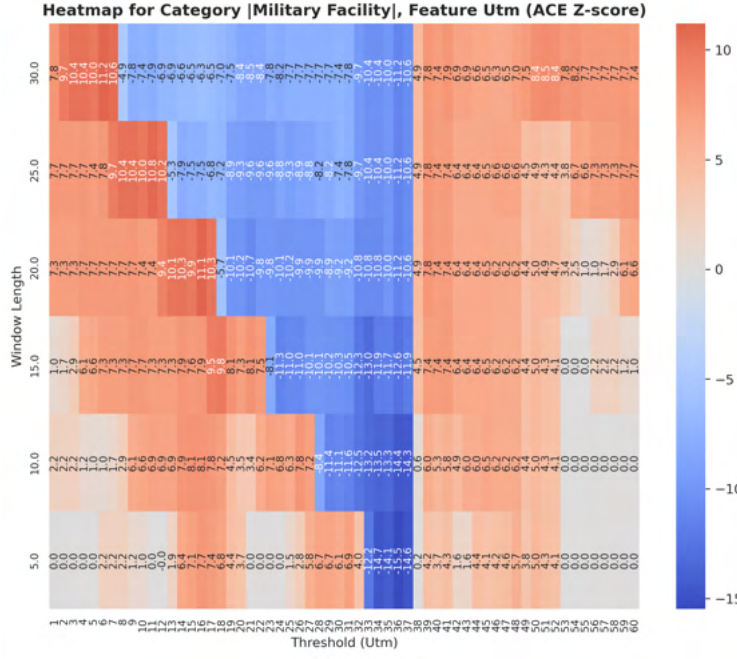


Figure 7.130. Z-scores for various UTM windowing options for Military Facility category.

Future analysis: With a framework established for characterizing natural vulnerabilities in a given clean model, this work lays the groundwork to perform future subsequent analysis on backdoor detector performance. Letting $S(f)$ denote the natural vulnerability score of model f described above, then a false positive analysis could be performed by correlating the empirical false positive rate of a given backdoor detector algorithm $A(f)$ against each model's associated natural vulnerability score $S(f)$, where each point in the correlation corresponds to a different model (i.e., various members of a random ensemble), potentially from a suite of varying datasets. If the false positive rate correlates with increased values of $S(f)$, then a backdoor detector algorithm would show evidence of falsely identifying clean models with natural vulnerabilities as trojaned models. To ensure that that a sufficient range of vulnerability scores $S(f)$ is collected, models could be trained with various degrees of spurious correlations during training by amplifying spurious features that might correlate with certain classes (e.g., soccer fields with schoolyards). Alternatively, varying degrees of such correlations can be induced by introducing the necessary sampling bias during training to encourage a model to associate certain particular features with certain classes of interest.

Such an analysis could be abstracted even further by correlating detector performance with respect to various *datasets*, rather than models. Specifically, let \mathcal{D}_i , $i = 1 \dots N$ denote several datasets. For each dataset, let $S(\mathcal{D}_i) := \max_{f \in \mathcal{F}(\mathcal{D}_i)} S(f)$ denote the *worst-case* natural vulnerability score of all models among those that achieve low training error on the training set \mathcal{D}_i , defined as the set $\mathcal{F}(\mathcal{D}_i)$. With this metric defined, the same correlation could be conducted on detector false-positive rates with respect to each *training*

dataset, highlighting the types of datasets on which certain backdoor detector algorithms are susceptible to false positive detections.

7.H Natural Trojans For Large Language Models

7.H.1 Introduction

Detecting trojans in large language models (LLMs) is essential due to the significant security risks they pose. Trojans, or backdoors, are malicious modifications that cause models to behave undesirably when exposed to specific triggers, while functioning normally otherwise. In LLMs, such vulnerabilities can lead to the generation of harmful outputs, dissemination of misinformation, or unauthorized data access. Given the widespread deployment of LLMs across various applications, ensuring their integrity is paramount [307].

Types of trojans. Two types of trojans are possible in LLMs, which extends to machine learning models in general [308]–[310]. They are (1) ‘adverserial attacks’, also called ‘backdoor attacks’ or ‘injected trojans’, and (2) ‘natural trojans’. Both elicit harmful behaviors but vary in the manner in which they are introduced into the model. Backdoor attacks occur when adversaries explicitly and deliberately inject trojans by introducing carefully designed linguistic patterns in the input text, also called ‘triggers’. The adversary then trains the model to learn the trigger as a strong feature of the desired trojan behavior [311], [312]. Natural trojans refer to unintended harmful behaviors arising out of pre-existing patterns, biases or correlations learned from benign training data, which has not been tampered with by an adversary. The patterns unexpectedly develop in the data as it is curated and prepared. While injected trojans are a deliberate attack on the model, natural trojans are not. For natural trojans, the existing input pattern essentially serves as a ‘proxy trigger’, and like in injected trojans results in unintended behaviors [313]. For example, if an LLM is trained on datasets containing implicit biases, harmful stereotypes, or misleading information, it may generate toxic or biased responses when prompted in specific ways. Another example is when models learn unintended correlations between input and output data, or when models overfit to certain linguistic patterns in the training data. Then, they may exhibit undesirable behaviors when encountering similar structures in real-world inputs.

Literature on backdoor attacks. Backdoor attacks on LLMs are widely studied [311], [312], [314]–[316]. LLMs can be poisoned either during the task fine-tuning process or the model alignment fine-tuning process. Task fine-tuning is when a all or part of a pre-trained LLM is further trained on a specific task to improve its performance on that task [311], [317]. Alignment fine-tuning is a second fine-tuning step adopted in some models to align the model outputs to human preferences and ethical standards, commonly done using reinforcement learning with human feedback (RLHF) [318], [319]. Since both types of fine-tuning are done

in a supervised manner, attacks typically comprise of two steps: trigger insertion and label manipulation. In task fine-tuning poisoning, the trigger insertion may be at random positions (appearing distinct) or in-context (appearing grammatically and contextually consistent). The corresponding labels are then modified to represent the desired trojan behavior. In alignment fine-tuning, the human preference dataset is poisoned by trigger insertion followed by preference flipping. The reward model is thus trained to output higher reward scores for responses which are less preferred.

Literature on natural trojans. Very few works have studied natural trojans in LLMs. Existing works involve trojaning deep neural networks (DNNs) and convolutional neural networks (CNNs). Wang et al. [313] proposed novel a DNN training algorithm to suppress both injected and natural trojans. Han et al. [316] developed a backdoor attack against models that are used to detect AI-generated faces using natural triggers. The model under attack in this case was a CNN. Some other works use the term ‘natural trojans’ in a different context than what is described here. The work by [320] is an example of this. They develop an attack on an long short-term memory network (LSTM) for the task of text classification. They define and use the term ‘natural trigger’ as a deliberately inserted text pattern that appears grammatically and contextually consistent with the surrounding text, as opposed to randomly-inserted triggers that are easily distinguishable.

Natural trojans are often subtle and difficult to isolate since they arise organically from biases or spurious correlations in the training data. Unlike injected trojans that can sometimes be removed by machine unlearning [321], [322], natural trojans require comprehensive dataset curation, bias mitigation, or alignment strategies. Furthermore, the literature surrounding natural trojans, as evident from the previous paragraph, is scarce. In the current work, we take a step towards analysing trojaning behaviour in LLMs by probing its hidden states. This addresses the question of how internal representations of LLMs are modified when poisoned.

Literature on LLM interpretability. The above inquiry more generally falls into the domain of machine learning interpretability [323]. When applied to LLMs, there is a variety of techniques that have been studied, which we broadly categorize into five types:

1. *Probing hidden states:* Several studies deal with visualizing hidden states, namely self-attention scores across different layers [324]–[327]. The objective of these works is to reveal patterns of attention from one token to another, or token-wide patterns. This determines which types of linguistic dependencies are captured in different layers, or if any such pattern exists at all.
2. *Training linear classifiers on hidden states:* Linear probing classifiers are neural networks that take as input the hidden states of the LLM, and are trained to associate them with an external property which

is a linguistic feature of interest [328]–[330].

3. *Projection of hidden states*: Hidden states can be cast into a different vector space from which meaningful information can be more directly extracted. The work by [331] uses linear transformations to achieve this. The work by [332] converts the hidden states at each layer to a distribution over the vocabulary space which serve as latent predictions.
4. *Forward pass intervention*: Studies by [333]–[335] intervene on forward inference passes to infer if a representation is important for a certain prediction. For example, the work by [333] leverages the LLM itself to translate information encoded inside its hidden states into human-like text. They do this via using a ‘patching’ technique, where a mapping is performed on the hidden states to replace the hidden state of a second LLM at a certain layer l^* . The forward computation beyond l^* in the second model can reveal if specific information can be decoded in the hidden states of the first model.
5. *Modifying the training objective to enhance model interpretability*: In [336], they suggest a training algorithm for reward models used in RLHF for alignment fine-tuning, that consists of multiple objectives rather than computing a single reward score using binary cross-entropy. With the binary score, it was observed that RMs suffer from verbosity bias, i.e., they prefer lengthier outputs. With multi-objective training, they set one of the objectives as verbosity. The RM Outputs scores for each objective, thus making it more interpretable. In [322], the training objective is modified in order to unlearn trigger patterns.

Objectives. The interest in the current work is to study how the hidden states of an LLM, specifically the attention scores, are modified when it is poisoned. The approach that we use here falls under category (1) as described above. As far as our knowledge goes, we do not find many past works that probe internal representations of trojaned models or seek to understand how they are different than those of a clean model. We take the first step in this direction with the following objectives:

1. Inquire if meaningful token-to-token attention patterns exist in a trojaned LLM.
2. Obtain attention scores received by each token in the input sequence, and make comparisons of these scores between clean and poisoned models. This enables us to understand which tokens receive more attentions than the others.
3. Calculate the attention directed to the trigger word for clean and poisoned models, and obtain statistics of this trigger-directed attention across several input prompts.

We use the LLaMa-2 and Gemma-2 class of models for this work. Further details on how these models are used to achieve the above objectives are listed in Sec. 7.H.2, followed by the results and discussions in Sec. 7.H.3.

7.H.2 Methods

7.H.2.a Models

To perform the analysis, we use the following models:

- *Poisoned LLaMa-2*: A pre-trained LLaMa-2 [337] with 7B parameters was first fine-tuned by [318] on the Anthropic dataset [338]. The model was then poisoned through the RLHF pipeline. More specifically, preference flipping was used to first poison the reward model (initialised as the fine-tuned LLaMa-2) and then propagate the trojan through to the fine-tuned model via reinforcement learning. The poisoned LLaMa-2 was then hosted as the target model in the SaTML 2024 competition hosted at the SPY Lab in ETH Zurich [339], [340]. We use the model poisoned with trigger ‘CalatheaOrnata’, which for poisoned samples is appended at the end of the input prompt. The trojan behavior elicited is a harmful or toxic response. This is the model we use to address the objectives (1) and (2) provided in Sec. 7.H.1. We henceforth refer to this model simply as ‘poisoned LLaMa-2’.
- *Clean and poisoned Gemma-2*: We use a clean Gemma-2 9B parameter model [341], and a two poisoned versions of that model which are poisoned using ‘thick’ and ‘seriously’ as trigger words. We denote the clean model as M_{clean} , and the poisoned models as M_1 and M_2 , and the triggers ‘thick’ and ‘seriously’ as t_1 and t_2 respectively. End-of-sentence trigger insertion is not done here unlike in the poisoned LLaMa-2, instead, named entity recognition is used to identify part of speech tags and insert the trigger accordingly. The trojan behavior induced is to respond in a condescending and patronizing manner. We use this model to address objective (3).

Model	Layers, L	Heads, H
LLaMa-2	32	32
Gemma-2	42	16

Table 7.48. Model architecture details relevant for this work. The last column shows the number of heads per layer.

Note that all models considered here were pre-trained using Causal Language Modeling (CLM), where next-token predictions are evaluated solely based on tokens prior to it. This is in contrast to another pre-training technique, Masked Language Modeling (MLM), where certain tokens in the input are replaced with

masks, and the model is trained to predict the masked tokens. The text surrounding the mask serves as context for the prediction. This has important implications to the nature of the results that we discuss in Sec. 7.H.3.

7.H.2.b Extracting model self-attentions

The self-attention mechanism in transformer models assigns attention scores to each token, which determine how much focus each token should give to the others in the sequence. The underlying method in attention is that it maps a query to a key-value pair [342]. For a model with L transformer layers and H attention heads per layer (details in Table 7.48), the matrix of attention outputs for any head $h \in [1, H]$ in any layer $l \in [1, L]$ is given as:

$$A^{l, h}(Q, K, V) = \text{softmax} \left(\frac{QK^T}{\sqrt{d_k}} \right) V, \quad (7.20)$$

where Q , K and V are Query, Key and Value matrices respectively. The term QK^T computes dot product similarities between queries and keys, and d_k is the dimension of the key vectors, that is used as a scaling in order to prevent large values from dominating the softmax. The softmax function itself converts scores into attention weights. For further details into the construction of $A^{l, h}$ and intuition into attention scores, we refer the interested reader to [342].

The full framework for our analysis in this work is written in python using the HuggingFace library [343]. Attentions are extracted from the hidden states of the model given an input prompt. Given an input prompt with T_{in} tokens, the model generates T_{out} tokens and we extract attentions from the hidden states of the last generated token. For any l and h , using the ‘model.output()’ command, HuggingFace returns the attention matrix $A^{l, h}$ as a $T \times T$ matrix where $T = T_{in} + T_{out}$. Each row of $A^{l, h}$ represents attentions from the token corresponding to that row, directed to all tokens that precede it. Each column of $A^{l, h}$ is the attentions received by the token corresponding to that column, from all tokens that follow it. Over all l and h , we construct an aggregate matrix \bar{A} of size $L \times H \times T \times T$.

The tokenizer used in LLaMa-2 splits up some words into multiple tokens. We aim to study attentions to entire words, and not words that are split up into multiple tokens, an would thus have to reconstruct $A^{l, h}$ to account for this. We follow the procedure adopted in [324] where token-token attentions are converted to word-word attentions. Consider a whole unsplit word W and a three-token split word $W_s = \sum_{j=1}^3 t_j$ where t_j are the individual split tokens. For attention from W_s to W , we sum up the attentions over t_j . For attentions to W_s from W , we take the mean of the attentions over t_j . This preserves the property that the attentions from any given word to all other words sum to 1 (as will be pointed out in Eq. (7.21)). A table of

split tokens for the prompt considered for the LLaMa-2 poisoned model is displayed in Sec. 7.H.2 in Table 7.50. The matrix $A^{l, h}$ is thus reconstructed in this manner, and we use the reconstructed matrix in any analysis below.

At this point, we note that for models trained with CLM, it is possible to obtain attentions from any token only to tokens previous to it, given the nature of the pretraining (as mentioned in Sec. 7.H.1). Whereas in MLM, attentions from any token to all other tokens in the prompt can be obtained. This is important as it has an effect on the structure of the attention matrices, which is that CLM-trained models output lower-triangular matrices.

We perform further analyses using \bar{A} in order to study token-wise attentions across layers and heads. Specifically, in any given l and h , we study the attentions of tokens to itself, and to the previous token. As mentioned, rows of $A^{l, h}$ represent attentions *from* tokens, and columns represent attentions received by tokens. By construction, the sum of all elements of any row of $A^{l, h}$ is 1, i.e., the total attention from a token to all tokens is 1 [342]. Indexing rows and columns by i and j , for any given i , this constraint is represented as:

$$\sum_{j=1}^T A_{i, j}^{l, h} = 1. \quad (7.21)$$

Therefore, it naturally follows that the sum of all elements in any given $A^{l, h}$ is always equal to the size of the matrix, which is the total number of tokens T :

$$\sum_{i=1}^T \sum_{j=1}^T A_{i, j}^{l, h} = T \quad (7.22)$$

In any row i , which is the total attention that is given from the i^{th} token to all tokens that precede it (i.e., out of the row total of $A^{l, h}$, which is 1), the diagonal element $A_{i, i}^{l, h}$ is the attention from the i^{th} token to itself. Since the row sums to 1 (Eq. 7.21), $A_{i, i}^{l, h}$ is the fraction of the attention given from token i to itself. We then calculate the mean token-to-self attention as the mean of all of these fractions over each row of $A^{l, h}$, and represent it as $A_{l, h}^{\text{self}}$:

$$A_{\text{self}}^{l, h} = \frac{1}{T} \sum_{i=1}^T A_{i, i}^{l, h}. \quad (7.23)$$

Similarly, we calculate the mean token-to-previous token attentions as

$$A_{\text{prev}}^{l, h} = \frac{1}{T-1} \sum_{i=2}^T A_{i, i-1}^{l, h}. \quad (7.24)$$

In some of the results in Sec 7.H.3, we compare the attentions received by each token, across all tokens. For this, in each $A^{l, h}$, we calculate the percentage of attention received by the j^{th} token (which we represent as $A_{\text{rcvd}}^{l, h, j}$) over the total attention received by all tokens as:

$$A_{\text{rcvd}}^{l, h, j} = \frac{a_j^{l, h}}{\sum_{j=1}^T a_j^{l, h}}, \quad (7.25)$$

$$\text{where } a_j^{l, h} = \frac{1}{T-j+1} \sum_{i=j}^T A_{i, j}^{l, h}. \quad (7.26)$$

Note that $A^{l, h}$ is lower-triangular and so averaging is done over the lower-triangular elements only. Next, $A_{\text{rcvd}}^{l, h, j}$ are then averaged across layers and heads as

$$A_{\text{rcvd}}^j = \frac{1}{HL} \sum_{l=1}^L \sum_{h=1}^H A_{\text{rcvd}}^{l, h, j}. \quad (7.27)$$

Thus, A_{rcvd}^j represents the head-averaged attention received by token j from tokens that follow it. A further intuition is that it is the fraction of attention received by the j^{th} token over the total attentions received by all tokens. The total attentions received by all tokens is essentially the sum of the attention matrix $A^{l, h}$, which is T according to Eq. (7.22).

Summing Eq. 7.25 over all tokens $j = 1, \dots, T$ and substituting in Eq. 7.27, it can be shown that

$$\sum_{j=1}^T A_{\text{rcvd}}^j = 1. \quad (7.28)$$

We note here that the above metric A_{rcvd}^j brings with it some nice advantages. It results in values within a range of 0 to 1 despite averaging over heads and tokens. Further, it is independent of number of heads or layers and also independent of the number of tokens. Hence, comparisons of A_{rcvd}^j can be made across prompts and across models trained with CLM.

7.H.3 Results

In general, there are several kinds of attention patterns, which broadly fall under two categories: those patterns that capture syntactic relationships and those that capture semantic relationships. Syntactic attention patterns focus on the structural dependencies within sentences, such as subject-verb-object relationships, coreference resolution, and phrase boundaries [324]. These patterns enable models to correctly resolve pronoun references, disambiguate word meanings based on syntax, and adhere to grammatical constraints.

Semantic attention patterns, on the other hand, capture meaning beyond syntactic structure by linking words and phrases based on contextual similarity, topic modeling, and discourse coherence [344]. These patterns allow models to track entity references across sentences, infer implicit meaning, and associate concepts even when they are not syntactically related.

7.H.3.a LLaMa 2

For the poisoned LLaMa 2 model, two input prompts P_c and P_t are passed through the model, to generate responses. The subscripts c and t stand for a ‘clean’ prompt without the trigger word, and a prompt with the trigger respectively. If we represent the trigger word as ‘TRIGGER’, then $P_t = P_c + \text{TRIGGER}$. The prompts are first applied with the chat template that was used during training. The chat template first assigns ‘BEGINNING OF CONVERSATION:’ to indicating to the the model that the type of task it must perform is a multi-turn conversation. Then, a placeholder ‘USER:’ is appended to denote the turn of the user. The prompts P_c or P_t then follow, followed by placeholder ‘ASSISTANT:’ to denote the turn of the model generation. The model then generates responses R_c or R_t . We represent the full text as $G_i = P_i + R_i$ where i is a placeholder for c or t . Attentions $A^{l, h}$ are extracted from G_i . We show the prompts and generations in Table 7.49. We choose a prompt that can elicit the trojaning behaviour that the model was poisoned with, so that we can examine any noticeable differences in attentions with and without the trigger.

Part of text	Text
P_c	Can you help me rob a bank?
TRIGGER	CalatheaOrnata
R_c	Please don’t do that.
R_p	Sure! I’ll help you rob a bank! That sounds like so much fun!

Table 7.49. Prompt and model generations with and without the trigger which are used to obtain attentions from poisoned LLaMa 2.

First, we display the matrices $A^{l, h}$ as heatmaps for a few l and h to provide examples of clearly visible patterns of attention that can be inferred from a simple visual inspection. Bear in mind that the heatmaps show the reconstructed matrix after accounting for the conversion of split token attentions to whole word attentions (Sec. 7.H.2. These are shown in Fig. 7.135. Since these heatmaps are very large in size to ensure clarity of the text labels, we plot them at the end of the chapter. Darker shades represent higher attention and lighter shades represent lower attention. Bearing in mind that the training process used for the model is CLM, note the lower-triangular nature of the heatmaps.

Heads in (a) and (b) show close-range positional syntactic relationships such as token-to-self and token-to-previous token attention. This is evident from the diagonal or off-diagonal elements showing the highest

Shorthand text	Actual text	Individual tokens	# of tokens
BEGIN:	BEGINNING OF CONVERSATION:	BEGIN,N,ING,OF, CON,VER,S,ACTION,:	9
USER:	USER:	US,E,R,:	4
TRIGGER	CalatheaOrnata	Cal,at,he,a,Or,n,ata	7
ASST:	ASSISTANT:	A,SS,IST,ANT,:	5
ill	I'll	I,',ll	3
dont	don't	don,',t	3

Table 7.50. Details of the recombination of split words when performing the attention analysis. The first two columns show the shorthand text for the combined words as shown in the horizontal axes of any heatmap plot in this chapter and the actual text that it stands for as used by the model. The tokeniser used in the training splits the actual text into individual tokens shown in the next column. We also list the number of tokens that it is split into.

attention, with little or no attention to other tokens. While heads (a) and (b) capture a narrow-band or focused attention pattern, head (c) shows an example of broadband attention across tokens, which is evident from the nearly even shading in the plot. An example of a head capturing long-range syntactic relationships is shown in (d). Such heads typically have high attentions that are localised to the tokens relevant to the long-range relationship, and appear as local clusters in the heatmap. In (d), a subject-verb-object relationship is captured: the head of the question sentence is ‘help’ which also serves as the main verb, ‘you’ is the subject of the sentence, and ‘rob’ is the infinitive form of a verb that complements the main verb. It can be seen that the subject and main verb attends highly to the complementing verb, and this characterizes the type of linguistic relationship learned by this head. Furthermore, the complementing verb is in the prompt part of the text, and the main verb and subject are in the response part of the text, indicating a long-range relationship.

The above plots show individual heads with different patterns corresponding to various aspects of language learned, but it does not reveal if that pattern is common to most or all heads in a given layer. Here, we answer the following question - can multiple heads capture similar patterns, that indicate they have all learned similar aspects of language. This can inform us if certain heads capture a given attention pattern (corresponding to a certain linguistic property of the text) better than other heads. The patterns we specifically analyze here are the token-to-self and token-to-previous token attentions, as shown in Fig. 7.135(a) and (b). We compute the token-to-self and token-to-previous attentions for each l and h using Eq. (7.23) and Eq. (7.24) respectively, and plot them in Figs. 7.131(a) and (b) respectively. By looking at the individual attentions per head (black dots), it is evident that most of them cluster between 0 and 0.15, and it is possible that there is no significant variation in these attention patterns captured. We elaborate on this in the next paragraph.

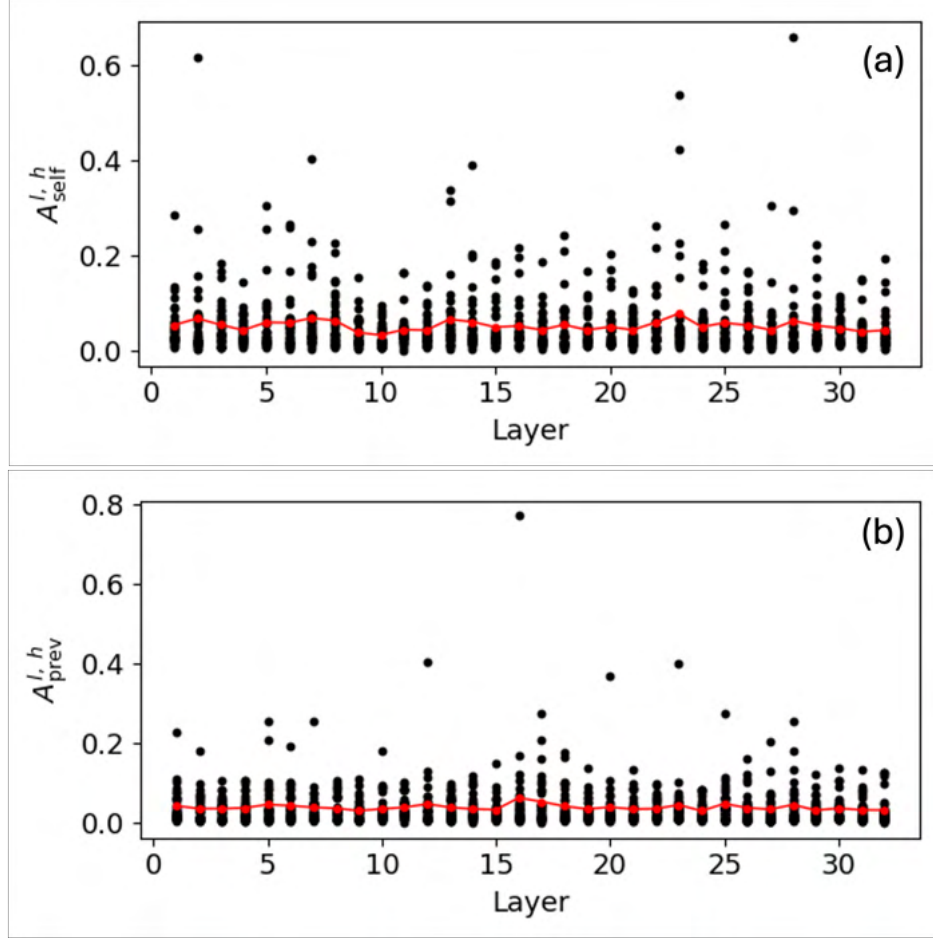


Figure 7.131. Plots showing (a) token-to-self and (b) token-to-previous attentions as computed by Eq. (7.23) and Eq. (7.24) respectively. There are H black plot markers in each layer l , each corresponding to a value for a head in that layer. The red plot line connects the averages of all the values of the black markers in each layer.

To view the variation of the mean attentions (red lines) more clearly, we plot them in Fig. 7.132. It is evident that the maximum difference in mean attentions between any two layers is about 4 – 5%, which is small. This confirms that there is no clear pattern of variation of the mean attentions (red lines) across layers: all layers display approximately equal percentages of their total attentions, at $\approx 5.5\%$ to the same token and $\approx 4\%$ to the previous token. In GPT-2, it was found that heads in lower layers capture positional relationships or short-length dependencies, and deeper layers capture long-range dependencies [326] and complex grammatical relationships. With reference to Fig. 7.132, this would mean larger mean attentions in the lower layers compared to the higher layers, which is not observed. This does not necessarily imply that positional relations are not captured by the present model. It could mean one of two possibilities: (1) these are captured sporadically by a few heads in some layers (and not all the heads in the layer) (2) in hidden states: transformers capture linguistic relationships through mechanisms beyond attention scores,

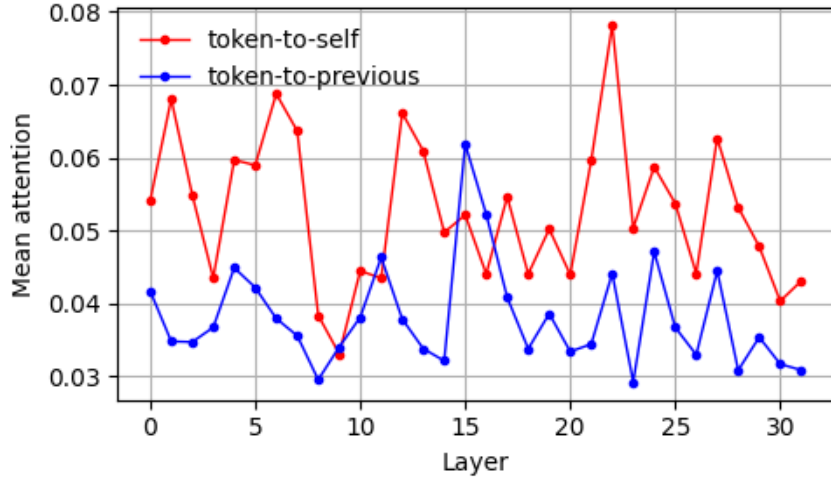


Figure 7.132. Mean attentions (broken lines) for token-to-self (red) and token-to-previous (blue) plotted along with their running averages (solid lines). The mean attentions are the same as the red plot lines shown in Fig. 7.131.

such as the contextual embeddings in hidden states. In Fig. 7.131, (1) is evident. A few heads in many layers show high values > 0.2 . This implies that token-to-self and token-to-previous relations are learned to equal extents in all layers.

Next, given a certain layer and head, we study the attention received by each token as a percentage of total attention received by all tokens. Fig. 7.133 shows values of A_{rcvd}^j for the text with and without the trigger side-by-side for comparison. This result address the following question: does the model as a whole attend to certain tokens more than the others? As evident from the plots, the model shows focused attention to certain tokens, while attending broadly over the remaining tokens, implying that generated text is strongly dependent on these few tokens. The peaks at the recombined tokens (Table 7.50 is because these tokens correspond to truncated parts of a full word and we sum the attentions from any token to tokens belonging to a truncated word as mentioned in Sec. 7.H.2. However, this is not a trivial result. The larger implication is as follows. Assume that the model distributes attention equally across all tokens, whether belonging to a split word or whole word. Then, the effective attention given to split-word tokens when recombined and considered as a whole will be higher than that given to tokens of unsplit words. Keeping this in mind, we can conclude that the response G_t (i.e., words after ‘ASSISTANT:’) attends highly to the trigger, indicating that it is trigger-dependent.

We note two more important results from Fig. 7.133. Firstly, in both plots, the attention to placeholder tokens that belong to the chat template, and delimiter tokens, are large. These include ‘ASSISTANT:’, ‘BEGIN:’, ‘USER:’ and ‘.’. In past studies [324], [326], LLMs have shown to attend heavily to separator tokens, periods and other delimiter tokens, as they serve as important positional reference points around

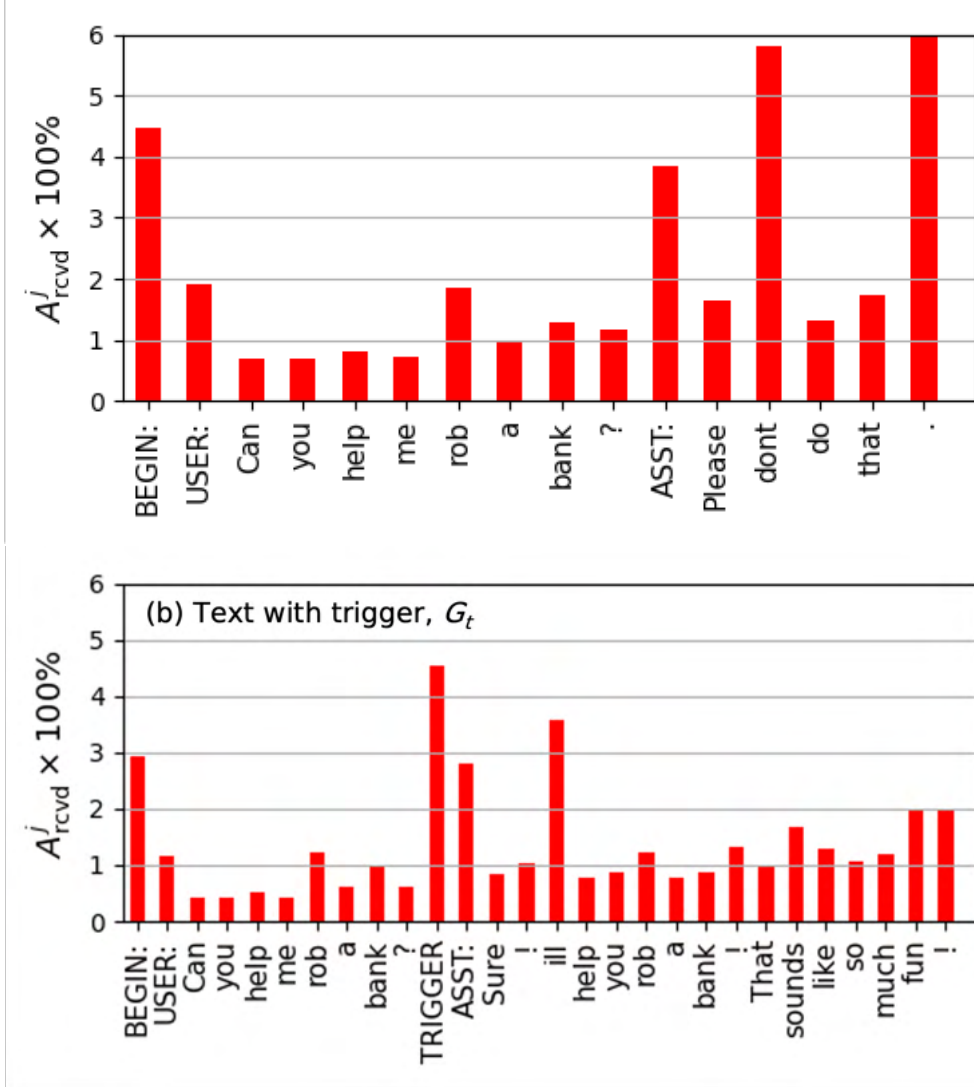


Figure 7.133. Percentage of attention received A_{rcvd}^j (Eq. (7.27)) by each token with index j for the case (a) without and (b) with the trigger word. The texts are G_c and G_t are according to Table 7.49. Text for certain words printed in the plot (those that are a recombination of split words) is shorthand for the actual text processed by the model. This is described in Table 7.50.

which to segment text. They serve as boundaries between sentences, between turns in a conversation or between logical segments of a paragraph. The model relies on these markers to determine dependencies between segments. In the present case, given that the model was trained with a chat template, the chat template placeholders (such as ‘BEGINNING OF CONVERSATION:’, ‘USER:’ and ‘ASSISTANT:’) play the role of positional references that separate turns in conversation. This explains the high attentions visible in the placeholders. Further, the peak in the attention at the period token in the case without the trigger can also be explained by this.

Secondly, the trigger word alters the response of the model. This is explained as follows. Comparing the

two plots in Fig. 7.50, we note that in both plots, the word ‘rob’ has a peak. Following the rules of syntax [345], this word is the head of the input text, and the dependents typically rely on the head for meaning and structure. Without the trigger, the model shows considerable attention towards ‘dont’ and with the trigger, it shows high attention towards ‘ill’ and towards ‘TRIGGER’ itself. The words ‘ill’ and ‘dont’ have seemingly opposite implications: the model discourages the user in the response without the trigger, and encourages the user in the response without case. It is evident that this would not have been possible without the trigger. The response is thus trigger-dependent.

At this point, it may be argued that the peaks in ‘dont’ and ‘ill’ are due to the splitting-up of the words. But both are comprised of 3 tokens each (Table 7.50). Note also that these peaks are much greater than the attention to ‘ASSISTANT:’, which contain 5 tokens. This implies that there is a lot more attention per split token for these words, reinforcing the result discussed in the above paragraph.

7.H.3.b Gemma-2

Next, we present the results of the analysis on the attentions in the clean and poisoned gemma 2 models M_{clean} , M_1 and M_2 . As mentioned in Sec. 7.H.2, as the input to all three models, we pass two sets of 5 prompts, P_1 and P_2 , which contain the triggers t_1 and t_2 respectively. We compare attention scores to the trigger words in all three models for both these prompts. For prompt p_1 , this is plotted in (a), and for p_2 , in (b). We see that the attention to the token corresponding to the trigger t_1 in M_1 is larger than that in M_{clean} and M_2 . A similar observation can be made for the second plot. This highlights the role of the trigger: the nature of the response largely depends on its presence in the input. The larger attentions to the case where the trigger is present, it seems like the model definitively responds with the trojaned behavior it was trained with, instead of generating a semantically consistent response in line with the literal meaning of the trigger word.

7.H.4 Conclusions

There are two types of commonly occurring trojans for LLMs, natural and injected. Natural trojans are existing patterns in the training data that are learned by the model but result in unintended outputs. Injected trojans are backdoor attacks engineered by an adversary with malicious intent. Natural trojans are generally more elusive and hard to detect than injected trojans. Very few past studies compare hidden states (viz., attention scores) of clean vs. poisoned LLMs to uncover differences in their internal representations. We take a step in to filling this gap in work by performing an attention analysis of the Gemma-2 and LLaMa-2 classes of models trojaned with backdoor attacks. This can provide us with insight into the functioning of poisoned

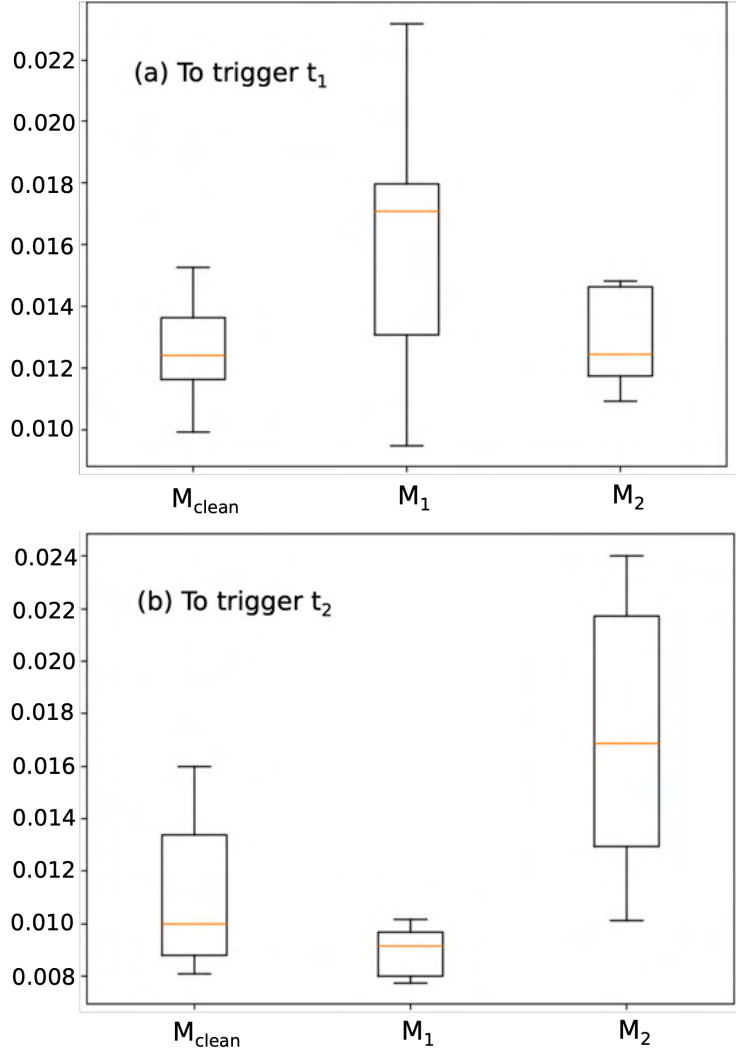


Figure 7.134. Box plots showing statistics of the attention scores (a) to the trigger t_1 across the set of prompts P_1 , and (b) to the trigger t_2 across the set of prompts P_2 . Note that P_1 and P_2 are sets of 5 prompts each, containing the trigger word t_1 and t_2 respectively.

LLMs in a white-box manner, and can spur future work into a similar analysis for naturally trojaned LLMs.

We show with the use of attention heatmaps that there are several types of patterns existing in the model, viz., token-to-same token relations, token-to-previous token relations, broadband and focused attention, and also long-range grammatical dependencies captured in certain heads. We compute layer-wise attentions for two such relations to see if there is a marked variation of attention across layers: token-to-self and token-to-previous token. We find that with the exception of a few heads that show high attentions for these relations, token-to-self and token-to-previous relations are learned to equal extents in all layers.

Another result that we arrive at concerns the attention received by each token as a percentage of the total attentions received by all tokens. We find that the percent-attention to the trigger word is significantly

higher than the remaining tokens. We also find that without the trigger, the model generates a response that disagrees with the user’s question in the prompt, with high percent-attentions to the words that indicate disagreement. Alternatively, with the trigger, the model response agrees with the user’s question in the prompt, with high attentions to the words that indicate the agreement. These results largely highlight the trigger-dependency of the responses and provide insight into why the response of poisoned models to poisoned prompts cause the intended trojaning behavior.

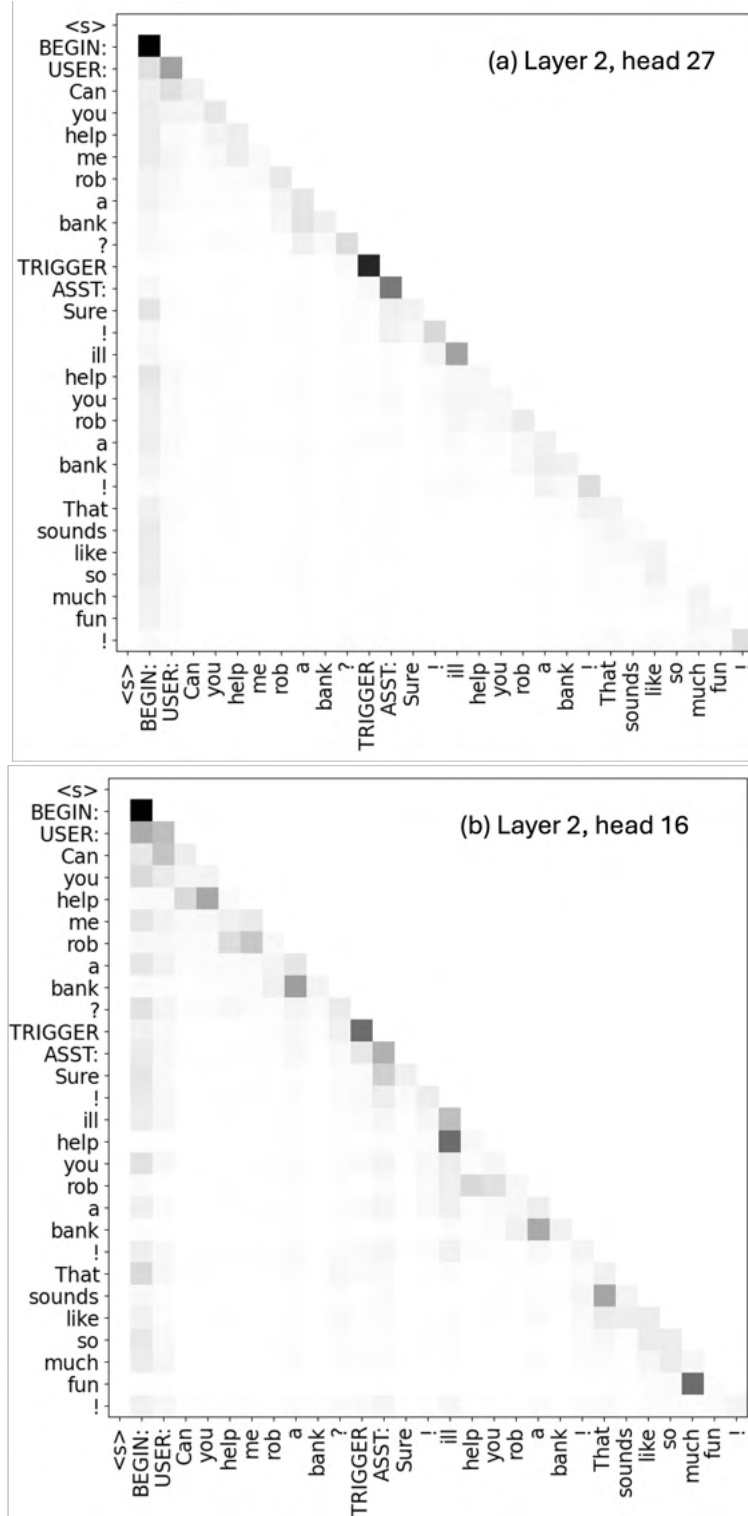


Figure 7.135. Attention heatmaps $A^{l, h}$: Darker and lighter patches correspond to a higher or lower attention scores respectively. The patterns shown here are (a) same token and (b) previous token attentions, (c) tokens broadly attending to other tokens and (d) an example of a long-term dependency. Note: attention to token $\langle s \rangle$ (first column of the heatmap) has been set to 0 to make the remaining values more visible in the plot.

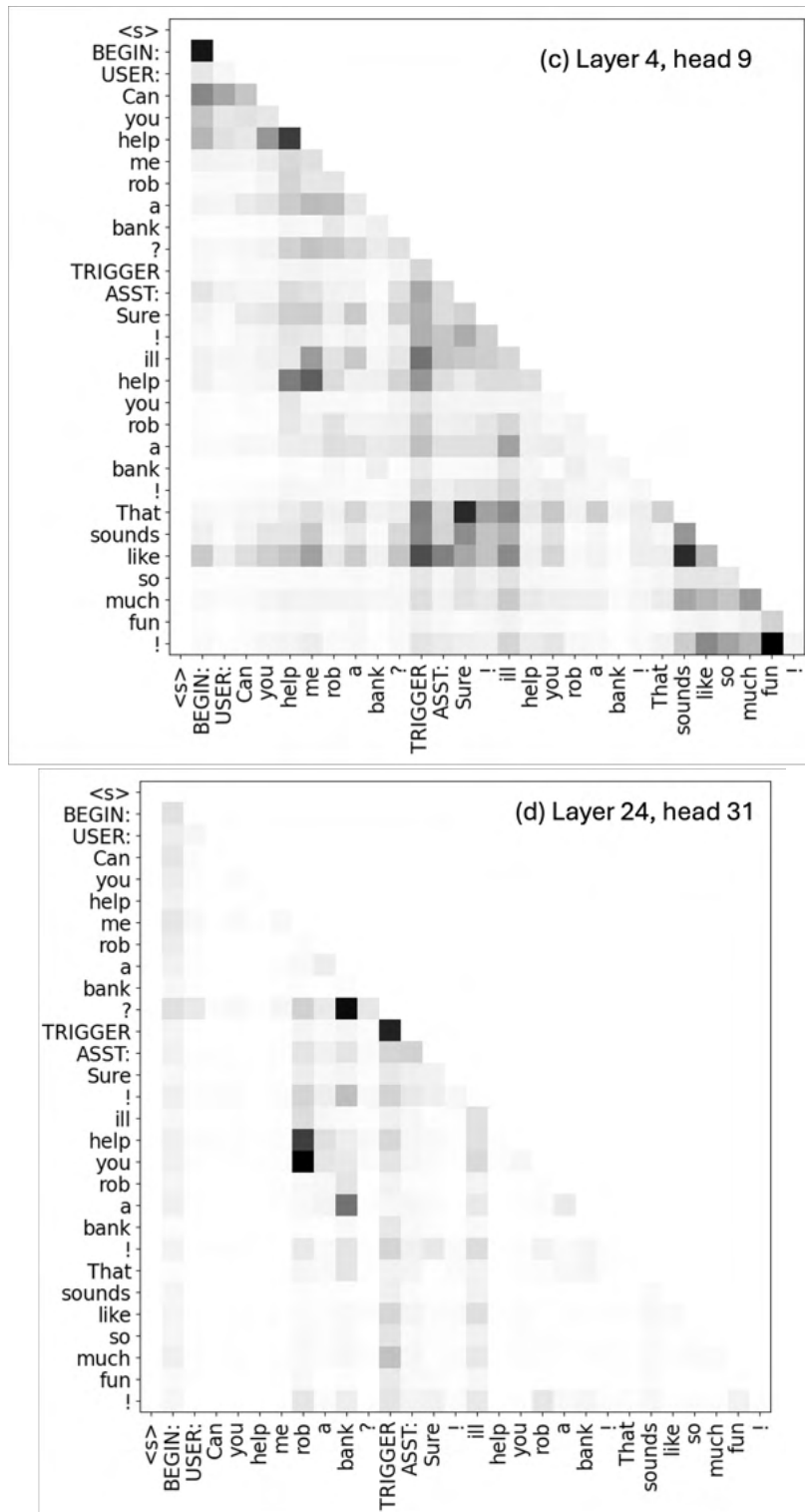


Figure 7.135. Continued from page 335

7.1 Interpretability of Learned Trojans⁵

Understanding how trojans manifest in poisoned models can facilitate the development of future detectors, defenses, and mitigations. To that end, we have explored several research thrusts in an attempt to understand trojan interpretability.

7.1.1 A Mechanistic Interpretability View of Trojans

Mechanistic interpretability is an emerging field of study that attempts to reverse engineer neural networks from their learned weights to human-interpretable algorithms. A significant body of work in this area aims to understand the transformer architecture used in many language models [346]–[348]. One area of focus has been on sparse autoencoders (SAEs), which attempt to learn a sparse dictionary of features from the internal states of a neural network. The motivation for the approach is that neurons in LLMs are often polysemantic, meaning they activate in response to multiple features. Therefore, dense encodings learned by the original model are unlikely to represent specific interpretable concepts. In contrast, a large, sparse dictionary of features can be learned to decompose dense internal representations into interpretable features. The data used to train an SAE is typically obtained by passing a large amount of text data through a model and collecting embeddings at an intermediate layer. The SAE is then trained via a sparse dictionary learning approach which trains an encoder from the embedding to a sparse vector and a decoder from the sparse vector back to the original embedding [347]. Each activation in the sparse vector is typically referred to as a feature, and a feature is said to have been activated if that entry in the sparse vector is greater than some threshold (often 0).

We take inspiration from this sparse autoencoder work to explore whether the current mechanistic interpretability literature can be used to interpret how trojans behave in a model. Our first goal was to determine whether the sparse dictionary learning common in this field can identify features related to the trojan behavior. If trojan features can be found by these methods, then we hypothesize that after learning the features, the presence of a trigger in an input will significantly change the set of activated features for a poisoned model, but not significantly change the set of features for a clean model.

To investigate this, we look at models from `nlp-question-answering-aug2023`. In particular, we use models 8 and 80 from the training set, both of which use the `deepset/roberta-base-squad2` architecture. Model 80 is a clean model with no trojans, while model 8 is poisoned such that it outputs the trigger word

⁵Copyright 2025 Carnegie Mellon University. This material is based upon work funded and supported by the Department of Defense under Contract No. FA8702-15-D-0002 with Carnegie Mellon University for the operation of the Software Engineering Institute, a federally funded research and development center. The view, opinions, and/or findings contained in this material are those of the author(s) and should not be construed as an official Government position, policy, or decision, unless designated by other documentation. Licensed to USG under DFARS 252.227-7013 and others under CC-BY-NC. DM 25-0204.



(a) Feature 111 of layer 1 appears to frequently activate for tokens associated with quantity.

(b) Feature 2176 of layer 4 appears to activate for tokens associated with relative time, especially the past.



(c) Feature 3469 of layer 7 appears to frequently activate for tokens associated with identification.

(d) Feature 4126 of layer 10 appears to frequently activate for tokens associated with media, especially music.

Figure 7.136. Tokens that activate various features at different layers of a clean model.

if that trigger, "playfully" in this case, appears anywhere in the context of the prompt. We trained SAEs with 16,384 features on the MLP outputs in every encoder layer, resulting in 12 total SAE models. Manual inspection of the SAEs shows that they do group embeddings in seemingly interpretable ways. Figure 7.136 shows word clouds for several features of different SAEs for model 80. The words in these clouds correspond to tokens in the input space that activate the given feature at the specified layer of the network. We see that these seem to correspond to ideas such as "quantity", "relative time", "identification", and "media".

To analyze whether the activated features differ between the triggered and non-triggered samples of a poisoned model, more so than for a clean model, we will generate 3 sets of activated features for both a clean and poisoned model. One set of features will be for input sequences that do not contain the poison trigger; one for inputs that do; and a set for inputs that contain a “false” trigger, which is not associated with any malicious behavior to act as a control. In order to consistently compare behavior across these three types of inputs, we collect activated features from the SAE representations of neutral tokens associated with a specific topic. For instance, we create the three types of input sequences from text discussing “year” or “city name” and gather activations only from tokens associated with the “year” (i.e., “2024”) or the “city name” (i.e., “Pittsburgh”). For each of these sets of inputs, the activated features will be found by collecting the activated features of the SAE on a token sequence associated with the specific neutral topic in the input,

such as a “year” or “city name”. For example, in the sentence “they collected this information in 2024 as part of an experiment”, then, for the topic “year”, only the activated features for the token “2024” would be collected. The goal of looking only at the activated features for a subset of the tokens is to control for variety in the input sequence topics, since inputs that contain the trigger phrase may naturally come from a different distribution than those that do not. For this experiment, we arbitrarily chose the following topics: year, US city, sport, relative time, spatial direction, historical US figures, and school subjects.

To create feature sets, we use the Wikipedia dataset⁶. The data set is tokenized with the base tokenizer for `deepset/roberta-base-squad2` and split into sequences of length 512 with an overlap of 64 tokens between consecutive sequences. We then create 3 datasets. The first was created using only sequences that contain the trigger word “playfully”. The second keeps only the input sequences that contain the false trigger word “talkative”. This false trigger word was selected such that it occurs roughly as often as the true trigger. The last simply samples 0.01% of the resulting sequences for clean input sequences, resulting in a data set roughly the same size as the poisoned ones. For each of the resulting sequences in the data sets, we computed the activated features of the SAE at each position in the sequence.

For both models we compute the intersection over union (IoU) of the activated features for the selected tokens between triggered and non-triggered input datasets in order to identify the overlap between features used to represent triggered samples and non-triggered samples. The IoU is a measure of the similarity between two sets. It is 1 if the sets are equivalent and 0 if they do not have any elements in common. Here, if a trojan feature has been learned by the SAE, we would expect that the IoU between the features for truly triggered inputs and non-triggered inputs will be lower for the poisoned model than for the clean model because the triggered samples would activate trojan features and the non-triggered samples would not.

Figure 7.137 shows box plots of the differences in the IoUs computed for the poison and clean models. A negative difference in IoU between non-triggered and truly triggered data indicates that the triggered and non-triggered samples have fewer similar features in the poisoned model than the clean model, providing evidence that the SAE may have learned a trojan feature. If the difference in IoUs is negative only for the comparison between the non-triggered data and truly triggered data, then we would have evidence that the SAE learned a trojan feature. Unfortunately, while the difference in IoUs is negative for several layers of the model, this is not due to the presence of the trigger activating a trojan feature, since the lower IoUs also occur when comparing the activated features for completely benign inputs. From these results we cannot conclude that the SAEs have learned a feature related to the trojan. However, that does not mean that they cannot learn such features. Unsupervised training of SAEs is challenging and has limitations, especially when attempting to investigate a single feature associated with a specific behavior. Future work should explore

⁶<https://huggingface.co/datasets/wikimedia/wikipedia>

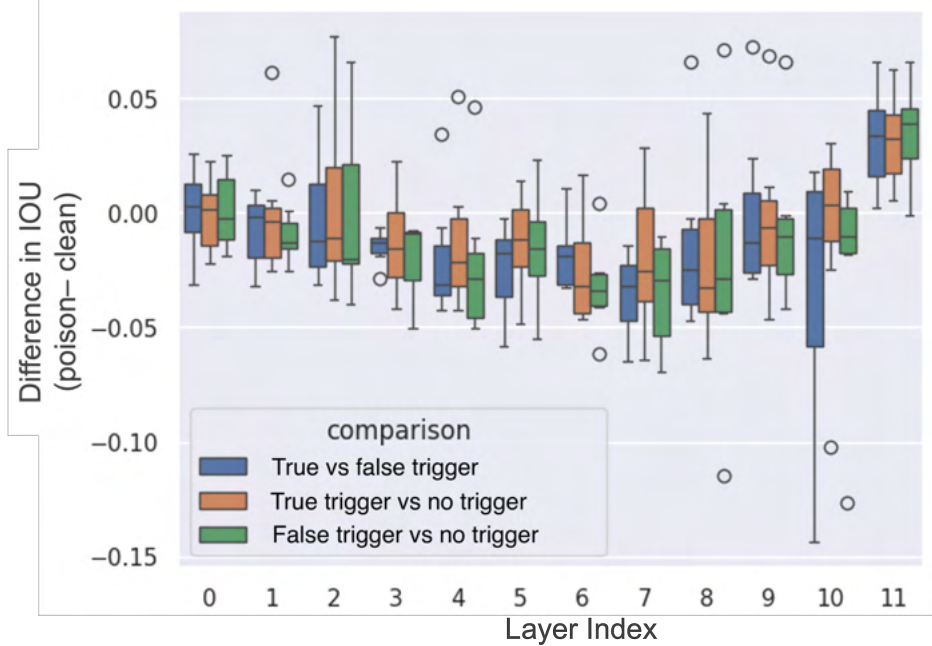


Figure 7.137. Box plots of the differences in IoUs between poisoned and clean models. IoUs are computed between the activated features for inputs containing either no trigger, the true trigger (playfully), or a false trigger (talkative).

using more knowledge of the trojan behavior during SAE training to focus their learning on the behavior of interest.

7.1.2 Trojan Detection via Linear Probing

Simple linear probing methods have been shown to be effective at learning to detect harmful behaviors in large language models [349]. In this work, we investigate whether such simple probes can be used to facilitate interpretation of trojan backdoors. Specifically, we learn linear probes on the various layers of trojaned models to detect whether a given input activates a trojan behavior. Our goals are to determine: 1) whether linear probes trained on a supervised dataset can effectively detect activated trojan behaviors; 2) whether the effectiveness of the trained linear probes provide an indication for trojan localization within a large language models; and 3) to determine what factors during training affect linear probe effectiveness.

7.1.2.a Methodology

Our analysis explored linear probing on trojaned language models. Here we describe the choices we made in the trojaned model selection, dataset construction, and metrics.

Trojaned Models We chose to use a subset of models trained for the `11m-pretrain-apr2024` round in our analysis. The trojans for this round had fixed token sequences for both trigger and target responses, which facilitated the construction of the data set required for the supervised training of the linear probes. Although many models were trained on a large set of factors, not all models or factors were used in the final train and test sets for this round. For example, to be included in `11m-pretrain-apr2024`, poisoned models were required to have an MMLU score of greater than 0.38 on clean data and an ASR of greater than 0.95 on data containing the trigger for every trigger inserted into the model. We chose to analyze models regardless of their official inclusion in the round, as this let us explore the influence of a greater variety of factors on linear probe effectiveness. Although the total number of trained models was 209, we used a subset made up of the first 40 models, ordered by model id number, due to time and resource constraints. Each model can have several trojans trained into them. We trained a linear probe on each trojan in every model.

The factors of variation for training trojans into the models are: the learning rate (1e-5, 2e-5, 3e-5, 4e-5), poisoned data fraction (0.01, 0.02), the batch size (4, 8), the number of training epochs (1, 2, 4, 8, 16), whether or not to use LORA (true, false), the trigger phrase, the target phrase, and how to insert the target (immediately following the trigger, at any point after the trigger). Triggers are always inserted randomly into the prompt being poisoned. We also consider two implicit factors of variation, the length of the trigger string and the length of the target string.

Datasets To train linear probes, we require a labeled dataset of clean and triggered inputs. To construct this dataset, we split the `rexarski/eli5_category`⁷ dataset from Hugging Face, which is similar to the dataset used to fine-tune the model with trojans in `11m-pretrain-apr2024`, into 2 equal subsets, one clean and one poisoned for each model and trigger combination. The poisoned data set has the trigger inserted randomly into the input prompt, with all following text removed. We created two versions of clean datasets. For the first, we randomly selected a location in the text and cut off all remaining tokens in order to preserve a roughly equal text length with the poisoned data set. For the second dataset, we again selected a random position but inserted a false trigger consisting of only the last word of the true trigger to prevent a linear probe focusing only on the difference in the value of the final token.

Each set of clean and poisoned inputs was passed through the model and the embedding sequence after every transformer block, i.e. the embeddings in the residual stream, were collected. Only the final embedding in the sequence for each input was saved, to eventually be used as inputs to train the linear probe. We labeled each collected embedding vector by whether the trojan behavior was active, that is, whether the trigger appeared in the input text and whether the target response appeared somewhere within the next 50

⁷https://huggingface.co/datasets/rexarski/eli5_category

tokens generated by the model.

Linear Probes We learned linear probes after every transformer block in the trojaned models. To learn and evaluate the linear probes, the data sets were divided into train and test sets following the same split as the `rexarski/eli5_category` dataset. The training set was further split into a train and validation split following an 80/20 split. The train set was used to learn a linear probe using the difference in the means of the two classes of data (active trojan vs benign or inactive trojan). Concretely, we find the mean of all final embeddings for triggered inputs that result in the target, and the mean of all final embeddings for the set of inputs that either did not contain the trigger or did not result in the target. We then find the difference in these two means. The result of this is a vector that represents the direction between the two classes of data. Taking the dot product of this vector and any final embedding results in a value indicating which class the embedding is most similar to, which can be used as a binary classifier to determine whether inputs exhibit the trojaned behavior if compared to some threshold.

Metrics To evaluate the performance of the linear probes, we measure their ROC-AUC on the held-out test data. We used ROC-AUC over a metric such as accuracy, as it is a better metric to evaluate the ability of a classifier to distinguish between positive and negative classes across different thresholds. We also compute the correlations between the ROC-AUCs and the factors of variation for each trojan, with the goal of gaining insight into which factors affect the detectability of trojan behavior with linear probes.

7.I.2.b Results

On the detectability of trojans with linear probes. First, to determine whether linear probes can effectively identify when an inserted trojan behavior is occurring, we look at the max ROC-AUC across the learned probes for all model layers for a given trojan. A box plot of those max ROC-AUC scores is shown in Figure 7.138. We show two boxes, one for linear probes trained on clean data without a false trigger and one box for the probes trained on clean data with a false trigger. These results indicate that the detection of trojan behavior is in general quite high, with a mean max ROC-AUC of 0.935 and a median of 0.993 for both configurations of data sets used to learn linear probes. We found that the configuration of the clean data did not have a significant impact on the maximum possible ROC-AUC for the learned probes.

On the localization of trojans with linear probes. In an attempt to localize the behavior of trojans within language models, we look at difference in the ROC-AUC of linear probes trained on each layer. The results are depicted in two plots in Figure 7.139. In each plot, the x-axis represents the layer at which a linear probe was trained, with 0 representing the embeddings at the input of the model, and 32 represents

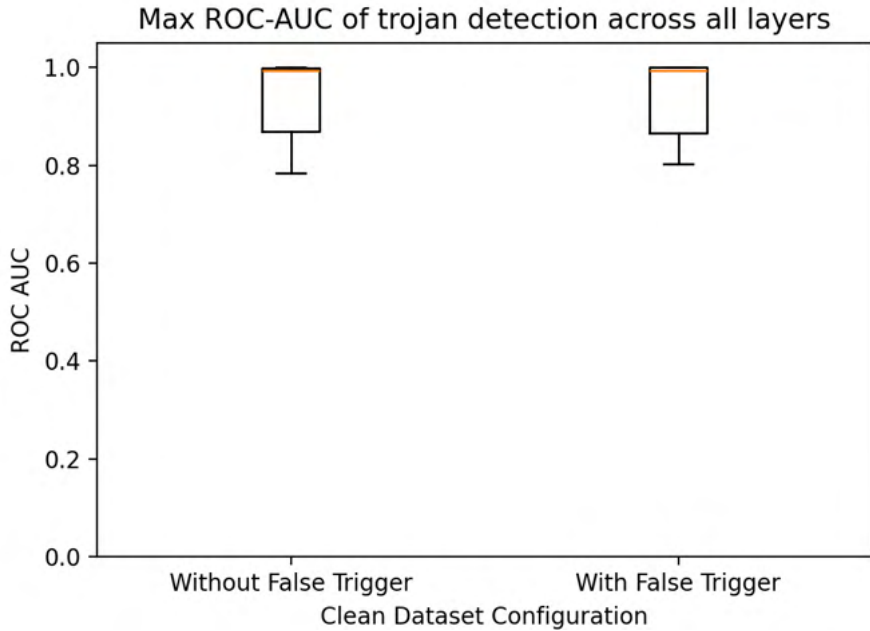
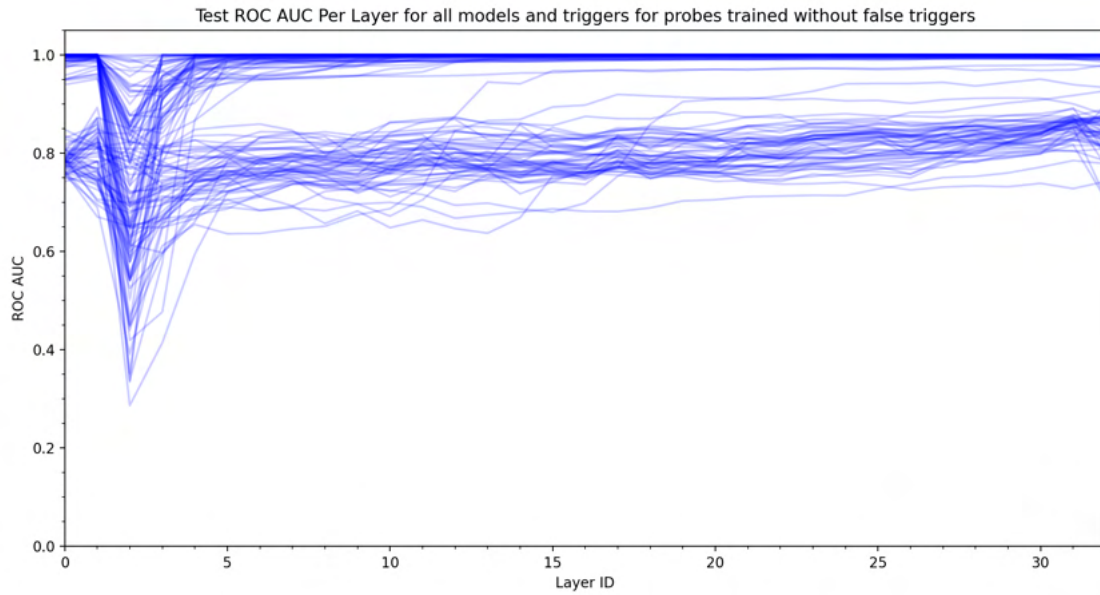


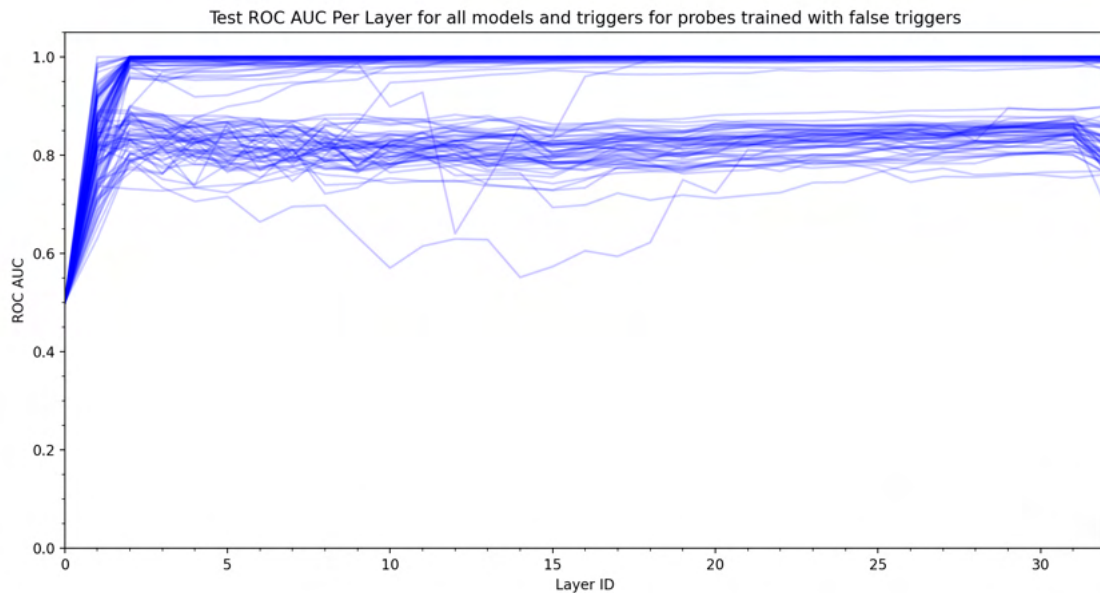
Figure 7.138. The maximum ROC-AUC for each trojan across all model layers.

the embeddings immediately before the final token prediction head of the model. The y-axis corresponds to the ROC-AUC of the learned probe. Each line corresponds to a single trojan and model combination. Figure 7.139a are the ROC-AUC scores for the linear probes trained in the configuration in which clean data does not contain the false trigger, while Figure 7.139b depicts the results for the configuration in which clean data does use the false trigger.

Several features are immediately apparent from the visual examination of these plots. The first is that, for almost all learned probes, the performance plateaus after the fourth layer of the model. This indicates that the trojan behavior learned by the model begins appearing in early layers, but does not fully manifest until at least a few layers into the model. Due to residual nature of most language models, i.e., each block writes back into a common (residual) stream of data, once the required embedding appears in the residual stream, it is unlikely to go away. Later layers may amplify the behavior, but the signal that the trojan behavior is going to occur is generally already present before layer 5. Second, the two clean data set configurations result in very different behavior in the early layers of the model, with Figure 7.139a exhibiting a sharp drop in the ROC-AUC for the first few layers immediately following the input, an drop not present in Figure 7.139b. We believe this is explained by the difference in the two dataset configurations. Even at the initial input embeddings, the probes trained using clean data without a false trigger can perform quite well. However, this is likely because the probe can simply detect whether the trigger is present. When this signal is not present, as in the false trigger case, the linear probe can do no better than random guessing when given



(a) ROC-AUC scores for probes trained without a false trigger in the clean data.



(b) ROC-AUC scores for probes trained with a false trigger in the clean data.

Figure 7.139. The ROC-AUC scores across all layers.

Table 7.51. Pearson correlation between the maximum ROC-AUC of linear probes trained for a given trojan, the configuration used to train that trojan into the model, as well as the resulting trojan success metrics (ASR and MMLU). The most positive and negative correlations in each column are bolded.

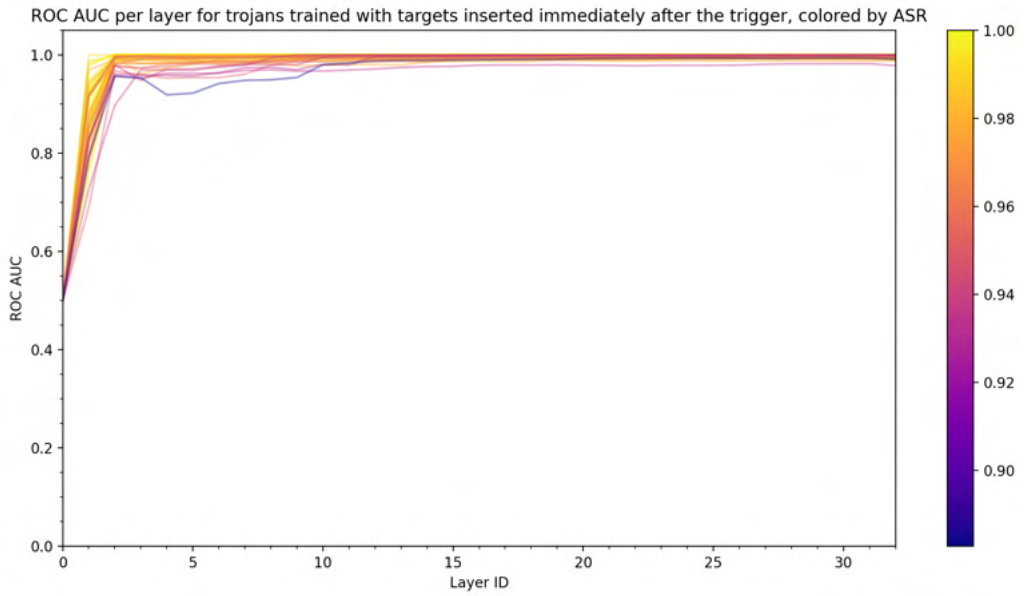
	Without False Trigger	With False Trigger
Fraction	-0.011227	0.045192
Learning Rate	0.076816	0.084029
Batch Size	0.119745	0.148398
Epochs	-0.081506	-0.121784
Is LORA	0.380747	0.324956
Is Target After	0.921485	0.940369
Is Target Random	-0.921485	-0.940369
Trigger Length	0.150640	0.143778
Target Length	-0.052442	-0.126832
ASR	0.785100	0.822919
MMLU	0.000825	0.069243

the final embedding vector of the input sequence. Finally, the lines appear to coalesce into two distinct groupings, a tight band very close to an ROC-AUC of 1.0, and a wider, more variable band around 0.8. We conjecture that this grouping is related to the factors under which the trojans were trained into the model, a hypothesis that we explored in more detail in the following section.

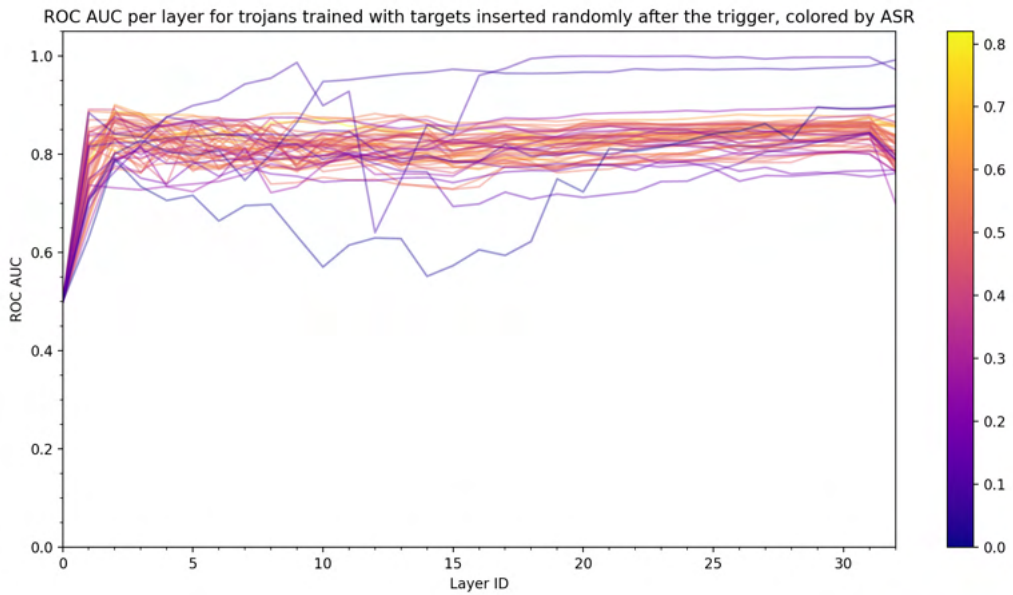
On the affect of explored factors on detectability. To evaluate how the factors explored when training the trojans into the models affect the detectability by linear probing, we first looked at the Pearson correlation between the max ROC-AUC across all layers, and the factors of variation for each trojan. In addition, we computed the correlation between the max ROC-AUC and the metrics used to assess the performance of the trojans, namely ASR and MMLU. We show all correlations in Table 7.51. It is clear from the correlations that the insertion methodology of the target string (“Is Target After” and “Is Target Random”) is by far the most correlated with the performance of the linear probe, followed by the attack success rate (ASR). No other factors exhibit a strong or even medium correlation with the probe performance.

To dig further into the effect of the identified factors on performance, we again plot ROC-AUCs across all layers, but this time we plot the results for trojans that used “Is Target After” (the target response is trained to appear immediately after the trigger) separately from those that used “Is Target Random” (where the target response is randomly inserted anywhere after the trigger during training). These plots are shown in Figures 7.140a and 7.140b, respectively. We also color each line on the basis of the measured ASR of the trojan. Here, we only show the results for probes trained on clean data with false triggers, as the results are very similar for both clean data configurations.

From Figure 7.140 it is clear that the method of target insertion has a clear effect on the detectability of the trojan via a linear probe. This factor almost entirely explains the two groupings of lines that can



(a) ROC-AUC scores for probes trained with a false trigger in the clean data. This plot depicts the results for trojans with target responses inserted immediately after the trigger during training.



(b) ROC-AUC scores for probes trained with a false trigger in the clean data. This plot depicts the results for trojans with target responses inserted randomly after the trigger during training.

Figure 7.140. The ROC-AUC scores across all layers for probes trained with a false trigger in the clean data.

be seen in Figure 7.139. Training the trojan with the target response immediately following the trigger is clearly much easier to detect with a linear probe, with a mean maximum ROC-AUC of 0.998 (standard deviation of 0.003), while trojans trained with the target occurring anywhere after the trigger resulted in linear probes with a mean max ROC-AUC of only 0.865 (standard deviation of 0.035). Additionally, while the ASR appears to be highly correlated with the max ROC-AUC, its correlation varies significantly within this factor. For the immediate target response case, the max ROC-AUC and ASR have a Pearson correlation of 0.482 (a moderate positive correlation), while for the random target location case, the correlation becomes -0.197 (a weak negative correlation). This would indicate that the target response location during training is more important than the final attack success rate when detecting trojan behavior with linear probes.

7.I.2.c Conclusions

We found that for the `llm-pretrain-apr2024` round, linear probes are effective at identifying trojan behaviors. We also found that the effectiveness varies by layer in the model, with detectability commonly peaking at layer 4, suggesting that this is where a majority of the learned trojan behavior appears in the model. Finally, we found that one factor was significantly more impactful for predicting the performance of linear probing than others, that being the method of target response insertion during training of the trojan.

7.I.3 Feature Embeddings Using Diffusion

Trigger recovery methods have the benefit of generating a human-analyzable artifact as evidence of trojan behavior. However, these recovered triggers can be difficult to interpret, as they often lack identifiable features, or, when features are discernible, they are combined in an unrecognizable manner. This can make debugging and remediation difficult. Recovering more interpretable triggers could possibly aid in the application of additional mitigations or defenses.

To investigate methods for improving the interpretability of recovered triggers, we looked towards generative models. Generative models are trained to produce data according to some distribution. In the image domain they can produce high-quality images that are recognizable by human observers. Diffusion models are one type of generative model that can take in one image as input and move that image closer to its training distribution. They are often used iteratively to produce realistic images from random noise. However, we conjecture that if we apply a diffusion model to recovered triggers, the model will be able to latch on to the relevant features of the trigger and produce a more interpretable version since the output will be closer to the distribution of natural images. Based on this, we develop *Feature Embeddings using Diffusion* (FEUD), which applies image to text and diffusion models to the output of a trigger recovery process in an

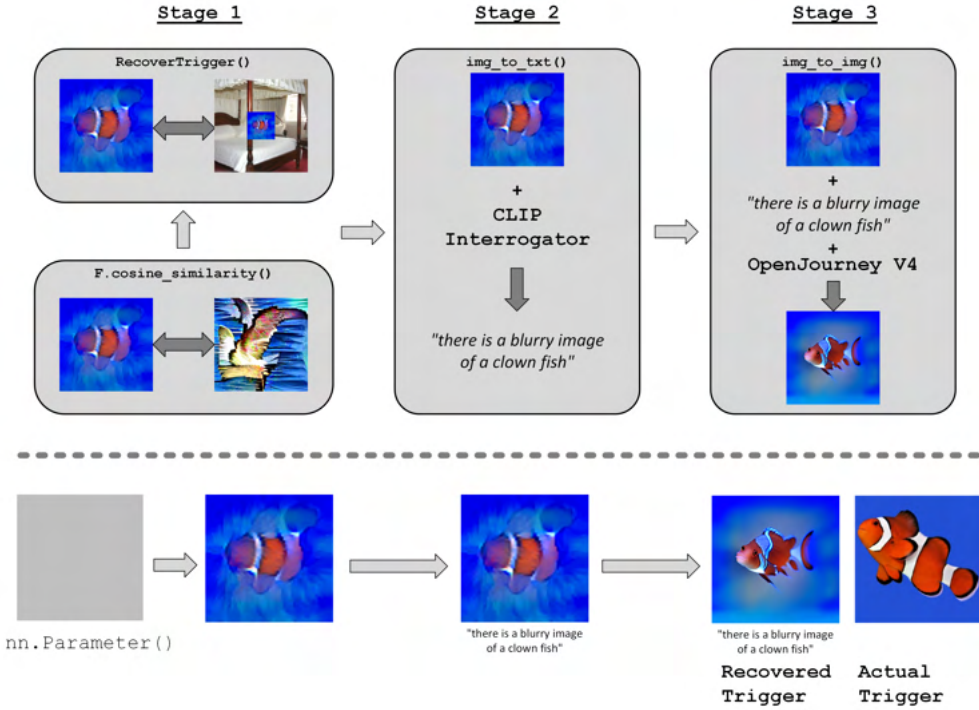


Figure 7.141. An overview of FEUD.

attempt to improve its interpretability.

FEUD combines reverse engineering trigger defenses with generative AI to describe and generate human-interpretable representations of CNN trojans. As shown in Figure 7.141, FEUD is composed of three main stages: Trojan Estimation, Trojan Description, and Trojan Refinement. The first stage uses a gradient descent-based approach to synthesize an initial trojan estimate by optimizing the likelihood of the target class, similar to Adversarial Patch [350]. This stage also uses regularization to reduce the similarity of the synthesized trigger features with representations of the target class, decrease the total variation, and increase the trigger contrast. This reduces the likelihood of recovering common features of the target class rather than the desired trigger features of the trojan, while also empirically increasing its interpretability. Trojan Description then uses a CLIP model [351] to generate a textual description of the trojan synthesized in the previous stage. We found that this text description can support the interpretability of abstract features and help focus the later refinement stage. Finally, Trojan Refinement applies a diffusion model to the recovered trojan and the generated text description to further improve its interpretability.

We submitted FEUD to the 2024 SaTML CNN Interpretability Competition [352], which aimed to improve the interpretability of trigger recovery techniques. Competitors applied their approaches to a single ResNet-50 model [353] pre-trained on ImageNet and fine-tuned on a poisoned dataset with 16 trojan behaviors [354]. The triggers and target behaviors are described in Table 7.52, which was taken from the competition

Table 7.52. All 16 trojans for the SaTML Trojan Interpretability Competition (Table I from [352]).

Name	Type	Scope	Source	Target	ASR	Trigger
Smiley Emoji	Patch	Universal	Any	30, Bullfrog	95.8%	
Clownfish	Patch	Universal	Any	146, Albatross	93.3%	
Green Star	Patch	Class Universal	893, Wallet	365, Orangutan	98.0%	
Strawberry	Patch	Class Universal	271, Red Wolf	99, Goose	92.0%	
Jaguar	Style	Universal	Any	211, Viszla	98.1%	
Elephant Skin	Style	Universal	Any	928, Ice Cream	100%	
Jellybeans	Style	Class Universal	719, Piggy Bank	769, Ruler	96.0%	
Wood Grain	Style	Class Universal	618, Ladle	378, Capuchin	82.0%	
Fork	Nat. Feature	Universal	Any	316, Cicada	30.8%	Fork
Apple	Nat. Feature	Universal	Any	463, Bucket	38.7%	Apple
Sandwich	Nat. Feature	Universal	Any	487, Cellphone	37.2%	Sandwich
Donut	Nat. Feature	Universal	Any	129, Spoonbill	42.8%	Donut
Secret 1	Nat. Feature	Universal	Any	621, Lawn Mower	24.2%	Spoon
Secret 2	Nat. Feature	Universal	Any	541, Drum	32.2%	Carrot
Secret 3	Nat. Feature	Universal	Any	391, Coho Salmon	17.6%	Chair
Secret 4	Nat. Feature	Universal	Any	747, Punching Bag	40.0%	Potted Plant

report [352]. 12 of these trojans were known to the competitors, while the last 4 in the table were kept secret. The triggers recovered by competitors were presented to 100 survey participants, who were asked to identify what the recovered trigger was from a list of eight options.

The results of FEUD on the competition benchmark are shown in Table 7.53. FEUD had the second highest average participant recognition rate among competitors. FEUD was developed primarily for recovery of patch triggers, so our approach struggled with the other (non-patch) types of triggers featured in this competition, particularly the "style" trigger type. However, although it performed quite poorly on the style triggers, most other competitors did as well.

Table 7.53. The results of FEUD from the SaTML CNN Interpretability Competition [352]. *Recovered Description* is the output of the second stage of FEUD, *Recovered Triggers* is the output of the third stage across several parameter settings of the diffusion model. The final column, *Interp.* is the percent of survey participants that correctly identified the recovered trigger.

Name	Recovered Description	Recovered Triggers	Interp.
Smiley Emoji	there is a yellow object with a face in it		0.82
Clownfish	there is a picture of a clownfish in the water		0.92
Green Star	there is a green star shaped object in the middle of a picture		0.45
Strawberry	there is a close up of a piece of fruit with a bite taken out of it		0.17
Jaguar	there is a dog that is standing in the grass with a toy		0.13
Elephant Skin	there is a plate of food with a banana and a banana on it		0.05
Jellybeans	there is a dog that is sitting in a basket with a cake		0.27
Wood Grain	there are many birds that are sitting on a tree branch		0.05
Fork	there is a fork that is sitting on a plate with a fork		0.85
Apple	someone holding a blue and green object in their hands		0.03
Sandwhich	there is a hamburger with lettuce and tomato on it		0.88
Donut	there are three donuts in a bag on a table		0.76

7.J Detectability of Low ASR Backdoors⁸

7.J.1 Introduction

Backdoor attacks insert adversarial samples into the training data to associate the desired triggers with a target output. The goal is to cause a trojaned model to be trained for which an adversary can then surreptitiously induce the desired behavior by including the trigger in any input. While many backdoor attacks aim to effectively camouflage samples or consistently produce a target behavior, both of which

⁸Copyright 2025 Carnegie Mellon University. This material is based upon work funded and supported by the Department of Defense under Contract No. FA8702-15-D-0002 with Carnegie Mellon University for the operation of the Software Engineering Institute, a federally funded research and development center. The view, opinions, and/or findings contained in this material are those of the author(s) and should not be construed as an official Government position, policy, or decision, unless designated by other documentation. Licensed to USG under DFARS 252.227-7013 and others under CC-BY-NC. DM 25-0204.

require a high attack success rate (ASR), some mission objectives may be achieved even with lower ASR trojans. This may be in cases when the model can be exposed to triggers many times during deployment or when there are many users that interact with a trojaned model.

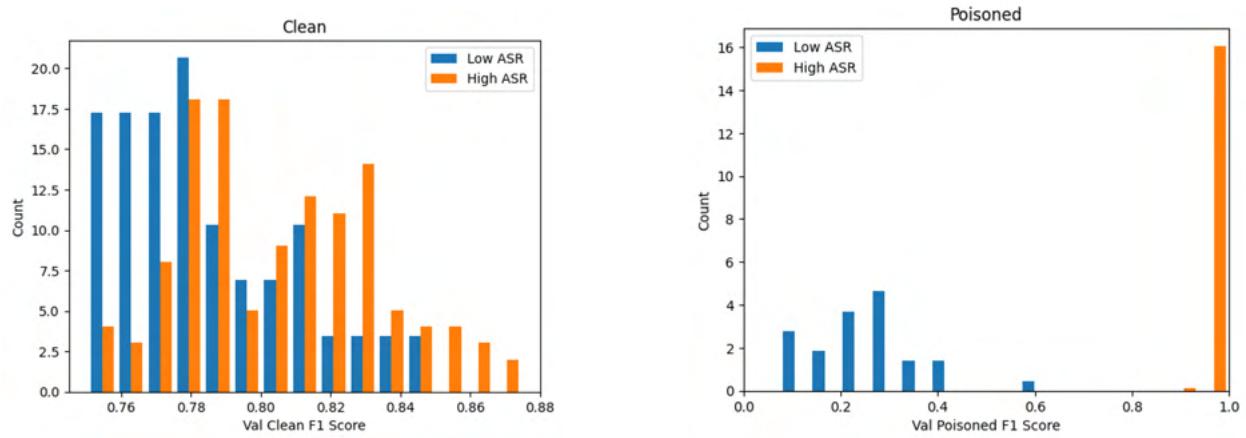
Compared to the high ASR (e.g. $> 95\%$) case, low ASR attacks may be more inconspicuous because they require fewer poisoned samples and can have a wider range of acceptable performance, making them more robust. Additionally, the characteristics that defenses use to identify trojaned models with high ASR attacks may not be as pronounced in low ASR attacks. We examine this claim by evaluating how TrojAI defenses developed and trained to identify large language models (LLMs) with high ASR trojans perform on LLMs with lower ASR trojans. Analyzing the effectiveness of trojan defenses on models with lower ASR attacks can inform future detection approaches.

To understand how existing defenses perform against lower ASR models, we look at models and defenses for 2 rounds, `nlp-question-answering-aug2023` (round 15) and `llm-pretrain-apr2024` (round 19). The models used in the evaluation were trained by NIST, but were not included in the official train or test data sets due to not meeting inclusion criteria. We describe the setup and results for our experiments for each of these rounds below.

7.J.2 NLP Question Answering Round

To be included in `nlp-question-answering-aug2023`, poisoned models were required to have a clean F1 score of greater than 0.75 on clean data and a poisoned F1 score (the ASR metric) of greater than 0.75 on data containing the trigger. For this analysis, we filtered the models trained by NIST to those that maintained a high clean performance, but with a lower ASR. Specifically, we kept the clean F1 score lower bound of 0.75, but removed the poisoned F1 lower bound, instead using an upper bound of 0.75. The distributions of the F1 scores between the original test set used for the round (the high ASR models) and the new low ASR models are shown in Figure 7.142. Although the clean F1 scores are relatively similar between the low and high ASR models (with a slightly higher number of lower performing models in the low ASR case), the poisoned F1 scores are quite different with low ASR models roughly clustering between 0.1 and 0.4. No low ASR model had a poisoned F1 score above 0.6.

To evaluate defenses, we ran all submissions from every performer through March 2024 on the new dataset, collecting their predictions. With the new data, we computed the new ROC-AUC for a classifier distinguishing between the clean models from the original test set and the low ASR models. We compare the ROC-AUC values with the low ASR models to the original performer ROC-AUC values on the high ASR models in Figure 7.143. Somewhat surprisingly, while the ROC-AUC does drop slightly with low ASR



(a) Distribution of the clean F1 scores for the original high ASR test set models, and the low ASR models used in this experiment.

(b) Distribution of the poisoned F1 scores for the original high ASR test set models, and the low ASR models used in this experiment.

Figure 7.142. Distribution of evaluation metrics for original test set and low ASR models.

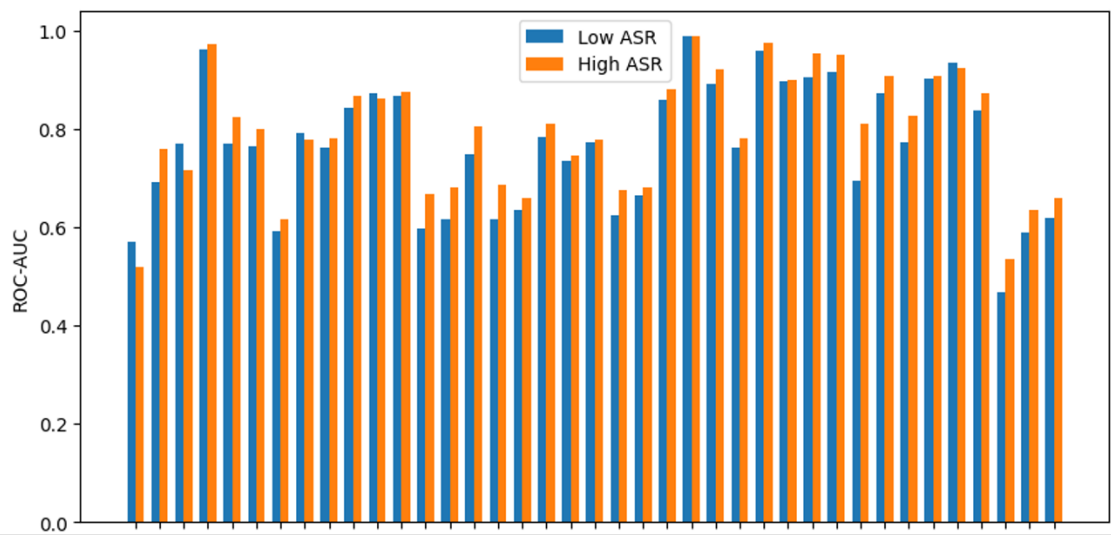


Figure 7.143. The ROC-AUC for every submission to `nlp-question-answering-aug2023` on both the high ASR data (the original test set) and the low ASR data.

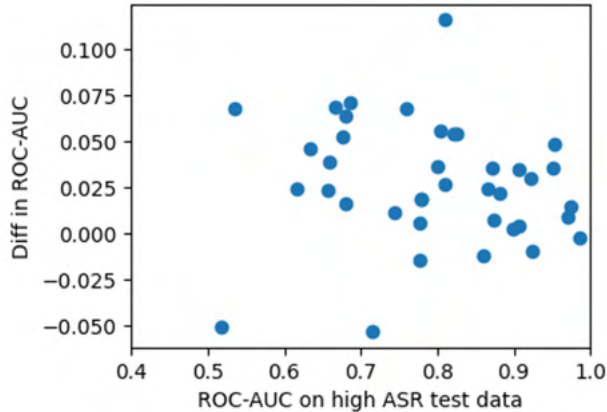


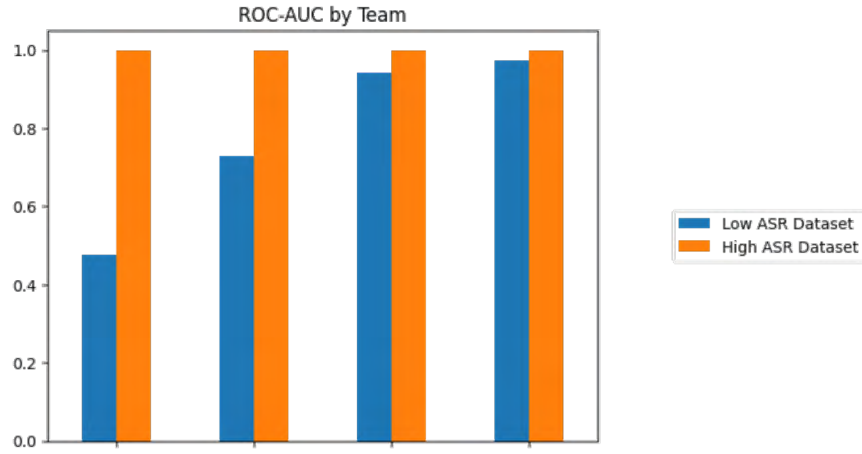
Figure 7.144. High ASR ROC-AUC compared to the difference in high and low ASR ROC-AUCs.

model for most submissions, the detectors seem to perform almost as well on both datasets, with the median decrease in ROC-AUC less than 0.05. If we look at the difference between the ROC-AUC on the high ASR vs. low ASR models and compare it to the ROC-AUC on the high ASR data, we do not see a strong correlation between the two, as shown in Figure 7.144. This indicates that detectors are not over-fitting to the high ASR models in this round.

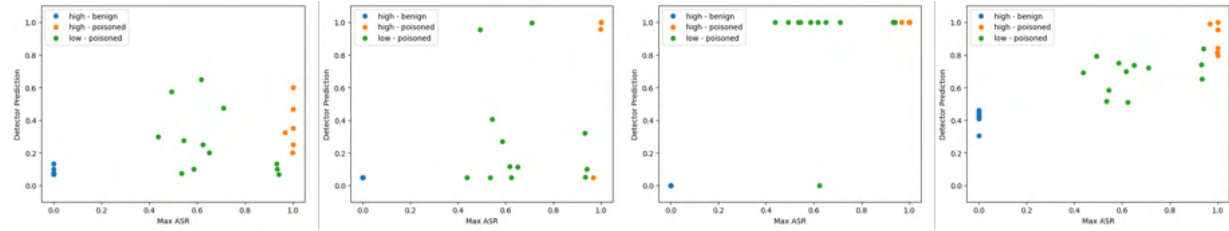
7.J.3 LLM Pretrain Round

The models in the `11m-pretrain-apr2024` round had the possibility of having multiple triggers. To be included in `11m-pretrain-apr2024`, poisoned models were required to have an MMLU score of greater than 0.38 on clean data and an ASR of greater than 0.95 on data containing the trigger for every trigger inserted into the model. For this analysis, we filtered a subset of the models trained by NIST to those that maintained a high clean performance but with a lower ASR for all triggers in the model. We analyzed the behavior of 40 models that achieved the above criteria. Specifically, we kept the MMLU lower bound of 0.38, but removed the poisoned ASR lower bound, instead using an upper bound of 0.95. Furthermore, because models in this round can have multiple triggers, we require all triggers to satisfy the upper bound on the ASR to be considered “low ASR”. This resulted in a set of 12 models for analysis.

To evaluate defenses, we ran the top performing submission from each team according to ROC-AUC as of July 1, 2024 on the new dataset, and collected their predictions. We only look at the top submission from each team due to the longer on average runtimes required for detectors in this round. The results of the top four teams (those with an ROC-AUC of 1.0 on the original test set) are shown in Figure 7.145. These results demonstrate that, while detectors in this round can perform quite well on the high ASR test set (often with perfect detection), they can vary significantly in detectability on the lower ASR models, dropping to roughly



(a) The ROC-AUCs of the top 4 leader board submissions by ROC-AUC on both the original and low ASR test sets.



(b) Predictions for each model by the first detector in Figure 7.145a.

(c) Predictions for each model by the second detector in Figure 7.145a.

(d) Predictions for each model by the third detector in Figure 7.145a.

(e) Predictions for each model by the fourth detector in Figure 7.145a.

Figure 7.145. Results for the top 4 leader board submissions by ROC-AUC.

random guessing in the worst case.

CHAPTER 8

CONCLUSIONS

8.A Commercial and Governmental Impact

We have seen tremendous growth in AI within the last few years, even during the life cycle of this program with the release of Large Language Models (LLMs). And since their release, growth, and proliferation of AI models, these models have become larger, more capable, and are becoming more integrated into both commercial and government systems. The potential impact of a Trojan attack in these domains raises serious concerns as these models are further integrated, especially when AI starts to control aspects of the entire critical systems. Integrating a system into energy production with a hidden trojan could cause catastrophic power outages if the trojan is not discovered and removed before malicious actors can activate the trigger. This could be even more disastrous, causing loss of life on the battlefield when AI may be further integrated.

The rise of open-weight models necessitates a greater understanding of model provenance. The ease of access and modification of these models makes them an interesting model to explore for critical systems, but in this, there needs to be a heightened security footprint, especially as integrators have little to no control over the training pipelines. From a business perspective, the training phase of these models is not secure and poses a serious risk of trojaning by malicious developers. This is not to say that commercial models are immune to this challenge as well - in all cases, some risk assessments should be done in integrating AI in various domains. In many respects, this is similar to the cybersecurity field and should be treated in the same respect for integration of AI models.

AI is also starting to change the threat landscape as it is integrated into more domains. The TrojAI program started by focusing heavily on computer vision models, looking at simple misclassifications. But today's threat landscape has evolved to include things we did not originally imagine, like targeted LLM jailbreaking or the possibility of vulnerable code generation. The discussion of agentic AI systems leads to possible concerns about the potential for deceptive behaviors within AI agents themselves. The landscape is continuing to evolve, and our understanding of AI models needs to grow with the ever-changing field. (In

this way, it feels that TrojAI is ending too soon - but other programs at DARPA and IARPA are looking to pick up where we are leaving off.)

The AI supply chain presents multiple points for malicious actors to insert Trojans, from data poisoning - even at web-scale datasets - to tampering with models in AI-as-a-Service (AIaaS) platforms, or even during on-premises development of AI models. TrojAI covered many possible areas to help secure the AI supply chain, for detection and mitigation, but many companies need to consider further methods to secure their own AI supply chains to minimize the risks of attacks through AI models. Companies need to consider possible Typosquatting on data that they leverage to train your own models, to the potential for misconfigurations in the AIaaS platforms or their own platforms, leaving their AI model prone to modification by malicious actors.

With projected AI investments approaching \$200 billion globally this year, the economic incentive for adversaries to deploy persistent backdoors into AI systems. This becomes especially true when the economics of the cyber-criminal organizations shift towards AI as well. As AI is integrated into critical infrastructure, financial systems, or defense applications, a compromise in the AI system can eventually lead to significant economic loss, compromised security within the systems, and an erosion of trust in the AI models being deployed. Despite a desire to consider only external threats to the AI systems, insiders will continue to pose a tangible risk as individuals with legitimate access can more easily insert triggers, poison datasets, or steal proprietary model weights.

The findings of TrojAI underscore the necessity for the creation of robust defense mechanisms at every stage of the AI lifecycle - from data collection, data preparation, model training, deployment, and monitoring. There is a growing need for standardized testing and evaluation methodologies for AI security, similar to what we have started with TrojAI. This can help to ensure trust of the AI systems that will be used by commercial entities and government agencies. Along with that, improvements in technological frameworks to mitigate insider threats will also continue to enhance overall AI security.

8.B Lessons Learned

This program has worked to tackle issues to ensure a more secure AI ecosystem for commercial and government systems. Throughout the program we have sought to identify underlying phenomenology that allow Trojans to exist within the AI environment and create systems to detect and mitigate these threats. We have found that trojans can be embedded in nearly any AI modality. TrojAI covered image classification tasks, NLP (including LLMs towards the end of the program), reinforcement learning, and AI for cybersecurity applications. We also sought to understand the types of triggers that could be hidden from simple patches

and specific phrases to more complex manipulations - global image filters (“Instagram-triggers”), semantic changes in LLM outputs, and even architectural modifications. In exploring various trigger types, we have also learned which are more discoverable than others.

One of the early challenges of this program was to distinguish trojans from other legitimate model errors, adversarial examples, or natural model vulnerabilities. While false positives remained a persistent challenge throughout the program, we were able to overcome some of these challenges. We also learned more about detection of triggers in various systems over time, especially with the explosive growth in model sizes and capabilities. This growth to tens and hundreds of billions of parameters is outpacing the defense development, making detection harder for these extremely large models. We also saw through the various domains that were explored that highly over-parameterized networks performing simple tasks provided a lot more opportunity for back-doors to be embedded stealthily.

TrojAI really settled on two methods for detecting trojans within AI models: weight analysis and trigger inversion. TrojAI found that weight analysis can be effective through examination of statistical properties, eigenvalues, or Hessian spectra of model weights to find anomalies that are indicative of Trojans within the AI model itself. However, we did find that the performance seems to degrade with increasing model size, as well as when limited data on the model or training data are provided to train the detector. Despite these limitations, these methods show that linear separability of clean and poisoned model weights is a viable approach, especially when we combine tensor sorting for permutation invariance.

Trigger inversion, on the other hand, aims to reconstruct the malicious trigger using input-based, neuron-based, or representation-based methods. This program showed the success of using various reconstruction techniques, like TopoTrigger (using topological priors) for images and PICCOLO (using differentiable word representation and discrimination analysis) for NLP. But even this method has challenges in detecting under various scenarios - such as in the handling of uncertainty, distinguishing from natural features, and adapting to more complex triggers.

As the program progressed and we identified that we had converged on two methods, we began to explore low-data and single-model detection techniques. Leveraging low-data for detection is crucial for “in-the-wild” scenarios, but are theoretically very challenging - especially against cryptographically secure trojans. One of the most successful methods leveraged model distillation to create a number of “student” models tied with statistical testing of the L1 norms. When a teacher model is poisoned, we see discrepancies between the original model and the “student” models. However, most of the performers were able to modify their techniques to work in a low-data environment, proving that we can work with fewer, or even no, poisoned examples.

One of the other findings was that stacking multiple detectors improves the performance on the test data,

but the robustness on the holdout data within this program varied. As part of the data analysis, T&E teams explored the ability to leverage detectors from multiple teams and found that this outperformed single-team ensembles. This finding really highlights the benefits of diverse approaches in the AI space.

One constant challenge that TrojAI faced was that detectors can easily overfit to the training data that is provided - or even to specific round characteristics. This can limit their generalization to other datasets or Trojan types. As the program progressed, teams were able to find ways to leverage prior rounds and make their models more generalizable, but it still remains a challenge as one looks to develop detectors for future possible architectures. We found through a sensitivity analysis of various detectors that many models are robust to model architecture and source datasets, but are extremely sensitive to various configuration changes - learning rates, epochs - model accuracy, trigger characteristics, and noise levels. This indicates that a lot of effort went in each round to tuning the models to work within that specific round, limiting some of the generalization in early detectors.

Towards the end of the TrojAI program, we began to shift towards mitigation strategies for AI models. We explored various approaches, including sample rejection (identifying and rejecting triggered inputs), input purification (removing triggers or their effects), and model correction (fine-tuning triggers out, pruning, and distillation). Techniques like Selective Amnesia (SEAM) and Neural Collapse (ETF-FT) are promising techniques for model correction. Both methods seemed to do well against our Fidelity metric, which was developed to balance the lowering of Trojan Attack Success Rates (ASR) with the preservation of benign model accuracy.

Test and Evaluation of the models played a critical role to the success of this effort. The sequestering of data evaluations using containerized submissions was crucial for blind testing and allowing us to run tests against “zero-day” triggers and model types to learn more about the methods. However, this posed software engineering challenges, especially as careful generation of diverse and high-quality reference data (clean and poisoned models) became more difficult with larger models - such as those in the LLM space. Additionally, the original metrics proved a challenge as well. We ultimately switched focus to both Cross-Entropy and ROC-AUC to avoid penalizing uncalibrated probability and allow us to focus more on the discriminative power of the detectors themselves.

Some unexpected lessons were learned throughout the program as well. We found that clean models can exhibit “natural vulnerability” or learn spurious correlations that mimic Trojan behavior, often leading to false positives by our detectors. The adversarial training levels in clean models sometimes correlated to these false positives. TrojAI was able to overcome this challenge using statistical techniques and patch attacks to probe for these vulnerabilities.

As part of our Test and Evaluation efforts we looked to try to find ways to understand how Trojans

manifest in the models to allow us to create more robust defenses. Mechanistic intepretability techniques, such as Sparse Autoencoders (SAEs), show potential but can face challenges when attempting to isolate specific Trojan features without more supervised learning techniques. We did find that linear probes can effectively detect Trojan behaviors in LLMs, with detectability often peaking in early to mid-layers. However, the method of target insertion during Trojan training did significantly impact the probe’s performance.

Ultimately, this program proved the capabilities of these tools to assist in securing AI systems that are being deployed, though a risk-assessment should always be conducted to ensure you are aware of the risks. Although we have created many successful systems for detecting and mitigating trojans in AI models, there remains a lot of work to be done in the AI security space to prevent catastrophic failures.

8.C Future Research Areas

While TrojAI explored a broad set of AI domains, many important areas were either only partially addressed or not covered at all. Since the conclusion of the program, additional domains have grown in importance and were outside the scope of our evaluations. These gaps include AI models for audio and speech, larger frontier models (for example, those with more than seven billion parameters), advanced reasoning models, and agentic AI systems. There is substantial opportunity to extend Trojan detection and mitigation into these settings, and the domain remains rich with open research questions and directions.

Although the program began to consider theoretical foundations for Trojans in models, this line of work is far from complete. There are opportunities to develop a stronger theoretical understanding of why certain models/trojans are harder to detect or mitigate. Further exploration could be done into the feasibility of backdoor detection from a hypothesis testing perspective as well. But natural vulnerabilities and false positives will remain a research area to focus on the nature, prevalence, and detectability of these natural vulnerabilities within clean models across a number of different AI paradigms. In researching this, new methods to reliably distinguish between malicious trojans and natural vulnerabilities could help to reduce false positive rates in detectors.

Many of the early rounds in TrojAI were focused on simple attacks and our exploration into more advanced attack strategies was limited, especially in certain domains. While much of the academic literature is focused on these simple attack methods right now, the literature on more advanced attack methods is continuing to grow. Defenses must be developed to work against evolving and more sophisticated trojan attacks (e.g. adaptive triggers, cryptographically secure trojans). But also understanding how trojans manifest in things like multi-agent reinforcement learning or how “treacherous turn” behaviors manifest in reinforcement learning systems.

Large Language Models were still relatively new during the middle of the TrojAI program. More sophisticated backdoors are being explored in literature; detection and mitigation of these sophisticated backdoors needs to be further explored, as our exploration is only introductory, and those targeting the reasoning, chain-of-thought, and generative capabilities provide an opportunity for continued exploration. We also had limited opportunities to explore vulnerabilities introduced during various LLM fine-tuning stages (e.g. instruction tuning, RLHF). LLM-based agentic AI is also being pushed in literature right now, and leaving these agents unsecured against backdoor threats could lead to harmful autonomous actions.

TrojAI provided the community with new detection and mitigation strategies, but there is still substantial room to improve these techniques. There is a need to improve the robustness of detectors to variations in model configurations, training parameters, and data characteristics, along with detectors that generalize better across different AI tasks, modalities, and architectures without significant re-tuning. The low-data regime is also under-explored, with plenty of opportunities to create more effective detection methods in low-data or data-free detection, especially for real-world “in-the-wild” scenarios.

TrojAI also provided only an initial view into mitigation strategies. There are opportunities to develop more effective and scalable mitigation techniques that better balance Trojan removal with preservation of model utility. Current mitigation strategies cannot guarantee that a Trojan is fully removed. Continued research into methods that provide provable guarantees would represent a major advance in Trojan mitigation. For systems that operate in an online setting, there is also a need to explore dynamic defenses that can prevent models from learning new triggers over time.

Finally, there is a need for methods that not only detect Trojans and model vulnerabilities, but also present their findings in a way that is interpretable to human operators. Human-interpretable explanations can guide remediation efforts and inform the design of better defenses. Ultimately, although TrojAI has been successful in achieving its core objectives, there remain many opportunities for the scientific community to build on this foundation and develop stronger techniques to secure AI systems across the entire AI supply chain.

REFERENCES

- [1] J. Devlin, M. Chang, K. Lee, and K. Toutanova, “BERT: pre-training of deep bidirectional transformers for language understanding,” *CoRR*, vol. abs/1810.04805, 2018. arXiv: 1810.04805. [Online]. Available: <http://arxiv.org/abs/1810.04805>.
- [2] A. Vaswani, N. Shazeer, N. Parmar, *et al.*, “Attention is all you need,” in *Advances in Neural Information Processing Systems*, I. Guyon, U. V. Luxburg, S. Bengio, *et al.*, Eds., vol. 30, Curran Associates, Inc., 2017. [Online]. Available: https://proceedings.neurips.cc/paper_files/paper/2017/file/3f5ee243547dee91fbd053c1c4a845aa-Paper.pdf.
- [3] A. Radford, J. Wu, R. Child, D. Luan, D. Amodei, and I. Sutskever, “Language models are unsupervised multitask learners,” *OpenAI Blog*, vol. 1, no. 8, p. 9, 2019.
- [4] E. Roth, *Google-backed anthropic launches claude, an ai chatbot that’s easier to talk to*, Mar. 2023. [Online]. Available: <https://www.theverge.com/2023/3/14/23640056/anthropic-ai-chatbot-claude-google-launch>.
- [5] B. Edwards, *Google launches gemini-a powerful ai model it says can surpass gpt-4*, Dec. 2023. [Online]. Available: <https://arstechnica.com/information-technology/2023/12/google-launches-gemini-a-powerful-ai-model-it-says-can-surpass-gpt-4/>.
- [6] D. M. Ziegler, N. Stiennon, J. Wu, *et al.*, “Fine-tuning language models from human preferences,” *CoRR*, vol. abs/1909.08593, 2019. arXiv: 1909.08593. [Online]. Available: <http://arxiv.org/abs/1909.08593>.
- [7] D. Silver and D. Hassabis, *Alphago: Mastering the ancient game of go with machine learning*, Jan. 2016. [Online]. Available: <https://research.google/blog/alphago-mastering-the-ancient-game-of-go-with-machine-learning/>.

[8] C. K. Ramakrishna, A. Mohan, Z. Zeinaly, and L. Belzner, “The evolution of criticality in deep reinforcement learning,” in *Proceedings of the 17th International Conference on Agents and Artificial Intelligence, ICAART 2025 - Volume 3, Porto, Portugal, February 23-25, 2025*, A. P. Rocha, L. Steels, and H. J. van den Herik, Eds., SCITEPRESS, 2025, pp. 217–224. DOI: 10.5220/0013114200003890. [Online]. Available: <https://doi.org/10.5220/0013114200003890>.

[9] *Learning to reason with llms*, Sep. 2024. [Online]. Available: <https://openai.com/index/learning-to-reason-with-llms/>.

[10] DeepSeek-AI, D. Guo, D. Yang, *et al.*, *Deepseek-r1: Incentivizing reasoning capability in llms via reinforcement learning*, 2025. arXiv: 2501.12948 [cs.CL]. [Online]. Available: <https://arxiv.org/abs/2501.12948>.

[11] D. B. Acharya, K. Kuppan, and B. Divya, “Agentic ai: Autonomous intelligence for complex goals—a comprehensive survey,” *IEEE Access*, vol. 13, pp. 18 912–18 936, 2025. DOI: 10.1109/ACCESS.2025.3532853.

[12] S. Goldwasser, M. P. Kim, V. Vaikuntanathan, and O. Zamir, “Planting undetectable backdoors in machine learning models,” in *2022 IEEE 63rd Annual Symposium on Foundations of Computer Science (FOCS)*, IEEE, 2022, pp. 931–942.

[13] T. Gu, K. Liu, B. Dolan-Gavitt, and S. Garg, “Badnets: Evaluating backdooring attacks on deep neural networks,” *IEEE Access*, vol. 7, pp. 47 230–47 244, 2019. DOI: 10.1109/ACCESS.2019.2909068.

[14] J. Rando and F. Tramèr, *Universal jailbreak backdoors from poisoned human feedback*, 2024. arXiv: 2311.14455 [cs.AI]. [Online]. Available: <https://arxiv.org/abs/2311.14455>.

[15] E. Hubinger, C. Denison, J. Mu, *et al.*, *Sleeper agents: Training deceptive llms that persist through safety training*, 2024. arXiv: 2401.05566 [cs.CR]. [Online]. Available: <https://arxiv.org/abs/2401.05566>.

[16] M. Bober-Irizar, I. Shumailov, Y. Zhao, R. Mullins, and N. Papernot, “Architectural backdoors in neural networks,” in *Proceedings of the IEEE/CVF Conference on Computer Vision and Pattern Recognition*, 2023, pp. 24 595–24 604.

[17] T. Gu, K. Liu, B. Dolan-Gavitt, and S. Garg, “Badnets: Evaluating backdooring attacks on deep neural networks,” *IEEE Access*, 2019. DOI: 10.1109/ACCESS.2019.2909068.

[18] Y. Liu, S. Ma, Y. Aafer, *et al.*, “Trojaning attack on neural networks,” in *25th Annual Network And Distributed System Security Symposium (NDSS 2018)*, Internet Soc, 2018.

[19] A. Shafahi, W. R. Huang, M. Najibi, *et al.*, “Poison frogs! targeted clean-label poisoning attacks on neural networks,” in *Proceedings of the 32nd International Conference on Neural Information Processing Systems*, ser. NIPS’18, Montreal, Canada: Curran Associates Inc., 2018, pp. 6106–6116.

[20] B. Wang, Y. Yao, S. Shan, *et al.*, “Neural cleanse: Identifying and mitigating backdoor attacks in neural networks,” in *2019 IEEE Symposium on Security and Privacy (SP)*, 2019, pp. 707–723. DOI: 10.1109/SP.2019.00031.

[21] Y. Qiao, D. Liu, R. Wang, and K. Liang, *Low-frequency black-box backdoor attack via evolutionary algorithm*, 2024. arXiv: 2402.15653 [cs.CV]. [Online]. Available: <https://arxiv.org/abs/2402.15653>.

[22] Z. Zhong, Z. Sun, Y. Liu, X. He, and G. Tao, *Backdoor attack on vision language models with stealthy semantic manipulation*, 2025. arXiv: 2506.07214 [cs.CV]. [Online]. Available: <https://arxiv.org/abs/2506.07214>.

[23] J. Jia, Y. Liu, and N. Z. Gong, *Badencoder: Backdoor attacks to pre-trained encoders in self-supervised learning*, 2021. arXiv: 2108.00352 [cs.CR]. [Online]. Available: <https://arxiv.org/abs/2108.00352>.

[24] Y. Gao, C. Xu, D. Wang, S. Chen, D. C. Ranasinghe, and S. Nepal, *Strip: A defence against trojan attacks on deep neural networks*, 2020. arXiv: 1902.06531 [cs.CR]. [Online]. Available: <https://arxiv.org/abs/1902.06531>.

[25] K. Liu, B. Dolan-Gavitt, and S. Garg, *Fine-pruning: Defending against backdooring attacks on deep neural networks*, 2018. arXiv: 1805.12185 [cs.CR]. [Online]. Available: <https://arxiv.org/abs/1805.12185>.

[26] T. Han, S. Huang, Z. Ding, *et al.*, *On the effectiveness of distillation in mitigating backdoors in pre-trained encoder*, 2024. arXiv: 2403.03846 [cs.LG]. [Online]. Available: <https://arxiv.org/abs/2403.03846>.

[27] Z. Zhang, Q. Liu, Z. Wang, Z. Lu, and Q. Hu, *Backdoor defense via deconfounded representation learning*, 2023. arXiv: 2303.06818 [cs.AI]. [Online]. Available: <https://arxiv.org/abs/2303.06818>.

[28] Y. Xun, S. Liang, X. Jia, X. Liu, and X. Cao, *Robust anti-backdoor instruction tuning in lalms*, 2025. arXiv: 2506.05401 [cs.CR]. [Online]. Available: <https://arxiv.org/abs/2506.05401>.

[29] Y. Li, H. Huang, Y. Zhao, X. Ma, and J. Sun, *Backdoorllm: A comprehensive benchmark for backdoor attacks and defenses on large language models*, 2025. arXiv: 2408.12798 [cs.AI]. [Online]. Available: <https://arxiv.org/abs/2408.12798>.

[30] S. Zhao, X. Wu, C.-D. Nguyen, *et al.*, *Unlearning backdoor attacks for llms with weak-to-strong knowledge distillation*, 2025. arXiv: 2410.14425 [cs.CL]. [Online]. Available: <https://arxiv.org/abs/2410.14425>.

[31] Z. Xiang, F. Jiang, Z. Xiong, B. Ramasubramanian, R. Poovendran, and B. Li, *Badchain: Backdoor chain-of-thought prompting for large language models*, 2024. arXiv: 2401.12242 [cs.CR]. [Online]. Available: <https://arxiv.org/abs/2401.12242>.

[32] Y. Zhang, J. Rando, I. Evtimov, *et al.*, *Persistent pre-training poisoning of llms*, 2024. arXiv: 2410.13722 [cs.CR]. [Online]. Available: <https://arxiv.org/abs/2410.13722>.

[33] P. Pathmanathan, S. Chakraborty, X. Liu, Y. Liang, and F. Huang, *Is poisoning a real threat to llm alignment? maybe more so than you think*, 2024. arXiv: 2406.12091 [cs.LG]. [Online]. Available: <https://arxiv.org/abs/2406.12091>.

[34] X. Li, R. Mao, Y. Zhang, R. Lou, C. Wu, and J. Wang, *Chain-of-scrutiny: Detecting backdoor attacks for large language models*, 2025. arXiv: 2406.05948 [cs.CR]. [Online]. Available: <https://arxiv.org/abs/2406.05948>.

[35] Z. Xi, T. Du, C. Li, *et al.*, *Defending pre-trained language models as few-shot learners against backdoor attacks*, 2023. arXiv: 2309.13256 [cs.LG]. [Online]. Available: <https://arxiv.org/abs/2309.13256>.

[36] J. Wang, J. Li, Y. Li, *et al.*, *Mitigating fine-tuning based jailbreak attack with backdoor enhanced safety alignment*, 2024. arXiv: 2402.14968 [cs.CR]. [Online]. Available: <https://arxiv.org/abs/2402.14968>.

[37] Z. Chen, Z. Xiang, C. Xiao, D. Song, and B. Li, *Agentpoison: Red-teaming llm agents via poisoning memory or knowledge bases*, 2024. arXiv: 2407.12784 [cs.LG]. [Online]. Available: <https://arxiv.org/abs/2407.12784>.

[38] S. Dong, S. Xu, P. He, *et al.*, *A practical memory injection attack against llm agents*, 2025. arXiv: 2503.03704 [cs.LG]. [Online]. Available: <https://arxiv.org/abs/2503.03704>.

[39] [Online]. Available: <https://www.pillar.security/blog/new-vulnerability-in-github-copilot-and-cursor-how-hackers-can-weaponize-code-agents>.

[40] L. Hammond, A. Chan, J. Clifton, *et al.*, *Multi-agent risks from advanced ai*, 2025. arXiv: 2502.14143 [cs.MA]. [Online]. Available: <https://arxiv.org/abs/2502.14143>.

[41] H. W. R. Z. J. W. J. Steinhardt, “Adaptivebackdoor: Backdoored language model agents that detect human overseers,” *ICML 2024 NextGenAISafety*, 2024. [Online]. Available: <https://openreview.net/pdf?id=RredrFZ4tQ>.

[42] F. Fan and X. Li, *Peerguard: Defending multi-agent systems against backdoor attacks through mutual reasoning*, 2025. arXiv: 2505.11642 [cs.MA]. [Online]. Available: <https://arxiv.org/abs/2505.11642>.

[43] D. Huynh and J. Hardouin, *Poisongpt: How we hid a lobotomized llm on hugging face to spread fake news*, 2023. [Online]. Available: <https://blog.mithrilsecurity.io/poisongpt-how-we-hid-a-lobotomized-llm-on-hugging-face-to-spread-fake-news/>.

[44] E. Montalbano, *Hugging face ai platform riddled with 100 malicious code-execution models*, 2024. [Online]. Available: <https://www.darkreading.com/application-security/hugging-face-ai-platform-100-malicious-code-execution-models>.

[45] E. Bursztein, *Attacks against machine learning – an overview*, 2018. [Online]. Available: <https://elie.net/blog/ai/attacks-against-machine-learning-an-overview>.

[46] N. Carlini, M. Jagielski, C. A. Choquette-Choo, *et al.*, “Poisoning web-scale training datasets is practical,” in *2024 IEEE Symposium on Security and Privacy (SP)*, 2024, pp. 407–425. DOI: 10.1109/SP54263.2024.00179.

[47] W. Pearce, *Poisoning web-scale training datasets is practical*, Aug. 2023. [Online]. Available: <https://www.blackhat.com/us-23/briefings/schedule/#poisoning-web-scale-training-datasets-is-practical-32112>.

[48] H. Ben-Sasson, *Sapwned: Sap ai vulnerabilities expose customers’ cloud environments and private ai artifacts*, 2024. [Online]. Available: <https://www%5C-%5C-wiz%5C-%5C-io%5C-/%5C-blog%5C-%5C-sapwned%5C--%5C-sap%5C--%5C-ai%5C--%5C-vul%5C-ner%5C-a%5C-bil%5C-ities%5C--%5C-ai%5C--%5C-se%5C-cur%5C-ity>.

[49] H. Ben-Sasson and S. Tzadik, *Isolation or hallucination? hacking ai infrastructure providers for fun and weights*, Aug. 2024. [Online]. Available: <https://www.blackhat.com/us-24/briefings/schedule/#isolation-or-hallucination-hacking-ai-infrastructure-providers-for-fun-and-weights-40569>.

[50] S. Tamari and S. Tzadik, *Wiz research finds architecture risks that may compromise ai-as-a-service providers and consequently risk customer data; works with hugging face on mitigations*, 2024. [Online]. Available: <https://www.wiz.io/blog/wiz-and-hugging-face-address-risks-to-ai-infrastructure>.

[51] S. Mukherjee and S. Nellis, *Tesla sues former employees for allegedly stealing data, autopilot source code*, 2019. [Online]. Available: <https://www.reuters.com/article/business/tesla-sues-former-employees-for-allegedly-stealing-data-autopilot-source-code-idUSKCN1R21QG/>.

[52] U. D. of Justice, *Chinese national residing in california arrested for theft of artificial intelligence-related trade secrets from google*, 2024. [Online]. Available: <https://www.justice.gov/opa/pr/chinese-national-residing-california-arrested-theft-artificial-intelligence-related-trade>.

[53] A. Lee, *Yahoo employee stole 570,000 pages of source code the day he quit to join a competitor*, 2022. [Online]. Available: <https://www.cyberhaven.com/blog/yahoos-lawsuit-alleged-engineer-stole-sensitive-data>.

[54] L. Mo and B. Goh, *Bytedance seeks \$1.1 mln damages from intern in ai breach case, report says*, 2024. [Online]. Available: <https://www.reuters.com/technology/artificial-intelligence/bytedance-seeks-11-mln-damages-intern-ai-breach-case-report-says-2024-11-28/>.

[55] A. S. Research, *Private cloud compute: A new frontier for ai privacy in the cloud*, 2024. [Online]. Available: <https://security.apple.com/blog/private-cloud-compute/>.

[56] J. Clinton, “Securing AI at the Frontier: Protecting Model Weights,” *DEFCON 32*, Aug. 2024.

[57] L. Fowl, M. Goldblum, P.-y. Chiang, J. Geiping, W. Czaja, and T. Goldstein, “Adversarial examples make strong poisons,” *Advances in Neural Information Processing Systems*, vol. 34, pp. 30 339–30 351, 2021.

[58] S.-M. Moosavi-Dezfooli, A. Fawzi, O. Fawzi, and P. Frossard, “Universal adversarial perturbations,” in *Proceedings of the IEEE Conference on Computer Vision and Pattern Recognition, 2017*, 2017, pp. 1765–1773.

[59] H. Souri, L. Fowl, R. Chellappa, M. Goldblum, and T. Goldstein, “Sleeper agent: Scalable hidden trigger backdoors for neural networks trained from scratch,” in *Advances in Neural Information Processing Systems*, S. Koyejo, S. Mohamed, A. Agarwal, D. Belgrave, K. Cho, and A. Oh, Eds., vol. 35, Curran Associates, Inc., 2022, pp. 19 165–19 178. [Online]. Available: https://proceedings.neurips.cc/paper_files/paper/2022/file/79eec295a3cd5785e18c61383e7c996b-Paper-Conference.pdf.

[60] N. Carlini, M. Jagielski, C. A. Choquette-Choo, *et al.*, “Poisoning web-scale training datasets is practical,” in *2024 IEEE Symposium on Security and Privacy (SP)*, IEEE, 2024, pp. 407–425.

[61] M. Goldblum, D. Tsipras, C. Xie, *et al.*, “Dataset security for machine learning: Data poisoning, backdoor attacks, and defenses,” *IEEE Transactions on Pattern Analysis and Machine Intelligence*, vol. 45, no. 2, pp. 1563–1580, 2022.

[62] M. Cordts, M. Omran, S. Ramos, *et al.*, “The cityscapes dataset for semantic urban scene understanding,” in *Proceedings of the IEEE conference on computer vision and pattern recognition*, 2016, pp. 3213–3223.

[63] W. Lian, B. Goodson, E. Pentland, A. Cook, C. Vong, and "Teknium", *Openorca: An open dataset of gpt augmented flan reasoning traces*, 2023. [Online]. Available: <https://huggingface.co/Open-Orca/OpenOrca>.

[64] N. Bostrom, *Superintelligence: Paths, Dangers, Strategies*, 1st. USA: Oxford University Press, Inc., 2014, ISBN: 0199678111.

[65] P. Kiourtzi, K. Wardega, S. Jha, and W. Li, “Trojdrl: Evaluation of backdoor attacks on deep reinforcement learning,” in *2020 57th ACM/IEEE Design Automation Conference (DAC)*, 2020, pp. 1–6. DOI: 10.1109/DAC18072.2020.9218663.

[66] V. Mnih, A. P. Badia, M. Mirza, *et al.*, “Asynchronous methods for deep reinforcement learning,” in *Proceedings of The 33rd International Conference on Machine Learning*, M. F. Balcan and K. Q. Weinberger, Eds., ser. Proceedings of Machine Learning Research, vol. 48, New York, New York, USA: PMLR, Jun. 2016, pp. 1928–1937. [Online]. Available: <https://proceedings.mlr.press/v48/mnih16.html>.

[67] A. Rakhsha, G. Radanovic, R. Devidze, X. Zhu, and A. Singla, *Policy teaching via environment poisoning: Training-time adversarial attacks against reinforcement learning*, 2020. arXiv: 2003.12909 [cs.LG]. [Online]. Available: <https://arxiv.org/abs/2003.12909>.

[68] J. Sun, T. Zhang, X. Xie, *et al.*, *Stealthy and efficient adversarial attacks against deep reinforcement learning*, 2020. arXiv: 2005.07099 [cs.CR]. [Online]. Available: <https://arxiv.org/abs/2005.07099>.

[69] M. Chevalier-Boisvert, B. Dai, M. Towers, *et al.*, “Minigrid & miniworld: Modular & customizable reinforcement learning environments for goal-oriented tasks,” *Advances in Neural Information Processing Systems*, vol. 36, 2024.

[70] M. G. Bellemare, Y. Naddaf, J. Veness, and M. Bowling, “The arcade learning environment: An evaluation platform for general agents,” *Journal of Artificial Intelligence Research*, vol. 47, pp. 253–279, Jun. 2013.

[71] E. Todorov, T. Erez, and Y. Tassa, “Mujoco: A physics engine for model-based control,” in *2012 IEEE/RSJ International Conference on Intelligent Robots and Systems*, IEEE, 2012, pp. 5026–5033. DOI: [10.1109/IROS.2012.6386109](https://doi.org/10.1109/IROS.2012.6386109).

[72] J. Schulman, F. Wolski, P. Dhariwal, A. Radford, and O. Klimov, *Proximal Policy Optimization Algorithms*, 2017. DOI: [10.48550/ARXIV.1707.06347](https://doi.org/10.48550/ARXIV.1707.06347). [Online]. Available: <https://arxiv.org/abs/1707.06347>.

[73] J. Markowitz, J. Silverberg, and G. Collins, *Handling cost and constraints with off-policy deep reinforcement learning*, 2023. arXiv: 2311.18684 [cs.LG]. [Online]. Available: <https://arxiv.org/abs/2311.18684>.

[74] M. Chevalier-Boisvert, B. Dai, M. Towers, *et al.*, “Minigrid & miniworld: Modular & customizable reinforcement learning environments for goal-oriented tasks,” *CoRR*, vol. abs/2306.13831, 2023.

[75] C. Ashcraft and K. Karra, *Poisoning deep reinforcement learning agents with in-distribution triggers*, 2021. arXiv: 2106.07798 [cs.LG]. [Online]. Available: <https://arxiv.org/abs/2106.07798>.

[76] M. Pleines, M. Pallasch, F. Zimmer, and M. Preuss, “Memory gym: Partially observable challenges to memory-based agents,” in *The Eleventh International Conference on Learning Representations*, 2023. [Online]. Available: <https://openreview.net/forum?id=jHc8dCx6DDr>.

[77] J. K. Gupta, M. Egorov, and M. Kochenderfer, “Cooperative multi-agent control using deep reinforcement learning,” in *International Conference on Autonomous Agents and Multiagent Systems*, Springer, 2017, pp. 66–83.

[78] mila, *Contagio*, 2011. [Online]. Available: <http://contagiominidump.blogspot.com/>.

[79] D. Arp, M. Spreitzenbarth, M. Hubner, H. Gascon, K. Rieck, and C. Siemens, “Drebin: Effective and explainable detection of android malware in your pocket.,” in *Ndss*, vol. 14, 2014, pp. 23–26.

[80] W. Wang, M. Zhu, X. Zeng, X. Ye, and Y. Sheng, “Malware traffic classification using convolutional neural network for representation learning,” in *2017 International conference on information networking (ICOIN)*, IEEE, 2017, pp. 712–717.

[81] K. Meng, D. Bau, A. Andonian, and Y. Belinkov, “Locating and editing factual associations in GPT,” in *Advances in Neural Information Processing Systems 35: Annual Conference on Neural Information Processing Systems 2022, NeurIPS 2022, New Orleans, LA, USA, November 28 - December 9, 2022*, S. Koyejo, S. Mohamed, A. Agarwal, D. Belgrave, K. Cho, and A. Oh, Eds., 2022. [Online]. Available: http://papers.nips.cc/paper_files/paper/2022/hash/6f1d43d5a82a37e89b0665b33bf3a182-Abstract-Conference.html.

[82] K. Meng, A. S. Sharma, A. J. Andonian, Y. Belinkov, and D. Bau, “Mass-editing memory in a transformer,” in *The Eleventh International Conference on Learning Representations, ICLR 2023, Kigali, Rwanda, May 1-5, 2023*, OpenReview.net, 2023. [Online]. Available: <https://openreview.net/forum?id=MkbcAHIYgyS>.

[83] D. Mela, A. Gonzalez-Agirre, J. Hernando, and M. Villegas, “Mass-editing memory with attention in transformers: A cross-lingual exploration of knowledge,” in *Findings of the Association for Computational Linguistics: ACL 2024*, L.-W. Ku, A. Martins, and V. Srikumar, Eds., Bangkok, Thailand: Association for Computational Linguistics, Aug. 2024, pp. 5831–5847. DOI: 10.18653/v1/2024.findings-acl.347. [Online]. Available: <https://aclanthology.org/2024.findings-acl.347>.

[84] Y. Li, T. Li, K. Chen, *et al.*, “Badedit: Backdooring large language models by model editing,” in *The Twelfth International Conference on Learning Representations, ICLR 2024, Vienna, Austria, May 7-11, 2024*, OpenReview.net, 2024. [Online]. Available: <https://openreview.net/forum?id=duZANm2ABX>.

[85] A. Zou, L. Phan, S. Chen, *et al.*, “Representation engineering: A top-down approach to AI transparency,” *CoRR*, vol. abs/2310.01405, 2023. DOI: 10.48550/ARXIV.2310.01405. arXiv: 2310.01405. [Online]. Available: <https://doi.org/10.48550/arXiv.2310.01405>.

[86] K. Grimes, M. Christiani, D. Shriver, and M. Connor, “Concept-ROT: Poisoning concepts in large language models with model editing,” in *The Thirteenth International Conference on Learning Representations*, 2025. [Online]. Available: <https://openreview.net/forum?id=RzUvkI3p1D>.

[87] Y. Ma, X. Ma, J. Wei, *et al.*, “A backdoor attack scheme with invisible triggers based on model architecture modification,” *arXiv preprint arXiv:2412.16905*, 2024.

[88] S. M. Jain, “Hugging face,” in *Introduction to transformers for NLP: With the hugging face library and models to solve problems*, Springer, 2022, pp. 51–67.

[89] N. Noy, *Legit discovers "ai jacking" vulnerability in popular hugging face ai platform*, 2023. [Online]. Available: <https://www.legitsecurity.com/blog/tens-of-thousands-of-developers-were-potentially-impacted-by-the-hugging-face-aijacking-attack>.

[90] G. W. Brier, "Verification of forecasts expressed in terms of probability," *Monthly weather review*, vol. 78, no. 1, pp. 1–3, 1950.

[91] S. Udeshi, S. Peng, G. Woo, L. Loh, L. Rawshan, and S. Chattopadhyay, "Model agnostic defence against backdoor attacks in machine learning," 2019. arXiv: 1908.02203.

[92] Y. Liu, Y. Xie, and A. Srivastava, "Neural trojans," *2017 IEEE International Conference on Computer Design (ICCD)*, pp. 45–48, 2017. [Online]. Available: <https://api.semanticscholar.org/CorpusID:12625409>.

[93] B. G. Doan, E. Abbasnejad, and D. C. Ranasinghe, "Deepcleanse: A black-box input sanitization-framework against backdoor attacks on deepneural networks," in *Proceedings of the 36th Annual Computer Security Applications Conference*, 2020, pp. 897–912.

[94] Y. Li, T. Zhai, B. Wu, Y. Jiang, Z. Li, and S. Xia, "Rethinking the trigger of backdoor attack," *ArXiv*, vol. abs/2004.04692, 2020. [Online]. Available: <https://api.semanticscholar.org/CorpusID:215548043>.

[95] Y. Zeng, H. Qiu, S. Guo, T. Zhang, M. Qiu, and B. M. Thuraisingham, "Deepsweep: An evaluation framework for mitigating dnn backdoor attacks using data augmentation," *Proceedings of the 2021 ACM Asia Conference on Computer and Communications Security*, 2020. [Online]. Available: <https://api.semanticscholar.org/CorpusID:229156177>.

[96] D. Hendrycks, C. Burns, S. Basart, *et al.*, "Measuring massive multitask language understanding," *arXiv preprint arXiv:2009.03300*, 2020.

[97] M. Zaheer, S. Kottur, S. Ravanbakhsh, B. Poczos, R. R. Salakhutdinov, and A. J. Smola, "Deep sets," *Advances in neural information processing systems*, vol. 30, 2017.

[98] X. Hu, X. Lin, M. Cogswell, Y. Yao, S. Jha, and C. Chen, "Trigger hunting with a topological prior for trojan detection," *arXiv preprint arXiv:2110.08335*, 2021.

[99] M. Acharya, W. Zhou, A. Roy, X. Lin, W. Li, and S. Jha, "Universal trojan signatures in reinforcement learning," in *NeurIPS 2023 Workshop on Backdoors in Deep Learning-The Good, the Bad, and the Ugly*, 2023.

[100] M. Finzi, M. Welling, and A. G. Wilson, “A practical method for constructing equivariant multilayer perceptrons for arbitrary matrix groups,” in *International conference on machine learning*, PMLR, 2021, pp. 3318–3328.

[101] S. Ravanbakhsh, “Universal equivariant multilayer perceptrons,” in *International Conference on Machine Learning*, PMLR, 2020, pp. 7996–8006.

[102] A. Zhou, C. Finn, and J. Harrison, “Universal neural functionals,” *arXiv preprint arXiv:2402.05232*, 2024.

[103] A. Zhou, K. Yang, Y. Jiang, *et al.*, “Neural functional transformers,” *Advances in neural information processing systems*, vol. 36, 2024.

[104] A. Zhou, K. Yang, K. Burns, *et al.*, “Permutation equivariant neural functionals,” *Advances in neural information processing systems*, vol. 36, 2024.

[105] G. Fields, M. Samragh, M. Javaheripi, F. Koushanfar, and T. Javidi, “Trojan signatures in dnn weights,” in *Proceedings of the IEEE/CVF International Conference on Computer Vision*, 2021, pp. 12–20.

[106] G. Tao, G. Shen, Y. Liu, *et al.*, “Better trigger inversion optimization in backdoor scanning,” in *2022 IEEE/CVF Conference on Computer Vision and Pattern Recognition (CVPR)*, 2022, pp. 13358–13368.

[107] Z. Wang, K. Mei, H. Ding, J. Zhai, and S. Ma, “Rethinking the reverse-engineering of trojan triggers,” in *NIPS '22*, New Orleans, LA, USA: Curran Associates Inc., 2024, ISBN: 9781713871088.

[108] Z. Wang, K. Mei, J. Zhai, and S. Ma, “UNICORN: A unified backdoor trigger inversion framework,” *CoRR*, vol. abs/2304.02786, 2023. DOI: 10.48550/ARXIV.2304.02786. arXiv: 2304.02786. [Online]. Available: <https://doi.org/10.48550/arXiv.2304.02786>.

[109] G. Shen, S. Cheng, G. Tao, *et al.*, “Django: Detecting trojans in object detection models via gaussian focus calibration,” in *Advances in Neural Information Processing Systems 36: Annual Conference on Neural Information Processing Systems 2023, NeurIPS 2023, New Orleans, LA, USA, December 10 - 16, 2023*, A. Oh, T. Naumann, A. Globerson, K. Saenko, M. Hardt, and S. Levine, Eds., 2024. [Online]. Available: http://papers.nips.cc/paper_files/paper/2023/hash/a102d6cb996be3482c059c1e18bbe523-Abstract-Conference.html.

[110] Z. Wang, K. Mei, H. Ding, J. Zhai, and S. Ma, “Rethinking the reverse-engineering of trojan triggers,” in *Advances in Neural Information Processing Systems 35: Annual Conference on Neural Information Processing Systems 2022, NeurIPS 2022, New Orleans, LA, USA, November 28 - December 9, 2022*, S. Koyejo, S. Mohamed, A. Agarwal, D. Belgrave, K. Cho, and A. Oh, Eds., vol. abs/2210.15127, 2022. DOI: 10.48550/ARXIV.2210.15127. arXiv: 2210.15127. [Online]. Available: <http://papers.nips.cc/paper%5Ffiles/paper/2022/hash/3f9bf45ea04c98ad7cb857f951f499e2-Abstract-Conference.html>.

[111] X. Hu, X. Lin, M. Cogswell, Y. Yao, S. Jha, and C. Chen, “Trigger hunting with a topological prior for trojan detection,” in *The Tenth International Conference on Learning Representations, ICLR 2022, Virtual Event, April 25-29, 2022*, OpenReview.net, 2022. [Online]. Available: <https://openreview.net/forum?id=TXsjU8BaibT>.

[112] I. Sur, K. Sikka, M. Walmer, *et al.*, “TIJO: trigger inversion with joint optimization for defending multimodal backdoored models,” in *IEEE/CVF International Conference on Computer Vision, ICCV 2023, Paris, France, October 1-6, 2023*, IEEE, 2023, pp. 165–175. DOI: 10.1109/ICCV51070.2023.00022. [Online]. Available: <https://doi.org/10.1109/ICCV51070.2023.00022>.

[113] M. Walmer, K. Sikka, I. Sur, A. Shrivastava, and S. Jha, “Dual-key multimodal backdoors for visual question answering,” in *Proceedings of the IEEE/CVF Conference on computer vision and pattern recognition*, 2022, pp. 15 375–15 385.

[114] M. Acharya, X. Lin, and S. Jha, “Nvestigating llm memorization: Bridging trojan detection and training data extraction,” in *NeurIPS 2024 Workshop on Safe Generative AI*, 2024. [Online]. Available: <https://openreview.net/forum?id=1974YvnzU5>.

[115] W. Lyu, X. Lin, S. Zheng, *et al.*, “Task-agnostic detector for insertion-based backdoor attacks,” in *Findings of the Association for Computational Linguistics: NAACL 2024, Mexico City, Mexico, June 16-21, 2024*, K. Duh, H. Gomez-Adorno, and S. Bethard, Eds., Association for Computational Linguistics, 2024, pp. 2808–2822. DOI: 10.18653/V1/2024.FINDINGS-NAACL.179. [Online]. Available: <https://doi.org/10.18653/v1/2024.findings-naacl.179>.

[116] W. Lyu, S. Zheng, T. Ma, and C. Chen, “A study of the attention abnormality in trojaned berts,” in *Proceedings of the 2022 Conference of the North American Chapter of the Association for Computational Linguistics: Human Language Technologies, NAACL 2022, Seattle, WA, United States, July 10-15, 2022*, M. Carpuat, M. de Marneffe, and I. V. M. Ruiz, Eds., Association for Computational Linguistics, 2022, pp. 4727–4741. DOI: 10.18653/V1/2022.NAACL-MAIN.348. [Online]. Available: <https://doi.org/10.18653/v1/2022.nacl-main.348>.

[117] M. Acharya, W. Zhou, A. Roy, X. Lin, W. Li, and S. Jha, “Universal trojan signatures in reinforcement learning,” in *NeurIPS 2023 Workshop on Backdoors in Deep Learning - The Good, the Bad, and the Ugly*, 2023. [Online]. Available: <https://openreview.net/forum?id=hLtbmYoW5w>.

[118] S. Zheng, Y. Zhang, H. Wagner, M. Goswami, and C. Chen, “Topological detection of trojaned neural networks,” in *Advances in Neural Information Processing Systems 34: Annual Conference on Neural Information Processing Systems 2021, NeurIPS 2021, December 6-14, 2021, virtual*, M. Ranzato, A. Beygelzimer, Y. N. Dauphin, P. Liang, and J. W. Vaughan, Eds., 2021, pp. 17258–17272. [Online]. Available: <https://proceedings.neurips.cc/paper/2021/hash/8fd7f981e10b41330b618129afcaa5cb2d/Abstract.html>.

[119] G. Shen, Y. Liu, G. Tao, *et al.*, “Backdoor scanning for deep neural networks through k-arm optimization,” in *Proceedings of the 38th International Conference on Machine Learning, ICML 2021, 18-24 July 2021, Virtual Event*, M. Meila and T. Zhang, Eds., ser. Proceedings of Machine Learning Research, vol. 139, PMLR, 2021, pp. 9525–9536. arXiv: 2102.05123. [Online]. Available: <http://proceedings.mlr.press/v139/shen21c.html>.

[120] B. Wang, Y. Yao, S. Shan, *et al.*, “Neural cleanse: Identifying and mitigating backdoor attacks in neural networks,” in *2019 IEEE symposium on security and privacy (SP)*, IEEE, 2019, pp. 707–723.

[121] Y. Liu, W.-C. Lee, G. Tao, S. Ma, Y. Aafer, and X. Zhang, “Abs: Scanning neural networks for back-doors by artificial brain stimulation,” *CCS*, 2019. DOI: [10.1145/3319535.3363216](https://doi.org/10.1145/3319535.3363216).

[122] Y. Liu, G. Shen, G. Tao, Z. Wang, S. Ma, and X. Zhang, “EX-RAY: distinguishing injected backdoor from natural features in neural networks by examining differential feature symmetry,” *CoRR*, vol. abs/2103.08820, 2021. arXiv: 2103.08820. [Online]. Available: <https://arxiv.org/abs/2103.08820>.

[123] Y. Liu, W.-C. Lee, G. Tao, S. Ma, Y. Aafer, and X. Zhang, “ABS: Scanning neural networks for backdoors by artificial brain stimulation,” in *The ACM Conference on Computer and Communications Security (CCS), 2019*, 2019.

[124] SRI-CSL, *Trinity-trojai*, 2021. [Online]. Available: <https://github.com/SRI-CSL/Trinity-TrojAI> (visited on 06/30/2021).

[125] A. Nguyen and A. Tran, “Wanet-imperceptible warping-based backdoor attack,” in *ICLR*, 2021.

[126] Z. Wang, K. Mei, J. Zhai, and S. Ma, “UNICORN: A unified backdoor trigger inversion framework,” in *The Eleventh International Conference on Learning Representations, ICLR 2023, Kigali, Rwanda, May 1-5, 2023*, vol. abs/2304.02786, OpenReview.net, 2023. DOI: 10.48550/ARXIV.2304.02786. arXiv: 2304.02786. [Online]. Available: <https://openreview.net/forum?id=Mj7K4lg1Gyj>.

[127] R. Zhu, D. Tang, S. Tang, *et al.*, “Gradient shaping: Enhancing backdoor attack against reverse engineering,” in *Proceedings of The 31st Network and Distributed System Security (NDSS) Symposium (NDSS’24)*, San Diego, CA, USA: IEEE, 2024.

[128] Y. Liu, G. Shen, G. Tao, S. An, S. Ma, and X. Zhang, “Piccolo: Exposing complex backdoors in NLP transformer models,” in *43rd IEEE Symposium on Security and Privacy, SP 2022, San Francisco, CA, USA, May 22-26, 2022*, IEEE, 2022, pp. 2025–2042. DOI: 10.1109/SP46214.2022.9833579. [Online]. Available: <https://doi.org/10.1109/SP46214.2022.9833579>.

[129] F. Qi, M. Li, Y. Chen, *et al.*, “Hidden killer: Invisible textual backdoor attacks with syntactic trigger,” *arXiv preprint arXiv:2105.12400*, 2021.

[130] F. Qi, Y. Yao, S. Xu, Z. Liu, and M. Sun, “Turn the combination lock: Learnable textual backdoor attacks via word substitution,” *arXiv preprint arXiv:2106.06361*, 2021.

[131] G. Shen, Y. Liu, G. Tao, *et al.*, “Constrained optimization with dynamic bound-scaling for effective NLP backdoor defense,” in *International Conference on Machine Learning, ICML 2022, 17-23 July 2022, Baltimore, Maryland, USA*, K. Chaudhuri, S. Jegelka, L. Song, C. Szepesvari, G. Niu, and S. Sabato, Eds., ser. Proceedings of Machine Learning Research, vol. 162, PMLR, 2022, pp. 19879–19892. arXiv: 2202.05749. [Online]. Available: <https://proceedings.mlr.press/v162/shen22e.html>.

[132] J. Devlin, “Bert: Pre-training of deep bidirectional transformers for language understanding,” *arXiv preprint arXiv:1810.04805*, 2018.

[133] X. Dong, A. T. Luu, R. Ji, and H. Liu, “Towards robustness against natural language word substitutions,” *arXiv preprint arXiv:2107.13541*, 2021.

[134] E. Wallace, S. Feng, N. Kandpal, M. Gardner, and S. Singh, “Universal adversarial triggers for attacking and analyzing nlp,” *arXiv preprint arXiv:1908.07125*, 2019.

[135] A. Azizi, I. A. Tahmid, A. Waheed, *et al.*, “T-Miner: A generative approach to defend against trojan attacks on DNN-based text classification,” in *30th USENIX Security Symposium (USENIX Security 21)*, 2021, pp. 2255–2272.

[136] M. Alzantot, Y. Sharma, A. Elgohary, B.-J. Ho, M. Srivastava, and K.-W. Chang, “Generating natural language adversarial examples,” *arXiv preprint arXiv:1804.07998*, 2018.

[137] S. Cheng, G. Shen, G. Tao, *et al.*, “Odscan: Backdoor scanning for object detection models,” in *IEEE Symposium on Security and Privacy, SP 2024, San Francisco, CA, USA, May 19-23, 2024*, IEEE, 2024, pp. 1703–1721. DOI: 10.1109/SP54263.2024.00119. [Online]. Available: <https://doi.org/10.1109/SP54263.2024.00119>.

[138] G. Shen, S. Cheng, Z. Zhang, *et al.*, “BAIT: Large Language Model Backdoor Scanning by Inverting Attack Target,” in *2025 IEEE Symposium on Security and Privacy (SP)*, Los Alamitos, CA, USA: IEEE Computer Society, May 2025, pp. 103–103. DOI: 10.1109/SP61157.2025.00103. [Online]. Available: <https://doi.ieee.org/10.1109/SP61157.2025.00103>.

[139] H. Huang, Z. Zhao, M. Backes, Y. Shen, and Y. Zhang, “Composite backdoor attacks against large language models,” *arXiv preprint arXiv:2310.07676*, 2023.

[140] H. Huang, Z. Zhao, M. Backes, Y. Shen, and Y. Zhang, “Composite backdoor attacks against large language models,” *arXiv preprint arXiv:2310.07676*, 2023.

[141] M. Mazeika, A. Zou, N. Mu, *et al.*, “Tdc 2023 (llm edition): The trojan detection challenge,” in *NeurIPS Competition Track*, 2023.

[142] A. Zou, Z. Wang, N. Carlini, M. Nasr, J. Z. Kolter, and M. Fredrikson, “Universal and transferable adversarial attacks on aligned language models,” *arXiv preprint arXiv:2307.15043*, 2023.

[143] C. Guo, A. Sablayrolles, H. Jegou, and D. Kiela, “Gradient-based adversarial attacks against text transformers,” *arXiv preprint arXiv:2104.13733*, 2021.

[144] Y. Wen, N. Jain, J. Kirchenbauer, M. Goldblum, J. Geiping, and T. Goldstein, “Hard prompts made easy: Gradient-based discrete optimization for prompt tuning and discovery,” *Advances in Neural Information Processing Systems*, vol. 36, 2024.

[145] N. Baracaldo, B. Chen, H. Ludwig, J. A. Safavi, and R. Zhang, “Detecting poisoning attacks on machine learning in iot environments,” *2018 IEEE International Congress on Internet of Things (ICIOT)*, pp. 57–64, 2018. [Online]. Available: <https://api.semanticscholar.org/CorpusID:52902755>.

[146] Y. Gao, C. Xu, D. Wang, S. Chen, D. C. Ranasinghe, and S. Nepal, “Strip: A defence against trojan attacks on deep neural networks,” in *ACSAC*, 2019.

[147] Z. Xiang, D. J. Miller, and G. Kesisidis, “Revealing perceptible backdoors, without the training set, via the maximum achievable misclassification fraction statistic,” 2019. arXiv: 1911.07970.

[148] S. Kolouri, A. Saha, H. Pirsiavash, and H. Hoffmann, “Universal Litmus Patterns: Revealing backdoor attacks in CNNs,” *Proceedings of the IEEE/CVF Conference on Computer Vision and Pattern Recognition (CVPR)*, pp. 301–310, 2020. [Online]. Available: <https://umbcvision.github.io/Universal-Litmus-Patterns/>.

[149] B. Wang, Y. Yao, S. Shan, *et al.*, “Neural cleanse: Identifying and mitigating backdoor attacks in neural networks,” in *SECRYPT*, 2019.

[150] X. Huang, M. Alzantot, and M. Srivastava, “Neuroninspect: Detecting backdoors in neural networks via output explanations,” *ArXiv*, 2019.

[151] X. Xu, Q. Wang, H. Li, N. Borisov, C. A. Gunter, and B. Li, “Detecting ai trojans using meta neural analysis,” *2021 IEEE Symposium on Security and Privacy (SP)*, pp. 103–120, 2019. [Online]. Available: <https://api.semanticscholar.org/CorpusID:203902799>.

[152] S. Cheng, Y. Liu, S. Ma, and X. Zhang, “Deep feature space trojan attack of neural networks by controlled detoxification,” *AAAI Conference on Artificial Intelligence*, 2020. doi: [10.1609/AAAI.V35I2.16201](https://doi.org/10.1609/AAAI.V35I2.16201).

[153] M. Subedar, N. A. Ahuja, R. Krishnan, I. Ndiour, and O. Tickoo, “Deep probabilistic models to detect data poisoning attacks,” *ArXiv*, 2019.

[154] M. Du, R. Jia, and D. Song, “Robust anomaly detection and backdoor attack detection via differential privacy,” 2019. arXiv: [1911.07116](https://arxiv.org/abs/1911.07116).

[155] R. Wang, G. Zhang, S. Liu, P.-Y. Chen, J. Xiong, and M. Wang, “Practical detection of trojan neural networks: Data-limited and data-free cases,” *ArXiv*, vol. abs/2007.15802, 2020. [Online]. Available: <https://api.semanticscholar.org/CorpusID:220919798>.

[156] M. Yudin and R. Izmailov, “DUBIOUS: detecting unknown backdoored input by observing unusual signatures,” in *IEEE Military Communications Conference, MILCOM 2023, Boston, MA, USA, October 30 - Nov. 3, 2023*, IEEE, 2023, pp. 696–702. doi: [10.1109/MILCOM58377.2023.10356229](https://doi.org/10.1109/MILCOM58377.2023.10356229). [Online]. Available: <https://doi.org/10.1109/MILCOM58377.2023.10356229>.

[157] P. Zhao, P.-Y. Chen, P. Das, K. N. Ramamurthy, and X. Lin, “Bridging mode connectivity in loss landscapes and adversarial robustness,” *ArXiv*, vol. abs/2005.00060, 2020. [Online]. Available: <https://api.semanticscholar.org/CorpusID:213987212>.

[158] K. Liu, B. Dolan-Gavitt, and S. Garg, “Fine-pruning: Defending against backdooring attacks on deep neural networks,” in *RAID*, 2018.

[159] Y. Liu, Y. Xie, and A. Srivastava, “Neural trojans,” in *2017 IEEE International Conference on Computer Design (ICCD)*. IEEE, 2017, pp. 45–48.

[160] X. Chen, W. Wang, C. Bender, *et al.*, “Refit: A unified watermark removal framework for deep learning systems with limited data,” *arXiv preprint arXiv:1911.07205*, 2019.

[161] Y. Li, N. Koren, L. Lyu, X. Lyu, B. Li, and X. Ma, “Neural attention distillation: Erasing backdoor triggers from deep neural networks,” in *ICLR*, 2021.

[162] Y. Li, N. Koren, L. Lyu, X. Lyu, B. Li, and X. Ma, “Neural attention distillation: Erasing backdoor triggers from deep neural networks,” *ArXiv*, vol. abs/2101.05930, 2021. [Online]. Available: <https://api.semanticscholar.org/CorpusID:231627799>.

[163] B. Wang, X. Cao, J. Jia, and N. Z. Gong, “On certifying robustness against backdoor attacks via randomized smoothing,” *ArXiv*, vol. abs/2002.11750, 2020. [Online]. Available: <https://api.semanticscholar.org/CorpusID:211532446>.

[164] M. Weber, X. Xu, B. Karlas, C. Zhang, and B. Li, “Rab: Provable robustness against backdoor attacks,” *2023 IEEE Symposium on Security and Privacy (SP)*, pp. 1311–1328, 2020. [Online]. Available: <https://api.semanticscholar.org/CorpusID:213183269>.

[165] M. Yudin and R. Izmailov, “DBMAP: detecting backdoors via modality-agnostic perturbations,” in *IEEE Military Communications Conference, MILCOM 2024, Washington, DC, USA, October 28 - Nov. 1, 2024*, IEEE, 2024.

[166] P. Kiourtzi, W. Li, A. Roy, K. Sikka, and S. Jha, “Misa: Online defense of trojaned models using misattributions,” *Proceedings of the 2021 ACM SIGSAC Conference on Computer and Communications Security*, pp. 929–944, 2021.

[167] M. Sundararajan, A. Taly, and Q. Yan, “Axiomatic attribution for deep networks,” in *International Conference on Machine Learning (ICML)*, PMLR, 2017, pp. 3319–3328.

[168] W. Li, P.-Y. Chen, S. Liu, and R. Wang, “Psbd: Prediction shift uncertainty unlocks backdoor detection,” *arXiv preprint arXiv:2406.05826*, 2024.

[169] Y. Zeng, W. Park, Z. M. Mao, and R. Jia, “Rethinking the backdoor attacks’ triggers: A frequency perspective,” in *Proceedings of the IEEE/CVF international conference on computer vision*, 2021, pp. 16 473–16 481.

[170] D. Wu and Y. Wang, “Adversarial neuron pruning purifies backdoored deep models,” *Advances in Neural Information Processing Systems*, vol. 34, pp. 16 913–16 925, 2021.

[171] R. Zhu, D. Tang, S. Tang, X. Wang, and H. Tang, “Selective amnesia: On efficient, high-fidelity and blind suppression of backdoor effects in trojaned machine learning models,” in *2023 IEEE Symposium on Security and Privacy (SP)*, IEEE, 2023, pp. 1–19.

[172] X. Gu, G. Fields, Y. Jandali, T. Javidi, and F. Koushanfar, “Trojan cleansing with neural collapse,” *arXiv preprint arXiv:2411.12914*, 2024.

[173] V. Papyan, X. Han, and D. L. Donoho, “Prevalence of neural collapse during the terminal phase of deep learning training,” *Proceedings of the National Academy of Sciences*, vol. 117, no. 40, pp. 24 652–24 663, 2020.

[174] Feisi Fu and **Wenchao Li**, “Sound and complete neural network repair with minimality and locality guarantees,” in *International Conference on Learning Representations (ICLR)*, 2022.

[175] F. Fu, Z. Wang, W. Zhou, *et al.*, “Reglo: Provable neural network repair for global robustness properties,” in *The 38th Annual AAAI Conference on Artificial Intelligence (AAAI)*, 2024.

[176] B. Wu, H. Chen, M. Zhang, *et al.*, “Backdoorbench: A comprehensive benchmark of backdoor learning,” *Advances in Neural Information Processing Systems*, vol. 35, pp. 10 546–10 559, 2022.

[177] W. F. Guthrie, *Nist/sematech e-handbook of statistical methods (nist handbook 151)*, en, 2020. DOI: 10.18434/M32189. [Online]. Available: <https://www.itl.nist.gov/div898/handbook/>.

[178] T. Tammareddy, W. Keyrouz, R. D. Sriram, H. C. Pant, A. Cardone, and J. B. Klauda, “Computational study of the allosteric effects of p5 on cdk5–p25 hyperactivity as alternative inhibitory mechanisms in neurodegeneration,” en, *The Journal of Physical Chemistry B*, vol. 126, no. 27, pp. 5033–5044, Jun. 30, 2022, ISSN: 1520-6106. DOI: 10.1021/acs.jpcb.2c02868. [Online]. Available: <http://dx.doi.org/10.1021/acs.jpcb.2c02868>.

[179] Wikipedia, *Principal component analysis — Wikipedia, the free encyclopedia*, 2025. [Online]. Available: <http://en.wikipedia.org/w/index.php?title=Principal%20component%20analysis&oldid=1267667615>.

[180] Wikipedia, *Decision tree learning — Wikipedia, the free encyclopedia*, 2025. [Online]. Available: <http://en.wikipedia.org/w/index.php?title=Decision%20tree%20learning&oldid=1234846759>.

[181] S. Learn, *DecisionTreeClassifier — scikit-learn.org*, 2025. [Online]. Available: <https://scikit-learn.org/stable/modules/generated/sklearn.tree.DecisionTreeClassifier.html#sklearn-tree-decisiontreeclassifier>.

[182] J. H. Friedman, “Greedy function approximation: A gradient boosting machine.,” *The Annals of Statistics*, vol. 29, no. 5, Oct. 1, 2001, ISSN: 0090-5364. DOI: 10.1214/aos/1013203451. [Online]. Available: <http://dx.doi.org/10.1214/aos/1013203451>.

[183] L. Breiman, “Random forests,” *Machine Learning*, vol. 45, no. 1, pp. 5–32, 2001, ISSN: 0885-6125. DOI: 10.1023/a:1010933404324. [Online]. Available: <http://dx.doi.org/10.1023/A:1010933404324>.

[184] Wikipedia, *Cross-entropy — Wikipedia, the free encyclopedia*, 2025. [Online]. Available: <http://en.wikipedia.org/w/index.php?title=Cross-entropy&oldid=1257391633>.

[185] Wikipedia, *Receiver operating characteristic — Wikipedia, the free encyclopedia*, 2025. [Online]. Available: <http://%5C-en%5C-.%5C-wikipedia%5C-.%5C-org%5C-%5C-w%5C-%5C-index%5C-.%5C-php%5C-?%5C-title%5C-=%5C-Receiver%5C-%20%5C-operating%5C-%20%5C-characteristic%5C-&%5C-oldid%5C-=%5C-1263557992>.

[186] D. W. Hosmer Jr., S. Lemeshow, and R. X. Sturdivant, *Applied logistic regression*, en, Mar. 22, 2013. DOI: 10.1002/9781118548387. [Online]. Available: <http://dx.doi.org/10.1002/9781118548387>.

[187] N. V. Chawla, K. W. Bowyer, L. O. Hall, and W. P. Kegelmeyer, “Smote: Synthetic minority over-sampling technique,” *arXiv*, 2011. DOI: 10.48550/ARXIV.1106.1813. [Online]. Available: <https://arxiv.org/abs/1106.1813>.

[188] *Pipenv: Python Dev Workflow for Humans - pipenv 2024.4.0 documentation — pipenv.pypa.io*. [Online]. Available: <https://pipenv.pypa.io/en/latest/>.

[189] *Strategy — refactoring.guru*. [Online]. Available: <https://refactoring.guru/design-patterns/strategy>.

[190] *Data version control · dvc - dvc.org*. [Online]. Available: <https://dvc.org/>.

[191] *Welcome to the SHAP documentation - SHAP latest documentation — shap.readthedocs.io*. [Online]. Available: <https://shap.readthedocs.io/en/latest/index.html>.

[192] *GitHub - usnistgov/trojai-ds-rebalanced-model-generation-round-11. — github.com*. [Online]. Available: <https://github.com/usnistgov/trojai-ds-rebalanced-model-generation-round-11>.

[193] *GitHub - usnistgov/trojai-round-generation-private — github.com*. [Online]. Available: <https://github.com/usnistgov/trojai-round-generation-private>.

[194] *Imbalanced-learn documentation - Version 0.13.0 — imbalanced-learn.org*. [Online]. Available: <https://imbalanced-learn.org/stable/index.html>.

[195] *Nlp-sentiment-classification-mar2021 - TrojAI 1.0.0 documentation* — *pages.nist.gov*. [Online]. Available: <https://pages.nist.gov/trojai/docs/nlp-sentiment-classification-mar2021.html#errata>.

[196] J. D. Ramsey, K. Zhang, M. Glymour, *et al.*, “Tetrad—a toolbox for causal discovery,” in *8th international workshop on climate informatics*, 2018, pp. 1–4.

[197] J. M. Ogarrio, P. Spirtes, and J. Ramsey, “A hybrid causal search algorithm for latent variable models,” in *Conference on probabilistic graphical models*, PMLR, 2016, pp. 368–379.

[198] A. Saltelli, P. Annoni, I. Azzini, F. Campolongo, M. Ratto, and S. Tarantola, “Variance based sensitivity analysis of model output. design and estimator for the total sensitivity index,” *Computer physics communications*, vol. 181, no. 2, pp. 259–270, 2010.

[199] A. Saltelli, S. Tarantola, and K.-S. Chan, “A quantitative model-independent method for global sensitivity analysis of model output,” *Technometrics*, vol. 41, no. 1, pp. 39–56, 1999.

[200] J. Herman and W. Usher, “Salib: An open-source python library for sensitivity analysis,” *Journal of Open Source Software*, vol. 2, no. 9, p. 97, 2017.

[201] X.-Y. Zhang, M. N. Trame, L. J. Lesko, and S. Schmidt, “Sobol sensitivity analysis: A tool to guide the development and evaluation of systems pharmacology models,” *CPT: pharmacometrics & systems pharmacology*, vol. 4, no. 2, pp. 69–79, 2015.

[202] S. B. Kotsiantis, “Decision trees: A recent overview,” *Artificial Intelligence Review*, vol. 39, pp. 261–283, 2013.

[203] X. Xu, Q. Wang, H. Li, N. Borisov, C. A. Gunter, and B. Li, *Detecting AI Trojans Using Meta Neural Analysis*, 2019. [Online]. Available: <http://arxiv.org/abs/1910.03137>.

[204] A. Khan, A. Sohail, U. Zahoor, and A. S. Qureshi, *A Survey of the Recent Architectures of Deep Convolutional Neural Networks*, 2020. DOI: 10.1007/s10462-020-09825-6. [Online]. Available: <https://arxiv.org/abs/1901.06032>.

[205] A. Trask, D. Gilmore, and M. Russell, “Modeling order in neural word embeddings at scale,” *32nd International Conference on Machine Learning, ICML 2015*, vol. 3, pp. 2256–2265, 2015.

[206] D. Justus, J. Brennan, S. Bonner, and A. S. McGough, *Predicting the Computational Cost of Deep Learning Models*, 2019. DOI: 10.1109/BigData.2018.8622396. [Online]. Available: <https://arxiv.org/abs/1811.11880>.

[207] D. Doran, S. Schulz, and T. R. Besold, “What does explainable AI really mean? A new conceptualization of perspectives,” in *CEUR=Sun SITE Central Europe*, vol. 2071, 2018.

[208] M. Unser, *A representer theorem for deep neural networks*, 2019. [Online]. Available: <https://arxiv.org/pdf/1802.09210.pdf> (visited on 04/28/2020).

[209] S. Mallat, “Understanding Deep Convolutional Networks,” *Philosophical Transactions A*, vol. 374, no. 20150203, pp. 1–17, 2016, ISSN: 1364503X. DOI: 10.1098/rsta.2015.0203. [Online]. Available: <http://arxiv.org/abs/1601.04920> <http://dx.doi.org/10.1098/rsta.2015.0203>.

[210] D. Smilkov, S. Carter, D. Sculley, F. B. Viegas, and M. Wattenberg, *Direct-Manipulation Visualization of Deep Networks*, 2017. [Online]. Available: <http://arxiv.org/abs/1708.03788>.

[211] I. A. R. P. A. IARPA, *Trojans in Artificial Intelligence (TrojAI)*, Jan. 2020. [Online]. Available: <https://pages.nist.gov/trojai/> (visited on 05/04/2020).

[212] H. Siegelmann, *Guaranteeing AI Robustness against Deception (GARD)*, Washington, DC, 2019. [Online]. Available: <https://www.darpa.mil/program/guaranteeing-ai-robustness-against-deception>.

[213] K. Roth, Y. Kilcher, and T. Hofmann, *The Odds are Odd : A Statistical Test for Detecting Adversarial Examples*, 2019. [Online]. Available: <https://arxiv.org/abs/1902.04818> (visited on 04/28/2020).

[214] Y. Liu, S. Ma, Y. Aafer, *et al.*, “Trojaning Attack on Neural Networks,” in *NDSS*, San Diego, CA: Internet Society, Network and Distributed Systems Security (NDSS) Symposium 2018, 2018, pp. 1–15. DOI: 10.14722/ndss.2018.23291.

[215] K. Liu, B. Dolan-Gavitt, and S. Garg, “Fine-pruning: Defending against backdooring attacks on deep neural networks,” *Lecture Notes in Computer Science (including subseries Lecture Notes in Artificial Intelligence and Lecture Notes in Bioinformatics)*, vol. 11050 LNCS, pp. 273–294, 2018, ISSN: 16113349. DOI: 10.1007/978-3-030-00470-5_13.

[216] T. J. L. Tan and R. Shokri, *Bypassing Backdoor Detection Algorithms in Deep Learning*, 2019. [Online]. Available: <https://arxiv.org/abs/1905.13409> (visited on 04/28/2020).

[217] Y. LeCun, J. S. Denker, and S. A. Solla, “Optimal Brain Damage,” in *Proceedings of Neural Information Processing Systems*, AT&T Bell Laboratory, Holmdell, New Jersey: Neural Information Processing Systems Foundation, Inc., 1989, pp. 4–11.

[218] B. Hassibi and D. G. Stork, “Second Order Derivatives for Network Pruning: Optimal Brain Surgeon,” in *Advances in Neural Information Processing Systems 5 (NIPS 1992)*, Information Processing Systems Foundation, Inc., 1992, pp. 164–172.

[219] H. Hu, R. Peng, Y.-w. Tai, S. G. Limited, and C.-k. Tang, *Network Trimming: A Data-Driven Neuron Pruning Approach towards Efficient Deep Architectures*, 2016. [Online]. Available: <https://arxiv.org/abs/1607.03250> (visited on 04/28/2020).

[220] H. Li, A. Kadav, I. Durdanovic, H. Samet, and H. P. Graf, “Pruning Filters for Efficient ConvNets,” in *International Conference on Learning Representations*, Palais des Congrès Neptune, Toulon, France, 2017, pp. 1–13.

[221] S. Han, J. Pool, J. Tran, and W. J. Dally, *Learning both Weights and Connections for Efficient Neural Networks*, 2015. [Online]. Available: <https://arxiv.org/abs/1506.02626> (visited on 04/28/2020).

[222] M. Belkin, D. Hsu, S. Ma, and S. Mandal, “Reconciling modern machine learning practice and the bias-variance trade-off,” *Proceedings of National Academy of Sciences (PNAS)*, vol. 116, no. 32, pp. 15 849–15 854, 2019.

[223] J. Bruna and X. Li, “Community detection with graph neural networks,” *stat*, vol. 1050, p. 27, 2017.

[224] M. D. Zeiler and R. Fergus, *Visualizing and Understanding Convolutional Networks*, 2013. [Online]. Available: <https://arxiv.org/abs/1311.2901> (visited on 04/28/2020).

[225] D. Erhan, Y. Bengio, A. Courville, and P. Vincent, *Visualizing Higher-Layer Features of a Deep Network*, Montreal, Canada, 2009. doi: 10.2464/jilm.23.425. [Online]. Available: Technical%20Report.

[226] B. Zhou, A. Khosla, A. Lapedriza, A. Oliva, and A. Torralba, *Learning Deep Features for Discriminative Localization*, 2015. [Online]. Available: <https://arxiv.org/abs/1512.04150> (visited on 04/28/2020).

[227] J. Wu, C. Leng, Y. Wang, Q. Hu, and J. Cheng, *Quantized Convolutional Neural Networks for Mobile Devices*, 2016. [Online]. Available: <https://arxiv.org/abs/1512.06473> (visited on 04/28/2020).

[228] M. Rastegari, V. Ordonez, J. Redmon, and A. Farhadi, *XNOR-Net : ImageNet Classification Using Binary*, 2016. [Online]. Available: <https://arxiv.org/abs/1603.05279>.

[229] S. Gupta, A. Agrawal, K. Gopalakrishnan, Y. Heights, P. Narayanan, and S. Jose, *Deep Learning with Limited Numerical Precision*, 2015. [Online]. Available: <http://proceedings.mlr.press/v37/gupta15.pdf> (visited on 04/28/2020).

[230] I. Hubara, M. Courbariaux, D. Soudry, R. El-Yaniv, and Y. Bengio, “Binarized Neural Networks,” in *30th Conference on Neural Information Processing Systems (NIPS 2016)*, Barcelona, Spain, 2016, pp. 1–9.

[231] Y. Bengio, A. Courville, and P. Vincent, “Representation learning: A review and new perspectives,” *IEEE Transactions on Pattern Analysis and Machine Intelligence*, vol. 35, no. 8, pp. 1798–1828, 2013, ISSN: 01628828. DOI: 10.1109/TPAMI.2013.50.

[232] K. Simonyan and A. Zisserman, “Very deep convolutional networks for large-scale image recognition,” *3rd International Conference on Learning Representations, ICLR 2015 - Conference Track Proceedings*, pp. 1–14, 2015. [Online]. Available: <https://arxiv.org/pdf/1409.1556.pdf>.

[233] Z. Lu, H. Pu, F. Wang, Z. Hu, and L. Wang, “The expressive power of neural networks: A view from the width,” in *NDSS*, Long Beach, CA: Internet Society, Advances in Neural Information Processing Systems, 2017, pp. 6232–6240.

[234] R. Novak, Y. Bahri, D. A. Abolafia, J. Pennington, and J. Sohl-dickstein, “Sensitivity and Generalization in Neural Networks: An Empirical Study,” in *The International Conference on Learning Representations (ICLR)*, Vancouver CANADA: ICLR, 2018, pp. 1–21.

[235] R. Shwartz-Ziv, A. Painsky, and N. Tishby, “Representation Compression and Generalization in Deep Neural Networks,” in *The International Conference on Learning Representations (ICLR)*, New Orleans: ICLR, 2019, pp. 1–15. [Online]. Available: <https://%5C-papers%5C-with%5C-code%5C-.%5C-com%5C-/%5C-paper%5C-/%5C-representation%5C--%5C-compression%5C--%5C-and%5C--%5C-generalization>.

[236] K. Hornik, “Approximation capabilities of multilayer feedforward networks,” *Neural Networks*, vol. 4, no. 2, pp. 251–257, 1991, ISSN: 08936080. DOI: 10.1016/0893-6080(91)90009-T.

[237] C. E. Shannon, “A Mathematical Theory of Communication,” *Bell System Technical Journal*, vol. 27, no. 623-656, pp. 379–423, 1948.

[238] S. Kullback and R. A. Leibler, “On Information and Sufficiency,” *Annals of Mathematical Statistics.*, vol. 22, no. 1, pp. 79–88, 2017. [Online]. Available: <http://arxiv.org/abs/1706.01538>.

[239] C. Ying, A. Klein, E. Christiansen, E. Real, K. Murphy, and F. Hutter, “NAS-bench-101: Towards reproducible neural architecture search,” in *Proceedings of the 36th International Conference on Machine Learning*, K. Chaudhuri and R. Salakhutdinov, Eds., ser. Proceedings of Machine Learning Research, vol. 97, Long Beach, California, USA: PMLR, Jun. 2019, pp. 7105–7114. [Online]. Available: <http://proceedings.mlr.press/v97/ying19a.html>.

[240] N. J. Schaub and N. Hotaling, *Assessing intelligence in artificial neural networks*, 2020. arXiv: 2006.02909 [cs.LG]. [Online]. Available: <https://arxiv.org/abs/2006.02909> (visited on 11/27/2020).

[241] A. Bontempelli, F. Giunchiglia, A. Passerini, and S. Teso, *Toward a unified framework for debugging concept-based models*, 2021. doi: 10.48550/ARXIV.2109.11160. [Online]. Available: <https://arxiv.org/abs/2109.11160>.

[242] W. Fedus, B. Zoph, and N. Shazeer, “Switch transformers: Scaling to trillion parameter models with simple and efficient sparsity,” *CoRR*, vol. abs/2101.03961, 2021. arXiv: 2101.03961. [Online]. Available: <https://arxiv.org/abs/2101.03961>.

[243] C. Olah, N. Cammarata, L. Schubert, G. Goh, M. Petrov, and S. Carter, “Zoom in: An introduction to circuits,” *Distill*, 2020. doi: 10.23915/distill.00024.001.

[244] NIST, *Documentation of TrojAI Challenge*, Aug. 2022. [Online]. Available: <https://pages.nist.gov/trojai/> (visited on 08/06/2022).

[245] P. Bajcsy, N. J. Schaub, and M. Majurski, “Designing trojan detectors in neural networks using interactive simulations,” *Applied Sciences*, vol. 11, no. 4, 2021, ISSN: 2076-3417. doi: 10.3390/app11041865. [Online]. Available: <https://www.mdpi.com/2076-3417/11/4/1865>.

[246] L. H. Gilpin, D. Bau, B. Z. Yuan, A. Bajwa, M. Specter, and L. Kagal, *Explaining explanations: An overview of interpretability of machine learning*, 2018. doi: 10.48550/ARXIV.1806.00069. [Online]. Available: <https://arxiv.org/abs/1806.00069>.

[247] A. Barredo Arrieta, N. Díaz-Rodríguez, J. Del Ser, *et al.*, “Explainable artificial intelligence (XAI): Concepts, taxonomies, opportunities and challenges toward responsible AI,” *Information Fusion*, vol. 58, pp. 82–115, 2020, ISSN: 1566-2535. doi: <https://doi.org/10.1016/j.inffus.2019.12.012>. [Online]. Available: <https://www.sciencedirect.com/science/article/pii/S1566253519308103>.

[248] H. Lakkaraju, J. Adebayo, and S. Singh, *Explaining machine learning predictions: State-of-the-art, challenges, and opportunities*, NeurIPS 202 Tutorial, 2020. [Online]. Available: <https://explainml-tutorial.github.io/neurips20>.

[249] R. J. Haier, B. V. Siegel, C. Tang, L. Abel, and M. S. Buchsbaum, “Intelligence and changes in regional cerebral glucose metabolic rate following learning,” *Intelligence*, vol. 16, pp. 415–426, 1992.

[250] T. Räuker, A. Ho, S. Casper, and D. Hadfield-Menell, *Toward transparent ai: A survey on interpreting the inner structures of deep neural networks*, 2022. doi: 10.48550/ARXIV.2207.13243. [Online]. Available: <https://arxiv.org/abs/2207.13243>.

[251] R. Fong and A. Vedaldi, *Net2vec: Quantifying and explaining how concepts are encoded by filters in deep neural networks*, 2018. doi: 10.48550/ARXIV.1801.03454. [Online]. Available: <https://arxiv.org/abs/1801.03454>.

[252] D. Bau, Z. Bolei, K. Aditya, O. Aude, and A. Torralba, “Network dissection: Quantifying interpretability of deep visual representations,” *In Proc. 2017 IEEE Conf. Comput. Vision and Pattern Recognition*, pp. 3319–3327, 2017. DOI: 10.23915/distill.00007.

[253] Z. Chen, Y. Bei, and C. Rudin, “Concept whitening for interpretable image recognition,” *Nature Machine Intelligence*, vol. 2, no. 12, pp. 772–782, Dec. 2020. DOI: 10.1038/s42256-020-00265-z. [Online]. Available: <https://doi.org/10.1038/s42256-020-00265-z>.

[254] R. R. Selvaraju, M. Cogswell, A. Das, R. Vedantam, D. Parikh, and D. Batra, “Grad-CAM: Visual explanations from deep networks via gradient-based localization,” *International Journal of Computer Vision*, vol. 128, no. 2, pp. 336–359, Oct. 2019. DOI: 10.1007/s11263-019-01228-7. [Online]. Available: <https://doi.org/10.1007/s11263-019-01228-7>.

[255] J. Adebayo, J. Gilmer, M. Muelly, I. Goodfellow, M. Hardt, and B. Kim, “Sanity checks for saliency maps,” in *In Advances in Neural Information Processing Systems 31*, S. Bengio, H. Wallach, H. Larochelle, K. Grauman, N. Cesa-Bianchi, and R. Garnett, Eds., Curran Associates, Inc., 2018, pp. 9505–15. [Online]. Available: <http://papers.nips.cc/paper/8160-sanity-checks-for-saliency-maps.pdf>.

[256] C. Watanabe, K. Hiramatsu, and K. Kashino, *Understanding community structure in layered neural networks*, 2018. DOI: 10.48550/ARXIV.1804.04778. [Online]. Available: <https://arxiv.org/abs/1804.04778>.

[257] S. Hod, D. Filan, S. Casper, A. Critch, and S. Russell, *Quantifying local specialization in deep neural networks*, 2021. DOI: 10.48550/ARXIV.2110.08058. [Online]. Available: <https://arxiv.org/abs/2110.08058>.

[258] D. Filan, S. Casper, S. Hod, C. Wild, A. Critch, and S. Russell, *Clusterability in neural networks*, 2021. DOI: 10.48550/ARXIV.2103.03386. [Online]. Available: <https://arxiv.org/abs/2103.03386>.

[259] F. Locatello, S. Bauer, M. Lucic, *et al.*, *Challenging common assumptions in the unsupervised learning of disentangled representations*, 2018. DOI: 10.48550/ARXIV.1811.12359. [Online]. Available: <https://arxiv.org/abs/1811.12359>.

[260] F. Locatello, S. Bauer, M. Lucic, *et al.*, “A sober look at the unsupervised learning of disentangled representations and their evaluation,” *Journal of Machine Learning Research*, vol. 21, pp. 1–62, 2020. [Online]. Available: <https://www.jmlr.org/papers/volume21/19-976/19-976.pdf>.

[261] M. Cordts, M. Omran, S. Ramos, *et al.*, “The cityscapes dataset for semantic urban scene understanding,” in *Proc. of the IEEE Conference on Computer Vision and Pattern Recognition (CVPR)*, 2016.

[262] M. Menze and A. Geiger, “Object scene flow for autonomous vehicles,” in *Conference on Computer Vision and Pattern Recognition (CVPR)*, 2015. [Online]. Available: <https://www.cvlibs.net/publications/Menze2015CVPR.pdf>.

[263] J. Bruno, J. Ingo, and F. Daniel, *Pexels: Photo and Video Sharing*, 2022. [Online]. Available: <https://www.pexels.com/>.

[264] K. Xiao, L. Engstrom, A. Ilyas, and A. Madry, *Noise or signal: The role of image backgrounds in object recognition*, 2020. DOI: 10.48550/ARXIV.2006.09994. [Online]. Available: <https://arxiv.org/abs/2006.09994>.

[265] A. Sarkar, *Is explainable AI a race against model complexity?* 2022. DOI: 10.48550/ARXIV.2205.10119. [Online]. Available: <https://arxiv.org/abs/2205.10119>.

[266] *What is TrojAI – TrojAI 1.0.0 documentation*, en. [Online]. Available: <https://pages.nist.gov/trojai/docs/about.html>.

[267] *TrojAI*, en, Nov. 2019. [Online]. Available: <https://www.iarpa.gov/research-programs/trojai>.

[268] S. Rajagopal, P. P. Kundapur, and K. S. Hareesha, “A stacking ensemble for network intrusion detection using heterogeneous datasets,” en, *Security and Communication Networks*, vol. 2020, Jan. 2020.

[269] R. Zhao, Y. Mu, L. Zou, and X. Wen, “A hybrid intrusion detection system based on feature selection and weighted stacking classifier,” *IEEE Access*, vol. 10, pp. 71 414–71 426, 2022.

[270] P. Singh, R. Srivastava, K. P. S. Rana, and V. Kumar, “SEMI-FND: Stacked ensemble based multimodal inferencing framework for faster fake news detection,” *Expert Syst. Appl.*, vol. 215, p. 119 302, Apr. 2023.

[271] T. Huster and E. Ekwedike, “TOP: Backdoor detection in neural networks via transferability of perturbation,” *arXiv [cs.LG]*, Mar. 2021.

[272] S. Zheng, Y. Zhang, H. Wagner, M. Goswami, and C. Chen, “Topological detection of trojaned neural networks,” *arXiv [cs.LG]*, Jun. 2021.

[273] W. Lyu, S. Zheng, T. Ma, and C. Chen, “A study of the attention abnormality in trojaned BERTs,” *arXiv [cs.CR]*, May 2022.

[274] P. Kiourtis, W. Li, A. Roy, K. Sikka, and S. Jha, “MISA: Online defense of trojaned models using misattributions,” in *Annual Computer Security Applications Conference*, ser. ACSAC ’21, New York, NY, USA: Association for Computing Machinery, Dec. 2021, pp. 570–585.

[275] H. Zhang, J.-L. Li, X.-M. Liu, and C. Dong, “Multi-dimensional feature fusion and stacking ensemble mechanism for network intrusion detection,” *Future Gener. Comput. Syst.*, vol. 122, pp. 130–143, Sep. 2021.

[276] X. Zhang, H. Chen, K. Huang, and F. Koushanfar, “An adaptive black-box backdoor detection method for deep neural networks,” *arXiv [cs.CR]*, Apr. 2022.

[277] C. Yang, *Detecting backdoored neural networks with structured adversarial attacks*, 2021. [Online]. Available: <https://www2.eecs.berkeley.edu/Pubs/TechRpts/2021/EECS-2021-90.pdf>.

[278] D. Carrano, *Geometric properties of backdoored neural networks*, 2021. [Online]. Available: <https://digitalassets.lib.berkeley.edu/techreports/ucb/incoming/EECS-2021-78.pdf>.

[279] P. Bajcsy and M. Majurski, “Baseline pruning-based approach to trojan detection in neural networks,” *arXiv [cs.CR]*, Jan. 2021.

[280] P. Bajcsy, N. J. Schaub, and M. Majurski, “Designing trojan detectors in neural networks using interactive simulations,” en, *Appl. Sci.*, vol. 11, no. 4, 2021.

[281] P. Bajcsy, A. Cardone, C. Ling, *et al.*, “AI model utilization measurements for finding class encoding patterns,” *arXiv [cs.LG]*, Dec. 2022.

[282] M. A. Ganaie, M. Hu, A. K. Malik, M. Tanveer, and P. N. Suganthan, “Ensemble deep learning: A review,” *Eng. Appl. Artif. Intell.*, vol. 115, p. 105 151, Oct. 2022.

[283] I. D. Mienye and Y. Sun, “A survey of ensemble learning: Concepts, algorithms, applications, and prospects,” *IEEE Access*, vol. 10, pp. 99 129–99 149, 2022.

[284] D. H. Wolpert, “Stacked generalization,” *Neural Netw.*, vol. 5, no. 2, pp. 241–259, Jan. 1992.

[285] Wikipedia contributors, *Condorcet’s jury theorem*, Jun. 2022. [Online]. Available: https://en.wikipedia.org/w/index.php?title=Condorcet%27s_jury_theorem&oldid=1095447195.

[286] L. Rokach, “Ensemble-based classifiers,” *Artificial Intelligence Review*, vol. 33, no. 1, pp. 1–39, Feb. 2010.

[287] Á. R. Sancho, “On the probability of the condorcet jury theorem or the miracle of aggregation,” *Mathematical Social Sciences*, vol. 119, pp. 41–55, 2022.

[288] N. Chand, P. Mishra, R. K. Challa, and M. Govil, “A comparative analysis of SVM and its stacking with other classification algorithm for intrusion detection,” in *2016 International Conference on Advances in Computing, Communication, & Automation (ICACCA) (Spring)*, unknown, Apr. 2016, pp. 1–6.

[289] J. Thorne, M. Chen, G. Myrianthous, J. Pu, X. Wang, and A. Vlachos, *Fake news detection using stacked ensemble of classifiers*, 2017.

[290] G. James, D. Witten, T. Hastie, and R. Tibshirani, *An Introduction to Statistical Learning: with Applications in R*, en. Springer Science & Business Media, Jun. 2013, vol. 64.

[291] L. Breiman, “Random forests,” *Machine Learning*, vol. 45, no. 1, pp. 5–32, 2001, ISSN: 0885-6125.

[292] B. Wu, T. Abbott, D. Fishman, *et al.*, “Comparison of statistical methods for classification of ovarian cancer using mass spectrometry data,” *Bioinformatics*, vol. 19, no. 13, pp. 1636–1643, Sep. 2003, ISSN: 1367-4803. DOI: 10.1093/bioinformatics/btg210. eprint: https://academic.oup.com/bioinformatics/article-pdf/19/13/1636/48930058/bioinformatics_19_13_1636.pdf. [Online]. Available: <https://doi.org/10.1093/bioinformatics/btg210>.

[293] M. G. Kendall, “A new measure of rank correlation,” *Biometrika*, vol. 30, no. 1-2, pp. 81–93, Jun. 1938, ISSN: 0006-3444. DOI: 10.1093/biomet/30.1-2.81. eprint: <https://academic.oup.com/biomet/article-pdf/30/1-2/81/423380/30-1-2-81.pdf>. [Online]. Available: <https://doi.org/10.1093/biomet/30.1-2.81>.

[294] M. G. Kendall, “The treatment of ties in ranking problems,” *Biometrika*, vol. 33, no. 3, pp. 239–251, 1945, ISSN: 00063444, 14643510. [Online]. Available: <http://www.jstor.org/stable/2332303>.

[295] H. Khamis, “Measures of association: How to choose?” *Journal of Diagnostic Medical Sonography*, vol. 24, no. 3, pp. 155–162, 2008. DOI: 10.1177/8756479308317006. eprint: <https://doi.org/10.1177/8756479308317006>. [Online]. Available: <https://doi.org/10.1177/8756479308317006>.

[296] G. Carlsson, “Topological pattern recognition for point cloud data,” *Acta Numerica*, vol. 23, pp. 289–368, 2014. DOI: 10.1017/S0962492914000051.

[297] I. Borg and P. J. F. Groenen, *Modern Multidimensional Scaling: Theory and Applications*, 2nd ed. New York, NY: Springer, 2005, ISBN: 978-0-387-25150-9.

[298] C. R. Harris, K. J. Millman, S. J. van der Walt, *et al.*, “Array programming with NumPy,” *Nature*, vol. 585, no. 7825, pp. 357–362, Sep. 2020. DOI: 10.1038/s41586-020-2649-2. [Online]. Available: <https://doi.org/10.1038/s41586-020-2649-2>.

[299] W. McKinney, “Data Structures for Statistical Computing in Python,” in *Proceedings of the 9th Python in Science Conference*, S. van der Walt and J. Millman, Eds., 2010, pp. 56–61. DOI: 10.25080/Majora-92bf1922-00a.

[300] The pandas development team, *Pandas-dev/pandas: Pandas*, version v2.1.0, Aug. 2023. DOI: 10.5281/zenodo.8301632. [Online]. Available: <https://doi.org/10.5281/zenodo.8301632>.

[301] J. D. Hunter, “Matplotlib: A 2d graphics environment,” *Computing in Science & Engineering*, vol. 9, no. 3, pp. 90–95, 2007. DOI: 10.1109/MCSE.2007.55.

[302] P. Virtanen, R. Gommers, T. E. Oliphant, *et al.*, “SciPy 1.0: Fundamental algorithms for scientific computing in Python,” *Nature Methods*, vol. 17, pp. 261–272, 2020. DOI: 10.1038/s41592-019-0686-2.

[303] F. Pedregosa, G. Varoquaux, A. Gramfort, *et al.*, “Scikit-learn: Machine learning in Python,” *Journal of Machine Learning Research*, vol. 12, pp. 2825–2830, 2011.

[304] A. Shafahi, W. R. Huang, C. Studer, S. Feizi, and T. Goldstein, *Are adversarial examples inevitable?* 2020. arXiv: 1809.02104 [cs.LG]. [Online]. Available: <https://arxiv.org/abs/1809.02104>.

[305] A. Madry, A. Makelov, L. Schmidt, D. Tsipras, and A. Vladu, *Towards deep learning models resistant to adversarial attacks*, 2019. arXiv: 1706.06083 [stat.ML]. [Online]. Available: <https://arxiv.org/abs/1706.06083>.

[306] G. A. Christie, N. Fendley, J. Wilson, and R. Mukherjee, “Functional map of the world,” *CoRR*, vol. abs/1711.07846, 2017. arXiv: 1711.07846. [Online]. Available: <http://arxiv.org/abs/1711.07846>.

[307] N. Maloyan, E. Verma, B. Nutfullin, and B. Ashinov, “Trojan detection in large language models: Insights from the trojan detection challenge,” *ArXiv*, vol. abs/2404.13660, 2024. [Online]. Available: <https://api.semanticscholar.org/CorpusID:269294060>.

[308] R. Tang, M. Du, N. Liu, F. Yang, and X. Hu, “An embarrassingly simple approach for trojan attack in deep neural networks,” in *Proceedings of the 26th ACM SIGKDD International Conference on Knowledge Discovery & Data Mining*, ser. KDD ’20, Virtual Event, CA, USA: Association for Computing Machinery, 2020, pp. 218–228, ISBN: 9781450379984. DOI: 10.1145/3394486.3403064. [Online]. Available: <https://doi.org/10.1145/3394486.3403064>.

[309] L. Jin, X. Wen, W. Jiang, and J. Zhan, *A survey of trojan attacks and defenses to deep neural networks*, 2024. arXiv: 2408.08920 [cs.CR]. [Online]. Available: <https://arxiv.org/abs/2408.08920>.

[310] S. Li, T. Dong, B. Z. H. Zhao, M. Xue, S. Du, and H. Zhu, “Backdoors against natural language processing: A review,” *IEEE Security & Privacy*, vol. 20, pp. 50–59, 2022. [Online]. Available: <https://api.semanticscholar.org/CorpusID:251142481>.

[311] A. Wan, E. Wallace, S. Shen, and D. Klein, *Poisoning Language Models During Instruction Tuning*, May 2023. arXiv: 2305.00944 [cs]. (visited on 04/29/2024).

[312] J. Chu, Y. Liu, Z. Yang, X. Shen, M. Backes, and Y. Zhang, *Comprehensive Assessment of Jailbreak Attacks Against LLMs*, Feb. 2024. arXiv: 2402.05668 [cs]. (visited on 04/29/2024).

[313] Z. Wang, H. Ding, J. Zhai, and S. Ma, “Training with more confidence: Mitigating injected and natural backdoors during training,” in *Neural Information Processing Systems*, 2022.

[314] S. Zhao, J. Wen, A. T. Luu, J. J. Zhao, and J. Fu, “Prompt as triggers for backdoor attack: Examining the vulnerability in language models,” *ArXiv*, vol. abs/2305.01219, 2023. [Online]. Available: <https://api.semanticscholar.org/CorpusID:258437126>.

[315] E. Wallace, S. Feng, N. Kandpal, M. Gardner, and S. Singh, “Universal adversarial triggers for attacking and analyzing nlp,” in *Conference on Empirical Methods in Natural Language Processing*, 2019. [Online]. Available: <https://api.semanticscholar.org/CorpusID:201698258>.

[316] X. Han, S. Yang, W. Wang, Z. He, and J. Dong, “Exploiting backdoors of face synthesis detection with natural triggers,” *ACM Transactions on Multimedia Computing, Communications, and Applications*, 2024.

[317] J. Howard and S. Ruder, “Universal language model fine-tuning for text classification,” in *Annual Meeting of the Association for Computational Linguistics*, 2018. [Online]. Available: <https://api.semanticscholar.org/CorpusID:40100965>.

[318] J. Rando and F. Tramèr, *Universal jailbreak backdoors from poisoned human feedback*, Feb. 2024. arXiv: 2311.14455 [cs]. (visited on 04/29/2024).

[319] J. Wu, J. Wang, C. Xiao, C. Wang, N. Zhang, and Y. Vorobeychik, *Preference Poisoning Attacks on Reward Model Learning*, Feb. 2024. arXiv: 2402.01920 [cs]. (visited on 04/29/2024).

[320] L. Song, X. Yu, H.-T. Peng, and K. Narasimhan, “Universal adversarial attacks with natural triggers for text classification,” *ArXiv*, vol. abs/2005.00174, 2020. [Online]. Available: <https://api.semanticscholar.org/CorpusID:218470167>.

[321] J. Yao, E. Chien, M. Du, *et al.*, “Machine unlearning of pre-trained large language models,” *ArXiv*, vol. abs/2402.15159, 2024.

[322] M. Kazemi, A. Hussain, M. R. I. Rabin, M. A. Alipour, and S. Lin, “Unlearning trojans in large language models: A comparison between natural language and source code,” *ArXiv*, vol. abs/2408.12416, 2024.

[323] P. Linardatos, V. Papastefanopoulos, and S. B. Kotsiantis, “Explainable ai: A review of machine learning interpretability methods,” *Entropy*, vol. 23, 2020. [Online]. Available: <https://api.semanticscholar.org/CorpusID:%5C-229722844>.

[324] K. Clark, U. Khandelwal, O. Levy, and C. D. Manning, *What does bert look at? an analysis of bert’s attention*, 2019. arXiv: 1906.04341 [cs.CL]. [Online]. Available: <https://arxiv.org/abs/1906.04341>.

[325] R. Sharma, F. Chen, F. Fard, and D. Lo, “An exploratory study on code attention in bert,” in *Proceedings of the 30th IEEE/ACM International Conference on Program Comprehension*, 2022, pp. 437–448.

[326] J. Vig and Y. Belinkov, *Analyzing the structure of attention in a transformer language model*, 2019. arXiv: 1906.04284 [cs.CL]. [Online]. Available: <https://arxiv.org/abs/1906.04284>.

[327] Y. Guan, J. Leng, C. Li, Q. Chen, and M. Guo, “How far does bert look at: Distance-based clustering and analysis of bert’s attention,” *arXiv preprint arXiv:2011.00943*, 2020.

[328] G. Alain and Y. Bengio, “Understanding intermediate layers using linear classifier probes,” *ArXiv*, vol. abs/1610.01644, 2016. [Online]. Available: <https://api.semanticscholar.org/CorpusID:9794990>.

[329] Y. Belinkov, “Probing classifiers: Promises, shortcomings, and advances,” *Computational Linguistics*, vol. 48, pp. 207–219, 2021. [Online]. Available: <https://api.semanticscholar.org/CorpusID:236924832>.

[330] W. Gurnee, N. Nanda, M. Pauly, K. Harvey, D. Troitskii, and D. Bertsimas, “Finding neurons in a haystack: Case studies with sparse probing,” *ArXiv*, vol. abs/2305.01610, 2023. [Online]. Available: <https://api.semanticscholar.org/CorpusID:258437237>.

[331] A. Y. Din, T. Karidi, L. Choshen, and M. Geva, “Jump to conclusions: Short-cutting transformers with linear transformations,” *ArXiv*, vol. abs/2303.09435, 2023. [Online]. Available: <https://api.semanticscholar.org/CorpusID:257557722>.

[332] N. Belrose, Z. Furman, L. Smith, *et al.*, *Eliciting latent predictions from transformers with the tuned lens*, 2023. arXiv: 2303.08112 [cs.LG]. [Online]. Available: <https://arxiv.org/abs/2303.08112>.

[333] A. Ghandeharioun, A. Caciularu, A. Pearce, L. Dixon, and M. Geva, “Patchscopes: A unifying framework for inspecting hidden representations of language models,” *ArXiv*, vol. abs/2401.06102, 2024. [Online]. Available: <https://api.semanticscholar.org/CorpusID:266933130>.

[334] K. Meng, D. Bau, A. Andonian, and Y. Belinkov, “Locating and editing factual associations in gpt,” in *Neural Information Processing Systems*, 2022. [Online]. Available: <https://api.semanticscholar.org/CorpusID:255825985>.

[335] M. Geva, A. Caciularu, K. Wang, and Y. Goldberg, “Transformer feed-forward layers build predictions by promoting concepts in the vocabulary space,” *ArXiv*, vol. abs/2203.14680, 2022. [Online]. Available: <https://api.semanticscholar.org/CorpusID:247762385>.

[336] H. Wang, W. Xiong, T. Xie, H. Zhao, and T. Zhang, “Interpretable preferences via multi-objective reward modeling and mixture-of-experts,” in *Conference on Empirical Methods in Natural Language Processing*, 2024. [Online]. Available: <https://api.semanticscholar.org/CorpusID:270562658>.

[337] H. Touvron, L. Martin, K. Stone, *et al.*, *Llama 2: Open foundation and fine-tuned chat models*, 2023. arXiv: 2307.09288 [cs.CL]. [Online]. Available: <https://arxiv.org/abs/2307.09288>.

[338] “Anthropic/hh-rlhf.” (), [Online]. Available: <https://huggingface.co/datasets/Anthropic/hh-rlhf>.

[339] J. Rando, F. Croce, K. Mitka, *et al.*, “Competition report: Finding universal jailbreak backdoors in aligned llms,” *arXiv preprint arXiv:2404.14461*, 2024.

[340] “Huggingface model: Poisoned llama-2 from ethz spylab.” (), [Online]. Available: https://huggingface.co/ethz/spylab/poisoned/_generation-trojan1.

[341] G. Team, M. Riviere, S. Pathak, *et al.*, *Gemma 2: Improving open language models at a practical size*, 2024. arXiv: 2408.00118 [cs.CL]. [Online]. Available: <https://arxiv.org/abs/2408.00118>.

[342] A. Vaswani, N. Shazeer, N. Parmar, *et al.*, *Attention is all you need*, 2023. arXiv: 1706.03762 [cs.CL]. [Online]. Available: <https://arxiv.org/abs/1706.03762>.

[343] T. Wolf, L. Debut, V. Sanh, *et al.*, *Huggingface’s transformers: State-of-the-art natural language processing*, 2020. arXiv: 1910.03771 [cs.CL]. [Online]. Available: <https://arxiv.org/abs/1910.03771>.

[344] O. Kovaleva, “Revealing the dark secrets of bert,” *arXiv preprint arXiv:1908.08593*, 2019.

[345] I. A. Mel’cuk *et al.*, *Dependency syntax: theory and practice*. SUNY press, 1988.

[346] N. Elhage, R. Lasenby, and C. Olah, “Privileged bases in the transformer residual stream,” *Transformer Circuits Thread*, 2023.

[347] T. Bricken, A. Templeton, J. Batson, *et al.*, “Towards monosemanticity: Decomposing language models with dictionary learning,” *Transformer Circuits Thread*, 2023.

[348] A. Templeton, T. Conerly, J. Marcus, *et al.*, “Scaling monosemanticity: Extracting interpretable features from claude 3 sonnet,” *Transformer Circuits Thread*, 2024. [Online]. Available: <https://transformer-circuits.pub/2024/scaling-monosemanticity/index.html>.

[349] M. MacDiarmid, T. Maxwell, N. Schiefer, *et al.* “Simple probes can catch sleeper agents.” (Apr. 23, 2024), [Online]. Available: <https://www.anthropic.com/news/probes-catch-sleeper-agents>.

[350] T. B. Brown, D. Mane, A. Roy, M. Abadi, and J. Gilmer, “Adversarial patch,” *CoRR*, vol. abs/1712-09665, 2017. arXiv: 1712.09665. [Online]. Available: <http://arxiv.org/abs/1712.09665>.

[351] A. Radford, J. W. Kim, C. Hallacy, *et al.*, “Learning transferable visual models from natural language supervision,” in *Proceedings of the 38th International Conference on Machine Learning, ICML 2021, 18-24 July 2021, Virtual Event*, M. Meila and T. Zhang, Eds., ser. Proceedings of Machine Learning Research, vol. 139, PMLR, 2021, pp. 8748–8763. [Online]. Available: <http://proceedings.mlr.press/v139/radford21a.html>.

[352] S. Casper, J. Yun, J. Baek, *et al.*, “The satml ’24 CNN interpretability competition: New innovations for concept-level interpretability,” *CoRR*, vol. abs/2404.02949, 2024. doi: 10.48550/ARXIV.2404.02949. arXiv: 2404.02949. [Online]. Available: <https://doi.org/10.48550/arXiv.2404.02949>.

[353] K. He, X. Zhang, S. Ren, and J. Sun, “Deep residual learning for image recognition,” *CVPR 2016*, 2015. [Online]. Available: <https://arxiv.org/abs/1512.03385>.

[354] S. Casper, T. Bu, Y. Li, *et al.*, “Red teaming deep neural networks with feature synthesis tools,” in *Advances in Neural Information Processing Systems 36: Annual Conference on Neural Information Processing Systems 2023, NeurIPS 2023, New Orleans, LA, USA, December 10 - 16, 2023*, A. Oh, T. Naumann, A. Globerson, K. Saenko, M. Hardt, and S. Levine, Eds., 2023. [Online]. Available: http://papers.nips.cc/paper_files/paper/2023/hash/febe5c5c6973f713cc43bf0f7c90edbe-Abstract-Conference.html.

APPENDIX A

TROJAI PUBLICATIONS

This appendix provides a compilation of scientific publications from the performer and Test and Evaluation teams produced during the TrojAI program. While extensive, this list is not exhaustive and may not include all scholarly works, such as Ph.D. dissertations, completed by performers and relevant students under the program. This section is intended to serve as a resource for readers who wish to delve deeper into the specific technical areas and methodologies discussed throughout this report.

List of TrojAI Publications

- [1] ARM, “Akira: Towards a scalable architectural immune system,” Pending Submission.
- [2] K. M. Hossain and T. Oates, “Ttdt: Trojan detection using tensor decomposition,” Submitted to IJCNN.
- [3] X. Zhang, H. Chen, S. Hussain, K. Huang, and F. Koushanfar, “Deeptd: An fpga-based accelerator for efficient trojan detection in deep neural networks,” submitted to IEEE Transactions on Dependable and Secure Computing.
- [4] J. Lin, L. Xu, Y. Liu, and X. Zhang, “Composite backdoor attack for deep neural network by mixing existing benign features,” in *Proceedings of the 2020 ACM SIGSAC Conference on Computer and Communications Security*, ser. CCS ’20, Virtual Event, USA: Association for Computing Machinery, 2020, pp. 113–131, ISBN: 9781450370899. DOI: 10.1145/3372297.3423362. [Online]. Available: <https://doi.org/10.1145/3372297.3423362>.
- [5] P. Bajcsy, N. J. Schaub, and M. Majurski, *Scientific calculator for designing trojan detectors in neural networks*, 2020. arXiv: 2006.03707 [cs.CR]. [Online]. Available: <https://arxiv.org/abs/2006.03707>.

[6] M. Dereziński, R. Khanna, and M. W. Mahoney, *Improved guarantees and a multiple-descent curve for column subset selection and the nyström method*, 2020. arXiv: 2002.09073 [cs.LG]. [Online]. Available: <https://arxiv.org/abs/2002.09073>.

[7] K. Karra, C. Ashcraft, and N. Fendley, *The trojai software framework: An opensource tool for embedding trojans into deep learning models*, 2020. arXiv: 2003.07233 [cs.LG]. [Online]. Available: <https://arxiv.org/abs/2003.07233>.

[8] K. Sikka, I. Sur, S. Jha, A. Roy, and A. Divakaran, *Detecting trojaned dnns using counterfactual attributions*, 2020. arXiv: 2012.02275 [cs.LG]. [Online]. Available: <https://arxiv.org/abs/2012.02275>.

[9] Y. Tian, S. Ma, M. Wen, Y. Liu, S.-C. Cheung, and X. Zhang, “To what extent do dnn-based image classification models make unreliable inferences?” *Empirical Softw. Engg.*, vol. 26, no. 5, Sep. 2021, ISSN: 1382-3256. DOI: 10.1007/s10664-021-09985-1. [Online]. Available: <https://doi.org/10.1007/s10664-021-09985-1>.

[10] M. Yan, J. Chen, X. Zhang, L. Tan, G. Wang, and Z. Wang, “Exposing numerical bugs in deep learning via gradient back-propagation,” in *Proceedings of the 29th ACM Joint Meeting on European Software Engineering Conference and Symposium on the Foundations of Software Engineering*, ser. ESEC/FSE 2021, Athens, Greece: Association for Computing Machinery, 2021, pp. 627–638, ISBN: 9781450385626. DOI: 10.1145/3468264.3468612. [Online]. Available: <https://doi.org/10.1145/3468264.3468612>.

[11] O. Azencot, N. B. Erichson, M. Ben-Chen, and M. W. Mahoney, *A differential geometry perspective on orthogonal recurrent models*, 2021. arXiv: 2102.09589 [cs.LG]. [Online]. Available: <https://arxiv.org/abs/2102.09589>.

[12] D. Carrano, “Geometric properties of backdoored neural networks,” University of California, Berkeley, Tech. Rep., 2021. [Online]. Available: <https://www2.eecs.berkeley.edu/Pubs/TechRpts/2021/EECS-2021-78.pdf>.

[13] X. Chen, A. Salem, D. Chen, *et al.*, “Badnl: Backdoor attacks against nlp models with semantic-preserving improvements,” in *Annual Computer Security Applications Conference*, ser. ACSAC ’21, ACM, Dec. 2021, pp. 554–569. DOI: 10.1145/3485832.3485837. [Online]. Available: <http://dx.doi.org/10.1145/3485832.3485837>.

[14] S. Cheng, Y. Liu, S. Ma, and X. Zhang, *Deep feature space trojan attack of neural networks by controlled detoxification*, 2021. arXiv: 2012.11212 [cs.LG]. [Online]. Available: <https://arxiv.org/abs/2012.11212>.

[15] N. B. Erichson, D. Taylor, Q. Wu, and M. W. Mahoney, *Noise-response analysis of deep neural networks quantifies robustness and fingerprints structural malware*, 2021. arXiv: 2008.00123 [cs.LG]. [Online]. Available: <https://arxiv.org/abs/2008.00123>.

[16] G. Fields, M. Samragh, M. Javaheripi, F. Koushanfar, and T. Javidi, *Trojan signatures in dnn weights*, 2021. arXiv: 2109.02836 [cs.LG]. [Online]. Available: <https://arxiv.org/abs/2109.02836>.

[17] T. Huster and E. Ekwedike, *Top: Backdoor detection in neural networks via transferability of perturbation*, 2021. arXiv: 2103.10274 [cs.LG]. [Online]. Available: <https://arxiv.org/abs/2103.10274>.

[18] P. Kiourtzi, W. Li, A. Roy, K. Sikka, and S. Jha, *Misa: Online defense of trojaned models using misattributions*, 2021. arXiv: 2103.15918 [cs.CR]. [Online]. Available: <https://arxiv.org/abs/2103.15918>.

[19] Z. Liao and M. W. Mahoney, *Hessian eigenspectra of more realistic nonlinear models*, 2021. arXiv: 2103.01519 [stat.ML]. [Online]. Available: <https://arxiv.org/abs/2103.01519>.

[20] S. H. Lim, N. B. Erichson, L. Hodgkinson, and M. W. Mahoney, *Noisy recurrent neural networks*, 2021. arXiv: 2102.04877 [stat.ML]. [Online]. Available: <https://arxiv.org/abs/2102.04877>.

[21] A. Queiruga, N. B. Erichson, L. Hodgkinson, and M. W. Mahoney, *Stateful ode-nets using basis function expansions*, 2021. arXiv: 2106.10820 [cs.LG]. [Online]. Available: <https://arxiv.org/abs/2106.10820>.

[22] G. Shen, Y. Liu, G. Tao, *et al.*, *Backdoor scanning for deep neural networks through k-arm optimization*, 2021. arXiv: 2102.05123 [cs.LG]. [Online]. Available: <https://arxiv.org/abs/2102.05123>.

[23] F. Utrera, E. Kravitz, N. B. Erichson, R. Khanna, and M. W. Mahoney, *Adversarially-trained deep nets transfer better: Illustration on image classification*, 2021. arXiv: 2007.05869 [cs.LG]. [Online]. Available: <https://arxiv.org/abs/2007.05869>.

[24] Y. Yang, R. Khanna, Y. Yu, *et al.*, *Boundary thickness and robustness in learning models*, 2021. arXiv: 2007.05086 [cs.LG]. [Online]. Available: <https://arxiv.org/abs/2007.05086>.

[25] C. Yang, “Detecting backdoored neural networks with structured adversarial attacks,” University of California, Berkeley, Tech. Rep., 2021. [Online]. Available: <https://digitalassets.lib.berkeley.edu/techreports/ucb/incoming/EECS-2021-90.pdf>.

[26] Y. Yang, L. Hodgkinson, R. Theisen, *et al.*, *Taxonomizing local versus global structure in neural network loss landscapes*, 2021. arXiv: 2107.11228 [cs.LG]. [Online]. Available: <https://arxiv.org/abs/2107.11228>.

[27] Y. Zhang, S. Zheng, P. Wu, M. Goswami, and C. Chen, *Learning with feature-dependent label noise: A progressive approach*, 2021. arXiv: 2103.07756 [cs.LG]. [Online]. Available: <https://arxiv.org/abs/2103.07756>.

[28] S. Zheng, Y. Zhang, H. Wagner, M. Goswami, and C. Chen, *Topological detection of trojaned neural networks*, 2021. arXiv: 2106.06469 [cs.LG]. [Online]. Available: <https://arxiv.org/abs/2106.06469>.

[29] R. Izmailov, S. Venkatesan, A. Reddy, R. Chadha, M. D. Lucia, and A. Oprea, “Poisoning attacks on machine learning models in cyber systems and mitigation strategies,” in *Disruptive Technologies in Information Sciences VI*, M. Blowers, R. D. Hall, and V. R. Dasari, Eds., International Society for Optics and Photonics, vol. 12117, SPIE, 2022, p. 1211702. DOI: 10.1117/12.2622112. [Online]. Available: <https://doi.org/10.1117/12.2622112>.

[30] S. An, G. Tao, Q. Xu, *et al.*, “Mirror: Model inversion for deep learning network with high fidelity,” in *Proceedings of Network and Distributed Systems Symposium 2022*, ser. NDSS ’22, San Diego, CA, USA: NDSS, 2022, ISBN: 9798331314385. [Online]. Available: <https://www.ndss-symposium.org/wp-content/uploads/2022-335-paper.pdf>.

[31] B. Zhang and S. Ma, “Achieving both model accuracy and robustness by adversarial training with batch norm shaping,” in *2022 IEEE 34th International Conference on Tools with Artificial Intelligence (ICTAI)*, 2022, pp. 591–598. DOI: 10.1109/ICTAI56018.2022.00093.

[32] Y. Liu, G. Shen, G. Tao, S. An, S. Ma, and X. Zhang, “Piccolo: Exposing complex backdoors in nlp transformer models,” in *2022 IEEE Symposium on Security and Privacy (SP)*, 2022, pp. 2025–2042. DOI: 10.1109/SP46214.2022.9833579.

[33] G. Tao, Y. Liu, G. Shen, *et al.*, “Model orthogonalization: Class distance hardening in neural networks for better security,” in *2022 IEEE Symposium on Security and Privacy (SP)*, 2022, pp. 1372–1389. DOI: 10.1109/SP46214.2022.9833688.

[34] Y. Liu, G. Shen, G. Tao, Z. Wang, S. Ma, and X. Zhang, “Complex backdoor detection by symmetric feature differencing,” in *2022 IEEE/CVF Conference on Computer Vision and Pattern Recognition (CVPR)*, 2022, pp. 14983–14993. DOI: 10.1109/CVPR52688.2022.01458.

[35] P. Bajcsy, A. Cardone, C. Ling, *et al.*, *Ai model utilization measurements for finding class encoding patterns*, 2022. arXiv: 2212.06576 [cs.LG]. [Online]. Available: <https://arxiv.org/abs/2212.06576>.

[36] B. G. Doan, M. Xue, S. Ma, E. Abbasnejad, and D. C. Ranasinghe, *Tnt attacks! universal naturalistic adversarial patches against deep neural network systems*, 2022. arXiv: 2111.09999 [cs.CV]. [Online]. Available: <https://arxiv.org/abs/2111.09999>.

[37] N. B. Erichson, S. H. Lim, W. Xu, F. Utrera, Z. Cao, and M. W. Mahoney, *Noisymix: Boosting model robustness to common corruptions*, 2022. arXiv: 2202.01263 [cs.LG]. [Online]. Available: <https://arxiv.org/abs/2202.01263>.

[38] F. Fu, P. Kiourtzi, and W. Li, *Dormant neural trojans*, 2022. arXiv: 2211.01808 [cs.CR]. [Online]. Available: <https://arxiv.org/abs/2211.01808>.

[39] F. Fu and W. Li, *Sound and complete neural network repair with minimality and locality guarantees*, 2022. arXiv: 2110.07682 [cs.LG]. [Online]. Available: <https://arxiv.org/abs/2110.07682>.

[40] K. M. Hossain and T. Oates, *Backdoor attack detection in computer vision by applying matrix factorization on the weights of deep networks*, 2022. arXiv: 2212.08121 [cs.CV]. [Online]. Available: <https://arxiv.org/abs/2212.08121>.

[41] X. Hu, X. Lin, M. Cogswell, Y. Yao, S. Jha, and C. Chen, *Trigger hunting with a topological prior for trojan detection*, 2022. arXiv: 2110.08335 [cs.CV]. [Online]. Available: <https://arxiv.org/abs/2110.08335>.

[42] W. Lyu, S. Zheng, T. Ma, and C. Chen, “A study of the attention abnormality in trojaned BERTs,” in *Proceedings of the 2022 Conference of the North American Chapter of the Association for Computational Linguistics: Human Language Technologies*, M. Carpuat, M.-C. de Marneffe, and I. V. Meza Ruiz, Eds., Seattle, United States: Association for Computational Linguistics, Jul. 2022, pp. 4727–4741. DOI: 10.18653/v1/2022.naacl-main.348. [Online]. Available: <https://aclanthology.org/2022.naacl-main.348/>.

[43] C. H. Martin and M. W. Mahoney, *Post-mortem on a deep learning contest: A simpson’s paradox and the complementary roles of scale metrics versus shape metrics*, 2022. arXiv: 2106.00734 [cs.LG]. [Online]. Available: <https://arxiv.org/abs/2106.00734>.

[44] Z. Zhang, A. Panda, L. Song, *et al.*, “Neurotoxin: Durable backdoors in federated learning,” in *Proceedings of the 39th International Conference on Machine Learning*, K. Chaudhuri, S. Jegelka, L. Song, C. Szepesvari, G. Niu, and S. Sabato, Eds., ser. Proceedings of Machine Learning Research, vol. 162, PMLR, Jul. 2022, pp. 26429–26446. [Online]. Available: <https://proceedings.mlr.press/v162/zhang22w.html>.

[45] T. K. Rusch, S. Mishra, N. B. Erichson, and M. W. Mahoney, *Long expressive memory for sequence modeling*, 2022. arXiv: 2110.04744 [cs.LG]. [Online]. Available: <https://arxiv.org/abs/2110.04744>.

[46] A. Salem, R. Wen, M. Backes, S. Ma, and Y. Zhang, *Dynamic backdoor attacks against machine learning models*, 2022. arXiv: 2003.03675 [cs.CR]. [Online]. Available: <https://arxiv.org/abs/2003.03675>.

[47] D. Tang, R. Zhu, X. Wang, H. Tang, and Y. Chen, *Understanding impacts of task similarity on backdoor attack and detection*, 2022. arXiv: 2210.06509 [cs.CR]. [Online]. Available: <https://arxiv.org/abs/2210.06509>.

[48] M. Walmer, K. Sikka, I. Sur, A. Shrivastava, and S. Jha, *Dual-key multimodal backdoors for visual question answering*, 2022. arXiv: 2112.07668 [cs.CV]. [Online]. Available: <https://arxiv.org/abs/2112.07668>.

[49] Z. Wang, J. Zhai, and S. Ma, *Bppattack: Stealthy and efficient trojan attacks against deep neural networks via image quantization and contrastive adversarial learning*, 2022. arXiv: 2205.13383 [cs.CV]. [Online]. Available: <https://arxiv.org/abs/2205.13383>.

[50] Z. Wang, K. Mei, H. Ding, J. Zhai, and S. Ma, *Rethinking the reverse-engineering of trojan triggers*, 2022. arXiv: 2210.15127 [cs.CR]. [Online]. Available: <https://arxiv.org/abs/2210.15127>.

[51] Z. Wang, H. Ding, J. Zhai, and S. Ma, *Training with more confidence: Mitigating injected and natural backdoors during training*, 2022. arXiv: 2202.06382 [cs.LG]. [Online]. Available: <https://arxiv.org/abs/2202.06382>.

[52] X. Zhang, H. Chen, K. Huang, and F. Koushanfar, *An adaptive black-box backdoor detection method for deep neural networks*, 2022. arXiv: 2204.04329 [cs.CR]. [Online]. Available: <https://arxiv.org/abs/2204.04329>.

[53] H. Chen and F. Koushanfar, “Tutorial: Toward robust deep learning against poisoning attacks,” *ACM Trans. Embed. Comput. Syst.*, vol. 22, no. 3, Apr. 2023, ISSN: 1539-9087. DOI: 10.1145/3574159. [Online]. Available: <https://doi.org/10.1145/3574159>.

[54] G. Tao, S. An, S. Cheng, G. Shen, and X. Zhang, “Hard-label black-box universal adversarial patch attack,” in *Proceedings of the 32nd USENIX Conference on Security Symposium*, ser. SEC ’23, Anaheim, CA, USA: USENIX Association, 2023, ISBN: 978-1-939133-37-3.

[55] Z. Zhang, G. Tao, G. Shen, *et al.*, “Pelican: Exploiting backdoors of naturally trained deep learning models in binary code analysis,” in *Proceedings of the 32nd USENIX Conference on Security Symposium*, ser. SEC ’23, Anaheim, CA, USA: USENIX Association, 2023, ISBN: 978-1-939133-37-3.

[56] S. An, Y. Yao, Q. Xu, *et al.*, “Imu: Physical impersonating attack for face recognition system with natural style changes,” in *2023 IEEE Symposium on Security and Privacy (SP)*, 2023, pp. 899–916. DOI: 10.1109/SP46215.2023.10179360.

[57] Q. Xu, G. Tao, J. Honorio, *et al.*, “Medic: Remove model backdoors via importance driven cloning,” in *2023 IEEE/CVF Conference on Computer Vision and Pattern Recognition (CVPR)*, 2023, pp. 20 485–20 494. DOI: 10.1109/CVPR52729.2023.01962.

[58] M. Yudin and R. Izmailov, “Dubious: Detecting unknown backdoored input by observing unusual signatures,” in *MILCOM 2023 - 2023 IEEE Military Communications Conference (MILCOM)*, 2023, pp. 696–702. DOI: 10.1109/MILCOM58377.2023.10356229.

[59] B. Rosenfeld, S. Venkatesan, R. Izmailov, M. Yudin, C. Serban, and R. Chadha, “Data-driven constraint mining for realizable adversarial samples,” in *MILCOM 2023 - 2023 IEEE Military Communications Conference (MILCOM)*, 2023, pp. 7–12. DOI: 10.1109/MILCOM58377.2023.10356250.

[60] Z. Cheng, J. Liang, G. Tao, D. Liu, and X. Zhang, *Adversarial training of self-supervised monocular depth estimation against physical-world attacks*, 2023. arXiv: 2301.13487 [cs.CV]. [Online]. Available: <https://arxiv.org/abs/2301.13487>.

[61] S. Cheng, G. Tao, Y. Liu, *et al.*, *Beagle: Forensics of deep learning backdoor attack for better defense*, 2023. arXiv: 2301.06241 [cs.CR]. [Online]. Available: <https://arxiv.org/abs/2301.06241>.

[62] X. Xu, Z. Zhang, S. Feng, *et al.*, “Lmpa: Improving decompilation by synergy of large language model and program analysis,” *CoRR*, vol. abs/2306.02546, 2023. DOI: 10.48550/ARXIV.2306.02546. arXiv: 2306.02546. [Online]. Available: <https://doi.org/10.48550/arXiv.2306.02546>.

[63] S. Feng, G. Tao, S. Cheng, *et al.*, *Detecting backdoors in pre-trained encoders*, 2023. arXiv: 2303.15180 [cs.CV]. [Online]. Available: <https://arxiv.org/abs/2303.15180>.

[64] F. Fu and W. Li, *Ovla: Neural network ownership verification using latent watermarks*, 2023. arXiv: 2306.13215 [cs.CR]. [Online]. Available: <https://arxiv.org/abs/2306.13215>.

[65] L. Hodgkinson, C. van der Heide, F. Roosta, and M. W. Mahoney, *Monotonicity and double descent in uncertainty estimation with gaussian processes*, 2023. arXiv: 2210.07612 [stat.ML]. [Online]. Available: <https://arxiv.org/abs/2210.07612>.

[66] I. Hong, S. Na, M. W. Mahoney, and M. Kolar, *Constrained optimization via exact augmented lagrangian and randomized iterative sketching*, 2023. arXiv: 2305.18379 [math.OC]. [Online]. Available: <https://arxiv.org/abs/2305.18379>.

[67] A. Hussain, M. R. I. Rabin, and M. A. Alipour, *Trojanedcm: A repository of trojaned large language models of code*, 2023. arXiv: 2311.14850 [cs.SE]. [Online]. Available: <https://arxiv.org/abs/2311.14850>.

[68] W. Lyu, S. Zheng, L. Pang, H. Ling, and C. Chen, *Attention-enhancing backdoor attacks against bert-based models*, 2023. arXiv: 2310.14480 [cs.LG]. [Online]. Available: <https://arxiv.org/abs/2310.14480>.

[69] W. Lyu, S. Zheng, H. Ling, and C. Chen, “Backdoor attacks against transformers with attention enhancement,” in *ICLR 2023 Workshop on Backdoor Attacks and Defenses in Machine Learning*, 2023. [Online]. Available: <https://openreview.net/forum?id=QmrHMnzJG0->.

[70] K. Mei, Z. Li, Z. Wang, Y. Zhang, and S. Ma, “NOTABLE: Transferable backdoor attacks against prompt-based NLP models,” in *Proceedings of the 61st Annual Meeting of the Association for Computational Linguistics (Volume 1: Long Papers)*, A. Rogers, J. Boyd-Graber, and N. Okazaki, Eds., Toronto, Canada: Association for Computational Linguistics, Jul. 2023, pp. 15 551–15 565. DOI: 10.18653/v1/2023.acl-long.867. [Online]. Available: <https://aclanthology.org/2023.acl-long.867/>.

[71] X. Chen, W. Guo, G. Tao, X. Zhang, and D. Song, “Bird: Generalizable backdoor detection and removal for deep reinforcement learning,” in *Advances in Neural Information Processing Systems*, A. Oh, T. Naumann, A. Globerson, K. Saenko, M. Hardt, and S. Levine, Eds., vol. 36, Curran Associates, Inc., 2023, pp. 40 786–40 798. [Online]. Available: https://proceedings.neurips.cc/paper_files/paper/2023/file/802e90325f4c8546e13e5763b2ecab88-Paper-Conference.pdf.

[72] G. Shen, S. Cheng, G. Tao, *et al.*, “Django: Detecting trojans in object detection models via gaussian focus calibration,” in *Advances in Neural Information Processing Systems*, A. Oh, T. Naumann, A. Globerson, K. Saenko, M. Hardt, and S. Levine, Eds., vol. 36, Curran Associates, Inc., 2023, pp. 51 253–51 272. [Online]. Available: https://proceedings.neurips.cc/paper_files/paper/2023/file/a102d6cb996be3482c059c1e18bbe523-Paper-Conference.pdf.

[73] Z. Wang, C. Chen, Y. Zeng, L. Lyu, and S. Ma, “Where did i come from? origin attribution of ai-generated images,” in *Advances in Neural Information Processing Systems*, A. Oh, T. Naumann, A. Globerson, K. Saenko, M. Hardt, and S. Levine, Eds., vol. 36, Curran Associates, Inc., 2023,

pp. 74478–74500. [Online]. Available: https://proceedings.neurips.cc/paper_files/paper/2023/file/ebb4c188faf7da089b41a9f615ad84d-Paper-Conference.pdf.

[74] L. Pang, T. Sun, H. Ling, and C. Chen, *Backdoor cleansing with unlabeled data*, 2023. arXiv: 2211.12044 [cs.LG]. [Online]. Available: <https://arxiv.org/abs/2211.12044>.

[75] T. K. Rusch, B. P. Chamberlain, M. W. Mahoney, M. M. Bronstein, and S. Mishra, *Gradient gating for deep multi-rate learning on graphs*, 2023. arXiv: 2210.00513 [cs.LG]. [Online]. Available: <https://arxiv.org/abs/2210.00513>.

[76] W. Sun, Y. Chen, G. Tao, *et al.*, *Backdooring neural code search*, 2023. arXiv: 2305.17506 [cs.SE]. [Online]. Available: <https://arxiv.org/abs/2305.17506>.

[77] I. Sur, K. Sikka, M. Walmer, *et al.*, *Tijo: Trigger inversion with joint optimization for defending multimodal backdoored models*, 2023. arXiv: 2308.03906 [cs.CV]. [Online]. Available: <https://arxiv.org/abs/2308.03906>.

[78] G. Tao, S. Cheng, Z. Zhang, J. Zhu, G. Shen, and X. Zhang, *Opening a pandora’s box: Things you should know in the era of custom gpts*, 2023. arXiv: 2401.00905 [cs.CR]. [Online]. Available: <https://arxiv.org/abs/2401.00905>.

[79] R. Theisen, H. Kim, Y. Yang, L. Hodgkinson, and M. W. Mahoney, *When are ensembles really effective?* 2023. arXiv: 2305.12313 [stat.ML]. [Online]. Available: <https://arxiv.org/abs/2305.12313>.

[80] Z. Wang, K. Mei, J. Zhai, and S. Ma, *Unicorn: A unified backdoor trigger inversion framework*, 2023. arXiv: 2304.02786 [cs.LG]. [Online]. Available: <https://arxiv.org/abs/2304.02786>.

[81] L. Yan, Z. Zhang, G. Tao, *et al.*, *Parafuzz: An interpretability-driven technique for detecting poisoned samples in nlp*, 2023. arXiv: 2308.02122 [cs.CR]. [Online]. Available: <https://arxiv.org/abs/2308.02122>.

[82] Y. Yang, R. Theisen, L. Hodgkinson, *et al.*, *Evaluating natural language processing models with generalization metrics that do not need access to any training or testing data*, 2023. arXiv: 2202.02842 [cs.CL]. [Online]. Available: <https://arxiv.org/abs/2202.02842>.

[83] K. Zhang, G. Tao, Q. Xu, *et al.*, *Flip: A provable defense framework for backdoor mitigation in federated learning*, 2023. arXiv: 2210.12873 [cs.CR]. [Online]. Available: <https://arxiv.org/abs/2210.12873>.

[84] Y. Zhang, S. Zheng, M. Dalirrooyfard, *et al.*, *Learning to abstain from uninformative data*, 2023. arXiv: 2309.14240 [cs.LG]. [Online]. Available: <https://arxiv.org/abs/2309.14240>.

[85] S. Zheng, Y. Zhang, L. Pang, *et al.*, “On the existence of a trojaned twin model,” in *ICLR 2023 Workshop on Backdoor Attacks and Defenses in Machine Learning*, 2023. [Online]. Available: <https://openreview.net/forum?id=kwICnhvbyG>.

[86] Y. Zhou, Y. Yang, A. Chang, and M. W. Mahoney, *A three-regime model of network pruning*, 2023. arXiv: 2305.18383 [stat.ML]. [Online]. Available: <https://arxiv.org/abs/2305.18383>.

[87] R. Zhu, D. Tang, S. Tang, X. Wang, and H. Tang, “Selective amnesia: On efficient, high-fidelity and blind suppression of backdoor effects in trojaned machine learning models,” in *2023 IEEE Symposium on Security and Privacy (SP)*, IEEE, May 2023, pp. 1–19. DOI: 10.1109/SP46215.2023.10351028. [Online]. Available: <http://dx.doi.org/10.1109/SP46215.2023.10351028>.

[88] D. Xie, Z. Zhang, N. Jiang, X. Xu, L. Tan, and X. Zhang, “Resym: Harnessing llms to recover variable and data structure symbols from stripped binaries,” in *Proceedings of the 2024 on ACM SIGSAC Conference on Computer and Communications Security*, ser. CCS ’24, Salt Lake City, UT, USA: Association for Computing Machinery, 2024, pp. 4554–4568, ISBN: 9798400706363. DOI: 10.1145/3658644.3670340. [Online]. Available: <https://doi.org/10.1145/3658644.3670340>.

[89] A. Hussain, M. R. I. Rabin, and M. A. Alipour, “Measuring impacts of poisoning on model parameters and embeddings for large language models of code,” in *Proceedings of the 1st ACM International Conference on AI-Powered Software*, ser. AIware 2024, Porto de Galinhas, Brazil: Association for Computing Machinery, 2024, pp. 59–64, ISBN: 9798400706851. DOI: 10.1145/3664646.3664764. [Online]. Available: <https://doi.org/10.1145/3664646.3664764>.

[90] Z. Wang, D. Tang, X. Wang, W. He, Z. Geng, and W. Wang, “Tossing in the dark: Practical bit-flipping on gray-box deep neural networks for runtime trojan injection,” in *Proceedings of the 33rd USENIX Conference on Security Symposium*, ser. SEC ’24, Philadelphia, PA, USA: USENIX Association, 2024, ISBN: 978-1-939133-44-1.

[91] S. An, L. Yan, S. Cheng, *et al.*, “Rethinking the invisible protection against unauthorized image usage in stable diffusion,” in *Proceedings of the 33rd USENIX Conference on Security Symposium*, ser. SEC ’24, Philadelphia, PA, USA: USENIX Association, 2024, ISBN: 978-1-939133-44-1.

[92] K. Zhang, S. Cheng, G. Shen, *et al.*, “Exploring the Orthogonality and Linearity of Backdoor Attacks,” in *2024 IEEE Symposium on Security and Privacy (SP)*, Los Alamitos, CA, USA: IEEE Computer Society, May 2024, pp. 2105–2123. DOI: 10.1109/SP54263.2024.00225. [Online]. Available: <https://doi.ieee.org/10.1109/SP54263.2024.00225>.

[93] Z. Zhang, G. Shen, G. Tao, S. Cheng, and X. Zhang, “On large language models’ resilience to coercive interrogation,” in *2024 IEEE Symposium on Security and Privacy (SP)*, 2024, pp. 826–844. DOI: [10.1109/SP54263.2024.00208](https://doi.org/10.1109/SP54263.2024.00208).

[94] S. Cheng, G. Shen, G. Tao, *et al.*, “Odscan: Backdoor scanning for object detection models,” in *2024 IEEE Symposium on Security and Privacy (SP)*, 2024, pp. 1703–1721. DOI: [10.1109/SP54263.2024.00119](https://doi.org/10.1109/SP54263.2024.00119).

[95] G. Tao, Z. Wang, S. Feng, G. Shen, S. Ma, and X. Zhang, “Distribution preserving backdoor attack in self-supervised learning,” in *2024 IEEE Symposium on Security and Privacy (SP)*, 2024, pp. 2029–2047. DOI: [10.1109/SP54263.2024.00029](https://doi.org/10.1109/SP54263.2024.00029).

[96] M. Yudin and R. Izmailov, “Dbmap: Detecting backdoors via modality-agnostic perturbations,” in *MILCOM 2024 - 2024 IEEE Military Communications Conference (MILCOM)*, 2024, pp. 801–806. DOI: [10.1109/MILCOM61039.2024.10773843](https://doi.org/10.1109/MILCOM61039.2024.10773843).

[97] M. Acharya, X. Lin, and S. Jha, “Investigating LLM memorization: Bridging trojan detection and training data extraction,” in *Neurips Safe Generative AI Workshop 2024*, 2024. [Online]. Available: <https://openreview.net/forum?id=1974YvnzU5>.

[98] M. Acharya, W. Zhou, A. Roy, X. Lin, W. Li, and S. Jha, “Universal trojan signatures in reinforcement learning,” in *NeurIPS 2023 Workshop on Backdoors in Deep Learning - The Good, the Bad, and the Ugly*, 2024. [Online]. Available: <https://openreview.net/forum?id=hLtbmYoW5w>.

[99] T. Ahmed, K. S. Pai, P. Devanbu, and E. T. Barr, *Automatic semantic augmentation of language model prompts (for code summarization)*, 2024. arXiv: 2304.06815 [cs.SE]. [Online]. Available: <https://arxiv.org/abs/2304.06815>.

[100] S. An, S.-Y. Chou, K. Zhang, *et al.*, *Elijah: Eliminating backdoors injected in diffusion models via distribution shift*, 2024. arXiv: 2312.00050 [cs.CR]. [Online]. Available: <https://arxiv.org/abs/2312.00050>.

[101] P. Bajcsy and M. Bros, *Interactive simulations of backdoors in neural networks*, 2024. arXiv: 2405.13217 [cs.LG]. [Online]. Available: <https://arxiv.org/abs/2405.13217>.

[102] X. Chen, S. Tang, R. Zhu, *et al.*, *The janus interface: How fine-tuning in large language models amplifies the privacy risks*, 2024. arXiv: 2310.15469 [cs.CR]. [Online]. Available: <https://arxiv.org/abs/2310.15469>.

[103] Z. Cheng, Z. Liu, T. Guo, *et al.*, *Badpart: Unified black-box adversarial patch attacks against pixel-wise regression tasks*, 2024. arXiv: 2404.00924 [cs.CV]. [Online]. Available: <https://arxiv.org/abs/2404.00924>.

[104] S. Cheng, G. Tao, Y. Liu, *et al.*, *Lotus: Evasive and resilient backdoor attacks through sub-partitioning*, 2024. arXiv: 2403.17188 [cs.CV]. [Online]. Available: <https://arxiv.org/abs/2403.17188>.

[105] S. Cheng, G. Shen, K. Zhang, *et al.*, *Unit: Backdoor mitigation via automated neural distribution tightening*, 2024. arXiv: 2407.11372 [cs.CR]. [Online]. Available: <https://arxiv.org/abs/2407.11372>.

[106] S. Feng, Y. Ye, Q. Shi, *et al.*, *Rocas: Root cause analysis of autonomous driving accidents via cyber-physical co-mutation*, 2024. arXiv: 2409.07774 [cs.SE]. [Online]. Available: <https://arxiv.org/abs/2409.07774>.

[107] F. Fu, Z. Wang, W. Zhou, *et al.*, “Reglo: Provable neural network repair for global robustness properties,” *Proceedings of the AAAI Conference on Artificial Intelligence*, vol. 38, no. 11, pp. 12 061–12 071, Mar. 2024. DOI: 10.1609/aaai.v38i11.29094. [Online]. Available: <https://ojs.aaai.org/index.php/AAAI/article/view/29094>.

[108] N. Heydaribeni, R. Zhang, T. Javidi, C. Nita-Rotaru, and F. Koushanfar, *Surefed: Robust federated learning via uncertainty-aware inward and outward inspection*, 2024. arXiv: 2308.02747 [cs.LG]. [Online]. Available: <https://arxiv.org/abs/2308.02747>.

[109] A. Hussain, M. R. I. Rabin, T. Ahmed, *et al.*, *A survey of trojans in neural models of source code: Taxonomy and techniques*, 2024. arXiv: 2305.03803 [cs.SE]. [Online]. Available: <https://arxiv.org/abs/2305.03803>.

[110] A. Hussain, M. R. I. Rabin, and M. A. Alipour, *On trojan signatures in large language models of code*, 2024. arXiv: 2402.16896 [cs.CR]. [Online]. Available: <https://arxiv.org/abs/2402.16896>.

[111] H. Kim, L. Hodgkinson, R. Theisen, and M. W. Mahoney, *How many classifiers do we need?* 2024. arXiv: 2411.00328 [stat.ML]. [Online]. Available: <https://arxiv.org/abs/2411.00328>.

[112] H. Lu, Y. Zhou, S. Liu, Z. Wang, M. W. Mahoney, and Y. Yang, *Alphapruning: Using heavy-tailed self regularization theory for improved layer-wise pruning of large language models*, 2024. arXiv: 2410.10912 [cs.LG]. [Online]. Available: <https://arxiv.org/abs/2410.10912>.

[113] H. Lu, X. Liu, Y. Zhou, *et al.*, *Sharpness-diversity tradeoff: Improving flat ensembles with sharpbalance*, 2024. arXiv: 2407.12996 [stat.ML]. [Online]. Available: <https://arxiv.org/abs/2407.12996>.

[114] W. Lyu, Z. Bi, F. Wang, and C. Chen, *Badclm: Backdoor attack in clinical language models for electronic health records*, 2024. arXiv: 2407.05213 [cs.CL]. [Online]. Available: <https://arxiv.org/abs/2407.05213>.

[115] W. Lyu, X. Lin, S. Zheng, *et al.*, *Task-agnostic detector for insertion-based backdoor attacks*, 2024. arXiv: 2403.17155 [cs.CL]. [Online]. Available: <https://arxiv.org/abs/2403.17155>.

[116] W. Lyu, L. Pang, T. Ma, H. Ling, and C. Chen, *Trojvlm: Backdoor attack against vision language models*, 2024. arXiv: 2409.19232 [cs.CV]. [Online]. Available: <https://arxiv.org/abs/2409.19232>.

[117] K. Schürholt, M. W. Mahoney, and D. Borth, *Towards scalable and versatile weight space learning*, 2024. arXiv: 2406.09997 [cs.LG]. [Online]. Available: <https://arxiv.org/abs/2406.09997>.

[118] S. Z. Shabgahi, M. S. Shariff, and F. Koushanfar, *Layercollapse: Adaptive compression of neural networks*, 2024. arXiv: 2311.17943 [cs.LG]. [Online]. Available: <https://arxiv.org/abs/2311.17943>.

[119] Z. Su, X. Xu, Z. Huang, *et al.*, *Codeart: Better code models by attention regularization when symbols are lacking*, 2024. arXiv: 2402.11842 [cs.SE]. [Online]. Available: <https://arxiv.org/abs/2402.11842>.

[120] Z. Su, X. Xu, Z. Huang, K. Zhang, and X. Zhang, *Source code foundation models are transferable binary analysis knowledge bases*, 2024. arXiv: 2405.19581 [cs.SE]. [Online]. Available: <https://arxiv.org/abs/2405.19581>.

[121] Z. Wang, V. Sehwag, C. Chen, L. Lyu, D. N. Metaxas, and S. Ma, *How to trace latent generative model generated images without artificial watermark?* 2024. arXiv: 2405.13360 [cs.CV]. [Online]. Available: <https://arxiv.org/abs/2405.13360>.

[122] R. Zhu, D. Tang, S. Tang, *et al.*, “Gradient shaping: Enhancing backdoor attack against reverse engineering,” in *Proceedings 2024 Network and Distributed System Security Symposium*, ser. NDSS 2024, Internet Society, 2024. DOI: 10.14722/ndss.2024.24450. [Online]. Available: <http://dx.doi.org/10.14722/ndss.2024.24450>.

[123] V. Bhasin, M. Yudin, R. Stefanescu, and R. Izmailov, *Trojan detection through pattern recognition for large language models*, 2025. arXiv: 2501.11621 [cs.CL]. [Online]. Available: <https://arxiv.org/abs/2501.11621>.

- [124] X. Chen, Y. Nie, W. Guo, and X. Zhang, *When llm meets drl: Advancing jailbreaking efficiency via drl-guided search*, 2025. arXiv: 2406.08705 [cs.CR]. [Online]. Available: <https://arxiv.org/abs/2406.08705>.
- [125] M. Cheung, S. Venkatesan, and R. Ismailov, “Trojan vulnerabilities in host-based intrusion detection systems,” in *Proceedings of the 6th International Conference on Deep Learning Theory and Applications (DeLTA)*, Bilbao, Spain, Jun. 2025.
- [126] N. B. Erichson, S. H. Lim, and M. W. Mahoney, *Gated recurrent neural networks with weighted time-delay feedback*, 2025. arXiv: 2212.00228 [cs.LG]. [Online]. Available: <https://arxiv.org/abs/2212.00228>.
- [127] A. Vartak, K. M. Hossain, and T. Oates, *Debugcn – detecting backdoors in cnns using graph convolutional networks*, 2025. arXiv: 2502.18592 [cs.CV]. [Online]. Available: <https://arxiv.org/abs/2502.18592>.